

Advanced Functional Porous Materials and their Hybrid Composites for Energy-Efficient Chemical Separation Application

विद्या वाचस्पति की
उपाधि की अपेक्षाओं की आंशिक पूर्ति में प्रस्तुत शोध प्रबंध

A thesis submitted in partial fulfillment of the requirements of the degree of

Doctor of Philosophy

द्वारा / By

सहेल फजल / Sahel Fajal

पंजीकरण सं. / Registration No.: 20173525

शोध प्रबंध पर्यवेक्षक : प्रो. सुजीत के. घोष

Thesis Supervisor: Prof. Sujit K. Ghosh



भारतीय विज्ञान शिक्षा एवं अनुसंधान संस्थान पुणे
INDIAN INSTITUTE OF SCIENCE EDUCATION AND RESEARCH PUNE

2023

Dedicated to

Maa and Abba (My Parents)

भारतीय विज्ञान शिक्षा एवं अनुसंधान संस्थान पुणे
INDIAN INSTITUTE OF SCIENCE EDUCATION AND RESEARCH PUNE

डॉ. होमी भाभा मार्ग, पुणे 411008, महाराष्ट्र, भारत | Dr. Homi Bhabha Road, Pune 411008, Maharashtra, India
T +91 20 2590 8001 W www.iiserpune.ac.in



Certificate

It is hereby certified that the work described in this thesis entitled "*Advanced Functional Porous Materials and their Hybrid Composites for Energy-Efficient Chemical Separation Application*" submitted by *Mr. Sahel Fajal* was carried out by the candidate, under my supervision. The work presented here or any part of it has not been included in any other thesis submitted previously for the award of any degree or diploma from any other university or institution.

Date: 8/12/2023

A handwritten signature in blue ink, appearing to be "Sujit K. Ghosh".

Prof. Sujit K. Ghosh

Research Supervisor

Email: sghosh@iiserpune.ac.in

Contact No.: +91(20)25908076

भारतीय विज्ञान शिक्षा एवं अनुसंधान संस्थान पुणे
INDIAN INSTITUTE OF SCIENCE EDUCATION AND RESEARCH PUNE

डॉ. होमी भाभा मार्ग, पुणे 411008, महाराष्ट्र, भारत | Dr. Homi Bhabha Road, Pune 411008, Maharashtra, India
T +91 20 2590 8001 W www.iiserpune.ac.in



Declaration

I declare that this written submission represents my ideas in my own words and wherever other's ideas have been included; I have adequately cited and referenced the original sources. I also declare that I have adhered to all principles of academic honesty and integrity and have not misrepresented or fabricated or falsified any idea/ data/ fact/ source in my submission. I understand that violation of the above will cause for disciplinary action by the institute and can evoke penal action from the sources which have thus not been properly cited or from whom proper permission has not been taken when needed.

Date: 08th-Dec.-2023

Sahel Fajal
Sahel Fajal

Reg. Id: 20173525

Acknowledgement

At the very outset, I would like to take the opportunity to convey my deepest gratitude to my research supervisor **Prof. Sujit K. Ghosh** for his continuous support and motivation throughout my PhD tenure. I feel his illimitable encouragement has propelled my research in forward direction. It has been an immense privilege for me to work under his supervision. I believe that his inspiring guidance has helped me to design and execute different rational research projects successfully. Thank you very much Sir for all your diligent efforts, trust in me and most importantly for being such a wonderful guide.

I sincerely acknowledge both the former directors of Indian Institute of Science Education and Research (IISER) Pune, Prof. K. N. Ganesh and Prof. J. B. Udgaonkar, and the current director Prof. S. S. Bhagwat for providing world-class facilities and having a vibrant research environment. I am also extremely thankful to my research advisory committee (RAC) members, **Prof. Bhagavatula LV Prasad** (Director of the Centre for Nano and Soft Matter Sciences (CeNS), Bangalore), **Prof. Nirmalya Ballav** (Professor and Chair, Chemistry; Associate Dean (Research and Development) Chemistry, IISER Pune) for their valuable suggestions, advices and support during the annual RAC meetings. I am grateful to Prof. Nirmalya Ballav (Chair, Chemistry Department) and all other faculty members of the department of chemistry for being approachable for any help and maintaining such research friendly healthy environment in the department. I sincerely thank all the collaborators - especially Dr. Mandar M. Shirolkar (University of Technology of China), Dr. Neeladri Das (Indian Institute of Technology, Patna), Dr. Arun Torris (National Chemical Laboratory, Pune), who assisted me in completion of different projects.

It has been a great privilege for me to be a part of the 'Microporous Materials Lab' and I am extremely grateful to the all-past and present members of the team. I would like to thank all the lovable and dear members of the team: the alumni (Dr. Sanjog Nagarkar, Dr. Biplab Joarder, Dr. Biplab Manna, Dr. Soumya Mukherjee, Dr. Avishek Karmakar, Dr. Tarak Nath Mandal, Dr. Aamod V. Desai, Dr. Partha Samanta, Dr. Samraj Mollick, Dr. Shivani Sharma, Dr. Yogeshwar D. More, Dr. Arunabha Sen, Dr. Subhajit Dutta, Dr. Sumanta Let, Dr. Debanjan Mahato, Satyam Saurabh, among many), and the present team (Writakshi Mandal, Gourab Kumar Dam, Dipanjan

Majumder, Kishalay Biswas, Anirban Roy, Dipayan Ghosh, to name a few). Thank you very much all for your significant contribution, help and providing friendly environment in the lab. My sincere thanks go out for all my seniors: Soumya da, Avishek da, Tarak da, Aamod da, Partha da and Samraj da, for your guidance, support and valuable suggestions. Series of long discussion sessions and fun-filled sharing of individual work-experiences combined with assimilation of individual ideas has helped me a lot to expand the horizon of scientific knowledge and have inculcated the ideology to work as an integral team member, and to even rise as a team leader at a few occasions. I would to mention that it was an immense pleasure to work with all of you and I feel I have learnt many things from you people. Of them, I have worked most of the time with Samraj da, Tarak da, Aamod da, Partha da: thank you all for teaching me many lessons. Apart from my seniors, I would like to express my special appreciation to all my lab members, because without them this journey would not have been as exciting and memorable as it has been. I would consider myself lucky to have a batch-mate and friend like Writakshi, Sumanta Subhajit, Arunabha and Debanjan with whom I had maximum overlap in time and spent most of the time in lab. I consider it a blessing to have had Writakshi as a classmate and friend. We had many highs and lows during our long, cherished friendship, and we both encouraged the other to reach their best potential. I'd count myself lucky to have had a close relationship with Writakshi, who is a wonderful colleague and a good friend. I am appreciative of his excellent friendship, for keeping me inspired (especially for providing the driving force to write my first Angew Chem paper), and for helping with my study. I really admire their depth of understanding in different subjects (which has helped a lot during this tenure) and mesmerizing skills. I am grateful to her wonderful friendship and contributions in my researches. The innumerable experiences over the years in our esteemed lab-space has taught me to value the importance of a good work atmosphere. I would like to acknowledge the prompt and unconditional assistance from Gourab, Dipanjan, Kishalay, Anirban, Dipayan whenever required. I am especially thankful to Writakshi, Sumanta and Subhajit for their invaluable support during the last phase of my PhD. A number of special friends, Atikur (IIT Patna), Mofizur (IGCAR), Javed (IISER Pune), Samim (IIT-ISM Dhanbad): all of them have been special in their individual ways. I would like to express my heartfelt thanks to Ma'am (Dr. Sudarshana Mukherjee) for her friendly advises.

Throughout these five years, no matter the circumstance, two people have consistently stood by my side. They are the ones who were geographically the most distant ones. As a single child, I was unable to do any duty to help my aging parents (Maa and Abbu), who have strongly supported my education, like no one else. I have relied on my parents' support and encouragement throughout the challenging times as my lone savior, and I honestly feel that without them, I would not have been able to complete the few steps I have taken to advance in my job. Tiny footsteps have been taken to move ahead in my career.

I would like to convey my deepest regards towards my old school and university teachers who have encouraged me throughout different stages of life. I am also very much thankful to Dr. Aminul Islam (Aligarh Muslim University, India) for inspired me to pursue a PhD degree. I would like to express my sincere regards towards all the faculty members (especially, Prof. Mohd. Akram, Dr. M. Shahid and Dr. Md. Musawwer Khan) of Aligarh Muslim University (AMU), India, for their lessons and support during my Bachelor and Masters study. I am also thankful to Prof. M. Shakir (AMU, India) for providing me the opportunity to carry out my Masters project in his lab. For the smooth progress in a long course, the support of technical and administrative staff is equally important. I thank Dr. Umesha reddy Kacherki and Anuradha for library support, technical staff of IISER Pune – Mr. Parveen Nasa, Ms. Archana, Mr. Mahesh Jadhav, Mr. Nilesh Dumbre, Mr. Anil, Mr. Yatish, Mr. Ganesh Dimbar, Mr. Sandeep Kanade, Mr. Nitin, Ms. Megha, Mr. Sandeep and administrative staff – Mr. Mayuresh, Ms. Nayana, Mr. Tushar, Ms. Vrushali, Mr. Suresh, Mr. Prabhas, Ms. Priyadarshani for their prompt assistance at multiple occasions.

I acknowledge Department of Science and Technology (DST) Inspire, India for providing me fellowship. I would also like to thank John Wiley & Sons (Wiley-VCH), American Chemical Society (ACS), Royal Society of Chemistry (RSC), Nature Publishing Group (NPG), Elsevier for publishing a number of my research and review articles that I managed to publish in my PhD tenure. I would also like to thank the 5th European Conference on Metal Organic Frameworks and Porous Polymers(EuroMOF2023) at Granada, Spain (24-27, September, 2023) for inviting me to present my work in the form of a poster and in parallel, SERB-ITS (DST-India) for generously providing me the requisite travel grant to attend the same. A number of conference organizers including MTIC, CRSI, SESTEC, BRNS, SPSI-Macro, etc. have provided me many opportunities to present

my research works in the form of oral presentations and poster formats, which have definitively given me a lot of confidence to rely upon my own caliber. IISER Pune and its director has always remained supportive of such participations, which had further supported my cause, each time I approached.

I wish to thank all my friends for their support and help at different stages of my life, especially, Atikur, Mofizur, Javed, Samim, Kamruzzaman and so on.... I thank my batchmates like Writakshi, Rapti, Nilanjana, Kuddus, Sumit, Vikas, Surajit, Aman, Nitesh, Majeet to whom I could turn to for any help or suggestion without any hesitation. I thank all my batch-mates (August-2017) and Chemphilic team. I would like to acknowledge Rahi da (IISER Pune), my uncle (Mr. Jaynal Abedin) for his constant support and friendly advices, and I wish Nishad Abedin all the best for this future. I also want to acknowledge various vendors such as Mr. Krishna Ji, Mr. Godbole Ji, and others for their timely support by providing essential chemicals and other materials. I apologize in advance for not being able to take all of your names, but am sure; it would not offend you largely.

Finally, I would want to remark that even though everything wonderful has an end, the PhD experience I had at IISER Pune, which will soon come to an end, will always hold a special place in my heart. It has taught me to grow as a person unlike anything else, and I will cherish many of the moments I have experienced here. It is evident that I shall miss this location.

- Sahel Fajal

Contents

1. General Introduction on Advanced Functional Porous Materials Addressing Chemical Separation Challenges

1.1	Porous Materials: A brief account	1.2-1.3
1.2	Advanced Functional Porous Materials (AFPMs)	1.3-1.14
1.3	Hybrid Composite Porous Materials	1.14-1.17
1.4	Shaping of Advanced Functional Porous Materials (AFPMs)	1.18-1.18
1.5	Applications of Advanced Functional Porous Materials (AFPMs)	1.18-1.23
1.6	Functional Applications: Chemical Separation	1.23-1.29
1.7	Overview of the thesis-work	1.30-1.32
1.8	References	1.32-1.37

Section-A: Advanced Functional Porous Organic Materials for Separation of Toxic Gases and Water Contaminants

A1-A2

2. Unraveling Mechanistic Insights into Covalent Organic Frameworks for Highly Efficient Sequestration of Organic Iodides from Simulated Nuclear Waste

2.1	Introduction	2.2-2.5
2.2	Experimental	2.6-2.15
2.3	Results and Discussion	2.15-2.18
2.4	ROIs Sequestration Studies	2.18-2.26
2.5	Conclusion	2.26-2.27
2.6	Appendix Section	2.28-2.68
2.7	References	2.69-2.71

3. Ordered Macro/Microporous Ionic Organic Framework for Efficient Separation of Toxic Pollutants from Water

3.1	Introduction	3.2-3.4
3.2	Experimental	3.4-3.12

3.3	Results and Discussion	3.13-3.17
3.4	Capture Study	3.17-3.23
3.5	Conclusion	3.23-3.23
3.6	Appendix Section	3.24-3.64
3.7	References	3.65-3.67

Section-B: Hybrid Composite Porous Materials for Sequestration of Toxic Chemical Species from Water and Gas Phase B1-B2

4. Trap Inlaid Cationic Hybrid Composite Material for Efficient Segregation of Toxic Chemicals from Water

4.1	Introduction	4.2-4.4
4.2	Experimental	4.5-4.13
4.3	Results and Discussion	4.13-4.17
4.4	Capture Study	4.18-4.24
4.5	Conclusion	4.24-4.24
4.6	Appendix Section	4.25-4.62
4.7	References	4.63-4.66

5. Nano-snare Implanted Ultralight Crystalline Hybrid Composite Material for Multiple Cooperative Interactions Mediated Efficient Sequestration of Radioiodine

5.1	Introduction	5.2-5.5
5.2	Experimental	5.5-5.15
5.3	Results and Discussion	5.16-5.20
5.4	Iodine Sequestration Study	5.20-5.30
5.5	Conclusion	5.31-5.31
5.6	Appendix Section	5.32-5.85
5.7	References	5.86-5.88

6. Summary, Critical Comments and Perspectives 6.1-6.4

Synopsis

The fundamental objective behind the research work which are included in the thesis is to design and development of various advanced functional porous materials (AFPMs) for the separation of different toxic chemicals. In the pursuit of mitigating environmental challenges such as pollution, climate change, and resource depletion, the development of advanced functional porous materials has emerged as a promising avenue for innovative solutions. Advanced functional porous materials which represents a broad domain is majorly consists of metal-organic frameworks (MOFs), metal-organic gel (MOG), metal-organic polyhedra (MOPs), (built on metal-ligand co-ordination bond), covalent-organic frameworks (COFs), porous organic polymer (POPs), (built on covalent linkages between functional synthons), and their hybrid composites. These materials, characterized by their intricate porous structures due to diverse synthetic tunability and tailored chemical properties within the infinite architecture enabling the materials to act as functional host matrix. The pores can be designed by adding the required functional groups, which produces an exceptional host-guest supramolecular interaction. Because of these properties, these porous materials are garnering increasing attention for their ability to sequester and efficiently separate various substances from the surroundings. From greenhouse gas capture to the removal of hazardous pollutants from air and water, advanced functional porous materials have demonstrated remarkable versatility and effectiveness in addressing pressing global issues. Additionally, the versatility of AFPMs makes them invaluable tools in applications ranging from gas and solvent separation, chemical or pollutant adsorption or sequestration, gas storage, heterogeneous catalysis, small molecule recognition, electro-catalysis, batteries, supercapacitor, drug delivery etc. In this thesis work I have demonstrated how to conduct a methodical investigation to create innovative porous materials tailored for particular applications using various synthetic strategies. These newly developed AFPMs are employed as a method for the sequestration application of particular guest species that are environmentally hazardous. On the basis of the principles of ion exchange and host-guest interactions, efforts have been made to design functional porous frameworks and their hybrid composites, such as MOF/MOG, MOP, COF, etc., for the effective separation of various toxic gases (radioactive organic iodides and iodine species) and water contaminants (organic pollutants and inorganic metal-oxoanionic species).

Chapter 1. General Introduction on Advanced Functional Porous Materials Addressing Chemical Separation Challenges

In this section a brief discussion about various advanced functional porous materials (AFPMs), including MOF, MOG, MOP, COFs, POPs, and their hybrid composites towards various potential applications are

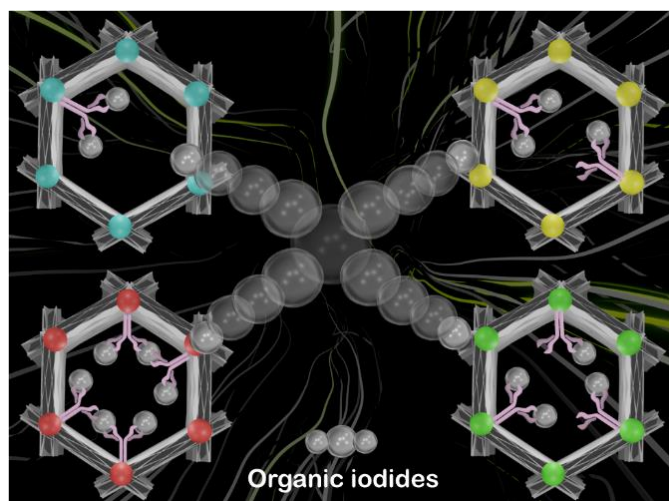
included. Definition, classification, synthetic and functionalization strategies, different properties and various applications of MOFs, MOGs, MOPs, COFs, and POPs have been discussed further. In addition to this, discussion about the macroscopic shaping of AFPMs along with synthesis and application of porous hybrid composite materials are provided. One of the key applications for porous materials is as a tool for the sequestration of different harmful gaseous species and water contaminants that support a clean environment. Environmental pollution has been defined, categorised, and traced back to a variety of noxious substances, radioactive species, and hazardous compounds. The importance, scope and limitation of current adsorption or separation techniques and sorbent materials has been discussed. Further, it has also been explored the potential for strategically designing and synthesizing a variety of functionalized advanced porous materials for the effective separation of these chemicals from both air and water. Finally, the opportunity, scope and challenges with both pros and cons of AFPMs towards real-world chemical separation application was discussed.

Section-A: Advanced Functional Porous Organic Materials for Separation of Toxic Gases and Water Contaminants

In the ongoing pursuit of addressing environmental challenges and ensuring the safety and well-being of our communities, the development of advanced functional porous organic materials such as covalent organic frameworks (COFs) and porous organic polymers (POPs) has emerged as a promising solution for the separation of toxic gases and water contaminants. This innovative field of materials science combines the versatility of porous organic frameworks with sophisticated chemical design to create tailored materials that exhibit exceptional selectivity and efficiency in capturing and removing harmful pollutants from both air and water sources. With the increasing concerns over air quality and water pollution, the quest for efficient, sustainable, and scalable separation technologies has led to the exploration of these cutting-edge materials, ushering in a new era of environmental remediation and protection. In this context, this report delves into the fascinating realm of advanced functional porous organic materials and their pivotal role in mitigating the threats posed by toxic gases (such as radioactive organic iodides) and water contaminants (such as organic pollutants and metal-based oxoanions). This section of the thesis contains two chapters i.e. chapter-2 and chapter-3. In chapter-2, a systematic investigation of optimization of structural functional sites to modulate the organic iodides capture performance has been demonstrated with a series of crystalline porous organic frameworks (COFs). Next, in chapter-3, a chemically robust macro-micro hierarchical porous positively charged viologen organic network material is fabricated and utilized for selective separation of organic and inorganic toxic pollutants from water.

Chapter 2. Optimization of Structural Functional Sites to Modulate the Radioactive Organic Iodide Capture Performance of Crystalline Porous Organic Frameworks

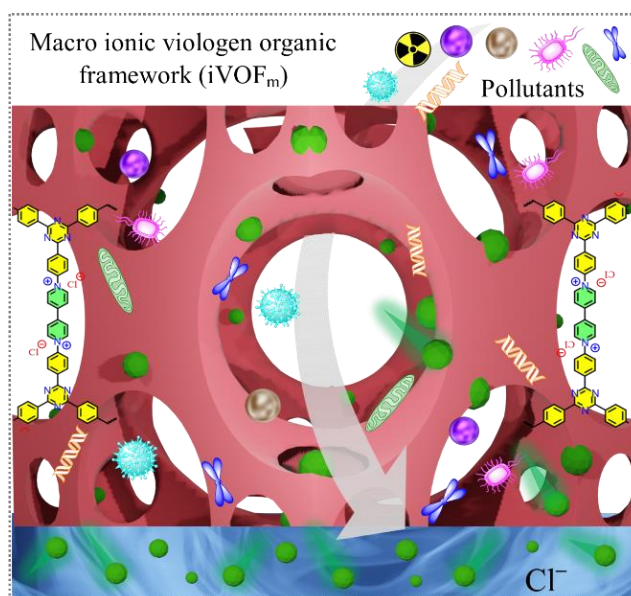
Recent decades have seen a significant advancement in nuclear energy as a substitute high power density and low-carbon energy source in light of the forthcoming global energy and environmental catastrophe. The emission of volatile radioactive chemicals such organic iodides, which must be removed before releasing the off-gas, constitutes a particular concern with nuclear reactors, though. These chemicals include methyl iodide (CH_3I) and ethyl iodide ($\text{CH}_3\text{CH}_2\text{I}$) both of which are extremely dangerous to the environment and human health. By altering the amount of N-heteroatomic sites in a series of chemically stable porous covalent organic frameworks (COF-A to D), in this work, we showed how a strategic analysis can be used to understand the significance of integrated functionalities within the frameworks in organic iodide sequestration. As a result, the porosity or surface area as well as the N-heteroatomic or heterocyclic moieties, such as the imine, pyridine, and triazine sites of these COFs, were observed to positively correlate with the CH_3I adsorption capacity. Through the N-methylation reaction mechanism, all of the COFs had substantial CH_3I sorption capabilities in both static and dynamic conditions. COF-A stood out among them for having an extremely high CH_3I adsorption capacity at 348 K in a static environment because of its large surface area and an abundance of nucleophilic groups, specifically imine functionality.



Journal of Materials Chemistry A, 2023, 11, 26580-26591.

Chapter 3. Ordered Macro/Microporous Ionic Organic Framework for Efficient Separation of Toxic Pollutants from Water

In order to gain better performance, fast mass diffusion is a crucial need for a few applications, such as segregation of pollutants by porous materials. Large open pores and easy and complete accessibility to functional recognition sites enable rapid mass movement across porous materials. In this regard, one of the most effective strategy would be to introduce macroporosity into these materials, giving access to large openpores that allow for unrestricted analyte transport and complete exposure to interaction sites. Additionally, the difficulty of combining macroporosity with ionic functioning could open up a remarkable path to an exceptional method of environmental remediation, but this avenue is still unexplored. Here, we developed an easy-to-tune synthetic technique for the fabrication of a positively charged hierarchically porous organized, interconnected macro-structure of viologen-unit grafted organic framework. Together, the organized large macropores and strong electrostatic interaction coming from the materials' ionic structure revealed highly rapid removal rates for a variety of organic and inorganic anionic hazardous contaminants from water. The enhanced removal efficiency of the compound towards guest anions was attributed to the efficient mass transport through the inter-connected ordered hierarchically porous structure of the materials, which was further experimentally established by the pH-dependent study and comparative uptake performance of meso- and nonporous identical chemical structures.



Angewandte Chemie International Edition, 2023, 62, e202214095.

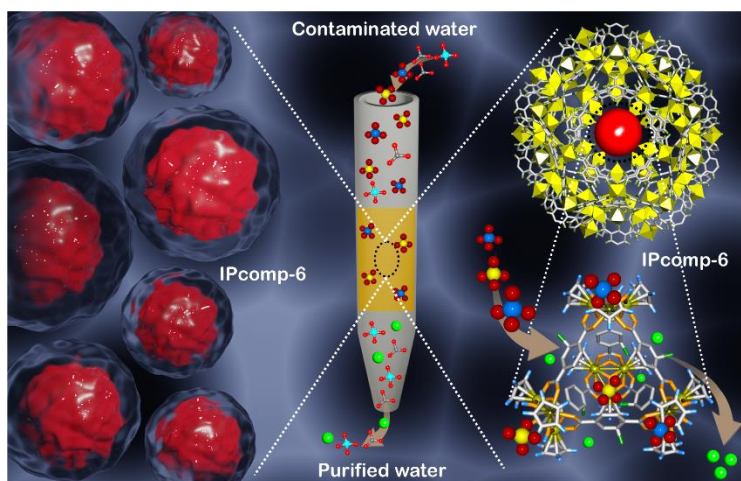
Section-B: Hybrid Composite Porous Materials for Sequestration of Toxic Water Pollutants and Radioiodine Species

The sequestration of toxic water pollutants, such as toxic heavy metal-based oxoanions and radioiodine species presents a critical challenge in the realm of environmental protection and nuclear safety. In recent years, significant strides have been made in developing advanced solutions through the integration of hybrid composite porous materials. These materials can be fabricated by combining different porous materials, in order to enhance their performance. These innovative materials represent a convergence of various functional components, including inorganic, organic, and nanoscale elements, synergistically designed to address the complex task of sequestering and immobilizing harmful waterborne contaminants and radioiodine species. As concerns about water quality and nuclear waste management intensify, the advent of these hybrid composite porous materials has become instrumental in providing efficient, reliable, and sustainable methods for sequestering pollutants that pose serious threats to both public health and the environment. This report delves into the captivating realm of hybrid composite porous materials, exploring their role as a transformative pathway in the sequestration of toxic water pollutants and radioiodine species, thereby advancing our capabilities in safeguarding our water resources and managing nuclear hazards. This section of the thesis contains two chapters i.e. chapter-4 and chapter-5. In chapter-4, efficient and selective removal of a group of toxic metal-based oxoanions from contaminated natural ground water and simulated industrial waste water system has been demonstrated by developing a metal-organic polyhedra incorporated metal-organic gel-based cationic hybrid composite material. Thereafter, in chapter-5, another hybrid composite material has been fabricated by covalently threading an amino functional metal-organic polyhedra with a covalent organic framework for effectively and selectively sequester iodine species from both contaminated air and water medium.

Chapter 4. Trap Inlaid Cationic Hybrid Composite Material for Efficient Segregation of Toxic Chemicals from Water

The segregation of metal-based oxoanions, particularly the arsenate has recently garnered significant scientific interest as they are potentially harmful pollutants that cause serious water pollution. Despite the fact that a number of excellent adsorbents have been utilized to manage chemicals well, their restricted microporous nature, non-monolithic applicability, relatively sluggish kinetics, and low selectivity prevented their widespread real-time application. In this work, we developed an innovative anion exchangeable hybrid composite lightweight material, which combines a hierarchically porous metal-

organic gel with stable cationic metal-organic polyhedra that are programmed with specific oxoanions trapping moieties. The hybrid composite was found to exhibit extremely rapid and selective segregation efficiency toward several hazardous oxoanions, such as HAsO_4^{2-} , SeO_4^{2-} , ReO_4^- , CrO_4^{2-} , and MnO_4^- in water. In the presence of 100-fold additional interfering anions, the material was able to selectively remove trace HAsO_4^{2-} even at low concentrations to well below the As(V) limit in drinking water set by the WHO. Additionally, in both batch and dynamic column exchange sorption experiments, the hybrid material was found to effectively remove arsenate from natural drinking water samples and simulated industrial effluent samples.

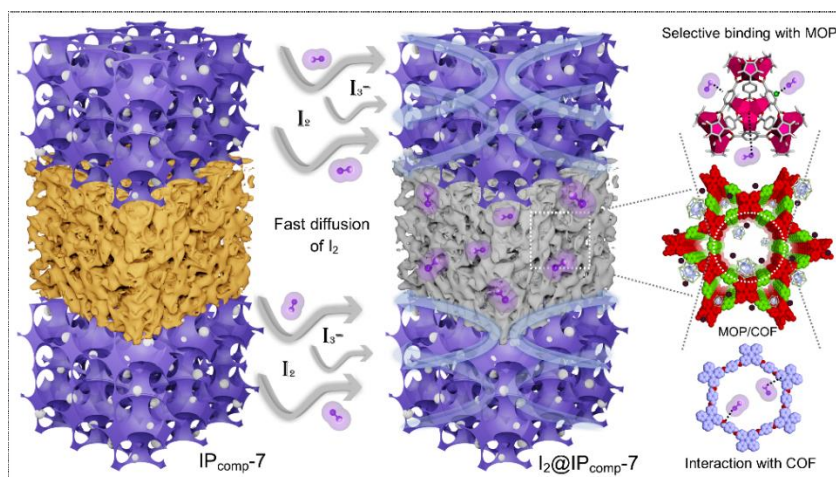


Angewandte Chemie International Edition, 2022, 61, e202203385.

Chapter 5. Nano-snare Implanted Ultralight Crystalline Hybrid Composite Material for Multiple Cooperative Interactions Mediated Efficient Sequestration of Radioiodine

Effective management of radioactive nuclear waste, such as the sequestration of radioiodine, has received considerable scientific interest recently given the significance of sustainable nuclear energy. Although, a number of sorbents have been reported for the adsorption of iodine, the absence of appropriate design methodologies makes it extremely difficult to build effective adsorbent with significantly improved segregation properties for widespread practical application. Considering this, in this work, a hybrid composite crystalline aerogel material has been created using a novel hybridization synthetic strategy by covalently combining a stable cationic discrete metal-organic polyhedron (MOP) with an imine-

functionalized covalent organic framework (COF). The synthesized lightweight composite material exhibit multifunctional properties such as large surface area with hierarchical macro-micro porosity different functional active binding sites, including imine, amine and metal chelating sites, which collectively interact with iodine species. The hybrid composite was found to demonstrate ultrafast adsorption kinetics, high adsorption capacity, retention efficiency, reusability, and recovery towards molecular iodine and different iodine species in both vapor phase and water medium. With these qualities, the proposed nano-adsorbent beat the majority of the previously reported adsorbents in terms of ultrahigh vapor-phase iodine absorption capacity in both static and dynamic condition. In addition, it was discovered that the material could rapidly and selectively remove iodine or polyiodides from a variety of complicated water matrixes when there was an abundance of interferences present, both at high and trace concentrations.



Nature Communication, 2024, 15, 1278.

Chapter 6. Summary, Critical Comments and Perspectives

The insights obtained from the library of task-specific advanced functional porous materials and their hybrid composites mentioned in chapters 2–5 have been attempted to be summarized in this chapter. The crucial role of some key design parameters, multifunctional properties as well as structure modulation have been discussed. The experimental outcomes of the current thesis work on advanced functional porous materials and their porous hybrid composites towards energy-intensive separation of various chemicals, particularly those fostering environmental sustainability is documented in comparison to state-of-art materials. Finally, along with few critical comments we put forward our viewpoints on the challenges and opportunities of these materials toward real-world chemical separation application.

Abbreviations

g	Gram
mg	Miligram
min	Minutes
mL	Milliliter
mmol	Milli moles
cm	Centimeter
RT	Room Temperature
MOF	Metal-Organic Framework
MOP	Metal-Organic Polyhedra
MOG	Metal-Organic Gel
MOC	Metal-Organic Cage
COF	Covalent Organic Framework
POP	Porous Organic Polymer
DMF	N,N'-dimethylformamide
DMAc	N,N'-dimethylacetamide
MeOH	Methanol
EtOH	Ethanol
THF	Tetrahydrofuran
SCXRD	Single-Crystal X-Ray Diffraction
PXRD	Powder X-Ray Diffraction
FT-IR	Fourier transform infra-red spectroscopy
TGA	Thermo-gravimetric Analysis
UV	Ultraviolet
FE-SEM	Field Emission Scanning Electron Microscopy
NMR	Nuclear Magnetic Resonance
EDX	Energy Dispersive X-ray Analysis
ICP-AES	Inductively Coupled Plasma Atomic Emission Spectroscopy
ICP-MS	Inductively Coupled Plasma Mass Spectroscopy
CP-MAS	Cross-Polarization Magic-Angle-Spinning
AFM	Atomic force microscopy
HRTEM	High-resolution transmission electron microscopy
DRS	Diffuse Reflectance Spectroscopy
ITC	Isothermal Titration Calorimetry
CT	Computed Tomography
XPS	X-ray Photoelectron Spectroscopy

Rights and Permissions

Chapter 2:

Reprinted (adapted) with permission from *J. Mater. Chem. A*, 2023, **11**, 26580-26591. Copyright 2023: Royal Society of Chemistry.

<https://doi.org/10.1039/D3TA04995G>.

Chapter 3:

Reprinted (adapted) with permission from *Angew. Chem. Int. Ed.* 2023, **62**, e202214095, Copyright 2023: John Wiley and Sons.

<https://doi.org/10.1002/anie.202214095>.

Chapter 4:

Reprinted (adapted) with permission from *Angew. Chem. Int. Ed.* 2022, **61**, e202203385, Copyright 2022: John Wiley and Sons.

<https://doi.org/10.1002/anie.202203385>.

Chapter 5:

Reprinted (adapted) with permission from *Nature Communications* 2024, **15**, 1278, Copyright 2024: Springer Nature.

<https://doi.org/10.1038/s41467-024-45581-9>.

Research Publications

Included in Thesis:

1. Unraveling Mechanistic Insights in Covalent Organic Frameworks for Highly Efficient Sequestration of Organic Iodides from Simulated Nuclear Waste
Sahel Fajal, Dipanjan Majumder, Writakshi Mandal, Sumanta Let, Gourab K. Dam, Mandar M. Shirolkar and Sujit K. Ghosh.
[J. Mater. Chem. A, 2023, 11, 26580-26591.](#)
2. Ordered Macro/Microporous Ionic Organic Framework for Efficient Separation of Toxic Pollutants from Water
Sahel Fajal, Atikur Hassan, Writakshi Mandal, Mandar M. Shirolkar, Sumanta Let, Neeladri Das and Sujit K. Ghosh.
[Angew. Chem. Int. Ed. 2023, 62, e202214095. \(Selected as Inside Front Cover page\)](#)
3. Trap Inlaid Cationic Hybrid Composite Material for Efficient Segregation of Toxic Chemicals from Water
Sahel Fajal, Writakshi Mandal, Samraj Mollick, Yogeshwer D. More, Arun Torris, Satyam Saurabh, Mandar M. Shirolkar and Sujit K. Ghosh.
[Angew. Chem. Int. Ed. 2022, 61, e202203385. \(Selected as Hot Article & Front Cover page\)](#)
4. Ultralight crystalline hybrid composite material for highly efficient sequestration of radioiodine
Sahel Fajal, Sahel Fajal, Writakshi Mandal, Arun Torris, Dipanjan Majumder, Sumanta Let, Arunabha Sen, Fayis Kanheerampockil, Mandar M. Shirolkar and Sujit K. Ghosh.
[Nat. Comm., 2024, 15, 1278.](#)

(† - indicates equal contribution)

Not Included in Thesis:

5. Unfolding the Role of Building Units of MOFs with Mechanistic Insight towards Selective Metal Ions Detection in Water
Sahel Fajal[†], Writakshi Mandal[†], Dipanjan Majumder, Mandar M Shirolkar, Yogeshwar D. More and Sujit K. Ghosh.
[Chem. Eur. J. 2022, 28, e202104175.](#)
-

6. Preferential Separation of Radioactive TcO_4^- Surrogate from a Mixture of Oxoanions by a Cationic MOF
Sahel Fajal, Dipayan Ghosh, Writakshi Mandal and Sujit K. Ghosh
Chem. Commun., 2024, **60**, 1884-1887.
 7. Porous Organic Polymers (POPs) for Environmental Remediation
Sahel Fajal, Subhajit Dutta and Sujit K. Ghosh.
Mater. Horiz., 2023, **10**, 4083–4138.
 8. Selective and sensitive recognition of Fe^{3+} ion by a Lewis basic functionalized chemically stable metal-organic framework (MOF)
Sahel Fajal, Partha Samanta, Subhajit Dutta and Sujit K. Ghosh.
Inorganica Chimica Acta 2019, **502**, 1193592.
 9. Nanotrap Grafted Anion Exchangeable Hybrid Materials for Efficient Removal of Toxic Oxoanions from Water
Samraj Mollick, **Sahel Fajal**, Satyam Saurabh, Dabanjan Mahato and Sujit K. Ghosh.
ACS Cent. Sci. 2020, **6**, **9**, 1534–1541.
 10. Benchmark uranium extraction from seawater by an ionic macroporous metal-organic framework
Samraj Mollick, Satyam Saurabh, Yogeshwar D. More, **Sahel Fajal**, Mandar M. Shirolkar, Writakshi Mandal and Sujit K. Ghosh.
Energy Environ. Sci., 2022, **15**, 3462-3469.
 11. Unveiling the Impact of Diverse Morphology of Ionic Porous Organic Polymers with Mechanistic Insight on the Ultrafast and Selective Removal of Toxic Pollutants from Water
Writakshi Mandal, **Sahel Fajal**, Samraj Mollick, Mandar M. Shirolkar, Yogeshwar D. More, Satyam Saurabh, Debanjan Mahato and Sujit K. Ghosh.
ACS Appl. Mater. Interfaces 2022, **14**, 20042–20052.
 12. Selective and Sensitive Recognition of Specific Types of Toxic Organic Pollutants with a Chemically Stable Highly Luminescent Porous Organic Polymer (POP)
Writakshi Mandal, **Sahel Fajal**, Partha Samanta, Subhajit Dutta, Mandar M. Shirolkar, Yogeshwar D. More and Sujit K. Ghosh.
ACS Appl. Polym. Mater. 2022, **4**, **11**, 8633–8644.
 13. A Hydrolytically Stable Luminescent Cationic MOF for Selective Detection of Toxic Organic Arsenic in Water
Gourab K. Dam, **Sahel Fajal**, Subhajit Dutta, Sumanta Let, Aamod V. Desai and Sujit K. Ghosh.
-

- ACS Appl. Opt. Mater.* 2023, **1**, **7**, 1217–1226.
14. All Organic Porous Heterogeneous Composite with Antagonistic Sites as Cascade Catalyst for Continuous Flow Reaction
Sumanta Let, Gourab K. Dam, **Sahel Fajal** and Sujit K. Ghosh.
Chem. Sci., 2023, **14**, 10591-10601.
 15. Nanotrap Grafting in the Microenvironment of a Stable Ultramicroporous Anionic MOF for Efficient Uranium Extraction from Seawater
Yogeshwar D. More, Samraj Mollick, Satyam Saurabh, **Sahel Fajal**, Michele Tricarico, Subhajit Dutta, Mandar M. Shirolkar, Writakshi Mandal, Jin-Chong Tan and Sujit K. Ghosh.
Small, 2023, 2302014.
 16. Palladium anchored N-Heterocyclic Carbene in a Porous Organic Polymer (POP): A Heterogeneous Composite Catalyst for Eco-Friendly C-C Coupling
Sumanta Let, Gourab K. Dam, Partha Samanta, **Sahel Fajal**, Subhajit Dutta and Sujit K. Ghosh.
J. Org. Chem. 2022, **87**, **24**, 16655–16664.
 17. Post Engineering of a Chemically Stable MOF for Selective and Sensitive Sensing of Nitric Oxide.
Writakshi Mandal, Dipanjan Majumder, **Sahel Fajal**, Sumanta Let, Mandar M. Shirolkar and Sujit K. Ghosh.
Mol. Syst. Des. Eng., 2023, **8**, 756-766.
 18. Ionic Metal-Organic Frameworks (iMOFs): Progress and Prospects as Ionic Functional Materials
Subhajit Dutta, Yogeshwar D. More, **Sahel Fajal**, Writakshi Mandal, Gourab K. Dam and Sujit K. Ghosh.
Chem. Commun., 2022, **58**, 13676-13698.
 19. Selective and Sensitive Fluorescence Turn-on Detection of Cyanide Ions in Water by Post Metallization of a MOF
Debanjan Mahato, **Sahel Fajal**, Partha Samanta, Writakshi Mandal and Sujit K. Ghosh.
ChemPlusChem, 2022, **87**, e202100426.
 20. Covalent Organic Framework Featuring High Iodine Uptake for Li-ion Battery: Unlocking the Potential of Hazardous Waste
Satyam Saurabh, Samraj Mollick, Yogeshwar D. More, Abhik Banerjee, **Sahel Fajal**, Nikhil Kumar, Mandar M. Shirolkar, Satishchandra B. Ogale and Sujit K. Ghosh.
ACS Materials Lett. 2023, **5**, 2422–2430
 21. Post-synthetically modified metal-organic frameworks for sensing and capture of water pollutants
Soumya Mukherjee, Subhajit Dutta, Yogeshwar D. More, **Sahel Fajal** and Sujit K. Ghosh.
-

- Dalton Trans.*, 2021, **50**, 17832-17850.
22. Highly Stable and End-Group Tuneable Metal-organic Framework / polymer composite for Superior Triboelectric Nanogenerator Application
Yogeshwar D. More, Satyam Saurabh, Samraj Mollick, Sachin Kumar Singh, Subhajit Dutta, **Sahel Fajal**, Anil Prathamshetti, Mandar M. Shirolkar, Suresh Panchal, Minal Wable, Satishchandra Ogale and Sujit K. Ghosh.
Adv. Mater. Interfaces 2022, 2201713.
23. A Luminescent Cationic MOF for Bimodal Recognition of Chromium and Arsenic based Oxo-anions in Water
Subhajit Dutta, Sumanta Let, Mandar M Shirolkar, Aamod V. Desai, Partha Samanta, **Sahel Fajal**, Yogeshwar D. More and Sujit K. Ghosh.
Dalton Trans., 2021, **50**, 10133-10141.
24. Hybrid blue perovskite@metal-organic gel (MOG) nanocomposite: simultaneous improvement of luminescence property and stability
Samraj Mollick, Tarak Nath Mandal, Atanu Jana, **Sahel Fajal** and Sujit K. Ghosh.
Chem. Sci., 2019, **10**, 10524–10530.
25. Stabilizing Metal-Organic Polyhedra (MOP): Issues and Strategies
Samraj Mollick, **Sahel Fajal**, Soumya Mukherjee and Sujit K. Ghosh.
Chem. Asian J. 2019, **14**, 3096–3108.
26. Ultrastable Luminescent Hybrid Bromide Perovskite@MOF Nanocomposites for the Degradation of Organic Pollutants in Water
Samraj Mollick, Tarak Nath Mandal, Atanu Jana, **Sahel Fajal**, Aamod V. Desai, and Sujit K. Ghosh.
ACS Appl. Nano Mater., 2019, **2**, 1333-1340.
27. Luminescent cationic MOF and its polymer composite membrane elicit selective sensing of antibiotics and pesticides in water
Subhajit Dutta, Writakshi Mandal, Aamod V. Desai, **Sahel Fajal**, Gourab K. Dam, Soumya Mukherjee and Sujit K. Ghosh.
Mol. Syst. Des. Eng., 2023, **8**, 1483-1491.
28. Luminescent Metal-Organic Frameworks as Chemical Sensors
Yogeshwar D. More, **Sahel Fajal**, Subhajit Dutta and Sujit K. Ghosh.
Book Chapter of a book entitled “Materials for Chemical Sensors”, by Science Publishers CRC Press 2023).
-

Chapter 1

General Introduction on Advanced Functional Porous Materials Addressing Chemical Separation Challenges

1.1 Porous Materials

The historical roots of porous materials extend back to around 1500 BC, as documented in ancient Egyptian literature such as the Ebers Papyrus, describing the use of porous charcoal for medical procedures addressing indigestion.^[1] The history of porous materials is a multifaceted journey that encompasses geological, industrial, and scientific dimensions. Porosity, an inherent property woven into the fabric of nature, traditionally mandates the existence of permanent and interconnected voids accessible to gas molecules or liquids for a material to be deemed porous. The concept of porosity, or the presence of void spaces within a material, has roots in ancient times, with early thinkers like Archimedes considering the buoyancy of materials as an indicator of their porosity.^[2, 3] Nature showcases such porosity in biological tissues, rocks, charcoal, and soils, harnessing it for applications like water purification, filtration, and cooling since ancient Egyptian times. In the latter half of the 20th century, amidst early research on charcoal adsorption, a distinct category of porous materials, termed zeolites (from the Greek words "zeo" meaning "to boil" and "lithos" meaning "stone"), gained recognition among scientists.^[4] However, it wasn't until the 20th century that systematic studies on porous materials began, driven by advancements in analytical techniques and the growing recognition of their significance in various fields. Geologically, the exploration of porous materials gained prominence with the understanding of subsurface reservoirs. In the petroleum industry, the study of porous rocks, such as sandstone and limestone, became crucial for predicting fluid flow in oil and gas reservoirs. The ability of rocks to store and transport fluids became a central concern for geologists and engineers involved in oil exploration and extraction. In parallel, the development of synthetic porous materials marked a significant turning point. Zeolites, crystalline aluminosilicate minerals with well-defined pore structures, emerged as key players in the mid-20th century.^[5-7] Their use as catalysts in various industrial processes showcased the potential of tailoring porosity for specific applications. The discovery and synthesis of zeolites paved the way for the exploration of other synthetic porous materials, including metal-organic frameworks (MOFs), covalent organic frameworks (COFs), and porous polymers. Zeolites, with their ordered and tunable pore structures, found applications in catalysis, gas separation, and ion exchange.^[8] The ability to control the size and shape of pores in these materials opened up new possibilities for designing advanced materials with tailored properties. The development of MOFs, a class of crystalline materials composed of metal ions or clusters connected by organic linkers, brought a new level of versatility to porous materials. MOFs exhibit an exceptional range of structures and properties, making them suitable for gas storage, separation, catalysis, and sensing applications. Their high surface area and tunable pore sizes have led to extensive research and innovation in fields such as environmental remediation, drug delivery, and energy storage.^[9-11] In recent years, the exploration of porous materials has extended to other domains, such as porous ceramics, aerogels, and porous carbon materials. These materials find applications in diverse areas, including

thermal insulation, water purification, and energy storage devices.^[8] Overall, the history of porous materials is a narrative of evolving scientific understanding and technological innovation. From ancient musings on buoyancy to the sophisticated design of custom-made materials with tailored porosity, the journey reflects the intertwined threads of geology, chemistry, and engineering that have shaped our ability to manipulate and leverage the unique properties of porous materials for a myriad of applications.

Classifying porous materials based on pore size, microporous materials have pores smaller than 2 nanometers (nm), mesoporous materials have pores ranging from 2 to 50 nm, and macroporous materials boast pores larger than 50 nm (Figure 1.1).^[12] While conventional porous solids have long played an indispensable role in society, achieving target-specific applications proves challenging due to unclear structure-property relationships. Consequently, there is a pressing need to develop a new class of porous materials allowing molecular-level fine-tuning and customization. Enter advanced functional porous materials (AFPMS), a category that has emerged over the last two decades, signaling a renaissance in material engineering and chemistry. A growing global community of researchers is now engaged in this dynamic field, exploring limitless chemical and structural possibilities. The unique chemistry of organic, inorganic, or hybrid combinations in AFPMS presents exciting alternatives surpassing conventional porous solids in attractiveness and versatility.^[13-16] This transformative era in material science heralds a new frontier where tailor-made materials, with unprecedented functionalities, are within reach, opening avenues for ground-breaking applications (Figure 1.1).

1.2 Advanced Functional Porous Materials (AFPMS)

In recent times, there has been a significant surge in global research attention focused on advanced functional porous materials (AFPMS) owing to their distinctive attributes and the advantages they offer in terms of precise molecular-level control. AFPMS, characterized by a high specific surface area and tailor-made pores, can be meticulously designed and synthesized. Moreover, these materials can be rendered processable by transforming them into monolithic aerogels, molecular beads, or thin films, making them compatible with practical applications (Figure 1.1). Notably, AFPMS can exhibit stimuli-responsive behaviour, allowing them to reversibly switch between open and closed porous forms in response to external stimuli. Their superiority over conventional porous solids lies in the availability of a wide range of straightforward synthetic routes for developing AFPMS, a feature not commonly found in traditional porous materials.^[15-17]

Generally, there are two methods for constructing AFPMS. The first involves crafting organic-inorganic hybrid porous architectures using functional organic synthons and inorganic metal nodes. The second method utilizes purely organic functionalized molecular blocks to create metal-free porous organic

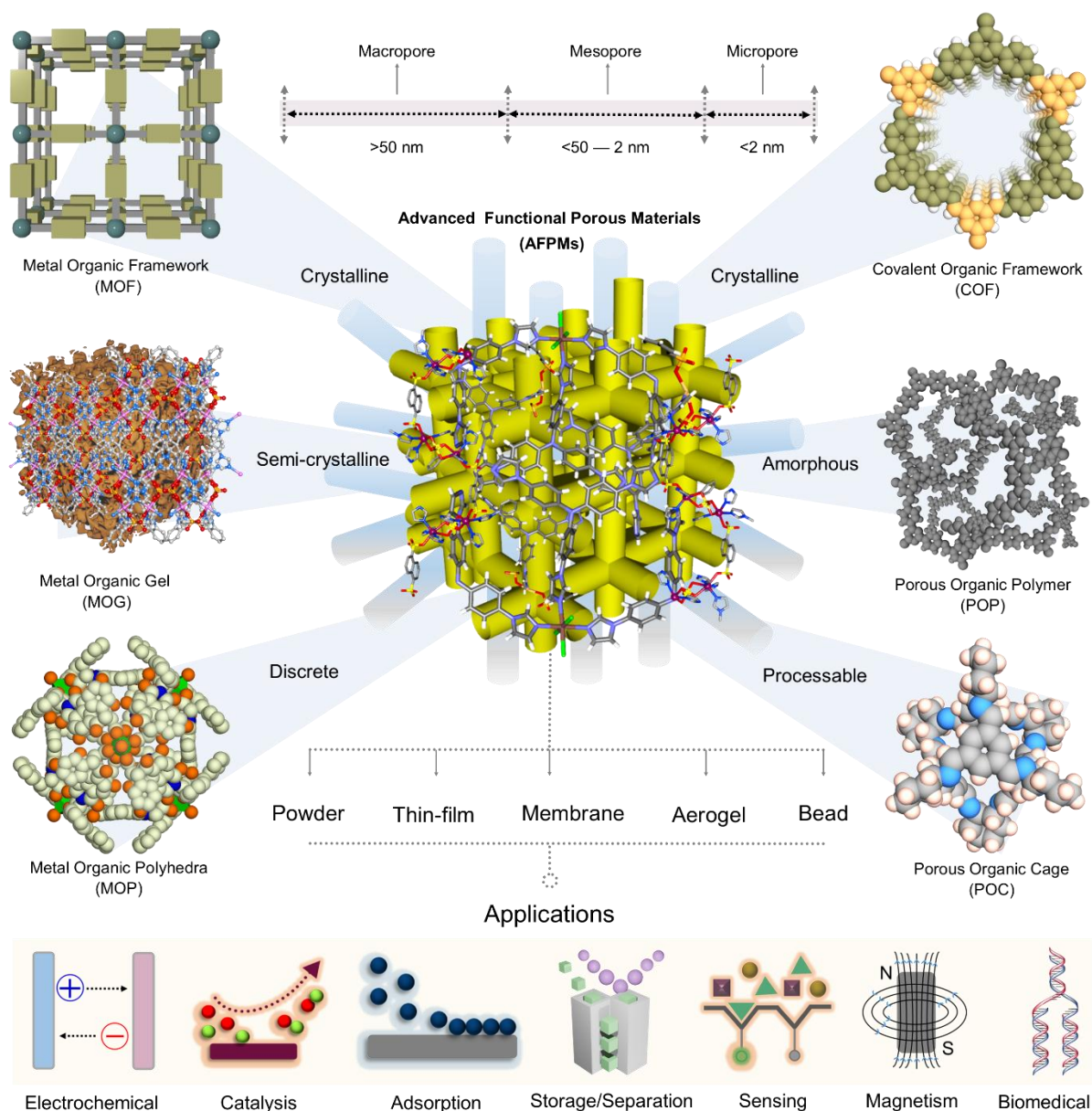


Figure 1.1: General schematic illustration of various types of advanced functional porous materials with their different properties, forms and applications.

materials by linking them through covalent bonds and noncovalent interactions (Figure 1.1). Based on these, the domain of advanced functional porous materials (AFPMs) can be broadly categorized into two sections: inorganic-organic hybrid porous materials and pure organic porous materials. Among them, the inorganic-organic hybrid porous materials consist of a large spectrum of materials, including metal-organic frameworks (MOFs) or porous coordination polymers (PCPs), metal-organic gels (MOGs), metal-organic polyhedra (MOPs).^[10, 11, 18-20] On the other hand, pure organic porous materials encompass porous organic polymers (POPs) or covalent organic frameworks (COFs), supramolecular organic frameworks (SOFs), hydrogen-bonded organic frameworks (HOFs), porous organic cages

(POCs), etc (Scheme 1.1).^[21-24] The key advantage of employing these strategies is the ability to carefully select functional moieties for synthesizing AFPMs, thereby imparting a task-specific nature to these materials. The building blocks are designed with application-specific functionality incorporated into the framework backbone, creating a porous scaffold that is interactive and functional based on the specific application requirements. Porous materials are a diverse class of substances characterized by the presence of voids, pores, or cavities within their structure. These voids create an internal surface area, often significantly larger than the external surface area, and can be tailored for specific applications. Porous materials find extensive use in various fields, including chemistry, materials science, geology, environmental science, and engineering. Here's a more detailed exploration of porous materials:

Classification:

Microporous Materials: These have pores with diameters less than 2 nm. Zeolites, activated carbon, and certain metal-organic frameworks (MOFs) fall into this category.

Mesoporous Materials: Pores in this category have diameters between 2 nm and 50 nm. Mesoporous silica materials, covalent organic frameworks (COFs), and some polymers are examples.

Macroporous Materials: These have larger pores, typically exceeding 50 nm. Foams, certain ceramics, and some polymers fall into this category.

Applications:

Catalysis: The high surface area and accessible pores of porous materials make them effective catalysts. Zeolites and MOFs, for instance, are used in various catalytic processes in the chemical industry.

Gas Storage and Separation: Porous materials are employed for storing gases, such as hydrogen, and for separating gas mixtures. This is crucial in applications like natural gas purification and carbon capture.

Adsorption: Porous materials can selectively adsorb molecules on their surfaces, making them valuable in applications like water purification, air filtration, and gas masks.

Drug Delivery: The controlled release of drugs is facilitated by porous materials, allowing for sustained and targeted delivery.

Sensing: Functionalized porous materials can be used in sensors for detecting specific molecules or ions.

Insulation: Certain porous materials, like aerogels, are known for their exceptional thermal insulation properties.

Examples of Advanced Functional Porous Materials (AFPMs):

Metal-Organic Frameworks (MOFs): Crystalline porous materials consisting of metal ions or clusters connected by organic ligands.

Metal-Organic Polyhedra (MOPs): Discrete crystalline porous materials consisting of metal ions or clusters connected by organic ligands.

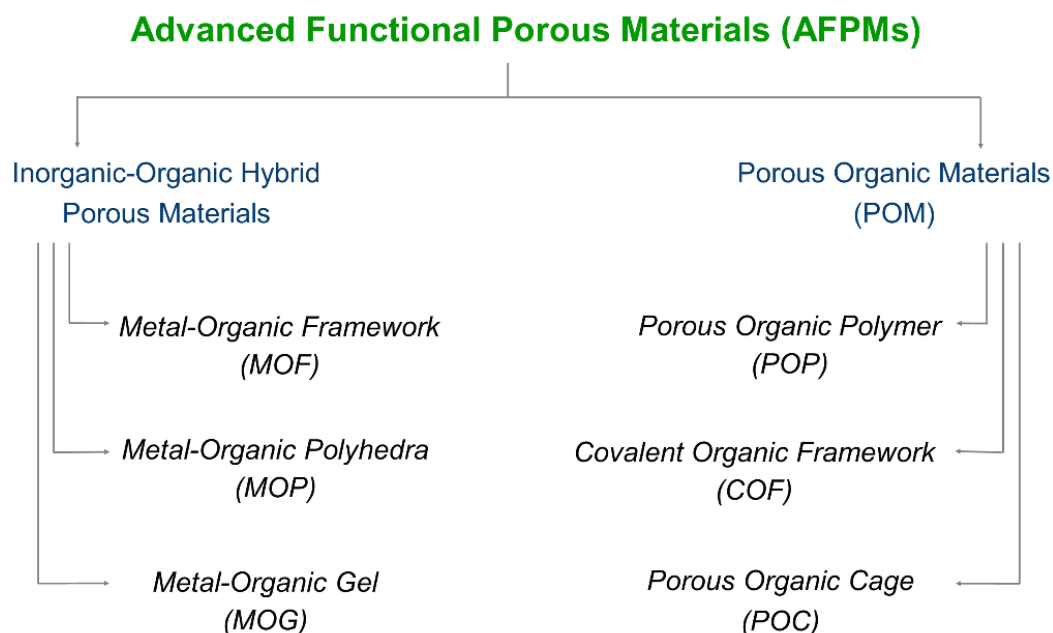
Metal-Organic Gels (MOGs): Semi-crystalline/amorphous soft porous materials consisting of metal ions or clusters connected by organic ligands.

Covalent Organic Frameworks (COFs): Crystalline organic polymers with regularly spaced pores.

Porous Organic Polymers (POPs): Amorphous polymers with intrinsic porosity, suitable for various applications.

Porous Organic Cages (POCs): Discrete organic molecules with intrinsic porosity.

Porous materials play a pivotal role in numerous scientific and industrial applications, offering a versatile platform for tailoring properties to meet specific needs. The ability to engineer these materials at the molecular and macroscopic levels opens up a wide range of possibilities for addressing challenges in energy, environmental sustainability, healthcare, and beyond.



Scheme 1.1: Classification of Advanced Functional Porous Materials (AFPMs).

1.2.1 Inorganic-Organic Hybrid Porous Materials

Inorganic-organic hybrid porous materials represent a versatile class of substances resulting from the integration of both inorganic and organic components into a unified porous structure. These materials often exhibit unique properties arising from the synergistic combination of the strengths of inorganic elements, such as metal ions or clusters, and the flexibility and functionality of organic ligands. The controlled assembly of these components leads to the formation of materials with tunable porosity, surface area, and chemical reactivity. Inorganic-organic hybrid porous materials find applications in various fields, including gas storage, catalysis, sensing, and drug delivery, owing to their customizable properties. The hybrid nature of these materials provides a platform for tailoring their characteristics to meet specific needs, making them valuable in the realm of materials science for diverse technological applications.^[18-20] This category of materials majorly consists of the following three classes of materials such as metal-organic frameworks (MOFs), metal-organic gels (MOGs), and metal-organic polyhedra (MOPs) (Scheme 1.1).

1.2.1.1 Metal-Organic Frameworks (MOFs)

Metal-organic frameworks (MOFs) represent a ground-breaking class of advanced functional porous materials that have garnered immense interest and research across scientific disciplines. These crystalline structures, often referred to as a subclass of coordination polymers, are characterized by a unique architecture consisting of metal ions or clusters interconnected by organic ligands and characterized by potential voids (Figure 1.2). The resulting three-dimensional framework exhibits exceptional porosity, with intricately designed pores and a remarkably high surface area. The versatility of MOFs lies in their tunable properties, allowing precise control over pore size, surface functionality, and overall structure.^[9-11] The synthesis of MOFs typically involves the coordination of metal nodes or clusters with organic ligands, with solvothermal, hydrothermal or room-temperature crystallization methods being commonly employed. The resulting porous structure serves as an ideal platform for a myriad of applications. The synthetic reaction media's solvent molecules commonly occupy the voids within the framework material. To access the space, these guest solvents must be removed from the MOF pores through vacuum treatment, heating, or a combination of both processes. Based on desolvation outcomes, MOFs are categorized into three generations: first, second, and third. After desolvation, first-generation frameworks lose structural integrity, while second-generation MOFs retain their framework structure. In contrast, third-generation MOFs, known as 'Dynamic frameworks,' exhibit flexible behavior, transforming into an alternate structure post-desolvation. A key feature is their reversible dynamicity, with the framework returning to its original structure after resolution.^[11] Another approach to functional MOF synthesis is 'post-synthetic modification (PSM).' This involves using a

MOF, synthesized through pre-synthetic strategies, with a functional subunit within the porous structure (Figure 1.2). It undergoes chemical transformation to generate structurally similar but functionally different porous MOFs. PSM is particularly valuable for synthesizing MOFs challenging to produce using conventional techniques.^[25] Functional MOFs can be classified based on charges into neutral MOFs and ionic MOFs (iMOFs). The carboxylate (-COOH) group in the organic linker typically binds metal nodes, forming neutral MOFs. Depending on the electrostatic nature, iMOFs are further classified into cationic and anionic frameworks (Figure 1.2).^[26, 27]

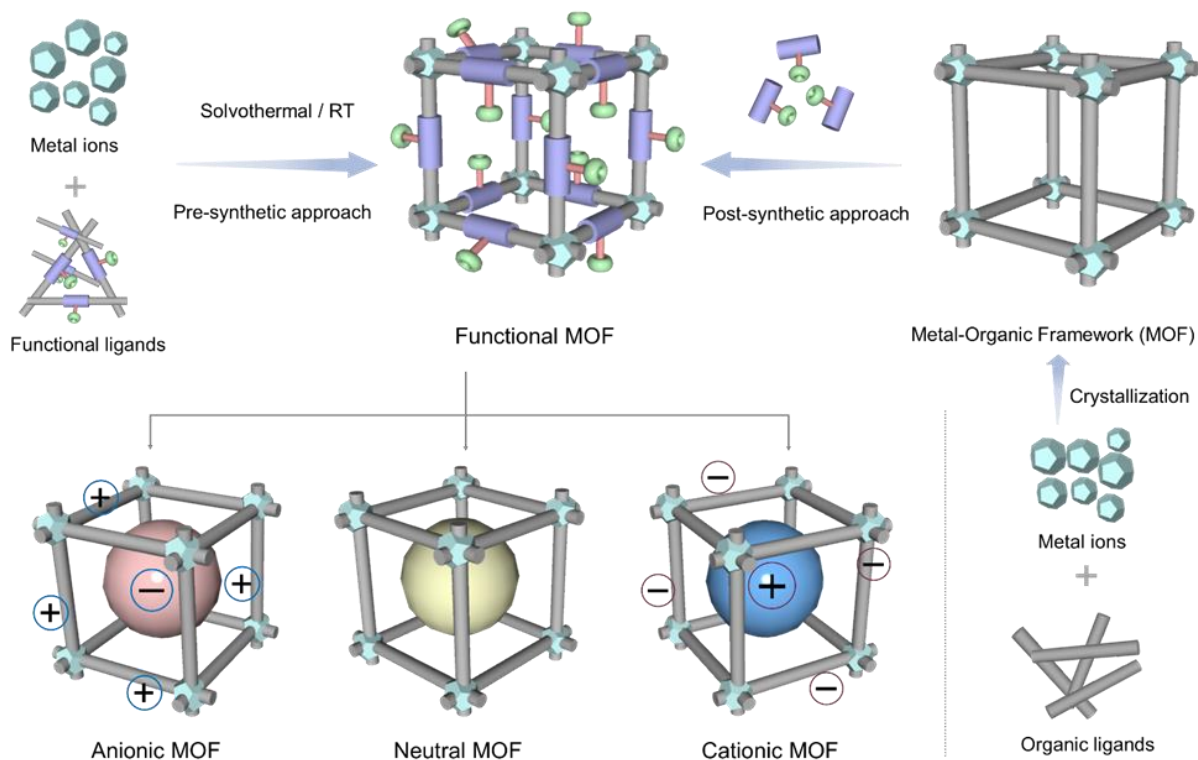


Figure 1.2: Schematic representation of synthesis and classifications of Metal-Organic Framework (MOF).

MOFs find application across diverse fields due to their structural properties and large surface area. Their pore dimensions and pendant functionalities enable host-guest chemistry. MOFs find application in diverse fields, and their utility is broad-ranging. Gas storage and separation represent prominent areas of application, leveraging the high surface area and tunable pores to selectively capture and store gases, including hydrogen for fuel cells. Luminescent MOFs (LMOFs) emit light upon external energy excitation and are employed in sensing various analytes. The luminescent properties of certain MOFs further extend their applications to areas such as recognition and host-guest chemistry, making them valuable tools in diverse scientific and technological endeavours.^[28] MOFs are also employed in

catalysis, where their active metal sites catalyze various chemical reactions. In drug delivery systems, the porous nature of MOFs allows for controlled encapsulation and release of pharmaceuticals. MOFs play a crucial role in environmental applications, particularly in water purification, owing to their ability to selectively adsorb contaminants.^[29] The classification of MOFs into different generations, each with distinct characteristics post-desolvation, adds an extra layer of complexity and adaptability to their applications. In the realm of clean energy, MOFs are pivotal for developing materials used in conductors, electrochemical applications, supercapacitors, and composite materials incorporating nanoparticles for energy and environmental applications.^[28-30]

However, challenges such as stability and scalability continue to drive ongoing research in the field of MOFs. Efforts are directed towards enhancing their stability under various conditions and developing scalable synthesis methods to unlock their full potential for practical applications. As researchers delve deeper into the intricacies of MOFs, the possibilities for innovation and discovery in materials science seem boundless, positioning MOFs as a cornerstone in the quest for advanced materials with unprecedented properties and applications.

1.2.1.2 Metal-Organic Gels (MOGs)

Metal-organic gels (MOGs) represent a cutting-edge class of materials that amalgamate the unique characteristics of metal-organic frameworks (MOFs) and soft materials like gels. These intriguing materials exhibit a gel-like consistency while incorporating the inherent porosity and structural features of MOFs. MOGs are formed through the self-assembly of metal ions or clusters with organic ligands, resulting in a three-dimensional gel network (Figure 1.3).^[31-33] The gelation process involves the formation of a viscoelastic structure, typically induced by factors like temperature, solvent conditions, or pH. What distinguishes MOGs is their dual nature – the ability to retain the ordered porosity of MOFs while displaying the deformability and responsiveness typical of gels. This combination of attributes renders MOGs highly adaptable for various applications. The synthesis of MOGs involves carefully selecting metal ions and organic ligands to achieve the desired gelation behavior. The resulting gel-like structures can be tuned to have specific mechanical properties, making them suitable for applications ranging from drug delivery to sensing. The porous nature of MOGs opens up possibilities for controlled release of encapsulated substances, making them promising candidates for targeted drug delivery systems. Additionally, their responsiveness to external stimuli, such as changes in temperature or pH, can be harnessed for applications in sensors and actuators. MOGs also hold potential in environmental and catalytic applications, leveraging their porosity and gel-like nature for efficient adsorption and separation processes. The combination of structural versatility and soft, gel-like characteristics positions MOGs as multifunctional materials with broad implications across fields such as materials science,

chemistry, and biotechnology.^[31-33] As research in this emerging field advances, the exploration of novel metal-organic gel systems and their innovative applications is expected to expand, unlocking new avenues for responsive and adaptable soft materials in diverse technological realms.

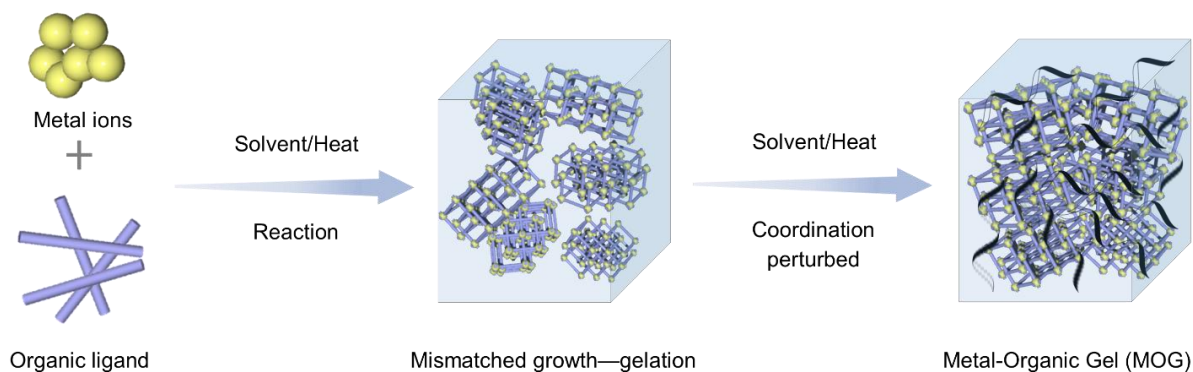


Figure 1.3: Schematic representation of synthesis of Metal-Organic Gel (MOG).

1.2.1.3 Metal-Organic Polyhedra (MOPs)

The term metal-organic polyhedra (MOP) was first introduced in the early 21st century. Unlike, MOFs, metal-organic polyhedra (MOPs) stand out as a captivating and intricate class of coordination compounds that form three-dimensional structures resembling polyhedra through the coordination-assisted self-assembly of metal ions or clusters with organic ligands (Figure 1.4).^[34-37] These polyhedral assemblies exhibit a diverse range of architectures, from simple geometric shapes to more complex structures with multiple metal nodes and ligands. The synthesis of MOPs involves carefully orchestrated coordination interactions between metal centers and organic ligands, leading to the formation of well-defined polyhedral structures. The nature of the metal ions and ligands used in the synthesis imparts specific properties to the resulting MOP, including porosity, functionality, and reactivity. MOPs find applications in various fields, including gas storage, catalysis, and sensing, owing to their well-defined structures and tunable properties. Their geometric precision and potential for functionalization make them promising candidates for the design of advanced materials with tailored properties, contributing to the growing landscape of supramolecular chemistry and materials science.^[34-37] As researchers continue to explore the vast design space of MOPs and their applications, these structures hold promise for innovations in diverse technological and scientific domains.

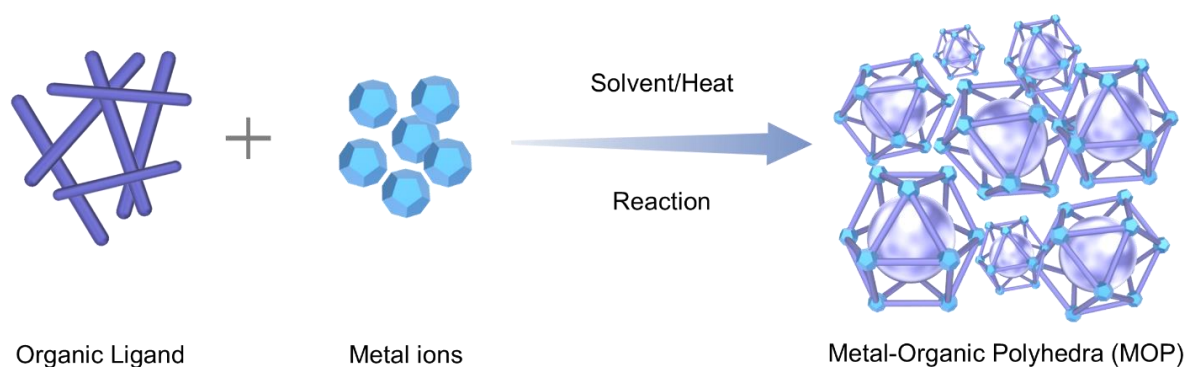


Figure 1.4: Schematic representation of synthesis of Metal-Organic Polyhedra (MOP).

1.2.2 Porous Organic Materials (POMs)

Porous organic materials (POMs) constitute a distinctive class of compounds characterized by their inherent porosity and predominantly organic composition. These materials feature a network of interconnected voids and channels created through the arrangement of organic building blocks, often incorporating functionalities like aromatic rings or organic linkers. POMs can exhibit high surface areas and tunable pore sizes, providing opportunities for selective adsorption, gas storage, and catalysis. The versatility of these materials is augmented by the ability to design and synthesize them with precise control over their structure and properties. Porous organic materials find applications in gas separation, water purification, and drug delivery, showcasing their significance in addressing challenges across environmental, energy, and biomedical domains.^[38-40] The major groups of materials that make up this category are mostly porous organic polymers (POPs), covalent organic frameworks (COFs), and porous organic cages (POCs) (Scheme 1.1).

1.2.2.1 Porous Organic Polymers (POPs)

Porous Organic Polymers (POPs) represent a dynamic and innovative class of materials that combine the structural integrity of polymers with inherent porosity, rendering them versatile and highly functional. These materials are characterized by an extended network of interconnected pores within their polymeric frameworks, creating a large surface area and diverse chemical functionalities. Owing to the absence of any long-range order in their molecular-level chemical structure, these materials demonstrated amorphous characteristics.^[40] The synthesis of POPs involves the polymerization of organic monomers, often containing aromatic or conjugated structures, leading to the formation of amorphous intricate three-dimensional networks with tunable porosity (Figure 1.5).^[41] What sets POPs

apart is their ability to offer precise control over pore size, shape, and surface chemistry through rational design and synthetic strategies. This tunability along with high chemical stability makes POPs ideal for a range of applications, including gas storage, catalysis, and molecular separation. Their unique combination of structural flexibility and porosity enables POPs to accommodate a wide array of guest molecules selectively.^[42] Moreover, the modular nature of POPs allows for tailored functionalities, enhancing their performance in applications such as water purification, sensing, and drug delivery. As research in this field advances, the development of new synthetic methodologies and a deeper understanding of structure-property relationships continue to expand the potential of porous organic polymers, positioning them at the forefront of materials science for addressing pressing challenges in areas such as sustainability, energy, and environmental remediation.^[40-44]

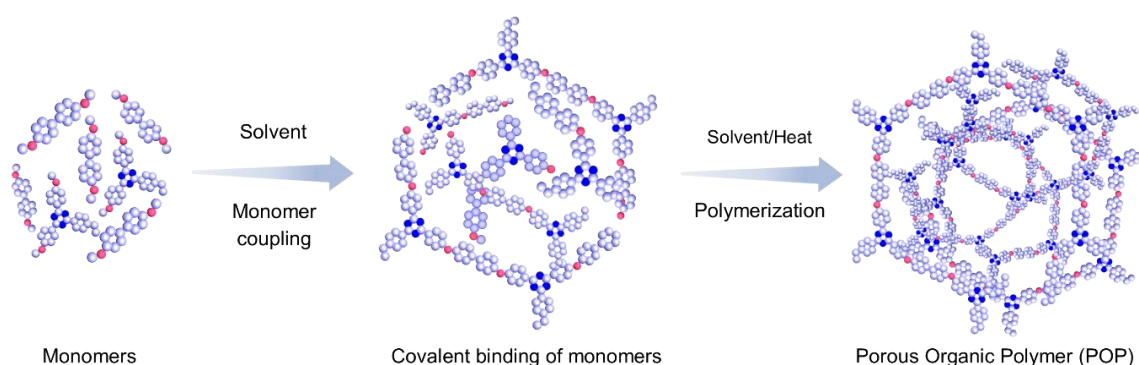


Figure 1.5: Schematic representation of synthesis of Porous Organic Polymers (POPs).

1.2.2.2 Covalent Organic Frameworks (COFs)

Covalent Organic Frameworks (COFs) stand at the forefront of advanced porous materials, representing a unique class characterized by their crystalline structures and covalent bonds linking organic building blocks. COFs are meticulously designed and synthesized through the formation of robust, ordered networks, where the organic components are connected by strong covalent bonds, leading to a stable and porous framework. The modular nature of COFs allows for precise control over their pore size, shape, and functionality, offering unprecedented tunability (Figure 1.6).^[45-48] This characteristic tunability, coupled with their high surface area, positions COFs as versatile materials with applications across various domains. They find utility in gas storage, catalysis, sensing, and molecular separation due to their tailored porosity, allowing for selective adsorption and controlled release of molecules. COFs also exhibit promise in electronic and optoelectronic devices, as their crystalline structures facilitate charge transport. Additionally, the potential for functionalization and post-synthetic modifications enhances their adaptability for diverse applications, such as drug delivery systems and

water purification.^[45-48] As research continues to unveil new synthetic strategies and further elucidate the structure-property relationships of COFs, these materials emerge as important contributors to the advancement of materials science, offering solutions to challenges in energy, environment, and technology.

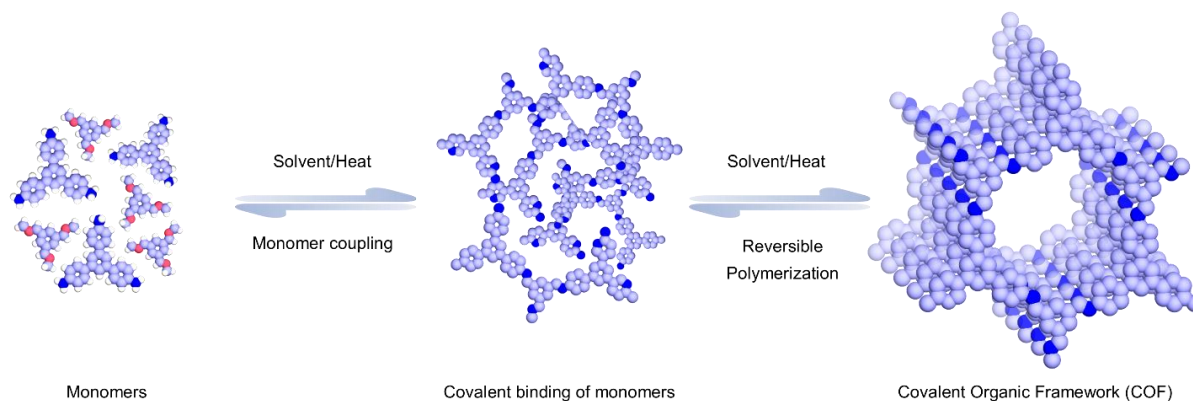


Figure 1.6: Schematic representation of synthesis of Covalent Organic Frameworks (COFs).

1.2.2.3 Porous Organic Cages (POCs)

Unlike, POPs or COFs, Porous Organic Cages (POCs) represent a highly intriguing and innovative class of porous materials that distinguish themselves by their cage-like discrete structures composed of covalently connected organic building blocks. These materials exhibit three-dimensional structures characterized by well-defined cavities and pores, resulting in materials with tailored porosity and exceptional surface area. The synthesis of POCs involves the judicious assembly of organic precursors through covalent bond formation, allowing for precise control over the cage dimensions and pore sizes (Figure 1.7).^[49] The modular nature of POCs enables the incorporation of diverse functionalities into the structure, expanding their potential applications. POCs have shown promise in various fields, including gas storage, separation, catalysis, and drug delivery, owing to their selective adsorption properties and tunable pore environments. Additionally, the ability to design POCs with specific chemical functionalities facilitates their integration into molecular recognition processes, making them valuable in sensing applications. The controlled and predictable nature of POC synthesis, along with the potential for post-synthetic modifications and solution-processable nature, positions these materials as versatile tools for addressing challenges in areas such as environmental remediation, sustainable energy, and biomedicine.^[49, 50] POCs are an interesting and promising class of porous materials that are adding to the growing field of advanced materials science as research in the subject develops.

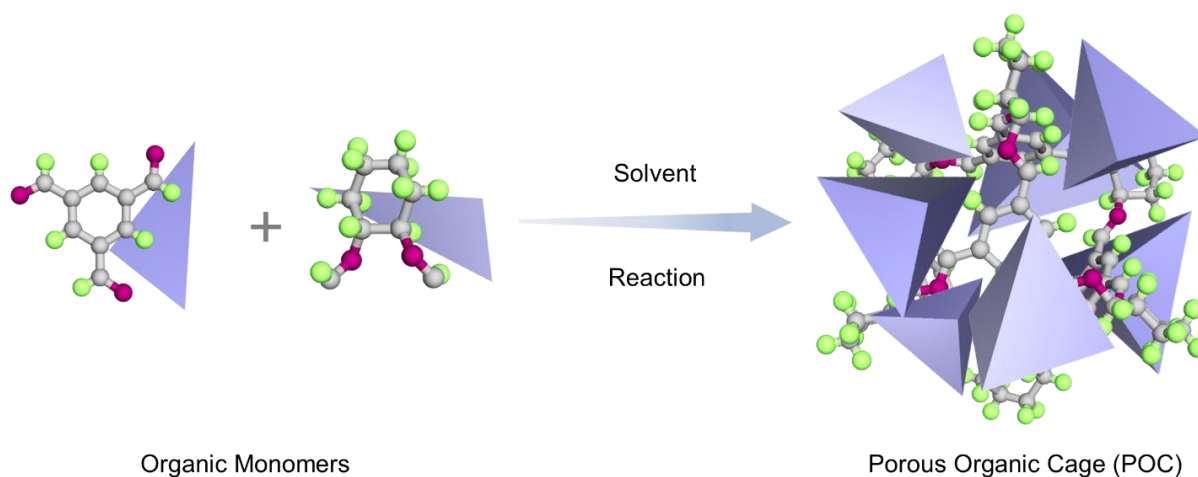


Figure 1.7: Schematic representation of synthesis of Porous Organic Cage (POC).

1.3 Hybrid Composite Porous Materials

Hybrid composite porous materials represent a versatile and innovative class of substances formed by combining distinct components, often inorganic and organic, to yield a material that possesses a synergistic combination of properties. Composite material refers to a blend of two or more substances that preserves their inherent characteristics or, in certain instances, displays enhanced and distinctive features compared to the individual components used independently.^[51-53] This class of materials typically exhibits a porous structure, offering a high surface area and tunable properties that arise from the unique interaction between the incorporated components. The combination of inorganic and organic elements enables precise tailoring of characteristics such as porosity, mechanical strength, and chemical reactivity. The hybrid nature of these materials often imparts multifunctionality, making them suitable for a diverse range of applications, including gas storage, catalysis, and environmental remediation. The ability to strategically choose and integrate different components allows for the optimization of performance and functionality, making hybrid composite porous materials a promising field in materials science with the potential to address challenges across various technological domains. The properties of composite materials rely on various factors, including the properties of the individual components, the relative quantities of each component, the size, shape, and distribution of the components, as well as the extent of interactions between the parent components. Generally, composite materials consist of a host matrix and functional guest species, where the guests contribute heightened activity and the host matrix often serves as a support. Porous materials are frequently employed as host matrices for support media, effectively immobilizing functional guest components to mitigate leaching and aggregation tendencies, resulting in a substantial enhancement in their reactivity. Moreover, these host matrices can

offer additional active sites that synergize with the guests in the composite material.^[53, 54] Advanced Functional Porous Materials (AFPMs) emerge as a compelling choice as a host matrix due to their customizable pore environment, consistent pore topologies, multiple functional locations, and framework flexibility. The selection of a suitable host matrix is facilitated by leveraging an extensive library of AFPMs, with simulation approaches commonly employed as an efficient screening method. Recently, various types of porous materials were found to be used as potential components to develop hybrid composite porous materials, which show effectiveness in numerous leading applications. Among them, MOP/MOF, MOP/COF, MOF/COF, POC/MOF, etc. are the most well-known examples.^[55-58] In the following section, a few synthetic strategies, properties, and applications of hybrid composite materials are discussed.

1.3.1 Composite Material Synthesis Techniques:

The size, form, and distribution of the guest species inside the host matrix determine how effective the composite material is. These crucial properties are greatly impacted by the development of straightforward production techniques, which also have a significant impact on the composite materials' overall performance efficiency. There aren't many methods for imploding foreign organisms into the host matrix.

1.3.1.1 Assembly of guest species inside the pre-synthesized host cavity: Using this method, the guest precursors are immobilized inside the host matrix that has already been synthesized, resulting in the generation of functioning guest species. The "ship-in-bottle" strategy is the name given to this widely employed technique.^[52, 59] Using a variety of methods, including vapor deposition, solid grinding, and solution infiltration, the guest precursors are initially impregnated into an AFPM matrix in this process before being converted to the necessary guest material. In this method, the guest species' ability to spread is restricted by the host pores, keeping them contained inside the pores. Nonetheless, there are still several issues with this method. When the guest species are in their synthetic environment, the host matrix ought to remain constant. A partial deterioration of the host species occurs as a result of the creation of greater size guest species (Figure 1.8). Exact control over the location, makeup, and structure of guest species inside the host cavity is challenging. The following are some techniques for the penetration of guest precursors into the host matrix:

(I) Chemical vapor deposition (CVD) method: One of the earliest techniques for encasing guest species in the host matrix is CVD. This process involves first impregnating precursor molecules into a host matrix's pores through sublimation, which is then broken down by heat or photochemical conditions. The maximum amount of the guest species can be loaded into the host matrix thanks to this approach's lack of solvent usage. The bigger guest species than the host matrix, which causes a partial

disruption of the framework, is the process's main drawback (Figure 1.8).^[52, 59] Furthermore, because it is hard to control the deposition process in a reproducible way, this process is still not fully understood.

(II) Solution infiltration method: In this method, the precursor solutions are used for liquid phase impregnation. During this process, the guest precursor solution is submerged in enough solution to seep into the host matrix's open cavity. The precursors are then reduced in order to generate the necessary guest species. The loading capacity is determined by how soluble the guest precursors are in the solution. Both the characteristics of the host matrix and the guest antecedents influence the distribution of guest species within it.^[52, 59] One drawback of this strategy is that it causes a large range of particle sizes to form within the host matrix (Figure 1.8).

(III) Incipient wetness impregnation: This method and solution impregnation are identical except for the reduction of the guest's precursor solution to a minimum. The solubility of guest precursors in appropriate solvents limits the maximum loading of guest species that can be achieved in this procedure without breaking the framework (Figure 1.8).

(IV) Solid-state grinding method: The infiltration of guest species into the porous host matrix can also be accomplished by solid-state grinding of volatile guest precursors without the need for any solvents. Precursor molecules are distributed evenly as a result of the volatile guest precursors sublimating to vapor and penetrating into the host matrix's voids during the grinding process. The embedded guest precursors are then reduced to create the desired small-sized guest species that are distributed throughout the host matrix. Without the need for solvents or post-infiltration washing procedures, the guest-loaded host matrix can be created fairly easily and efficiently through the grinding process.^[52, 59]

1.3.1.2 Construction of host around the guest species: In this method, the composite is synthesized by a host matrix that self-assembles around the pre-synthesized functional guest species to create the composite. This method is known as the "bottle-around-ship" or template synthesis technique. Pre-synthesized guest species are typically encased in the host framework rather than found in the cavities of the host matrix. This method not only avoids common problems like the guest species' tendency to aggregate on the outside surface and to partially destroy the host framework, but it also maintains the guest species' morphology, size, and composition. Because the guest species are synthesized before encapsulation, their particle size is not restricted to the aperture size of the host frameworks. Nevertheless, using this technique typically results in guest species self-nucleating outside of the host matrix. Moreover, guest elements are typically not able to endure the host matrix's reaction state.^[52, 59]

1.3.1.3 In situ encapsulation strategy: This method calls for mixing all of the components of the host matrix with functional guest precursors in an appropriate mixture so that the guest species and host framework can form simultaneously. Many aspects, such as precursor concentrations, solvent choice, reaction temperature, and modulators, have a significant impact on the balance of nucleation rates of both materials. Owing to its ease of use, low cost of production, and repeatability, this newly developed one-pot synthesis method is ideal for composite materials in real-world uses. Nevertheless, managing the development of these two distinct complexes is a challenging task because the guest species and the host matrix form simultaneously under the same reaction conditions.^[52, 59]

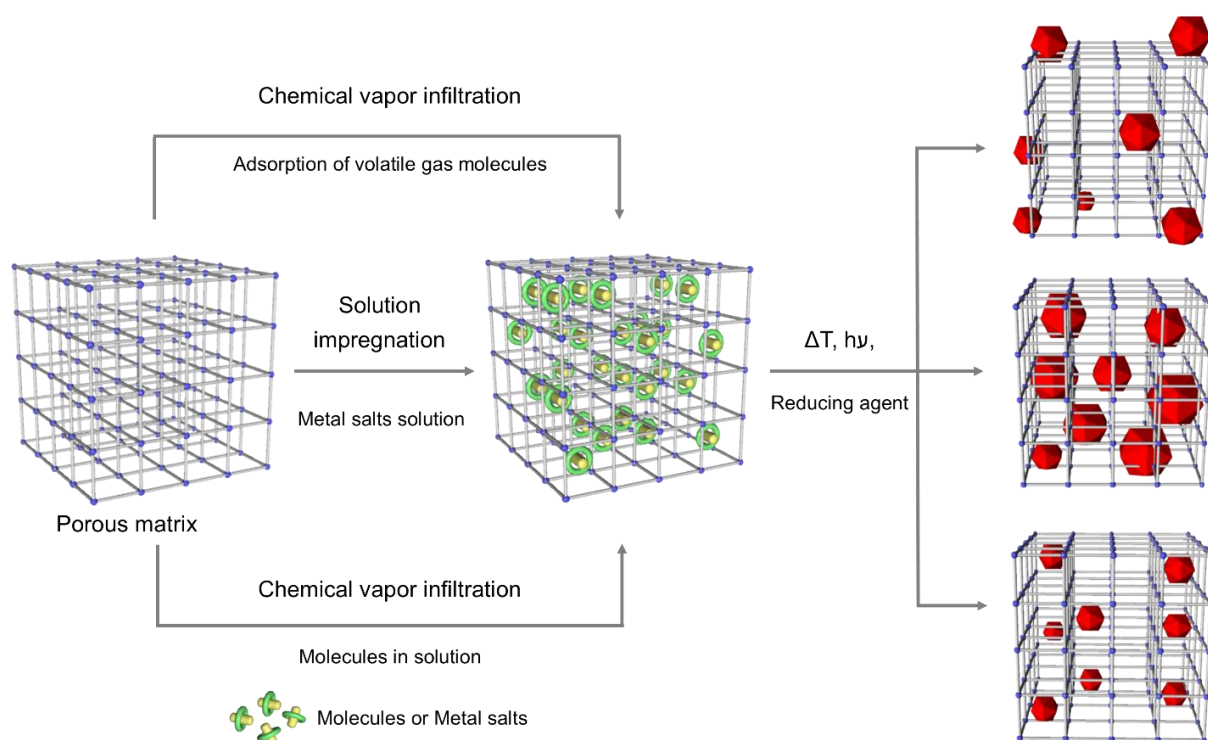


Figure 1.8: Schematic representation of strategies for synthesis of hybrid composite materials or growth of functional guest species into a pre-synthesized porous host matrix.

1.3.2 Examples of Hybrid Composite Porous Materials

Among the others, a few of the well-studied examples of advanced hybrid composite porous materials are polymer/metal-organic framework (MOF) composites, MOF/covalent organic framework (COF) composites, COF/metal-organic polyhedra (MOP) composites, MOP/metal-organic gel (MOG) composites, MOF/graphene oxide (GO) nanocomposites, COF/GO composites, MOP/MOG/MOG-Nano-cellulose/Carbon nanotube composite, POC/Hydrogel composites, etc.^[55-58]

1.4 Shaping of Advanced Functional Porous Materials

The shaping of advanced functional porous materials represents a crucial aspect in harnessing their unique properties for tailored applications. The design and fabrication of these materials involve intricate processes aimed at achieving specific forms while preserving their inherent porosity and functionality. Researchers employ various techniques, such as templating, supercritical CO₂ drying, freeze-drying, and sol-gel methods, to control the architecture and morphology of the materials. The shaping process is meticulously tuned to optimize parameters like pore size, surface area, and mechanical strength, ensuring the material's performance aligns with intended applications. The resulting structures, ranging from aerogels, foams, thin films, and membranes to intricate frameworks, play a pivotal role in applications such as catalysis, gas storage, and drug delivery. Among the various shapes of AFPMs, the development of aerogels holds significant importance due to their unique properties and versatile applications across various industries. Aerogels are renowned for their extremely low thermal conductivity, making them highly effective insulators. They are among the lightest solid materials, often composed of 90-99% air.^[60-63] This exceptional lightness makes them ideal for applications where weight reduction is critical, such as in lightweight materials for transportation vehicles, enabling fuel efficiency and improved performance. The high surface area and porosity of aerogels make them excellent candidates for applications involving adsorption and catalysis. They can be tailored for specific chemical or gas interactions, making them valuable in environmental remediation, water purification, and catalytic processes in chemical manufacturing. The shaping of advanced functional porous materials represents a dynamic field where innovation in fabrication techniques continues to drive the development of materials with enhanced properties and broader utility in diverse technological domains. For example, the macroscopic aerogel nature of MOG, COF, or any other AFPMs helps in the diffusion of a large amount of mass with ultrafast kinetics through the external large open void space, which further triggers the adsorption and catalytic performance of the materials.^[60-64] Thus, to achieve better performance, creating an aerogel or functional porous material membrane is advantageous.

1.5 Applications of Advanced Functional Porous Materials (AFPMS)

The applications of Advanced Functional Porous Materials (AFPMS) span a wide array of scientific and technological domains, owing to their unique properties and versatile nature. AFPMS find extensive use in gas storage and separation, where their tunable pore structures allow for selective adsorption of gases, crucial in fields such as clean energy storage and gas purification. In catalysis, AFPMS serve as effective catalyst support matrices, providing a high surface area and tailored environments for enhanced reactivity. The customizable pore environment and consistent topologies of AFPMS make them

excellent candidates for drug delivery systems, offering controlled release and targeted delivery of pharmaceuticals. Additionally, AFPMs play a pivotal role in environmental applications, particularly in water purification, where their porous matrices effectively immobilize contaminants. The unique features of AFPMs, including framework flexibility and multiple functional locations, make them ideal for applications in sensing and molecular recognition. Their adaptability as host matrices for encapsulating various functional guests positions AFPMs at the forefront of innovative materials, with continued research expected to uncover new applications and further enhance their impact on diverse technological fronts (Figure 1.9).^[65-77] A few of these applications are briefly discussed in the following section.

1.5.1 Gas Storage and Separation

The application of Advanced Functional Porous Materials (AFPMs) in gas storage and separation is particularly noteworthy, showcasing their pivotal role in addressing pressing challenges in energy and environmental domains. The tunable pore structures of AFPMs enable efficient gas storage, making them promising candidates for storing clean energy sources such as hydrogen. Clean energy and environmental solutions depend on the efficient adsorption and storage of gases such as carbon dioxide, hydrogen, and methane in gas storage facilities. AFPMs also exhibit exceptional capabilities in gas separation processes, where their selective adsorption properties allow for the separation of specific gases from complex mixtures. This is crucial in industrial settings, enabling the extraction of pure gases for various applications (Figure 1.9).^[65, 66, 77] The high surface area and customizable porosity of AFPMs contribute to their effectiveness in gas storage and separation, offering a versatile solution for enhancing energy storage technologies and mitigating environmental impacts associated with gas emissions. As research advances in this field, the continued development of AFPMs is anticipated to play a significant role in shaping the future of sustainable energy and gas purification technologies.

1.5.2 Sequestration of Toxic Pollutants

Advanced Functional Porous Materials (AFPMs) play a crucial role in the application of pollutant sequestration, offering innovative solutions to environmental challenges. AFPMs, with their tailored pore structures and high surface areas, serve as effective adsorbents for capturing and immobilizing various pollutants from air and water sources. These materials excel in removing contaminants such as heavy metals, organic pollutants, and toxic gases. The porous matrices of AFPMs provide sites for the selective adsorption of pollutants, preventing their release into the environment. This application is particularly significant in environmental remediation efforts, contributing to the purification of water sources and the reduction of air pollution. The versatility of AFPMs in pollutant sequestration positions them as valuable tools in sustainable environmental management, showcasing their potential to address critical issues related to pollution and contribute to the development of cleaner and healthier ecosystems

(Figure 1.9).^[71, 72, 78] As research in this field progresses, the continued exploration and refinement of AFPMs are expected to yield even more effective and tailored solutions for pollutant sequestration.

1.5.3 Heterogeneous Catalysis

In the realm of heterogeneous catalysis, Advanced Functional Porous Materials (AFPMs) emerge as pivotal catalyst support matrices, demonstrating remarkable efficiency and versatility. AFPMs, characterized by their tunable pore structures and high surface areas, provide an ideal platform for the immobilization of catalytically active species. These materials offer tailored environments that facilitate enhanced reactivity, making them invaluable in a wide range of catalytic processes.^[69] The porous matrices not only stabilize the catalytic components but also enable controlled access to active sites, influencing reaction kinetics and selectivity. AFPMs find application in various catalytic transformations, such as the synthesis of fine chemicals, environmental remediation, and energy conversion. The flexibility of AFPMs in accommodating different catalytic species and their ability to withstand harsh reaction conditions underscore their significance in advancing heterogeneous catalysis, offering a sustainable and efficient approach to catalytic processes with broad implications across industries (Figure 1.9).^[29, 70] As research in this field advances, AFPMs are poised to contribute significantly to the development of greener and more effective catalytic technologies.

1.5.4 Photo-catalysis and Electro-catalysis Applications

Advanced Functional Porous Materials (AFPMs) have been instrumental in advancing sustainable energy and environmental remediation through their role in both photo- and electro-catalysis. In photo-catalysis, AFPMs exhibit promising features for harnessing solar energy to drive catalytic reactions, as their porous architectures enable efficient light absorption and charge separation. This makes them valuable in applications such as water splitting for hydrogen production and the degradation of pollutants. In electro-catalysis, the tunable pore structures and high surface areas of AFPMs provide an ideal platform for immobilizing catalytically active species, enhancing reactivity and efficiency in various electrochemical processes.^[29] This includes applications in fuel cells, electrolyzers, and other energy conversion devices, where AFPMs act as robust catalyst support matrices. The adaptability of AFPMs in accommodating different catalytic species, coupled with their ability to withstand harsh reaction conditions, positions them as key contributors to the evolving landscape of green and sustainable catalytic technologies.^[69, 70] As research in this field progresses, AFPMs are poised to play a significant role in addressing challenges related to clean energy and environmental sustainability (Figure 1.9).

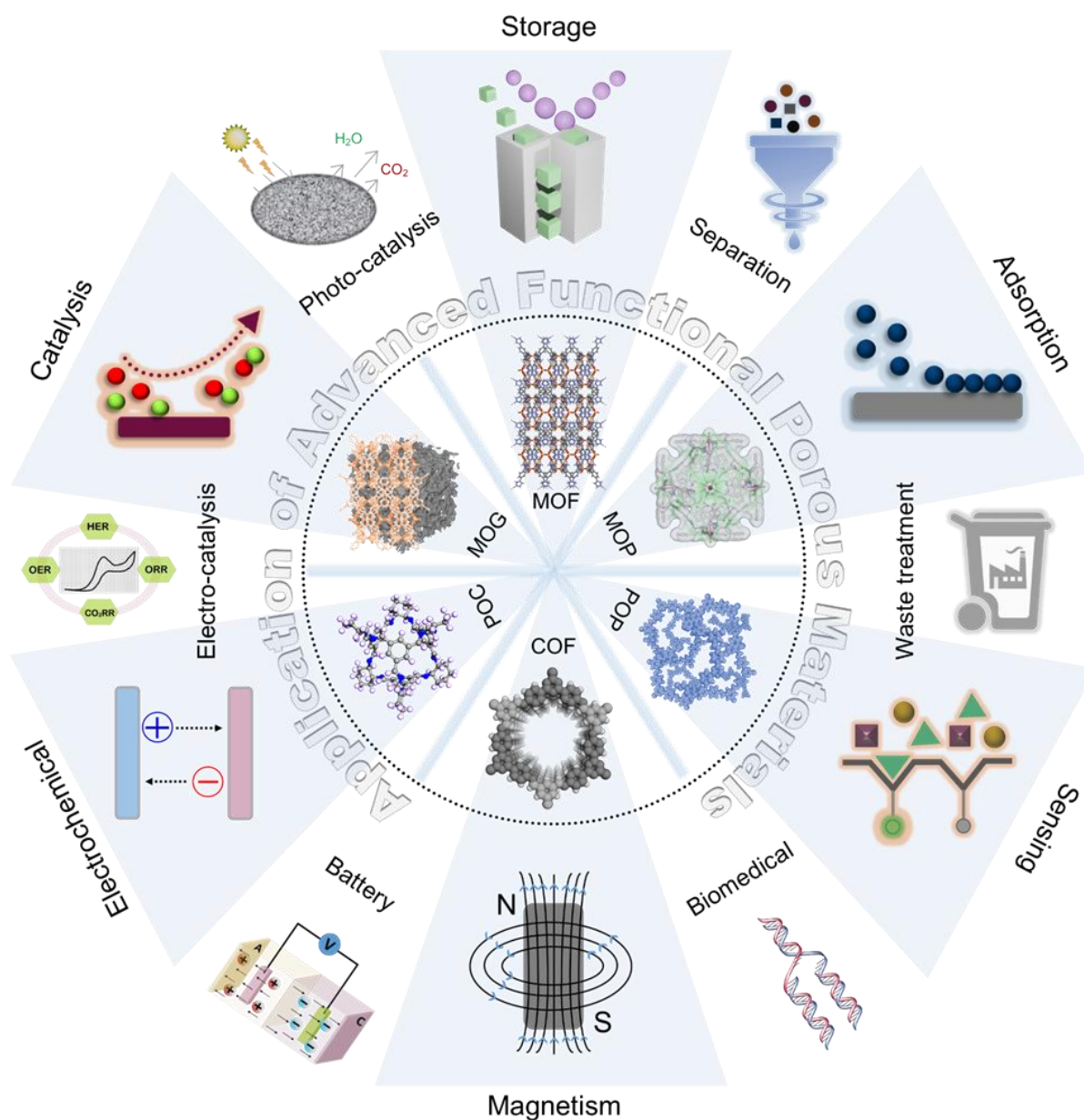


Figure 1.9: Schematic illustration of various applications of advanced functional porous materials.

1.5.5 Electrochemical Applications

Advanced Functional Porous Materials (AFPMs) exhibit a plethora of applications in electrochemistry, leveraging their unique properties to advance various energy storage and conversion technologies. The high surface area and tunable porosity of AFPMs make them excellent candidates for electrode materials in energy storage devices such as batteries and supercapacitors. The porous structures provide ample active sites for electrochemical reactions, facilitating efficient charge storage and rapid ion transport. Moreover, AFPMs play a crucial role in fuel cell technologies, acting as catalyst support

materials to enhance catalytic activity and durability. Their framework flexibility and multiple functional locations contribute to improved electro-catalytic performance. Additionally, AFPMs find applications in sensors, where their customizable pore environments enable the selective adsorption and detection of specific analytes.^[29-48] This versatility positions AFPMs as key players in advancing electrochemical technologies, offering solutions to challenges in energy storage, conversion, and sensing for a sustainable and technologically advanced future (Figure 1.9).

1.5.6 Molecular Recognition

Advanced Functional Porous Materials (AFPMs) show remarkable potential in the field of molecular recognition, which is beneficial for various applications related to sensing and selective adsorption. The tailored pore structures and multiple functional locations within AFPMs enable precise molecular recognition, allowing them to selectively capture and distinguish specific analytes from complex mixtures. This molecular sieving ability finds utility in sensors, where AFPMs can be designed to detect and respond to target molecules, showcasing their potential for applications in environmental monitoring, healthcare diagnostics, and security.^[28] Additionally, AFPMs serve as effective platforms for selective adsorption in separation processes, facilitating the purification of target molecules from mixtures. The customizable pore environments, consistent pore topologies, and framework flexibility of AFPMs collectively position them as powerful tools in molecular recognition, offering a versatile and adaptable solution to various challenges in analytical chemistry and materials science.^[28-48, 67] AFPMs will probably become more and more important in determining the direction of molecular recognition technologies as research progresses (Figure 1.9).

1.5.7 Magnetism Application

Advanced Functional Porous Materials (AFPMs) may not be primarily magnetized, but their special structural qualities and compositional flexibility make them interesting for use in magnetism-related domains. Customized magnetic functions can be achieved by designing AFPMs to include magnetic components or nanoparticles inside their porous frameworks. These materials find application in magnetic separation processes, where the porous matrices aid in the immobilization of magnetic nanoparticles for efficient removal of contaminants or targeted delivery in biomedical applications. AFPMs with magnetic components also show promise in magneto-responsive drug delivery systems, where external magnetic fields can be employed for controlled drug release. The versatility of AFPMs in accommodating magnetic elements and their porous nature makes them valuable in various technological applications where magnetic properties are leveraged for enhanced functionality.^[65-75] Although the field of magnetism in AFPMs is still developing, it is becoming increasingly evident that they have the ability to contribute to innovative technologies (Figure 1.9).

1.5.8 Biomedical Application

In the field of biomedical applications, Advanced Functional Porous Materials (AFPMs) hold immense promise due to their tailored structures and versatile functionalities. AFPMs can be engineered to serve as drug delivery carriers, leveraging their porous matrices to encapsulate and release pharmaceutical agents in a controlled and targeted manner. The high surface area and customizable pore environments of AFPMs make them ideal for loading therapeutic molecules, allowing for enhanced drug efficacy and reduced side effects. Moreover, the ability of AFPMs to immobilize biomolecules and exhibit biocompatibility positions them as excellent candidates for bio-sensing applications, facilitating the detection of specific biomarkers associated with diseases. AFPMs also find utility in tissue engineering, where their porous frameworks can support cell growth and provide a scaffold for regenerative medicine.^[73, 79] The adaptability of AFPMs in accommodating various functionalities and their compatibility with biological systems underscore their potential to revolutionize drug delivery, diagnostics, and regenerative medicine, contributing significantly to advancements in biomedical research and healthcare (Figure 1.9).

1.6 Chemical Separation

1.6.1 Overview and Importance in Various Industries and Environmental Contexts

Chemical separation procedures are essential methods used in many different sectors to separate and purify materials according to their chemical characteristics. These procedures are essential for assuring product quality, resolving environmental issues, and extracting pure components from complicated combinations. Chemical separation involves a number of techniques, each designed for a particular use case. Differential affinity between components and a stationary phase is the basis for chromatography, whereas distillation uses variations in boiling points to separate components in a liquid mixture. Membrane filtration, in contrast, divides materials according to variations in solubility or size.

The importance of chemical separation is evident in its widespread application across diverse industries. In the pharmaceutical sector, precise separation is essential for drug development, ensuring the purity and efficacy of medications. In the petrochemical industry, chemical separation processes such as distillation play a crucial role in refining crude oil into various valuable products like gasoline, diesel, and petrochemical feedstock. In the food and beverage industry, separation techniques are employed to purify and concentrate ingredients. Moreover, chemical separation is integral to the production of semiconductors, where highly pure materials are essential for electronic device fabrication.^[80-82]

Environmental contexts also highlight the significance of chemical separation. Wastewater treatment relies on separation processes to remove pollutants, ensuring that discharged water meets regulatory standards. Additionally, the remediation of contaminated sites involves separating harmful substances from the soil or groundwater, mitigating the environmental impact of industrial activities. Chemical separation contributes to sustainable practices by enabling the recycling of materials and reducing overall environmental pollution.^[80-85]

1.6.2 Significance of Advanced Porous Materials in Chemical Separation Processes

The significance of advanced porous materials in chemical separation processes lies in their unique properties and tailored design, which enable more efficient, selective, and sustainable separation methods compared to traditional techniques. These materials, including but not limited to metal-organic frameworks (MOFs), porous organic polymers (POPs), covalent organic frameworks (COFs), and hybrid composite materials offer distinct advantages that contribute to advancements in various industrial and environmental applications.^[86-90] Owing to the following unique characteristics these materials are exclusively used for sequestration of various chemicals both from air and water.

High Surface Area and Porosity: Advanced porous materials such as MOFs and COFs, typically possess large surface areas and well-defined pores. This characteristic provides an extensive contact area for interactions with target molecules, enhancing the adsorption and separation capacity of these materials.

Tailorable Pore Structures: The tunable nature of the pore structures in advanced porous materials allows for precise control over the size, shape, and functionality of the pores. This tunability enables the design of materials specifically tailored for the separation of target molecules, leading to enhanced selectivity and efficiency.

Selective Adsorption: Advanced porous materials exhibit selective adsorption properties, allowing them to preferentially capture certain molecules over others. This selectivity is crucial in industries such as pharmaceuticals, where the separation of closely related compounds is a common challenge.

Catalytic Properties: Some advanced porous materials also exhibit catalytic activity, enabling simultaneous separation and reaction processes. This dual functionality is particularly advantageous in applications such as catalysis and chemical synthesis.

Environmental Sustainability: The use of advanced porous materials in separation processes can contribute to environmentally sustainable practices. Their efficiency in capturing and isolating specific

components allows for the recycling of valuable materials and reduces the generation of waste, aligning with the principles of green chemistry.

Energy-Efficient Separation: Ongoing research explores the integration of advanced porous materials into novel separation technologies, with a focus on energy efficiency. Innovations in areas such as gas separation and molecular sieving contribute to more sustainable and cost-effective separation processes.

The significance of advanced porous materials in chemical separation processes stems from their unique properties and customizable structures, offering improved efficiency, selectivity, and sustainability compared to conventional separation methods. These materials contribute to advances in environmental stewardship and technology by playing a critical role in addressing complex separation challenges across industries.

1.6.3 Principles of Chemical Separation by Advanced Functional Porous Materials

The principles of chemical separation by advanced porous materials are grounded in the specific characteristics of these materials, such as their high surface area, tunable pore structures, and selective adsorption properties.^[86-90] Understanding these principles is crucial for designing and optimizing separation processes. A few of adsorption mechanisms are listed below:

Molecular Sieving: The porous nature of advanced materials allows for the size-based exclusion of molecules. Smaller molecules can penetrate and adsorb within the pores, while larger molecules are excluded. This molecular sieving effect is especially valuable for separating components with similar chemical properties but different sizes.

Surface Interactions: The surface of advanced porous materials often contains functional groups that can interact selectively with specific molecules. These interactions, such as hydrogen bonding or van der Waals forces, contribute to the adsorption of target molecules, providing a basis for separation.

Tailoring Materials for Targeted Separations: The ability to design and tailor the pore structures of advanced porous materials is a fundamental principle. Researchers and engineers can customize the size, shape, and chemical functionality of the pores to enhance the material's specificity for particular molecules or classes of compounds.

Selectivity and Specificity: Advanced porous materials exhibit selective adsorption, meaning they can preferentially adsorb certain molecules over others. This selectivity is determined by the interplay of pore size, shape, and surface chemistry. It enables the isolation of specific components from complex mixtures with high precision.

Equilibrium and Kinetics: The adsorption process by porous materials is governed by both thermodynamic equilibrium and kinetic considerations. Understanding the kinetics of adsorption and desorption is crucial for optimizing separation processes in terms of efficiency and speed.

Regeneration and Reusability: Advanced porous materials are designed to be reusable through regeneration processes. Owing to their heterogeneous nature, after adsorbing target molecules, these materials can often be regenerated by desorption or other means, allowing for multiple cycles of use without significant loss of performance.

1.6.4 Utility of Advanced Functional Porous Materials in Chemical Separation Application

Advanced functional porous materials have widely been used in chemical separation applications, including both industry and environment. A few these are listed below:

I. Applications in Industry:

Pharmaceutical Industry (Drug purification and synthesis), (Separation of complex chemical mixtures).

Petrochemical Industry (Hydrocarbon separation and purification), (Catalysis using porous materials).

II. Environmental Remediation:

Removal of pollutants from air (Radioactive wastes such as iodine, polyiodides, toxic gases, volatile organic compounds (VOCs), etc.).

Sustainable approaches to waste water treatment (Sequestration of metal ions, organic dyes, micro contaminants, etc.).

In this thesis, among these various field of chemical separation application, the separation of toxic species both from contaminated air and waste water has been successfully demonstrated by developing a range of different advanced functional porous materials and their hybrid composites.

1.6.5 Environmental Pollution

The term "environmental pollution," which describes the introduction of pollutants into the natural environment and their detrimental effects on ecosystems, human health, and biodiversity, is a pressing global issue. Pollution comes from a variety of sources, such as agriculture practices, transportation emissions, industrial activity, and inappropriate waste disposal. The two main types of pollution—water pollution and air pollution—each pose unique risks to the delicate balance of our planet. Pollutants like

greenhouse gases, hazardous chemicals, and plastic waste are released into the atmosphere, which not only deteriorates the quality of the air and water but also speeds up climate change. Urgent global efforts are necessary to reduce the effects of environmental pollution, promote sustainable practices, and protect the planet's health for coming generations as the world struggles with its effects.^[91-93]

A serious environmental problem, air pollution is caused by hazardous substances remaining in the atmosphere of the planet. These pollutants pose serious risks to both human health and the health of the planet as a whole. They are frequently released from industrial activities, vehicle emissions, and other human-made sources. Particulate matter, carbon monoxide, sulfur dioxide, nitrogen oxides, and ozone are examples of common air pollutants. One particular and worrisome aspect of environmental degradation is air pollution resulting from nuclear waste. Although the process of producing nuclear power doesn't release greenhouse gases, handling and disposing of radioactive waste does. Radioactive pollutants released into the air from nuclear facilities, accidents, or improper waste disposal can have severe consequences. Radioactive isotopes, such as iodine-131 and organic iodides, can be carried by air currents, leading to contamination of the atmosphere. This contamination poses a threat to human health, causing long-term health issues and increasing the risk of cancer. Furthermore, the release of radioactive materials into the atmosphere can have a wide range of ecological effects on wildlife and ecosystems. Sufficient protocols for the secure handling, transportation, and elimination of radioactive waste are imperative in order to alleviate the possible air pollution linked to these substances and ensure the enduring viability of nuclear energy as a means of energy.^[94-97]

Water pollution, stemming from both inorganic and organic pollutants, is a pervasive environmental challenge with wide-ranging consequences. Inorganic pollutants, such as heavy metals like mercury and lead, can enter water bodies through industrial discharges, agricultural runoff, or improper disposal of waste. Metal oxoanions such as arsenate (HAsO_4^{2-}), selenate (SeO_4^{2-}), chromate (CrO_4^{2-}), etc. are listed as highly toxic species in water by Environmental Protection Agency (EPA). These substances pose significant health risks to aquatic ecosystems and can accumulate in the food chain, impacting human health when contaminated water is consumed. On the other hand, organic pollutants, including organic dyes, antibiotics, pesticides, fertilizers, and various industrial chemicals, can contribute to water pollution through runoff and direct discharges. These substances can lead to nutrient imbalances, harmful algal blooms, and the degradation of water quality. The interplay of inorganic and organic pollutants leads to the degradation of water ecosystems, posing a threat to aquatic life, upsetting ecosystems, and compromising the accessibility of potable water for human consumption. To protect this essential resource, water pollution must be addressed through extensive regulatory measures, sustainable agricultural practices, enhanced waste management, and the creation of environmentally friendly technologies.^[93-99]

1.6.6 Role of Advanced Functional Porous Materials in Environmental Remediation

Advanced functional porous materials play a crucial role in environmental remediation by offering innovative and efficient solutions for the removal of pollutants from air, water, and soil. These materials, which include metal-organic frameworks (MOFs), covalent organic frameworks (COFs), porous organic polymers (POPs), and other porous structures, provide unique properties that make them well-suited for addressing environmental challenges (Figure 1.10).^[100-103] The high surface area and tunable porosity of advanced porous materials make them excellent candidates for adsorbing a wide range of contaminants. They can selectively capture pollutants such as heavy metals, organic compounds, and volatile organic compounds (VOCs) from air and water, contributing to the purification of these environmental matrices. The selectivity of advanced porous materials allows for the targeted removal of specific contaminants, even in the presence of complex mixtures. This capability is valuable in situations where the separation of one pollutant from a mixture of various substances is required for effective remediation. Many advanced porous materials exhibit a strong affinity for heavy metal oxoanions. This property is harnessed for the removal of toxic metals like arsenate, selenate, chromate, etc. from industrial wastewater, preventing their entry into ecosystems and potential harm to human health. Advanced porous materials are employed in water treatment processes to remove impurities, organic pollutants, and even microorganisms such as organic dyes, antibiotics, pharmaceuticals, etc. Their ability to selectively adsorb contaminants helps improve the quality of drinking water and protects aquatic ecosystems (Figure 1.10).^[100-105] Porous materials with tailored structures can selectively capture volatile organic compounds, which are prevalent air pollutants emitted from industrial processes and vehicular activities. Remediation of gaseous nuclear waste such as radioactive iodine, organic iodides, etc. are also highly important in terms of safe and effective development of nuclear industry as well as reducing the environmental pollution by eliminating these toxic species before discharging into the air (Figure 1.10). This is also crucial for effective management of nuclear waste and thus help in the development of low-carbon energy based nuclear industry. In together, this aids in reducing air pollution and mitigating associated health risks. Some advanced porous materials possess catalytic properties that can facilitate the degradation of pollutants. By promoting chemical reactions that break down contaminants into less harmful substances, these materials contribute to the overall remediation of polluted environments. Porous materials with hydrophobic properties are utilized in the cleanup of oil spills. These materials can selectively adsorb hydrophobic substances, such as oil and hydrocarbons, from water surfaces, offering an effective and environmentally friendly approach to mitigating the impact of oil spills. Advanced porous materials are employed for capturing and removing harmful gases, such as nitrogen oxides and sulfur dioxide, from industrial emissions. This application aids in reducing air pollution and meeting environmental regulations. In water remediation, advanced porous materials assist in the containment and removal of contaminants, preventing their migration into groundwater and

minimizing the long-term impact on ecosystems. This supports sustainable waste management practices. The multifaceted capabilities of advanced functional porous materials make them invaluable tools in environmental remediation efforts (Figure 1.10).^[100-107] Their use in selectively adsorbing and catalytically degrading pollutants contributes to the development of sustainable and efficient solutions for safeguarding the environment and public health.

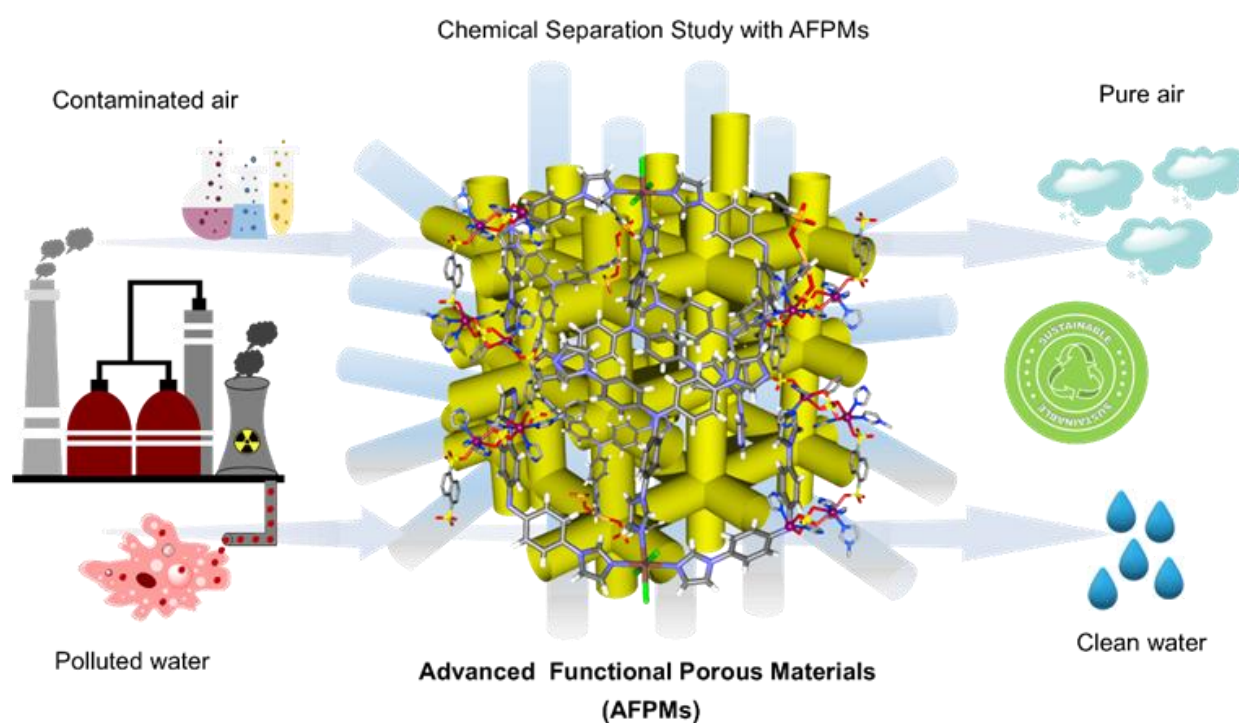


Figure 1.10: Schematic illustration of utilization of advanced functional porous materials towards chemical separation applications or remediation of environmental pollution.

1.6.7 Challenges and Opportunities of Advanced Functional Porous Materials in Chemical Separation Application

Although, an exclusive number of advanced porous materials have been successfully utilized for efficient chemical separation application, there are still many challenges that need to be addressed. These challenges are listed here. Some advanced porous materials may face challenges related to stability and durability, especially in harsh chemical environments. The continuous exposure to aggressive substances during separation processes can lead to degradation of the material over time, impacting its effectiveness. While advanced porous materials are designed to be reusable, the regeneration process may pose challenges. Efficient and cost-effective regeneration methods need to be

developed to ensure that the materials can maintain their performance over multiple cycles without significant degradation. Scaling up the production and application of advanced porous materials for industrial processes can be challenging. Achieving consistent material quality and reproducibility on a large scale is essential for widespread adoption but may encounter hurdles in terms of cost and feasibility. Achieving high selectivity in the separation of components from complex mixtures can be challenging. The presence of similar-sized molecules or closely related chemical species may lead to difficulty in achieving the desired level of specificity in certain applications. Some separation processes involving advanced porous materials may require elevated temperatures or pressure conditions, leading to increased energy consumption. Addressing energy efficiency challenges is crucial for the practical implementation of these materials in large-scale industrial settings. While challenges exist, the opportunities presented by advanced functional porous materials and their hybrid composite porous materials in chemical separation applications are vast. In this thesis, a few of efficient strategies have been documented to demonstrate the improved pollutants segregation efficiencies by developing novel functional porous materials. Continued research and innovation in material science, process optimization, and integration with other technologies hold the key to unlocking the full potential of these materials in addressing complex separation challenges across various industries.

1.7 Thesis Overview

The design and synthesis of task-specific advanced functional porous materials (AFPMS), such as covalent organic framework (COF), porous organic polymer (POP), and porous hybrid composite materials of metal-organic polyhedra (MOP) with metal-organic gel (MOG) and COF, are the primary areas of concentration for the current thesis work. These materials are intended to selectively and effectively sequester a variety of toxic chemicals from both water and air medium. Task-driven AFPMS and their hybrids were designed with a focus on function by carefully examining several crucial design factors, including the appropriate choice of monomers, the strategic modulation of the post-functionalization structure to impart the desired charge and functionalities, and the induction of hierarchical porosity toward target-specific applications. Leveraging on the molecular level configuration and macroscopic architecture control that AFPMS can offer, tailor made “nanospace” both in terms of hierarchical porosity, electrostatics and desired chemical specific functionalities was realized in all the scientific works presented in the current thesis. The overall thesis has two sections each of which is further sub-divided into two chapters. The first part of the thesis work describe the role of functionality, in terms of both chemical configuration and hierarchical porosity of porous organic materials (COFs and POPs) and their strategic utility as the ideal adsorbent for sequestration of toxic air and water contaminants. Subsequently, the second section of the thesis concentrates on the creation

and exploration of innovative hybrid composite porous materials for the effective sequestration of radioactive waste species and the successful segregation of emerging water contaminants, two urgent global issues that require prompt mitigation.

In the second chapter (chapter 2) in order to understand the role of framework integrated functionalities of porous organic materials towards sequestration of radioactive waste species such as organic iodides, a series of chemically stable porous covalent organic frameworks (COFs) have been synthesized by varying the number of N-heteroatomic sites. The results of this systematic strategy-driven study showed that the porosity or surface area of these COFs, as well as their N-heteroatomic or heterocyclic functions like imine, pyridine, and triazine sites, positively correlated with the methyl iodide (CH₃I) adsorption capability. This work offers guidance for the design and development of novel porous adsorbents, such as COFs, for pertinent adsorption applications. It also presents critical importance for understanding the toxic gas's adsorption mechanisms. Along this line, the knowledge gained from this work in terms of design, synthesis and role of tunable porosity and functionality of robust porous organic materials (POMs) was encouraged in the follow up work to demonstrate the role of higher order porosity such as macropores of POMs towards improved separation performance for a range of organic and inorganic toxic water pollutants, a charged chemically stable highly ordered macro-micro hierarchically porous organic network material was synthesized in chapter 3. The developed cationic interconnected macroporous viologen organic network material demonstrated ultrafast removal efficiency toward a range of organic and inorganic anionic toxic pollutants, including antibiotic molecules, organic dyes, metal oxyanions, etc. from water. Significantly, effective mass transport via the interconnected ordered hierarchically porous structure was identified as the cause of the compound's increased removal effectiveness towards guest anions.

On our effort in crafting task-specific advanced functional porous materials (AFPMS) for energy-efficient chemical separation application, we continued our endeavor zeroing on development of innovative hybrid composite porous materials. Because of their combined advantages and excellent performance, composite porous materials are starting to look more favorable than individual porous materials. According to this perspective, due to their distinctive and innovative qualities for task-specific applications, hybrid composite materials have grown in popularity and are now a subject of desired research. To accomplish this, in chapter 4, a unique anion exchangeable hybrid composite aerogel material was fabricated by embedding a stable cationic nanosized metal-organic polyhedra with a hierarchically porous metal-organic gel to utilize it as a potential adsorbent for metal-based group of toxic oxoanions. In water with an excessive amount of other coexisting anions, the composite scavenger showed very selective and rapid segregation efficiency towards several hazardous metal-oxoanions such as HAsO₄²⁻, SeO₄²⁻, ReO₄⁻, CrO₄²⁻, and MnO₄⁻. The material can successfully remove arsenate from both natural drinking water samples and simulated industrial effluent samples. It can also

selectively remove trace arsenate even at low concentrations, much below the As(V) limit in drinking water set by the WHO. In order to verify the composite's sustainability, its practical application was investigated using actual drinking water samples. Outstanding reusability performance and arsenate trapping effectiveness were noted. Inspired by the ingenious multifunctional properties of advanced hybrid composite porous materials, in next chapter 5, further effort has been made in order to develop another hybrid aerogel material by covalently joining of amino functional cationic metal-organic polyhedra (MOP) with imine functional dual pore-based covalent organic framework (COF). The light-weight composite material displayed large surface area with hierarchical macro-micro porosity and multifunctional active binding sites, which collectively interact with iodine, an emerging radioactive waste. The developed nano-adsorbent showed ultrahigh vapor phase iodine adsorption capacity in both static and dynamic conditions. Moreover, the composite was found to exhibit rapid adsorption kinetics towards both molecular iodine and polyiodide species in aqueous phase and organic solvent with high sorption capacity and thus provides scope for real time application. The mechanistic involvement of multifunctional binding sites such as metal nanocluster and heteroatom functionality, cationic nature of the hybrid was found to responsible behind the selective and fast adsorption of radioiodine.

1.8 Reference

- [1] Bryan, C. P. *Ancient Egyptian Medicine: The Papyrus Ebers*. (Ares Chicago, **1974**).
- [2] G. S. Day, F. Drake, H.-C. Zhou and M. M. Ryder, *Commun. Chem.*, **2021**, *4*, 114.
- [3] E. M. Diamond, and K. T. H. Farrer, *Mariner's Mirror*, **2005**, *91*, 548–553.
- [4] A. F. Cronstedt, , J. L. Schlenker, & G. H. Köhl, *Proceedings from the Ninth International Zeolite Conference*. (eds von Ballmoos, R., Higgins, J. B. & Treacy, M. M. J.) 3-9 (Butterworth-Heinemann, **1993**).
- [5] T. D. Bennett, F.-X. Coudert, S. L. James and A. I. Cooper, *Nat. Mat.*, **2021**, *20*, 1179-1187.
- [6] M. E. Davis, *Nature*, **2002**, *417*, 813-821.
- [7] A. Corma, *Chem. Rev.*, **1997**, *97*, 2373-2419.
- [8] A. G. Slater, A. I. Cooper, *Science*, **2015**, *348*, aaa8075.
- [9] H. Furukawa, K. E. Cordova, M. O'Keeffe and O. M. Yaghi, *Science*, **2013**, *341*, 6149.
- [10] H.-C. Zhou, J. R. Long and O. M. Yaghi, *Chem. Rev.*, **2012**, *112*, 673-674.
- [11] S. Horike, S. Shimomura and S. Kitagawa, *Nat. Chem.*, **2009**, *1*, 695-704.

- [12] F. Fajula, A. Galarneau, F. Di Renzo, *Microporous Mesoporous Mater.* **2005**, *82*, 227-239.
- [13] D. Zhao, P. K. Thallapally, C. Petit, J. Gascon, *ACS Sustainable Chem. Eng.*, **2019**, *7*, 7997-7998.
- [14] X.Y. Yang, L.-H. Chen, Y. Li, J. C. Rooke, C. Sanchez, B.-L. Su, *Chem. Soc. Rev.*, **2017**, *46*, 481-558.
- [15] J. Zhang, J. Chen, S. Peng, Z. Zhang, Y. Tong, P. W. Miller, X.-P. Yan, *Chem. Soc. Rev.*, **2019**, *48*, 2566-2595.
- [16] J. Yu, A. Corma, Y. Li, *Adv. Mater.* **2020**, *32*, 2006277.
- [17] M. J. Bojdys, M. I. E. Briggs, J. T. A. Jones, D. J. Adams, S. Y. Chong, M. Schmidtman and A. I. Cooper, *J. Am. Chem. Soc.*, **2011**, *133*, 16566-16571.
- [18] H.-C. Zhou and S. Kitagawa, *Chem. Soc. Rev.*, **2014**, *43*, 5415-5418.
- [19] D. J. Tranchemontagne, Z. Ni, M. O’Keeffe and Omar M. Yaghi, *Angew. Chem., Int. Ed.*, **2008**, *47*, 5136-5147.
- [20] N. Ahmad, H. A. Younus, A. H. Chughtai and F. Verpoort, *Chem. Soc. Rev.*, **2015**, *44*, 9-25.
- [21] M.A. Little and A. I. Cooper, *Adv. Funct. Mater.* **2020**, *30*, 1909842.
- [22] S. Yuan, X. Li, J. Zhu, G. Zhang, P. V. Puyvelde and B. V. Bruggen, *Chem. Soc. Rev.*, **2019**, *48*, 2665-2681.
- [23] D. Wu, F. Xu, B. Sun, R. Fu, H. He and K. Matyjaszewski, *Chem. Rev.*, **2012**, *112*, 3959-4015.
- [24] J. R. Holst, A. Trewin and A. I. Cooper, *Nat. Chem.*, **2010**, *2*, 915-920.
- [25] S. M. Cohen, *J. Am. Chem. Soc.*, **2017**, *139*, 2855-2863.
- [26] S. Dutta, Y. D. More, S. Fajal, W. Mandal, G. K. Dam, S. K. Ghosh, *Chem. Commun.*, **2022**, *58*, 13676-13698.
- [27] A. Karmakar, A. V. Desai and S. K. Ghosh, *Coord. Chem. Rev.*, **2016**, *307*, 313-341.
- [28] W. P. Lustig, S. Mukherjee, N. D. Rudd, A. V. Desai, J. Li, S. K. Ghosh, *Chem. Soc. Rev.* **2017**, *46*, 3242-3285.
- [29] Y.-S. Wei, M. Zhang, R. Zou, Q. Xu, *Chem. Rev.* **2020**, *120*, *21*, 12089–12174.
- [30] B. Li, H.-M. Wen, Y. Cui, W. Zhou, G. Qian, B. Chen, *Adv. Mater.* **2016**, *28*, 8819–8860.
- [31] J. K. Wychowaniec, H. Saini, B. Scheibe, D. P. Dubal, A. Schneemann, K. Jayaramulu, *Chem. Soc. Rev.*, **2022**, *51*, 9068–9126.

- [32] J. Hou, A. F. Sapnik, T. D. Bennett, *Chem. Sci.*, **2020**, *11*, 310–323.
- [33] K. Sumida, K. Liang, J. Reboul, I. A. Ibarra, S. Furukawa, P. Falcaro, *Chem. Mater.* **2017**, *29*, 2626–2645.
- [34] E.-Gonzalez, M. Y. Tsang, J. Troyano, G. A. Craig, S. Furukawa, *Chem. Soc. Rev.*, **2022**, *51*, 4876–4889.
- [35] E. J. Gosselin, C. A. Rowland, E. D. Bloch, *Chem. Rev.* **2020**, *120*, 8987–9014.
- [36] E. G. Percastegui, *Chem. Commun.*, **2022**, *58*, 5055–5071.
- [37] E.-S. M. El-Sayed, Y. D. Yuan, D. Zhao, D. Yuan, *Acc. Chem. Res.* **2022**, *55*, 1546–1560.
- [38] J.-S. M. Lee, A. I. Cooper, *Chem. Rev.* **2020**, *120*, 4, 2171–2214.
- [39] S. Das, P. Heasman, T. Ben, S. Qiu, *Chem. Rev.* **2017**, *117*, 1515–1563.
- [40] N. Chaoui, M. Trunk, R. Dawson, H. Schmidt, A. Thomas, *Chem. Soc. Rev.*, **2017**, *46*, 3302–3321.
- [41] S.-Y. Ding, W. Wang, *Chem. Soc. Rev.*, **2013**, *42*, 548–568.
- [42] Z. Qian, Z. J. Wang, K. A. I. Zhang, *Chem. Mater.* **2021**, *33*, 1909–1926.
- [43] J. Wu, F. Xu, S. Li, P. Ma, X. Zhang, Q. Liu, R. Fu, D. Wu, *Adv. Mater.* **2019**, *31*, 1802922.
- [44] Z. Qian, Z. J. Wang, K. A. I. Zhang, *Chem. Mater.* **2021**, *33*, 1909–1926.
- [45] A. P. Cote, A. I. Benin, N. W. Ockwig, M. O’Keeffe, A. J. Matzger, O. M. Yaghi, *Science* **2005**, *310*, 1166–1170.
- [46] N. Huang, P. Wang, D. Jiang, *Nat. Rev. Mat.* **2016**, *1*, 16068.
- [47] Z. Wang, S. Zhang, Y. Chen, Z. Zhang, S. Ma, *Chem. Soc. Rev.*, **2020**, *49*, 708–735.
- [48] D.-G. Wang, T. Qiu, W. Guo, Z. Liang, H. Tabassum, D. Xia, R. Zou, *Energy Environ. Sci.*, **2021**, *14*, 688–728.
- [49] T. Tozawa, J. T. A. Jones, S. I. Swamy, S. Jiang, D. J. Adams, S. Shakespeare, R. Clowes, D. Bradshaw, T. Hasell, S. Y. Chong, C. Tang, S. Thompson, J. Parker, A. Trewin, J. Bacsá, A. M. Z. Slawin, A. Steiner, A. I. Cooper, *Nat. Mat.* **2009**, *8*, 973–978.
- [50] X. Yang, Z. Ullah, J. F. Stoddart, C. T. Yavuz, *Chem. Rev.* **2023**, *123*, 4602–4634.
- [51] C. R. Kim, T. Uemura, S. Kitagawa, *Chem. Soc. Rev.* **2016**, *45*, 3828–3845.
- [52] C. Rosler, R. A. Fischer, *CrystEngComm*, **2015**, *17*, 199–217.

- [53] A. Aijaz, Q. Xu, *J. Phys. Chem. Lett.* **2014**, *5*, 1400-1411.
- [54] S. Dang, Q. Zhu, Q. Xu, *Nat. Rev. Mater.* **2017**, *3*, 17075.
- [55] Y. Li, M. Karimi, Y.-N. Gong, N. Dai, V. Safarifard, H.-L. Jiang, *Matter*, **2021**, *4*, 2230-2265.
- [56] Z. Chen, X. Li, C. Yang, K. Cheng, T. Tan, Y. Lv, Y. Liu, *Adv. Sci.* **2021**, 2101883.
- [57] Y. Liu, W. Zhou, W. L. Teo, K. Wang, L. Zhang, Y. Zeng, Y. Zhao, *Chem*, **2020**, *6*, 3172-3202.
- [58] Q. Liu, Y. Song, Y. Ma, Y. Zhou, H. Cong, C. Wang, J. Wu, G. Hu, M. O'Keeffe, H. Deng, *J. Am. Chem. Soc.* **2019**, *141*, *1*, 488-496.
- [59] L. Chen, R. Luque, Y. Li, *Chem. Soc. Rev.* **2017**, *46*, 4614-4630.
- [60] H. Kong, Y. Chen, G. Yang, B. Liu, L. Guo, Y. Wang, X. Zhou, G. Wei, *Nanoscale Horiz.*, **2022**, *7*, 112-140.
- [61] Y. Chen, L. Zhang, Y. Yang, B. Pang, W. Xu, G. Duan, S. Jiang, K. Zhang, *Adv. Mater.* **2021**, *33*, 2005569.
- [62] Z. Inonu, S. Keskin, C. Erkey, *ACS Appl. Nano Mater.* **2018**, *1*, 5959-5980.
- [63] L. Huang, J. Yang, Y. Zhao, H. Miyata, M. Han, Q. Shuai, Y. Yamauchi, *Chem. Mater.* **2023**, *35*, 2661-2682.
- [64] H. Dou, M. Xu, B. Wang, Z. Zhang, G. Wen, Y. Zheng, D. Luo, L. Zhao, A. Yu, L. Zhang, Z. Jiang, Z. Chen, *Chem. Soc. Rev.*, **2021**, *50*, 986-1029.
- [65] Q.-L. Zhu, Q. Xu, *Chem. Soc. Rev.* **2014**, *43*, 5468-5512.
- [66] B. Seoane, J. Coronas, I. Gascon, M. Etxeberria Benavides, O. Karvan, J. Caro, F. Kapteijn, J. Gascon, *Chem. Soc. Rev.* **2015**, *44*, 2421-2454.
- [67] Y. Cui, J. Zhang, H. He, G. Qian, *Chem. Soc. Rev.* **2018**, *47*, 5740-5785.
- [68] S. Fajal, S. Dutta, S. K. Ghosh, *Mater. Horiz.*, **2023**, *10*, 4083-4138.
- [69] A. Dhakshinamoorthy, H. Garcia, *Chem. Soc. Rev.* **2012**, *41*, 5262-5284.
- [70] P. Samanta, A. V. Desai, S. Let, S. K. Ghosh, *ACS Sustainable Chem. Eng.*, **2019**, *7*, 7456-7478.
- [71] M. Mon, R. Bruno, J. Ferrando-Soria, D. Armentano, E. Pardo, *J. Mater. Chem. A*, **2018**, *6*, 4912-4947.
- [72] T. Kitao, Y. Zhang, S. Kitagawa, B. wang, T. Uemura, *Chem. Soc. Rev.* **2017**, *46*, 3108-3133.

- [73] N. Ahmad, H. A. Younus, A. H. Chughtai, F. Verpoort, *Chem. Soc. Rev.* **2015**, *44*, 9-25.
- [74] K. Liu, X. Zhang, X. Meng, W. Shi, P. Cheng, A. K. Powell, *Chem. Soc. Rev.* **2016**, *45*, 2423-2439.
- [74] C. Liu, J. Wang, J. Wan, C. Yu, *Coord. Chem. Rev.* **2021**, *432*, 213743.
- [75] G. Cai, P. Yan, L. Zhang, H.-C. Zhou, H.-L. Jiang, *Chem. Rev.* **2021**, *121*, 12278–12326.
- [76] M. Kalaj, K. C. Bentz, S. Ayala, Jr., J. M. Palomba, K. S. Barcus, Y. Katayama, S. M. Cohen, *Chem. Rev.* **2020**, *120*, 16, 8267–8302.
- [77] Q. Qian, P. A. Asinger, M. J. Lee, G. Han, K. M. Rodriguez, S. Lin, F. M. Benedetti, A. X. Wu, W. S. Chi, Z. P. Smith, *Chem. Rev.* **2020**, *120*, 16, 8161–8266.
- [78] S. Rojas, P. Horcajada, *Chem. Rev.* **2020**, *120*, 16, 8378–8415.
- [79] W. Liang, P. Wied, F. Carraro, C. J. Sumby, B. Nidetzky, C.-K. Tsung, P. Falcaro, C. J. Doonan, *Chem. Rev.* **2021**, *121*, 1077–1129.
- [80] D. S. Sholl, R. P. Lively, *Nature* **2016**, *532*, 435–437.
- [81] C. A. Jaksland, R. Gani, K. M. Lien, *Chem. Eng. Sci.* **1995**, *50*, 511-530.
- [82] Choppin, G.R. (1999). Overview of Chemical Separation Methods and Technologies. In: Choppin, G.R., Khankhasayev, M.K. (eds) *Chemical Separation Technologies and Related Methods of Nuclear Waste Management*. NATO Science Series, vol 53. Springer, Dordrecht. https://doi.org/10.1007/978-94-011-4546-6_1
- [83] D. L. Gin, R. D. Noble, *Science* **2021**, *332*, 674-676.
- [84] Y. Jiang, Y. Hu, B. Luan, L. Wang, R. Krishna, H. Ni, X. Hu, Y. Zhang, *Nat. Comm.* **2023**, *14*, 401.
- [85] Y. Wang, R. J. Abergel, *J. Chem. Educ.* **2023**, *100*, 4, 1603–1612.
- [86] E. Favre, *Front. Chem. Eng.*, **2022**, *4*, 916054.
- [87] C. E. Wilmer, O. K. Farha, Y.-S. Bae, J. T. Hupp, R. Q. Snurr, *Energy Environ. Sci.*, **2012**, *5*, 9849-9856.
- [88] Y. Wu, B. M. Weckhuysen, *Angew. Chem. Int. Ed.* **2021**, *60*, 18930–18949.
- [89] R. L. Siegelman, E. J. Kim, J. R. Long, *Nat. Mat.* **2021**, *20*, 1060–1072.
- [90] Y.-S. Bae, R. Q. Snurr, *Angew. Chem. Int. Ed.* **2011**, *50*, 11586 – 11596.

- [91] M. Mon, R. Bruno, J. Ferrando-Soria, D. Armentano and E. Pardo, *J. Mater. Chem. A*, **2018**, *6*, 4912–4947.
- [92] WWAP (United Nations World Water Assessment Water for a Sustainable World; The United Nations World Water Development Report: UNESCO: Paris, **2015**; pp 1–67.
- [93] D. T. Sun, L. Peng, W. S. Reeder, S. M. Moosavi, D. Tiana, D. K. Britt, E. Oveisi and W. L. Queen, *ACS Cent. Sci.*, **2018**, *4*, 349-356.
- [94] A. J. Howarth, Y. Liu, J. T. Hupp and O. K. Farha, *CrystEngComm*, **2015**, *17*, 7245–7253.
- [95] Organic Pollutants in Water, ed. I. H. Suffet and M. Malaiyandi, American Chemical Society, Washington, DC, **1986**, vol. 214.
- [96] I. Ali, M. Asim and T. A. Khan, *J. Environ. Manage.* **2012**, *113*, 170–183.
- [97] E. M. Dias and C. Petit, *J. Mater. Chem. A*, **2015**, *3*, 22484–22506.
- [98] M. M. Mekonnen, A. Y. Hoekstra, *Sci. Adv.* **2016**, *2*, e1500323.
- [99] R. C. Ewing, F. N. von Hippel, *Science* **2009**, *325*, 151-152.
- [100] Y. Song, J. Phipps, C. Zhu, S. Ma, *Angew. Chem. Int. Ed.* **2023**, *62*, e202216724.
- [101] J. R. Werber, C. O. Osuji, M. Elimelech, *Nat. Rev. Mat.* **2016**, *1*, 16018.
- [102] A. A. Uliana, N. T. Bui, J. Kamcev, M. K. Taylor, J. J. Urban, J. R. Long, *Science* **2021**, *372*, 296-299.
- [103] S. Bolisetty, M. Peydayesh, R. Mezzenga, *Chem. Soc. Rev.*, **2019**, *48*, 463—487.
- [104] Q. Sun, B. Aguila, S. Ma, *Trends in Chemistry*, **2019**, *3*, 292-303.
- [105] B. Zheng, X. Lin, X. Zhang, D. Wu, K. Matyjaszewski, *Adv. Funct. Mater.* **2020**, *30*, 1907006.
- [106] J. Li, X. Wang, G. Zhao, C. Chen, Z. Chai, A. Alsaedi, T. Hayat, X. Wang, *Chem. Soc. Rev.*, **2018**, *47*, 2322—2356.
- [107] D. Banerjee, D. Kim, M. J. Schweiger, A. A. Kruger, P. K. Thallapally, *Chem. Soc. Rev.*, **2016**, *45*, 2724—2739.

Section A

**Advanced Functional Porous
Organic Materials for Separation of
Toxic Gases and Water
Contaminants**

In recent times, there has been a significant surge in global research attention focused on advanced functional porous materials (AFPMS) owing to their distinctive attributes and the advantages they offer in terms of precise molecular-level control. As was previously said, AFPMS can be broadly divided into two categories: pure organic porous materials and inorganic-organic hybrid porous materials. One of the methods used to manufacture metal-free porous organic materials is the construction of pure organic porous materials using only organic functionalized molecular blocks, which are connected by covalent bonds and noncovalent interactions. On the basis of this, the field of advanced functional porous materials comprises the following: hydrogen-bonded organic frameworks (HOFs), supramolecular organic frameworks (SOFs), covalent organic frameworks (COFs), porous organic polymers (POPs), porous organic cages (POCs), etc.^[1, 2] In this section, utility of functional porous organic materials such as COFs and POPs have been demonstrated. Porous organic materials (POMs) are materials made of organic building blocks arranged in a network of linked voids and channels. These materials frequently include organic linkers or aromatic rings as functionalities. POMs have the ability to display large surface areas and modify the size of their pores, which opens up possibilities for gas storage, catalysis, and selective adsorption. The capacity to precisely regulate the structure and properties of these materials during design and synthesis adds to their versatility. Applications for porous organic materials include water purification and gas separation demonstrating their importance in tackling issues in the environmental, and energy realms.^[3, 4]

This section consist of two chapters i.e. chapter 2 and chapter 3. In chapter 2, a systematic strategy-driven study has been performed to demonstrate the role of framework integrated functionalities along with textural properties of a series of covalent organic frameworks (COFs) towards efficient sequestration of toxic nuclear waste such as organic iodides from air medium. While in chapter 3, investigation of role of higher order porosity i.e. macro-micro hierarchical porosity over typical meso and micro porosity, towards improved separation of large organic persistence pollutants from water has been demonstrated by developing an ordered interconnected charged macro-micro porous viologen organic network material. In both these two chapters, the studies focuses on rational design and successful development of functionalized advanced organic porous materials for sequestration of toxic gaseous and water contaminants.

References:

- [1] J.-S. M. Lee, A. I. Cooper, *Chem. Rev.* **2020**, *120*, 4, 2171–2214.
- [2] J. Wu, F. Xu, S. Li, P. Ma, X. Zhang, Q. Liu, R. Fu, D. Wu, *Adv. Mater.* **2019**, *31*, 1802922.
- [3] S. Das, P. Heasman, T. Ben, S. Qiu, *Chem. Rev.* **2017**, *117*, 1515–1563.
- [4] Y. Song, Q. Sun, B. Aguila, S. Ma, *Adv. Sci.* **2019**, *6*, 1801410.

Chapter 2

Unraveling Mechanistic Insights into Covalent Organic Frameworks for Highly Efficient Sequestration of Organic Iodides from Simulated Nuclear Waste

2.1 Introduction

The usage of nuclear power for global energy systems has attracted significant interest and is predicted to increase in the near future due to the urgently growing needs for high-efficiency and economical, potential, and sustainable energy.^[1,2] In nuclear plants, during the generation of nuclear energy, the used nuclear fuel rods need to be reprocessed by dissolving in concentrated hot nitric acid. In this dissolution protocol, apart from the molecular iodine, nitric acid vapor, NO₂, and N₂O₅, another highly radioactive dissolved off-gas (DOG) species, organic iodides, e.g., methyl iodide (CH₃I) and ethyl iodide (CH₃CH₂I), are generated.^[3–5] Radioactive organic iodide (ROI) vapor is extremely harmful to living beings due to its substantially higher activity and has therefore attracted a significant amount of public attention, especially in the event of a nuclear disaster.^[5–7] Therefore, considering both the environmental as well as human health concerns along with future development and the safe generation of nuclear energy, efficient sequestration of these radioactive species from the air has attracted much research interest in recent years. However, it was found that trapping these ROI species is considerably difficult owing to their lower adsorption rate towards specific adsorbents (Ag@MOR)^[5–7] and poor retention efficiency. Past studies have established the use of solid sorbent-based fixed-bed technologies for radionuclide sequestration as more advantageous over other traditional methods owing to their relatively simple operation, cost-effectiveness, and high efficiency.^[8–12] Among the employed solid adsorbents, silver nanoparticles or ions impregnated or exchanged on silica, zeolites, alumina, activated carbon, aerogel, etc., have been explored as potential sorbents for the capture of radioiodine and ROIs.^[5, 7–12] However, their lower efficiency with poor selectivity, low sorption capacity, and weak retention ability limit their real-time utility towards ROI capture. Moreover, the high cost associated with the use of novel metals along with the poor regeneration capability, have kept these materials far from practical implementation. Most of these studies have focused on the capture of iodine but the investigation of ROIs sequestration is still limited. This has impelled researchers toward the development of new effective regenerable sorbent materials for the successful removal of radioactive ROIs from contaminated air.

In the past few years, rational design strategies have yielded several excellent advanced porous materials for the specific sequestration of ROI species. In this regard, metal–organic frameworks (MOFs)^[13–15] and porous organic polymers (POPs)^[16, 17] or covalent organic frameworks (COFs)^[18–20] are two widely-known porous materials constructed from the coordination of metal ions/clusters with organic linkers and with the covalent assembly of pure organic small molecules, respectively, which have been successfully tested for the capture of CH₃I or CH₃CH₂I.^[7, 21–26] These materials were found to exhibit excellent ROI adsorption capacities due to their collective properties of high porosity with large pore volume and tailored surface functionalities.^[21–25] Li et al. explored the potential of a chemically stable Cr-MOF (Cr-MIL), post-synthetically modified with tertiary amine binding sites, as an effective

molecular trap for the capture of radioactive organic iodides with high adsorption capacities and regeneration ability at a high temperature (150 °C) and at room temperature.^[7] Interestingly, under similar conditions, the CH₃I sorption capacity for this adsorbent was found to be higher than the commercially used adsorbent (Ag@MOR). On the other hand, as another promising class of adsorbents, POPs or COFs have been recently shown to exhibit outstanding ROI sorption performance.^[21–25] In a recent report, Dai et al. investigated the utility of a pillar[5]quinone-derived multi-microporous organic polymer with hydrophenazine linkages for excellent iodomethane capture, which was found to be higher than its analogous microporous hydrophenazine-linked organic polymers.^[25] In another interesting work, Wang reported the ultra-high adsorption capacity of methyl iodide (1.45 g g⁻¹) under static sorption conditions via the methylation of bipyridine groups of a nitrogen-rich COF (SCUCOF-2).^[23] Han et al. recently demonstrated the record high methyl iodide capture capacity (1.53 g g⁻¹) in static mode at room temperature by developing a rationally functionalized COF (COFTAPT). The adsorbent also revealed a high iodine (I₂) capture capacity in dynamic mode from a mixture of I₂ and CH₃I. Most importantly, the CH₃I sorption capacity was found to depend upon the structural-functional binding sites of the framework, whereas the textural properties (such as porosity, surface area, and pore volume) were found to be not related to the iodomethane adsorption capacity.^[22] All these pioneering works have explored effective individual strategies to develop functional porous materials based on excellent adsorbents for ROI capture. Among them, the doping of heteroatoms and incorporation of N-containing heterocyclic structural moieties, such as imine, pyridine, triazine, etc., are rational approaches for the potent sequestration of ROIs. However, a general study to demonstrate the systematic investigation of the ROI capture performance by fine-tuning functional recognition sites with a series of crystalline porous organic framework materials is still unexplored territory. In addition, a complete mechanistic understanding of the function of N-containing structural moieties along with the textural properties of COFs towards ROI capture is not precisely understood. Given that the radioactive organic iodides produced as nuclear waste from the treatment of spent nuclear fuel with a hot concentrated nitric acid solution, the high chemical, hydrolytic, thermal and radiological tolerance ability of the adsorbent in various harsh chemical conditions and reprocessing temperature is a preliminary requirement for the practical utilization of the sorbent. Most studies have been focused only on the adsorption capacity of ROI trapping either in dry or humid conditions, however, the effective sequestration of these species from highly acidic conditions along with operating temperature (~150 °C) and irradiation have hardly been explored. This might be because of the lower chemical, thermal and radiological stability of the developed adsorbents. Therefore, it is particularly important to develop effective adsorbents with high chemical, thermal and radiological tolerance pertaining to real-time application.

Taking these all aspects into consideration, herein, we deliberately chose a series of four imine COFs with well-defined porosity, constructed from the covalent threading of 2-hydroxybenzene-1,3,5-

tricarbaldehyde with four different triamines as illustrated in figure 2.1. The architecture of the structurally analogous COFs featured various N-containing heterocyclic structural moieties including benzene core tri-phenyl (for COF-A), pyridine core tri-phenyl (for COF-B), triazine core tri-phenyl (for COF-C), and triazine core tri-pyridine (for COF-D) as specific recognition sites that can facilitate variable interactions with ROIs. The microenvironment of these isostructural COFs was regulated by introducing functional sites on the organic linkers in the COF building units.

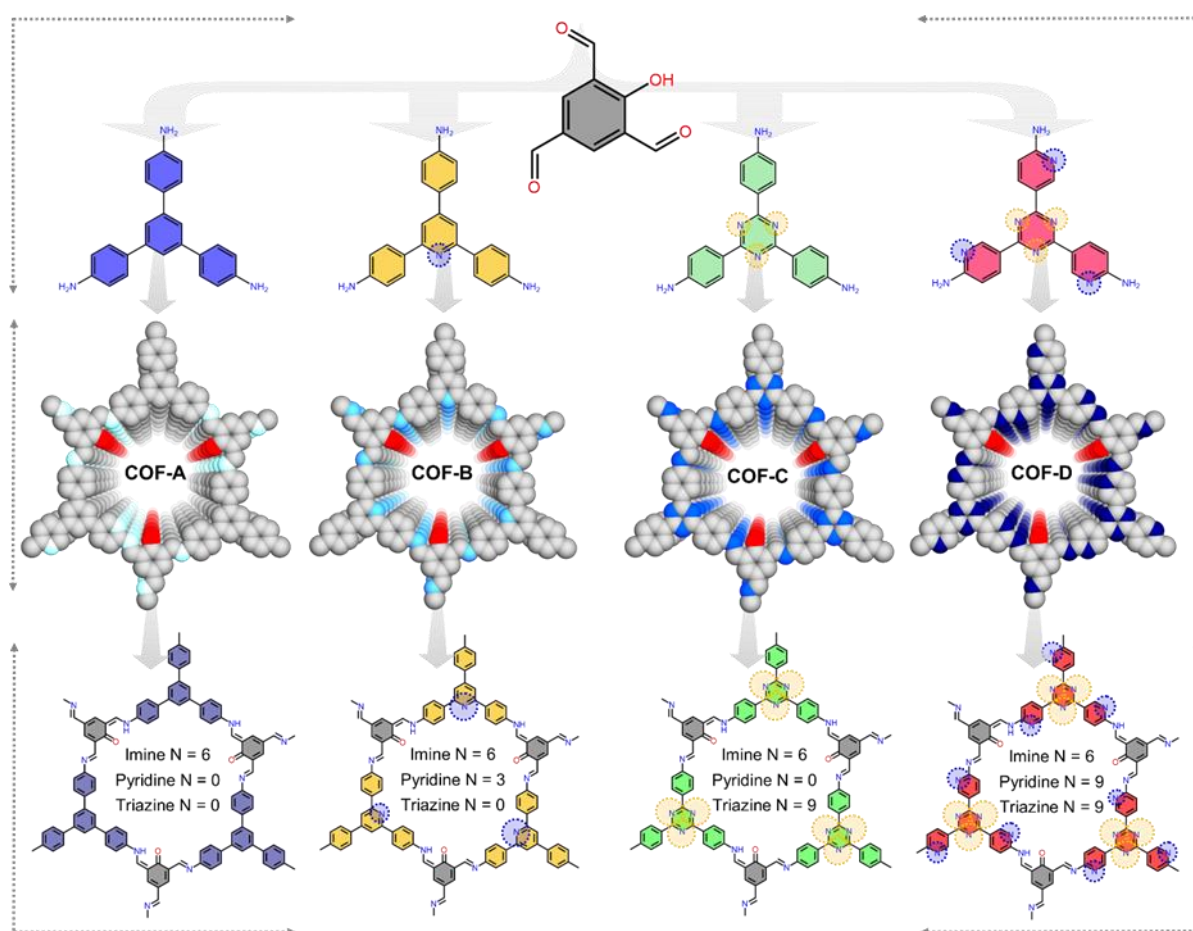
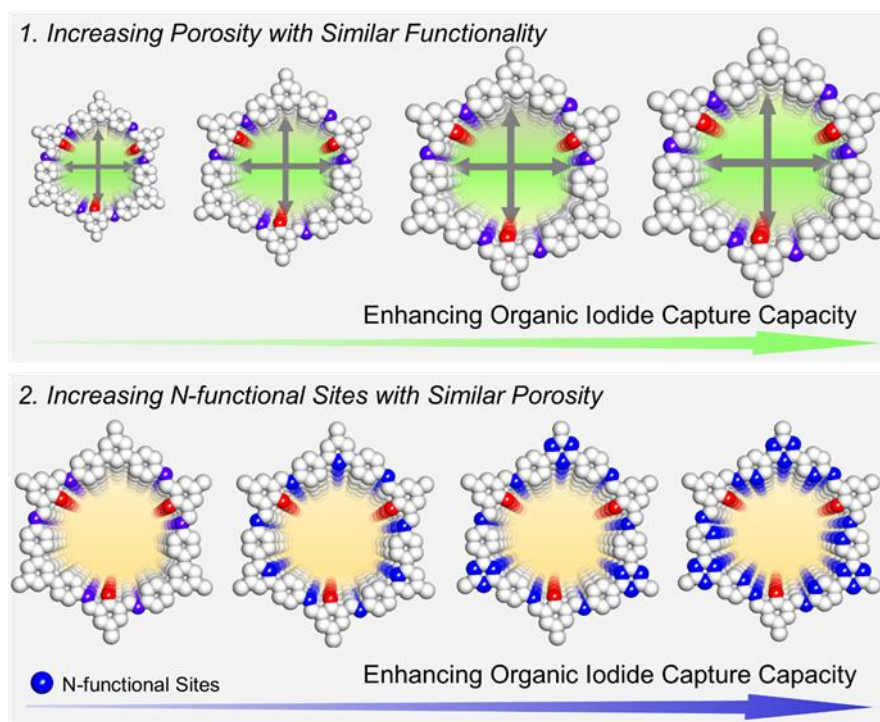


Figure 2.1: Schematic representation of synthesis, packing diagram and chemical structure of COF-A, COF-B, COF-C and COF-D with their respective precursors. The number of different N sites present in the unit of COFs structure.

The programmed functional moieties influence the interactions between the surface of the COFs and ROI species, therefore altering the affinity along with offering an understanding of the role of various N-containing sites in the sorption process of ROIs (Scheme 2.1). The detailed investigation revealed that under static conditions, moving from COF-A to COF-D, the ROIs' uptake capacities were found to

decrease systematically. Surprisingly, COF-A exhibited the highest ROI (both CH_3I and $\text{CH}_3\text{CH}_2\text{I}$) uptake capacity, which could be attributed to the dominant factor of porosity over extra surface functionality (Scheme 2.1). COF-A was found to exhibit high CH_3I capture capacities in both static and dynamic modes under all relevant conditions, including elevated temperatures ($\sim 150\text{ }^\circ\text{C}$), irradiation, and the presence of acid and moisture. Systematic studies further revealed that when these COFs were synthesized with identical porosities, interestingly, the ROI uptake capacities were found to correspond positively with the adsorbent's nitrogen content (Scheme 2.1). This phenomenon can be explained by the combined effect of more N-doped functional sites and textural properties such as large surface area, pore volume and pore size (Scheme 2.1). Moreover, these chemically stable efficient adsorbents were found to adsorb ROIs in a cyclic manner without largely compromising their sorption efficiencies. Both experimental characterizations and theoretical calculations were carried out in order to demonstrate the in-depth mechanistic insights behind such effective binding of ROIs with different N-functional sites of the COFs. Our research demonstrated that the fabrication and optimization of such adsorbents can be expanded to other materials by a rational integration of specific N-containing functional sites along with robust framework configuration, which may result in the development of various effective adsorbents with ultrahigh enrichment indexes for radioactive ROI species from nuclear waste.



Scheme 2.1: Schematic illustration for enhanced organic iodide capture capacity by (1) increasing porosity and (2) increasing N-functional sites of COFs.

2.2 Experimental

2.2.1. Materials: All the reagents, starting materials and solvents were commercially purchased from Sigma-Aldrich, TCI Chemicals and Spectrochem depending on their availability and used without further purification. 1, 3, 5-tris-(4-aminophenyl)-benzene was purchased from TCI chemicals.

2.2.2. Safety Note: Methyl iodide and ethyl iodide vapor is toxic in nature and proper protective gear (masks, gloves) is always to be used. The organic iodide capture protocol described in this report that uses acid (in dynamic sorption) in a packed tube at high temperature must be carried out under strict safety precautions.

2.2.3. General Characterizations and Physical Measurements:

2.2.3.1. Powder X-ray diffraction (PXRD): Powder X-ray diffraction (PXRD) experiments were performed on a Bruker D8 Advanced X-ray diffractometer at room temperature using Cu K α radiation ($\lambda = 1.5406 \text{ \AA}$) at a scan speed of $0.5^\circ \text{ min}^{-1}$ and a step size of 0.01° in 2θ .

2.2.3.2. Fourier transform infrared spectroscopy (FT-IR): The FT-IR spectra were acquired by using Bruker Optics ALPHA-II spectrophotometer using KBr pellet in $500\text{-}4000 \text{ cm}^{-1}$ range. The FT-IR data are reported with a wave number (cm^{-1}) scale in $500\text{-}4000 \text{ cm}^{-1}$ range.

2.2.3.3. Thermogravimetric analysis (TGA): Thermogravimetric analyses were recorded on Perkin-Elmer STA 6000 TGA analyzer by heating the samples from 40 to $800 \text{ }^\circ\text{C}$ under N_2 atmosphere with a heating rate of $10 \text{ }^\circ\text{C min}^{-1}$.

2.2.3.4. Solid-state nuclear magnetic resonance (NMR) spectroscopy: Solid-state ^{13}C cross-polarization-magic angle spinning (CP-MAS) spectra were conducted on a Bruker 500 MHz NMR spectrometer with a CP-MAS probe. Carbon chemical shifts are expressed in parts per million (δ scale).

2.2.3.5. X-ray photoelectron spectroscopy (XPS): As-obtained powder samples was stuck to conductive paste and then measured by X-ray photoelectron spectroscopy using K-Alpha+model (Thermo Fischer Scientific, UK) with Al K α source.

2.2.3.6. Nitrogen adsorption-desorption isotherm measurements: N_2 gas adsorption-desorption measurements were performed using BelSorp-Max instrument (Bel Japan). Prior to adsorption measurements, the activated samples were heated at $120 \text{ }^\circ\text{C}$ under vacuum for 12 hours using BelPrepvacII.

2.2.3.7. Field emission scanning electron microscopy (FESEM): The morphology of the materials was recorded with a Zeiss Ultra Plus field-emission scanning electron microscope (FESEM) with an integral charge compensator and embedded EsB and AsB detectors (Oxford X-max instruments 80 mm^2

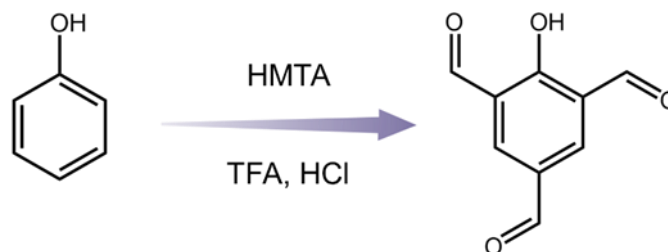
(Carl Zeiss NTS, GmbH). The samples were sputter-coated with a 5-10 nm Au film to reduce charging. The elemental analysis was carried out using voltage of 15 KV equipped with an EDX detector. Data acquisition was performed with an accumulation time of >600s.

2.2.3.8. Transmission electron microscopy (TEM): TEM, High-resolution TEM imaging and STEM-EDS were performed on the HRTEM (JEM-2200FS, JEOL) operating at acceleration voltage of 200 kV. For TEM analysis, all the samples were dispersed in isopropanol (0.5 mg/mL) and sonicated for 15 min. Then, the samples were left for 2 min, and the upper part of the solution was taken for preparing TEM samples on a lacey carbon-coated copper grid (Electron Microscopy Science, 200 mesh).

2.2.3.9. Zeta potential: Zeta potential measurements were performed on Anton Paar Litesizer 500 series instrument. Measurement cell: Omega cuvette Mat. No. 155765, Target temperature 25.0 °C, Equilibration time – (Series parameter), Henry factor 1.1 (Other), Adjusted voltage (Automatic Mode), Number of runs 20, Solvent – water.

2.2.3.10. UV-visible absorption spectra: UV-vis absorption studies were performed on a Shimadzu UV 3600 UV/vis spectrophotometer in an optical quartz cuvette (10 mm path length) over the entire range of 200-800 nm.

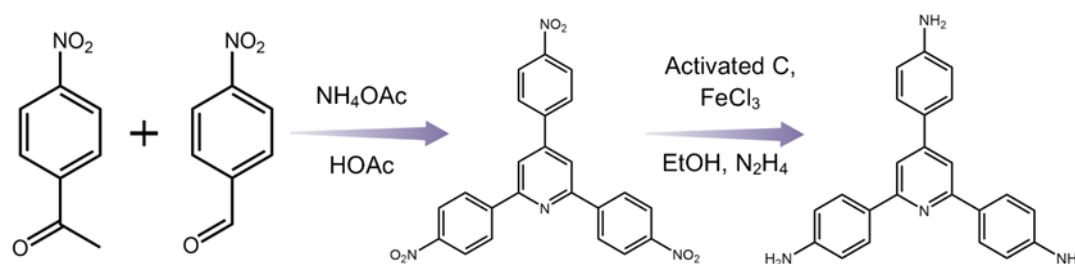
2.2.3.11. Synthesis of 2,4,6-triformyl phenol (TFP) or 2-hydroxybenzene-1,3,5-tricarbaldehyde: TFP was synthesized by following a previously reported procedure.^[27] A mixture of 6.9 g (65 mmol) of phenol was stirred with 70 mL of trifluoro acetic acid (TFA) and 20.1 g (143 mmol) of hexamethylenetetramine (HMTA) at ~125 °C for about 20 h. After that, the reaction mixture was then heated to 148-150 °C and held at that temperature for 3 hours. Thereafter, the mixture was cooled to ~120 °C, and treated with 100 mL of 3N HCl, and then heated at ~100 °C for half an hour, then cooled to room temperature slowly by overnight. The resulting mixture were then filtered in a glass frit and washed with water to give a brown crude powder. The brown powders were then recrystallized from DMF and the needle shaped crystals were obtained as final product.



Scheme 2.2: Synthesis scheme of 2-hydroxybenzene-1, 3, 5-tricarbaldehyde.

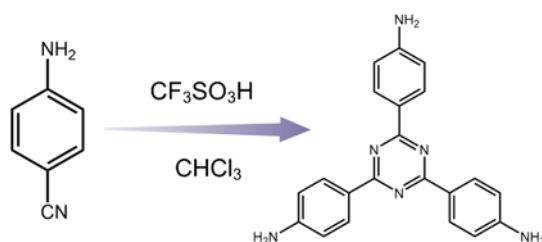
2.2.3.12. Synthesis of 4,4',4''-(pyridine-2,4,6-triyl)trianiline from 2,4,6-tris(4-nitrophenyl)pyridine: 4,4',4''-(pyridine-2,4,6-triyl)trianiline was synthesized by following a previously reported procedure.^[28] At first 2,4,6-tris(4-nitrophenyl)pyridine was synthesized.^[28] Briefly, 10 mmol of 4-Nitrobenzaldehyde and 20 mmol of 4-Nitroacetophenone were dissolved in 25 ml of acetic acid. Then 10 g of ammonium acetate was added to this mixture and refluxed at 110 °C for 3 hours. A dark red precipitate was filtered and washed with acetic acid and cold ethanol. After dried at ~80 °C, this dark red crude product was found as 2,4,6-tris(4-nitrophenyl)pyridine, which was further used in the next step for amine preparation.

In this step, 1.5 g of above 2,4,6-tris(4-nitrophenyl)pyridine was dissolved in 20 ml EtOH. Next, about 60 mg of ferric chloride hexahydrate and 200 mg of activated carbon were added to this solution and heated under reflux conditions for 30 mins. To this, 4 ml of hydrazine hydrate in 4 ml EtOH was added dropwise and the mixture was refluxed for 12 hours. Thereafter, the mixture was filtered as hot and the filtrate was poured in excess distilled water. A white yellow precipitate with high yield was appeared, which was filtered, washed with water and dried at 60°C overnight.



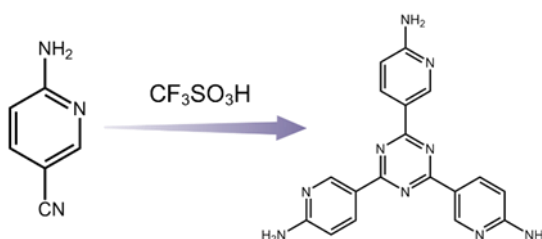
Scheme 2.3: Synthesis scheme of 4,4',4''-(pyridine-2,4,6-triyl)trianiline.

2.2.3.13. Synthesis of 2,4,6-tris(4-aminophenyl)-1,3,5-triamine: 2,4,6-tris(4-aminophenyl)-1,3,5-triamine was synthesized from 4-aminobenzonitrile via an acid catalyzed trimerisation reaction by following a previously reported protocol.^[29] In a typical synthesis 4-aminobenzonitrile (591 mg, 5.0 mmol) was mixed with ~35 ml of chloroform taken in a dry RB (25 ml) and then 5.0 ml of triflic acid was added slowly at 0 °C and stirred under an inert atmosphere for 3 days. After that, the reaction mixture was gently poured into a beaker containing crushed ice-water and neutralized by 2M NaOH solution to afford yellow colored precipitate. This precipitate was filtered and washed with distilled water and dried at 60 °C overnight to get pure product.



Scheme 2.4: Synthesis scheme of 2,4,6-tris(4-aminophenyl)-1,3,5-triazine.

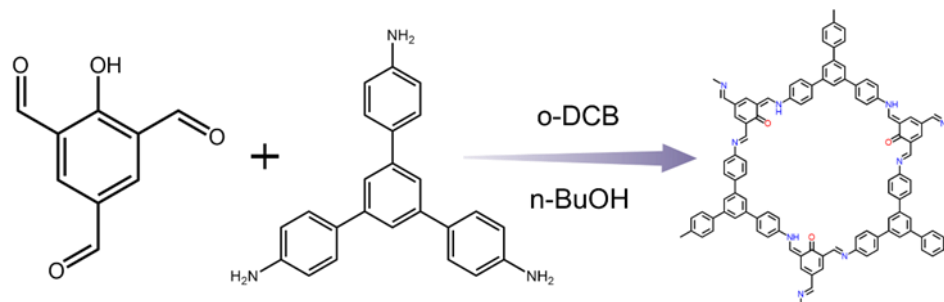
2.2.3.14. Synthesis of 5,5',5''-(1,3,5-triazine-2,4,6-triyl)tris(pyridin-2-amine): 5,5',5''-(1,3,5-triazine-2,4,6-triyl)tris(pyridin-2-amine) was synthesized from 6-Amino-3-pyridinecarbonitrile via an acid catalyzed trimerisation reaction by following a previously reported procedure.^[30] In a typical synthesis, 1.544 g (13.076 mmol) 6-Amino-3-pyridinecarbonitrile was taken in a round bottom flask at -20 °C. Then 8 mL of triflic acid (CF₃SO₃H) was added drop wise for 20 minutes. The resulting mixture was stirred for 24 h at room temperature in an inert atmosphere. Subsequently, the reaction mixture was quenched with distilled water and was neutralized by adding 2M NaOH solution until the pH was 7. At this pH, a pale yellow precipitate was observed which with further increase in pH it turns white. This white precipitate was filtered off and washed several times with distilled water. Next, the crude product was dried at 60 °C overnight to get the final product.



Scheme 2.5: Synthesis scheme of 5,5',5''-(1,3,5-triazine-2,4,6-triyl)tris(pyridin-2-amine).

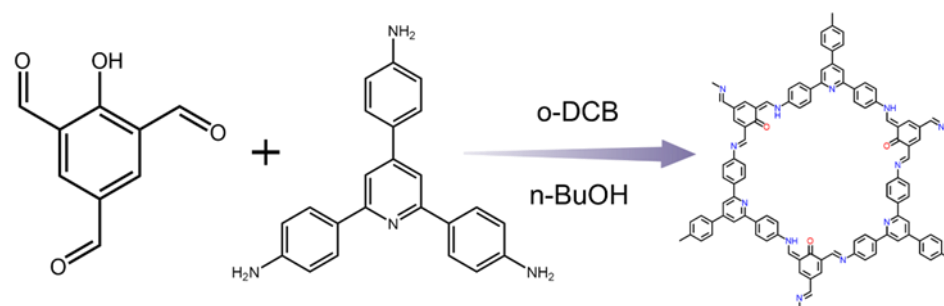
2.2.3.15. Synthesis of COF-A: COF-A was synthesized by following a previously reported procedure.^[27] 2-hydroxybenzene-1,3,5-tricarbaldehyde (14.3 mg, 0.08 mmol), 1,3,5-tris(4-aminophenyl)benzene (28.1 mg, 0.08 mmol), 0.5 mL of n-butanol, 0.5 mL of o-dichlorobenzene and 0.1 mL of 6 M aqueous acetic acid were added into a 20 mL glass vial. This mixture was sonicated for 15 mins. in order to get a homogenous dispersion. Then the tube was flash frozen at 77 K (liquid N₂ bath) and degassed. Thereafter, the tube was sealed and heated at 120 °C for 7 days. A dark red colored precipitate produced was collected by filtration. Then it was washed and solvent exchanged with

anhydrous tetrahydrofuran several times. The resultant precipitate was dried at 120 °C under vacuum for overnight to give a red coloured powder.



Scheme 2.6: Synthesis scheme of COF-A.

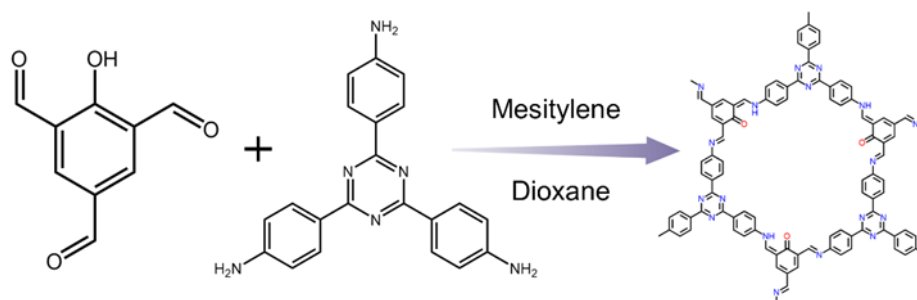
2.2.3.16. Synthesis of COF-B: COF-B was synthesized by following a previously reported procedure with slight modification.^[31] 70.5 mg of 4,4',4''-(pyridine-2,4,6-triyl)trianiline (0.2 mmol) and 36 mg of 2-hydroxybenzene-1,3,5-tricarbaldehyde (0.2 mmol) were added in a 20 mL glass tube and dissolved in 2.5 ml o-dichlorobenzene and 2.5 ml n-butanol mixture. After that 0.5 ml of 6M acetic acid was added to this mixture and was stirred well. Then the tube was flash frozen at 77 K (liquid N₂ bath), degassed and sealed. The contents in the sealed tube was heated at 120 °C for 3 days. After cooling to room temperature, the deep brown precipitate was filtered and washed with DMF, THF, MeOH. The powder was dried at 120 °C, overnight. The final product was cleaned through soxhlet extraction.



Scheme 2.7: Synthesis scheme of COF-B.

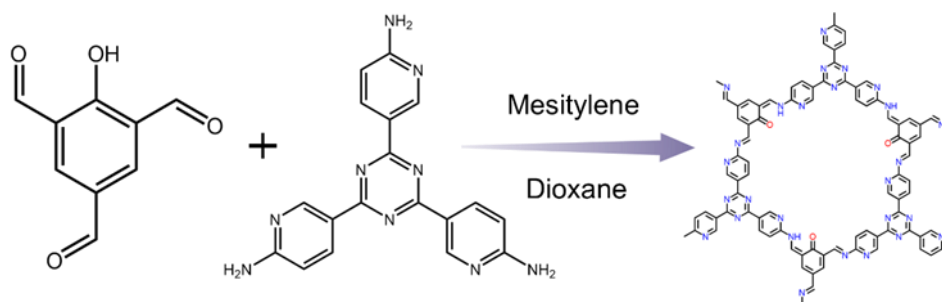
2.2.3.17. Synthesis of COF-C: COF-C was synthesized by following a previously reported procedure with slight modification.^[32] In a typical synthetic procedure a 20 mL of pyrex tube was charged with 26.72 mg (0.15 mmol) of 2-hydroxybenzene-1,3,5-tricarbaldehyde (TFP) and 53.17 mg (0.15 mmol) of 2,4,6-tris(4-aminophenyl)-1,3,5-triazine (TAPT). Then 2.5 mL of mesitylene and 2.5 mL of dioxane along with 0.5 mL of 6M acetic acid were added to the mixture. After that, the tube was sonicated for 15 minutes in order to get a homogenous dispersion. Then the tube was flash frozen at 77 K (liquid N₂ bath) and degassed. Thereafter, the tube was sealed and heated at 120 °C for 3 days. After 3 days the

sealed tube was taken out to obtain deep red-color material. Finally, it was collected and washed with dry solvents (methanol, acetone and THF) and dried at 120 °C for 6 hours.



Scheme 2.8: Synthesis scheme of COF-C.

2.2.3.18. Synthesis of COF-D: COF-D was synthesized by following a previously reported procedure with slight modification.^[30] 2-hydroxybenzene-1,3,5-tricarbaldehyde (53.5 mg, 0.3 mmol) and 5,5',5''-(1,3,5-triazine-2,4,6-triyl)tris(pyridin-2-amine) (107 mg, 0.3 mmol) were weighed into a Pyrex tube and were dissolved in 3 mL of dioxane and 3 mL of mesitylene and stirred until a red color was observed. To this mixture, 1.0 mL of stock acetic acid was added. Then the Pyrex tube was flash frozen in a liquid nitrogen bath and sealed. The Pyrex tube along with its contents was placed in an oven for heating at 120 °C for 5 days and gradually cooled to room temperature overnight. After cooling to room temperature, the dark-red colored precipitate was filtered and washed with DMF, THF, MeOH and THF. The final product was cleaned through soxhlet extraction and dried at 80 °C for 12 h.



Scheme 2.9: Synthesis scheme of COF-D.

2.2.3.19. Synthesis of COF-A1: The synthesis procedure of COF-A1 is almost similar to COF-A, however the precursor amount, solvent and catalyst was changed as following. 2-hydroxybenzene-1,3,5-tricarbaldehyde (26.8 mg, 0.15 mmol), 1,3,5-tris(4-aminophenyl)benzene (52.7 mg, 0.15 mmol), 2.5 mL of mesitylene, 2.5 mL of dioxan and 0.5 mL of 6 M aqueous acetic acid were added into a 20 mL glass vial. This mixture was sonicated for 15 mins. in order to get a homogenous dispersion. Then

the tube was flash frozen at 77 K (liquid N₂ bath) and degassed. Thereafter, the tube was sealed and heated at 120 °C for 3 days. Rest of the procedure is same as COF-A.

2.2.3.20. Synthesis of COF-A2: The synthesis procedure of COF-A2 is almost similar to COF-A, however the precursor amount, solvent and catalyst was changed as following. 2-hydroxybenzene-1,3,5-tricarbaldehyde (26.8 mg, 0.15 mmol), 1,3,5-tris(4-aminophenyl)benzene (52.9 mg, 0.15 mmol), 2.5 mL of mesitylene, 2.5 mL of dioxan and 1 mL of 6 M aqueous acetic acid were added into a 20 mL glass vial. This mixture was sonicated for 15 mins. in order to get a homogenous dispersion. Then the tube was flash frozen at 77 K (liquid N₂ bath) and degassed. Thereafter, the tube was sealed and heated at 120 °C for 3 days. Rest of the procedure is same as COF-A.

2.2.3.21. Synthesis of COF-A3: The synthesis procedure of COF-A3 is similar to COF-A, however the precursor amount, solvent and catalyst was changed as following. 2-hydroxybenzene-1,3,5-tricarbaldehyde (53.5 mg, 0.3 mmol), 1,3,5-tris(4-aminophenyl)benzene (105.4 mg, 0.3 mmol), 3 mL of mesitylene, 3 mL of dioxan and 0.5 mL of stock acetic acid were added into a 20 mL glass vial. This mixture was sonicated for 15 mins. in order to get a homogenous dispersion. Then the tube was flash frozen at 77 K (liquid N₂ bath) and degassed. Thereafter, the tube was sealed and heated at 120 °C for 3 days. Rest of the procedure is same as COF-A.

2.2.3.22. Synthesis of COF-D1: The synthesis procedure of COF-D1 is similar to COF-D, however the precursor amount, solvent and catalyst was changed as following. 2-hydroxybenzene-1,3,5-tricarbaldehyde (53.5 mg, 0.3 mmol), 5,5',5''-(1,3,5-triazine-2,4,6-triyl)tris(pyridin-2-amine (107mg, 0.3 mmol), 2.5 mL of mesitylene, 2.5 mL of dioxan and 1.5 mL of stock acetic acid were added into a 10 mL glass vial. This mixture was sonicated for 15 mins. in order to get a homogenous dispersion. Then the tube was flash frozen at 77 K (liquid N₂ bath) and degassed. Thereafter, the tube was sealed and heated at 120 °C for 3 days. Rest of the procedure is same as COF-D.

2.2.3.23. General Consideration: The aqueous solution of organic dyes were prepared by dissolving a certain amount of solid dye into deionized water and the different concentrations were obtained by diluting the stock solution with the proper amount of distilled water unless otherwise indicated. The concentrations of dyes during all the experiments were detected by UV-vis spectroscopic analysis. All the adsorption experiments were performed at ambient conditions. All the data has been collected three times through UV-vis analysis to plot the final adsorption results.

2.2.3.24. Vapor phase static organic iodide uptake studies: Typically, ~15 mg of desolvated COF sample was weighted in a small glass vial, and this vial was exposed to organic iodide (CH₃I or C₂H₅I) (~3 mL) at 75 °C (348 K) in a closed system. After the corresponding adsorption time, the glass vial was taken out, cooled to room temperature, and weighed. Organic iodide uptake capacity of the sample was calculated by the weight difference of glass vials before and after adsorption, using the formula:

$$W = ((m_2 - m_1)) / m_1 \times 100\%$$

Where, w ($\text{g}\cdot\text{g}^{-1}$) is the adsorption capacity of organic iodide uptake, m_1 (g) and m_2 (g) are the mass of compounds with the glass vial before and after being exposed to organic iodide vapor. The values of uptake capacity are the average values of at least three experiments. In case of other temperatures, such as 273 and 423 K, similar static CH_3I adsorption experiment was conducted in a closed system.

2.2.3.25. Recyclability test: To study the recyclability for CH_3I -loaded material in static system we followed a reported protocol with slight modification.^[22] Typically, a certain amount of CH_3I -loaded compound with maximum adsorption capacity was taken in an glass vial containing excess amount of ethanol and ultra-sonicated for a certain period of time. Thereafter, the regenerated samples were dried under vacuum at 120 °C overnight and then reused for the next cycle CH_3I adsorption test in static phase.

2.2.3.26. Retention ability test: To study the adsorption stability for methyl iodide-loaded material in static system, a certain amount of CH_3I -loaded material was taken in an open glass vial, and the vial was placed in an empty large bottle, which was placed open at room temperature and ambient pressure. After one day, the weight of the vial containing CH_3I -adsorbed material was recorded and the vial was placed back into the empty large bottle. The large bottle was opened to further continue the experiment for next 7 days.

2.2.3.27. Vapor phase dynamic methyl iodide uptake studies: The gaseous methyl iodide adsorption in dynamic system was performed in a home-built setup. At first, 20 mg of COF sample was packed into a glass column with glass wool filling the void space of both ends, which served as the adsorption cell. This adsorption cell along with a separate chamber containing methyl iodide was transferred into an oven and heated at 75 °C for desired time period. A nitrogen flow ($5 \text{ cm}^3/\text{min}$) passed through the methyl iodide vapor generator (inlet) to blow the methyl iodide vapor into the COF material in the adsorption cell. The effluent from the adsorption cell (outlet) was treated with 0.1 M NaOH solution. The adsorption capacity for methyl iodide was calculated from the weight difference of glass tubes before and after adsorption. The vapor phase dynamic methyl iodide capture study in the presence of nitric acid vapor was performed in a similar method taking HNO_3 in a separate glass vial along with the methyl iodide vial (Appendix 2.28).

2.2.3.28. Organic dyes capture experiments: The pollutant concentration was calculated by using UV-vis spectroscopy after establishing a standard curve at room temperature. The pollutant removal efficiency (%) by the adsorbent polymer under investigation was determined utilizing the following equation:

Removal efficiency = $((C_0 - C_t)/C_0) \times 100\%$

Where, C_0 (mM) and C_t (mM) represents the concentrations of pollutant solutions before and after adsorption, respectively.

The amount of pollutant adsorbed by the polymer was calculated from the following equation:

Adsorption capacity (q_t) = $((C_0 - C_t))/m \times M_w$

Where, q_t ($\text{mg} \cdot \text{g}^{-1}$) is the amount of pollutant adsorbed per gm of adsorbent material at time t (min). C_0 ($\text{mmol} \cdot \text{L}^{-1}$) and C_t ($\text{mmol} \cdot \text{L}^{-1}$) represent the initial and residual concentration of pollutant in the stock solution and filtrate, respectively; m (gm) is the mass of adsorbent used for the study. M_w ($\text{g} \cdot \text{mol}^{-1}$) is the molar mass of the dyes under consideration.

2.2.3.29. Organic dyes adsorption kinetics study: Initially 2 mL 0.1 mM aqueous stock solution of the respective organic dyes were taken in a UV cuvette and subsequently their initial absorbance was measured. 2 mg of COFs was added to the dye solution and the absorbance spectra of the supernatant solutions were recorded accordingly at different time intervals. The concentration of the dyes in the filtrate was determined by UV-Vis spectroscopy subsequently.

The adsorption kinetics were further quantified utilizing pseudo-second-order model from which the apparent rate constant k_{obs} can be obtained using following equation:

$$t/q_t = t/q_e + 1/k_{\text{obs}}q_e^2$$

Where, q_t and q_e are the adsorbate uptakes (mg adsorbate per gm of COFs) at time t (min) and at equilibrium, respectively, and k_{obs} is an apparent second-order rate constant ($\text{g} \cdot \text{mg}^{-1} \cdot \text{min}^{-1}$). The rate constant k_{obs} can be calculated from the intercept and slope of the plot of t/q_t against t .

2.2.3.30. Column-exchange based dye capture experiment: To check the dye removal efficiency of COF-A after CH_3I adsorption ($\text{CH}_3\text{I}@\text{COF-A}$), a column exchange-based sorption experiment was conducted by packing ~ 100 mg of $\text{CH}_3\text{I}@\text{COF-A}$ with ~ 5 gm of sand inside a U shaped glass column as bed for orange G (OG) as a model dye capture test (Appendix 2.62). Then different volume of stock 0.25 mmol OG aqueous solution was passed through the column bed with a flow rate of 0.5 mL/min, which was controlled by a water-flow-regulator, and the drops per minute was recorded with the help of a stopwatch. A bed-volume of ~ 2.1 mL of column eluted solution was collected in different containers. The concentration of the column eluted solutions were then analysed through UV-vis spectroscopy (Appendix 2.63).

2.2.3.31. Determination of electrostatic surface potential (ESP), binding sites and binding energy of different interactions:

Density functional theory (DFT) computations were performed using the Discovery Studio 2016 to derive the ESP surface of model monomers of COF-A, B, C and D. The geometry optimization of the monomers were carried out using hybrid B3LYP exchange correlation function and double numeric plus polarization (DNP) basis set with SCF density convergence of 1×10^{-6} . The electrostatic potential (ESP) on the van der Waals (VDW) surfaces (isodensity = 0.001 a.u.) of COF-A to COF-D monomers was derived based on its ground state electron density.

The Static binding energies (ΔE) at 0 K in vacuum were calculated using the following expression:

$$\Delta E = E(\text{COF} + \text{CH}_3\text{I}) - E(\text{COF}) - E(\text{CH}_3\text{I})$$

Where, E_x refers, respectively, to the total energies of the COF + CH₃I complex, the COF alone, and the CH₃I molecule respectively.

2.3 Results and Discussion

The construction of porous materials with custom polygon shapes, distinct pore sizes, and precisely defined pore environments are attractive for using two-dimensional (2D) COFs with identical 1D open channel pores.^[26, 33, 34] The keto-enol-based highly crystalline imine functionalized COFs are not only propitious for their high chemical stabilities but are also recognized as potential materials towards various leading applications such as catalysis, gas separation, sensing, energy storage, pollutants capture, and more, owing to their collective unique properties.^[35-42] Now, contemporary literature have presented report that imine functionality of Schiff-base COFs offer favourable interactions with methyl iodide.^[22] Nevertheless, although in case of C3-aldehyde based proton tautomerism induced keto-enol COFs exhibited remarkable chemical stabilities,^[43] due to their transformation to completely irreversible keto bonds, density of pure imine functionality becomes inaccessible^[44] to further interact with ROIs. This is particularly accurate in case of 1,3,5-triformylphloroglucinol aldehyde based Schiff-base COFs. Therefore, achieving high adsorption capacity of ROIs from strong chemical condition requires a perfect equilibrium between these factors. Considering this, in this study, all the judiciously selected COFs are imine-linked through the Schiff-base reaction between mono-hydroxy functionalized tri-aldehyde and triamine moieties to form 2D hexagonal microporous frameworks (Figure 2.1). A series of four different COFs were synthesized by the solvothermal condensation reaction of 2-hydroxybenzene-1,3,5-tricarbaldehyde with 1,3,5-tris(4-aminophenyl)benzene (for COF-A), 4,4',4''-(pyridine-2,4,6-triyl)trianiline (for COF-B), 2,4,6-tris(4-aminophenyl)-1,3,5-triamine (for COF-C), 5,5',5''-(1,3,5-triazine-2,4,6-triyl)tris(pyridin-2-amine) (for COF-D), respectively, under particular reaction condition, as described in the experimental section (Figure 2.1 and Scheme 2.6-2.9).^[38-41] The structure of the COFs indicated that one small repeating unit (amine periphery) of COF-A contains only

three imine-N sites. Whereas, in case of COF-A, COF-B, COF-C and COF-D, all have three imine-N (common in all the cases) as well as one pyridine-N, three triazine-N and three triazine-N with three extra pyridine-N sites, respectively (Figure 2.1). The structural characterizations of these COFs were performed by powder X-ray diffraction (PXRD), Fourier transform infrared (FTIR), solid-state ^{13}C cross-polarization magic-angle-spinning nuclear magnetic resonance (CP-MAS-NMR) spectroscopy, thermogravimetric analysis (TGA), X-ray photoelectron spectroscopy (XPS), low temperature nitrogen (N_2) gas sorption measurements, etc.

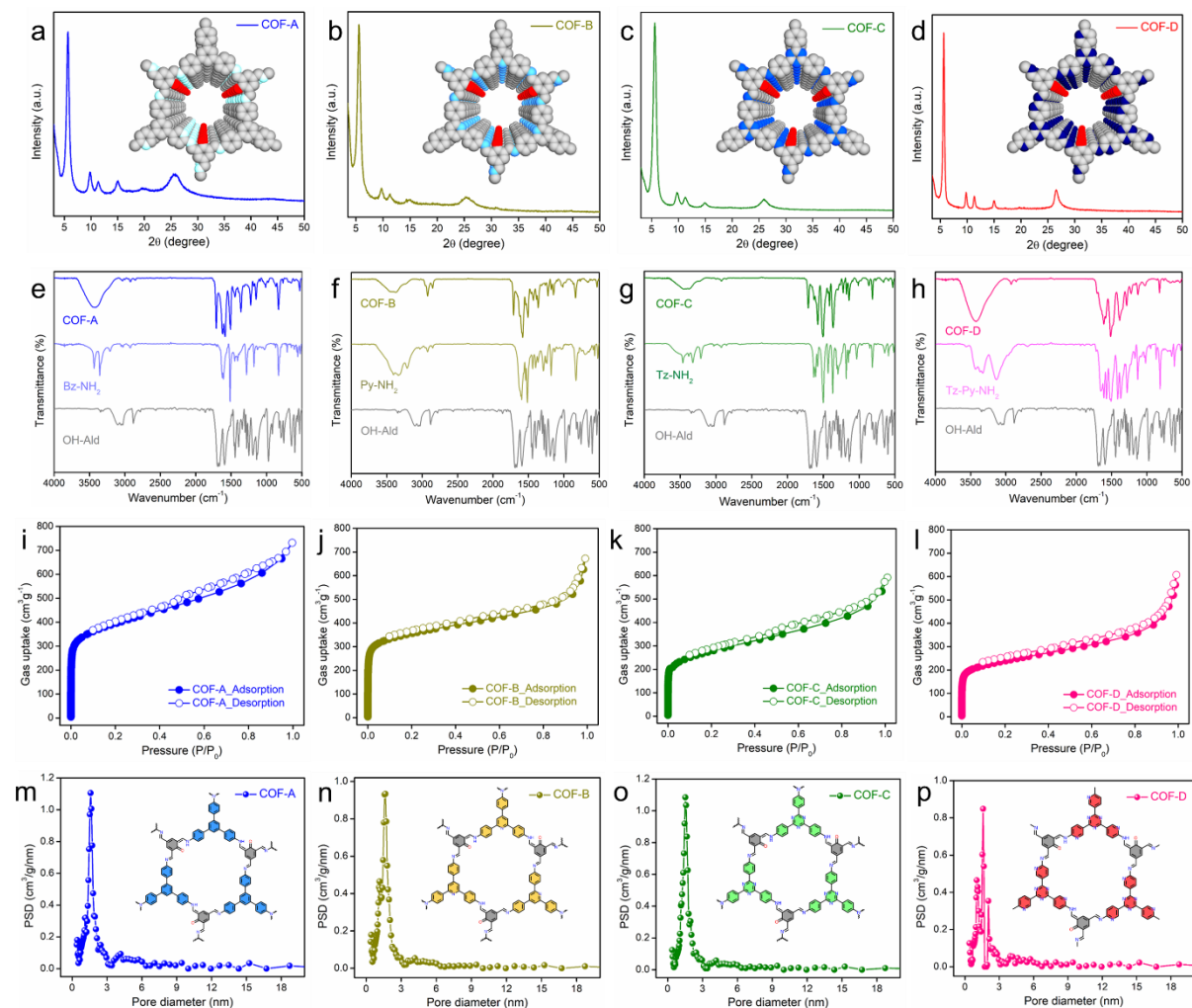


Figure 2.2: (a-d) Experimental PXRD patterns, (e-h) FTIR spectra of the COFs with their respective precursors, (i-l) N_2 gas adsorption-desorption data at 77 K, (m-p) NLDFT pore size distribution plots of COF-A, COF-B, COF-C and COF-D, respectively.

The experimental PXRD pattern of all the four COFs indicated highly crystalline nature with single-phase purity (Figure 2.2a-2.2d). The PXRD pattern of COF-A indicated intense peak at 5.68° along with other small peaks at 9.76 , 11.20 , 14.89 , and 25.16° , corresponding to reflections from (100), (110),

(200), (120), and (001) facets, respectively (Figure 2.2a).^[27] The obtained experimental data matches well with the reported eclipsed (AA) stacking mode of COF-A. Based on these results, COF-A possessed a 2D structure with honeycomb-like 1D open channel pores (Figure 2.2a).^[27] The crystalline structure of COF-B, C and D were also evaluated using PXRD analysis, which suggests similar 2D structural formation with eclipsed (AA) stacking mode (Figure 2.2b-2.2d).^[30-32] These analysis further suggested that all the COFs demonstrated isostructural porous framework with hexagonal 1D pores. Thereafter, the presence of C-NH stretching peak at $\sim 1678\text{ cm}^{-1}$, along with the appearance of C=N stretching bands at $\sim 1582\text{ cm}^{-1}$ as well as disappearance of stretching frequencies of -CH=O bands (aldehyde) at $\sim 1680\text{ cm}^{-1}$ and N-H stretching signals (primary amine -NH_2) at ~ 3450 , ~ 3325 and $\sim 3204\text{ cm}^{-1}$ in the FT-IR spectra of all the COFs confirmed the complete condensation of tri-aldehyde with respective tri-amine moieties (Figure 2.2e-2.2h). In addition, the intense peaks at ~ 1618 and 1503 cm^{-1} originating from C=O and C=C stretching, along with peaks associated with C=N and C-N bonds further confirmed the existence of β -ketoenamine form in all the four COFs, which is generated by the tautomerization between the Schiff bonds (-C=N-) and the β -positioned hydroxyl groups, giving rise to energetically favoured intralayer hydrogen bonding.^[27-30] The solid-state ^{13}C CP-MAS NMR spectra of all the COF samples further validated their proposed structures as a result of successful polycondensation reactions to form COFs, evidenced by the appearance of characteristic resonance peaks of imine carbons at 158.9 and 156.1 ppm and absence of peaks at ~ 190 ppm corresponding to aldehyde carbon (-CH=O) (Appendix 2.1-2.4). Moreover, the peaks corresponding to $\delta = 197$ ppm and $\delta = 114\text{--}124$ ppm appear due to the keto form (owing to the tautomerization of -OH groups) and aromatic sp^2 carbons of the frameworks, respectively. In addition, signals at ~ 149 ppm correspond to the sp^2 carbon attached to -OH moiety of all the COFs and signals at ~ 169 ppm correspond to the triazine ring carbon of COF-C and COF-D, respectively (Appendix 2.3, 2.4). Both the FTIR and solid-state ^{13}C CP-MAS NMR spectra validate that the different functional groups (such as triazine and/or pyridine) were introduced in the respective COFs structure (Figure 2.1). The TGA profiles for all the COFs under N_2 atmosphere indicated no significant weight loss up to ~ 350 to $\sim 450\text{ }^\circ\text{C}$, further suggesting the high thermal stability (Appendix 2.5-2.8). However, beyond $\sim 450\text{ }^\circ\text{C}$ the constant weight loss was due to the decomposition of organic moieties of the COFs. Furthermore, XPS was employed to investigate the surface composition along with chemical state of the COF structures. The XPS survey spectra of all the COFs displayed characteristic peaks of the elements, i.e., C, N and O (Appendix 2.9-2.12). The C 1s XPS spectra of the COFs exhibited peaks in the range of ~ 284.3 , ~ 285.6 , and $\sim 290.2\text{ eV}$, corresponding to aromatic carbon bond (-C=C-), carbon of imine (-C=N) or enol bond (-C-O) and carbon of keto bond (-C=O), respectively (Appendix 2.13).^[32, 45] Also, the O 1s core energy level XPS spectra indicated peaks at ~ 531.3 and $\sim 533.2\text{ eV}$, which are associated with the oxygen atom of -C-O and -C=O bonds, respectively (Appendix 2.14). Moreover, the deconvoluted N 1s XPS spectra of COF-A to COF-D revealed peaks at ~ 398.2 to $\sim 400.4\text{ eV}$ corresponds to the N of -C=N bond (imine, pyridine

and triazine groups) and secondary amine nitrogen, respectively (Appendix 2.15). Thereafter, the permanent porosity analysis, determination of specific surface area and pore size of the synthesized COFs were evaluated by the low temperature (77 K) N₂ gas adsorption-desorption measurement. The N₂ sorption data of all the COFs exhibited type-I adsorption isotherm with high and rapid N₂ uptake at low partial pressure that is characteristic to a microporous structure (Figure 2.2i-2.2l). However, the total gas uptake at 77 K of these COFs were found to be different and follow the order: COF-A>COF-B>COF-C>COF-D. The Brunauer–Emmet–Teller (BET) surface area of these COFs were calculated as 1560 m².g⁻¹ for COF-A, 1335 m².g⁻¹ for COF-B, 1185 m².g⁻¹ for COF-C and 1013 m².g⁻¹ for COF-D. Further, the pore size distribution of the COFs were estimated using nonlocal density functional theory (NLDFT) that revealed distribution of micropores with average pore diameter of ~1.3 nm to ~1.45 nm (Figure 2.2m-2.2p).

After these structural characterizations, the morphological investigation of these COFs were done by field emission scanning electron microscopy (FESEM) and transmission electron microscopy (TEM). The FESEM images of COF-A, COF-B and COF-C revealed agglomerated plait-spherical with surface porcupine like morphology (Appendix 2.16). However, COF-D exhibited hexagonal flake-like morphology with stacked microstructure (Appendix 2.16). Similar observation was noted in the TEM and high-resolution TEM (HR-TEM) images of these COFs, which validate the abundance of aggregated COF nanoflakes (Appendix 2.17 and 2.18). Moreover, the elemental composition of the COFs were determined with the help of elemental analysis, energy-dispersive X-ray spectroscopy (EDS) and corresponding mapping. All the COFs manifested the presence and homogeneous distributions of C, N and O elements throughout the structures (Appendix 2.19 and 2.20) (Appendix Table 2.1).

2.4 ROIs Sequestration Studies

We have conducted both the static and dynamic organic iodide sorption experiments after the successful synthesis and characterization of all the COFs in order to investigate the contribution of framework integrated functionality of porous COFs towards effective organic iodide [namely, methyl iodide (CH₃I) and ethyl iodide (CH₃CH₂I)] adsorption. Based on prior understanding of the forward dependence of CH₃I adsorption upon the functionality of porous frameworks,^[22] we hypothesized that among the synthesized COFs, COF-D should exhibit the highest organic iodide uptake capacity owing to its additional framework integrated heteroatom functionalities such as triazine, pyridine, and imine moieties. Further, the order of capacity should follow as COF-D>COF-C>COF-B>COF-A, provided all the COFs feature similar porosity. However, in our case we encountered an interesting result as describe below. Initially, the static CH₃I adsorption test was performed to investigate the saturation

capacity of all the COFs. In a typical experiment, organic iodide uptake of COFs was measured gravimetrically at 348 K under ambient pressure in various time intervals with three parallel experimental set-up (see the experimental section for details). The change in the weight of the adsorbents (COFs) after CH_3I adsorption was plotted as a function of time. The four COFs demonstrated high CH_3I capture capacity with fast uptake kinetics, however, the uptake amounts were different. Notably, it was found that the adsorption capacity of CH_3I reached $1.27 \text{ g}\cdot\text{g}^{-1}$ at 24 h, and the maximum uptake amount was $1.58 \text{ g}\cdot\text{g}^{-1}$ within 72 h for COF-A (Figure 2.3a). Surprisingly, for COF-B, C and D the saturation adsorption capacity of CH_3I were found to be as 1.37, 1.13 and $0.98 \text{ g}\cdot\text{g}^{-1}$, respectively within 72 h under similar conditions (Figure 2.3b-2.3d, Appendix 2.21). The CH_3I uptake kinetics of all the COFs were found to follow pseudo-second-order kinetic model (Appendix 2.22). It should be mentioned that the CH_3I uptake capacity in static condition at 348 K of COF-A is one of the highest among most of the reported materials (Appendix Table 2.2).

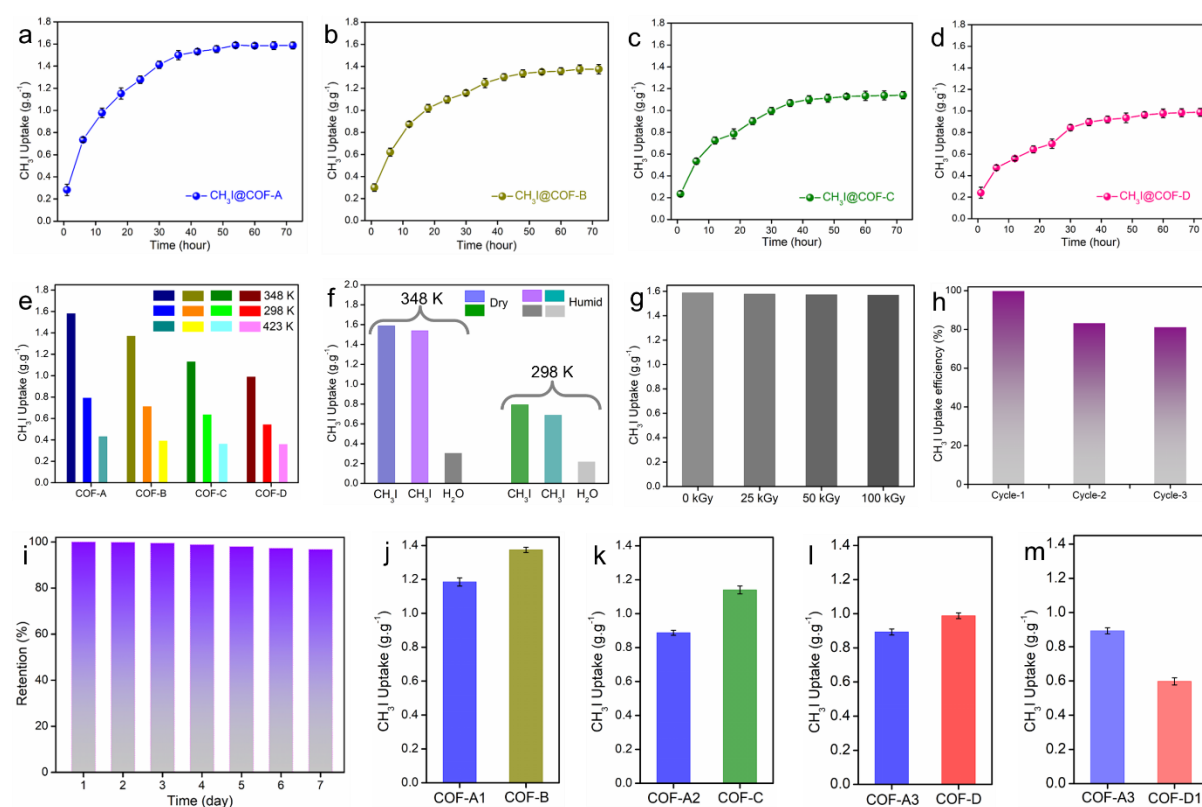


Figure 2.3: (a-d) CH_3I adsorption capacities of COF-A, COF-B, COF-C and COF-D, respectively, as a function of time at 348 K under static condition. (e) CH_3I uptake capacities of COF-A at 298, 348, and 423 K within 72 h. (f) Uptake capacities of CH_3I by COF-A in dry and humid condition at 298 and 348 K. (g) The CH_3I uptake capacities of COF-A upon β -irradiation. (h) The recyclability result of COF-A for CH_3I adsorption. (i) CH_3I retention efficiency of COF-A upon exposure to air at room

temperature. Comparison of CH₃I sorption capacities between (j) COF-A1 and COF-B, (k) COF-A2 and COF-C, (l) COF-A3 and COF-D, and (m) COF-A3 and COF-D1, respectively.

Furthermore, the uptake of CH₃I vapor at different temperature including room temperature (298 K), and industrial relevant temperature (423 K) were performed. At 298 K, COF-A to D exhibited 0.79, 0.71, 0.63 and 0.54 g.g⁻¹ CH₃I capture capacities, respectively (Figure 2.3e). Moreover, at 423 K, COF-A to D showed significantly lower CH₃I uptake capacities as 0.43, 0.39, 0.36 and 0.35 g.g⁻¹, respectively (Figure 2.3e). Note that at both 298 and 423 K temperature the saturation adsorption capacities of all the COFs were considerably lower than at 348 K. However, the order of these capacities of all the COFs were found as almost similar with previous (at 348 K), i.e., COF-A>COF-B>COF-C>COF-D.

That being said, in nuclear waste or off-gas stream, CH₃I vapor exist with moisture along with nitric acid and nitrogen oxides (i.e., NO₂).^[5] This means that the practical adsorbents should sufficiently stable toward water and high acidic conditions in addition to radiation stability. Therefore, the hydrolytic, chemical (acidic) and radiation stability of COF-A (as model adsorbent) was investigated by treating with aqueous 1M nitric acid solution and range of high doses of β -irradiation. As shown in appendix 2.23 COF-A remains intact even after treatment of HNO₃ solution for 24 h. Also, the PXRD patterns of β -irradiated (doses of ~25 to 100 kGy) samples revealed that COF-A retains its high crystalline nature, further indicating the radiation tolerance ability of the adsorbent (Appendix 2.24). The excellent chemical, radiation and thermal stability of the adsorbent (COF-A) enabled its utilization at elevated operating conditions required for radio-active nuclear waste disposal.

Considering the practical relevance, first, the uptake of CH₃I in the presence of humidity by COF-A in static condition was evaluated (see the experimental section for details). COF-A demonstrated very negligible depletion in the uptake capacity of CH₃I in humid condition as compared to dry condition at both 348 and 298 K (Figure 2.3f). Furthermore, CH₃I capture in the presence of 1M HNO₃ solution was tested, which resulted 1.47 g.g⁻¹ uptake capacity at 348 K. In addition, almost negligible compromise in the CH₃I sorption capacities were observed for COF-A upon irradiation of various doses of β -ray (Figure 2.3g). These data indicated the potential of COF-A toward effective organic iodide capture from simulated nuclear waste system, as humidity, acidity and irradiation has negligible impact on its adsorption capacity.

Next, motivated by the high adsorption capacity of CH₃I by COF-A, the recyclability test was performed. After the first cycle of capture, COF-A was regenerated by thorough washing with ethanol followed by drying was further used for next cycles of capture. Interestingly, from the recyclability test, COF-A was found to display high adsorption efficiency with more than ~80% in three successive adsorption/desorption cycles (Figure 2.3h). This data confirmed the excellent stability and long-term

usability of the adsorbent towards organic iodide capture. Furthermore, the retention proficiency was tested by exposing CH_3I laden COF-A to air at room temperature for 7 days. The CH_3I @COF-A was shown to maintain its weight with minimal loss after 7 days, indicating that the absorption is not caused by surface condensation but rather by the strong interaction between the structure of the COF and CH_3I molecules (Figure 2.3i). Thereafter, along with CH_3I , ethyl iodide ($\text{CH}_3\text{CH}_2\text{I}$) sorption test was performed for all the COFs to explore the general feasibility of the adsorbents towards toxic gas capture. Interestingly, similar trends in the capture capacities of ethyl iodide adsorption was observed by the COFs. The respective amounts of $\text{CH}_3\text{CH}_2\text{I}$ capacities under static dry condition was found as 0.76, 0.67, 0.59 and 0.55 g.g^{-1} for COF-A, B, C and D, respectively (Appendix 2.25).

Investigation to the role of various N-heteroatomic functional sites of these COFs along with the effect of their porosity towards organic iodide adsorption being the key targeted criterion, we further performed the following experiments. For this, we prepared three control COF-A samples, which were synthesized applying similar synthetic procedures as pristine COF-A, except the use of solvent and catalyst amount and combination. These analogues COFs have the identical chemical structure and composition as COF-A, and were denoted as COF-A1, COF-A2, and COF-A3. The PXRD analysis of all these COFs revealed formation of similar structural integrity with COF-A (Appendix 2.26). However, the crystalline nature of these COFs were found to be weak as compared to pristine COF-A. Moreover, the surface area analysis of these COFs showed significantly lower porosity with compared to pristine COF-A (Appendix 2.27). Interestingly, the N_2 sorption data (at 77 K) of COF-A1 indicated similar gas uptake with COF-B, indicating near identical surface area and pore volume (Appendix 2.27a). Also, the N_2 gas uptake and thus surface area of COF-A2 was found to be comparable but slightly lower than COF-C (Appendix 2.27b). On the other hand, COF-A3 revealed similar N_2 gas uptake and surface area with COF-D (Appendix 2.27c). After their synthesis and characterizations, we went ahead to perform the CH_3I capture with all these materials and further compared them. Under the similar experimental conditions, COF-A1 found to exhibit 1.18 g.g^{-1} CH_3I uptake capacity, which was significantly lower than COF-B (Figure 2.3j). Also, COF-A2 demonstrated 0.88 g.g^{-1} capacity within ~72 h, which was found to be lower than COF-C as well as COF-B and COF-A1 (Figure 2.3k). Notably, in case of COF-A3, the capacity was much lower than COF-D as well as COF-B, COF-C, COF-A1, and COF-A2 (Figure 2.3l). Now, all of these findings support the hypothesis that when comparing these isostructural COFs having similar functionality with different porosity, the CH_3I adsorption is positively depends upon their porosity. Additionally, the functionality of these COFs directly affects the CH_3I uptake when compared to COFs with similar porosity but different functionality. Again, to further validate this, we prepared another control COF-D sample (COF-D1) (see experimental section for details), which exhibit similar structural formation with COF-D, however displayed significantly lower N_2 gas uptake or surface area than COF-D and COF-A3, owing to its poor crystalline nature (Appendix

2.26d, 2.27d). Interestingly, the CH₃I adsorption capacity of COF-D1 was found to be much lower (0.53 g.g⁻¹), when compared with COF-A3 or COF-D (Figure 2.3m). This result further validate the role of framework integrated functionalities such as N-heterocyclic moieties or heteroatoms along with the porosity of COFs towards effective adsorption of organic iodide vapours. Inspired by the above interesting results, further, we sought to investigate the performance of the COFs towards dynamic CH₃I adsorption test. For this, an experimental setup was used for CH₃I capture at 348 K in dynamic condition under the flow of nitrogen as the carrier gas (see experimental and appendix section for detail) (Appendix 2.28). The dynamic test at dry condition resulted in saturation adsorption capacities of 0.71, 0.55, 0.42 and 0.4 g.g⁻¹ within 48 h for COF-A, B, C and D, respectively. It is important to note that a simulated experimental set-up was further constructed to evaluated the performance of COF-A under circumstances similar to spent nuclear fuel processing. As shown in appendix 2.28, the experimental device consists of CH₃I vapor generator along with water and nitric acid solution to mimic the industrial relevant conditions. Nitrogen gas conveyed CH₃I vapor, moisture, and nitric acid vapours into the sorption tube when it was permitted to pass through the generator. The COF powders packed in the center of the sorption tube increasingly darkened with subsequent adsorption of CH₃I vapours (Appendix 2.29). Next, after treating COF-A with CH₃I vapor in dynamic mode, the sorption capacity was calculated. COF-A powder exhibited 0.58 g.g⁻¹ uptake capacity, suggesting that it could effectively capture organic iodide vapours under simulated dissolver off-gas conditions. In addition to this, we have performed both the static and dynamic vapor phase elemental iodine adsorption test at 348 K with COF-A, which resulted maximum I₂ capture capacity as 4.19 and 2.11 g.g⁻¹, respectively. All of the aforementioned findings showed that these COFs may be used effectively as potential adsorbents in real spent nuclear fuel reprocessing.^[46-49]

Investigation of organic iodide-binding interactions mechanisms

We were motivated further to look into the potential interactions between the structures of the COFs and methyl iodide (CH₃I) because of the impressively adjustable organic iodide capture ability of the COFs. The investigation of CH₃I-binding interactions mechanism with COF-A to COF-D was assessed by FESEM-EDS, elemental mapping, XPS, solid-state ¹³C NMR, FT-IR, TGA and zeta potential analysis. Initially, the FESEM-EDS and the corresponding elemental mapping images of the CH₃I loaded COFs materials indicated the homogeneous distribution of iodine (from CH₃I) element throughout the surface of the compounds (Appendix 2.30, 2.31). This data confirmed the successful loading of CH₃I molecules within the framework of the COFs. Additionally, in case of CH₃CH₂I@COFs, similar observation was noted from the EDS data and elemental mapping images, indicated uptake of ethyl iodide by the COFs (Appendix 2.32, 2.33). It should be mentioned that after CH₃I capture the surface morphology of all the COFs were found remain almost unchanged, as revealed

from the respective FESEM images of $\text{CH}_3\text{I}@\text{COFs}$ (Appendix 2.34). Identical observation was found in case of $\text{CH}_3\text{CH}_2\text{I}@\text{COFs}$ (Appendix 2.35). These data validate the robust surface morphology of the compounds towards organic iodide sequestration. The TGA profiles of $\text{CH}_3\text{I}@\text{COFs}$ revealed continuous weight loss up to $\sim 350^\circ\text{C}$ upon heating indicated large amount of CH_3I trapped inside the pores of the COFs during adsorption (Appendix 2.36). The TGA profile of $\text{CH}_3\text{CH}_2\text{I}@\text{COFs}$ demonstrated similar thermal behaviour (Appendix 2.37). The PXRD data of the COFs after CH_3I adsorption showed no diffraction peaks when compared to pristine crystalline COFs, suggesting loss of order structure or transformation into amorphous architecture (Appendix 2.38). Furthermore, solid-state ^{13}C NMR spectra of CH_3I loaded COFs showed appearance of new intense peak at ~ 57 ppm to ~ 59 ppm, which was attributed to the C atoms of CH_3I molecules, indicating the successful grafting of CH_3I into the structure of the COFs (Figure 2.4a-2.4d). Moreover, such grafting of CH_3I resulted in salt formation through the methylation reactions occurred at different N sites of the COFs.^[22, 23]

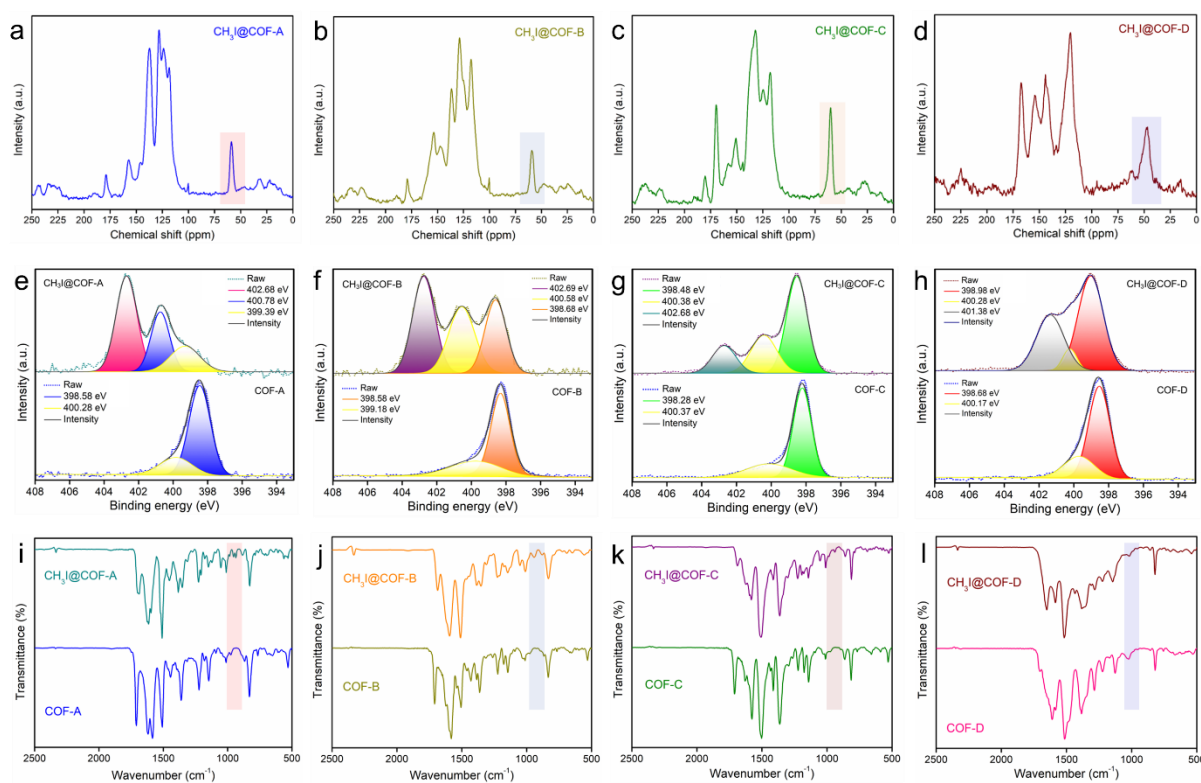


Figure 2.4: (a-d) ^{13}C solid-state NMR spectra of COF-A to D after adsorption of CH_3I at high temperature. (e-h) N 1s XPS spectra of COF-A to D, before and after CH_3I adsorption test. (i-l) FTIR spectra of COF-A to D, before and after CH_3I adsorption test, respectively.

Thereafter, XPS analysis was employed to understand the involvement of different functional sites or elements of COFs and their core energy level towards interaction with CH_3I . At first, compared to the

pristine COFs, the XPS survey spectra of CH₃I laden COFs displayed characteristic peaks at ~618.78 eV and ~630.28 eV corresponds to the I 3d_{5/2} and I 3d_{3/2} core energy level, respectively, which were generated owing to the presence of CH₃I molecules on the surface of the COFs (Appendix 2.39). Now, after the adsorption of CH₃I, the N 1s electron binding energies of COF-A at ~398.5 and ~400.2 eV corresponds to the N of –C=N bond and secondary amine nitrogen, respectively were found to shift from lower to higher binding energy, indicating significant interaction with CH₃I (Figure 2.4e).^[22, 23] Similar shifting of binding energies of N 1s was observed in case of COF-B, C and D after adsorption of CH₃I (Figure 2.4f-2.4h). In addition, the binding energies associated with N 1s of triazine and pyridine moieties of COF-B to COF-D were observed to be shifted towards relative higher binding energies, revealing involvement of these moieties towards interaction with CH₃I. Also, the appearance of new peaks at ~401.38 eV to ~402.69 eV for all the COFs A to D indicated strong interaction between N sites of COFs with CH₃I. Furthermore, in the FT-IR spectra of CH₃I@COFs, with compared to pristine COFs, the characteristic shift (~1 cm⁻¹) or intensity change of the C=N and C-N bonds vibrational frequency as well as appearance of band at ~939 cm⁻¹ indicated formation of new chemical bonds between the N sites of the COFs and CH₃I (Figure 2.4i-2.4l).^[22-25] This was further validated the formation of ionic species (-N-CH₃)+I⁻ upon adsorption of CH₃I. Similar result was observed in the case of CH₃CH₂I@COFs (Appendix 2.40). Notably, the bond frequency corresponds to C=C bond of the COFs were found to unaltered after the adsorption of CH₃I. That being said, all these results lend credence to the idea that CH₃I molecules are selectively anchored to the nucleophilic N sites through N-methylation processes rather than being adsorbed on the phenyl rings of the COFs. In addition to this, to further validate the formation of cationic surface of the COFs after trapping of CH₃I based on the methylation reaction, Zeta potential measurements were performed. With compared to the pristine COFs, the Zeta potential analysis of CH₃I@COFs displayed high positive values, suggested the transformation of neutral framework into cationic skeleton after CH₃I adsorption (Appendix 2.41, 2.42). These findings imply that nitrogen atoms in the frameworks from diverse functional moieties, including imine, triazine, pyridine, and secondary amine, are crucial in effectively enhancing the interactions between the COFs and the organic iodide molecules.

The above discussion established the fact that after the CH₃I adsorption the original neutral skeleton of all the COFs were converted into cationic one through methylation reaction, which further generated a large number of cationic center with exchangeable iodides as the free counter-ions. To cross-verify this, an anion-exchange study with CH₃I@COF-A using anionic organic dye, orange G (OG²⁻) was performed and monitored through UV-vis measurements (see appendix section for details). As a result of this dye elimination test, CH₃I@COF-A was found to sequester OG²⁻ rapidly from a 0.1 mmol stock aqueous solution within 30 sec of contact time (Appendix 2.43). Whereas, pristine COF-A demonstrated negligible dye removal efficiency within 30 sec of contact time as the UV-vis spectra

showed only a small reduction in the intensity even after longer period of time (Appendix 2.44). The removal efficiency or decrease in the concentration with respect to time profile of COF-A and CH₃I@COF-A exhibited ~21% and ~99% OG²⁻ capture efficiency within 1 min, respectively (Appendix 2.45). The rapid dye adsorption kinetics of CH₃I@COF-A with compared to COF-A clearly validate the conversion of neutral framework (COF-A) into cationic skeleton (CH₃I@COF-A). Furthermore, inspired by this result we have conducted a thorough organic toxics segregation study in the appendix section 2.6.5 (Appendix 2.43-2.65).

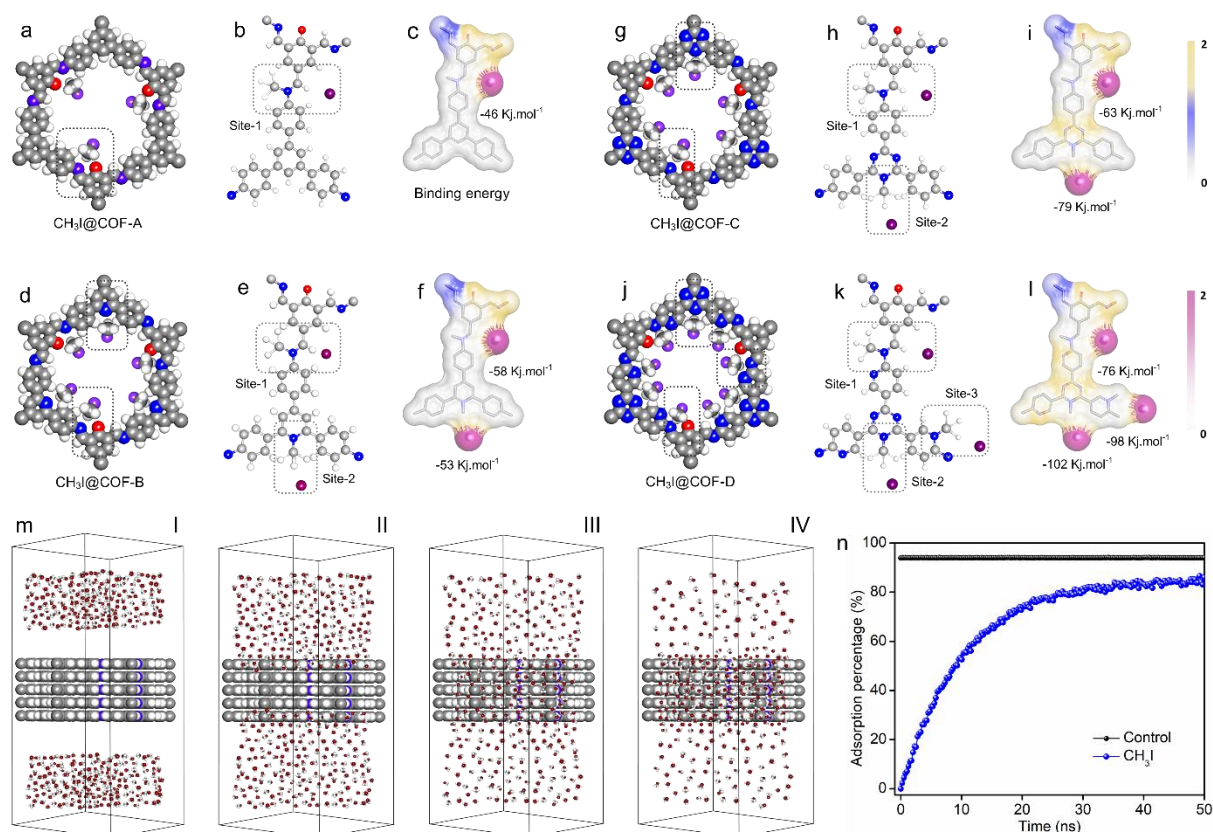


Figure 2.5: Density functional theory (DFT) calculations: (a-l) configurations for adsorption of CH₃I molecules with their corresponding binding energies and energy potential surface diagrams for different N-functional sites of COF-A, B, C, and D, respectively. Molecular simulations (MD) on the adsorption of CH₃I molecules into COF-A. (m) A time-series of snap-shots to show the adsorbing dynamics of CH₃I molecules into COF-A structure, (I-IV) 0, 10, 30, 50 ns, respectively. (n) Time evolution of the adsorption rate of CH₃I molecules (blue) in COF-A.

To gain more insight into the preferential binding sites of CH₃I, we further conducted the density functional theory (DFT) simulations study to evaluate the respective binding energies of CH₃I with the COFs. In the structure of COF-A to D, the nucleophilic N sites are majorly available in imine, pyridine

and triazine moieties. All of these sites are potential for interaction with CH_3I . To evaluate these interactions simulation studies were performed using B3LYP function considering the respective repeating units of the COFs as the model molecules to represent the structures of COF-A to D, as shown in figure 2.5 appendix 2.66. Primarily, COF-A has only one N-based binding site, i.e., imine functionality for interaction with CH_3I . The calculations revealed binding energy of $-46 \text{ kJ}\cdot\text{mol}^{-1}$ for this interaction (Figure 2.5a-2.5c). For COF-B, the binding energies for imine and pyridine sites were calculated as -58 and $-53 \text{ kJ}\cdot\text{mol}^{-1}$, respectively (Figure 2.5d-2.5f). The binding energies for imine and triazine sites for COF-C were found as -63 and $-79 \text{ kJ}\cdot\text{mol}^{-1}$, respectively (Figure 2.5g-2.5i).

Moreover, COF-D has three major CH_3I binding sites, such as imine, pyridine and triazine N-sites, which showed binding energies of -76 , -98 and $-102 \text{ kJ}\cdot\text{mol}^{-1}$, respectively (Figure 2.5j-2.5l). The simulation showed that the imine group in the COF structure is a most preferable sites for CH_3I adsorption.^[22] In addition to this, presence of other functionalities including pyridine and triazine groups in the adsorbent can serve as an additional platform to improve the ability to capture CH_3I vapor. These theoretical calculations matches with our experimental findings, which in aggregate concluded, extra framework functionality (N-nucleophilic sites) of COFs offer specific favourable adsorption sites for CH_3I molecules. We further investigated the adsorption dynamics of CH_3I molecules into the structure of COF-A using all-atom molecular dynamics (MD) simulations. The MD simulation was performed using GROMACS 2022. During interaction, van der Waals interaction was considered with simple cutoff scheme of 12 \AA and periodic boundary conditions. During interaction the five production runs of 50 ns repeats were performed. The time step of 2.0 fs was used and data collected for every 5 ps . Subsequently, supercells of dimension $3 \times 3 \times 3$ was created from SBU of COF-A and from I^- and $-\text{CH}_3$. Thereafter, the supercell of COF-A was interacted with the supercell composed of I^- and $-\text{CH}_3$. From the simulation it was observed that large number gaseous CH_3I molecules initially started diffusing and were rapidly absorbed into the hollow pores of COF-A structure (Figure 2.5m(I-IV)). The concentration of adsorbed CH_3I molecules in the COF-A structure were observed to increase over time. To describe this dynamics process, the adsorption rate of gaseous CH_3I molecules from the external environment into the structure of COF-A along with the simulation time were estimated. The simulation results are shown in figure 2.5n, which shows that initially for less than 10 ns the adsorption percentage of vapor phase CH_3I is above 50% and increased to about 80% within 30 ns and reaches almost 86% after 50 ns of contact time.

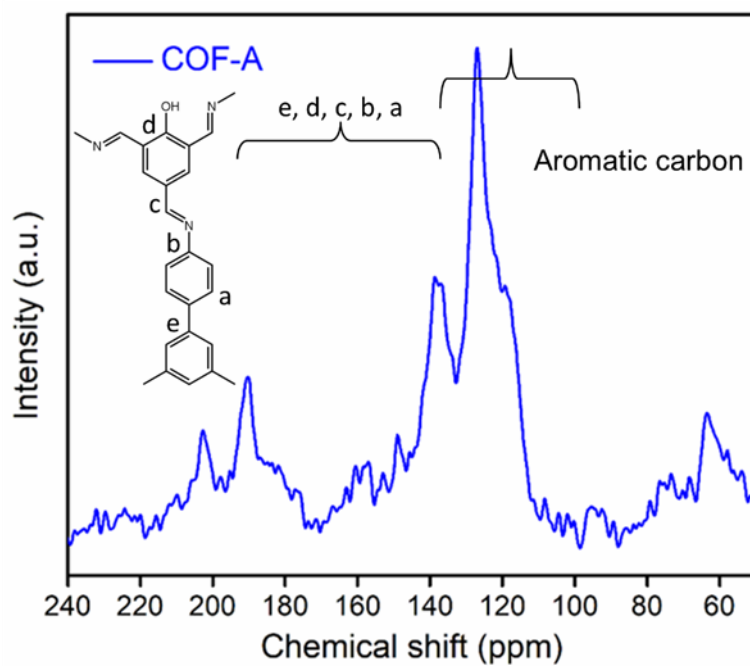
2.5 Conclusion

In summary, we demonstrated a systematic investigation to understand the role of framework integrated N-heterocyclic or heteroatomic nucleophilic functionalities in a series of isostructural chemically stable

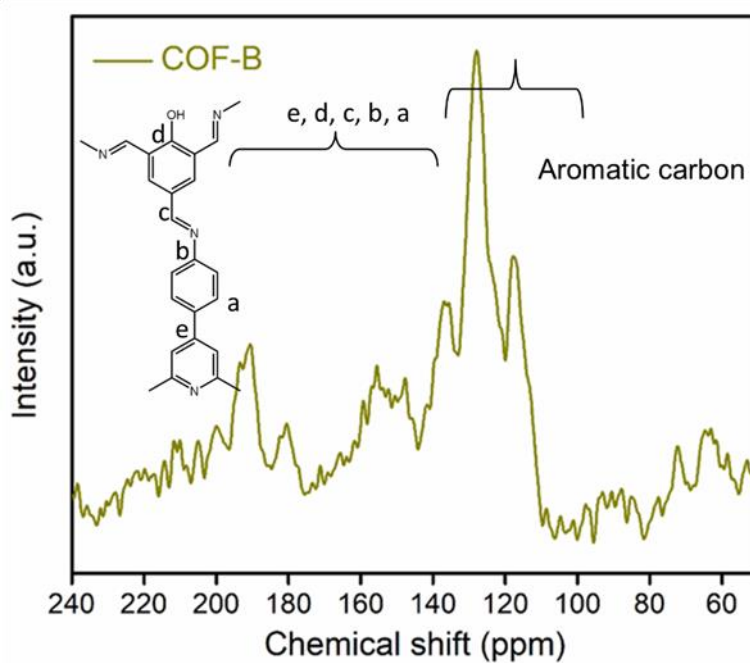
porous COFs towards selective and effective sequestration of organic iodide vapor. Among the synthesized COFs, COF-A, the less functionalized (only having imine groups) one exhibited highest CH₃I adsorption capacity, owing to its highest surface area and pore volume. However, the higher functionalized (with pyridine or triazine or both) COFs exhibited relatively low CH₃I uptake capacity, due to their less surface area compared to COF-A. Interestingly enough, when these COFs have comparable porosity, the CH₃I adsorption capacity was found to positively correlate with the N-contents of the COFs. Detailed experimental and theoretical calculations-based mechanistic studies revealed the optimized contribution of both porosity and various N-nucleophilic functional groups abundant in the structure of COFs synergistically reinforce and contribute toward the ultrahigh CH₃I adsorption capacity. COF-A was found to exhibit high CH₃I adsorption capacities at various relevant temperatures in dry, humid and acidic condition under both static and dynamic phase, further advocating the practical utility of this adsorbent towards real-time radionuclides sequestration. Satisfyingly, the static CH₃I sorption capacity at 348 K of COF-A was found to outperform most of the reported adsorbents. This work lays out a blueprint in terms of systematic molecular level materials engineering in order to harness augmented adsorption performance. Further, we believe the present findings will accelerate the development of COF-based adsorbents, and aid understanding rational modification of functional groups along with the porosity in solid-state materials for adsorption-based applications.

2.6 Appendix Section

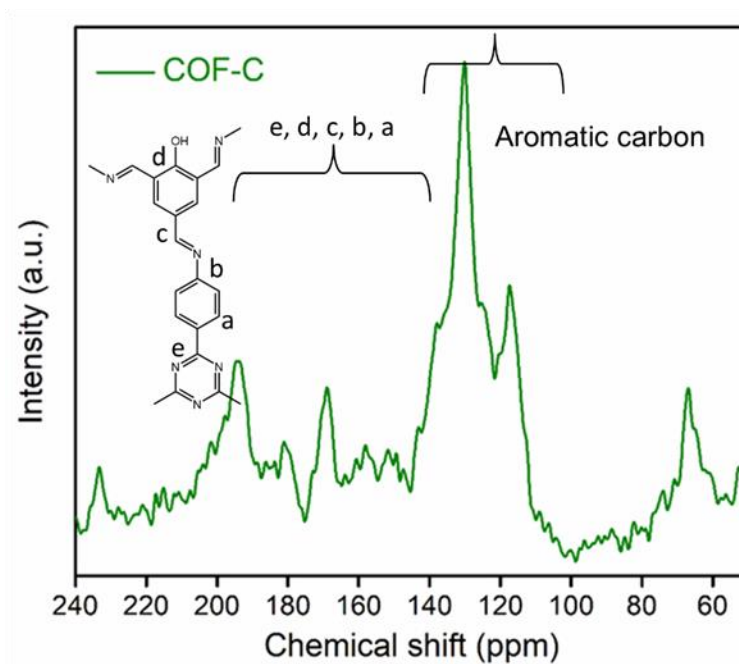
Appendix Section 2.6.1: Structural characterizations of the COFs



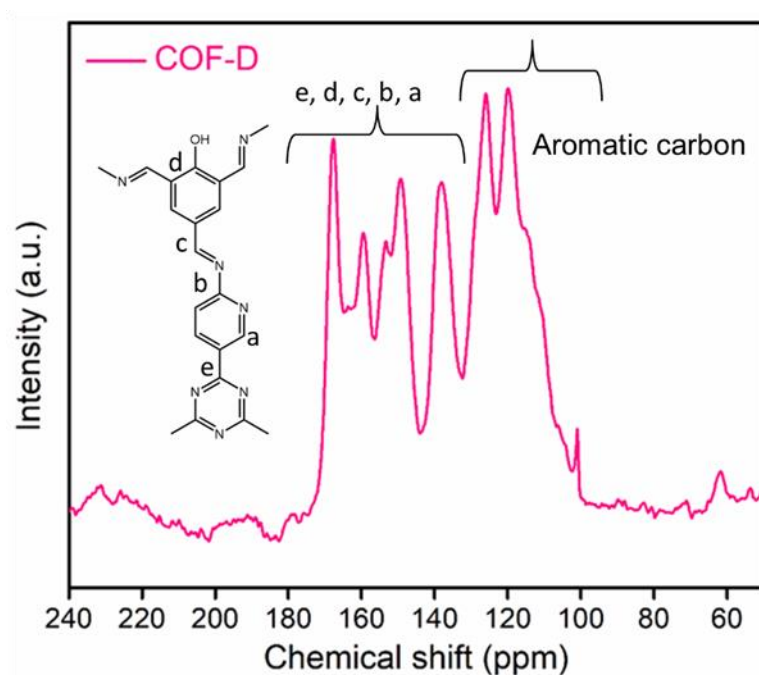
Appendix 2.1: Solid-state ^{13}C CP-MAS NMR spectra of COF-A.



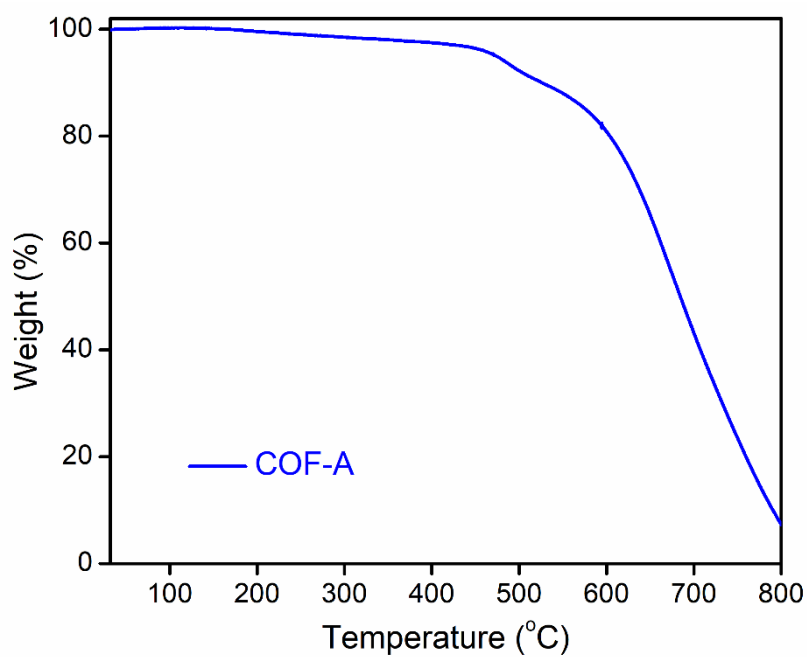
Appendix 2.2: Solid-state ^{13}C CP-MAS NMR spectra of COF-B.



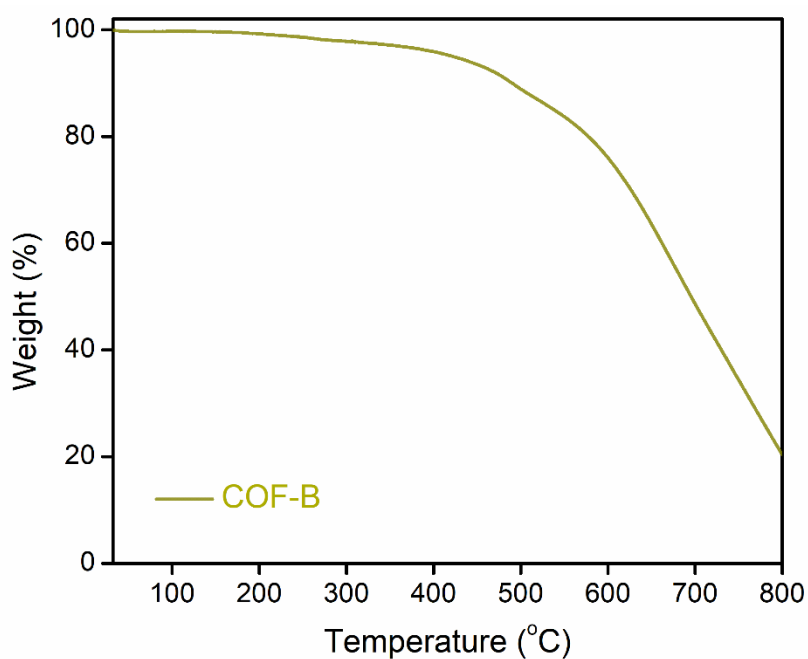
Appendix 2.3: Solid-state ^{13}C CP-MAS NMR spectra of COF-C.



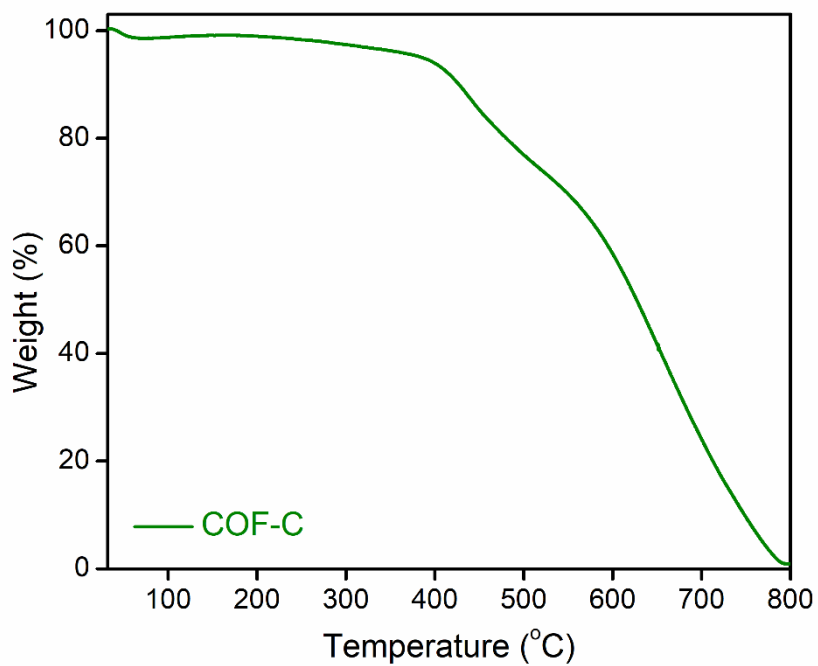
Appendix 2.4: Solid-state ^{13}C CP-MAS NMR spectra of COF-D.



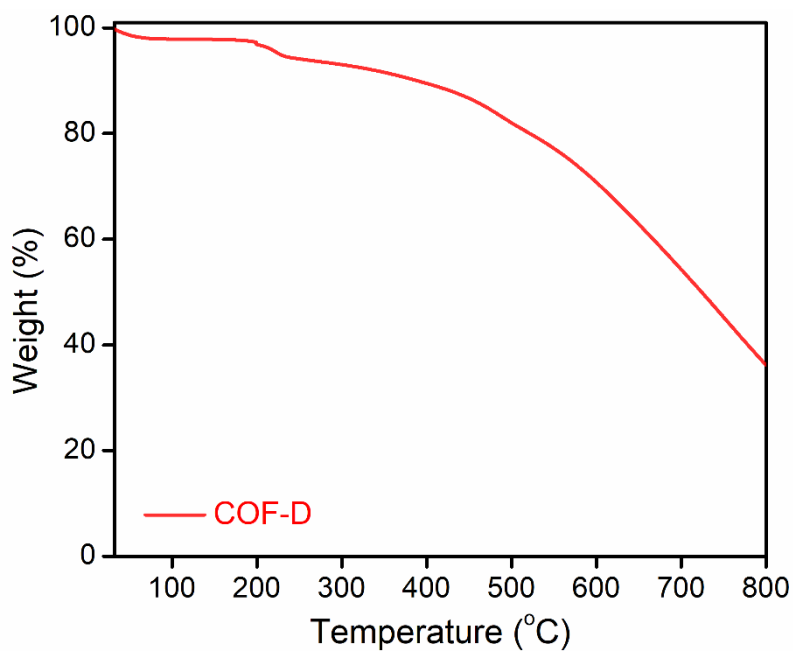
Appendix 2.5: TGA profile of COF-A.



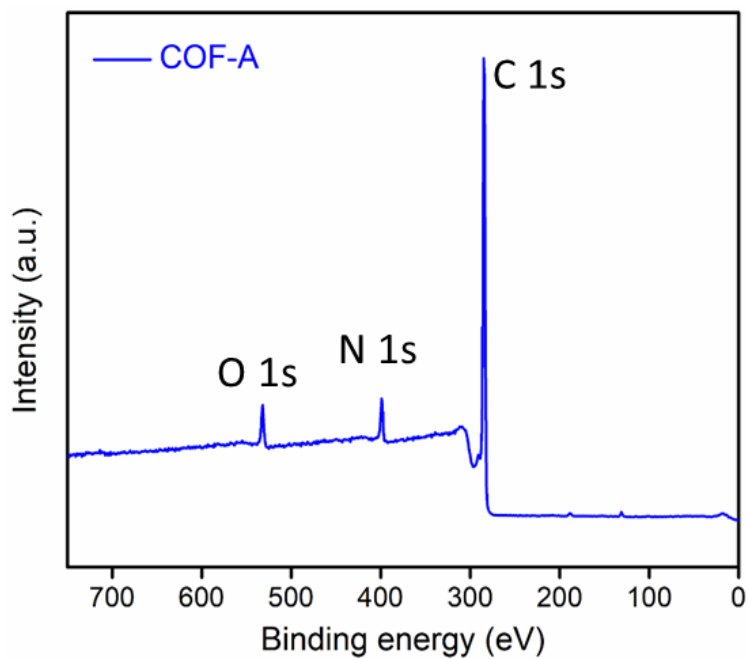
Appendix 2.6: TGA profile of COF-B.



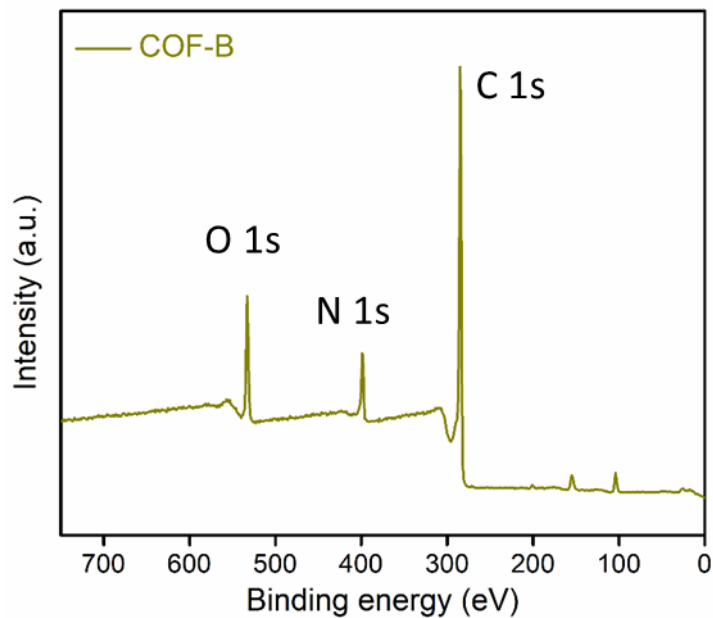
Appendix 2.7: TGA profile of COF-C.



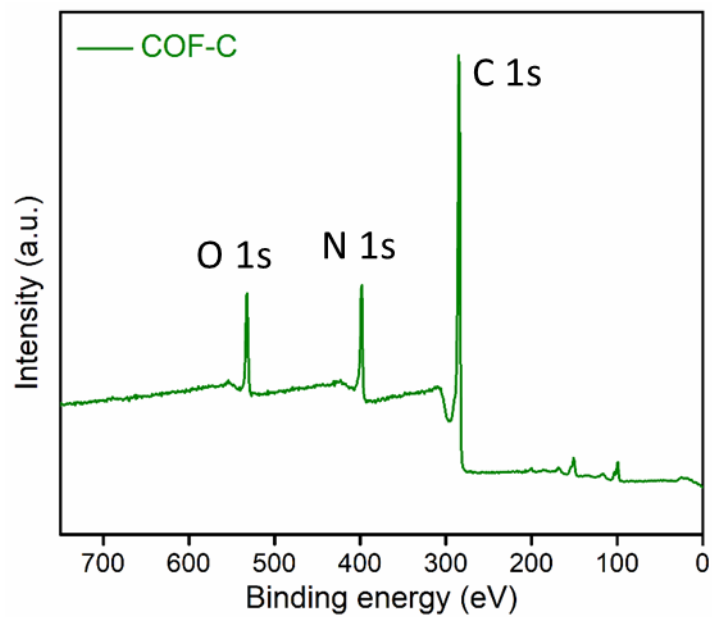
Appendix 2.8: TGA profile of COF-D.



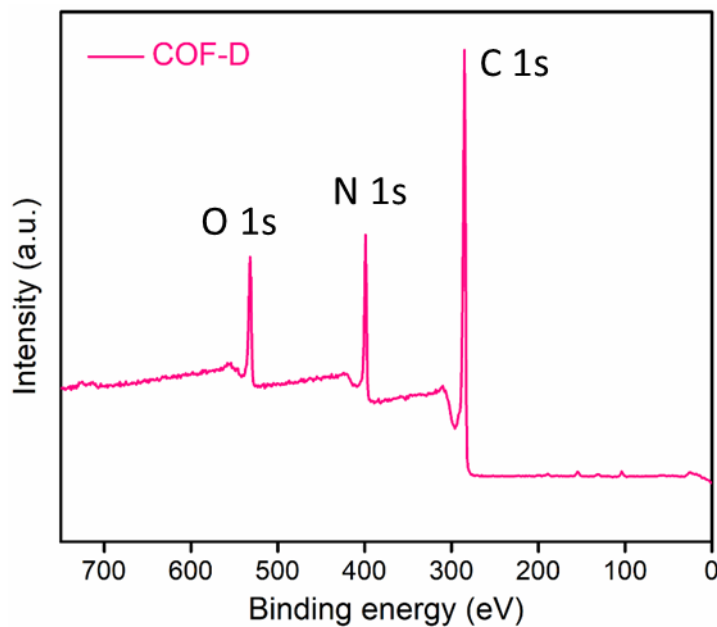
Appendix 2.9: XPS survey spectra of COF-A, showing the presence of C, N and O elements.



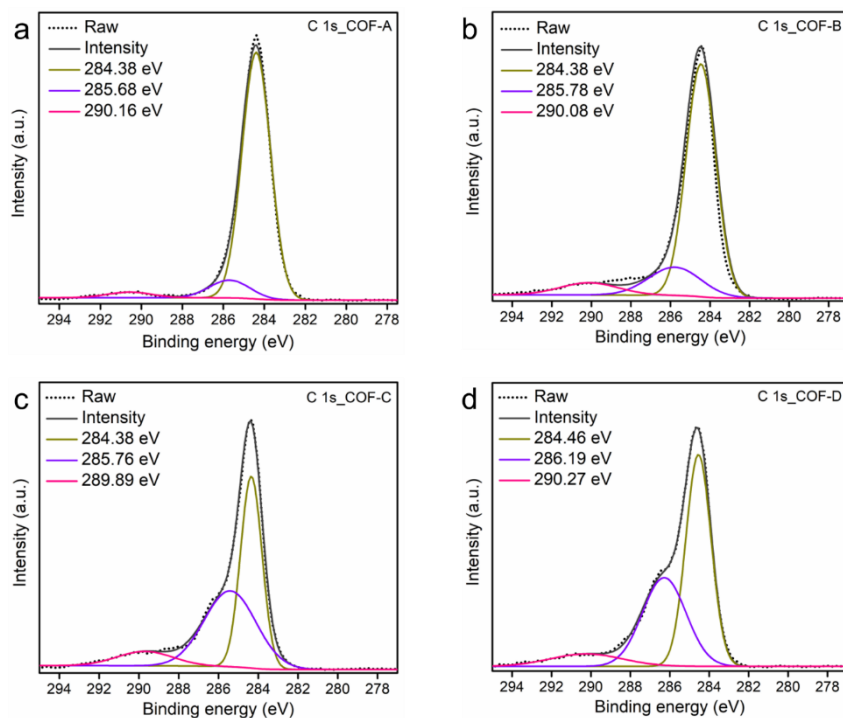
Appendix 2.10: XPS survey spectra of COF-B, showing the presence of C, N and O elements.



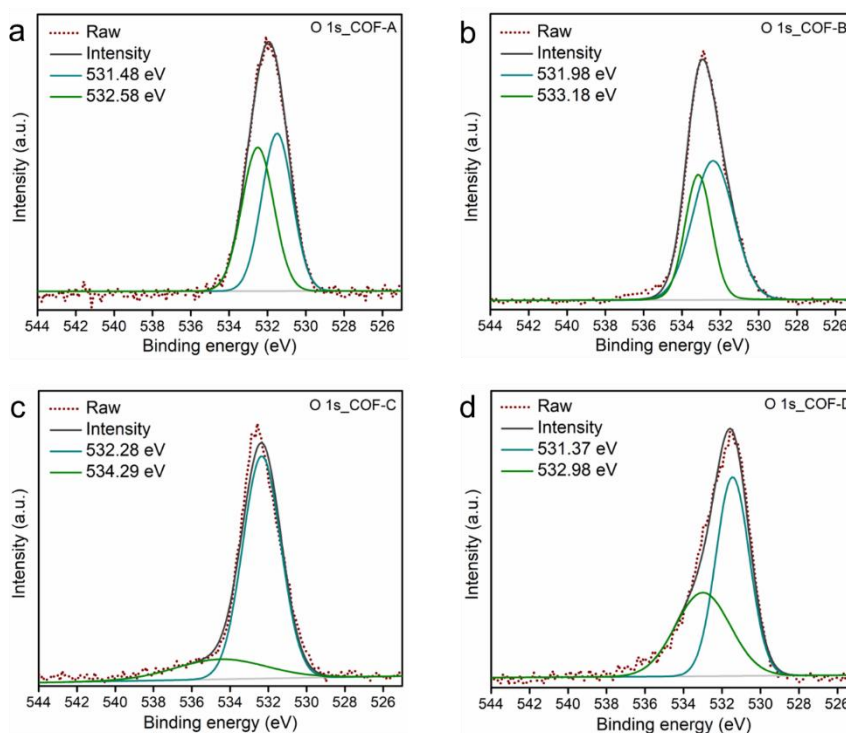
Appendix 2.11: XPS survey spectra of COF-C, showing the presence of C, N and O elements.



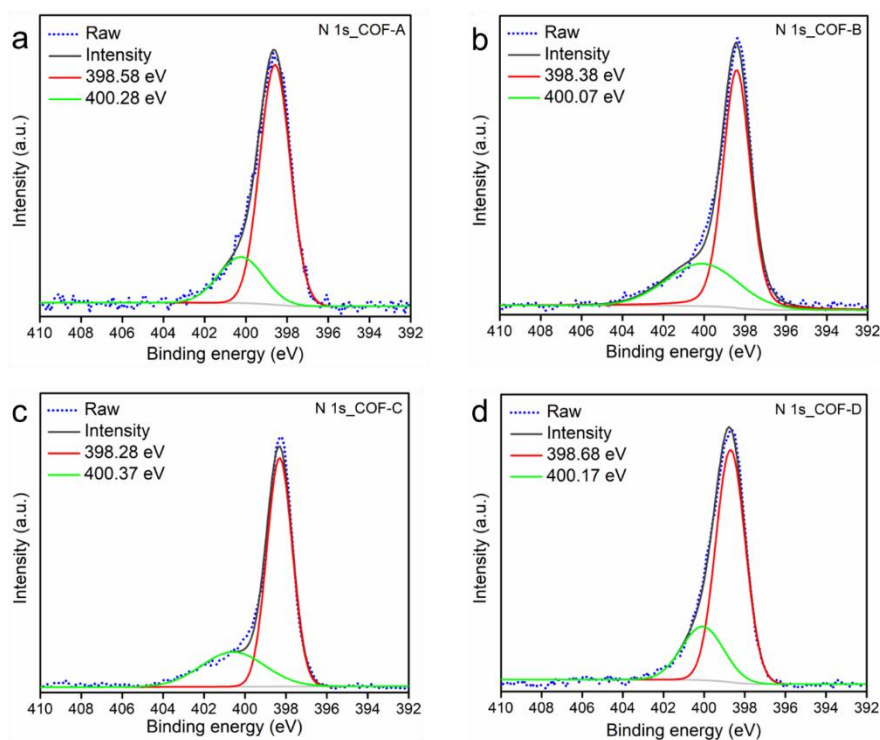
Appendix 2.12: XPS survey spectra of COF-D, showing the presence of C, N and O elements.



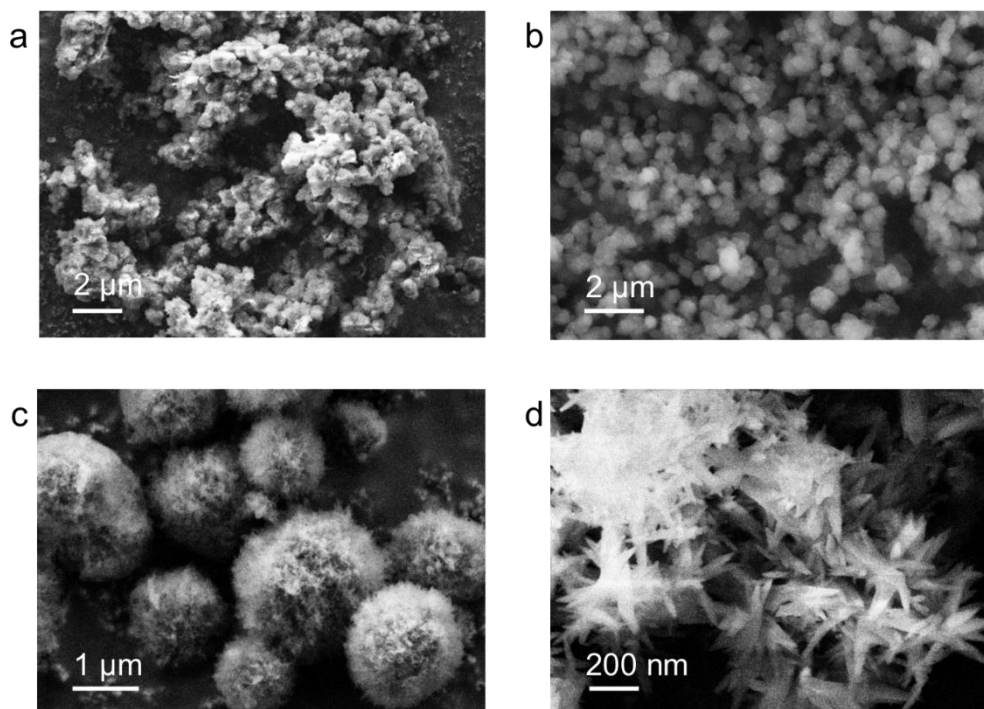
Appendix 2.13: C 1s XPS spectra of (a) COF-A, (b) COF-B, (c) COF-C, and (d) COF-D.



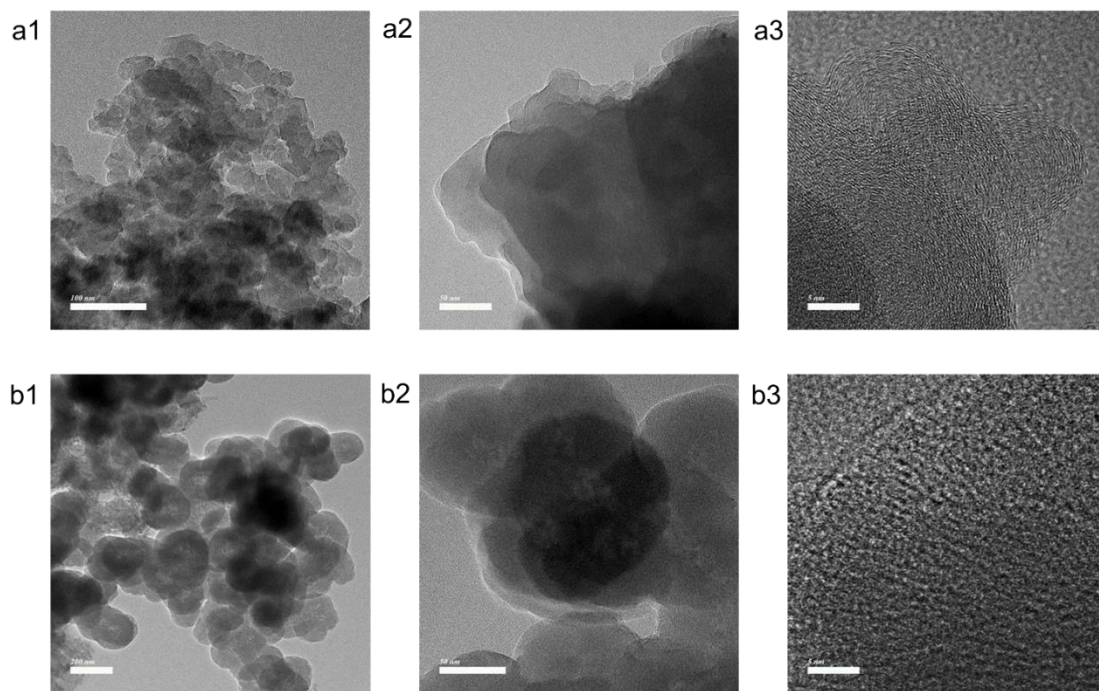
Appendix 2.14: O 1s XPS spectra of (a) COF-A, (b) COF-B, (c) COF-C, and (d) COF-D.



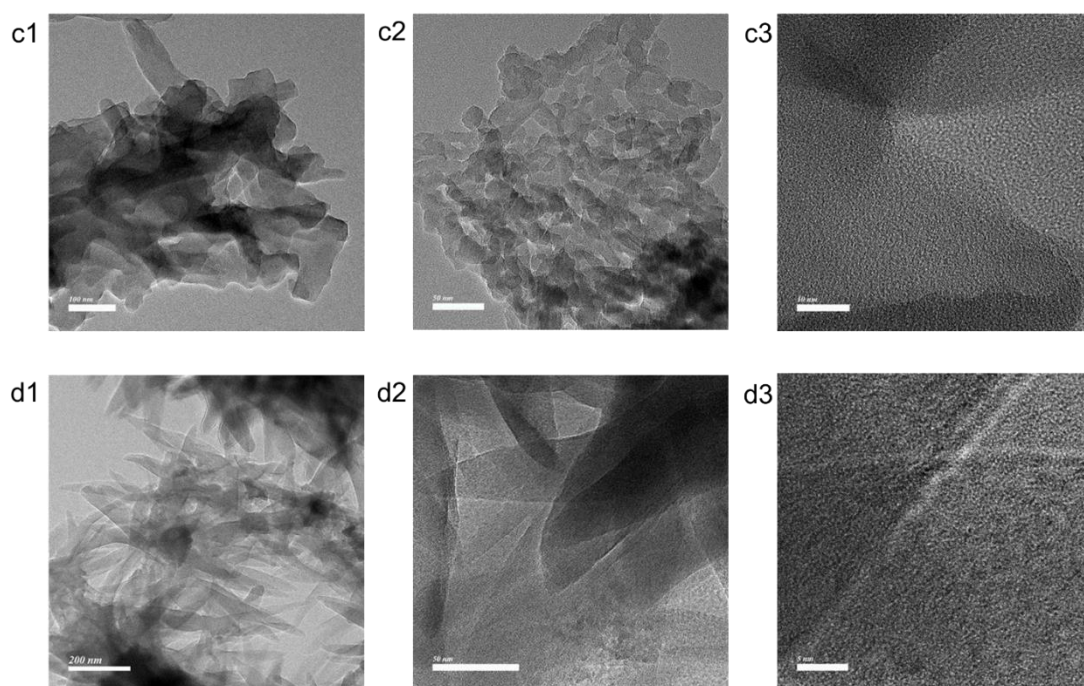
Appendix 2.15: N 1s XPS spectra of (a) COF-A, (b) COF-B, (c) COF-C, and (d) COF-D.



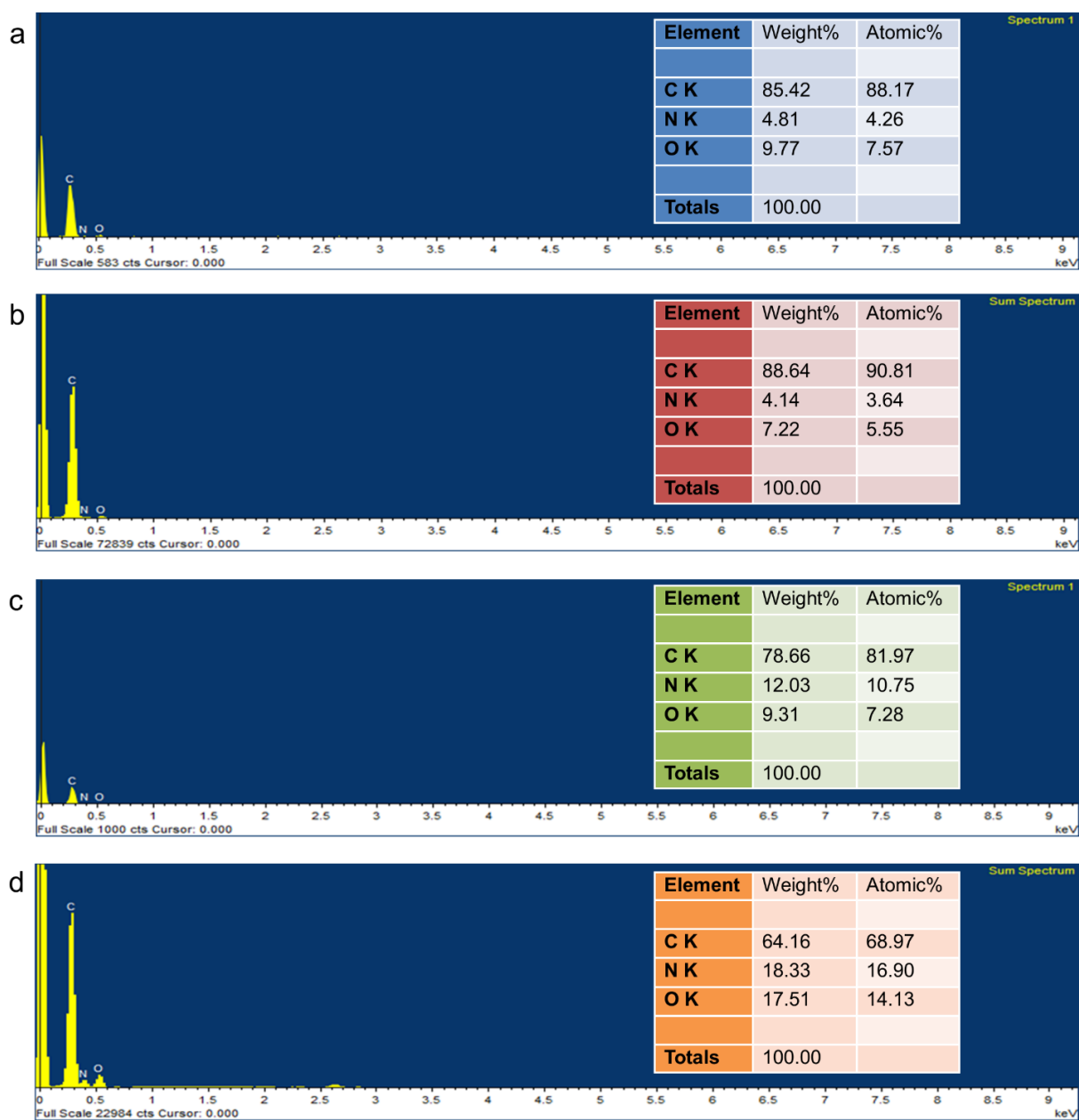
Appendix 2.16: FESEM images of (a) COF-A, (b) COF-B, (c) COF-C, and (d) COF-D.



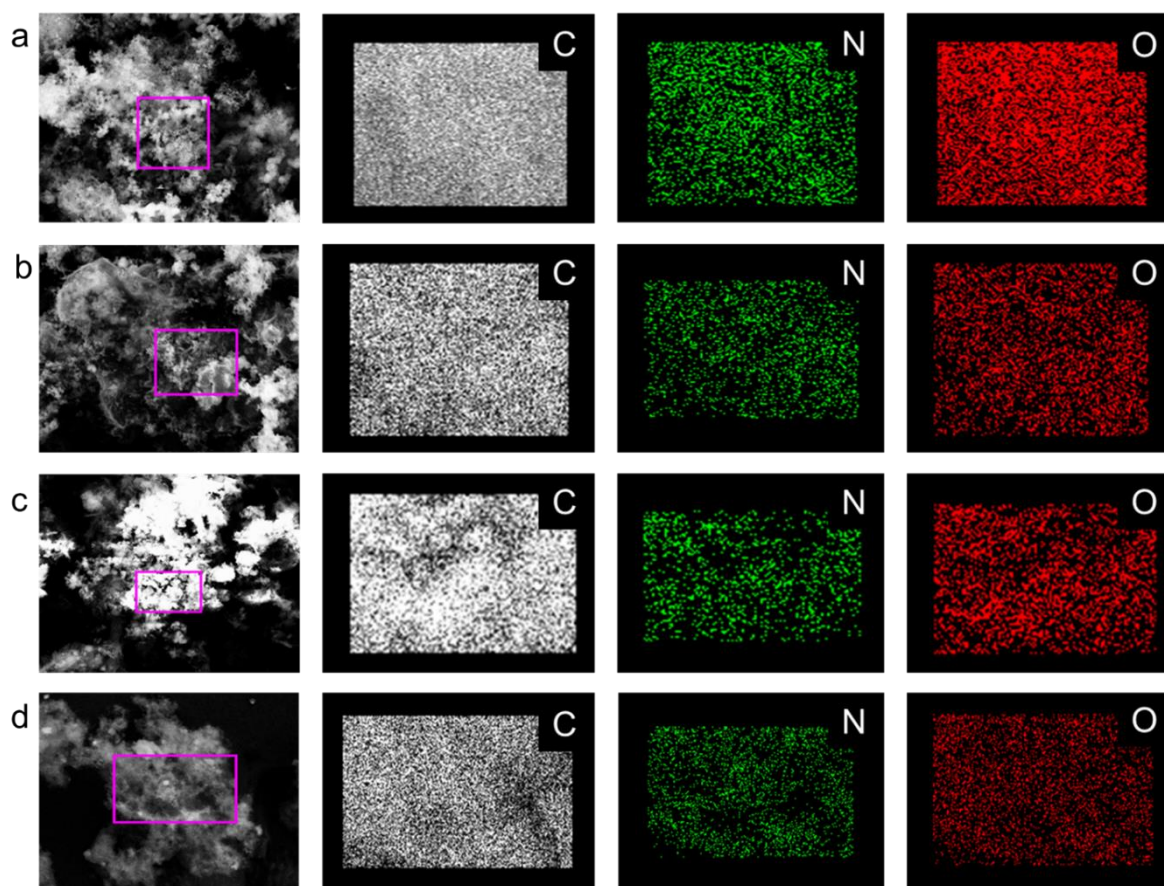
Appendix 2.17: TEM and HRTEM images of (a1-a3) COF-A and (b1-b3) COF-B.



Appendix 2.18: TEM and HRTEM images of (c1-c3) COF-C and (d1-d3) COF-D.



Appendix 2.19: Energy-dispersive X-ray spectroscopy (EDS) data from FESEM experiment of (a) COF-A, (b) COF-B, (c) COF-C, and (d) COF-D.

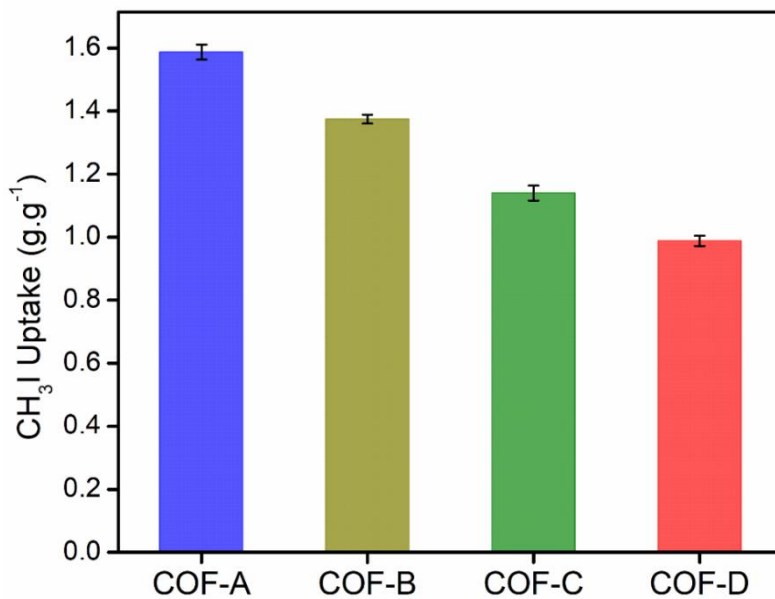
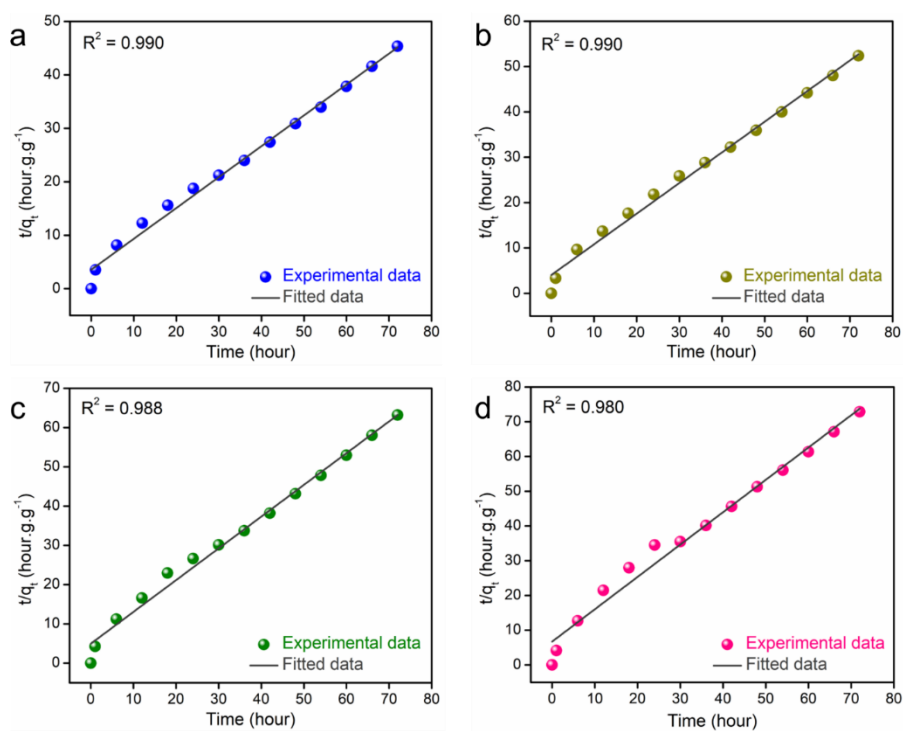


Appendix 2.20: Elemental mapping images from FESEM experiment of (a) COF-A, (b) COF-B, (c) COF-C, and (d) COF-D.

Appendix Table 2.1: Elemental analysis data of the COF-A, COF-B, COF-C and COF-D.

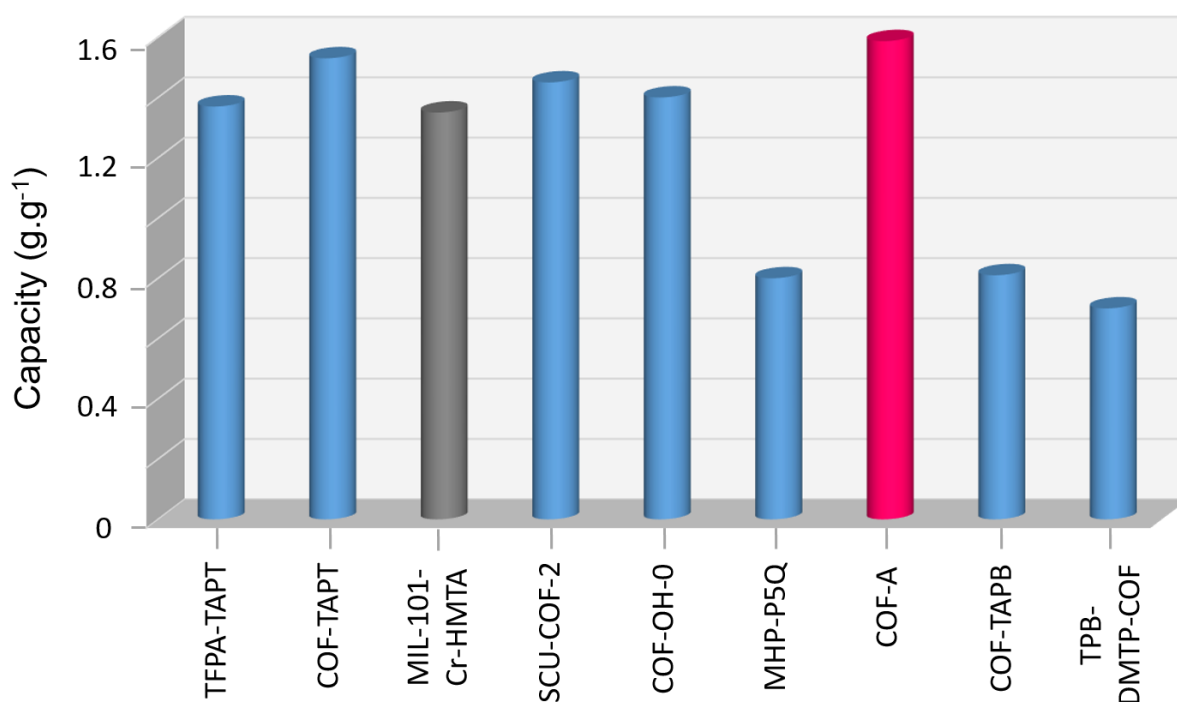
Samples	Theoretical content			Experimental content		
	C [%]	H [%]	N [%]	C [%]	H [%]	N [%]
COF-A	78.89	6.14	14.97	79.88	3.95	16.17
COF-B	76.47	5.79	17.74	77.82	3.99	18.19
COF-C	72.96	6.27	20.77	74.05	4.10	21.85
COF-D	68.26	5.51	26.23	69.14	3.75	27.11

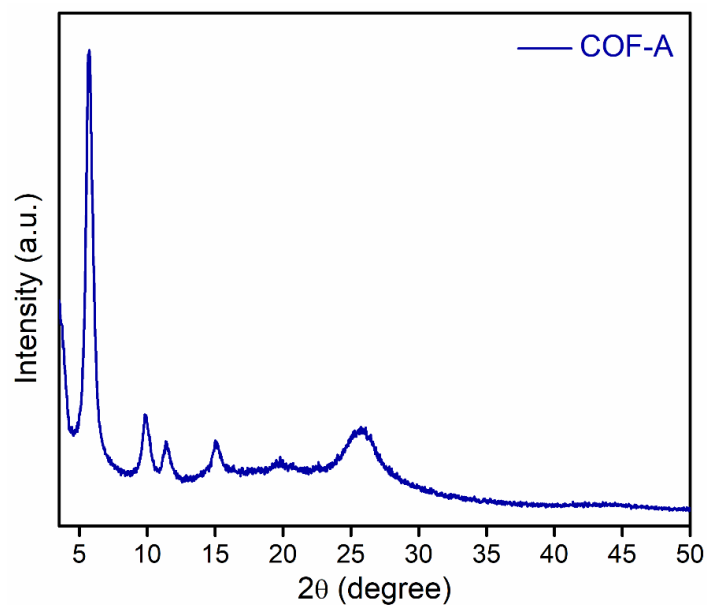
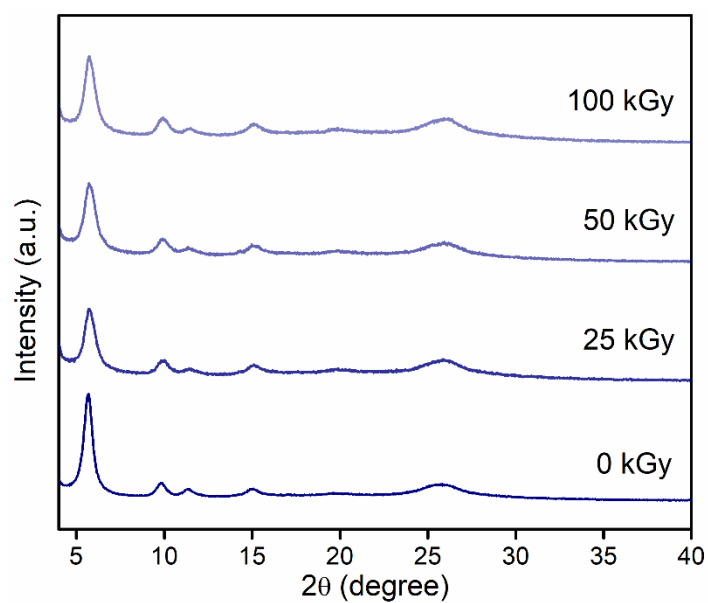
Appendix Section 2.6.2: Organic iodide capture study results

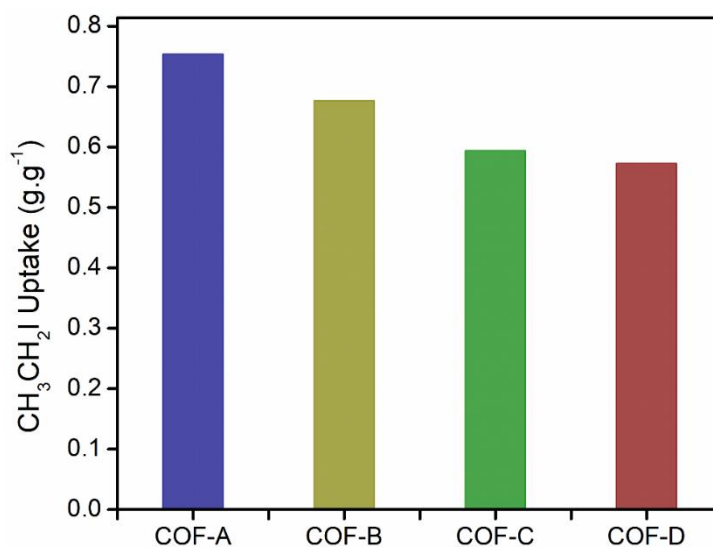
Appendix 2.21: Static CH₃I adsorption data of COF-A, COF-B, COF-C, and COF-D at 348 K.Appendix 2.22: Pseudo-second-order kinetic model fitting data of (a) COF-A, (b) COF-B, (c) COF-C, and (d) COF-D for CH₃I adsorption.

Appendix Table 2.2: Comparison table of static CH₃I adsorption data of various reported adsorbents.

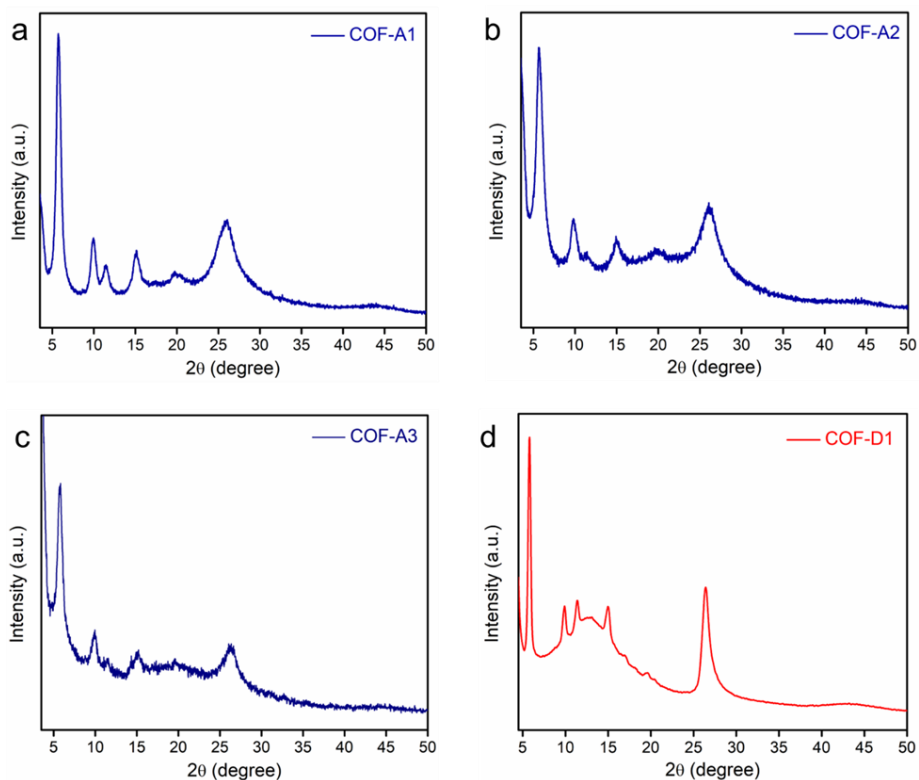
Sample	Temp.	CH ₃ I capacity	References
COF-A	348	1.58 g.g ⁻¹	This work
TFPA-TAPT	348	1.37 g.g ⁻¹	<i>Nat. Commun.</i> 2022 , <i>13</i> , 2878.
COF-TAPT	348	1.53 g.g ⁻¹	<i>Nat. Commun.</i> 2022 , <i>13</i> , 2878.
MIL-101-Cr-HMTA	348	1.35 g.g ⁻¹	<i>Nat. Commun.</i> 2017 , <i>8</i> , 485.
SCU-COF-2	348	1.45 g.g ⁻¹	<i>Chem</i> 2021 , <i>7</i> , 699–714.
COF-OH-0	348	1.4 g.g ⁻¹	<i>Angew. Chem. Int. Ed.</i> 2021 , <i>60</i> , 22432–22440.
MHP-P5Q	348	0.8 g.g ⁻¹	<i>Nat. Commun.</i> 2020 , <i>11</i> , 1086.
COF-TAPB	348	0.81 g.g ⁻¹	<i>Nat. Commun.</i> 2022 , <i>13</i> , 2878.
TPB-DMTP-COF	348	0.7 g.g ⁻¹	<i>Adv. Mat.</i> 2018 , <i>30</i> , 1801991.



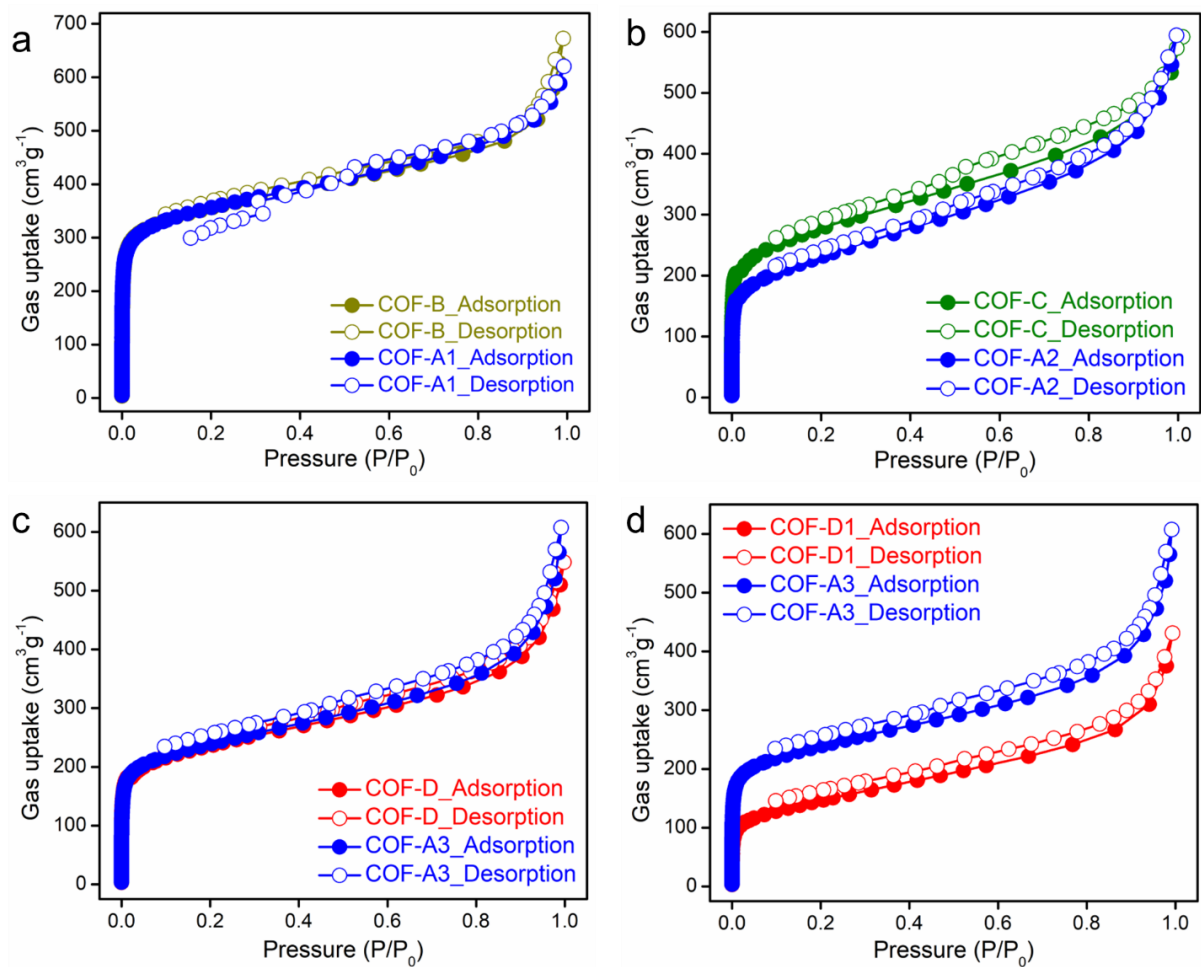
Appendix Section 2.6.3: Chemical stability test and CH₃I adsorption study.**Appendix 2.23: PXRD profile of acid (1M HNO₃) treated COF-A.****Appendix 2.24: PXRD profile of COF-A upon irradiation of different kGy radiation.**



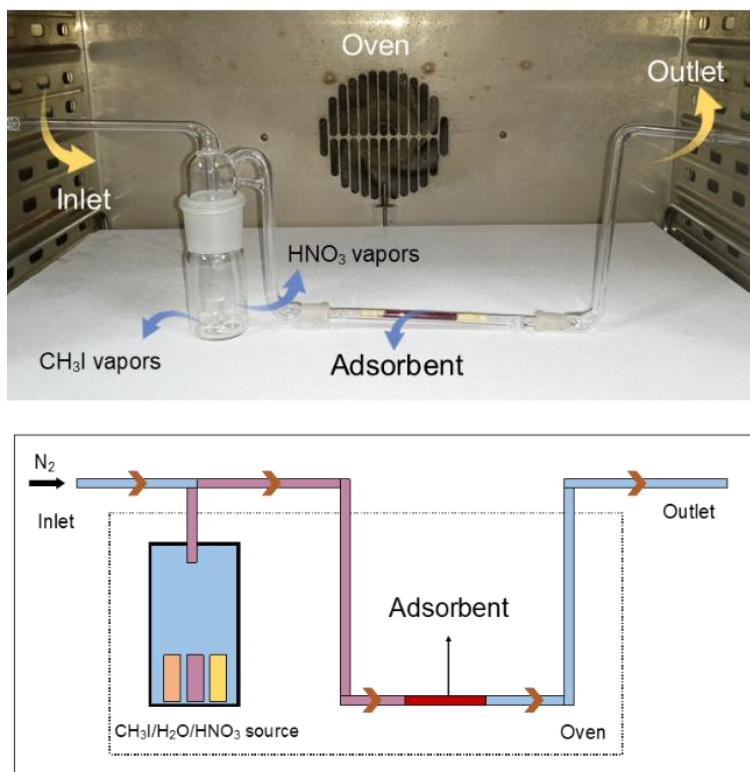
Appendix 2.25: Static adsorption capacities of CH₃CH₂I by COF-A at 348 K.



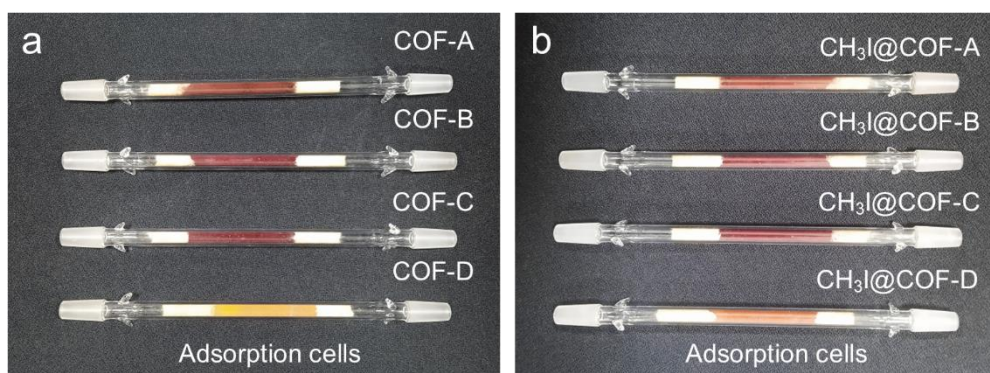
Appendix 2.26: PXRD patterns of (a) COF-A1, (b) COF-A2, (c) COF-A3, and (d) COF-D1.



Appendix 2.27: N_2 gas sorption data at 77 K of (a) COF-A1 and COF-B, (b) COF-A2 and COF-C, (c) COF-A3 and COF-D, and (d) COF-D1 and COF-A3.



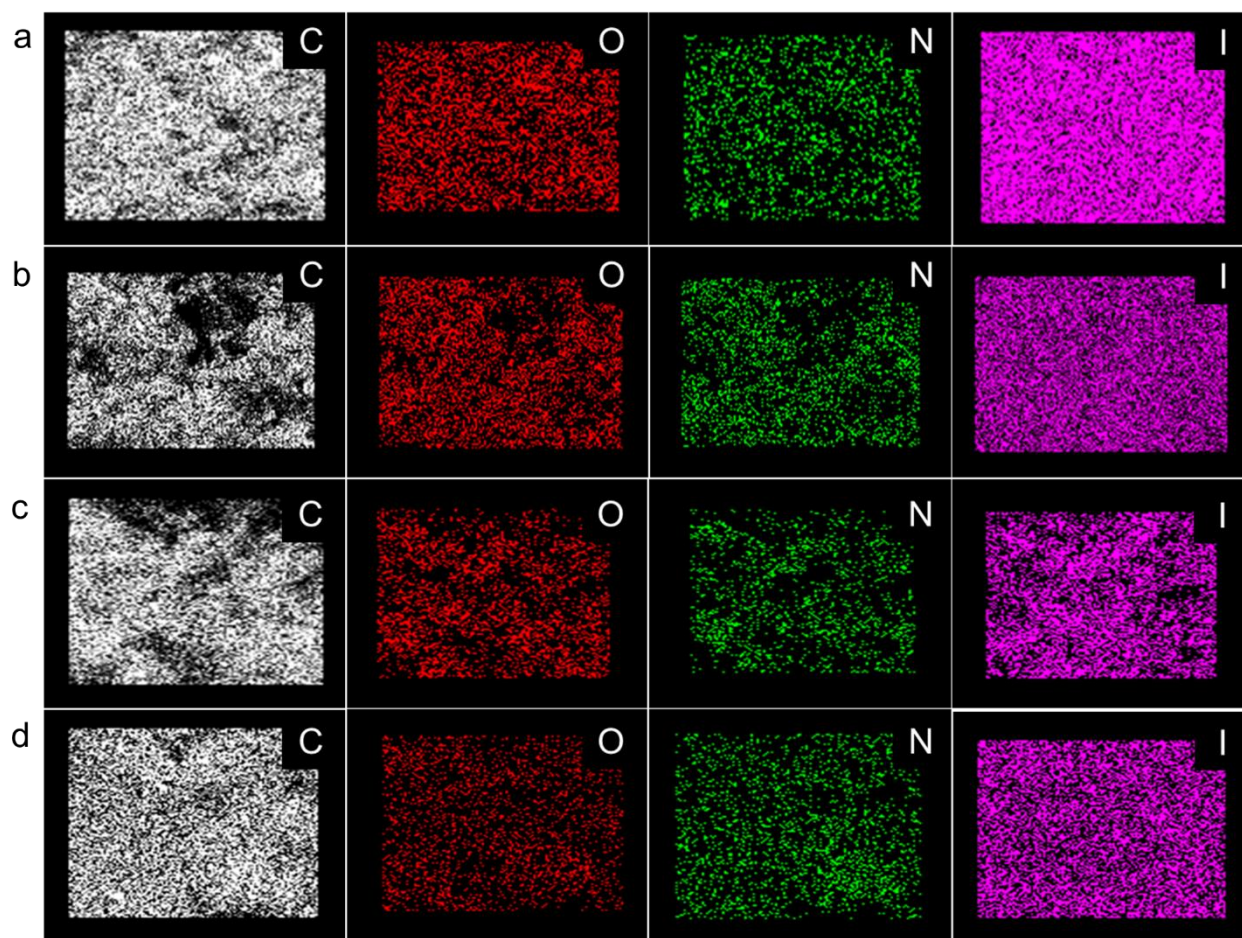
Appendix 2.28: Digital image and schematic diagram of experimental setup for vapor phase dynamic CH₃I capture test.



Appendix 2.29: Images of glass columns packed with COFs (a) before and (b) after adsorption of CH₃I.

Appendix Section 2.6.4: Post CH₃I adsorption characterizations.

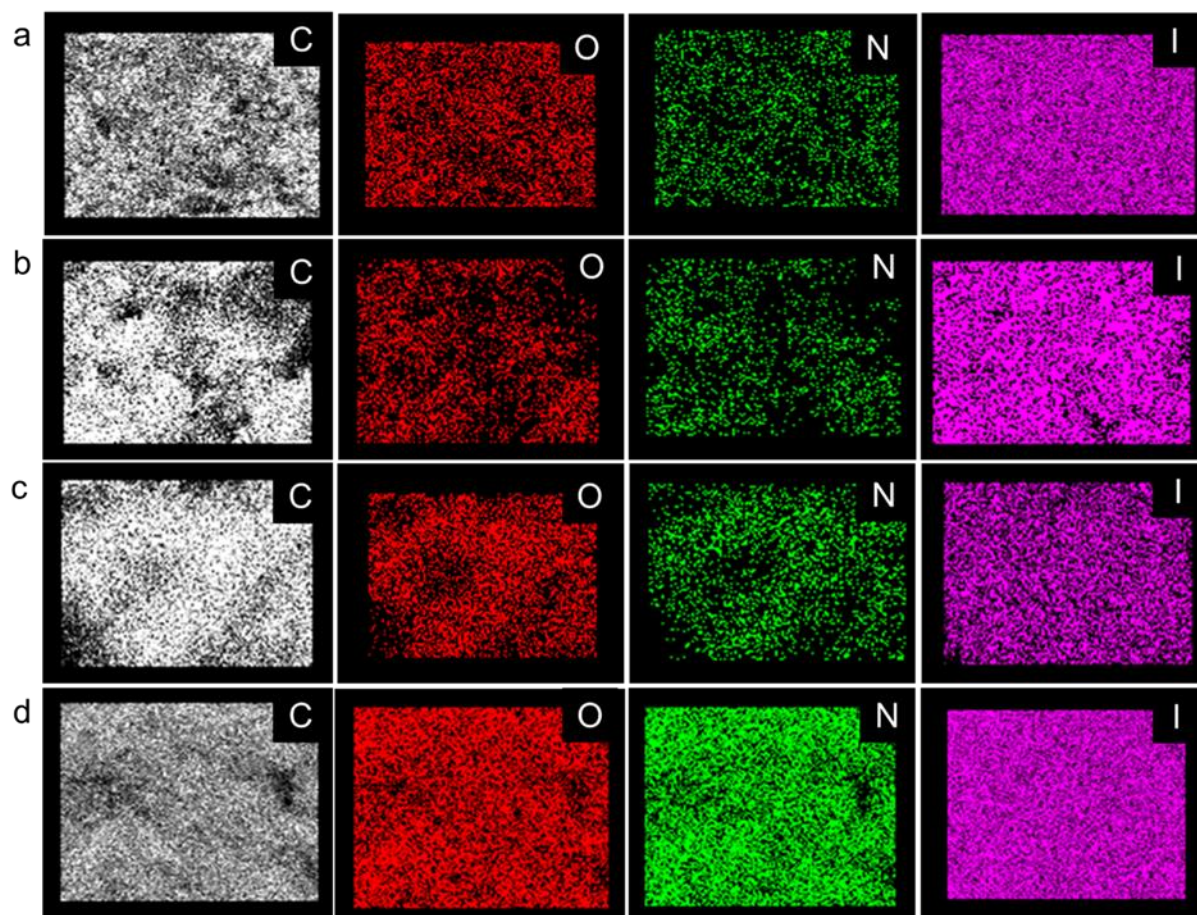
Appendix 2.30: Energy-dispersive X-ray spectroscopy (EDS) data from FESEM experiment of (a) CH₃I@COF-A, (b) CH₃I@COF-B, (c) CH₃I@COF-C, and (d) CH₃I@COF-D.



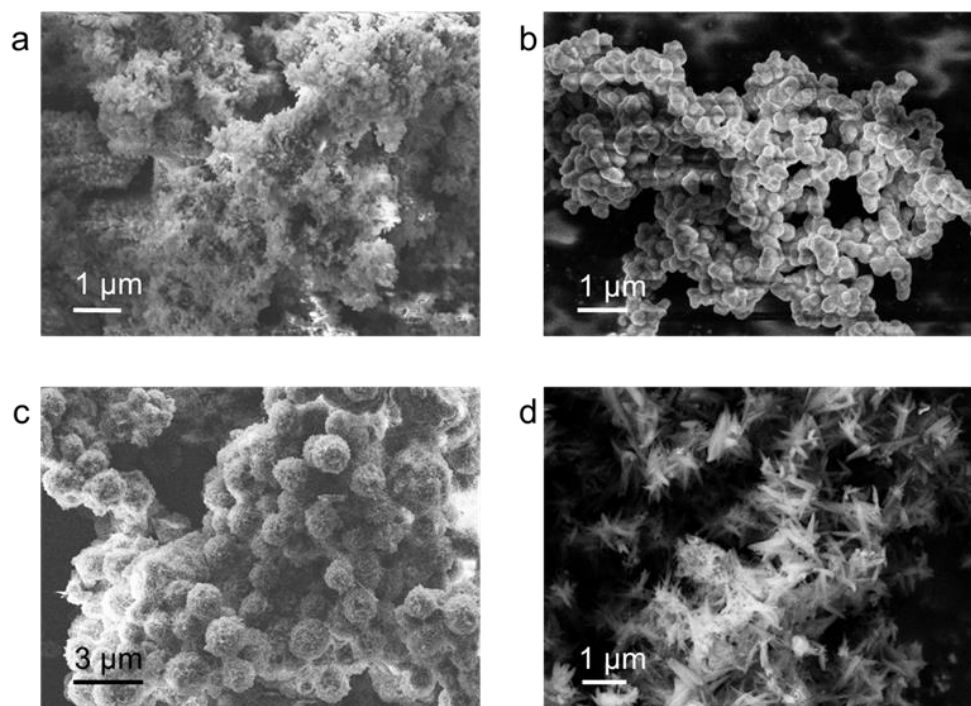
Appendix 2.31: Elemental mapping images from FESEM experiment of (a) CH₃I@COF-A, (b) CH₃I@COF-B, (c) CH₃I@COF-C, and (d) CH₃I@COF-D.



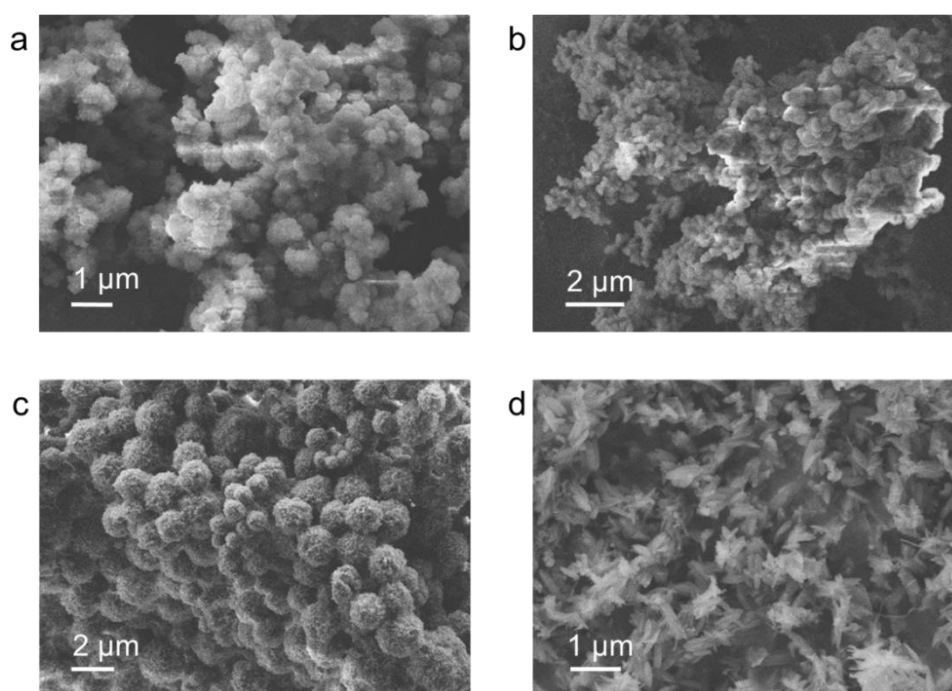
Appendix 2.32: Energy-dispersive X-ray spectroscopy (EDS) data from FESEM experiment of (a) $\text{CH}_3\text{CH}_2\text{I}@\text{COF-A}$, (b) $\text{CH}_3\text{CH}_2\text{I}@\text{COF-B}$, (c) $\text{CH}_3\text{CH}_2\text{I}@\text{COF-C}$, and (d) $\text{CH}_3\text{CH}_2\text{I}@\text{COF-D}$.



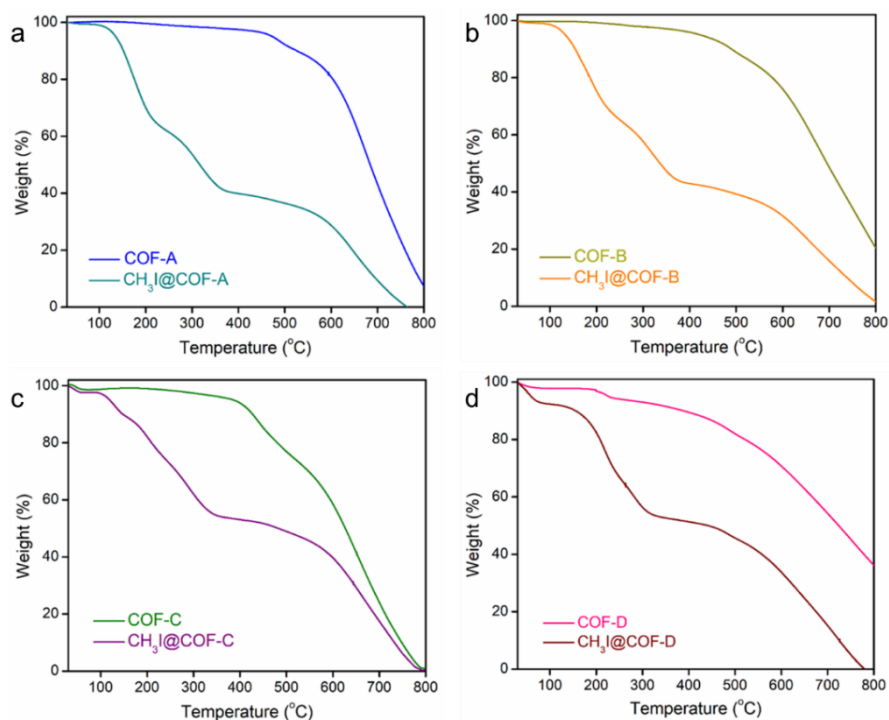
Appendix 2.33: Elemental mapping images from FESEM experiment of (a) CH₃CH₂I@COF-A, (b) CH₃CH₂I@COF-B, (c) CH₃CH₂I@COF-C, and (d) CH₃CH₂I@COF-D.



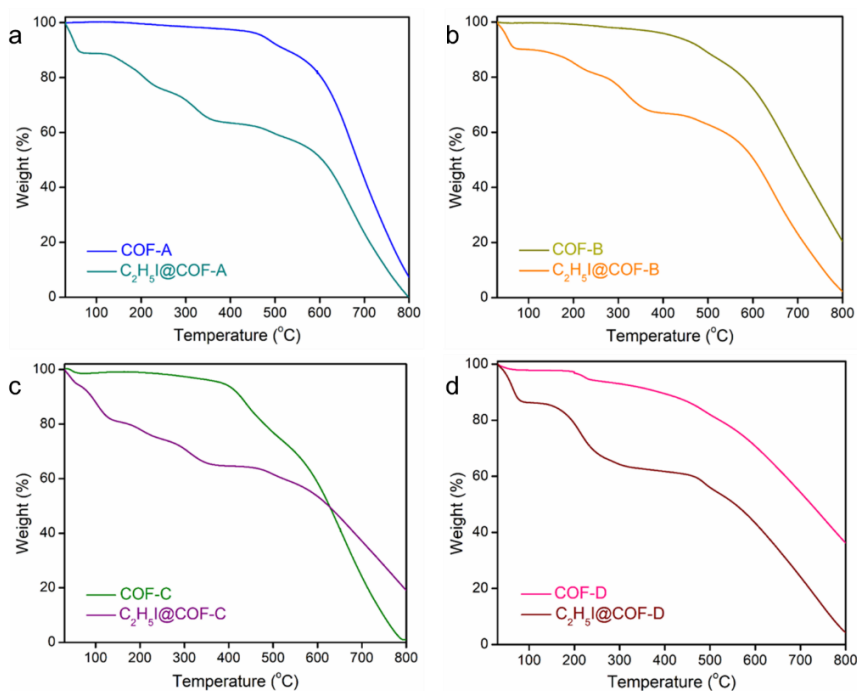
Appendix 2.34: FESEM images of (a) $\text{CH}_3\text{I}@\text{COF-A}$, (b) $\text{CH}_3\text{I}@\text{COF-B}$, (c) $\text{CH}_3\text{I}@\text{COF-C}$, and (d) $\text{CH}_3\text{I}@\text{COF-D}$.



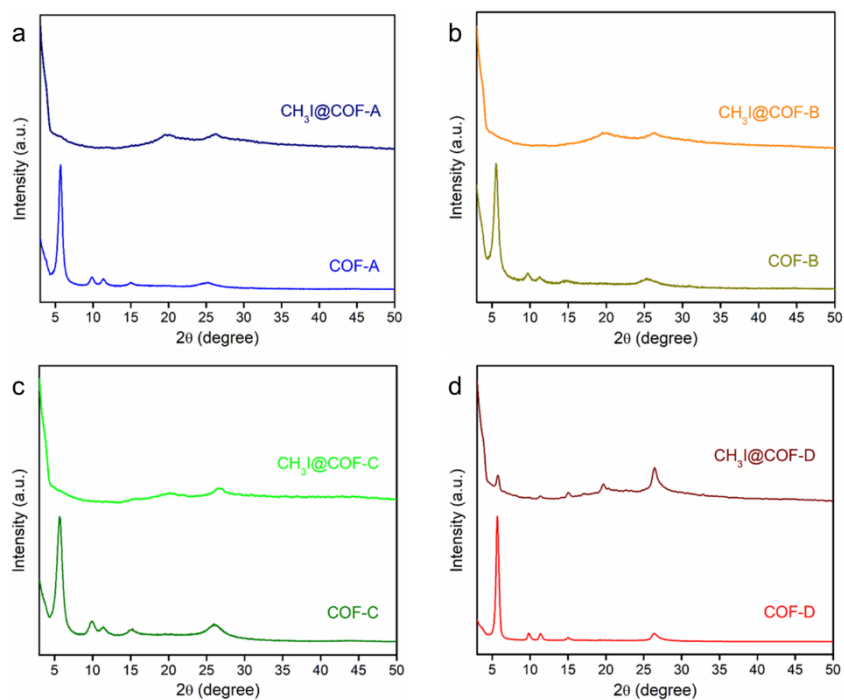
Appendix 2.35: FESEM images of (a) $\text{CH}_3\text{CH}_2\text{I}@\text{COF-A}$, (b) $\text{CH}_3\text{CH}_2\text{I}@\text{COF-B}$, (c) $\text{CH}_3\text{CH}_2\text{I}@\text{COF-C}$, and (d) $\text{CH}_3\text{CH}_2\text{I}@\text{COF-D}$.



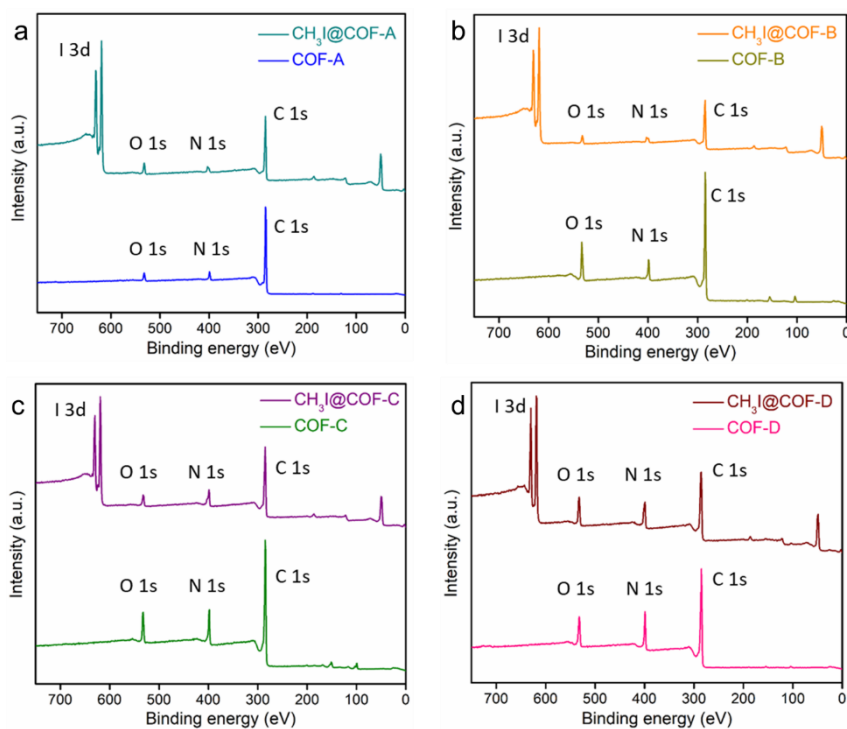
Appendix 2.36: TGA profiles of (a) CH₃I@COF-A, (b) CH₃I@COF-B, (c) CH₃I@COF-C, and (d) CH₃I@COF-D.



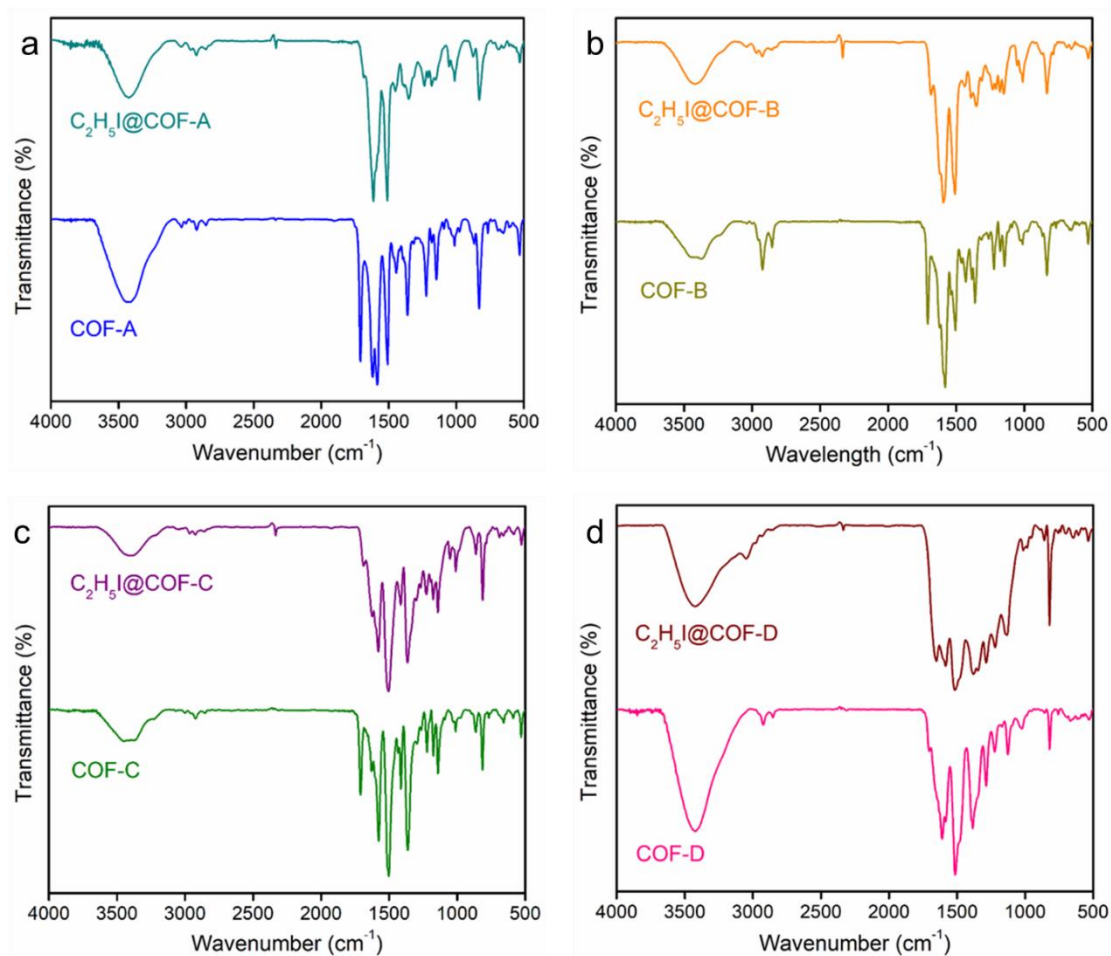
Appendix 2.37: TGA profiles of (a) CH₃CH₂I@COF-A, (b) CH₃CH₂I@COF-B, (c) CH₃CH₂I@COF-C, and (d) CH₃CH₂I@COF-D.



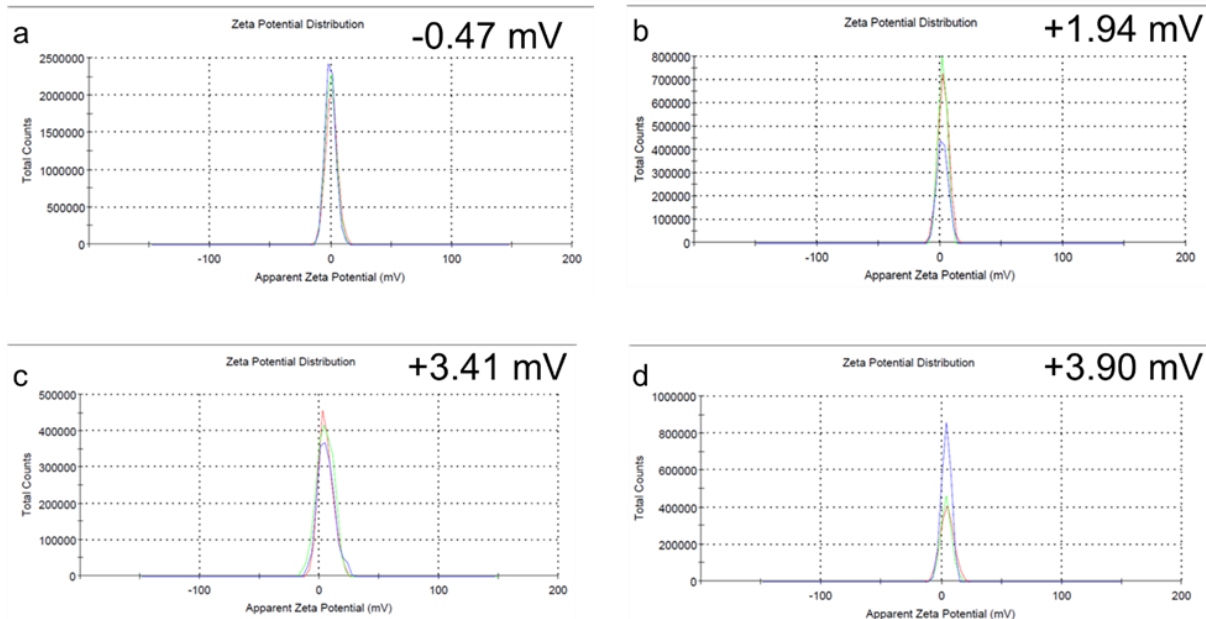
Appendix 2.38: PXRD patterns of (a) CH₃I@COF-A, (b) CH₃I@COF-B, (c) CH₃I@COF-C, and (d) CH₃I@COF-D.



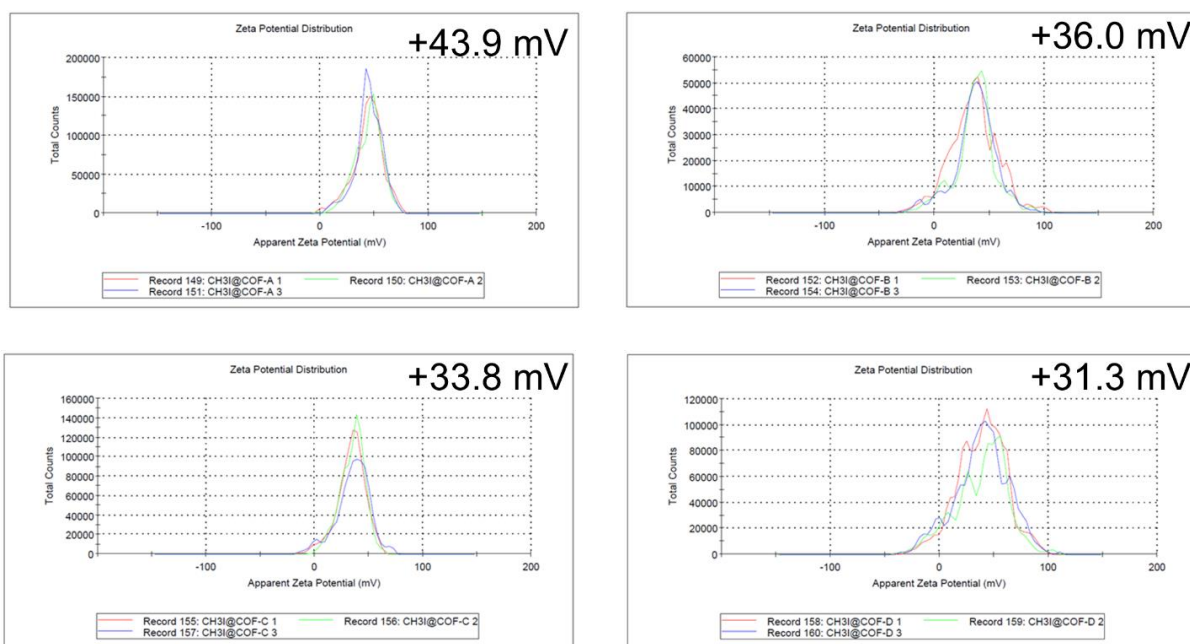
Appendix 2.39: XPS survey spectra of (a) CH₃I@COF-A, (b) CH₃I@COF-B, (c) CH₃I@COF-C, and (d) CH₃I@COF-D.



Appendix 2.40: FTIR spectra of (a) CH₃CH₂I@COF-A, (b) CH₃CH₂I@COF-B, (c) CH₃CH₂I@COF-C, and (d) CH₃CH₂I@COF-D.

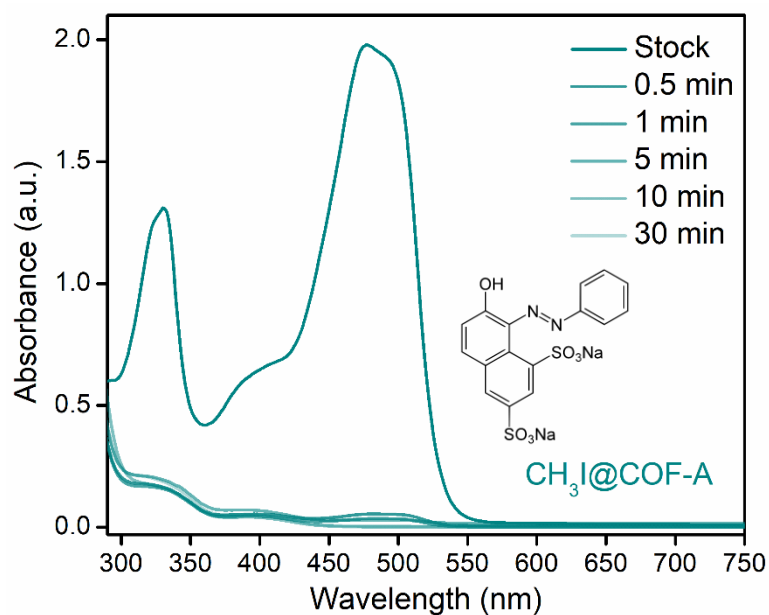
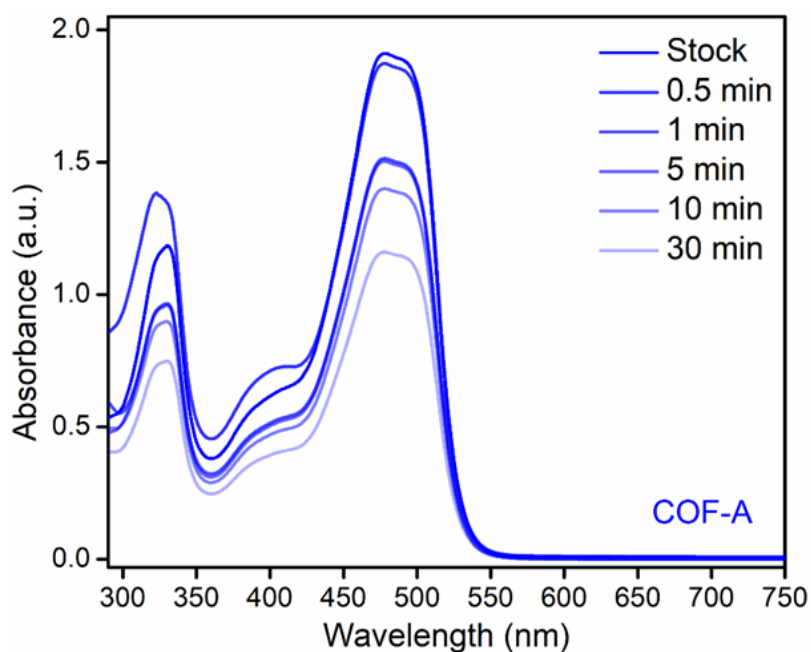


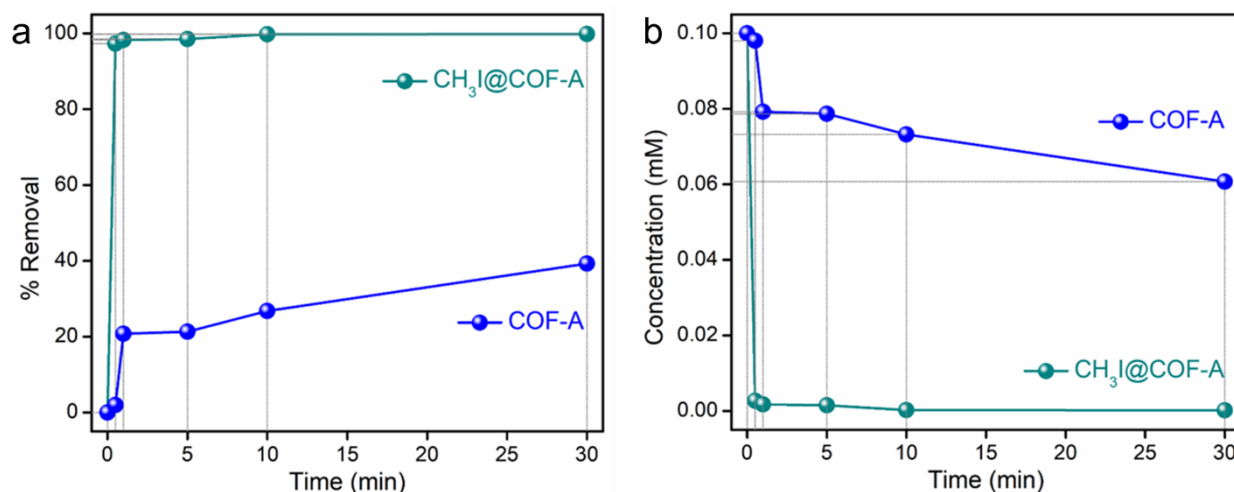
Appendix 2.41: Zeta potential data of (a) COF-A, (b) COF-B, (c) COF-C, and (d) COF-D.



Appendix 2.42: Zeta potential data of (a) CH₃I@COF-A, (b) CH₃I@COF-B, (c) CH₃I@COF-C, and (d) CH₃I@COF-D.

Appendix Section 2.6.5: Organic dye adsorption studies.

Appendix 2.43: UV-vis spectra of OG²⁻ dye upon treatment with CH₃I@COF-A.Appendix 2.44: UV-vis spectra of OG²⁻ dye upon treatment with COF-A.



Appendix 2.45: (a) Removal efficiency and (b) decrease in the concentration of OG²⁻ dye with time upon treatment of CH₃I@COF-A and COF-A.

Note: That being said, in the recent past, ionic porous materials having free exchangeable counter anions were extensively studied for successful sequestration of various contaminants from water. Furthermore, inspired by two independent perspectives, one is the outstanding organic toxics capture performance of the COFs after CH₃I adsorption, and another one is the importance of effective sequestration of organic persistent pollutants towards environmental remediation, we further sought to explore the potential of all CH₃I@COFs towards water treatment application by adsorptive removal of toxic organic dyes from water. Initially, as a typical dye, organic G (OG²⁻) was selected for evaluating the adsorption performances of the as-prepared CH₃I@COFs. The UV-vis spectroscopic analysis was performed to monitor the concentration of the dyes before and after the capture test. As a result, almost ~98%, ~83%, ~62% and ~46% OG²⁻ removal efficiency were observed in case of CH₃I@COF-A, B, C and D, respectively within 30 sec of contact time (Appendix 2.43-2.52). Similar test was performed with pristine COFs, which explored relatively very sluggish OG²⁻ removal kinetics as the UV-vis spectra showed no significant changes in the intensity after the capture test (Appendix 2.44-2.52). The removal efficiency or decrease in the concentration with respect to time profile of all the pristine COFs displayed only ~21%, ~7%, ~6% and ~4% removal efficiency towards OG²⁻ dye capture (Appendix 2.45, 2.52). Moreover, these dye adsorption results of the pristine COFs and after CH₃I adsorption were found to follow pseudo-second-order kinetics model with rate constant 1.048, 0.339, 0.151 and 0.0405 g.mg⁻¹.min⁻¹, for CH₃I@COF-A, B, C and D, respectively, towards OG²⁻ pollutant (Appendix 2.53). Whereas, the rate constant for COF-A, B, C and D were calculated as 0.0229, 0.0193, 0.0302 and 0.0213 g.mg⁻¹.min⁻¹, respectively (Appendix 2.54). All these findings indicated CH₃I loaded COFs, owing to their cationic charged surface demonstrated significant potential in the improved pollutants sequestration

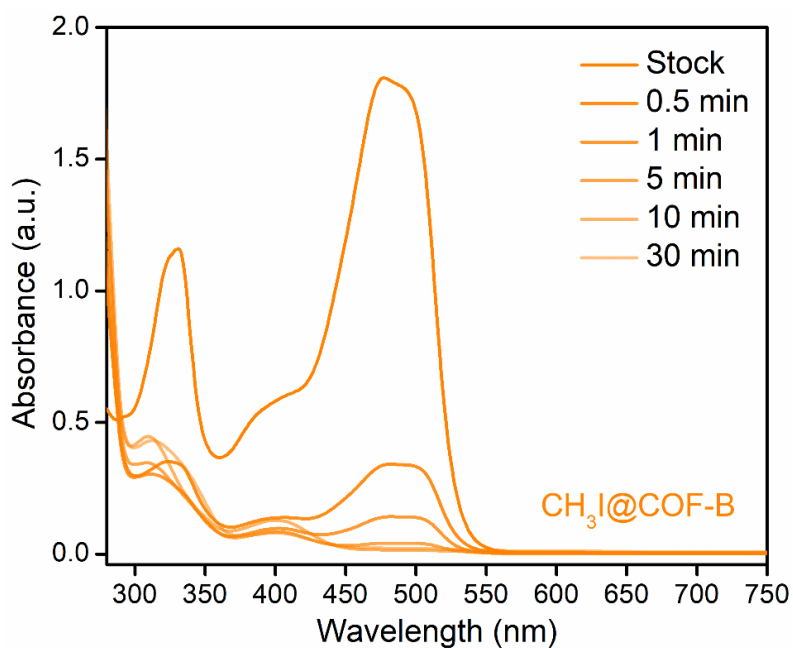
performance (Appendix 2.55). In addition, with compared to all, CH₃I@COF-A exhibited as the most promising candidate for the ultrafast removal of organic dye (OG²⁻) in water (Appendix 2.56).

Further, motivated by such excellent enrichment index towards OG²⁻ dye adsorption, the sorption performance of CH₃I@COF-A for other anionic dyes including alizarin red S (ARS), indigo carmine (IC) and methyl orange (MO) were also investigated. In a similar typical capture test, the UV-vis spectra of these dyes exhibited rapid diminishing of intensities with respect to time when treated with CH₃I@COF-A (Appendix 2.57). Interestingly, very fast kinetics of capture was observed in all the cases with the equilibrium reaching within less than 1 min. These results indicated excellent potency of CH₃I@COF-A in the effective adsorption of anionic dyes (OG, ARS, IC, and MO) in water medium, which was also associated with a distinct color change of the dye solutions visible to the naked eye (Appendix 2.58, 2.59). The ultrafast adsorption of anionic dyes by CH₃I@COF-A emphasize the fact that electrostatic interactions with Coulombic attractions are the significant prevailing factor in trapping these molecules.

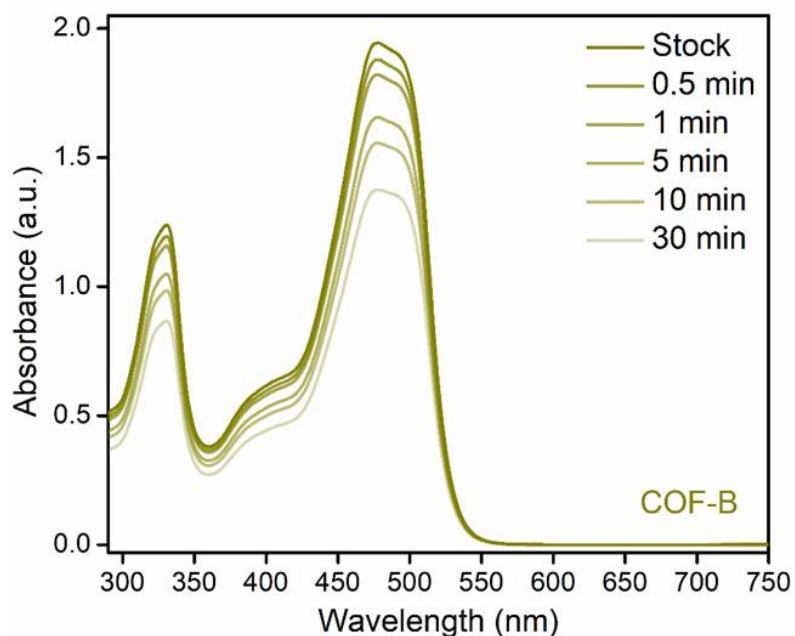
Next, the ability of CH₃I@COF-A to successfully and effectively adsorb anionic dyes owing to its cationic nature motivated us to investigate its selectivity based on charge specificity. For this we conducted the similar capture test with a cationic dye, methylene blue (MB) in water. CH₃I@COF-A exhibited negligible adsorption ability towards MB even after treatment of 30 min (Appendix 2.60). Additionally, a binary dye mixture-based adsorption investigation using dye molecules that were both cationic and anionic was conducted. CH₃I@COF-A was subjected to an equimolar combination of 1 mL anionic MO and 1 mL cationic MB in order to observe the adsorption behavior by UV-vis spectroscopy. Notice that under identical experimental circumstances, almost ~98% removal efficiency of the anionic MO dye was observed, whereas, only ~7% of the cationic methylene blue was removed, (Appendix 2.61). These findings support the electrostatic interactions' predominance in determining the contaminants' adsorption efficiency and the selective character of CH₃I@COF-A (Appendix 2.62). The color shift seen throughout the experiment provided more evidence of the selective adsorption behavior. After attaining equilibrium, the color of the mixed binary dye solution progressively shifted from green to blue, indicating the predominance of non-adsorbed methylene blue in the leftover stock solution (Appendix 2.63).

Further, a crucial consideration when assessing an adsorbent for practical applications is its column extraction ability. Therefore, it was also looked into whether CH₃I@COF-A was conceptually feasible for wastewater cleanup in real-time applications. We developed a fixed-bed stationary-phase column-based experimental setup to put this into practice (Appendix 2.63). In this typical experiment, a stock OG²⁻ dye solution was passed through a bed of CH₃I@COF-A with a flow rate of 0.5 mL.min⁻¹, and the column eluent solution was analyzed using UV-visible analysis (Appendix 2.64). As a result of breakthrough test, almost ~55 mL of outflow solution, OG²⁻ dye removal efficiency was over 93%

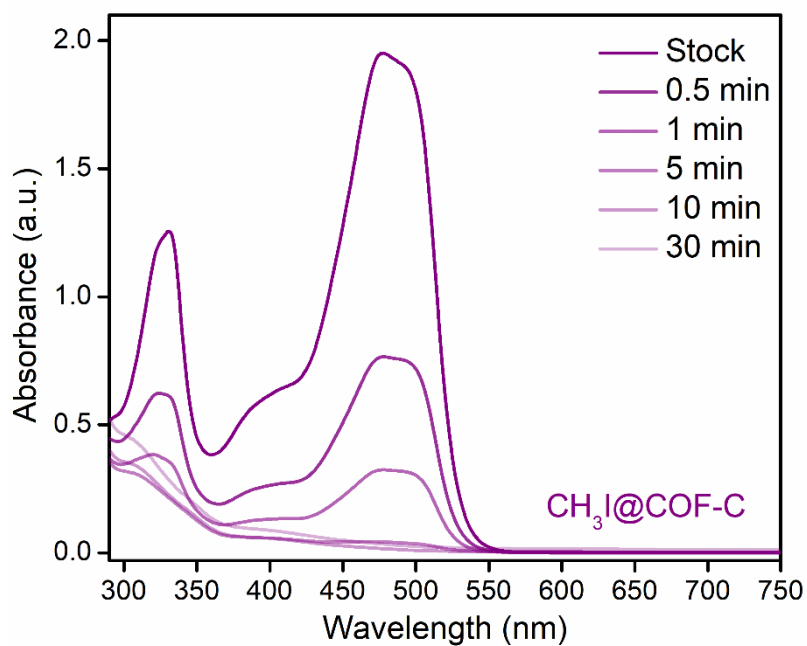
(Appendix 2.65). After which, the C/C_0 ratio was gradually increased until complete adsorbent saturation after ~ 107 mL of column eluent. This result showed the remarkable dynamic capture efficiencies of the adsorbent towards real-time waste-water treatment.



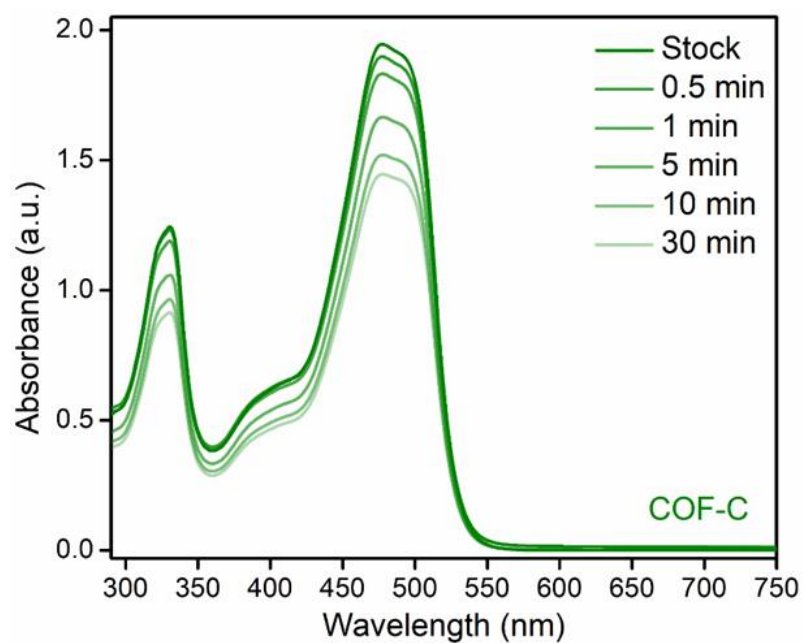
Appendix 2.46: UV-vis spectra of OG²⁻ dye upon treatment with CH₃I@COF-B.



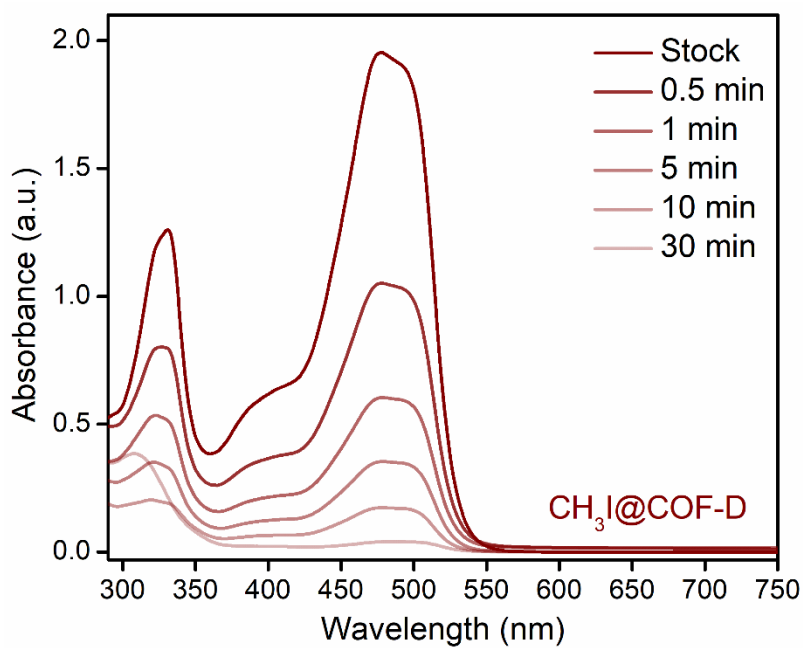
Appendix 2.47: UV-vis spectra of OG²⁻ dye upon treatment with COF-B.



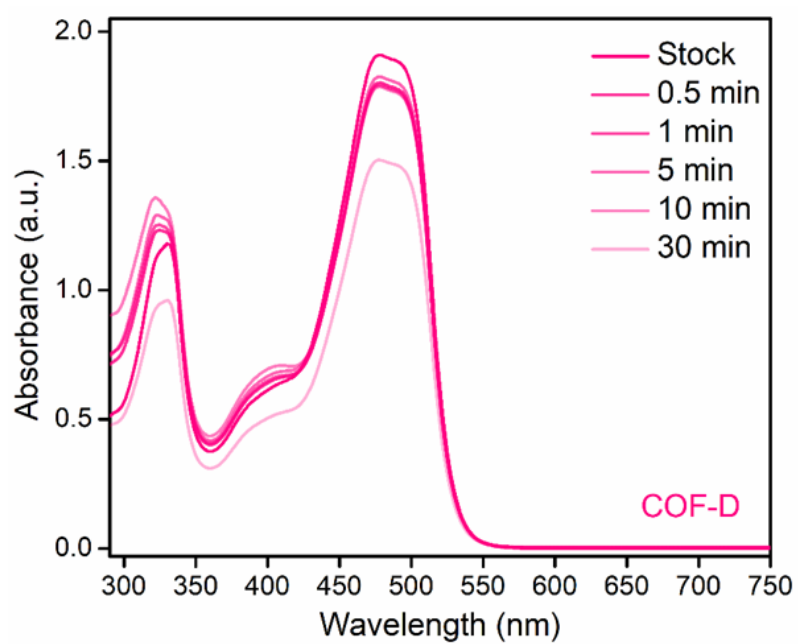
Appendix 2.48: UV-vis spectra of OG²⁻ dye upon treatment with CH₃I@COF-C.



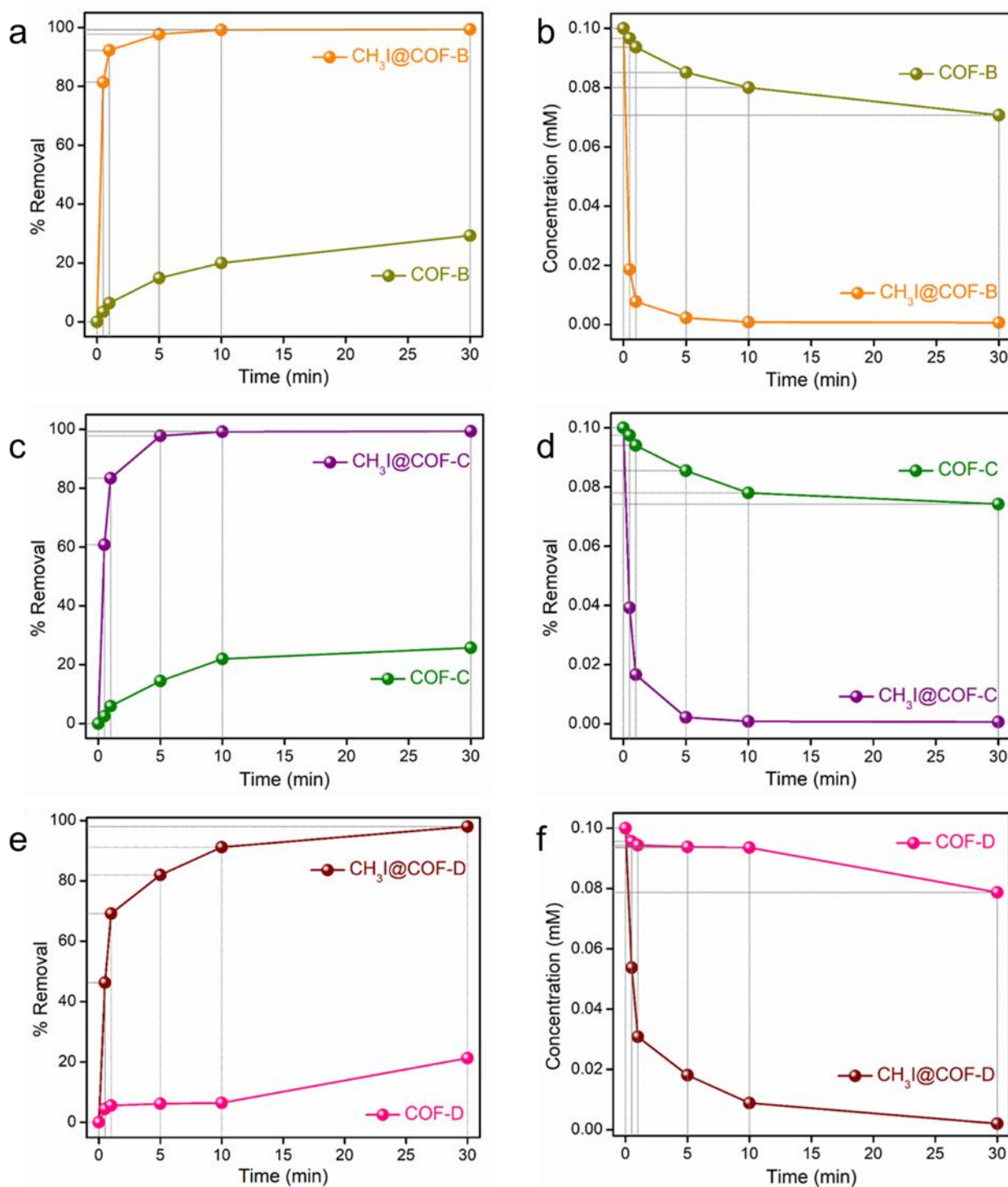
Appendix 2.49: UV-vis spectra of OG²⁻ dye upon treatment with COF-C.



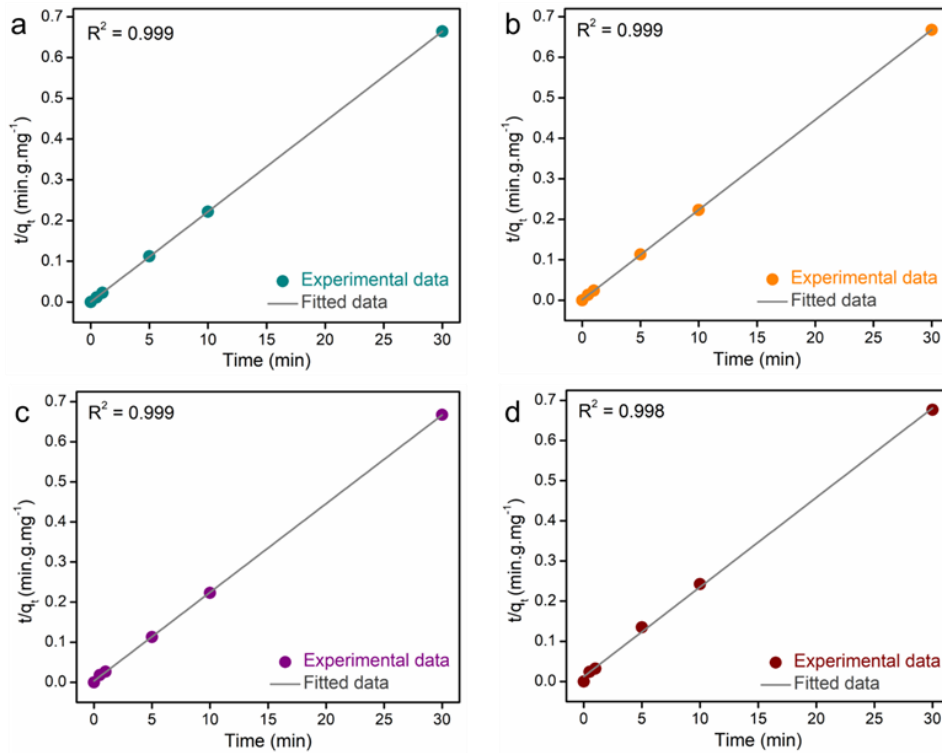
Appendix 2.50: UV-vis spectra of OG²⁻ dye upon treatment with CH₃I@COF-D.



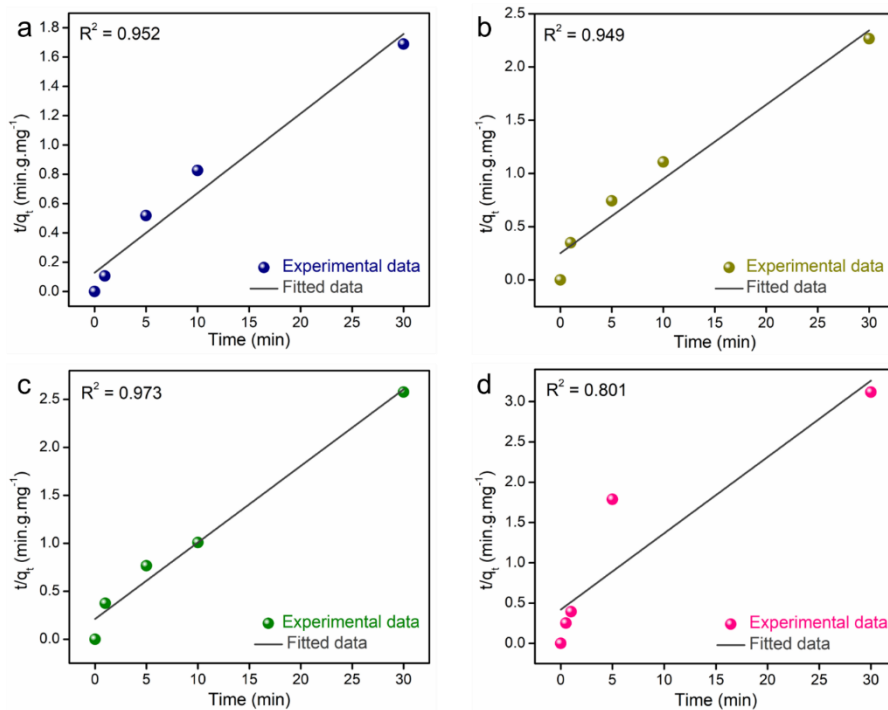
Appendix 2.51: UV-vis spectra of OG²⁻ dye upon treatment with COF-D.



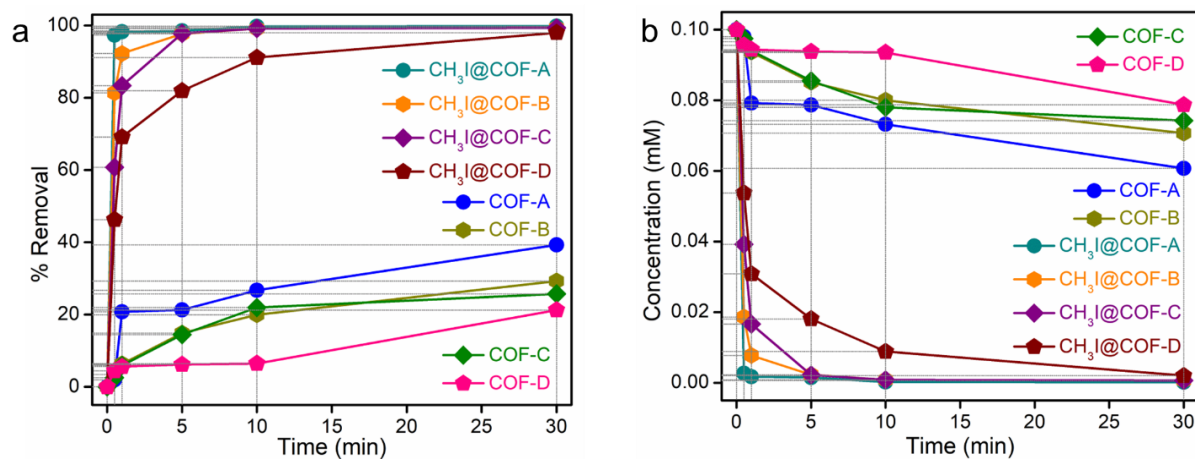
Appendix 2.52: (a, c, e) Removal efficiency and (b, d, f) decrease in the concentration of OG^{2-} dye with time upon treatment of $\text{CH}_3\text{I}@$ COF-B and COF-B, $\text{CH}_3\text{I}@$ COF-C and COF-C, and $\text{CH}_3\text{I}@$ COF-D and COF-D, respectively.



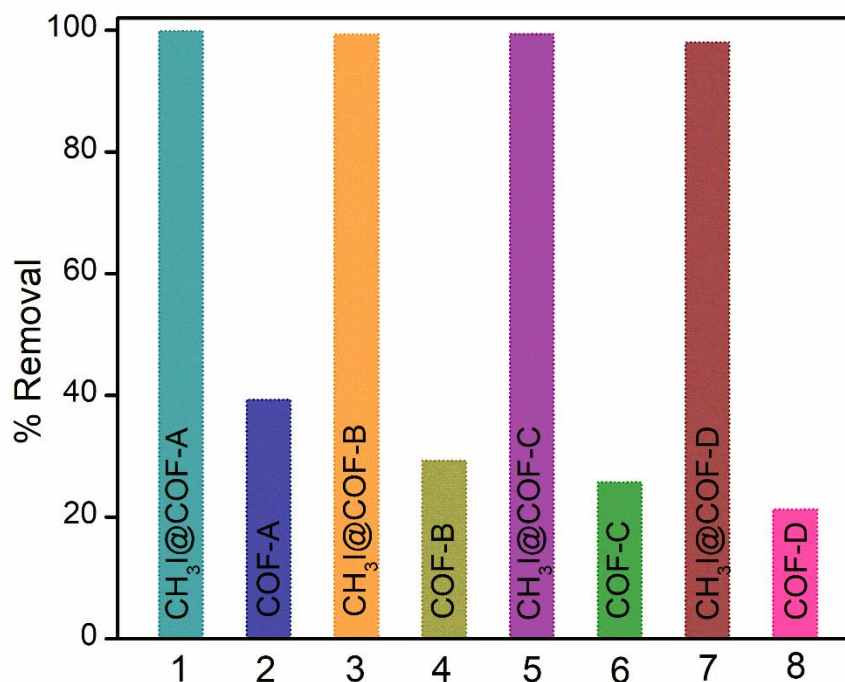
Appendix 2.53: Pseudo-second-order model fitting of adsorption of OG²⁻ dye by (a) CH₃I@COF-A, (b) CH₃I@COF-B, (c) CH₃I@COF-C, and (d) CH₃I@COF-D.



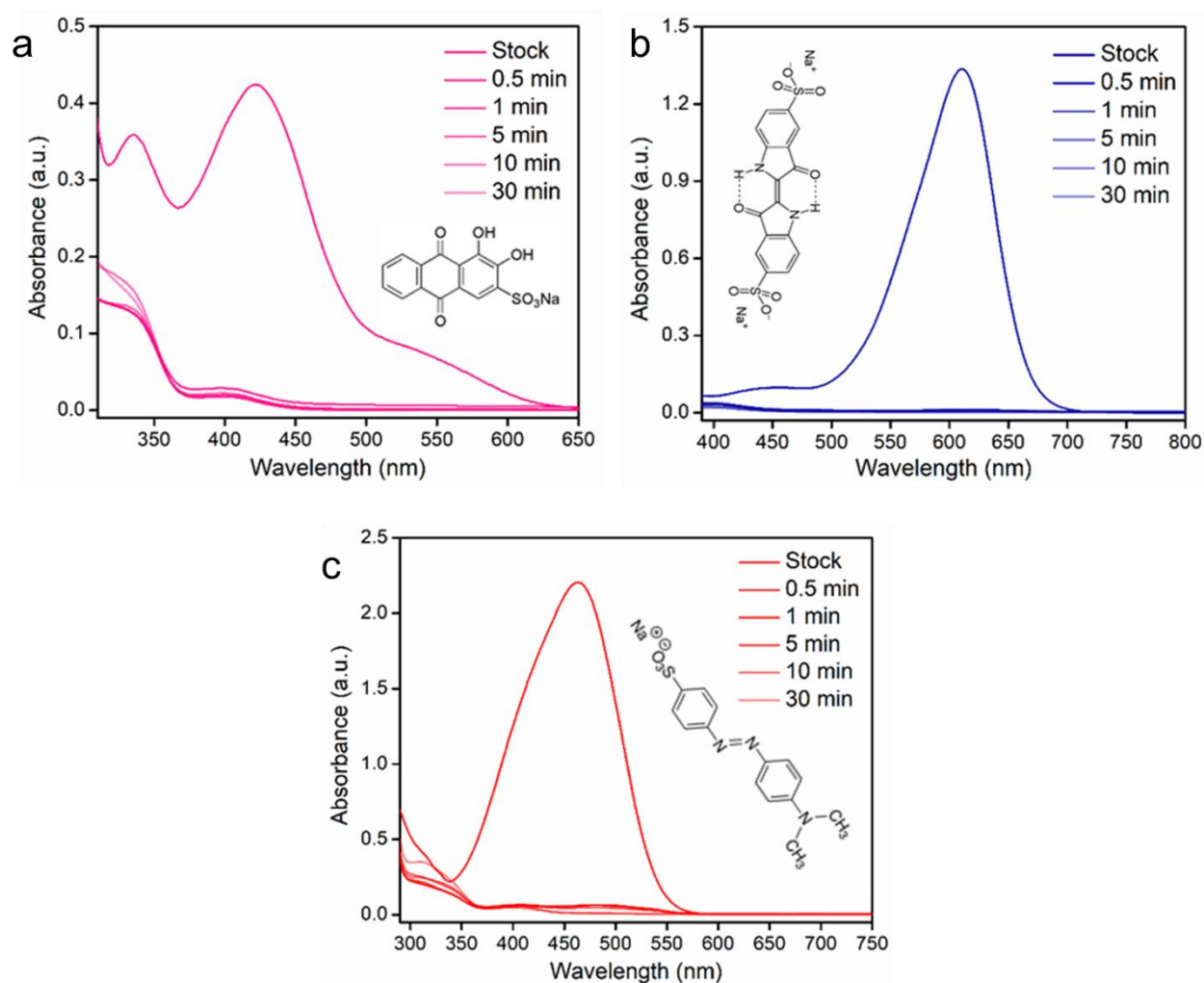
Appendix 2.54: Pseudo-second-order model fitting of adsorption of OG²⁻ dye by (a) COF-A, (b) COF-B, (c) COF-C, and (d) COF-D.
























Appendix 2.55: (a) Removal efficiency and decrease in the concentration of OG²⁻ dye with time upon treatment of CH₃I@COF-A and COF-A, CH₃I@COF-B and COF-B, CH₃I@COF-C and COF-C, and CH₃I@COF-D and COF-D, respectively.
























Appendix 2.56: (a) Removal efficiency of OG²⁻ aqueous solution by COF-A, B, C and D, before and after CH₃I adsorption.



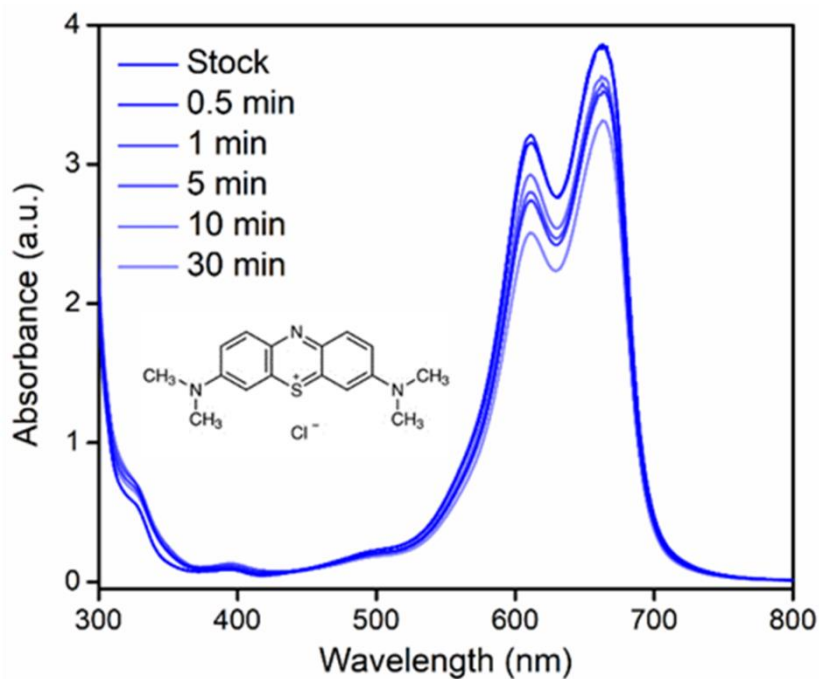
Appendix 2.57: UV-vis spectra of (a) alizarin red S (ARS), (b) indigo carmine (IC) and (c) methyl orange (MO) dyes upon treatment with $\text{CH}_3\text{I}@\text{COF-A}$.

Dye	Stock	0.5 min	1 min	5 min	10 min	30 min	60 min	
OG								---
IC								---
ARS								---

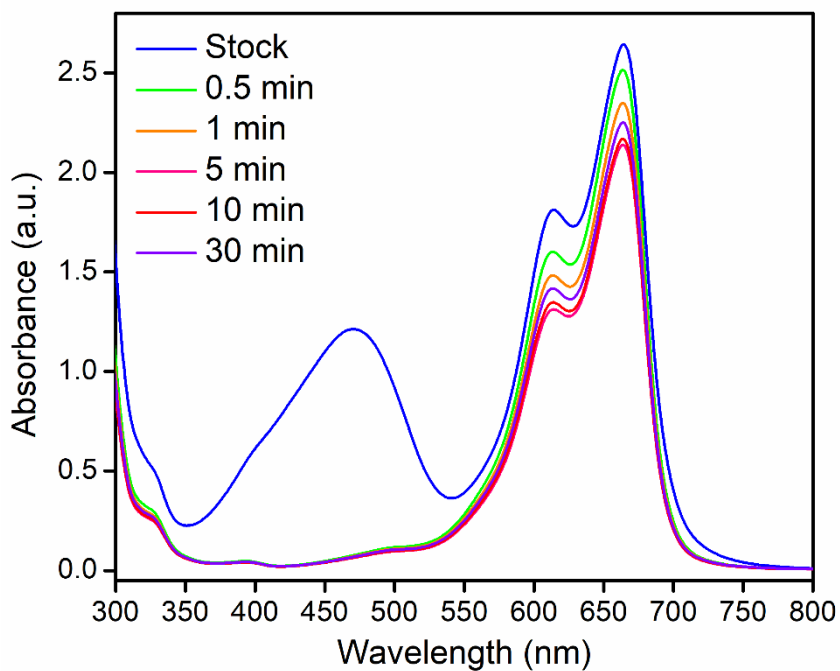
Appendix 2.58: Digital images of change in the colours of (a) orange G (OG), (b) indigo carmine (IC) and (c) alizarin red S (ARS), dyes with time upon treatment with $\text{CH}_3\text{I@COF-A}$.

Dye	Stock	0.5 min	1 min	5 min	10 min	30 min	60 min	
MB								MB
MO								---
MO + MB								MB

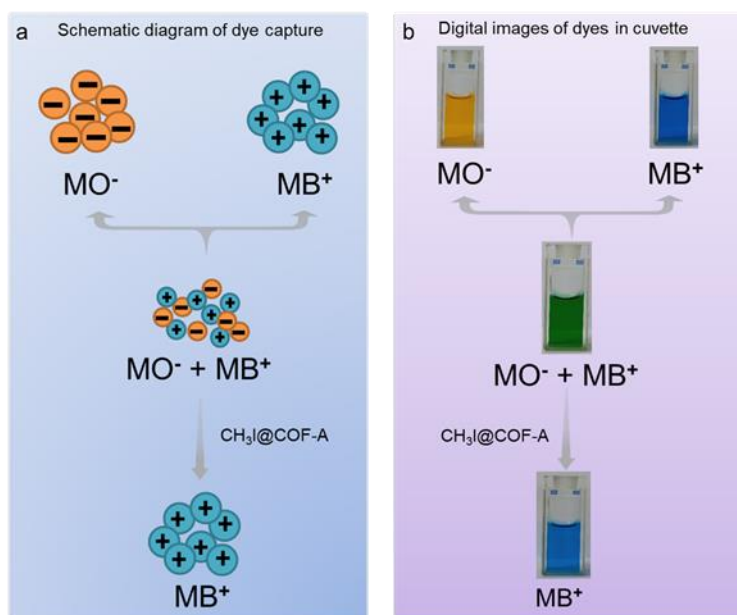
Appendix 2.59: Digital images of change in the colors of (a) methylene blue (MB), (b) methyl orange (MO) and (c) mixture of MB and MO, dyes with time upon treatment with $\text{CH}_3\text{I@COF-A}$.



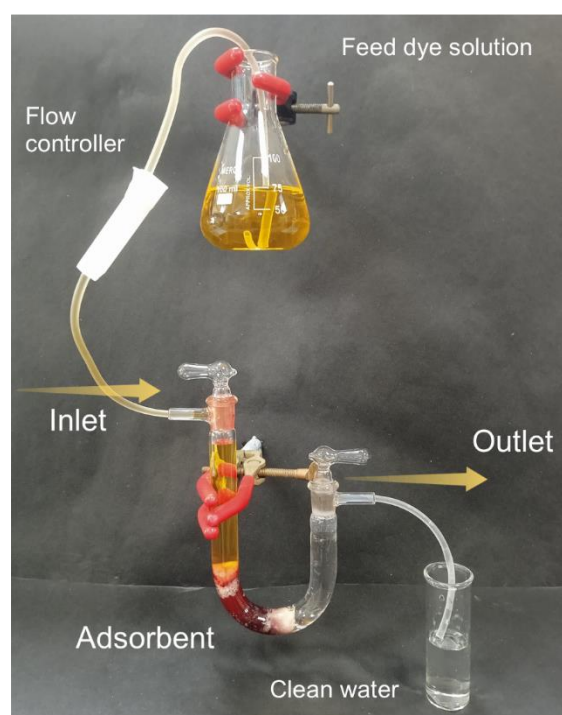
Appendix 2.60: UV-vis spectra of methylene blue (MB) dyes upon treatment with $\text{CH}_3\text{I}@\text{COF-A}$.



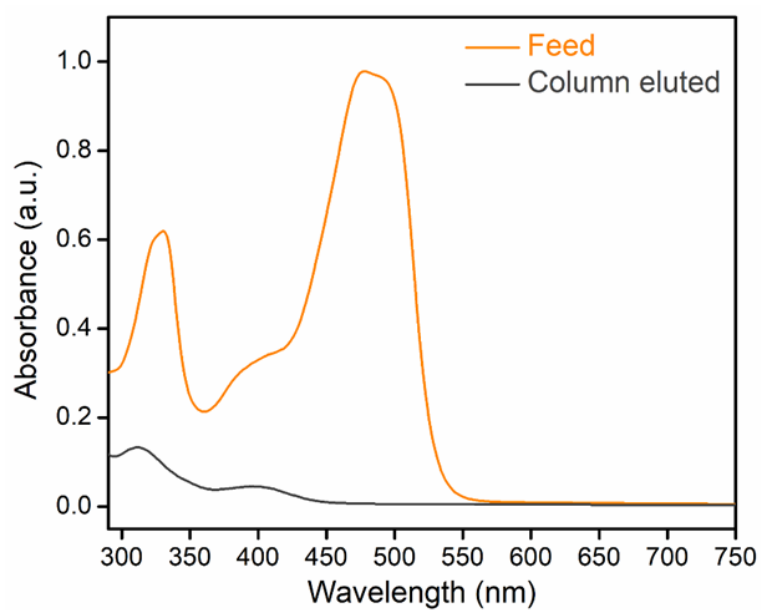
Appendix 2.61: UV-vis absorption spectra for the selective adsorption of MO from the binary mixture of MO-MB in water by $\text{CH}_3\text{I}@\text{COF-A}$.



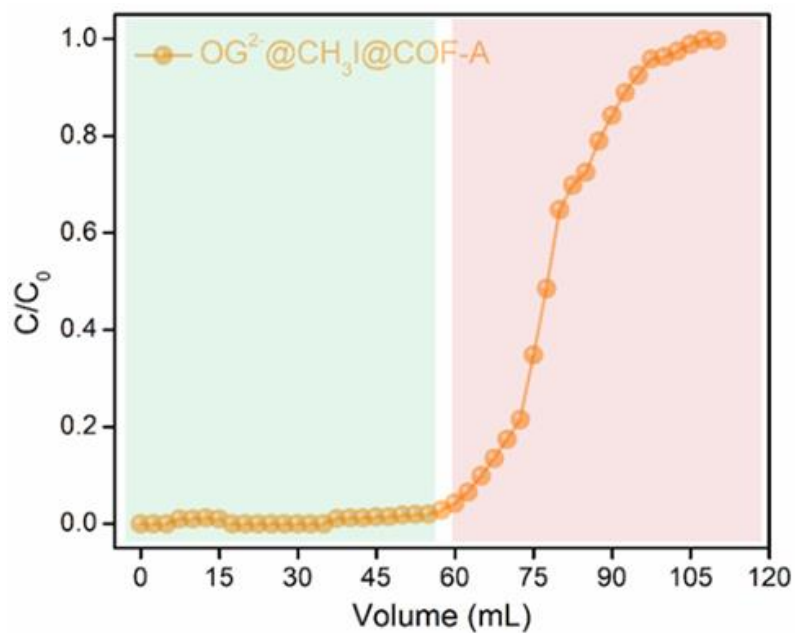
Appendix 2.62: (a) Schematic diagram and (b) images of selective capture of anionic MO dye over cationic MB dye in a binary mix dye capture test.



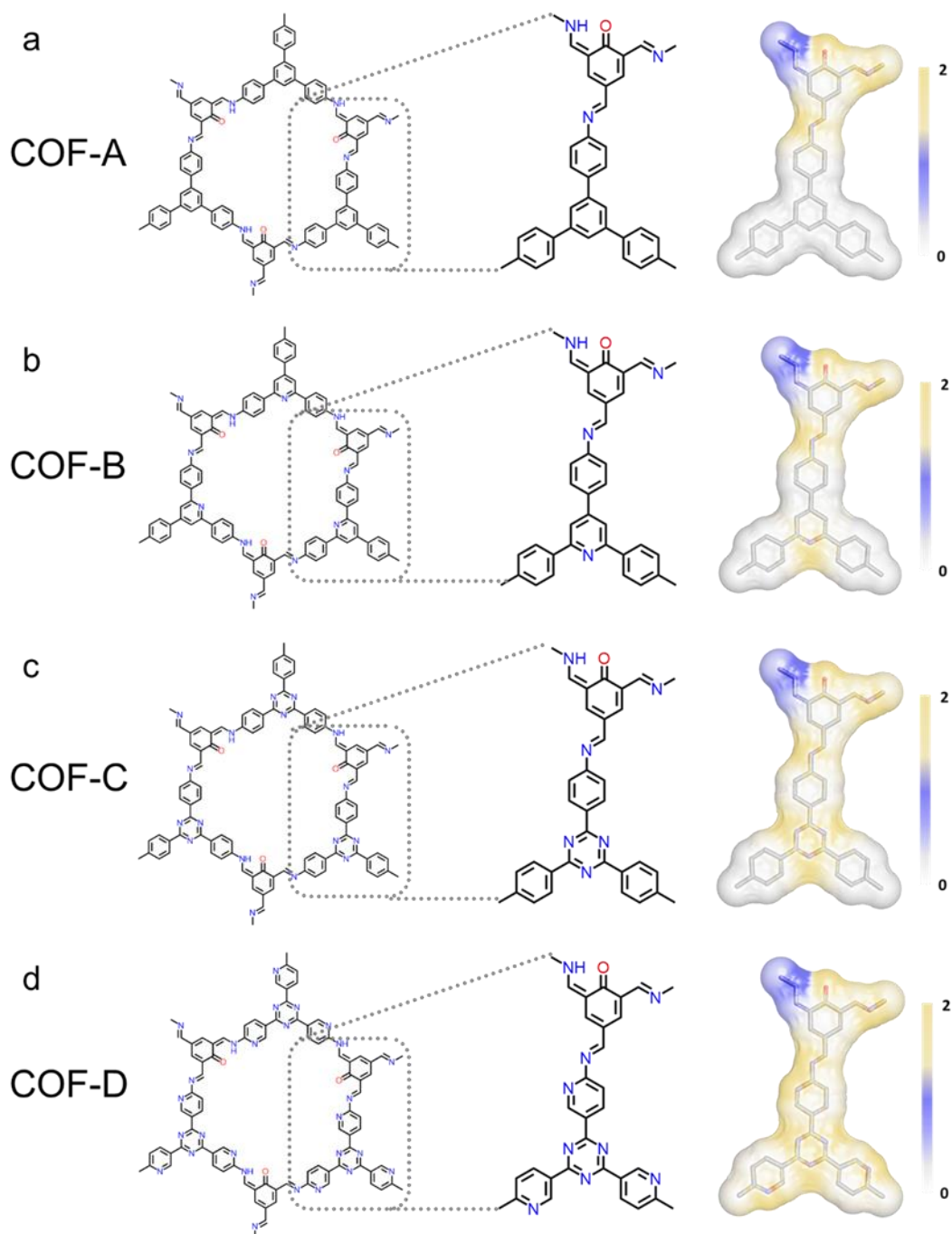
Appendix 2.63: Digital image of $CH_3I@COF-A$ based column setup for dynamic flow-through OG^{2-} dye capture test.



Appendix 2.64: UV-vis spectra of OG^{2-} dye upon treatment with $\text{CH}_3\text{I}@\text{COF-A}$ based fixed bed column.



Appendix 2.65: Breakthrough profile of dynamic column based OG^{2-} capture test by $\text{CH}_3\text{I}@\text{COF-A}$.



Appendix 2.66: Repeating units of the COFs as the model molecules to represent the structures of (a) COF-A, (b) COF-B, (c) COF-C, and (d) COF-D.

2.7 Reference

- [1] R.C. Ewing and F.N. von Hippel, *Science* **2009**, 325, 151–152.
- [2] Vienna, J. D. Nuclear Waste Vitrification in the United States: Recent Developments and Future Options. *Int. J. Appl. Glass Sci.* **2010**, 1, 309–321.
- [3] D. R. Haefner and T. J. Tranter, Methods of gas phase capture of iodine from fuel reprocessing off-gas: a literature survey, INL/EXT-07-12299, Idaho National Laboratory, Idaho Falls, ID, **2007**.
- [4] Treatment, conditioning and disposal of iodine-129, Technical Reports Series No. 276, IAEA, Vienna, **1987**.
- [5] T.C.T. Pham, S. Docao, I.C. Hwang, M.K. Song, D.Y. Choi, D. Moon, P. Oleynikov and K.B. Yoon, *Energy Environ. Sci.* **2016**, 9, 1050–1062.
- [6] S. H. Bruffey, R. T. Jubin, J. A. Report No. FCRD-MRWFD-2016-000357; ORNL/TM-2016/568 (**2016**).
- [7] B. Li, X. Dong, H. Wang, D. Ma, K. Tan, S. Jensen, B.J. Deibert, J. Butler, J. Cure, Z. Shi, T. Thonhauser, Y.J. Chabal, Y. Han and J. Li, *Nat. Commun.* **2017**, 8, 485.
- [8] S.W. Park, H.S. Park, W.K. Lee and H. Moon, *Separ. Technol.* **1995**, 5, 35–44.
- [9] C.M. González-García, J.F. González and S. Román, *Fuel Processing Technology* **2011**, 92, 247–252.
- [10] K.W. Chapman, P.J. Chupas and T.M. Nenoff, *J. Am. Chem. Soc.* **2010**, 132, 8897–8899.
- [11] K. Funabashi, T. Fukasawa and M. Kikuchi, *Nucl. Technol.* **1995**, 109, 366–372.
- [12] W. Hebel and G. Cottone, Radioactive Waste Management Series, Vol. 7 (Harwood Academic Publishers, **1982**).
- [13] H. Furukawa, K.E. Cordova, M. O’Keeffe and O.M. Yaghi, *Science* **2013**, 341, 6149.
- [14] H.-C. Zhou, J.R. Long and O.M. Yaghi, *Chem. Rev.* **2012**, 112, 673–674.
- [15] B. Li, H.-M. Wen, Y. Cui, W. Zhou, G. Qian and B. Chen, *Adv. Mater.* **2016**, 28, 8819–8860.
- [16] S. Fajal, S. Dutta and S.K. Ghosh, *Mater. Horiz.*, **2023**, 10, 4083–4138.
- [17] J. Wu, F. Xu, S. Li, P. Ma, X. Zhang, Q. Liu, R. Fu and D. Wu, *Adv. Mater.* **2019**, 31, 1802922.
- [18] X. Feng, X. Ding and D. Jiang, *Chem. Soc. Rev.* **2012**, 41, 6010.

- [19] D.-G. Wang, T. Qiu, W. Guo, Z. Liang, H. Tabassum, D. Xia and R. Zou, *Energy Environ. Sci.* **2021**, *14*, 688–728.
- [20] N. Huang, P. Wang and D. Jiang, *Nat. Rev. Mater.* **2016**, *1*, 16068.
- [21] T. Pan, K. Yang, X. Dong and Y. Han, *J. Mater. Chem. A* **2023**, *11*, 5460–5475.
- [22] Y. Xie, T. Pan, Q. Lei, C. Chen, X. Dong, Y. Yuan, W.A. Maksoud, L. Zhao, L. Cavallo, I. Pinnau and Y. Han, *Nat. Commun.* **2022**, *13*, 2878.
- [23] L. He, L. Chen, X. Dong, S. Zhang, M. Zhang, X. Dai, X. Liu, P. Lin, K. Li, C. Chen, T. Pan, F. Ma, J. Chen, M. Yuan, Y. Zhang, L. Chen, R. Zhou, Y. Han, Z. Chai and S. Wang, *Chem* **2021**, *7*, 699–714.
- [24] Y. Xie, T. Pan, Q. Lei, C. Chen, X. Dong, Y. Yuan, J. Shen, Y. Cai, C. Zhou, I. Pinnau and Y. Han, *Angew. Chem. Int. Ed.* **2021**, *60*, 22432–22440.
- [25] K. Jie, Y. Zhou, Q. Sun, B. Li, R. Zhao, D. Jiang, W. Guo, H. Chen, Z. Yang, F. Huang and S. Dai, *Nat. Commun.* **2020**, *11*, 1086.
- [26] W. Xie, D. Cui, S.-R. Zhang, Y.-H. Xu and D. Jiang, *Mater. Horiz.*, **2019**, *6*, 1571–1595.
- [27] G. H. Ning, Z. Chen, Q. Gao, W. Tang, Z. Chen, C. Liu, B. Tian, X. Li and K. P. Loh, *J. Am. Chem. Soc.* **2017**, *139*, 8897–8904.
- [28] W. Chen, W. Yan, S. Wu, Z. Xu, K. W. K. Yeung and C. Yi, *Macromol. Chem. Phys.* **2010**, *211*, 1803–1813.
- [29] R. Gomes, P. Bhanja and A. Bhaumik, *Chem. Commun.*, **2015**, *51*, 10050–10053.
- [30] S. Halder, R. Kushwaha, R. Maity and R. Vaidyanathan, *ACS Mater Lett.* **2019**, *1*, 490–497.
- [31] D. Chakraborty, S. Nandi, D. Mullangi, S. Halder, C. P. Vinod and R. Vaidyanathan, *ACS Appl Mater Interfaces* **2019**, *11*, 15670–15679.
- [32] S. Ruidas, A. Das, S. Kumar, S. Dalapati, U. Manna and A. Bhaumik, *Angew. Chem. Int. Ed.* **2022**, *61*, e202210507.
- [33] H. Xu, J. Gao and D. Jiang, *Nat. Chem.* **2015**, *7*, 905–912.
- [34] C. Qian, Q.-Y. Qi, G.-F. Jiang, F.-Z. Cui, Y. Tian and X. Zhao, *J. Am. Chem. Soc.* **2017**, *139*, 6736–6743.

- [35] R. K. Sharma, P. Yadav, M. Yadav, R. Gupta, P. Rana, A. Srivastava, R. Zboril, R. S. Varma, M. Antonietti and M. B. Gawande, *Mater. Horiz.*, **2020**, *7*, 411-454.
- [36] S. Fajal, A. Hassan, W. Mandal, M. M. Shirolkar, S. Let, N. Das and S. K. Ghosh, *Angew. Chem. Int. Ed.* **2023**, *62*, e02214095.
- [37] S. Fajal, W. Mandal, S. Mollick, Y. D. More, A. Torris, S. Saurabh, M. M. Shirolkar and S. K. Ghosh, *Angew. Chem. Int. Ed.* **2022**, *61*, e202203385.
- [38] W. Mandal, S. Fajal, S. Mollick, M. M. Shirolkar, Y. D. More, S. Saurabh, D. Mahato and S. K. Ghosh, *ACS Appl. Mater. Interfaces* **2022**, *14*, 20042–20052.
- [39] J. Wang, Z. Li, Y. Wang, C. Wei, K. Ai and L. Lu, *Mater. Horiz.*, **2019**, *6*, 1517–1525.
- [40] Z. Wang, S. Zhang, Y. Chen, Z. Zhang and S. Ma, *Chem. Soc. Rev.*, **2020**, *49*, 708–735.
- [41] J. Yang, F. Kang, X. Wang and Q. Zhang, *Mater. Horiz.*, **2022**, *9*, 121-146.
- [42] Y. Bai, L. Chen, L. He, B. Li, L. Chen, F. Wu, L. Chen, M. Zhang, Z. Liu, Z. Chai and S. Wang, *Chem* **2022**, *8*, 1442-1459.
- [43] S. Kandambeth, A. Mallick, B. Lukose, M. V. Mane, T. Heine and R. Banerjee, *J. Am. Chem. Soc.* **2012**, *134*, 19524–19527.
- [44] B.P. Biswal, S. Chandra, S. Kandambeth, B. Lukose, T. Heine and R. Banerjee, *J. Am. Chem. Soc.* **2013**, *135*, 5328–5331.
- [45] S. Ruidas, B. Mohanty, P. Bhanja, E. S. Erakulan, R. Thapa, P. Das, A. Chowdhury, S. K. Mandal, B. K. Jena and A. Bhaumik, *ChemSusChem* **2021**, *14*, 5057–5064.
- [46] T. Pan, X. Dong and Y. Han, *Nano Research* **2023**, *16*, 6308-6315.
- [47] Y. Zhang, L. He, T. Pan, J. Xie, F. Wu, X. Dong, X. Wang, L. Chen, S. Gong, W. Liu, L. Kang, J. Chen, L. Chen, Y. Han and S. Wang, *CCS Chem.* **2022**, *5*, 1540-1548.
- [48] A. Hassan, M. M. R. Mollah, S. Das and N. Das, *J. Mater. Chem. A*, **2023**, *11*, 17226-17236.
- [49] A. Hassan and N. Das, *ACS Appl. Polym. Mater.* **2023**, *5*, 7, 5349–5359.

Chapter 3

Ordered Macro/Microporous Ionic Organic Framework for Efficient Separation of Toxic Pollutants from Water

3.1 Introduction

Since the incarnation of the industrial revolution together with agriculture, human activities have generated various toxic anions as a potential water pollutants.^[1] Organic species such as dyes and antibiotics are considered as potentially toxic even at very low concentration.^[2] Environmental self-purification process is unable to degrade these complicated, highly-toxic, water soluble organic pollutants which further causes diverse health issues to the living organism.^[3] In addition, inorganic pollutants such as metal-based oxoanions and iodine present in wastewater are generated owing to rapid industrial development. These are also being tagged as carcinogenic and radioactive pollutants posing threat to the entire ecosystem.^[4, 5] Therefore, segregation of such hazardous water contaminants by innovative materials has received significant research attention in both scientific and industrial communities. Although, a variety of techniques have either been tested or are under consideration for water-purification, ion-exchange-based adsorption has been recently considered as favoured choice, owing to its high efficiency, selectivity, low cost and simplicity.^[6]

The past few years has witnessed revolutionary development of adsorption followed by ion-exchange-based separation by porous materials as potential alternatives to energy intensive sequestration process.^[7, 8] The removal mechanism in such materials are primarily governed by analyte diffusion followed by accessibility of the ion-exchangeable-sites within the pores.^[9, 10] In this regard, ionic porous organic-frameworks, such as viologen-based frameworks have gained immense interest and are considered more expedient over neutral frameworks, owing to its fascinating intrinsically charged potential porous nature.^[11, 12] Constructed from rigid covalent bonds, these are furnished with stronger electrostatic interactions that are suitable for host-guest recognition generated from the charged backbone of viologen-unit. Such ionic materials have shown promising application toward elimination of toxic anions from water.^[13-15] Although, until now, several synthetic strategies have reported been to construct ionic organic-network for specific sequestration of pollutants, these systematically developed strategies have been restricted to uniform pores.^[11, 16] Therefore, the pollutant separation performance, especially in terms of removal kinetics has been typically limited to a great extent due to inadequate mass-transfer through the small pores and less accessibility of active sites on account of pore blocking by the presence of free exchangeable counter anions in the cationic porous skeleton.^[17] Consequently, ionic porous organic-polymers have frequently demonstrated sluggish removal kinetics and poor sequestration efficacy towards decontamination of specific toxic pollutants from water.

The introduction of hierarchical porosity (meso or macro) into the microporous structure comes forth as an effective approach to surpass such fundamental cardinal issues. Simultaneously, this has led to development of materials with higher pore volume and easy accessibility of functional sites, shortening the diffusion paths and facilitating fast mass transfer.^[18, 19] Although, considerable efforts have been

made to construct mesoporous-skeleton by relative extendable ligand modification, only sporadic progress is observed in fabrication of macroporous structures.^[20, 21] Moreover, induction of macroporosity into the framework can be advantageous in order to improve the mass transport in pollutant removal applications.^[22] On the other hand, precise implantation of specific functionality (e.g., ionic nature) together with macroporosity could be more effective for fast and selective successful sequestration of targeted analytes. Although, breakthrough investigation of toxic organic pollutants elimination study was reported by inducing disordered macroporosity into the neutral microporous framework,^[23] the strategic construction of charged functionalized ordered macroporous organic-framework is highly desirable but it remains an unexplored territory.

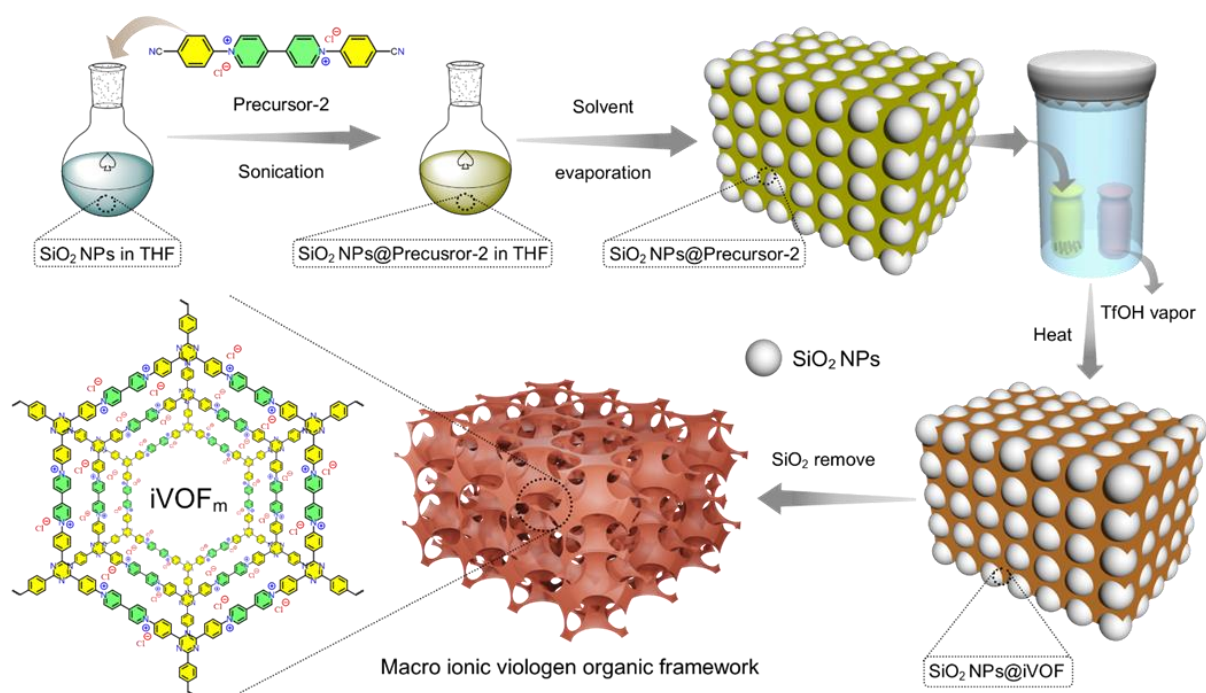


Figure 3.1: Schematic illustration of synthesis of iVOF_m utilizing solid-state acid vapor assisted synthetic strategy.

Under this backdrop, herein we report an effective approach to construct an anion-exchangeable ionic-functionalized ordered macro-microporous viologen-unit grafted organic-framework (iVOF_m, where, “i”, “VOF” and “m” stands for ionic, viologen-organic-framework, and macro, respectively) for water purification application by removing various toxic organic-inorganic anionic pollutants from water. Silica-nanoparticles template solid-state acid-vapor assisted synthetic strategy has been employed to deliberately incorporate macropores along with ionic moiety bearing free-exchangeable Cl⁻ ions (Figure 3.1). Furthermore, the size and number of macropores in the cationic backbone was finely-tuned by template-controllable-confinement synthetic strategy. The chemically robust iVOF_m demonstrated ultrafast capture kinetics toward a wide variety of organic inorganic hazardous anionic pollutants such

as, antibiotics, organic dyes, iodine and metal-based oxoanions, in water. The excellent removal efficiency (99% within 30 sec) in case of all pollutants was observed for iVOFm. Additionally, iVOFm have been further utilized as potential competent scavenger of SDM antibiotics from water with detailed investigation. iVOFm showed high uptake capacity, in a selective and recyclable manner with unprecedented sequestration of SDM in a wide pH range. Further, to explore the role of macroporosity of iVOFm upon fast separation of such anions, we utilized the systematic pH dependent SDM capture study as a key tool. The high removal efficiency (>60%) of cationic SDM at pH=1 was attributed to the enhanced transport of molecules through the hierarchical pores of iVOFm. To establish this hypothesis, both the reported mesoporous and nonporous assembly of iVOFm, having identical framework configuration were synthesized and used for SDM capture study. The SDM removal trends are in order of macro->meso->nonporous materials in both pH=7.13 and 1. This also demonstrated the role of macroporosity toward ultrafast and super-efficient anions removal efficiency by iVOFm. Finally, isothermal titration calorimetry and molecular dynamics simulation studies were performed to demonstrate the thermodynamically favourable strong interaction between the charged framework and model anions.

3.2 Experimental

3.2.1. Materials: Starting materials, 4,4'-Dipyridyl, 1-chloro-2,4-dinitrobenzene and tetraethyl-orthosilicate (TEOS) were purchased from Sigma-Aldrich. 4-aminobenzonitrile was purchased from TCI chemicals. Zinc chloride ($ZnCl_2$) and ammonium bifluoride (NH_4HF_2) was purchased from Alfa-Aesar. Triflic acid and all other solvents were purchased locally. The obtained chemicals were used without any further purification.

3.2.2. Safety Note: The synthesis protocol described in this article, that uses acid in a sealed tube must be carried out under strict safety precautions.

3.2.3. General Characterizations and Physical Measurements:

3.2.3.1 Fourier transform infrared spectroscopy (FT-IR): The IR spectra were acquired by using NICOLET 6700 FT-IR spectrophotometer using KBr pellet in 500-4000 cm^{-1} range.

3.2.3.2 Thermogravimetric analysis (TGA): Thermogravimetric analyses were recorded on Perkin-Elmer STA 6000 TGA analyzer by heating the samples from 40 to 800 $^{\circ}C$ under N_2 atmosphere with a heating rate of 10 $^{\circ}C\ min^{-1}$.

3.2.3.3 Field emission scanning electron microscopy (FESEM): The morphology of the materials was recorded with a Zeiss Ultra Plus field-emission scanning electron microscope (FESEM) with an

integral charge compensator and embedded EsB and AsB detectors (Oxford X-max instruments 80 mm² (Carl Zeiss NTS, GmbH). The samples were sputter-coated with a 5-10 nm Au film to reduce charging. The elemental analysis was carried out using voltage of 15 KV equipped with an EDX detector. Data acquisition was performed with an accumulation time of >600 s.

3.2.3.4 Transmission electron microscopy (TEM): For high-resolution TEM analysis, all the samples were dispersed in isopropanol (0.5 mg/mL) and sonicated for 30 min. Then, the samples were left for 2 min, and the upper part of the solution was taken for preparing TEM samples on a lacey carbon-coated copper grid (Electron Microscopy Science). TEM imaging and STEM-EDS were performed on the HRTEM (JEM-2200FS, JEOL) operating at acceleration voltage of 200 kV.

3.2.3.5 Solid-state nuclear magnetic resonance (NMR) spectroscopy: Solid-state ¹³C cross-polarization-magic angle spinning (CP-MAS) spectra were conducted on a Bruker 500 MHz NMR spectrometer with a CP-MAS probe. Carbon chemical shifts are expressed in parts per million (δ scale).

3.2.3.6 Powder X-ray diffraction (PXRD): Powder X-ray diffraction (PXRD) patterns were performed on a Bruker D8 Advanced X-ray diffractometer at room temperature using Cu K α radiation ($\lambda = 1.5406 \text{ \AA}$) at a scan speed of $0.5^\circ \text{ min}^{-1}$ and a step size of 0.01° in 2θ .

3.2.3.7 Nitrogen adsorption-desorption isotherm measurements: N₂ gas adsorption measurements were performed using BelSorp-Max instrument (Bel Japan). Prior to adsorption measurements, the activated samples were heated at 120 °C under vacuum for 12 hours using BelPrevacII.

3.2.3.8 Mercury intrusion porosimetry measurements: The macropores distribution was measured by mercury intrusion porosimetry (Anton Paar Quantachrome Instruments POREMASTER).

3.2.3.9 UV-visible absorption spectra: UV-vis absorption studies were performed on a Shimadzu UV 3600 UV /vis /NIR spectrophotometer in an optical quartz cuvette (10 mm path length) over the entire range of 200-800 nm.

3.2.3.10 X-ray photoelectron spectroscopy (XPS): As-obtained powder samples was stuck to conductive paste and then measured by X-ray photoelectron spectroscopy using K-Alpha+model (Thermo Fischer Scientific, UK) with Al K α source.

3.2.3.11 Electron paramagnetic resonance spectroscopy (EPR): Solid-state EPR spectra were recorded at room temperature (298 K) on CMS 8400 EPR spectrometer with a centerfield at 337 mT, sweep width of 20 mT, and power attenuation of 20 dB, and visualized with EPR Commander 6.0.

3.2.3.12 Zeta potential: Zeta potential measurements were performed on a Anton Paar Litesizer 500 series instrument. Measurement cell: Omega cuvette Mat. No. 155765, Target temperature 25.0 °C,

Equilibration time – (Series parameter), Henry factor 1.1 (Other), Adjusted voltage (Automatic Mode), Number of runs 20, Solvent – water.

3.2.3.13 Raman measurements: Raman spectra were acquired with an Xplora PLUS Raman microscope (Horiba Company) (785 nm laser and a 1200 lines/mm grating).

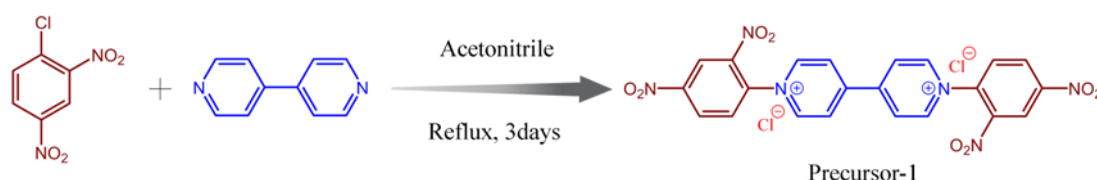
3.2.3.14 Electron tomography measurements: Electron tomography measurement has been carried out in TEM instrument, model-JEM2200FS, make-JEOL, operating at acceleration voltage of 200 kV. For electron tomography analysis, all the samples were dispersed in isopropanol (0.5 mg/mL) and sonicated for 10 min. Then the samples were left for 2 min, and the upper part of the solution was taken for preparing the samples on a lacey carbon-coated copper grid (Electron Microscopy Science). Thus, prepared copper grid was cut into two equal portions, among them one portion, loaded with compound was subjected to mount into the instrument.

3.2.3.15 Isothermal titration calorimetry: The ITC experiments were performed on a Malvern MicroCal PEAQ-ITC microcalorimeter having 20 (19+1) injection cycle method capacity, the sample volume of 280 μL with a sample cell size of 200 μL and injection syringe volume of 40 μL for each set of experiments.

3.2.3.16 FESEM image processing software: The FESEM images were processed using the image analysis software SPIP 6.0.9 (Image Metrology). MATLAB (by The MathWorks Inc.) was used for numerical calculations.

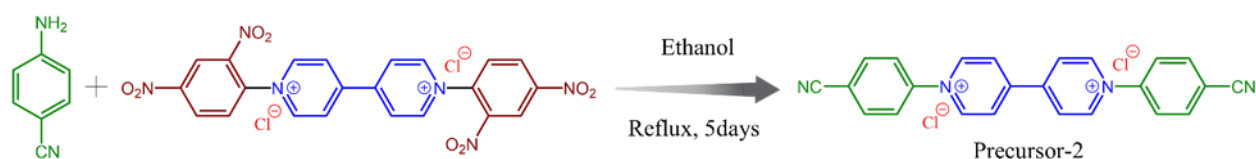
3.2.3.17 Electron tomography image processing software: The electron tomography images were processed using the image analysis software Visualiser Evo d Composer from JEOL for 3D image.

3.2.3.18 Synthesis of precursor-1: Precursor-1, 1,1'-bis(2,4-dinitrophenyl)-[4,4'-bipyridine]-1,1'-dium dichloride was synthesized according to the previously reported procedure without any modifications.^[24]



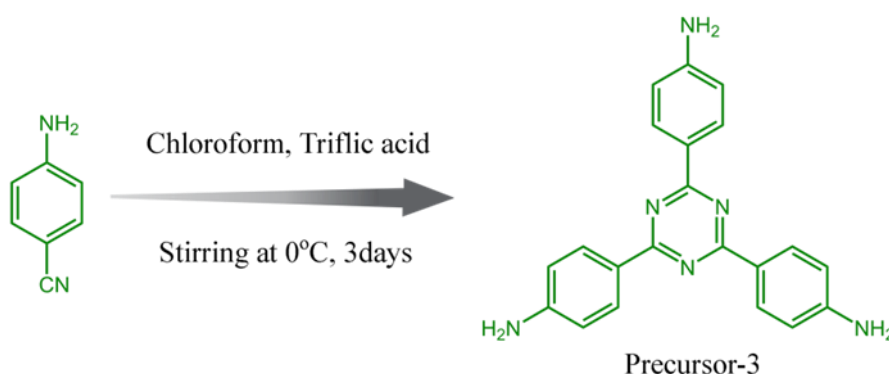
Scheme 3.1: Synthesis of precursor-1.

3.2.3.19 Synthesis of precursor-2: Precursor-2, 1,1'-bis(4-cyanophenyl)-[4,4'-bipyridine]-1,1'-dium dichloride was also synthesized according to the previously reported procedure without any modifications.^[25]



Scheme 3.2: Synthesis of precursor-2.

3.2.3.20 Synthesis of precursor-3: Precursor-3, 4,4',4''-(1,3,5-triazine-2,4,6-triyl) trianiline was synthesized from 4-aminobenzonitrile via an acid catalyzed trimerisation reaction by following a previously reported protocol.^[26]

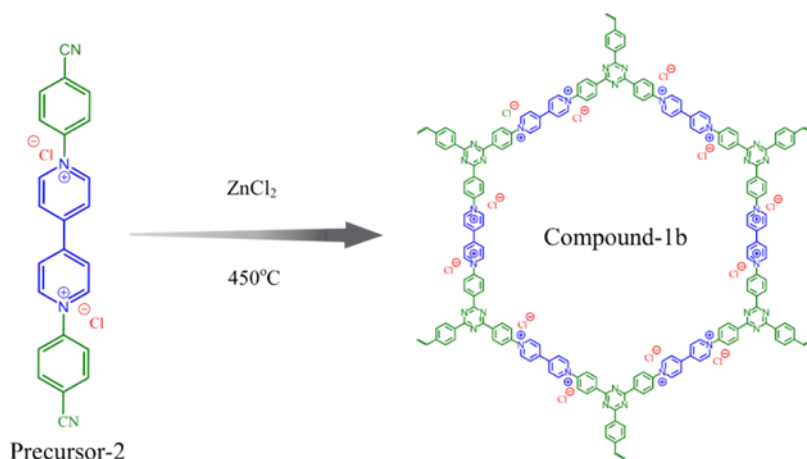


Scheme 3.3: Synthesis of precursor-3.

3.2.3.21 Synthesis of monodispersed silica nanoparticles: Monodisperse silica nanoparticles (SiO₂ NPs) were synthesized according to Stöber method.^[27] Briefly, 5 mL of tetraethylorthosilicate was slowly added to a stirring mixture of aqueous ethanolic solution (78 ml) and 32.8 wt% of ammonia aqueous solution (4.1 ml.) with vigorous stirring. Then, the above mixture was left to stand for 2 hours at room temperature to yield uniform silica nanoparticles. The precipitated silica microspheres were separated by centrifugation and washed with ethanol repeatedly. Finally, the compound was dried under vacuum at 80 °C. Further, to obtain different size-based silica nanoparticles, the temperature of the reaction system was gradually raised to 70 °C from room temperature. The silica nanoparticles with an average diameter of ~330, ~210 and ~160 nm was synthesized at a temperature of 25, 40 and 55 °C, respectively.^[28]

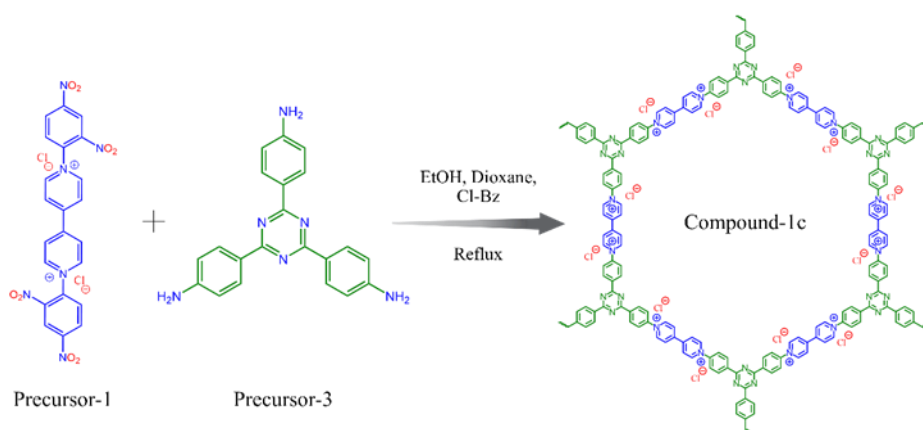
3.2.3.22 Synthetic procedure of macro ionic VOF (iVOFm) (Compound-1a): Macro ionic viologen organic framework (iVOFm) (Compound-1a) was synthesized according to the following protocol. In a clean 25 mL round-bottom flask, 90 mg of viologen monomer (Precursor-2) and 250 mg of as synthesized silica nanoparticle (as template) were well dispersed in 6 ml of tetrahydrofuran in an ultrasonic bath for 30 min. Then the solvent (THF) was removed using rotary evaporator. During this process of solvent evaporation, the viologen monomer precipitated out and filled the gaps between the 3D close-stacked silica spheres to form the initial SiO₂ NPs@viologen monomer composite precursor.^[29] Then thus formed composite precursor was carefully transferred into a small glass vial. After that the small vial with SiO₂ NPs@viologen monomer composite precursor was placed into a bigger glass vial with Teflon cap, in which there was another small vial containing ~0.45 mL of triflic acid. Then the big glass vial was degassed, refilled with nitrogen and sealed off followed by heating up to ~110 °C in a regular oven. After cooling the vessel down to room temperature, the product was immersed in water and washed with diluted ammonia solution and pure water to remove the residual TfOH. Thereafter, the silica templates were etched by using 15 ml of 4 M aqueous ammonium bifluoride (NH₄HF₂) solution. The resultant products were washed with pure water, THF, ethanol, acetone and aqueous NaCl solution, respectively, until the supernatant appeared clear. Finally, the product was dried under vacuum at 55 °C for further use (Figure 3.1).

3.2.3.23 Synthetic procedure of Compound-1b: Compound-1b, was synthesized according to the previously reported procedure.^[25] Precursor-2, 1,1'-bis(4-cyanophenyl)-[4,4'-bipyridine]-1,1'-dium dichloride and anhydrous ZnCl₂ (5 eq.) were transferred into a quartz ampoule under inert atmosphere. The ampoule was evacuated and sealed. After that the sealed ampoule was transferred into a temperature-programmed furnace and heated to 450 °C temperatures with a heating rate of 1°C/min and kept at that temperature for additional 48 h. After cooling to the room temperature, the ampoule was carefully opened. The obtained black solid was then grounded into a fine powder and washed with water in order to remove excess ZnCl₂. Then, the solid product was stirred in 1M HCl for 1 day and washed several times with water, THF, ethanol and acetone, respectively. Finally, the powder was dried at 120 °C for 12 h under vacuum to yield Compound-1b (Scheme 3.4).



Scheme 3.4: Synthesis of compound-1b via ionothermal reaction.

3.2.3.24 Synthetic procedure of Compound-1c: Compound-1c, was synthesized according to our previously reported protocol, via Zincke reaction.^[30] Precursor-1, 1,1'-bis(2,4-dinitrophenyl)-[4,4'-bipyridine]-1,1'-dium dichloride (560 mg, 0.75 mmol) and precursor-3, 4,4',4''-(1,3,5-triazine-2,4,6-triyl)trianiline (178 mg, 0.5 mmol) were introduced into a 50-mL Schlenk reaction tube. A total volume of 60 mL of 1:1:1 mixture of ethanol, 1,4 dioxane and chlorobenzene was added, and the Zincke reaction was carried out under refluxed condition for 2 days in nitrogen atmosphere. After that the solid product was subsequently cooled to room temperature and the precipitate was collected by filtration and washed with anhydrous ethanol, DMF, THF, MeCN, each by five times and with water several time, until the supernatant appeared clear. The solid product was dried overnight in a vacuum oven at 45 °C (Scheme 3.5).



Scheme 3.5: Synthesis of compound-1c through Zincke reaction.

3.2.3.25 Time dependent adsorption study: The standard procedure that we adopted for the adsorption experiments was as follows. The time dependent capture study of various analytes was performed in small vial equipped with magnetic stir bar with constant stirring rate of 550 r.p.m. Firstly, 2.5 mg of iVOFm was taken in 2.5 mL of certain concentration of each stock solution and stirred for selected time. The adsorbent was filtered off with syringe filter (0.22 μm). After that we recorded the corresponding absorbance spectra of the supernatant solution. The kinetic adsorption study was measured at different time interval. From this time dependent study, we calculated the removal % and decreasing concentration of the analytes with time using the following equations,

$$D_t = (C_0 - C_t) * 100 / C_0 = (A_0 - A_t) * 100 / A_0;$$

Where, D_t = exchange capacity, C_0 = initial concentration, A_0 = initial absorbance, C_t = final concentration, A_t = final absorbance at specific time.

Furthermore, kinetics data were fitted in a pseudo-second-order model with the help of the following equation,

$$Q_t = (k_2 Q_e^2 t) / (1 + k_2 Q_e t)$$

Where, t is the time in minutes, and Q_t and Q_e are the amounts of adsorbate (mg/g) on the adsorbent at different time intervals and at equilibrium respectively.

3.2.3.26 Adsorption isotherm experiment: In this experiment, 5 mg of the adsorbent was added to 5 mL of stock solution with different concentrations. The mixture was stirred at a constant speed of 550 rpm at room temperature for 12 hours. After equilibrium was established, the adsorbent was filtered off with syringe filter (0.22 μm), and the analytes concentration in the solution after adsorption was measured on a UV-vis spectrophotometer and further fitted with following equations,

Langmuir Model, $Q_e = (Q_m C_e) / (K_d + C_e)$; Where, C_e (ppm) and Q_e (mg/g) are the concentration of analyte at equilibrium and amount of analyte adsorbed at equilibrium respectively. Q_m (mg/g) is the maximum amount of analyte per mass of adsorbent to form a complete monolayer. K_d (mg/L) is a constant to the affinity of the binding sites.

Freundlich Model, $Q_e = K_f C_e^{1/n}$; Where, K_f and $1/n$ are the Freundlich model constant, indicating capacity and intensity of adsorption respectively.

However, it is due to the very high intensity of absorption maxima, we were unable to calculate the absorbance of high concentration SDM solution. Thus, the intensity maxima of the stock solution were measured by multiplying with the low concentration absorption maxima with certain values.

3.2.3.27 Study of adsorption in the presence of coexisting anions: In this study, we took ~100-fold-concentrated Cl^- , Br^- , SO_4^{2-} and NO_3^- ions as the competing anions and equimolar fulvic acid (FA) as

dissolved organic species, which are omnipresent in common water sources and waste waters. We took 10 ppm aqueous solution of targeted SDM antibiotic along with the hundred fold-concentrated competing anion and equimolar FA. To the mixture, 2.5 mg of activated iVOFm was added and stirred for 10 min. After that, the solution was filtered off to separate the compound, and the solution was characterized with UV-vis spectroscopy. The obtained solution was diluted 10 times to measure the UV-vis spectroscopy, and furthermore the relative capture efficiency of iVOFm in the presence of other anions was studied by comparison with a blank (Blank: only 10 ppm of the SDM was taken instead of a mixture).

3.2.3.28 Calculation of capacity: To calculate the capacity or the amount of SDM adsorbed per gram was determined by exposing 5 mg of activated iVOFm in 5 mL of the 500 ppm SDM solution for 12 hours under stirring conditions. After 12 hours, iVOFm was filtered out and the filtrate was used for further characterization. UV-vis measurements were carried out by diluting the solution. From the initial and final absorbance values of the SDM solutions we calculated the storage capacity of iVOFm using the following equation,

$$Q_m = \{(C_0 - C_t) * V\} / m;$$

Where, Q_m , C_0 , C_t , V and m are the capacity of the adsorbent, the initial concentration of the SDM solution, the concentration of the SDM solution at specific times, the volume of the solution and the mass used for the adsorbent respectively.

3.2.3.29 pH-dependent adsorption study: The effect of pH on capture study of SDM were recorded in a wide range of pH and compared with the data at pH=7.13 for relative performance. pH adjustments were made using 0.1 M HCl and 0.1 M NaOH in the pH range of 1 to 12.4 and the initial concentration of SDM solution was taken as 10 ppm. 2.5 mg iVOFm was immersed in 2.5 mL solution of 10 ppm SDM having different pH, and stirred for 1 hours at room temperature. After that UV-vis study was carried out to check the relative removal efficiency of iVOFm towards SDM.

3.2.3.30 Recyclability test of iVOFm: SDM loaded iVOFm was regenerated with excess diluted HCl and methanolic solution by keeping it for 8 hours. Reusability of the regenerated material was checked with the similar aforementioned standard procedure. After ~8 hours, the concentrations of the SDM solutions were measured by UV-vis spectroscopy. These studies were repeated for five cycles.

3.2.3.31 Column-exchange based capture experiment: To check the various toxic anions removal efficacy of the material (iVOFm), a column exchange-based sorption experiment was conducted by packing ~100 mg of iVOFm with ~5 gm of sand inside a glass column (bed length ~ 5 cm and diameter ~ 0.75 cm) as bed for anions capture (Appendix Scheme 3.6). Then different volume of stock [(0.1 mmol MO), (~50 ppm I₂+KI), (~50 ppm of KMnO₄) aqueous solution was individually passed through

the column bed with a flow rate of 0.5 mL/min, which was controlled by a water-flow-regulator, and the drops per minute was recorded with the help of a stopwatch. A bed-volume of ~2.5 mL of column eluted solution was collected in different container. The concentration of the respective anions in these solutions were then analyzed through UV-vis spectroscopy (Appendix Figure 3.33-3.35).

3.2.3.32 SDM removal study in real-water systems: For real-water system-based SDM capture analysis, different water samples (such as river water, lake water, sea water, potable water) were spiked with ~1 ppm of SDM to prepare the stock solution. 2.5 mg of iVOFm was mixed with 2.5 ml of this spiked solution. The solutions were stirred for 12 h to ensure sufficient contact time and after 12 h, suspensions were separated and solution was further analysis by UV-vis spectroscopy.

3.2.3.33 Breakthrough SDM capture study: 20 mg of compound was packed inside a glass column as bed for SDM capture. Then different volumes of stock ~50 ppm of SDM solution was passed through the column bed with a flow rate of 0.5 mL/min, which was controlled by a water-flow-regulator, and the drops per minute was recorded with the help of a stopwatch. A bed volume of ~5 mL of column eluted solution was collected in a different respective container. The concentration of SDM in these solutions were then analyzed through UV-vis spectroscopy analysis. The recyclability test of the column exchanged-based SDM capture study was performed by washing the column with pure water, followed by excess dilute HCl solution after each cycle. The filtrate of each cycle was collected at the bottom of the column. Before and after capture studies, the concentration of SDM solutions were analyzed.

3.2.3.34 Quantum calculation method: First-principles calculations based on density functional theory (DFT) were performed using Discovery Studio 2017 (Accelrys) program. The calculations were performed considering subunit (SBU) of the compound. We performed single-point energy calculation using three parameters B3LYP function. All the calculations were performed at fine quality calculation level. Initially, the molecular structure of selected unit of compound-1a was fully relaxed using geometry optimization, keeping Multiplicity factor to Auto mode with Double Numeric Plus Polarizing (DNP+) basis set and water as solvent. Subsequently, the structural simulation using simulated annealing technique was performed on geometry relaxed compound-1a to find plausible interaction site of the SDM. On the basis of ground state electron density, the electrostatic potential (ESP) on the van der Waals surfaces of iVOFm with SDM was derived (isodensity = 0.001 a.u.).

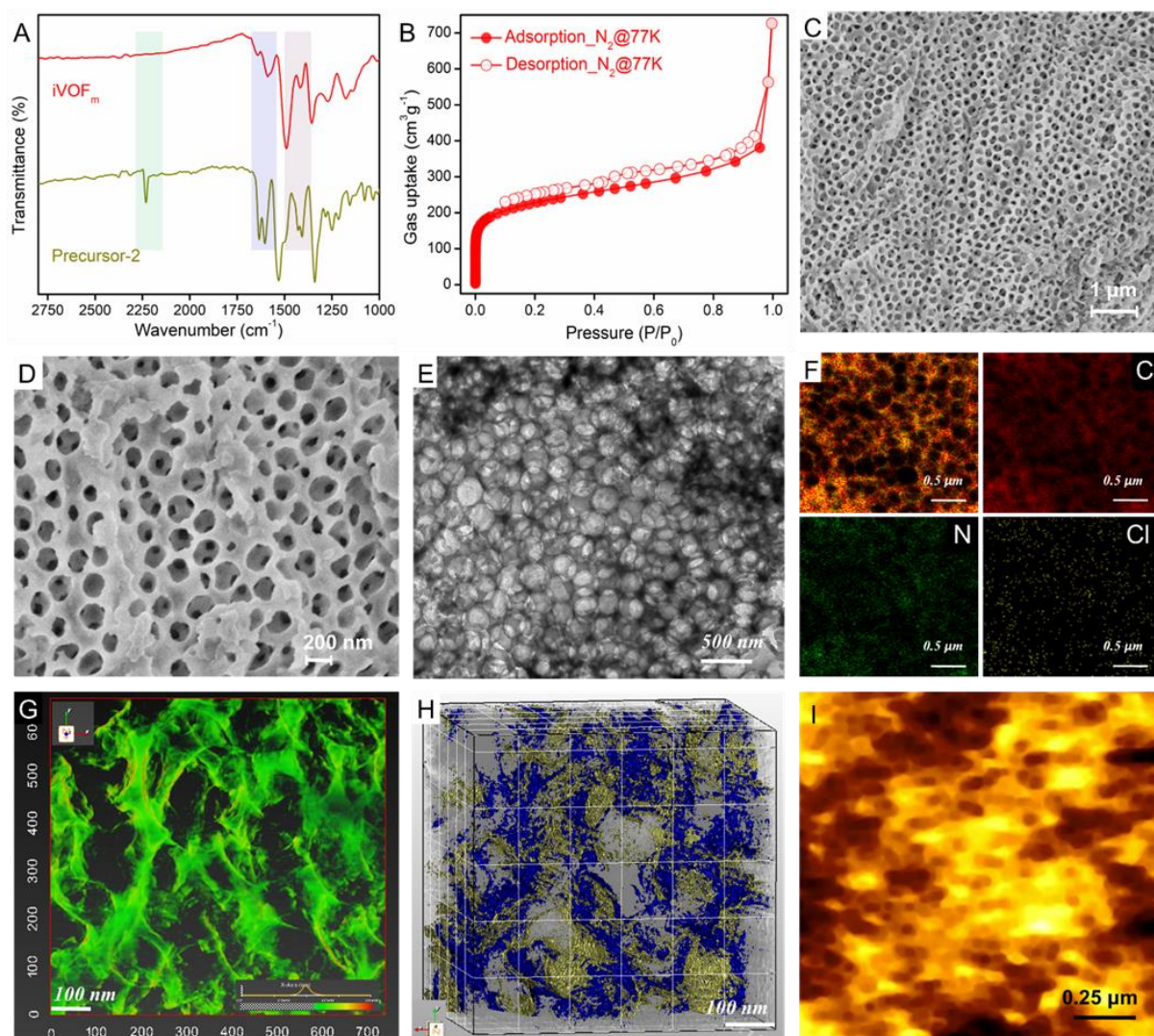
3.2.3.35 Molecular dynamics calculation: Using GROMACS 2022 we performed molecular dynamic (MD) simulations. For trajectory visualization and analysis VMD software was used. The simulation was carried out at 300 K with periodic boundary conditions. Using TIP3P water model, the water environment simulated. Initially, supercell of dimension 2X2X2 created from SBU of compound-1a. During simulation SBU was frozen and subsequently SDM was introduced. During interaction, van der Waals interaction was considered with simple cutoff scheme of 12 Å. During interaction the five

production runs of 50 ns repeats were performed. The time step of 2.0 fs was used and data collected for every 5 ps. The total accumulation time was more than 500 ns.

3.3 Results and Discussion

The hierarchical porous viologen based cationic organic-framework (iVOFm) was synthesized by introducing the viologen-units into the framework using cyanophenyl substituted viologen di-cation-unit through triflic acid (TfOH) vapor-assisted synthetic protocol in solid-phase as schematically represented in figure 3.1. Initially, the mono-dispersed silica-nanoparticles (SiO₂-NPs) have been synthesized and further used as template to systematically fabricate the macroporous network. Typically, the precursor-2 was well-mixed with silica-nanoparticles in THF solvent. Then the mixture was dried under pressure to obtain the tightly packed SiO₂-NPs@viologen monomer composite material which was later transferred into a small vial-in-vial setup, containing triflic acid in another vial. Finally, the resulting complete setup was heated during which period the polymerization reaction takes place. Finally, after removing the SiO₂-NPs, the desired macro ionic VOF (iVOFm) was obtained (experimental section for details). Insolubility of the compound in common solvents, primarily indicated the formation of the extended network. Further, thus prepared compound was thoroughly characterized by following techniques. The Fourier transform infrared (FT-IR) spectrum of iVOFm exhibited prominent peaks at 1495 and 1358 cm⁻¹, owing to the typical vibrational and stretching frequencies of aromatic C–N bonds, which demonstrated successful formation of triazine moiety (Figure 3.2A).^[31] In addition, the absence of the signal at 2235 cm⁻¹, the characteristic nitrile stretching of terminal cyano group of precursor-2 and the presence of signal at ~1639 and 1413 cm⁻¹ attributed to typical -C=N stretching of viologen salt, confirmed both the complete consumption of precursor-2 and construction of the bipyridinium subunits containing triazine network, respectively (Appendix 3.1).^[14, 25] Moreover, solid-state ¹³C cross-polarization-magic-angle-spinning (CP-MAS) NMR was employed to characterize iVOFm at molecular level, which demonstrated the characteristic peak of the sp² carbon of the triazine ring at 170 ppm, indicating the presence of triazine unit in the network (Appendix 3.2).^[32] Along with this, signals in the chemical shift range of 110-150 ppm can be assigned to the viologen moiety and other aromatic carbons of the framework structure (Appendix 3.2).^[31] Thereafter, thermal stability of the compound was investigated by performing thermogravimetric analysis (TGA) under nitrogen atmosphere. The TGA profile of iVOFm showed an initial weight loss due to the removal of solvent molecules from the structure and an excellent thermal stability >400 °C (Appendix 3.3). Moreover, to elucidate the porous nature and specific surface-area of iVOFm, low-temperature nitrogen sorption isotherm study was conducted. Figure 3.2B exhibited typical type-I isotherm with an additional sharp significant increase at high relative pressure in the nitrogen sorption study. This indicated

presence of microporous and induction of macroporous in iVOFm.^[21] The density functional theory (DFT) pore size distribution (PSD) was investigated from the N₂ porosity measurement of iVOFm (Appendix 3.4a). The Brunauer-Emmett-Teller surface area of iVOFm was calculated to be 815 cm³.g⁻¹. Further, the presence of macropores in iVOFm was confirmed by the mercury intrusion porosimetry, which explored the macroporous distribution in the range of ~20 to ~200 nm in the compound



(Appendix 3.4b and 3.4c).

Figure 3.2: A) FT-IR spectra, B) Nitrogen gas sorption, C) FESEM image, D) High-magnifying FESEM image, E) TEM image, F) STEM mapping image, G, H) 3D Electron tomography image, I) AFM image of iVOFm.

Further, the morphological evaluation of macroscopic structure of iVOFm was investigated by field emission scanning electron microscopy (FESEM), transmission electron microscopy (TEM), 3D electron-tomography and atomic force microscopy (AFM) analysis. The FESEM images of SiO₂-

nanoparticles indicated successful formation of SiO₂-NPs with an average diameter of 210 nm (Appendix 3.5). During the solvent (THF) evaporation process, the monodispersed silica-nanoparticles reorganized into a 3D close-stacked structure, and the viologen monomer precipitated out and filled the organized gaps between the silica-spheres to form the initial SiO₂-NPs@viologen monomer composite precursor. The silica-microspheres form a homogeneous stable suspension without any sedimentation. This aids in the fabrication of uniform and homogeneous SiO₂-NPs@VOF composite as revealed from the SEM image (Appendix 3.6). After the successful elimination of silica-template by salt etching method, the interconnected uniform ordered macroscopic structure of iVOFm throughout the large area of the material was observed (Figure 3.2C and Appendix 3.7). The high-magnification SEM images of iVOFm displayed the formation of uniform interconnected macroporous polymeric network with an average diameter of 210 nm (Figure 3.2D and Appendix 3.8). Additional SEM images suggested the uniformity of the macroporous construction throughout the material, along with rigid and robust macroscopic architecture of iVOFm, as no apparent collapse of the macro-skeleton has been observed after removing the silica-template (Appendix 3.9). In addition to this, TEM images also confirmed the interconnected ordered macroscopic structure of the iVOFm (Figure 3.2E and Appendix 3.10). Again, the homogeneous distribution of all the relevant elements in the TEM elemental mapping of iVOFm was investigated by energy dispersive spectroscopy (EDS) analysis (Figure 3.2F and Appendix 3.11). Moreover, from the color-modified SEM/TEM images, few randomly distributed small pores, connected with each-other through the macropores in the skeleton of the iVOFm was observed, which should be favourable for enhanced mass transfer, e.g., in the separation of pollutants from water (Appendix 3.12 and 3.13).^[23]

Moreover, to further insight into the hierarchical porous structure of iVOFm, 3D electron-tomography experiment was performed. Similar to TEM images, the cross-sectional electron-tomography images indicated homogeneous distribution of large open pores throughout the framework (Appendix 3.14). For better realization of the macrostructure, volume rendered 3D electron-tomography images have been reconstructed by probing a segment of iVOFm, which demonstrated the color-coded visualization of wide distribution bearing large nanometer size interconnected macropores throughout the volume of iVOFm (Figure 3.2G, 3.2H, Appendix 3.15 and 3.16). The homogeneous distribution of macropores throughout the structure was also visualized by the AFM image (Figure 3.2I). Furthermore, iVOFm demonstrated weak diffraction peaks at $2\Theta \sim 4.5^\circ$ correlating to the reflection from the (100) plane, indicating the existence of long-range molecular order as revealed from the PXRD data (Appendix 3.17).^[29, 33] We also observed, a broad diffraction peak at $2\Theta \sim 26^\circ$, indicating the existence of stacking structure in the polymeric network.^[14, 33]

Moreover, zeta-potential measurement showed positive surface charge (ζ -potential=+37.6mV), owing to the abundance of viologen subunits in the skeleton of the network (Appendix 3.18).^[14] Furthermore,

in order to evaluate the chemical stability, iVOFm was treated with 1M HCl and 1M NaOH aqueous solution, and further characterized by FT-IR, FESEM, TGA and N₂ sorption measurement. FT-IR data revealed no noticeable change in characteristic stretching frequencies advocating the chemical robustness of iVOFm in acidic and basic medium (Appendix 3.19). The TGA profile of acid-base treated samples showed identical thermal behaviours (Appendix 3.20). The FESEM images and N₂ sorption data demonstrated that iVOFm maintained its interconnected uniform ordered macroscopic morphological-features and structural robustness, respectively, even after acid-base treatment which further confirmed the high chemical stability of the compound (Appendix 3.21 and 3.22).

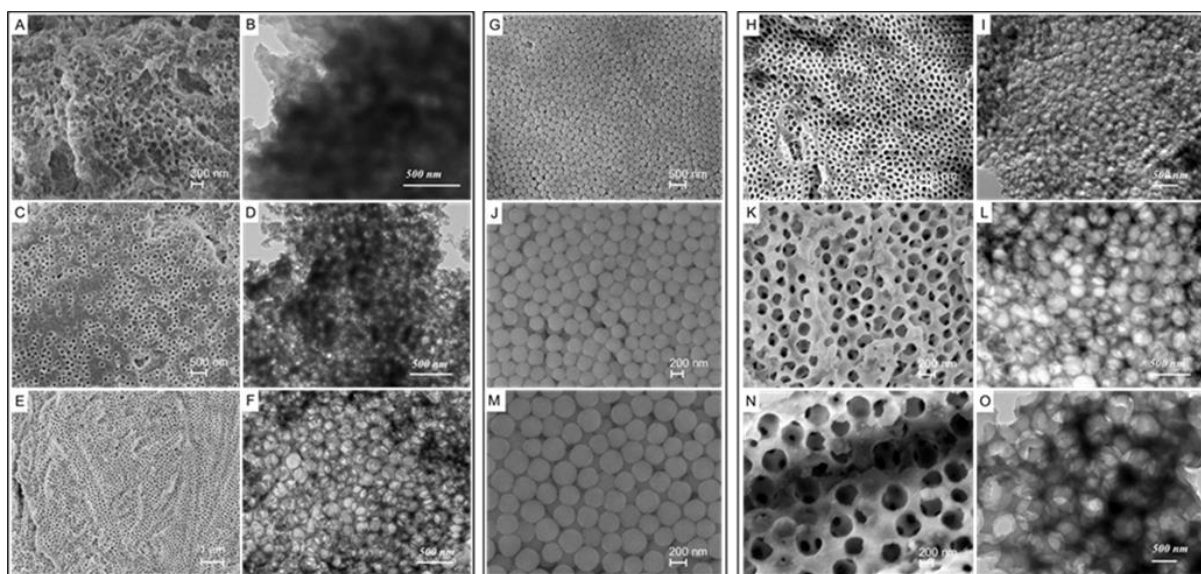


Figure 3.3: (A, C, E) FESEM, (B, D, F) TEM images of compounds, synthesized with 50, 150 and 250 mg of SiO₂-NPs, (G, J, M) FESEM images of SiO₂-NPs with size 160, 210 and 330 nm. (H, K, N) FESEM, (I, L, O) TEM images of the compounds, synthesized with 160, 210 and 330 nm size of silica-NPs, respectively.

Presumably, it can be hypothesized that the distribution and nature of macropores in iVOFm is majorly governed by the replica-template (SiO₂-NPs) amount and size used during the synthesis. This engrossing observation inspired us, further to investigate the influence of silica-nanoparticle amount and size-based macroscopic morphological diversification of the synthesized structure. At first, different amount of silica-particles (50, 150, 250, 350 mg) template was used to construct the respective macro polymers with viologen backbone, keeping the weight of the monomer constant in the initial step of polymerization. All compounds thus synthesized exhibited similar FT-IR patterns with iVOFm, demonstrating successful formation of the viologen-based polymer (Appendix 3.23). Both the FESEM and TEM images of the compounds, synthesized with 50 and 150 mg silica-template, illustrated fewer, inhomogeneous and less interconnected macroporous structure (Figure 3.3A-3.3D). This might be

attributed to the use of smaller number of templates. However, the morphology of the compounds, synthesized with 250 and 350 mg silica-template are well comparable, which is homogeneous and interconnected in nature (Figure 3.3E and 3.3F). Apart from this, different size of silica-nanoparticles (~160, ~210, ~330 nm) were employed to fabricate a series of VOF with various macro pore sizes (Figure 3.3G, 3.3J and 3.3M). As revealed from the FESEM and TEM images, the expected matching macro pore sizes (~160, ~210, ~330 nm) were observed in case of these compounds (Figure 3.3H-3.3O). Further, FT-IR spectra of these compounds indicated successful formation of the polymer (Appendix 3.24). Finally, these findings underscore the use of various amount and size of SiO₂-NPs as templates as a simple yet versatile strategy for the successful construction of cationic networks with variable macroporous architecture.

3.4 Capture Study

Chemically stable ionic framework materials are widely investigated as potential adsorbent for the elimination of various toxic pollutants from water.^[14, 15, 30] To this end, induction of macroporosity within the polymeric material can provide fast mass diffusion with unhindered transport of the specific target analytes. Therefore, in this study, the macro ionic framework (iVOFm) was deliberately employed in the removal of various organic-inorganic toxic pollutants from water (Appendix Section-3.6.3). The iVOFm demonstrated ultrafast (within ~30 sec) removal efficiency toward various types of environmentally relevant anionic pollutants such as dyes: Methyl Orange (MO) and Alizarin Red S (ARS), antibiotics: sulfadimethoxine (SDM) and sulfamethazine (SMT), oxoanions: potassium permanganate (KMnO₄) and potassium perrhenate (KReO₄), and iodine (I₂) (as polyiodides) in water (Figure 3.4A and Appendix 3.25). From the kinetics experiments it was found that removal of ~99% for SDM, ~96% for SMT, ~89% for MO, ~83% for ARS, ~99% for KMnO₄, ~97% for KReO₄, and ~95% for I₃⁻ in water was achieved within 30 sec from the respective aqueous solution by iVOFm (Figure 3.4B and Appendix 3.26-3.32). The rapid equilibrium efficiencies of iVOFm toward this diverse class of pollutants was attributed to the presence of macropores, distributed homogeneously throughout the cationic structure of iVOFm, which accelerated the diffusion of the analytes.^[23] Moreover, in order to check the order of capture efficiencies, the capacities of individual pollutants have been calculated, and further plotted against removal time. The pollutant uptake was found to follow pseudo-second-order model with a significant rate constant values (Figure 3.4C). Such fast removal kinetics of iVOFm towards dye molecules (MO and ARS), antibiotics (SDM and SMT) and oxoanions (KMnO₄ and KReO₄) were found to be well comparable with other reported porous materials (Appendix Table 3.2-3.5). Inspired by such rapid uptake, as a proof of concept toward practical implementation, a stationary-phase column-based MO, KMnO₄ and I₃⁻ capture experiments were performed with iVOFm. Results

exhibited ultrafast removal efficiencies, as the compound embedded column successfully decontaminated all the pollutants rapidly from aqueous media (Appendix 3.33).

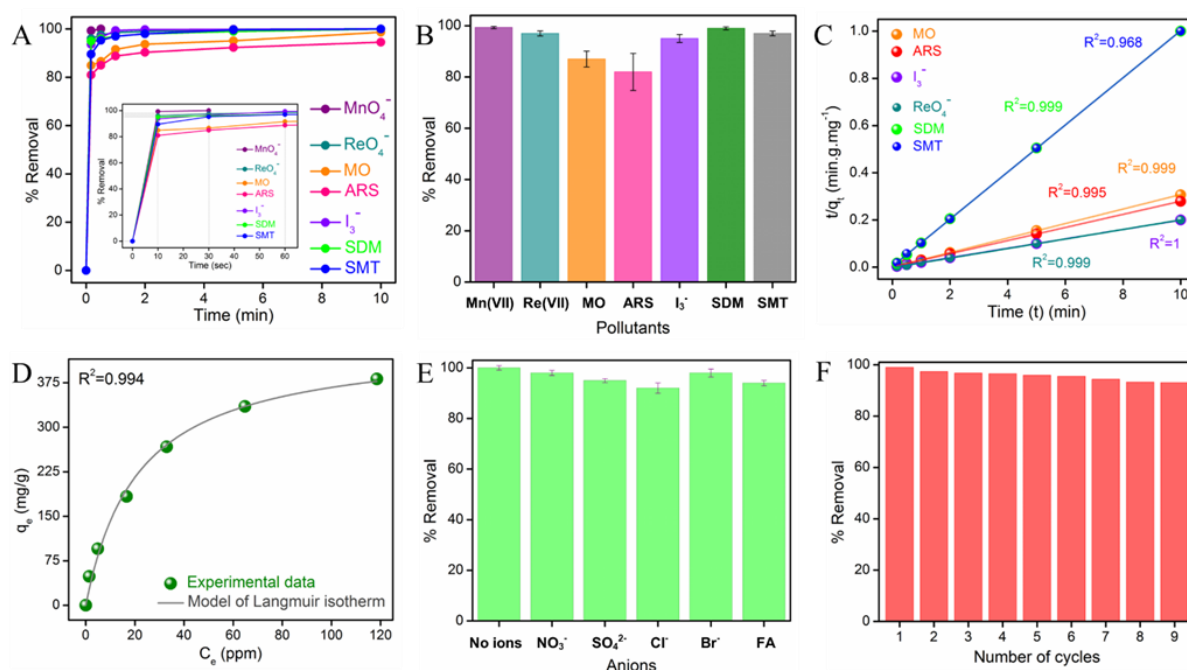


Figure 3.4: A) Removal kinetics of all pollutants, B) % removal of pollutants at time 30 sec, C) Pseudo-second-order fitting plots of pollutants, D) Langmuir isotherm model for SDM, E) Selective removal of SDM in presence of other species, F) Recyclability test result.

Among all the tested pollutants, iVOFm shows ultrafast removal (~100% within 60 sec) of SDM antibiotic from water with a high exchange capacity. The saturation uptake capacity for SDM was found to be 376 mg/g, which is believed to be one of the highest among the reported materials (Appendix Table 3.3). The sorption isotherm plot of SDM adsorption fitted well with the Langmuir isotherm model (Figure 3.4D). In real-world scenario waste-water contains number of other coexisting anions (NO_3^- , SO_4^{2-} , Cl^- , Br^-) as well as organic interferent like fulvic acid (FA) along with the SDM antibiotic.^[34] Further, we sought to explore the selective SDM capture experiment in the presence of ~100-fold excess of the aforementioned competitive analytes in water. Interestingly, it was found that iVOFm could remove SDM selectively with a high adsorption kinetics (99% removal in 60 sec) even in the presence of other excess concurrent anions and FA (Figure 3.4E). Moreover, the reusability of iVOFm was also performed, which resulted the excellent recyclability up to nine cycles with almost intact capture efficiency validating its potency and sustainability (Figure 3.4F).^[36] Also, the compound was found to exhibit high SDM removal efficiencies in different real water samples in batch sorption (Appendix 3.34) and column-based breakthrough sorption experiments (Appendix 3.35).

Hereafter, we move ahead to explore the underlying mechanism of such unprecedented anions segregation efficacy by iVOFm. We first try to elucidate the role of macropores of iVOFm toward fast separation of anions from water. For this, a following systematic pH dependent SDM capture study has been performed and the complete finding was used as a key strategy to understand the role of macroporosity upon enhanced removal performance. Considering the fact that the pH of antibiotic contaminated waste-water can vary in a wide pH range (from pH=1 to 12),^[34] we sought to investigate the effect of pH upon the SDM adsorption performance by iVOFm in both acidic and alkaline medium. An interesting observation in the adsorption trend was noted. After a very careful and discreet investigation upon SDM capture experiment at different pH, it was found that different sequestration efficiency of SDM by iVOFm has been observed at different pH range which can be explained by the structure-properties correlation of both SDM molecule and viologen subunit present in the framework. The maximum capture efficiency (~99%) was observed in the pH range of 6.44-7.2 (Figure 3.5A). Above pH 7.2 to 12 (alkaline media) there was a continuous decrease in the removal efficiency of iVOFm, as it reduced from ~99% to 84-65% (Figure 3.5A). Again, in the acidic medium (pH range of 2 to 6.44) the capture efficiency of iVOFm was found to decrease, as it drops to 81-78% from its maximum (99%) (Figure 3.5A). In addition, surprisingly, in more acidic condition (pH=1) iVOFm exhibited ~61% removal efficiency of SDM molecules (Figure 3.5A). Now, this intriguing observation can be explained on the basis of dissociation constants of SDM molecule, one at $pK_{a1}=1.30$ and the other at $pK_{a2}=6.21$,^[34] which suggest that below pH=1.30, SDM molecule exists in complete cationic form. Also, in the pH range from >1.30 to 6.21 it exists in its neutral form, while above pH>6.21 the anionic nature of SDM molecule is dominant in water (Figure 3.5B). On the other hand, it is well known that in alkaline medium the viologen units reduced to radical-cations form, from its di-cationic nature, which are subsist in acidic media (Figure 3.5B).^[35] The tunable pH dependent removal efficiency by iVOFm can be explained from the correlation between the pH-dependent structures of both viologen-subunits and analyte SDM molecules, with the experimental result, as described below (Figure 3.5A and 3.5B). As mention above, the maximum removal efficiency (>99%) was observed in the pH range of 6.4 to 7.2, which is attributed due to the maximum electrostatic interactions between the macroporous cationic surface of iVOFm and anionic SDM molecules (Figure 3.5B). In alkaline medium (pH>7.2 to 12), the continuous decrease in the removal efficiency can be explained due to lesser affinity of iVOFm toward anionic SDM, as in basic medium viologen di-cationic units get reduced to radical-cationic form (Appendix 3.36a).^[35] Moreover, the relatively greater decrease in the % removal of SDM in acidic pH range (pH=2 to 6.44) can be rationalized by considering the conversion of SDM molecules from its anionic form to neutral form ($pK_{a2}=6.21$) which demonstrated comparatively lower affinity than anionic SDM towards di-cationic form of viologen-units of iVOFm. It is noteworthy to mention that the relative increment in the % removal (~3-4%) in basic medium (pH>7.2 to 12) (84-65%) than acidic media (pH<6.21 to 1) (81-61%), may be due to the higher molecular interactions between anionic SDM

molecules and radical-cationic viologen units in basic media compared to relatively lower molecular interactions between the neutral SDM molecules and di-cationic viologen-units of iVOFm in acidic media. Moreover, the relative higher porosity of radical-cation form of viologen-units (in basic medium) with respect to di-cationic form of viologen-units (in acidic media) might be a significant reason behind this accession of removal efficiency (Appendix 3.36b).^[14] In addition, about ~61% removal efficiency of cationic SDM at pH=1 significantly indicated that adsorption is not only caused due to the electrostatic interaction, but macroporosity of iVOFm also plays a key role on the fast SDM adsorption. In a nutshell, considering the laid above discussion, along with the underlying integral rationale, i.e., electrostatic interactions and molecular interactions, macroporosity of iVOFm are other imperative requirements for such ultrafast, high SDM capture efficiency at different pH media.

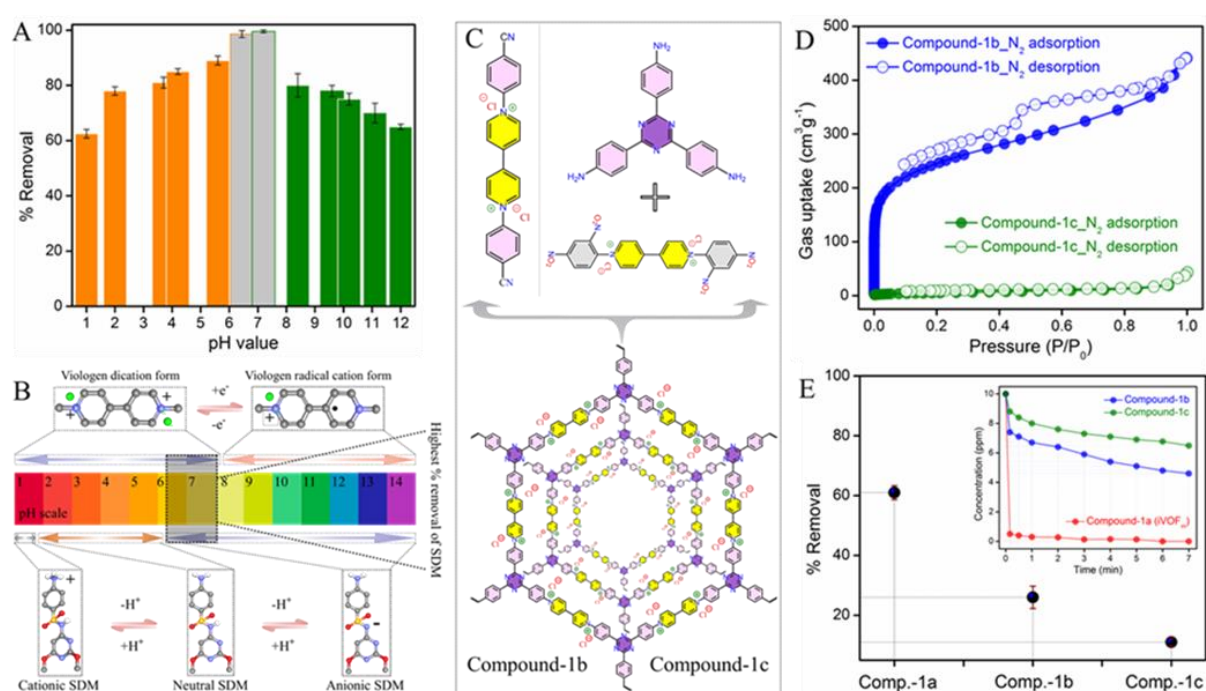


Figure 3.5: A) pH-dependent SDM removal study, B) Structures of viologen-subunit and SDM at different pH, C) Synthesis scheme of compound-1b and -1c, D) Nitrogen gas sorption data. (E) Relative SDM % removal of all compounds at pH=1, (inset, concentration decrease with time at pH=7.13).

Enthused from this afordiscussed observation, we went ahead to explore the role of macroporosity of iVOFm towards efficient anions capture in more details. Therefore, we synthesized two compounds having similar chemical structure with iVOFm, utilizing two reported protocols, (1) via ionothermal solid-state reaction, which produced micro-mesoporous charged network^[25] (compound-1b) and (2) via Zincke's reaction, which yielded a nonporous cationic viologen-organic-framework^[30] (Compound-1c) (Figure 3.5C). Thus, synthesized compounds have been thoroughly characterized by FT-IR, solid-state ¹³C-NMR, TGA, N₂ adsorption, FESEM, etc. (Appendix Section 3.6.4). Both FT-IR, solid-state ¹³C-

NMR and TGA profile of compound-1b and 1c indicated formation of polymeric network (Appendix 3.37-3.42). The morphology and elemental analysis of both compounds was characterized by FESEM-EDS (Appendix 3.43 and 3.44). Moreover, according to the reported literature, XPS, PXRD and Raman spectroscopy were employed to elucidated the chemical and electronic structure of compound-1b and -1c (Appendix 3.45-3.47).^[25, 30] Further, to establish the porosity of both compounds, nitrogen sorption measurements were performed. In case of compound-1b, high uptake of N₂ at low relative pressure (type I) and moderate uptake at high pressure (type IV) indicated the coexistence of both micropores and mesopores (Figure 3.5D).^[25] However, compound-1c demonstrated very low uptake of N₂ at 77K indicating low permanent porosity with less surface area (Figure 3.5D).^[30] After the successful characterization, thus synthesized compound-1b and 1c along with compound-1a (iVOFm) were employed toward SDM capture at pH=7.13 and pH=1. The comparative % removal of SDM by compound-1a, 1b and 1c, at pH = 7.13 are presented in figure 3.5E, Appendix 3.48 and 3.49, which indicated ~99%, ~32% and ~19% removal of SDM, respectively, within 1 min. Such high uptake (~99%) of SDM by compound-1a at pH = 7.13 might be attributed to the abundant macroporosity in synergy with strong molecular interactions between anionic SDM and cationic surface of compound-1a. Whereas, the relatively low percentage removal of SDM by compound-1b and 1c with respect to compound-1a can be explained by the reduced porosity of respective compounds, which makes the interactive surface less accessible for analytes inclusion.^[23] At pH=1, compound-1b and 1c demonstrated ~26% and ~11% removal efficiency, respectively, which is much lower than compound-1a (~61%) (Figure 3.5E). The reason behind these trends in capture efficiency of respective compounds can be described by the macro-microporous to meso-microporous to nonporous nature of compound-1a, 1b and 1c, respectively. This result suggested that inducing macroporosity within compound-1a (iVOFm) is indispensable in accomplishing the highest removal efficiency than comparatively less porous identical cationic compounds at pH=7.13 and 1. Again, after the pollutant removal experiment, no significant structural as well as morphological changes has been observed, which confirmed the robust nature of the iVOFm toward real-world water treatment application (Appendix 3.50 and 3.51). Additionally, the loading of SDM molecules into the pores of the compounds after capture experiment was characterized by FT-IR, SEM-EDS and N₂ sorption measurements (Appendix 3.50 and 3.51). This result demonstrated the advantage of order inter-connected macropores over less porous compounds toward achieving rapid and high degree of separation efficiency. Further, in order to validate the thermodynamically favourable interactions between SDM antibiotic and iVOFm, isothermal titration calorimetry (ITC) experiment was carried out. The ITC result indicated that the adsorption of anionic SDM molecules onto iVOFm is an exothermic process with negative Gibbs free energy, which suggested the strong binding affinity of SDM on iVOFm was a thermodynamically favourable process (Figure 3.6A and 3.6B).

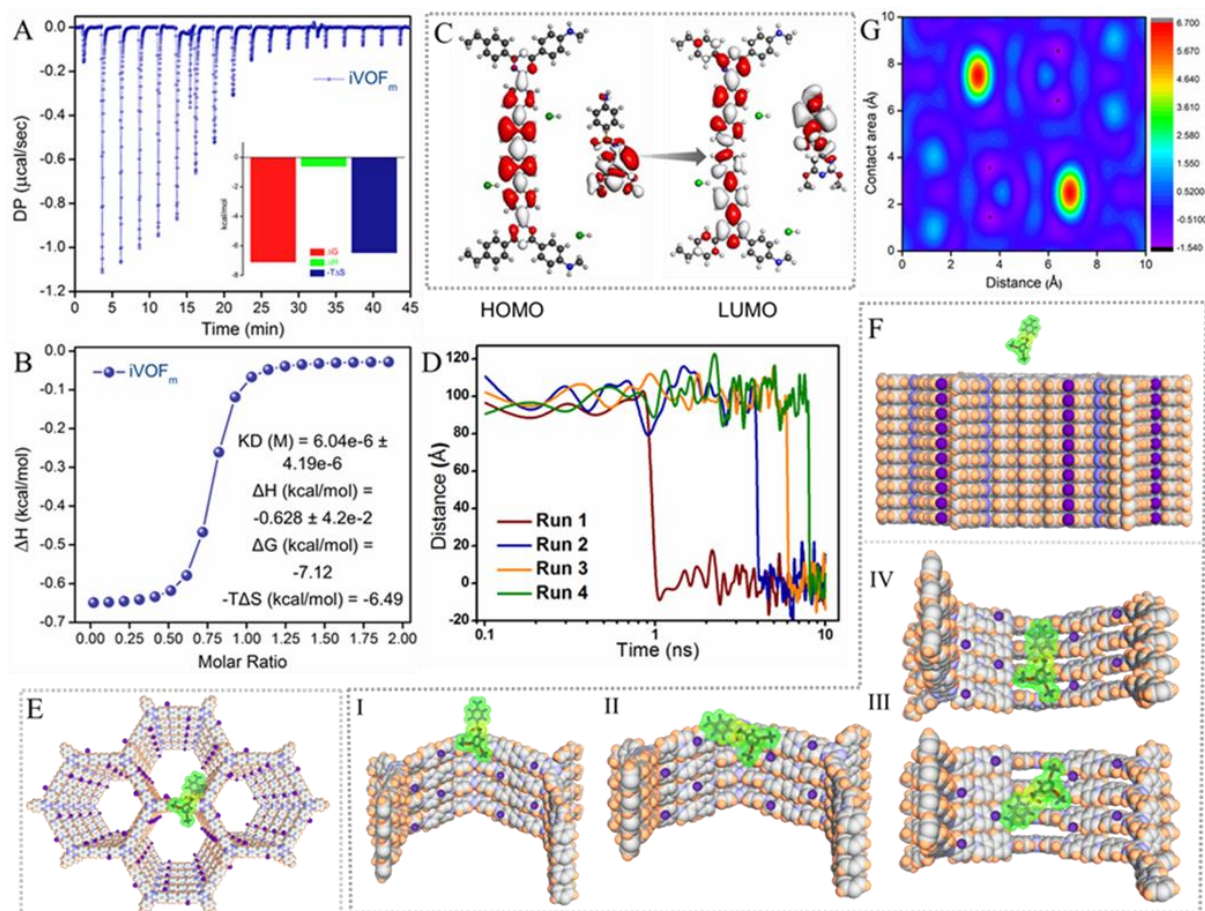


Figure 3.6: A) ITC thermogram with parameters, B) Heat of injection of SDM sorption, C) HOMO-LUMO energy profile, D) Runs of distance between center of mass of SDM and surface of iVOFm segment. Binding pattern of SDM along (E) top, (F) side-view, G) SDM binding-energy surface of the compound, (I-IV) simulation snapshots with different free binding energy.

Moreover, in order to get further insight on the experimental observation, the binding pattern and sorption pathway, molecular dynamics simulations study along with binding energy calculation of the interaction between the surface of iVOFm and SDM molecules has been done with the help of density functional theory (DFT). The simulation result validated the role of various supramolecular non-covalent interactions towards high and rapid SDM adsorption by iVOFm (Appendix Section 3.6.6). The HOMO-LUMO energy-state of the compound with the SDM molecule has been calculated, which indicated the presence of energy maxima and minima sites favourable for the interaction with minimum binding energy (Figure 3.6C). The binding energy of interaction was observed to be -123 kJ/mol. Thus, iVOFm is in ‘Switch-ON’ condition during the interaction with SDM. Further, in the simulation study, within a very short period of time (time~1ns), the SDM molecules were found to be absorbed into the cavity surface of the iVOFm, as showed by the decreased of center of mass with respect to the distance of SDM to the surface of the compound in the runs (Figure 3.6D-3.6F). These runs indicated the

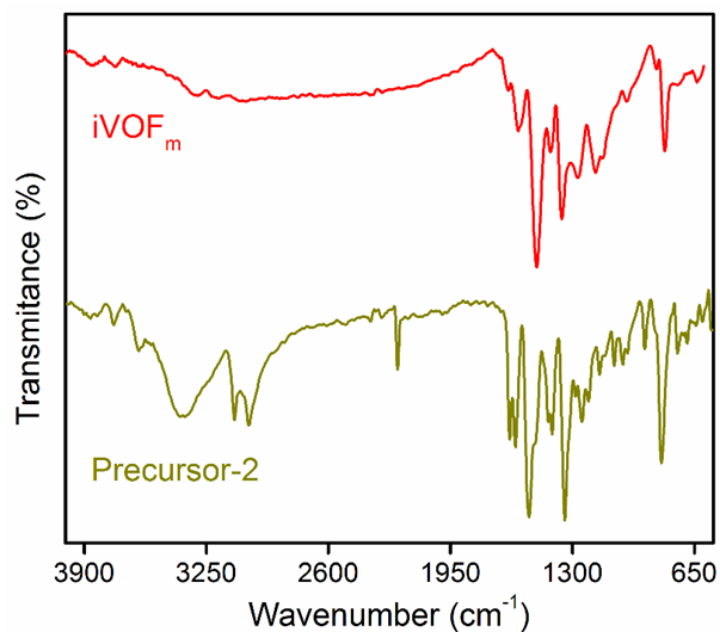
energetically favourable binding modes of SDM and iVOFm. The geometry-optimized structures for a minimized unit of iVOFm with SDM revealed crucial insights regarding the preferable binding sites (Appendix 3.55). Moreover, to further demonstrate the probable multiple binding modes and sorption patterns of SDM into the surface of the iVOFm, binding free energy has been calculated, which indicated different binding free energy basin located at different contact area ($A_{\text{cont.}}$) and distance ($D_{\text{com.}}$) between SDM and iVOFm (Figure 3.6G and Appendix 3.56). Interestingly, the binding energies for SDM molecule within the geometry-optimized unit of the compound were quite significant that elucidates the exceptional binding affinity along with high uptake competency. Additionally, the different configuration of binding of SDM with the cavity surface of the compound in corresponding to the free energy basins of the interactions has been demonstrated with the respective snapshots of specific SDM-iVOFm binding modes (Figure 3.6(I-IV)). Finally, the simulation data validate our experimental findings and further supports our understanding for the observed efficient separation performance of iVOFm towards SDM anions in water.

3.5 Conclusion

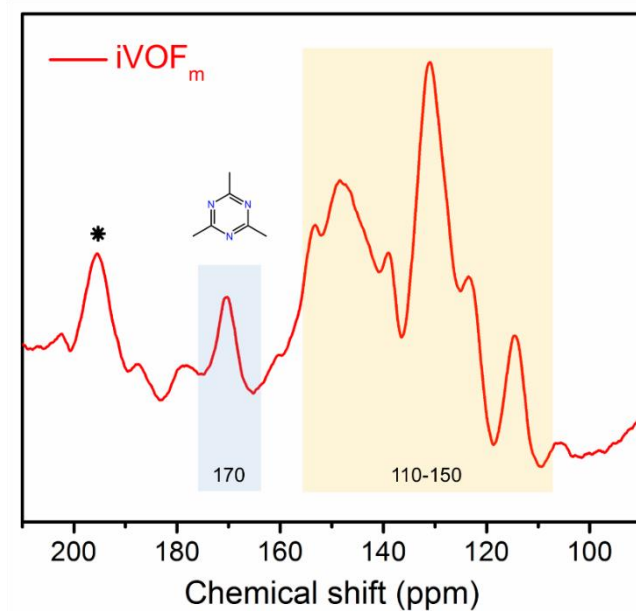
While targeting an effective method for significant enhancement in adsorption followed by ion-exchange performance of sorbent, we have developed a simple yet facile strategy to construct rare ionic hierarchical porous-organic-framework with order interconnected homogeneously distributed macropores, utilizing silica-nanoparticle mediated templating synthesis protocol. The use of specific size and amount of silica-template offers fine control over fabrication of specific size and amount of macropores on the polymeric material. Optimizing this strategy, we have succeeded in fabrication of an efficient ionic adsorbent, intentionally decorated with interconnected uniform macropores, which demonstrated excellent removal performance aided by enhanced diffusion towards a variety of toxic pollutants in water. The ultrafast sorption capability of the macroporous cationic scavenger was further compared with two identical structures with relatively less porous nature, which validated the role of large pores in the structure toward triggered pollutants separation application. Such efficient chemical segregation ability of iVOFm highlighted that this promising strategy is practically viable and can be extended for the construction of various other functional groups containing macro-microporous materials and further exploration toward task-specific applications.

3.6 Appendix Section

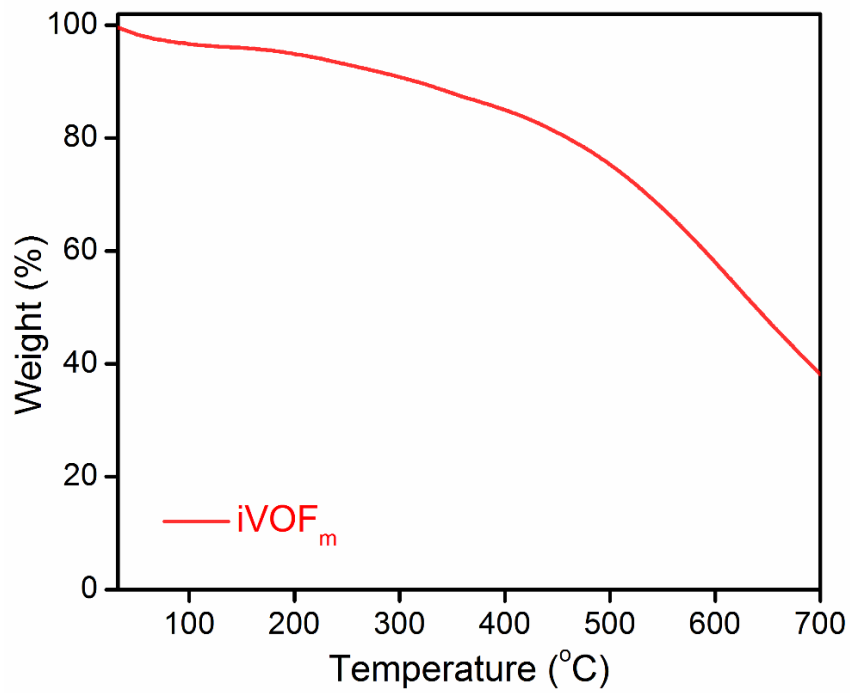
Appendix Section 3.6.1: Characterizations of iVOF_m



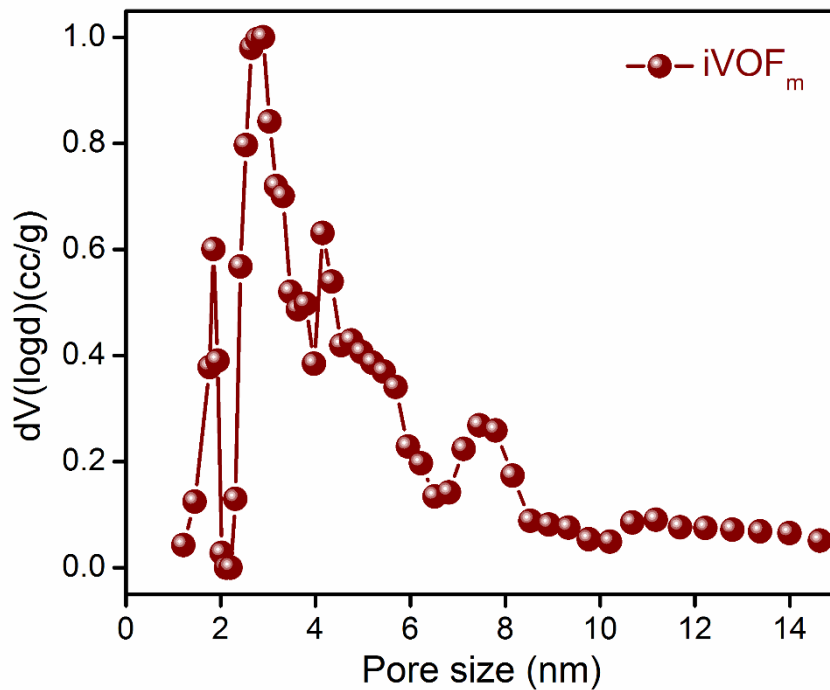
Appendix 3.1: FT-IR spectra of iVOF_m and its precursor-2, indicated formation of the material.



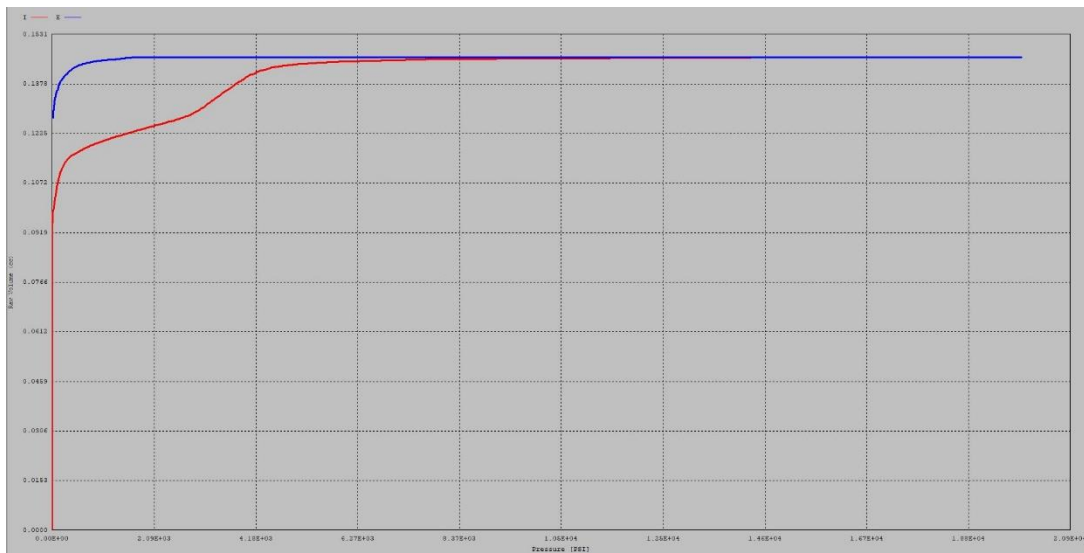
Appendix 3.2: ¹³C CPMAS NMR spectra of iVOF_m (The asterisks denote spinning side bands).



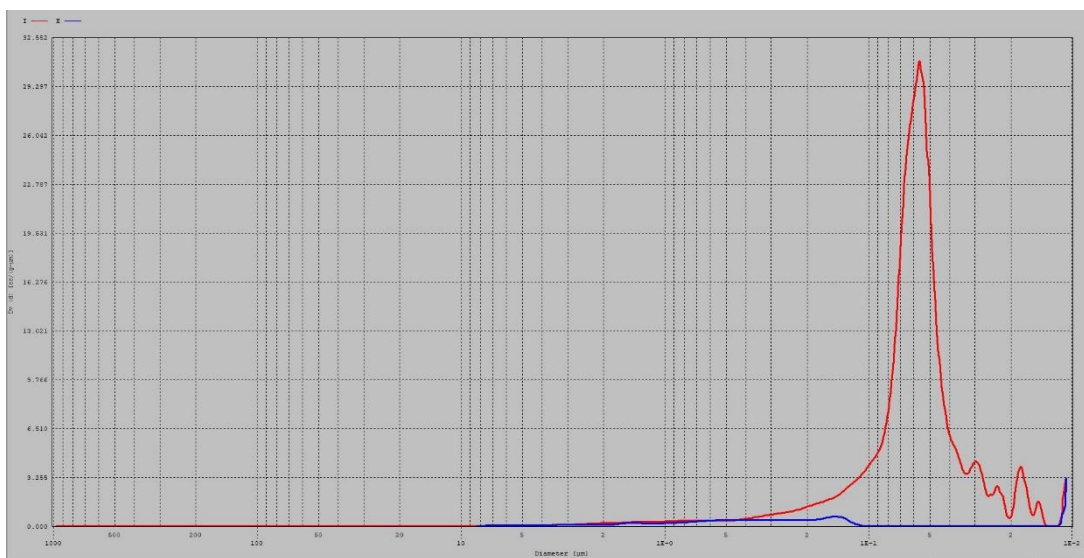
Appendix 3.3: Thermal gravimetric analysis (TGA) profile of $iVOF_m$.



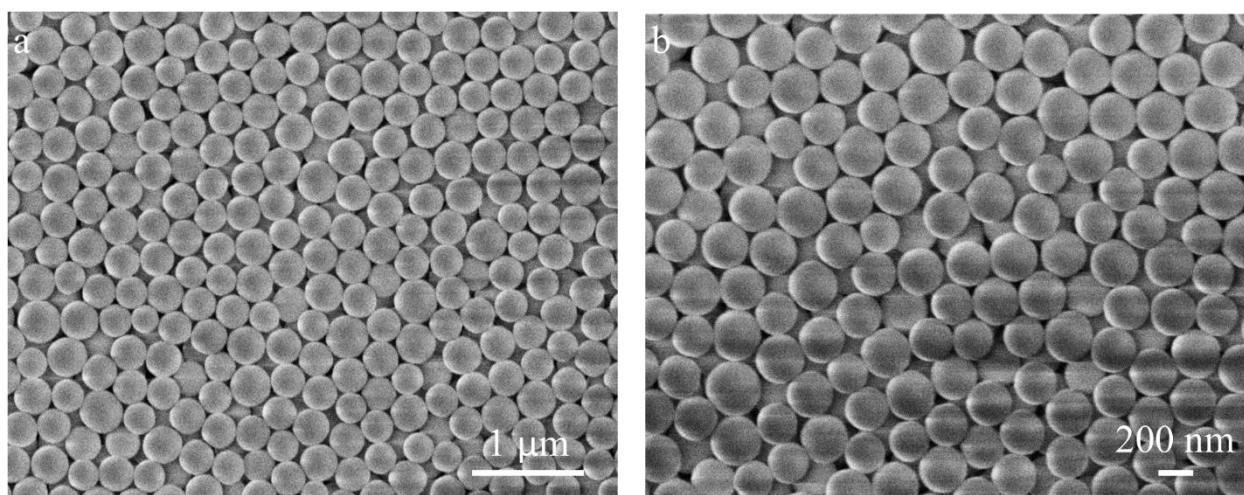
Appendix 3.4a: The DFT pore size distribution of $iVOF_m$ measured from the nitrogen sorption data.



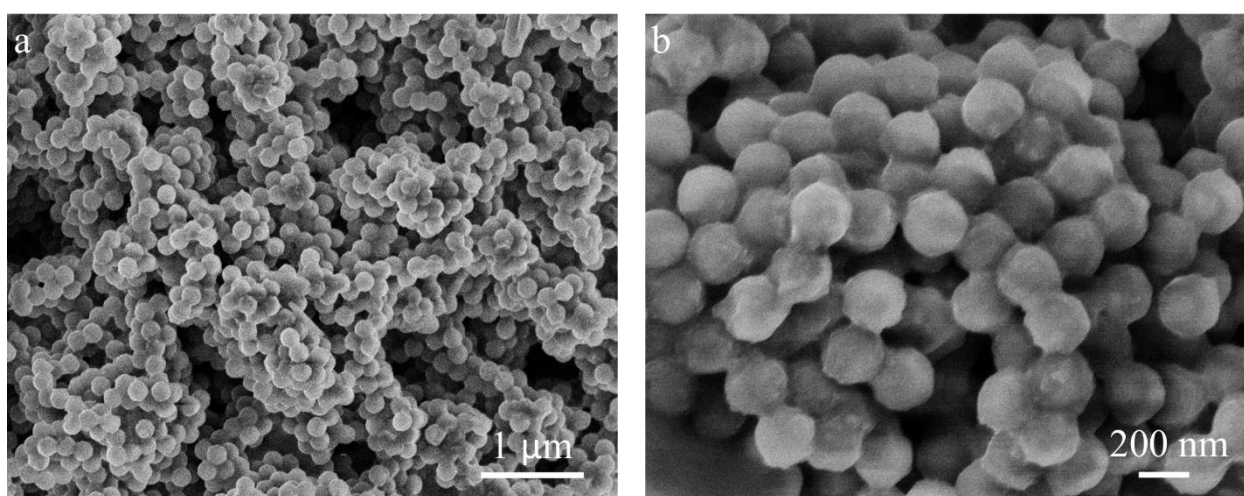
Appendix 3.4b: Intrusion and extrusion profile of iVOF_m measured by mercury intrusion porosimetry.



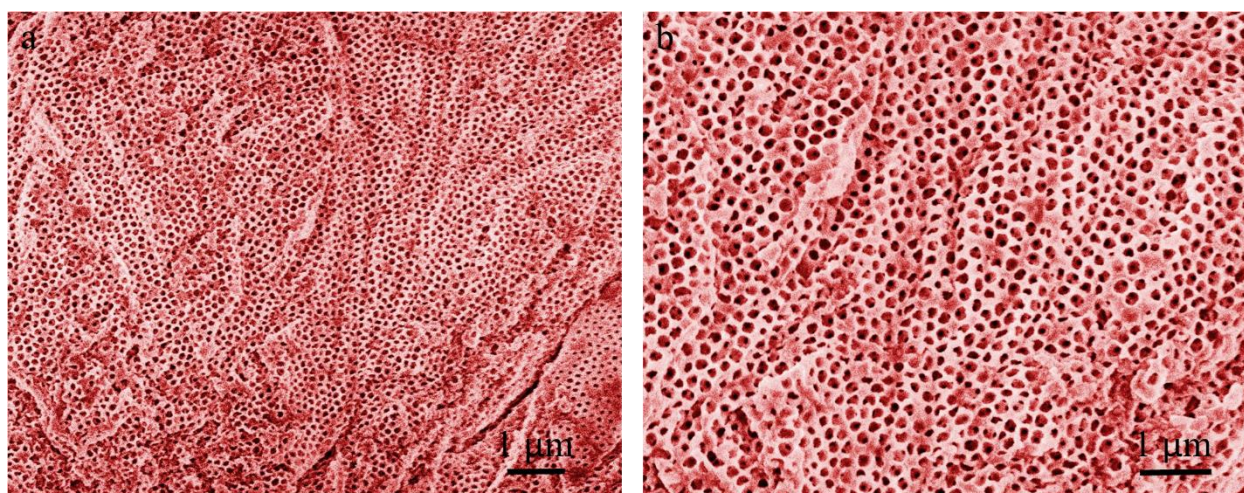
Appendix 3.4c: The pore size distribution of iVOF_m measured by mercury intrusion porosimetry.



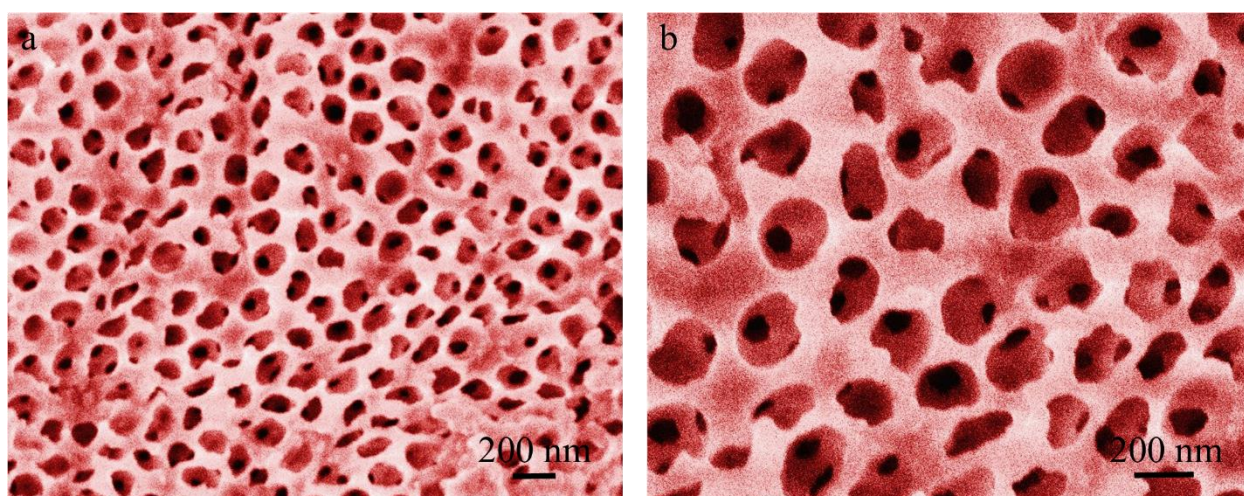
Appendix 3.5: FESEM images of monodisperse silica nanoparticles (SiO₂ NPs) in different magnification (a, b) with an average diameter of ~ 210 nm.



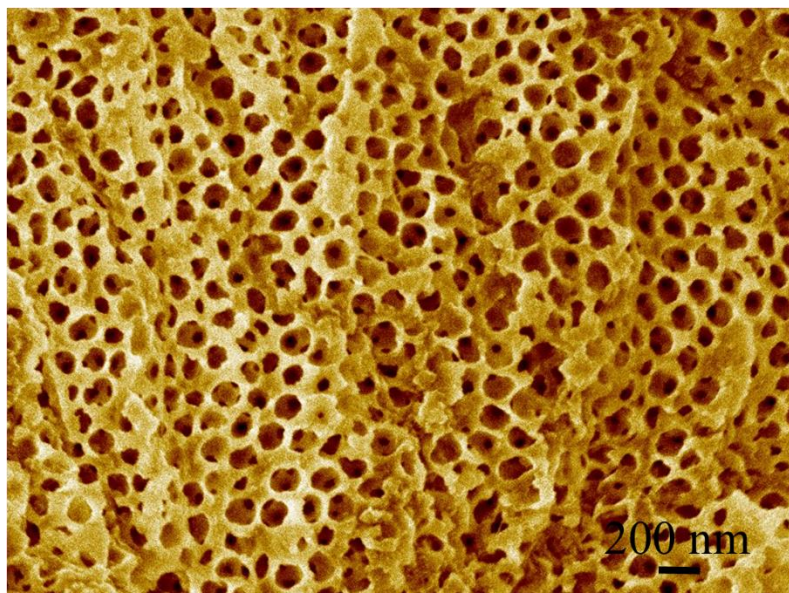
Appendix 3.6: FESEM images of SiO₂ NPs@VOF composite in different magnification (a, b).



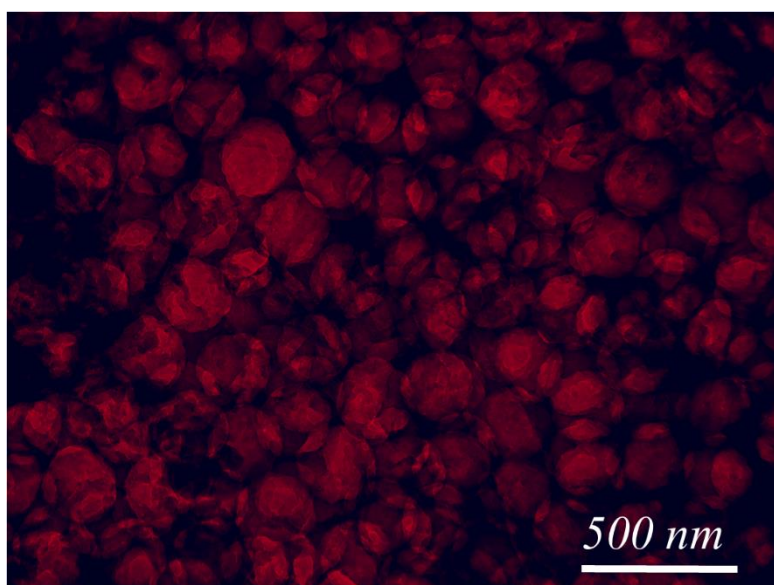
Appendix 3.7: Additional FESEM images of macro ionic VOF (iVOF_m) after removing the silica template. (Scale bar 1 micron) (The colour of the original images has been modified using mentioned software for better visualization).



Appendix 3.8: Additional high-magnification FESEM images of macro ionic VOF (iVOF_m) after removing the silica template. (Scale bar 200 nm) (The colour of the original images has been modified using mentioned software for better visualization).



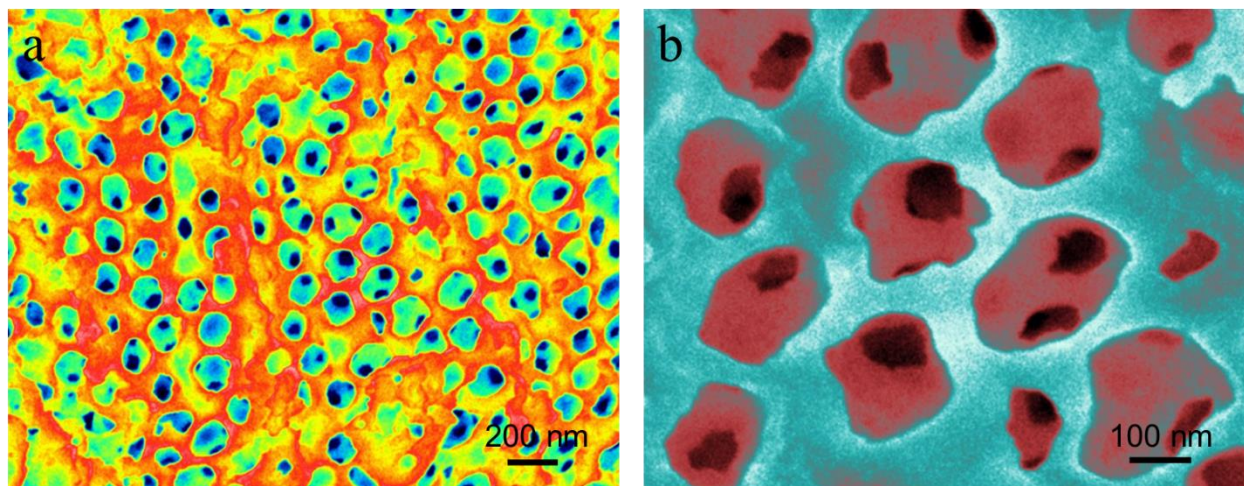
Appendix 3.9: Additional FESEM image of macro ionic VOF (iVOF_m). (Scale bar 200 nm) (The colour of the original images has been modified using mentioned software for better visualization).



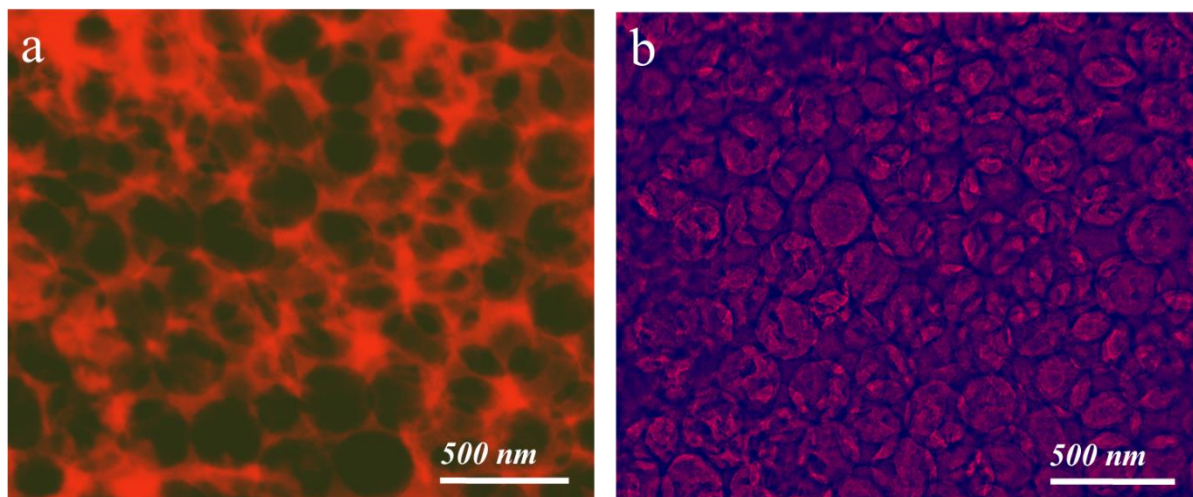
Appendix 3.10: Additional TEM image of macro ionic VOF (iVOF_m). (Scale bar 500 nm) (The colour of the original images has been modified using mentioned software for better visualization).



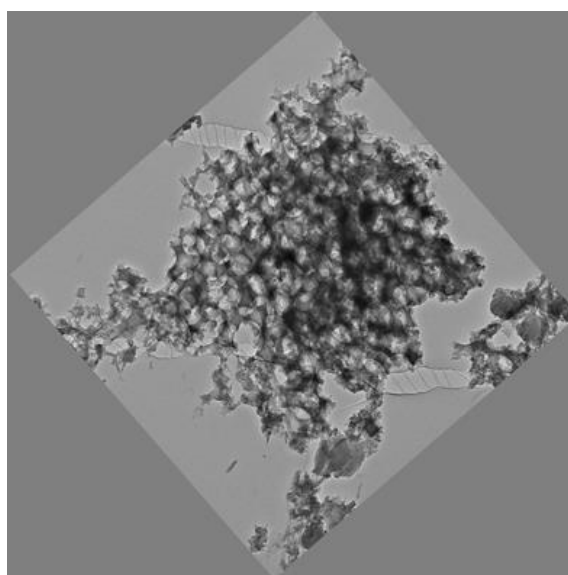
Appendix 3.11: EDS analysis of iVOF_m.



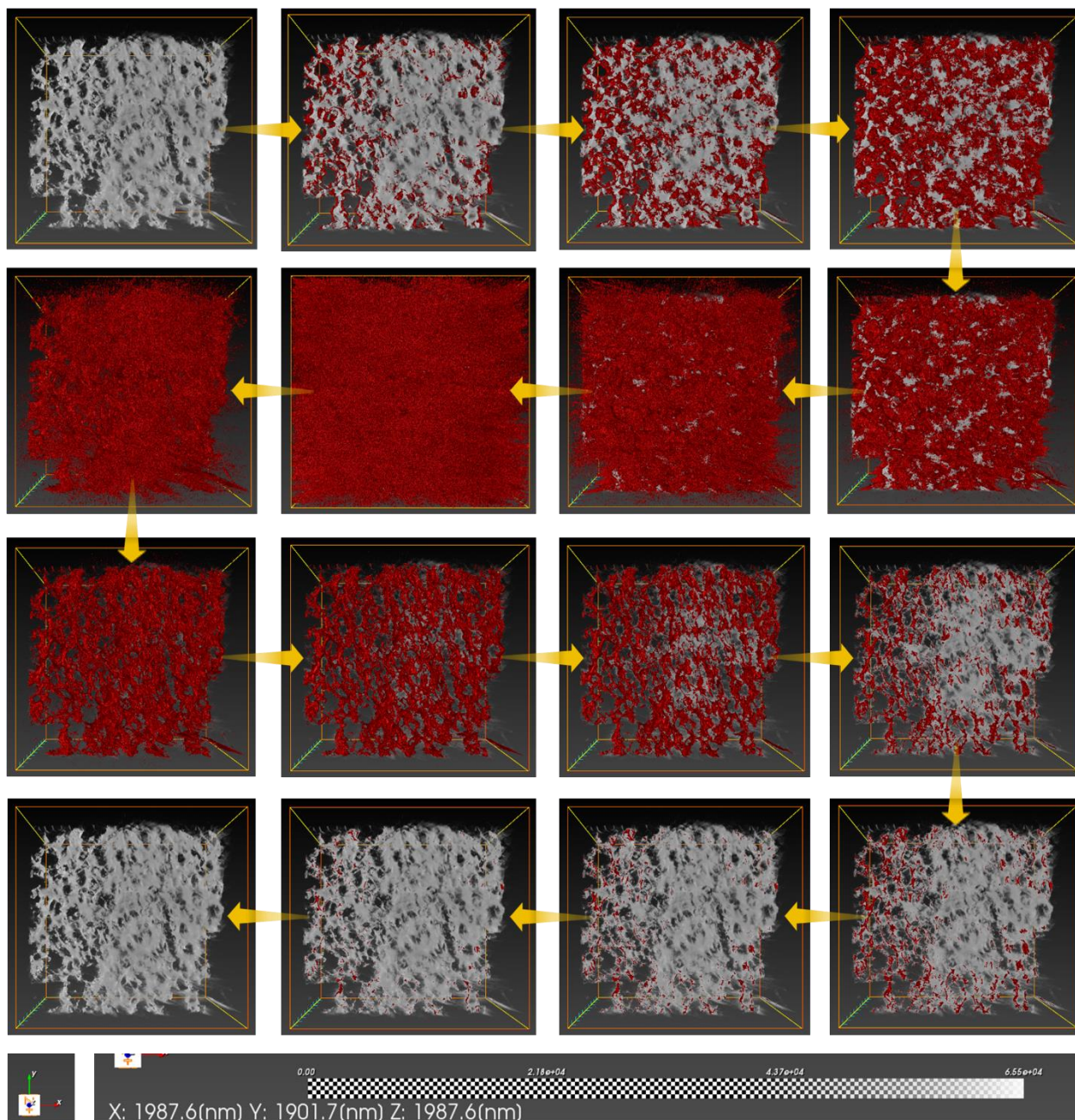
Appendix 3.12: High magnification colour-modified SEM images of iVOF_m showing few randomly distributed small pores, connected with each-other through the large macropores. (The color of the original images has been modified using mentioned software for better visualization).



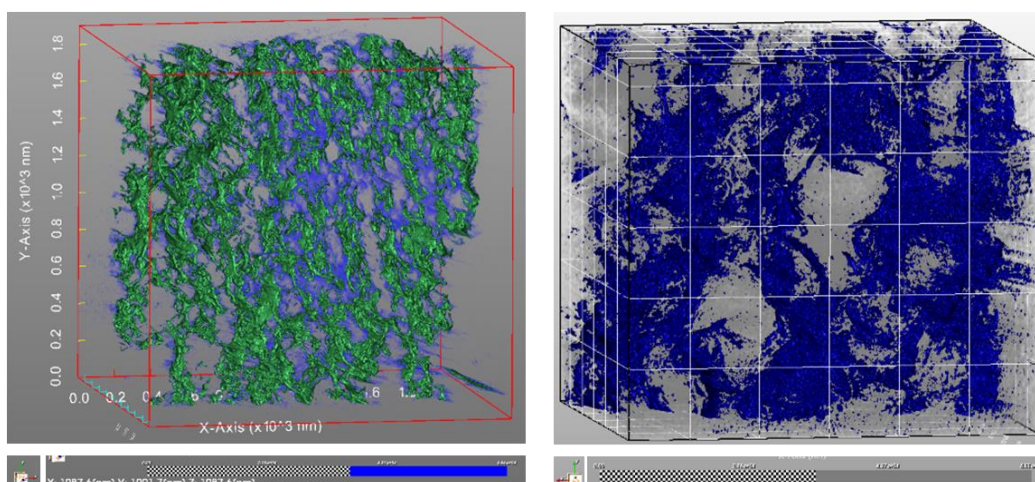
Appendix 3.13: High magnification colour-modified TEM images of iVOF_m showing few randomly distributed small pores, connected with each-other through the large macropores. (The color of the original images has been modified using mentioned software for better visualization).



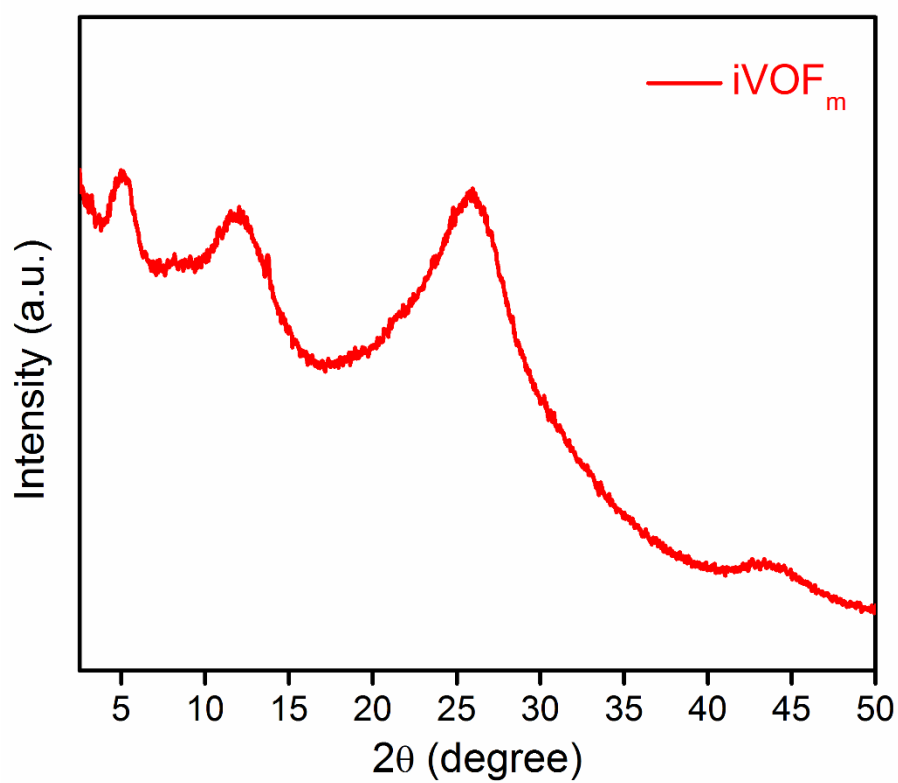
Appendix 3.14: 2D cross-sectional electron tomography image of iVOF_m.



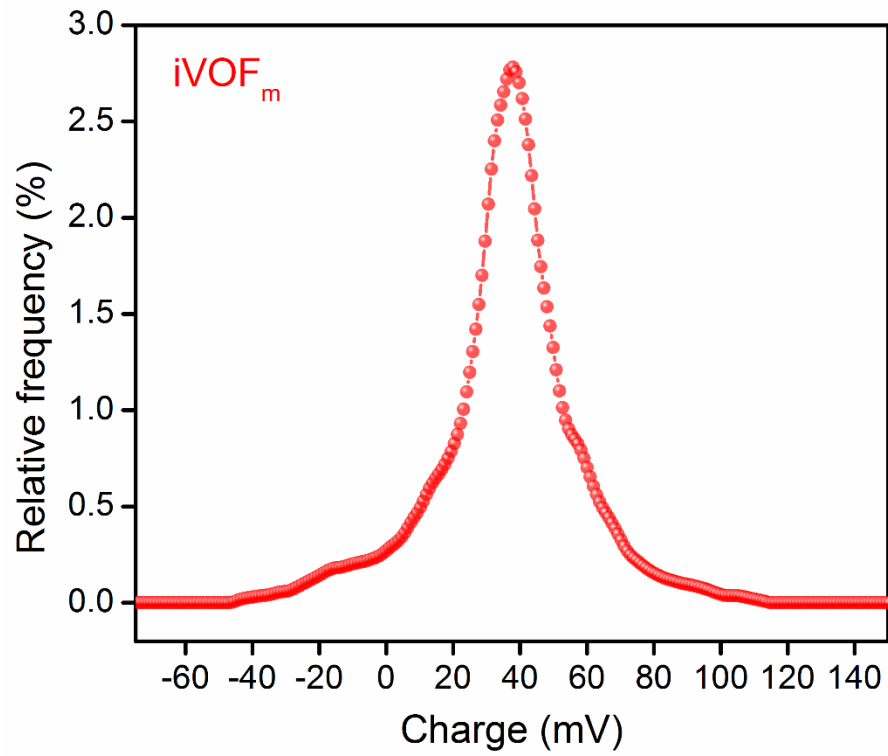
Appendix 3.15: Electron tomography 3D images of iVOF_m, showing homogeneous distribution of interconnected macropores throughout the cationic network of the material.



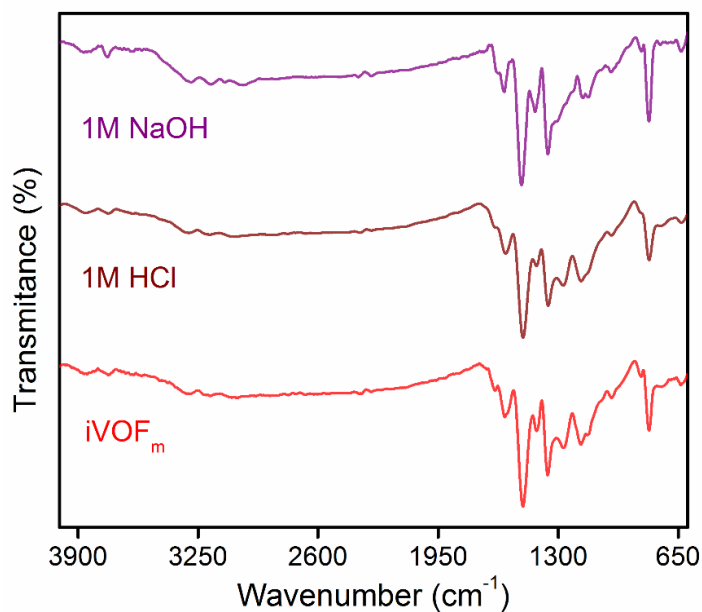
Appendix 3.16: High-magnifying electron tomography 3D images of $iVOF_m$.



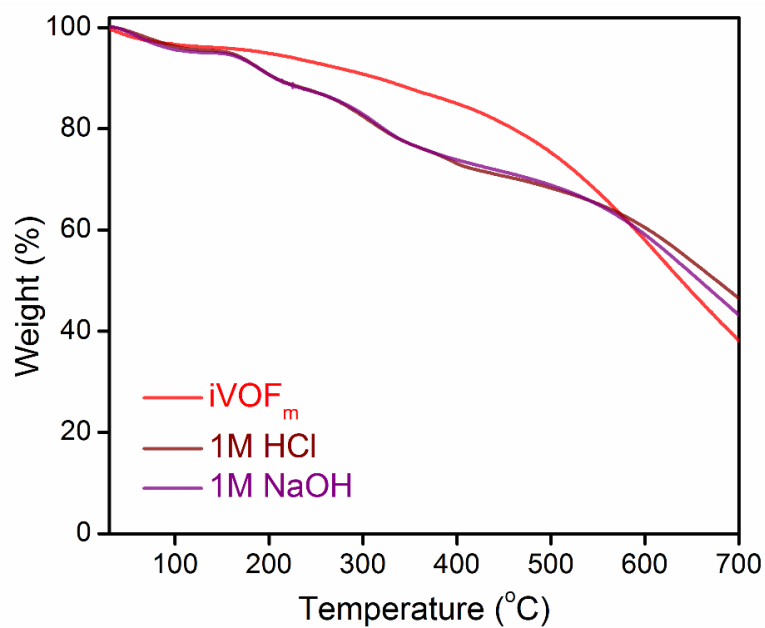
Appendix 3.17: PXRD pattern of $iVOF_m$.



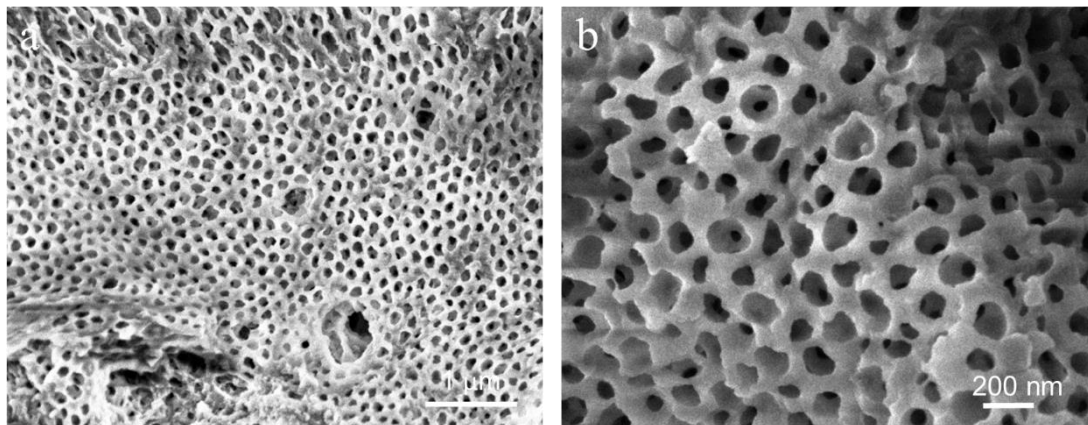
Appendix 3.18: Zeta potential measurement plot of iVOF_m shows an average charge of +37.6 mV.

Appendix Section 3.6.2: Chemical Stability Test of iVOF_m

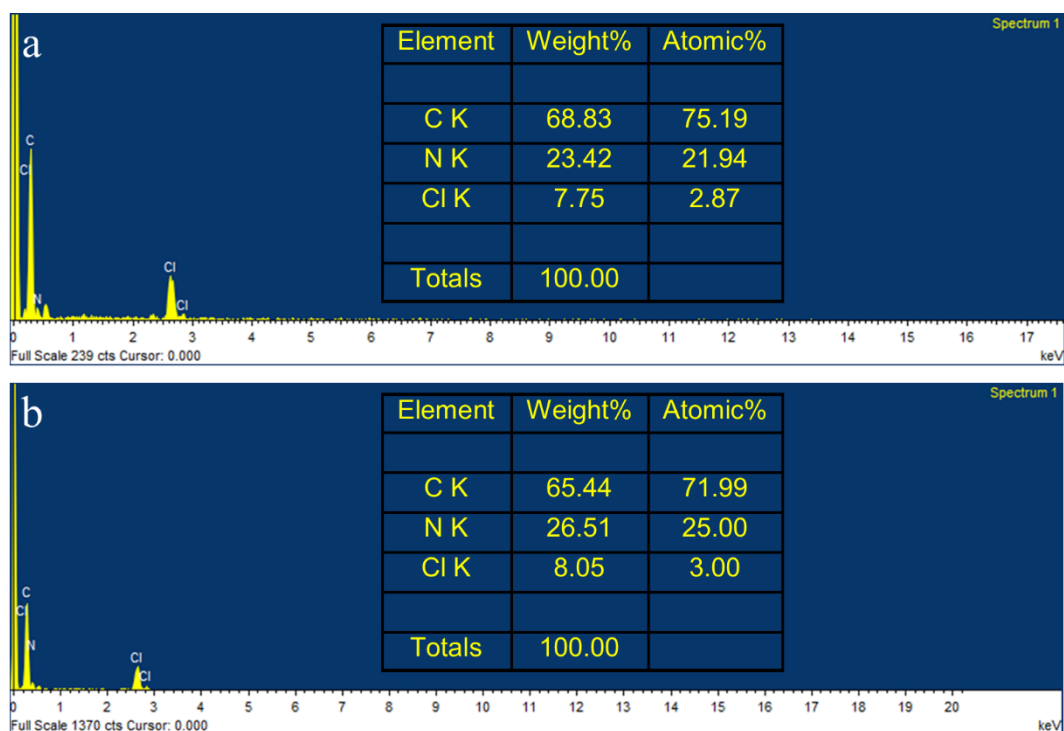
Appendix 3.19: FT-IR spectra of iVOF_m (red), 1 M HCl treated iVOF_m (wine) and 1 M NaOH treated iVOF_m (purple).



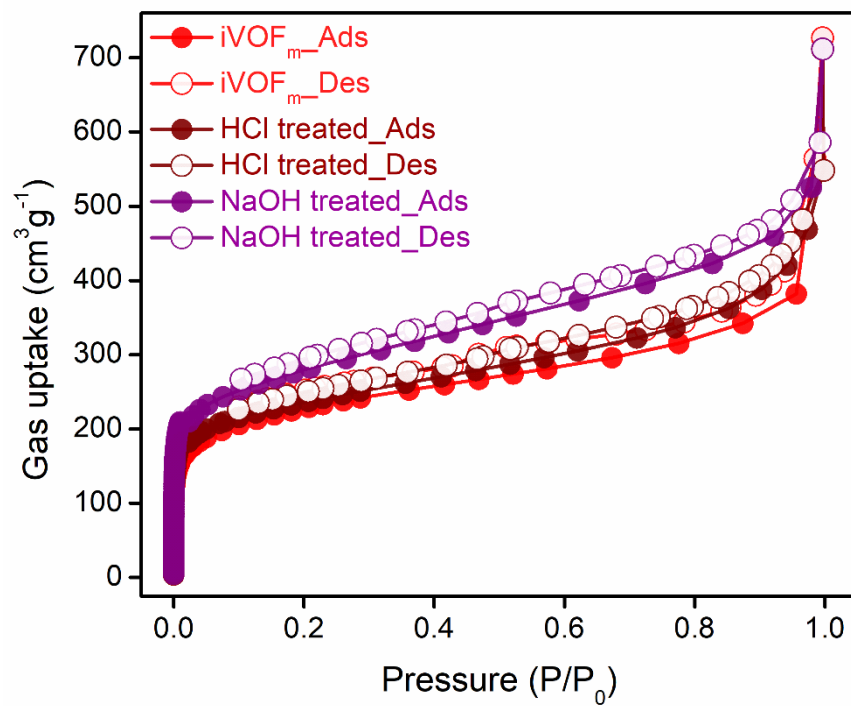
Appendix 3.20: (a) TGA profile of iVOF_m (red), 1 M HCl treated iVOF_m (wine) and 1 M NaOH treated iVOF_m (purple).



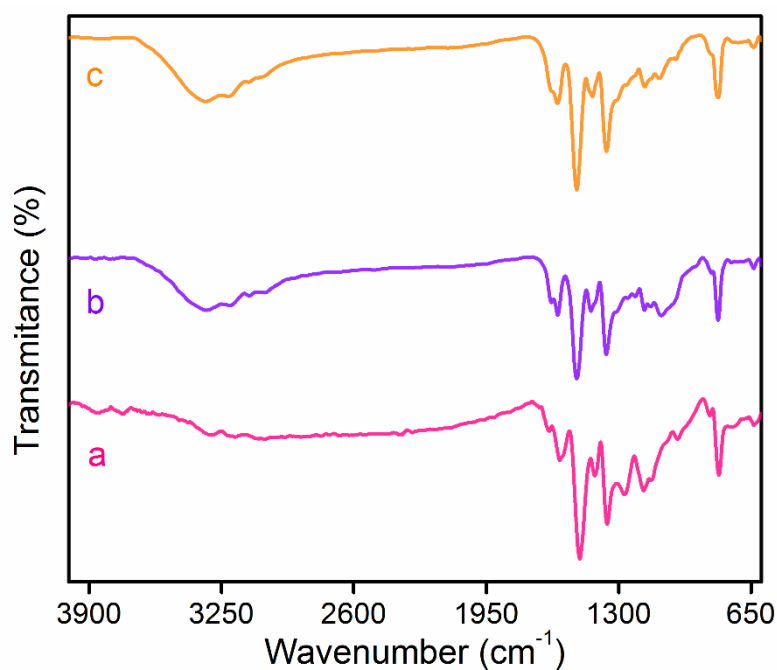
Appendix 3.21a: FESEM images of iVOF_m after treating with 1 M HCl (a) and 1 M NaOH (b).



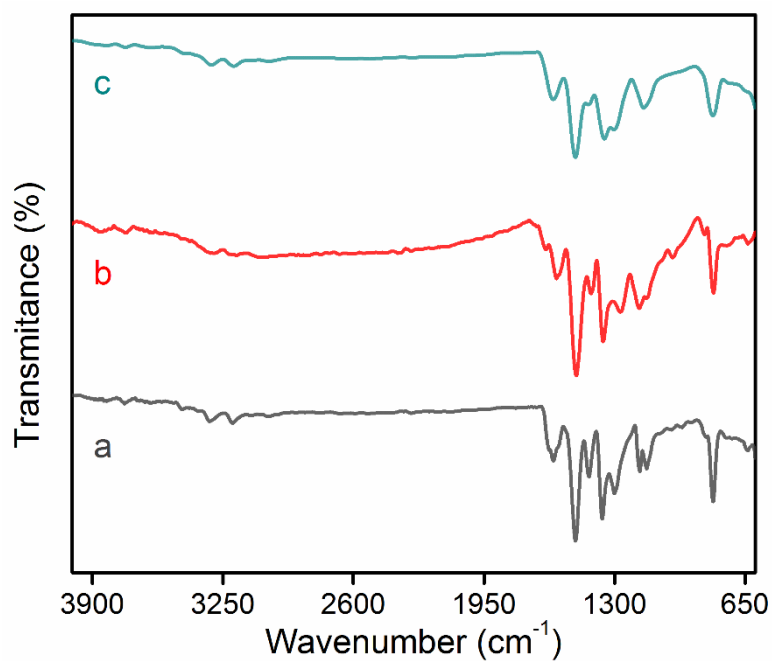
Appendix 3.21b: EDS analysis of iVOF_m after treating with 1 M HCl (a) and 1 M NaOH (b).



Appendix 3.22: Nitrogen sorption data (77 K) of iVOF_m after treating with 1 M HCl and 1 M NaOH.



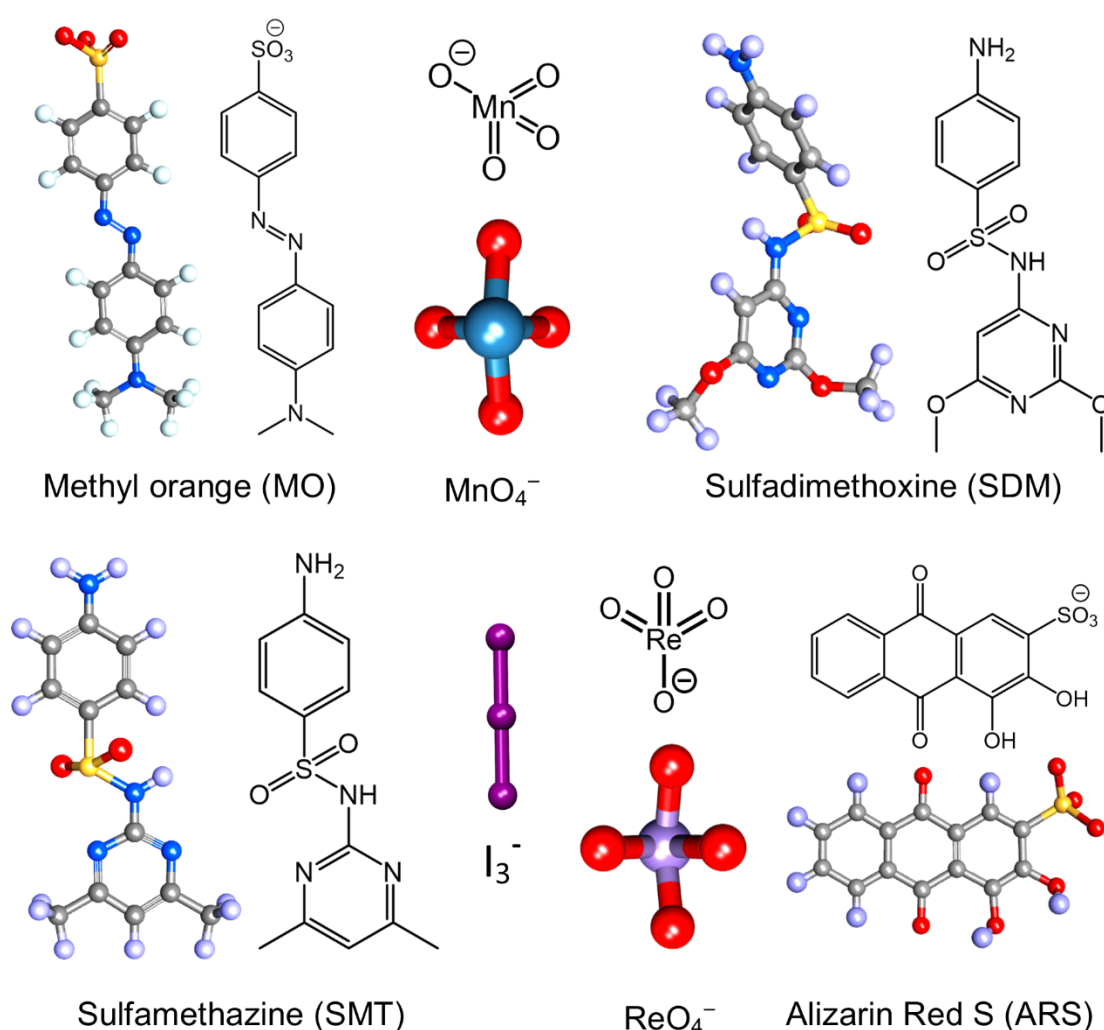
Appendix 3.23: FT-IR spectra of compound, synthesized with (a) ~250 mg, (b) ~150 mg and (c) ~50 mg of SiO_2 nanoparticles.



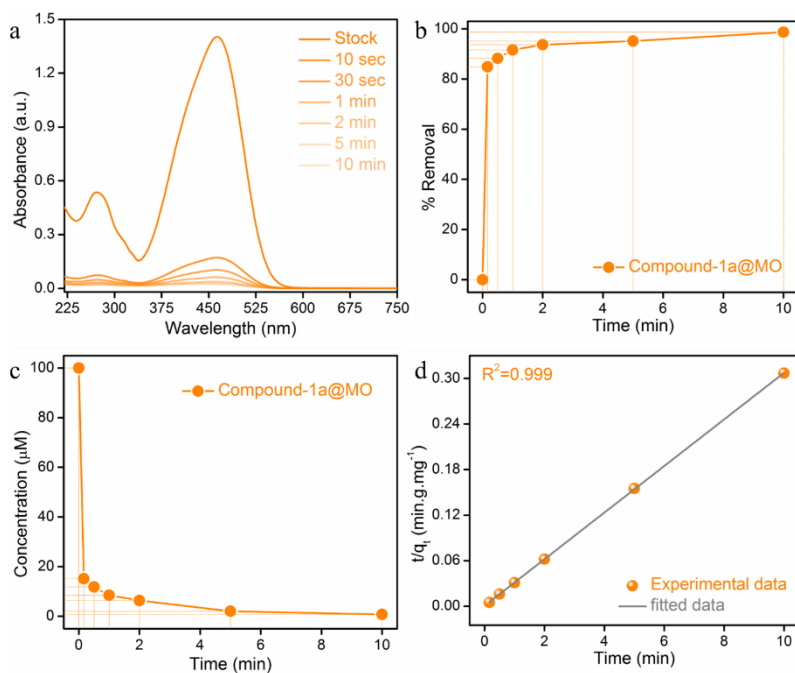
Appendix 3.24: FT-IR spectra of compound, synthesized with (a) ~160 nm, (b) ~210 nm and (c) ~330 nm of SiO_2 nanoparticles.

Appendix Section 3.6.3: Sorption Study

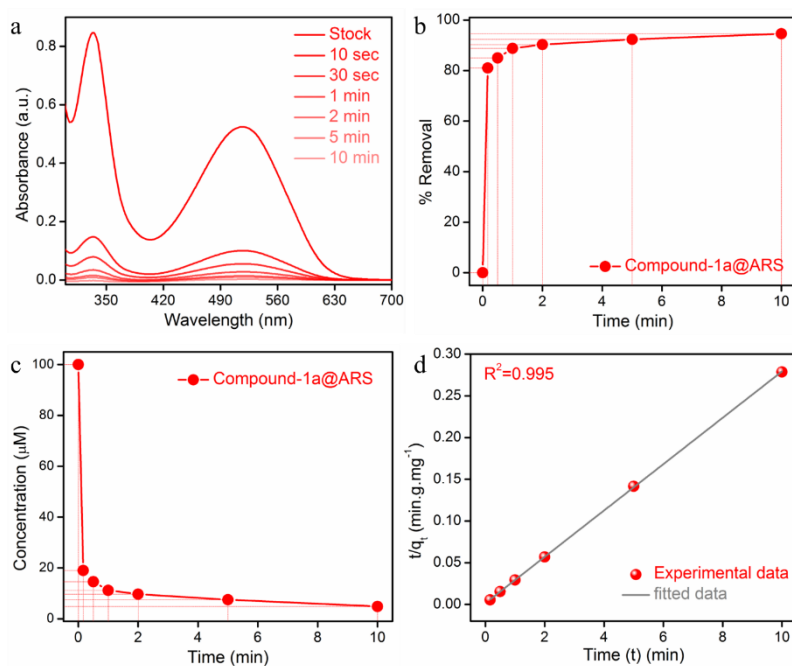
General consideration: All the adsorption kinetic studies has been carried out taking following respective concentration of different anionic analytes (Appendix 3.25) in pure aqueous solution. For organic dyes (methyl orange (MO) and alizarin red s (ARS)) the stock solution was prepared with 0.1 mmol of each dye in water. However, for the antibiotic solution (sulfadimethoxine (SDM) and sulfamethazine (SMT)), a stock solution of 10 ppm has been chosen for the kinetic study by iVOF_m. Further, in case of stock solution of oxoanions (potassium permanganate (KMnO₄) and potassium perrhenate (KReO₄)), the initial concentration was 50 ppm. Moreover, due to low intense absorption maximum, iodide (I₃⁻) stock solution (solution of I₂ and KI in DI water) was prepared at 50 ppm concentration.



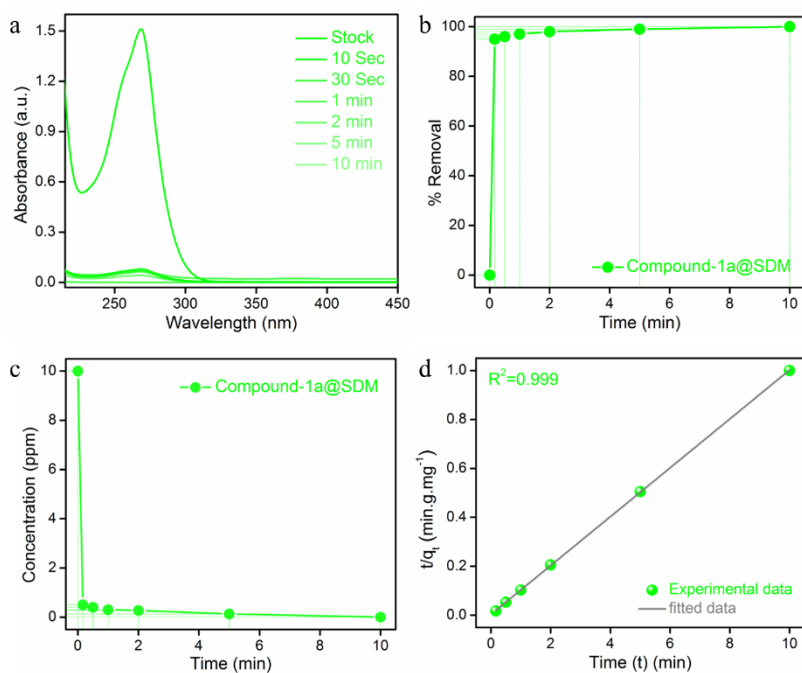
Appendix 3.25: Chemical structures of various organic-inorganic pollutants, used for capture study.



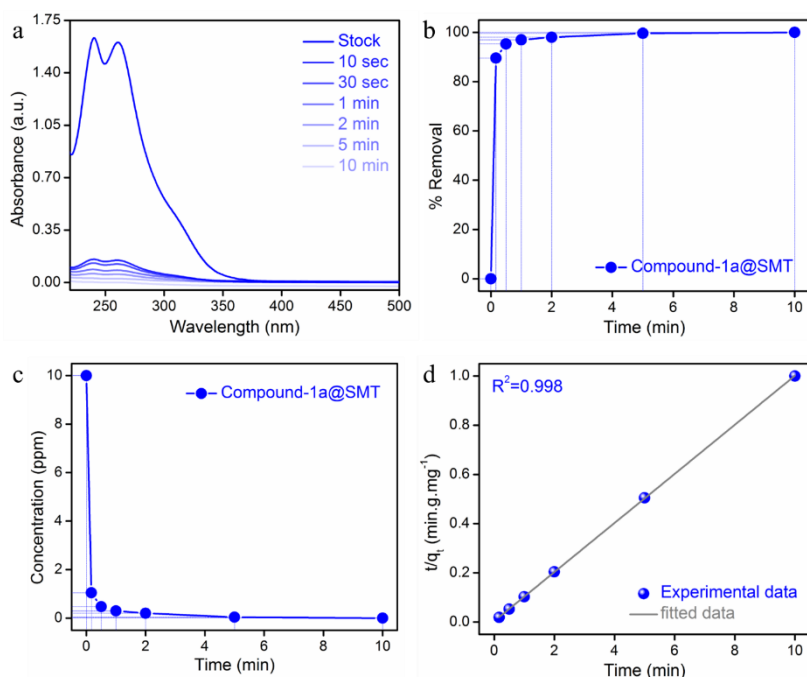
Appendix 3.26: Capture study of methyl orange (MO): (a) UV-vis spectra of MO shows diminishing in the absorbance with increasing time, (b) % removal vs time, (c) Decrease in the concentration with time, (d) Pseudo-second-order model fitting for MO capture.



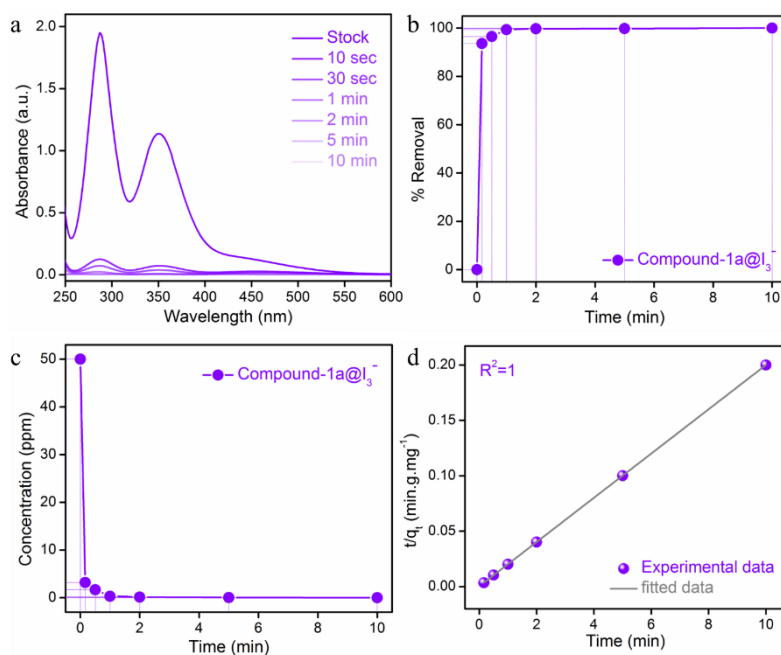
Appendix 3.27: Capture study of alizarin red S (ARS): (a) UV-vis spectra of ARS shows diminishing in the absorbance with increasing time, (b) % removal vs time, (c) Decrease in the concentration with time, (d) Pseudo-second-order model fitting for ARS capture.



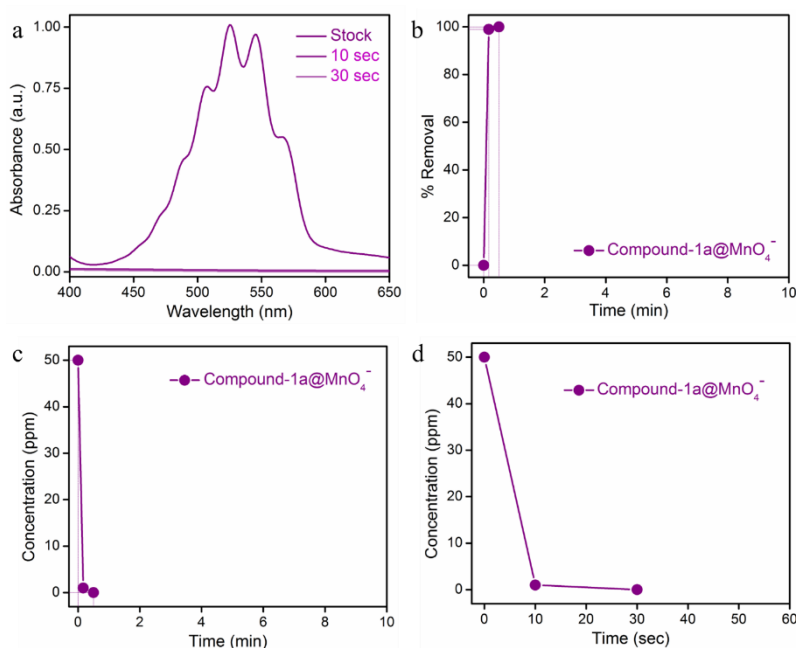
Appendix 3.28: Capture study of sulfadimethoxine (SDM): (a) UV-vis spectra of SDM shows diminishing in the absorbance with increasing time, (b) % removal vs time, (c) Decrease in the concentration with time, (d) Pseudo-second-order model fitting for SDM capture.



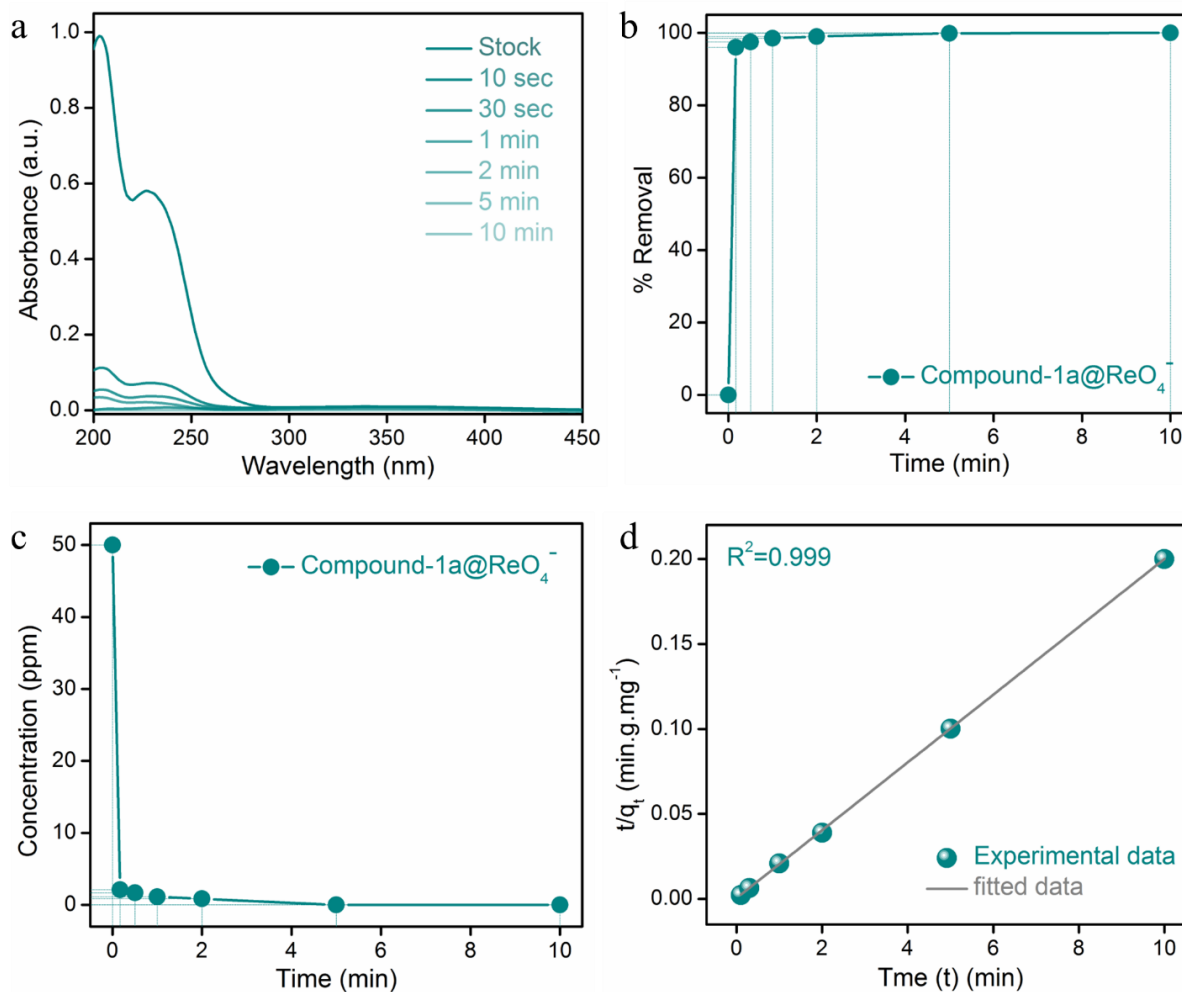
Appendix 3.29: Capture study of sulfamethazine (SMT): (a) UV-vis spectra of SMT shows diminishing in the absorbance with increasing time, (b) % removal vs time, (c) Decrease in the concentration with time, (d) Pseudo-second-order model fitting for SMT capture.



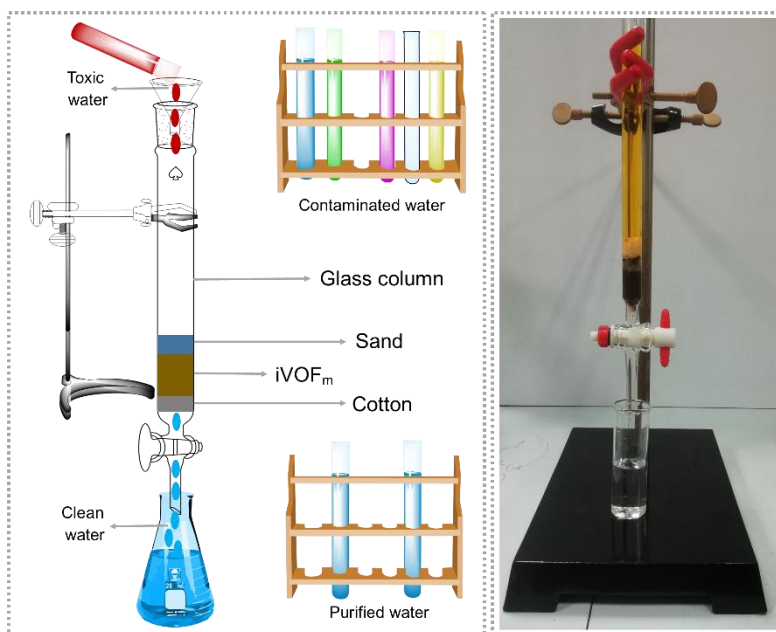
Appendix 3.30: Capture study of iodine with KI in water (I_3^-): (a) UV-vis spectra of I_2 shows diminishing in the absorbance with increasing time, (b) % removal vs time, (c) Decrease in the concentration with time, (d) Pseudo-second-order model fitting for I_2 capture.



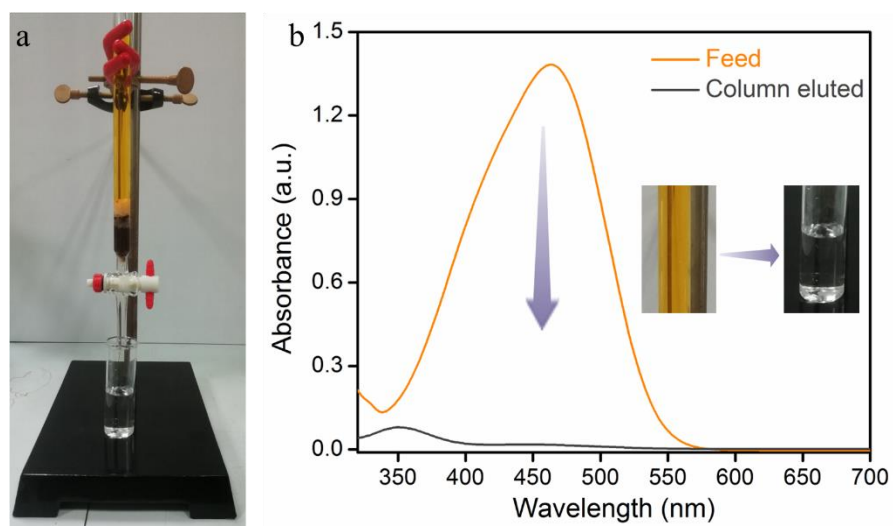
Appendix 3.31: Capture study of potassium permanganate ($KMnO_4$): (a) UV-vis spectra of MnO_4^- shows diminishing in the absorbance with increasing time, (b) % removal vs time, (c) Decrease in the concentration with time, (d) Pseudo-second-order model fitting for MnO_4^- capture.



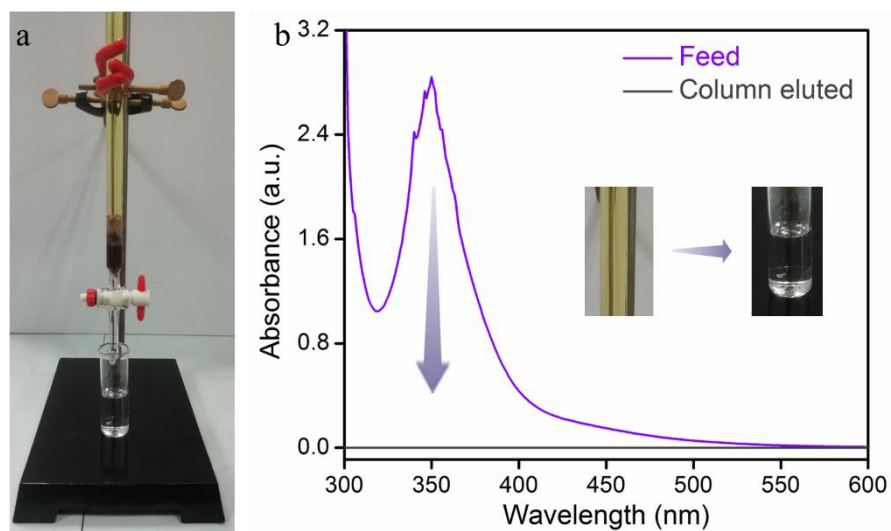
Appendix 3.32: Capture study of potassium perrhenate (KReO_4): (a) UV-vis spectra of ReO_4^- shows diminishing in the absorbance with increasing time, (b) % removal vs time, (c) Decrease in the concentration with time, (d) Pseudo-second-order model fitting for ReO_4^- capture.



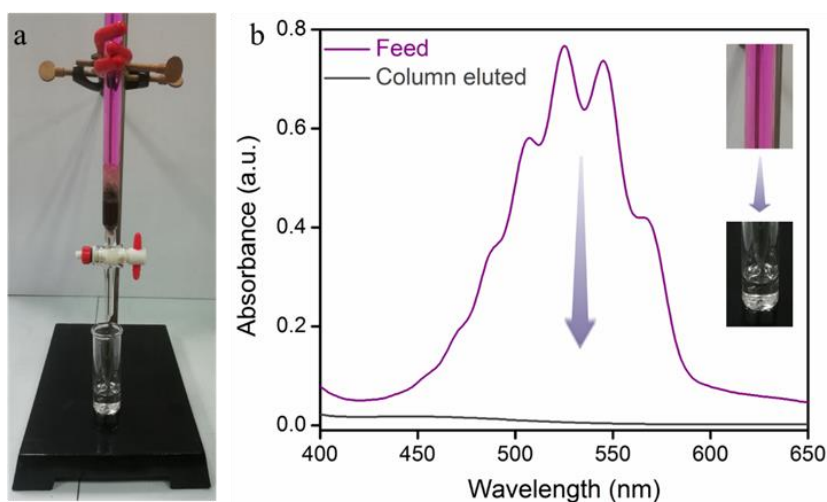
Appendix Scheme 3.6: Schematic diagram and digital image of experimental set-up of column-exchange based pollutants sorption experiment.



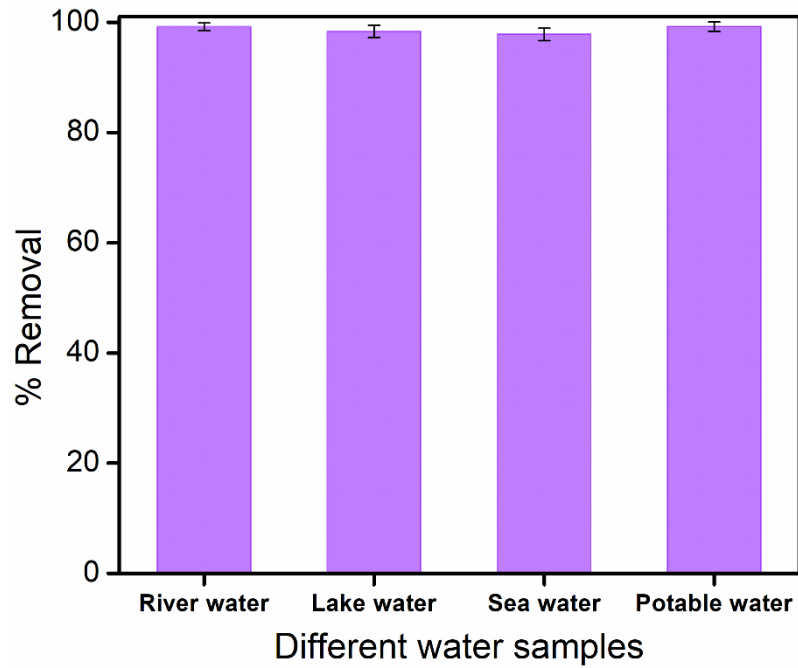
Appendix 3.33a: Column exchange-based capture study of methyl orange (MO): (a) Column setup for MO capture study, (b) UV-vis spectra of MO shows diminishing in the absorbance while passing through the iVOF_m embedded column bed.



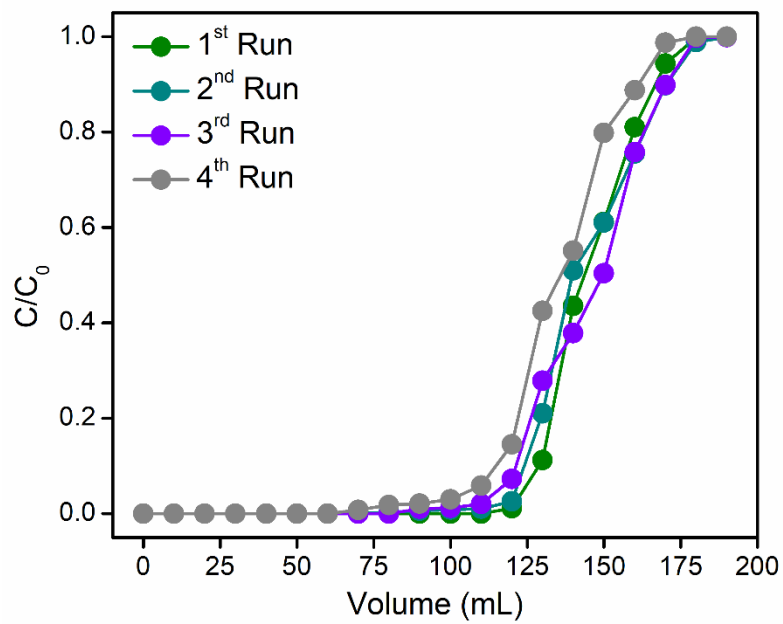
Appendix 3.33b: Column exchange-based capture study of iodine with KI in water (I_3^-): (a) Column setup for I_3^- capture study, (b) UV-vis spectra of I_3^- shows diminishing in the absorbance while passing through the iVOF_m embedded column bed.



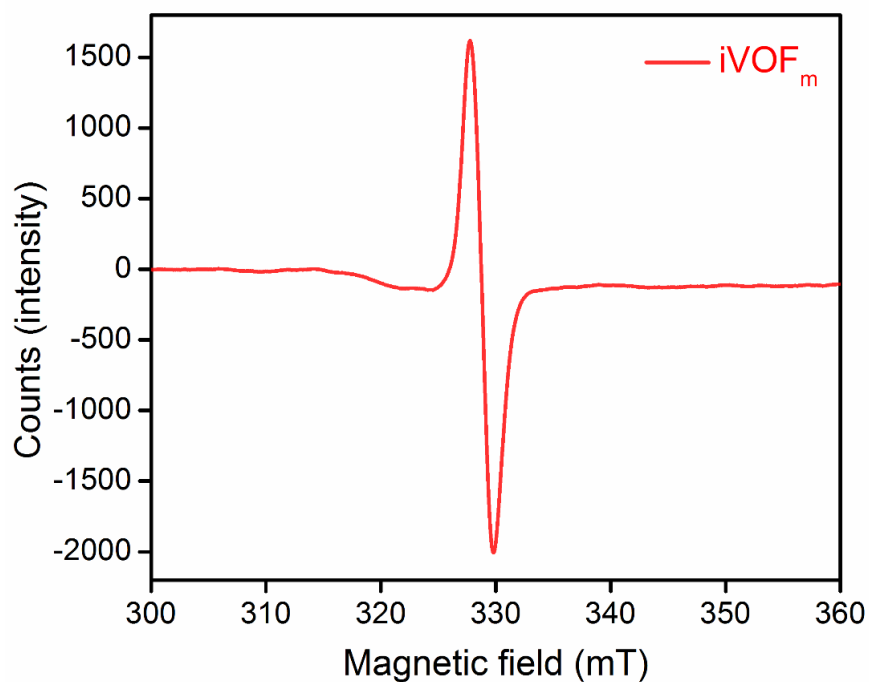
Appendix 3.33c: Column exchange-based capture study of potassium permanganate ($KMnO_4$): (a) Column setup for MnO_4^- capture study, (b) UV-vis spectra of MnO_4^- shows diminishing in the absorbance while passing through the iVOF_m embedded column bed.



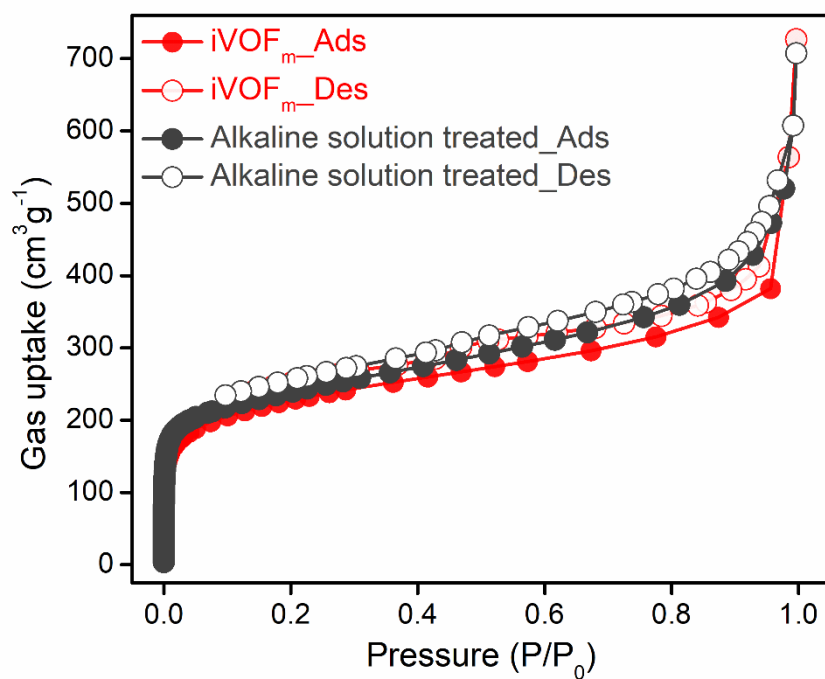
Appendix 3.34: SDM sorption data by iVOFm tested in different real water samples.



Appendix 3.35: Breakthrough SDM sorption data by iVOFm tested in 50 ppm water samples.

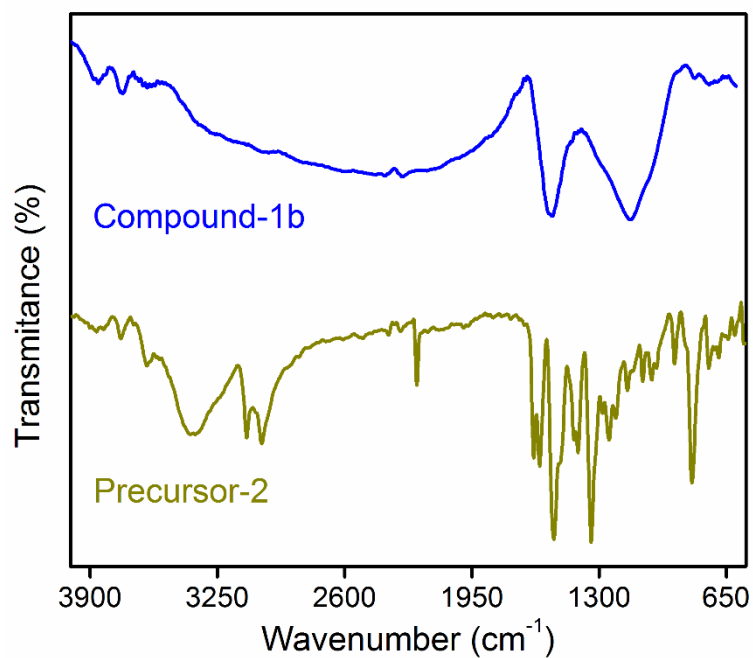


Appendix 3.36a: Solid-state EPR spectra of iVOF_m in alkaline medium.

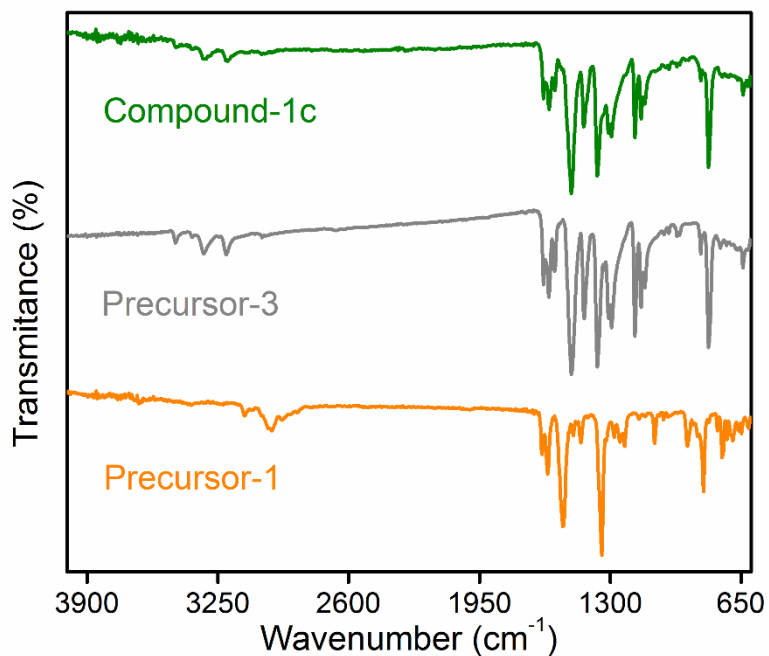


Appendix 3.36b: Nitrogen sorption data of iVOF_m in alkaline medium at 77K.

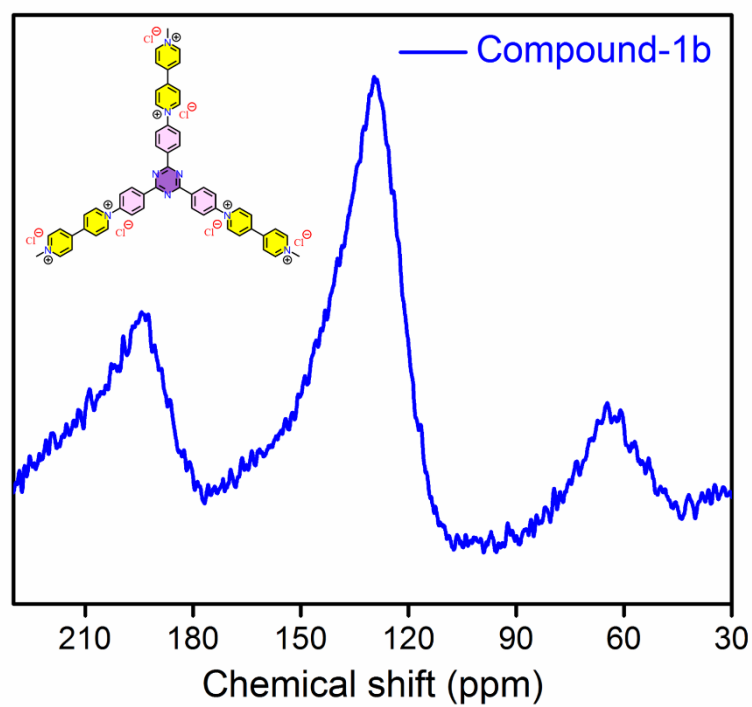
Appendix Section 3.6.4: Characterizations of Compound-1b, 1c and Relative SDM Capture



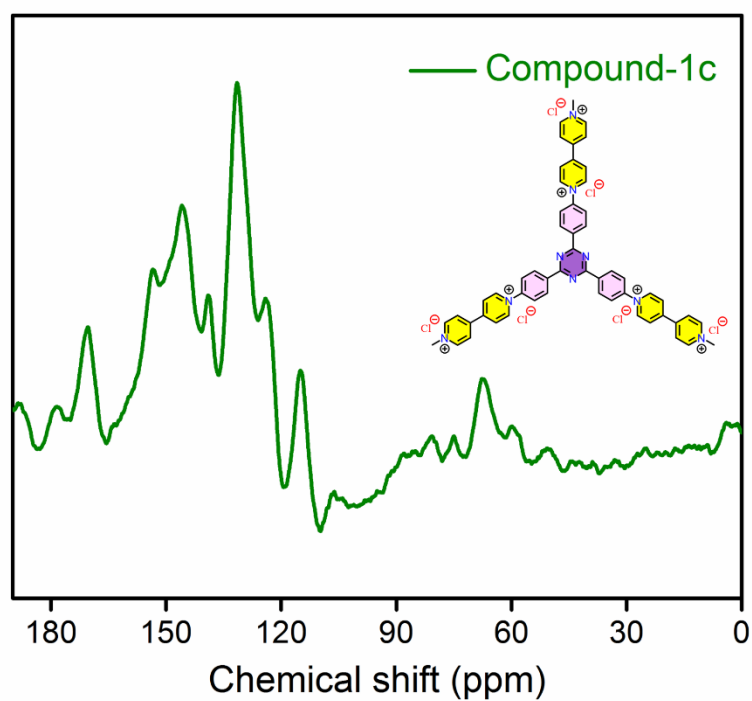
Appendix 3.37: FT-IR spectra of compound-1b with its precursor-2.



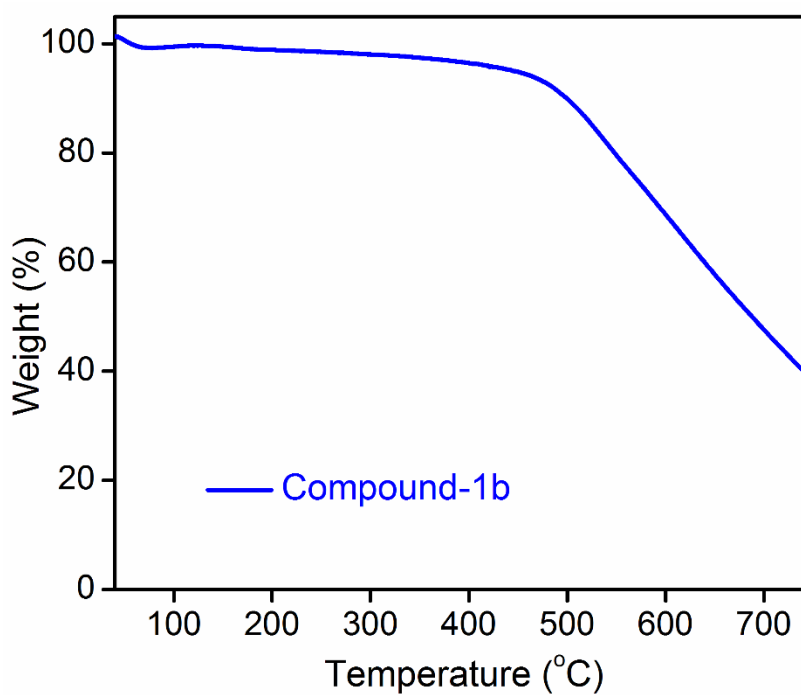
Appendix 3.38: FT-IR spectra of compound-1c with its precursor-1 and precursor-3.



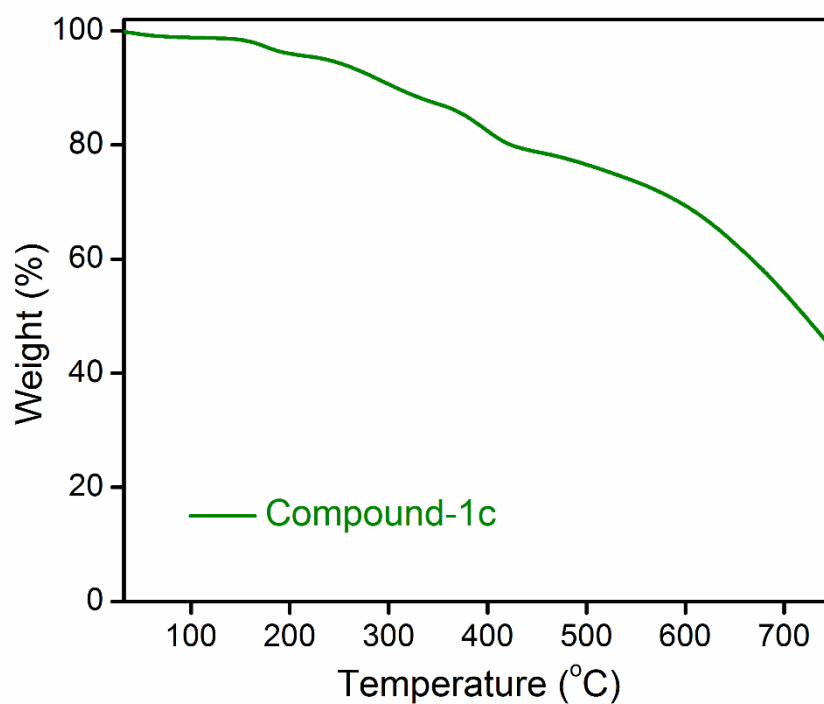
Appendix 3.39: ^{13}C CPMAS NMR spectra of compound-1b.



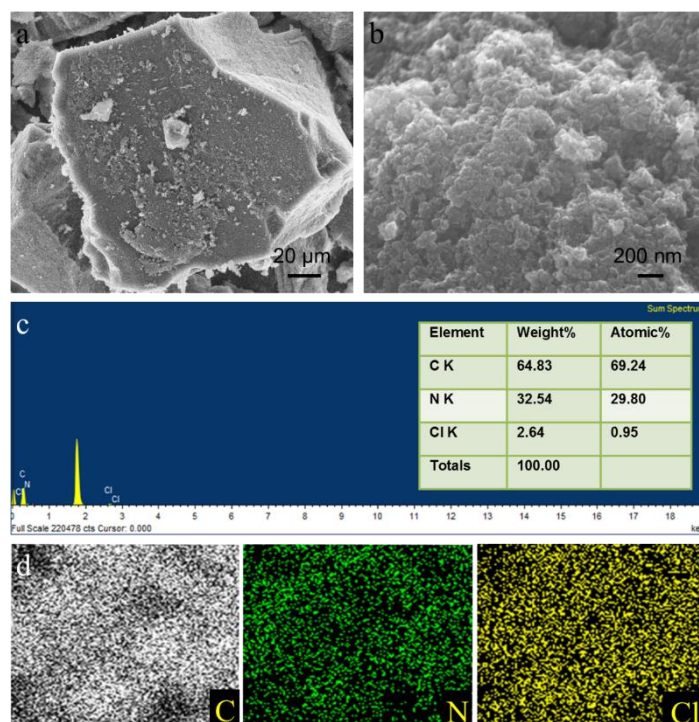
Appendix 3.40: ^{13}C CPMAS NMR spectra of compound-1c.



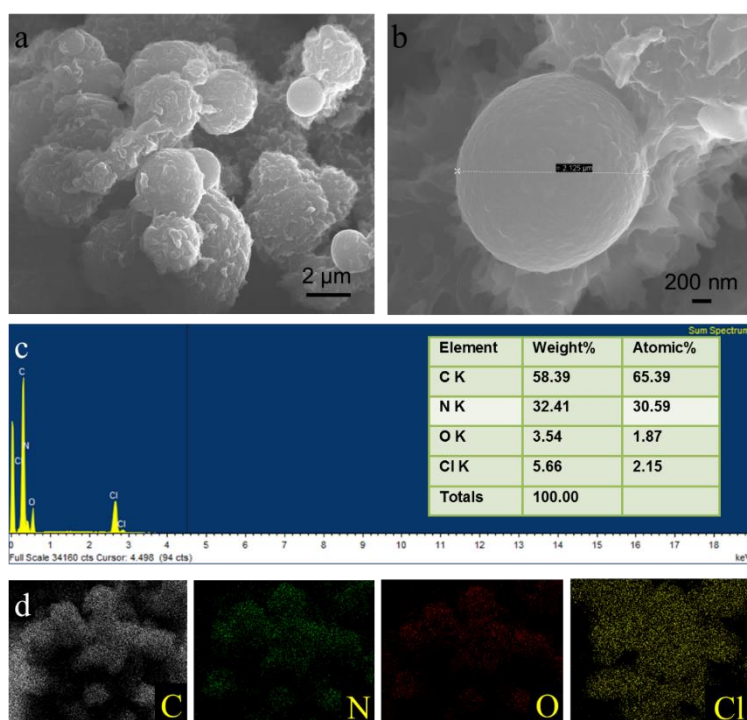
Appendix 3.41: TGA profile of compound-1b.



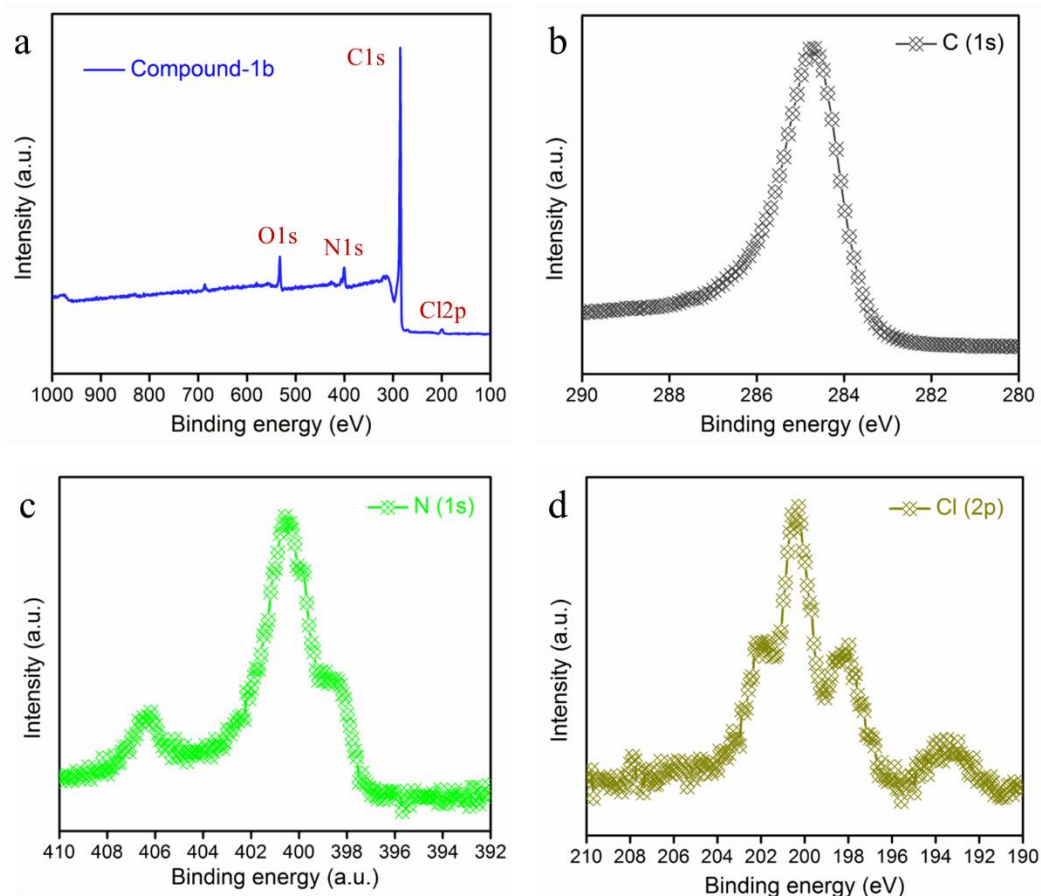
Appendix 3.42: TGA profile of compound-1c.



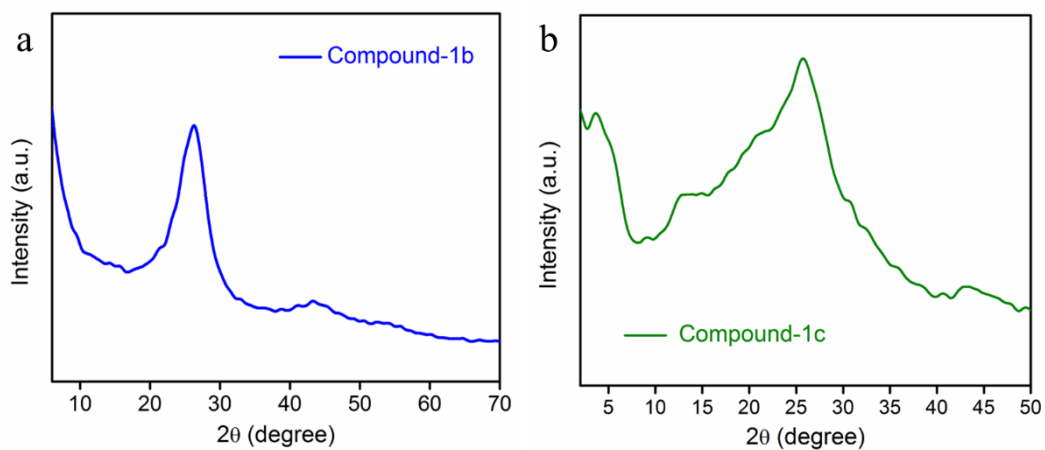
Appendix 3.43: (a, b) High and low magnifying FESEM images, (c) EDS data (element, carbon (C), nitrogen (N), chlorine (Cl)), and (d) Elemental mapping image of compound-1b.



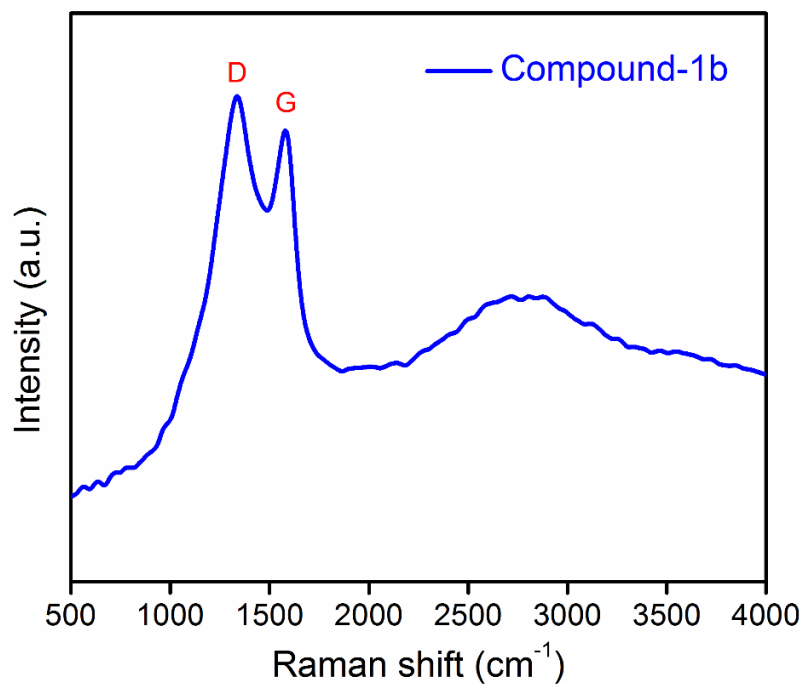
Appendix 3.44: (a, b) High and low magnifying FESEM images, (c) EDS data (element, carbon (C), nitrogen (N), oxygen (O), chlorine (Cl)), and (d) Elemental mapping image of compound-1c.



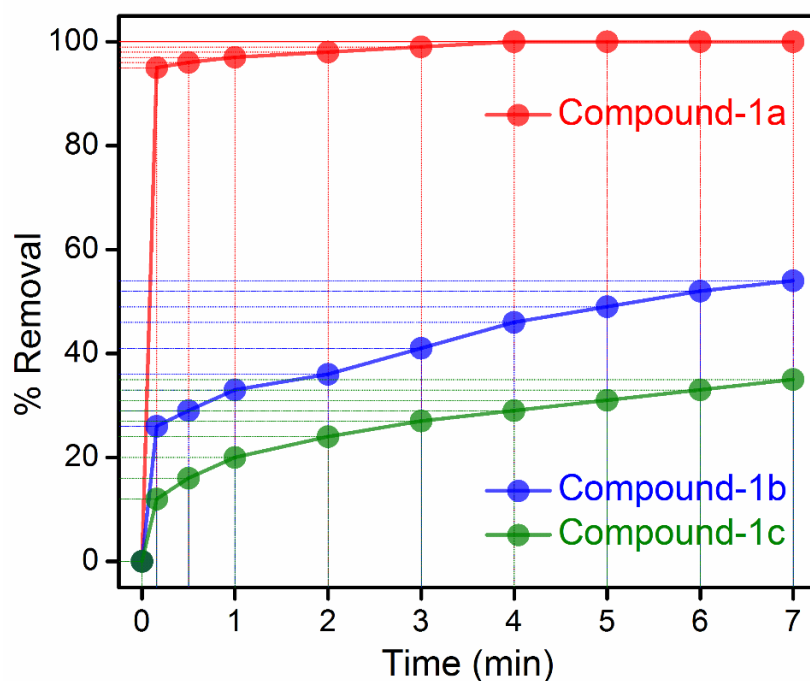
Appendix 3.45: X-ray photoelectron spectroscopy (XPS) analysis: (a) XPS survey spectra of compound-1b, (b, c, d) XPS spectra of C1s, N1s and Cl2p orbital, respectively. Which indicated formation of the material.



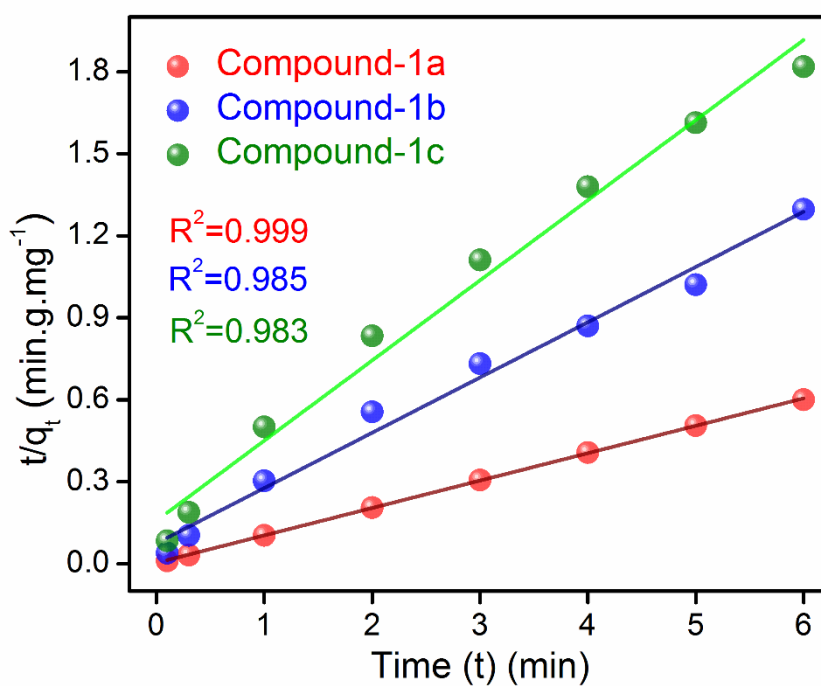
Appendix 3.46: Powder X-ray Diffraction (PXRD) analysis of (a) compound-1b and (b) compound-1c.



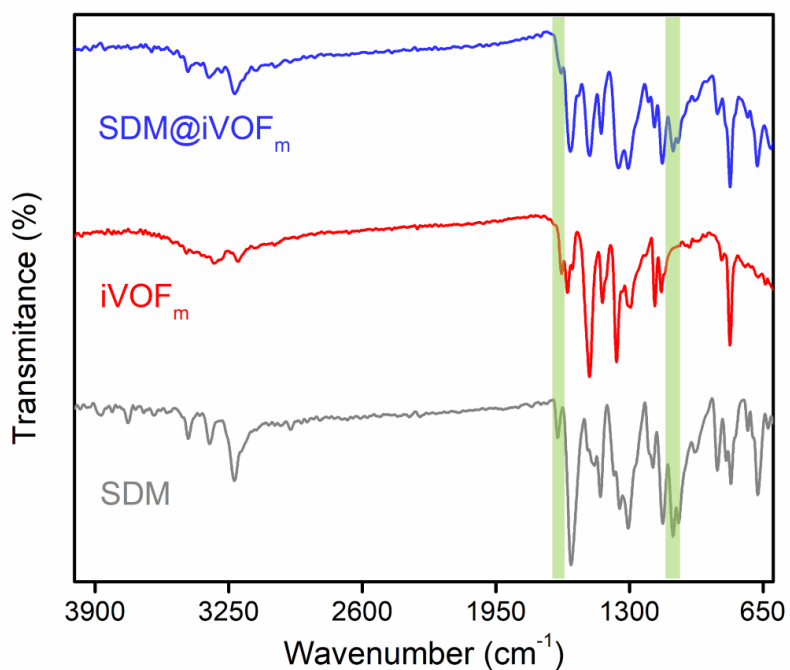
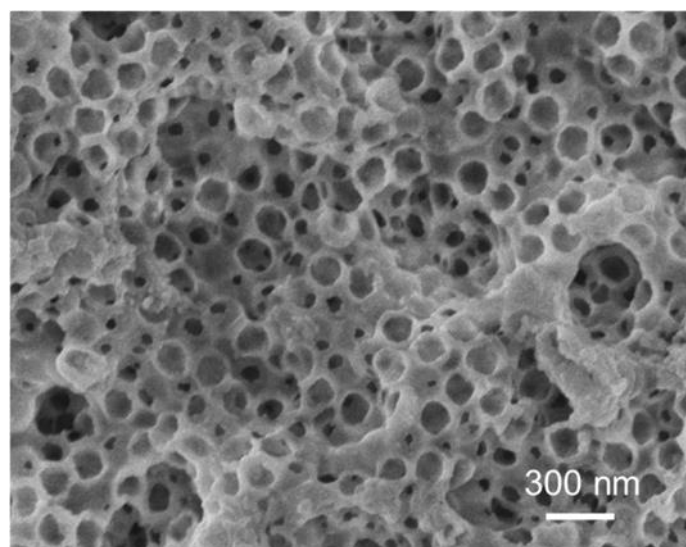
Appendix 3.47: Raman spectra of compound-1b, shows the dominant D and G band.

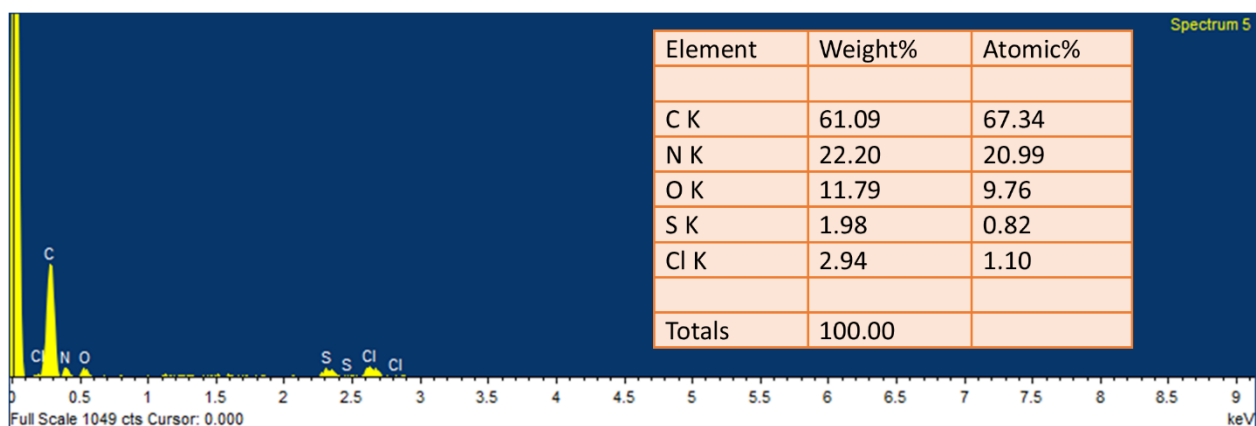


Appendix 3.48: Removal percentage of SDM molecule by compound-1a (iVOF_m), -1b and -1c at pH = 7.13.

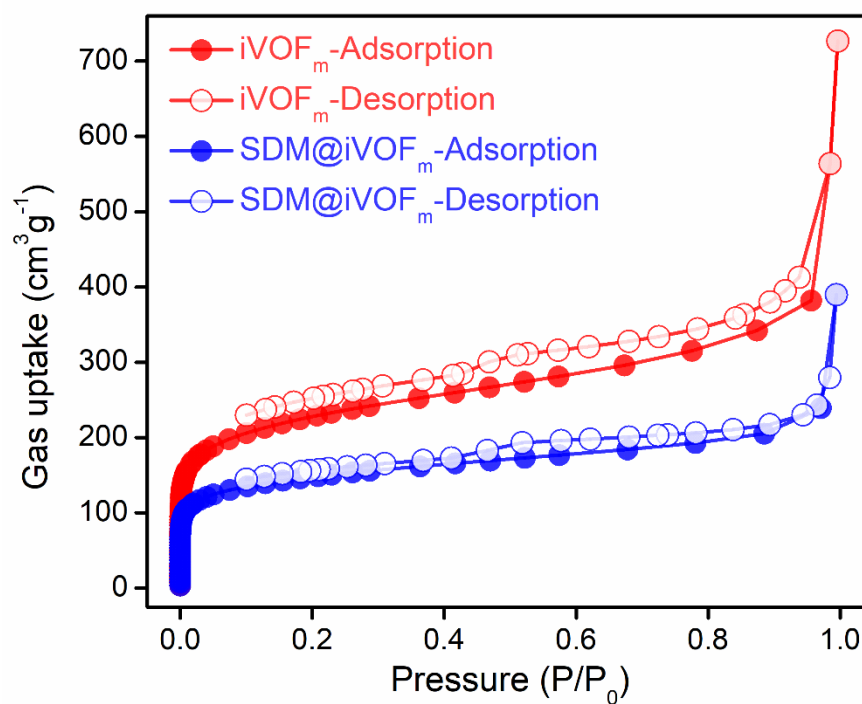


Appendix 3.49: Psuedo-second order model fitting for SDM molecule capture by compound-1a (iVOF_m), -1b and -1c at pH = 7.13.

Appendix Section 3.6.5: Post Adsorption Characterization of iVOF_mAppendix 3.50a: FT-IR spectra of SDM, iVOF_m and after sorption of SDM by iVOF_m.Appendix 3.50b: FESEM images of iVOF_m, after sorption study.

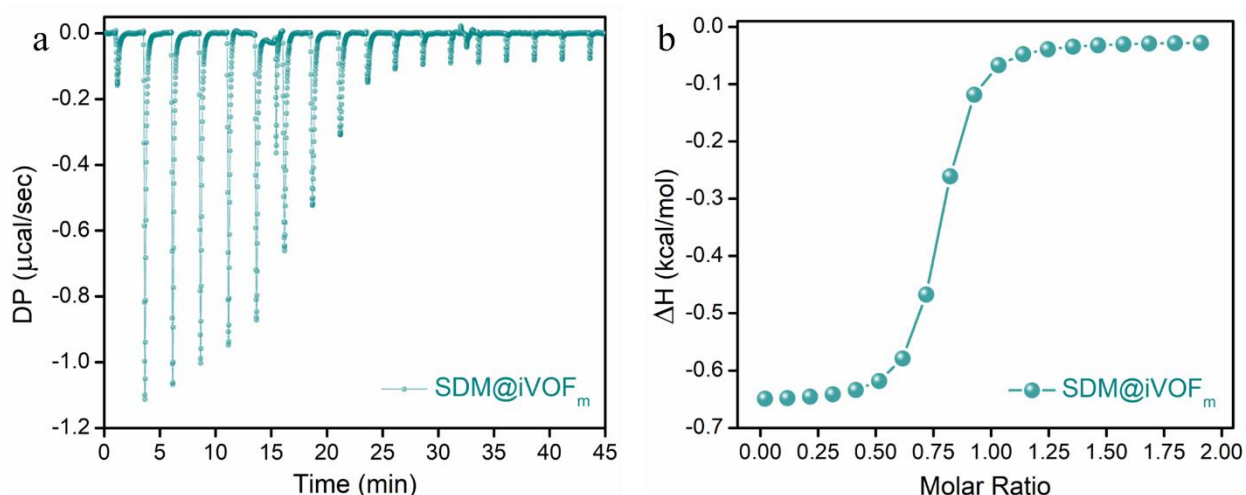


Appendix 3.51a: SEM-EDS data of $iVOF_m$, after SDM sorption study.

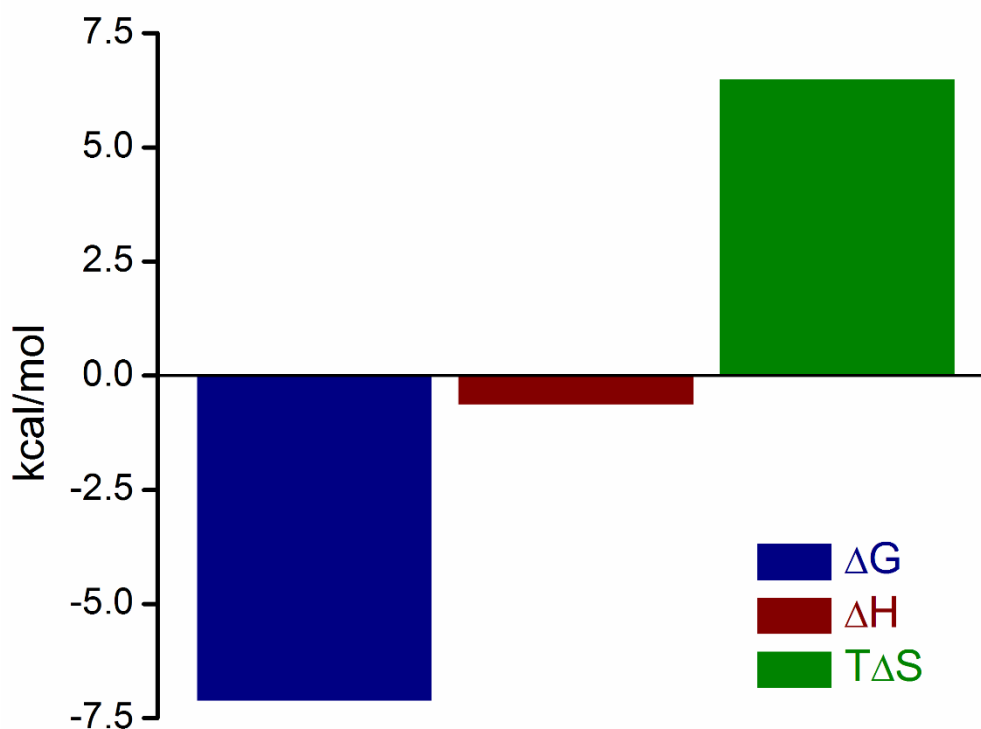


Appendix 3.51b: Nitrogen gas sorption data of $iVOF_m$, after SDM sorption study.

Isothermal titration calorimetry (ITC): Isothermal titration calorimetry (ITC) experiment has been conducted for the thermodynamic validation of such favourable interactions between the anionic SDM molecule and $i\text{VOF}_m$ in aqueous medium at $\text{pH} = 7.38$ (adjusted by 1M NaOH solution).^[37] ITC experiment quantitatively provides the change in enthalpy, entropy and Gibbs free energy associated with the adsorption followed by the ion-exchange process between adsorbent and adsorbate.^[38] In this typical experiment, first, the reference cell was filled with deionized water, and a homogeneous aqueous suspension of adsorbate ($i\text{VOF}_m$) (stock as, 2.5 mg compound in 10 mL of H_2O ($\text{pH} = 7.38$)) (consider as 1 mmol in the experiment) was poured into the sample cell and the 10 mmol concentration of adsorbent (SDM) aqueous solution ($\text{pH} = 7.38$) was placed into the syringe, while the complete mixture was stirring at 750 rpm. In this study, we recorded the thermograms for SDM molecule adsorption by the $i\text{VOF}_m$. The first injection of each titration was fixed at 0.4 μL . At least two titrations for each analyte-compound pair were collected. Data analysis was performed in y. MicroCal PEAQ-ITC analysis software. The heats of injection for blank titrations (analyte [SDM] into blank) were subtracted from the heats of injection into compound suspensions. The recorded thermogram (Figure 3.6a and Appendix 3.52) demonstrated a high association constant with the exothermic binding event along with the following thermodynamic parameters (Appendix 3.53 and Appendix Table 3.1). This result indicated the adsorption of SDM by $i\text{VOF}_m$ was thermodynamically favourable as the Gibbs free energy of the process was found to be negative with positive association constant (K_a) and negative entropy.^[39] Thus, these ITC data clearly indicated the similarities between the thermodynamic parameters and the bulk-scale experimental data of strong interactions between SDM molecule and $i\text{VOF}_m$ in water.



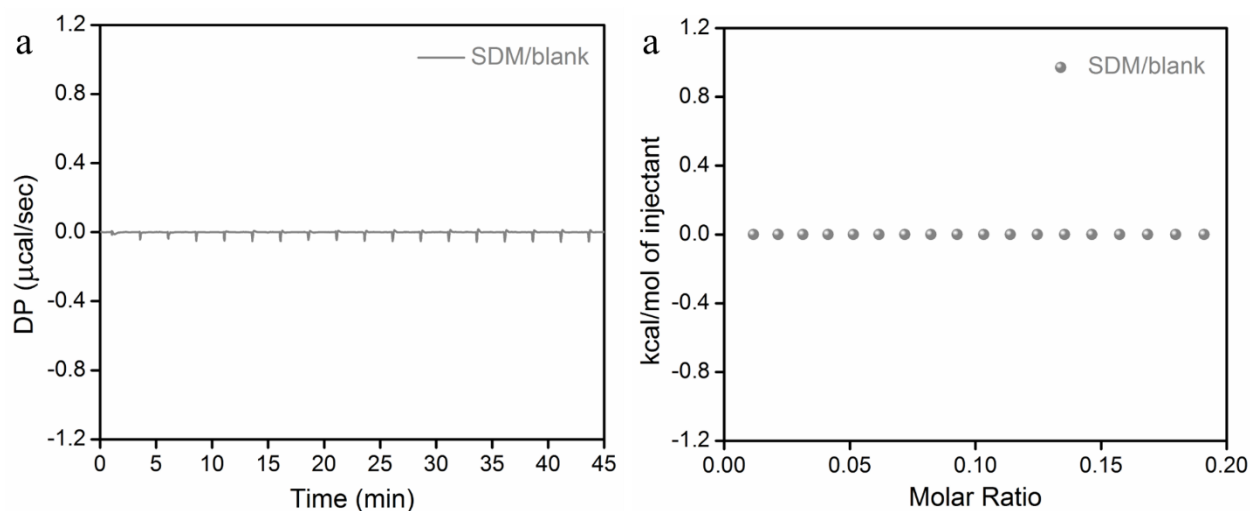
Appendix 3.52: (a) ITC thermogram of adsorption of SDM onto $i\text{VOF}_m$. (b) Corresponding single-site model fitted integrated heat data exhibited the exothermic binding phenomena of SDM in $i\text{VOF}_m$.



Appendix 3.53: Thermodynamic parameter, ΔH , $T\Delta S$, ΔG values for sorption of SDM on iVOF_m.

Appendix Table 3.1: Thermodynamic parameter of interaction between SDM molecules and iVOF_m in aqueous solution at pH = 7.38

Parameters	Values
Model	One set of sites
Cell (M)	1.00e-3
Syn (M)	10.0e-3
KD (M)	6.04e-6 ± 4.19e-6
ΔH (kcal/mol)	-0.628 ± 4.2e-2
ΔG (kcal/mol)	-7.12
$T\Delta S$ (kcal/mol)	6.49

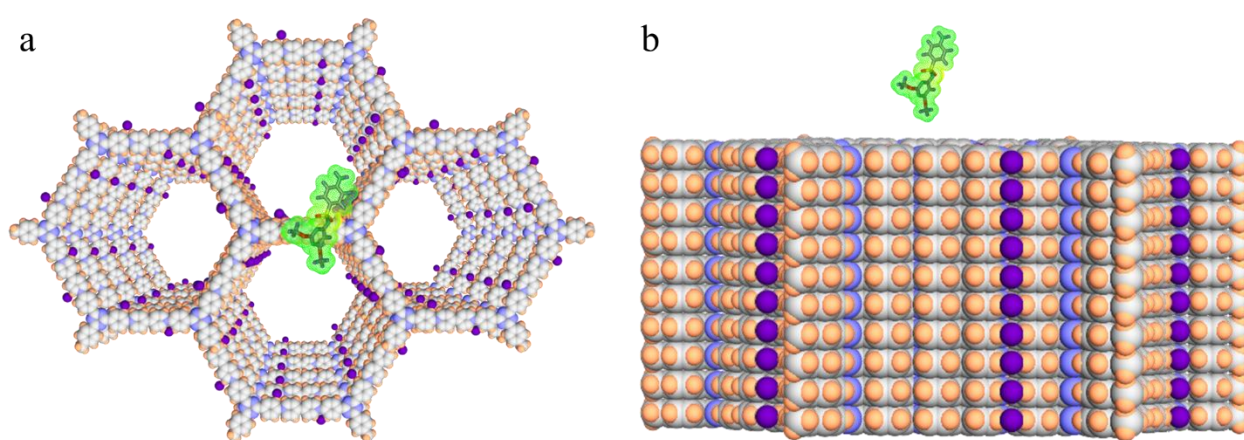


Appendix 3.54: (a) ITC thermogram of SDM with blank (water). (b) Corresponding integrated heat data of SDM with blank (water).

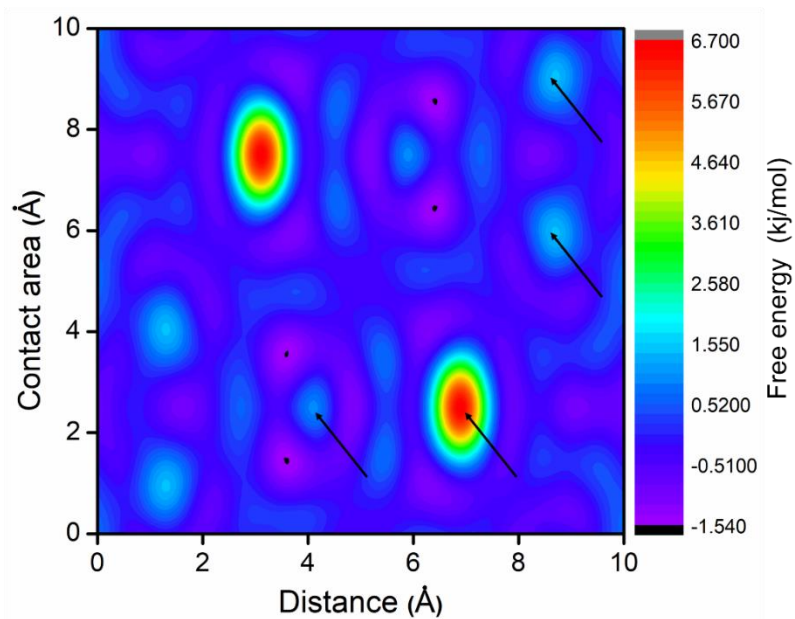
Appendix Section 3.6.6: Theoretical Studies and Binding Energy Calculation

Along with the different experimental investigation, theoretical calculation has also been carried out, utilizing density functional theory (DFT) studies, in order to further insight into the selective interaction of SDM molecule with $iVOF_m$. The binding energy of interaction of SDM with $iVOF_m$ was observed to be -123 kJ/mol, which is equivalent to -1.2 eV. Thus, SDM interaction with $iVOF_m$ making its HOMO-LUMO interaction favourable. Thus, $iVOF_m$ is in Switch ON condition during the interaction with SDM. (Figure 3.6c in the main text). The molecular dynamic simulation studies indicated that within a very short period of time (~ 1 ns) the SDM molecules was adsorbed into the potential large porous cavity of $iVOF_m$. However, in case of other individual runs, the time taken for adsorbed the SDM molecule by the $iVOF_m$ is greater than ~ 1 ns, as demonstrated by relatively slow decrease in the center of mass (COM) with the distances of SDM to the upper surface of the $iVOF_m$ (Figure 3.6d in the main text). This rapid decrease in the COM of SDM indicated strong binding possibility with the surface of $iVOF_m$ (Appendix 3.55). These individual runs suggests that the binding pattern between the SDM and $iVOF_m$ is energetically favourable. Now, to further elucidate the binding modes as well as sorption patterns of SDM inside the channels of $iVOF_m$, binding energy was calculated. The binding free energy was computed by $W(A_{cont}, D_{com}) = -K_b T \ln P(A_{cont}, D_{com})$, where K_b is the Boltzmann constant, T is the temperature, A_{cont} is the contact area between SDM and compound-1a, and D_{com} is the COM distances of SDM to the surface of $iVOF_m$, and $P(A_{cont}, D_{com})$ is the probability of finding SDM at position (A_{cont}, D_{com}) . The binding free energy surface profile demonstrated

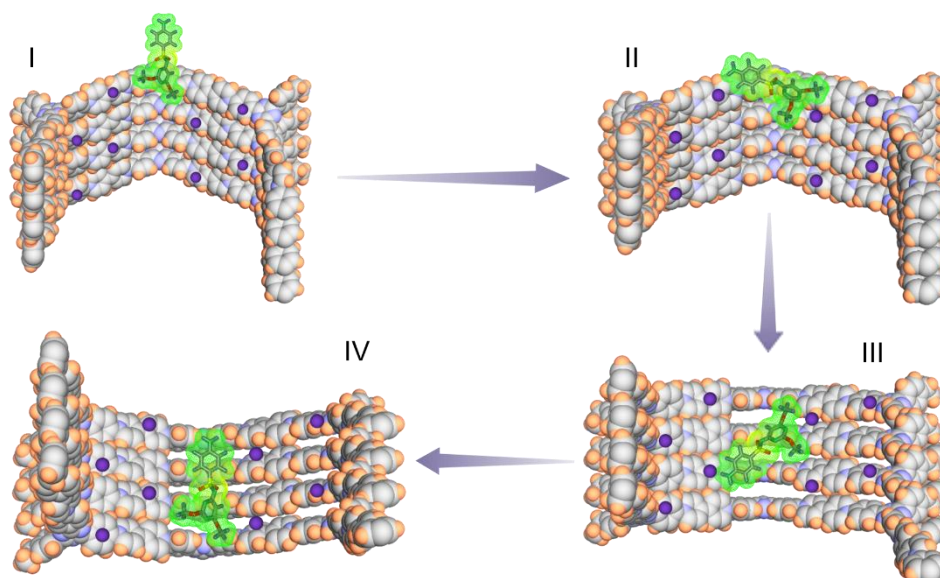
four individual free energy basins which are located at (i) 6.9 Å, 2.7 Å², (ii) 4.1 Å, 2.8 Å², (iii) 8.8 Å, 6.1 Å², (iv) 8.9 Å, 9.3 Å², respectively, with different binding energies (Appendix 3.56). These four individual binding free energy basins revealed four different binding modes of SDM with the surface of the iVOF_m (Appendix 3.57). These different binding modes explored the various non-covalent supramolecular interactions, such as hydrogen bonding interaction, Van-der-waals interaction, and plays key role behind such efficient capture of SDM by the iVOF_m in water medium.



Appendix 3.55: The top (a) and side (b) view of simulation pattern of SDM with the surface of iVOF_m.



Appendix 3.56: The SDM binding free energy surface with iVOF_m. The colour bar indicated the free energy (in kJ/mol).



Appendix 3.57: Snapshots of the specific binding of SDM with the surface of iVOF_m along with corresponding binding energies.

Appendix Section 3.6.7: Tables

Appendix Table 3.2: Comparison of this work with other related investigations of MO and ARS dye capture by various adsorbents. (N.D.: Not Done).

Compound name	Contact time for removal	Analyte	Reference
iVOF_m	5 min	MO	This work
iVOF_m	5 min	ARS	This work
3D-ionic-COF-1	30 min	MO	<i>J. Am. Chem. Soc.</i> 2017 , 139, 17771 – 17774
CX4-BD-1 COF CX4-BD-2 COF	120 min	MO	<i>J. Am. Chem. Soc.</i> 2021 , 143, 3407 – 3415
PCEC-C composite	720 min	MO ARS	<i>ACS Sustainable Chem. Eng.</i> 2017 , 5, 2, 1871–1880
VS4/CP nanocomposites	30 min	MO	<i>ACS Sustainable Chem. Eng.</i> 2017 , 5, 9, 7690–7699
CANEX sorbents	130 min	MO	<i>ACS Appl. Mater. Interfaces</i> 2018 , 10, 24, 20499–20511
SWCNT and MWCNT	65.0 and 100 min	ARS	<i>J. Phys. Chem. C</i> 2016 , 120, 32, 18296–18306
IPM-MOF-201	120 min	ARS	<i>iscience</i> , 2018 , 3, 21-30
CBA SSZ-13	300 min	ARS	<i>Journal of Hazardous Materials</i> , 2021 , 416, 125925
P5-P polymer	30 min	MO	<i>J. Mater. Chem. A</i> , 2017 , 5, 24217-24222
A-MnO ₂	120 min	MO	<i>J. Mater. Chem. A</i> , 2015 , 3, 19000-19010

Appendix Table 3.3: Comparison of this work with other related investigations of SDM, SMT and other antibiotics capture by various adsorbents. (N.D.: Not Done).

POP: Porous Organic Polymer, COF: Covalent Organic Framework, MOF: Metal-Organic Framework

Types of compound	Compound name	Initial conc.	Contact time	Analyte	Stability (Acid/Base)	Porosity	Capacity	Reference
POP	Compound-1a (iVOF _m)	50 ppm	1 min	SDM	1M HCl 1M NaOH	Micro/Macroporous	376 mg/g	This work
POP	TPFC-MIM	10 ppm	300 min	SDM	N.D.	Microporous	393.7 mg/g	<i>Ind. Eng. Chem. Res.</i> 2019 , 58, 16629–16635
carbon nanotubes	multiwalled carbon nanotubes	6.0 × 10 ⁻³ mmol/L	N.D.	SMX	N.D.	N.D.	23.8 mg/g	<i>Langmuir.</i> , 2009 , 25, 11608–11613

MOF	MIL-101(Cr)	10 mg/L	2 min	SDM	YES	Microporous	588.24 mg/g	<i>Journal of Molecular Liquids</i> , 2019 , 274, 632-638
carbon nanotubes	CNT	0.05–1.20 mg/L	N.D.	SDM	N.D.	Porous	16.3 mg/g	<i>Chem. Eng. J.</i> , 2017 , 312, 167-179
MOF	UiO-66-NH ₂	-	240 min	SMT	N.D.	Microporous	N.D.	<i>Faraday Discuss.</i> , 2021 , 231, 356-370
MOF-composite	MIL53(Fe)@percarbonate	0.02 mM	60 min	SMT	N.D.	Porous	N.D.	<i>Appl. Surf. Sci.</i> , 2018 , 457, 726–734
carbon nanotubes	CNF mats	50 µM	N.D.	SDM SMX	N.D.	N.D.	123 mg/g 32 mg/g	<i>ACS Appl. Mater. Interfaces</i> 2016 , 8, 18, 11431–11440
COF	TpMa-COF and TpMa-CON	10 ppm	3000 min	SMX	YES	Porous	N.D.	<i>ACS Appl. Mater. Interfaces</i> 2021 , 13, 35, 42035–42043
Metal salt	potassium permanganate	10 µmol L ⁻¹	120 min	SDM	N.D.	N.D.	N.D.	<i>Science of The Total Environment</i> , 2019 , 671, 705-713
Clay material	soil mediated by extracellular oxidoreductases	1 M)	72 h	SDM	N.D.	N.D.	N.D.	<i>Environmental Science and Pollution Research</i> , 2015 , 22(21), 16868-16874
MOF	cobalt(II)-based MOF	5 mg L ⁻¹	180 min	SMT SDZ	N.D.	N.D.	49.5 mg/g 48.2 mg/g	<i>Dalton Trans.</i> , 2020 , 49, 8959-8966
POP	microporous organic polymers	100 ppm	360 min	SMT	N.D.	Porous	483 mg/g	<i>Microporous Mesoporous Mater.</i> 2020 , 296, 109979
Activated Carbon	Activated Carbon	100 ppm	360 min	SMT	N.D.	N.D.	259 mg/g	<i>Microporous Mesoporous Mater.</i> 2020 , 296, 109979
Hydrogel	poly(HEA/NMMA)–CuS hydrogel	0.2 mM	360 min	SMX	N.D.	N.D.	3.8 mg/g	<i>Applied Catalysis B: Environmental</i> , 2017 , 217, 603-614
MOF	ZIF-8	100 mg/L	12 h	SMX	N.D.	N.D.	22 mg/g	<i>Catalysis Today</i> . 2018 , 301, 90–97
MOF	MDC-1000	100 mg/L	12 h	SMX	N.D.	N.D.	435 mg/g	<i>Catalysis Today</i> . 2018 , 301, 90–97
Activated Carbon	Commercial AC	100 mg/L	12 h	SMX	N.D.	N.D.	110 mg/g	<i>Catalysis Today.</i> , 2018 , 301, 90–97

Appendix Table 3.4: Comparison of this work with other related investigations of KReO₄ oxoanions capture by various adsorbents. (N.D.: Not Done).

Compound name	Contact time for removal	Reference
iVOF_m	1 min	This work

SCU-COF-1	1 min	<i>Chem. Sci.</i> 2019 , <i>10</i> , 4293-4305
IPcomp-3(200)	< 2 min	<i>ACS Cent. Sci.</i> 2020 , <i>6</i> , 1534-1541
α -MOC-1 and α -MOC-2	10 min	<i>ACS Appl. Nano Mater.</i> 2019 , <i>2</i> , 5824-5832
SCU-100 (ReO ₄ ⁻ /TcO ₄ ⁻)	30 min (TcO ₄ ⁻)	<i>Environ. Sci. Technol.</i> 2017 , <i>51</i> , 3471-3479
SBN	10 min	<i>Environ. Sci. Technol. Lett.</i> 2017 , <i>4</i> , 316-322
SCU-101 (ReO ₄ ⁻ /TcO ₄ ⁻)	10 min (TcO ₄ ⁻)	<i>J. Am. Chem. Soc.</i> 2017 , <i>139</i> , 14873-14876
SLUG-21	60 min	<i>J. Am. Chem. Soc.</i> 2010 , <i>132</i> , 7202-7209
Compound-1	60 min	<i>Chem. Sci.</i> 2018 , <i>9</i> , 7874-7881
PAF-1-F	24 h	<i>Chem. Eur. J.</i> 2016 , <i>22</i> , 17581-17584
iPOP-3	25 min	<i>Chem. Eur. J.</i> 2021 , <i>27</i> , 1-9
iPOP-4	30 min	<i>Chem. Eur. J.</i> 2021 , <i>27</i> , 1-9
TbDa-COF	2 min	<i>Chem.</i> 2020 , <i>6</i> , 2796-2809
bis-PC ₂ (Cl)@MIL-101	30 sec	<i>ACS Cent. Sci.</i> 2020 , <i>6</i> , 12, 2354-2361
SCU-CPN-1	30 sec	<i>Nat. Comm.</i> 2018 , <i>9</i> , 3007
CPN-tpm	20 min	<i>Small.</i> 2021 , <i>17</i> , 2007994
SCU-CPN-4	1 min	<i>ACS Cent. Sci.</i> 2021 , <i>7</i> , 1441-1450

Appendix Table 3.5: Comparison of this work with other related investigations of KMnO₄ oxoanions capture by various adsorbents. (N.D.: Not Done).

Compound name	Contact time for removal	Reference
iVOF_m	30 sec	This work
IPcomp-3(200)	< 2 min	<i>ACS Cent. Sci.</i> 2020 , <i>6</i> , 1534-1541
SLUG-21	48 h	<i>J. Am. Chem. Soc.</i> 2011 , <i>133</i> , 11110-11113
SLUG-21	96 h	<i>J. Am. Chem. Soc.</i> 2010 , <i>132</i> , 7202-7209
Compound-1	5 min	<i>Chem. Sci.</i> 2018 , <i>9</i> , 7874-7881
3D-ionic-COF-1	30 min	<i>J. Am. Chem. Soc.</i> 2017 , <i>139</i> , 17771-17774
1-SO ₄	24 h	<i>Angew. Chem. Int. Ed.</i> 2016 , <i>55</i> , 7811-7815
Tp-Pa-2-foam	<30 sec	<i>J. Am. Chem. Soc.</i> 2019 , <i>141</i> , 7572-7581
SCNU-Z1-Cl	16 min	<i>Inorg. Chem.</i> 2019 , <i>58</i> , 4, 2899-2909
1.NO ₃	>130 min	<i>ACS Appl. Mater. Interfaces</i> 2017 , <i>9</i> , 7202-7208

3.7 Reference

- [1] H. Wang, X. Ji, M. Ahmed, F. Huang, J. L. Sessler, *J. Mater. Chem. A* **2019**, *7*, 1394–1403.
- [2] S. Rojas, P. Horcajada, *Chem. Rev.* **2020**, *120*, 8378–8415.
- [3] X. L. Liu, H. W. Pang, X. W. Liu, Q. Li, N. Zhang, L. Mao, M. Q. Qiu, B. W. Hu, H. Yang, X. K. Wang, *Innovation* **2021**, *2*, 100076.
- [4] J. Li, X. Wang, G. Zhao, C. Chen, Z. Chai, A. Alsaedi, T. Hayat, X. Wang, *Chem. Soc. Rev.* **2018**, *47*, 2322–2356.
- [5] S. Fajal, W. Mandal, S. Mollick, Y.-D. More, A. Torris, S. Saurabh, M. M. Shirolkar, S. K. Ghosh, *Angew. Chem. Int. Ed.* **2022**, *61*, e202203385.
- [6] Q. Sun, B. Aguila, S. Ma, *Trends Chem.* **2019**, *1*, 292–303.
- [7] J. Huang, Y. Shi, G.-Z. Huang, S. Huang, J. Zheng, J. Xu, F. Zhu, G. Ouyang, *Angew. Chem. Int. Ed.* **2022**, *61*, e202206749.
- [8] J. Wang, S. Zhuang, *Coord. Chem. Rev.* **2019**, *400*, 213046.
- [9] Z. Wang, S. Zhang, Y. Chen, Z. Zhang, S. Ma, *Chem. Soc. Rev.* **2020**, *49*, 708–735.
- [10] W.-G. Bae, H. N. Kim, D. Kim, S.-H. Park, H. E. Jeong, K.-Y. Suh, *Adv. Mater.* **2014**, *26*, 675–700.
- [11] P. Zhang, Z. Wang, P. Cheng, Y. Chen, Z. Zhang, *Coord. Chem. Rev.* **2021**, *438*, 213873.
- [12] J. Ding, C. Zheng, L. Wang, C. Lu, B. Zhang, Y. Chen, M. Li, G. Zhai, X. Zhuang, *J. Mater. Chem. A* **2019**, *7*, 23337–23360.
- [13] S. M. Beladi-Mousavi, J. Klein, B. Khezri, L. Walder, M. Pumera, *ACS Nano* **2020**, *14*, 3434–3441.
- [14] T. Skorjanc, D. Shetty, F. Gándara, L. Ali, J. Raya, G. Das, M. A. Olson, A. Trabolsi, *Chem. Sci.* **2020**, *11*, 845–850.
- [15] L. He, S. Liu, L. Chen, X. Dai, J. Li, M. Zhang, F. Ma, C. Zhang, Z. Yang, R. Zhou, Z. Chai, S. Wang, *Chem. Sci.* **2019**, *10*, 4293–4305.
- [16] A. M. Evans, M. J. Strauss, A. R. Corcos, Z. Hirani, W. Ji, L. S. Hamachi, X. Aguilar-Enriquez, A. D. Chavez, B. J. Smith, W. R. Dichtel, *Chem. Rev.* **2022**, *122*, 442–564.

- [17] S. Mitra, S. Kandambeth, B. P. Biswal, M. A. Khayum, C. K. Choudhury, M. Mehta, G. Kaur, S. Banerjee, A. Prabhune, S. Verma, S. Roy, U. K. Kharul, R. Banerjee, *J. Am. Chem. Soc.* **2016**, *138*, 2823–2828.
- [18] K. Shen, L. Zhang, X. Chen, L. Liu, D. Zhang, Y. Han, J. Chen, J. Long, R. Luque, Y. Li, B. Chen, *Science* **2018**, *359*, 206–210.
- [19] L. Feng, K.-Y. Wang, G. S. Day, H.-C. Zhou, *Chem. Soc. Rev.* **2019**, *48*, 4823–4853.
- [20] R.-R. Liang, S. Y. Jiang, R.-H. A., X. Zhao, *Chem. Soc. Rev.* **2020**, *49*, 3920–3951.
- [21] X. Zhao, P. Pachfule, S. Li, T. Langenhahn, M. Ye, C. Schlesiger, S. Praetz, J. Schmidt, A. Thomas, *J. Am. Chem. Soc.* **2019**, *141*, 6623–6630.
- [22] A. K. Mohammed, S. Usgaonkar, F. Kanheerampockil, S. Karak, A. Halder, M. Tharkar, M. Addicoat, T. G. Ajithkumar, R. Banerjee, *J. Am. Chem. Soc.* **2020**, *142*, 8252–8261.
- [23] S. Karak, K. Dey, A. Torris, A. Halder, S. Bera, F. Kanheerampockil, R. Banerjee, *J. Am. Chem. Soc.* **2019**, *141*, 7572–7581.
- [24] S. Asaftei, E. De Clercq, *J. Med. Chem.* **2010**, *53*, 3480–3488.
- [25] O. Buyukcakir, S. H. Je, S. N. Talapaneni, D. Kim, A. Coskun, *ACS Appl. Mater. Interfaces* **2017**, *9*, 7209–7216.
- [26] R. Gomes, P. Bhanja, A. Bhaumik, *Chem. Commun.* **2015**, *51*, 10050–10053.
- [27] W. Stöber, A. Fink, E. Bohn, *J. Colloid and Interface Sci.* **1968**, *26*, 62–69.
- [28] S. Lee, *J. Ind. Eng. Chem.* **2019**, *77*, 426.
- [29] W. Huang, Z. J. Wang, B. C. Ma, S. Ghasimi, D. Gehrig, F. Laquai, K. Landfester, K. A. I. Zhang, *J. Mat. Chem. A* **2016**, *4*, 7555–7559.
- [30] P. Samanta, P. Chandra, S. Dutta, A. V. Desai, S. K. Ghosh, *Chem. Sci.* **2018**, *9*, 7874–7881.
- [31] L.-Z. Peng, P. Liu, Q.-Q. Cheng, W.-J. Hu, Y. A. Liu, J.-S. Li, B. Jiang, X.-S. Jia, H. Yang, K. Wen, *Chem. Commun.* **2018**, *54*, 4433–4436.
- [32] L. Liu, W.-D. Qu, K.-X. Dong, Y. Qi, W.-T. Gong, G.-L. Ning, J.-N. Cui, *Chem. Commun.* **2021**, *57*, 3339–3342.
- [33] S. Ren, M. J. Bojdys, R. Dawson, A. Laybourn, Y. Z. Khimyak, D. J. Adams, A. I. Cooper, *Adv. Mater.* **2012**, *24*, 2357–2361.

- [34] C. Wang, S. Zhang, F. Guo, Y. Ge, Y. Wang, H. Li, J. Hu, H. Liu, *Ind. Eng. Chem. Res.* **2019**, *58*, 16629–16635.
- [35] G. Das, T. Skorjanc, S. K. Sharma, F. Gándara, M. Lusi, D. S. Shankar Rao, S. Vimala, S. K. Prasad, J. Raya, D.-S. Han, R. Jagannathan, J.-C. Olsen, A. Trabolsi, *J. Am. Chem. Soc.* **2017**, *139*, 9558–9565.
- [36] Q. Zhang, M. Wahiduzzaman, S. Wang, S. Henfling, N. Ayoub, E. Gkaniatsou, F. Nouar, C. Sicard, C. Martineau, Y. Cui, G. Maurin, G. Qian, C. Serre, *Chem* **2019**, *5*, 1337–1350.
- [37] R. J. Drout, S. Kato, H. Chen, F. A. Son, K. -I. Otake, T. Islamoglu, R. Q. Snurr, O. K. Farha, *J. Am. Chem. Soc.* **2020**, *142*, 12357-12366.
- [38] E. Freire, O. L. Mayorga, M. Straume, *Anal. Chem.* **1990**, *62*, 950A-959A.
- [39] S. Kato, R. J. Drout, O. K. Farha, *Cell Rep. Phys. Sci.* **2020**, *1*, 100006.

Section B

Hybrid Composite Porous Materials for Sequestration of Toxic Chemical Species from Water and Gas Phase

A hybrid composite porous material is a combination of two or more porous materials that retains some of its inherent characteristics or, in certain cases, exhibits improved and unique properties as compared to the individual components utilized separately.^[1] The materials in this class usually have a porous structure, which allows them to have a high surface area and tunable properties due to the special interaction between the integrated components. It is possible to precisely control properties like porosity, mechanical strength, chemical reactivity, and stability by combining inorganic and organic constituents. These materials' hybrid nature frequently bestows multifunctionalities, rendering them appropriate for a wide range of uses, such as environmental remediation, gas storage, and catalysis.^[2] Composite materials are typically made up of a host matrix and functional guest species, where the host matrix frequently acts as a support and the guests provide increased activity. When used as host matrices for support media, porous materials effectively immobilize functional guest components to reduce leaching and aggregation tendencies and significantly increase their reactivity. Furthermore, in the composite material, these host matrices can provide extra active sites that complement the guests. Due to their various functional groups, consistent pore topologies, framework flexibility, and configurable pore environment, Advanced Functional Porous Materials (AFPMs) are an appealing option for both host and guest materials. It has recently been discovered that a variety of porous materials can be used to create hybrid composite porous materials, both as active guest materials and as porous supports. Among them, there are well-developed materials with a variety of applications, such as MOFs/COFs, MOPs/MOFs, MOPs/COFs, etc.^[3]

Based on all these rationale this section is also consist of two chapters: chapter 4 and chapter 5. In chapter 4, a hybrid composite porous material has been fabricated by embedding cationic Zr(IV)-based MOPs inside a hierarchical porous metal-organic gel (MOG) matrix. The developed hybrid was used for efficient segregation of a group of toxic metal-oxoanions from simulated wastewater system. While in chapter 5, an imine functional COF aerogel and an amino-functionalized cationic MOP were hybridized using a novel covalent hybridization technique to create another composite porous material. The hybrid COF aerogel was used to effectively sequester iodine or polyiodide species from both water and air media. The investigations in these two chapters center on the effective creation and rational layout of functionalized advanced hybrid composite porous materials for the sequestration of hazardous water and gaseous radioactive pollutants.

References:

- [1] C. R. Kim, T. Uemura, S. Kitagawa, *Chem. Soc. Rev.* **2016**, *45*, 3828-3845.
- [2] S. Dang, Q. Zhu, Q. Xu, *Nat. Rev. Mater.* **2017**, *3*, 17075.
- [3] Y. Liu, W. Zhou, W. L. Teo, K. Wang, L. Zhang, Y. Zeng, Y. Zhao, *Chem*, **2020**, *6*, 3172-3202.

Chapter 4

Trap Inlaid Cationic Hybrid Composite Material for Efficient Segregation of Toxic Chemicals from Water

4.1 Introduction

In terms of significant impact, the World Economic Forum documented water crisis as the largest worldwide risk.^[1] Due to accelerating urbanization along with rapid industrialization, an ever growing number of toxic contaminants are entering the fresh water supplies.^[2–4] In the priority list, the Environment Protection Agency (EPA) listed metal-based oxoanions as potential toxic inorganic pollutants in wastewater.^[5] In response, considering the escalating demand for clean water, coupled with the potential influence of these hazardous oxoanions in contaminated water, environmental remediation has attracted intense attention for sustainable life and has become a topical research interest in recent years.^[6, 7] Both environment and human health concerns are driving efforts to develop various efficient technologies to disinfect and decontaminate wastewater.^[8, 9] Among them, adsorption followed by ion-exchange-based purification techniques are emerging, and are considered as promising over other conventional methods.^[10, 11] Although several adsorbents have been devoted to remove waste from wastewater, the poor selectivity towards isolating trace toxic ions, in the presence of a high concentration of coexisting salts and slow removal kinetics limits the overall efficiency of the materials.^[12, 13] Therefore, to address these issues, tremendous development of effective regenerable materials with substantially improved segregation properties has received special attention. That being said, pioneering endeavours have been employed to identify efficient adsorbents for the removal of specific oxoanions from contaminated water.^[14–16] However, as a long-term battle, improvement in terms of high selectivity, fast kinetics and capacities towards a group of toxic oxoanions at trace concentration, from natural groundwater sources to point-of-use are still needed for practical application, which is unexplored due to the lack of rational synthetic strategies.

In this regard, by virtue of predesigned tunable reticular structure, advanced porous materials have been recognized as promising platforms for various leading applications.^[17–19] Recently, composite materials are emerging as advantageous over individual materials, owing to their collective benefits and effective performance.^[20, 21] Based on this view, hybrid composite materials have commanded research interest in recent years because of their unique and ingenious properties towards task-specific applications.^[22–24] Now, for host–guest hybrid composite material-based ideal adsorbents, the guest should be homogeneously distributed throughout the host matrix and decorated with functional groups that can strongly interact with the host matrix. In this context, discrete metal–organic polyhedra (MOP), a zero-dimensional crystalline material, constructed from predesigned organic linkers with a metal cluster, could be an ideal solution as a guest material and therefore attract interest in various applications, such as separation, catalysis, gas storage, sensing, biology, etc.^[25, 26] However, most of the MOPs are found to be less chemically stable which limits their practical utility in aqueous or chemical environments.^[27] In this regard, recently, Zr(IV)-based MOPs were recognized for their high chemical stabilities and thus have great potential towards different applications.^[28–30] Nevertheless, owing to the unavoidable

aggregation-induced blockage of the active sites, upon removal of the guest in the solid-state, unfortunately, MOPs are far from their conceivable capability.^[31] Again, attempts have been made to address these critical issues by encapsulating polyhedra into various porous matrices, such as metal–organic frameworks, silica, etc.,^[32, 33] but the heterogeneous nature of these host matrices restricts the practical utilization of the overall nanocomposite as a different workable, more coherent monolithic form, which are promising for separation applications. In a recent report, we demonstrated a strategic fabrication of an ionic hybrid material by covalently embedding stable cationic metal–organic polyhedra (MOP) with a covalent organic framework (COF) to develop a nanotrap as an efficient anion-exchange material.^[34] The synchronous existence of multifunctionalities enabled the rapid and efficient extraction of various toxic oxoanions from aqueous medium. However, the highly dispersed nature along with the non-monolithic applicability thwarted large-scale real-world applications. Considering this, here we envisioned that the use of a metal–organic gel (MOG) with a soft porous hybrid structure^[35] could be an ideal choice as an efficient host matrix for encasing guest-MOPs with an advantageous “bottle-around-ship” strategy to construct composite materials, having the characteristics of both a framework and a gel in terms of hierarchical porosity, high surface area, superior crack resistance capability for shaping.

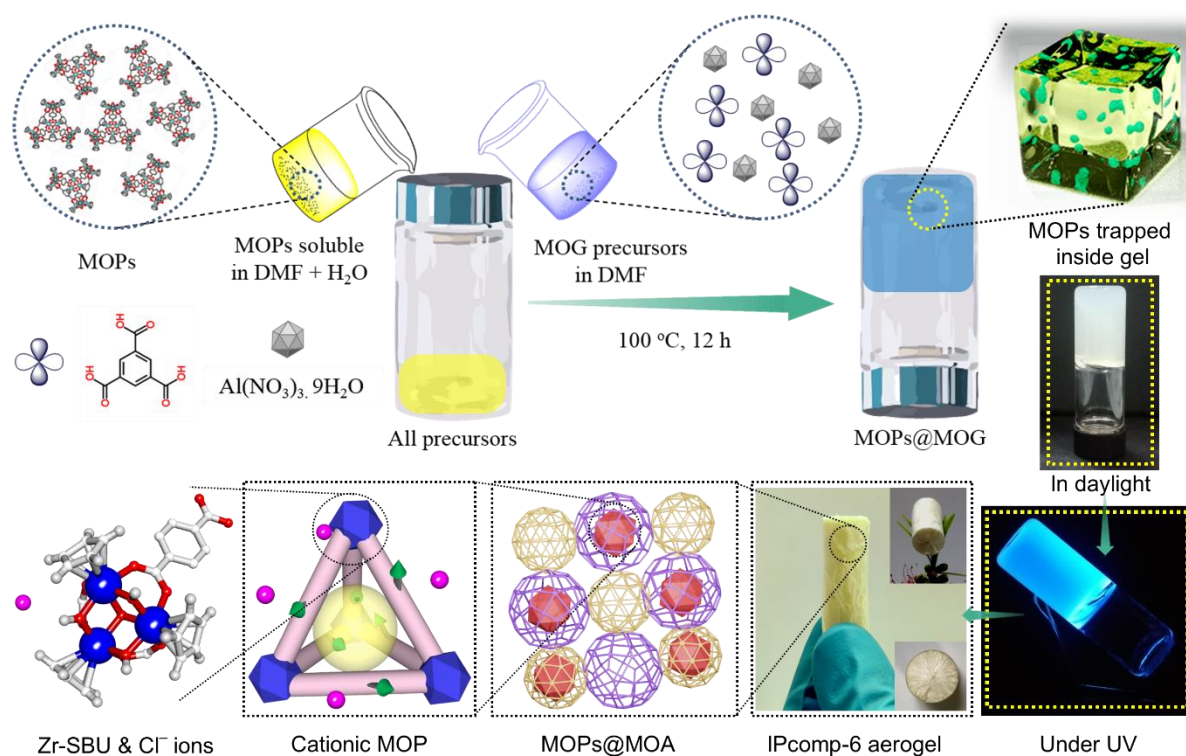
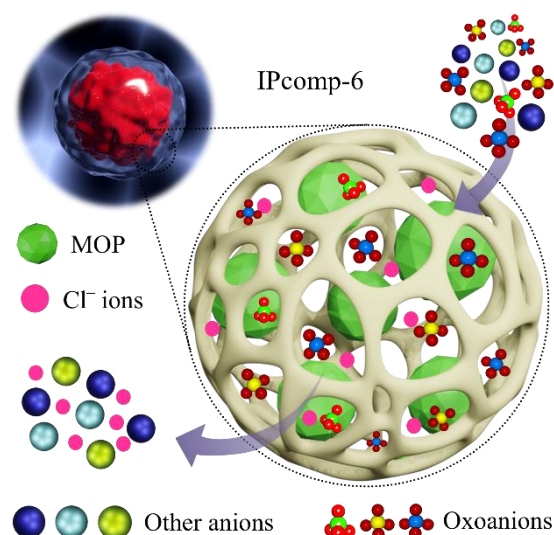


Figure 4.1 Schematic representation of the synthesis of cationic metal–organic polyhedra embedded metal–organic gel hybrid composite material (IPcomp-6). The free-standing wet-gel composite is

luminescent in nature. The lightweight aerogel form of IPcomp-6. The schematic illustration of the MOP exhibiting the Zr-SBU and free Cl^- ions inside the gel matrix.

The facile synthesis of metal–organic gel-based materials facilitate aerogel as well as xerogel monolithic architectures.^[36] However, the high-density nature of xerogel materials often suffers from assorted limitations such as volume shrinking upon drying, which subsequently obstructs the internal pores, and therefore restricts their efficiencies.^[37] The fabrication of ultralight, free-standing, stable, low-density sponge-like skeletal, aerogel materials without compromising their hierarchical porous properties is an effective alternative to address the aforementioned issues.^[38] In this regard, we have synthesized and shaped an efficient ionic hybrid composite aerogel material (hereafter denoted as IPcomp-6 (where “IP” stands for IISER Pune, and “comp” stands for composite)) with excellent anion-exchange ability by encapsulating a cationic MOP^[39] inside a hierarchically porous MOG,^[40] utilizing the “bottle-around-ship” encapsulation strategy (Figure 4.1).^[41] The strategic implantation of a multifunctionalized trap (MOP) with a stable host (MOG) is demonstrated for efficient removal of oxoanions (Scheme 4.1). The deliberately grafted $\text{Cp}_3\text{Zr}_3\text{O}(\text{OH})_3$ secondary building units (SBUs) of the MOP molecule result in high selectivity towards trapping various oxoanions,^[42] whereas, the amine group along with freely exchangeable Cl^- ions enhanced the anion-exchange process.^[43, 44] In addition, the host, MOG tied up the MOP molecules separately, boosts the diffusion of oxoanions towards the active nanotrap (MOP) through its hierarchically (micro to macro) porous nature. IPcomp-6 exhibited rapid and selective entrapment of different metalloid and metal-based oxoanions like HAsO_4^{2-} , SeO_4^{2-} , ReO_4^- , CrO_4^{2-} and MnO_4^- in the presence of a large excess of other coexisting common interfering anions in both high (~50 ppm) and ultralow (~1000 ppb) concentration. Thereafter, considering the pernicious consequences of arsenic in groundwater, IPcomp-6 was applied to the removal of arsenic from natural contaminated groundwater samples. It reduced the concentration of arsenic to much below the permissible limit for drinking water, set by world health organization (WHO) (<10 ppb).^[45] Such a fast and efficient adsorption performance by cooperative multifunctionalities of IPcomp-6 was further justified by various experimental and water-flow simulations as well as other theoretical calculation studies.



Scheme 4.1 Schematic representation of aqueous phase efficient removal of toxic oxoanions by IPcomp-6.

4.2 Experimental

4.2.1 Materials: All the reagents, starting materials and solvents were commercially purchased from Sigma-Aldrich, TCI Chemicals, Alfa aesar depending on their availability and used without further purification. All oxoanions salts are toxic in nature and proper protective gear (masks, gloves) is always to be used.

4.2.2 General Characterization and Physical Measurements:

4.2.2.1 Powder X-ray diffraction (PXRD): Powder X-ray diffraction (PXRD) experiments were performed on a Bruker D8 Advanced X-ray diffractometer at room temperature using Cu K α radiation ($\lambda = 1.5406 \text{ \AA}$) at a scan speed of $0.5^\circ \text{ min}^{-1}$ and a step size of 0.01° in 2θ .

4.2.2.2 Fourier transform infrared spectroscopy (FT-IR): The IR Spectra were acquired by using a Bruker Optics ALPHA-E spectrometer with a universal Zn-Se ATR (attenuated total reflection) accessory. FT-IR data are reported with a wave number (cm^{-1}) scale in $500\text{-}4000 \text{ cm}^{-1}$ range.

4.2.2.3 Thermogravimetric analysis (TGA): Thermogravimetric analyses were recorded on Perkin-Elmer STA 6000 TGA analyzer by heating the samples from 40°C to 800°C under N_2 atmosphere with a heating rate of $10^\circ \text{C min}^{-1}$.

4.2.2.4 Scanning electron microscopy (SEM): The morphology of the crystalline materials was recorded with a Zeiss Ultra Plus field-emission scanning electron microscope (FESEM) with an integral

charge compensator and embedded EsB and AsB detectors (Oxford X-max instruments 80 mm² (Carl Zeiss NTS, GmbH). The samples were sputter-coated with a 5-10 nm Au film to reduce charging. The elemental analysis was carried out using voltage of 15 KV equipped with an EDX detector. Data acquisition was performed with an accumulation time of 600s.

4.2.2.5 Transmission electron microscopy (TEM): TEM imaging and STEM-EDS were performed on the HRTEM (JEM-2200FS, JEOL) operating at an acceleration voltage of 200 kV. For TEM analysis, all the samples were dispersed in isopropanol and sonicated. Then, the samples were left for 2 min, and the upper part of the solution was taken for preparing TEM samples on a lacey carbon-coated copper grid (Electron Microscopy Science, 200 mesh).

4.2.2.6 Nitrogen adsorption-desorption isotherm measurements: N₂ gas adsorption measurements were performed using BelSorp-Max instrument (Bel Japan). Prior to adsorption measurements, the activated samples were heated at 120 °C under vacuum for 12 hours using BelPrepvacII.

4.2.2.7 X-ray photoelectron spectroscopy (XPS): As-obtained powder samples were stuck to conductive paste and then measured by X-ray photoelectron spectroscopy using K-Alpha+model (Thermo Fischer Scientific, UK) with Al K α source.

4.2.2.8 Nuclear magnetic resonance (NMR): ¹H and ¹³C NMR spectra were recorded on Bruker 400 MHz NMR spectrometer. The chemical shifts are expressed in parts per million (δ scale).

4.2.2.9 High-resolution mass spectroscopy (HRMS): The mass analysis of the MOPs was carried out using high-resolution mass spectrometry (HRMS-ESI-Q-TOF LC-MS) and Applied Bio system 4800 PLUS matrix-assisted laser desorption/ionization (MALDI) TOF/TOF analyzer.

4.2.2.10 Confocal laser scanning microscope (CLSM): Confocal laser scanning microscope (Zeiss, Oberkochen, Germany Model LSM 10) was used to achieve background free high-resolution images of all the compounds.

4.2.2.11 UV-visible absorption spectra: UV-vis absorption studies were performed on a Shimadzu UV 3600 UV /vis /NIR spectrophotometer in an optical quartz cuvette (10 mm path length) over the entire range of 200-800 nm.

4.2.2.12 Steady state photoluminescence spectra: The steady-state photoluminescence studies were recorded on a Fluorolog-3 spectrofluorometer (HORIBA Scientific).

4.2.2.13 Fluorescence measurements: All fluorescence measurements were done on Jobin Yvon Fluoromax-4 spectrofluorometer.

4.2.2.14 Inductively coupled plasma atomic absorption/emission spectrometry (ICP-AAS/AES) and mass spectrometry (ICP-MS): ICP-AAS analysis was performed on Thermo Scientific iCE 3000

Series. ICP-AES analysis was performed on ARCOS, Simultaneous ICP Spectrometer. ICP-MS was performed on Quadrupole inductively coupled plasma mass spectrometry (Q-ICP MS; Thermo Scientific iCAP Q) instrument. Multielement standards were purchased from inorganic ventures.

4.2.2.15 Supercritical CO₂ activation: Supercritical CO₂ activation process was performed using a TOUSIMIS Samdri instrument. A freshly filled liquid CO₂ cylinder was used for the experiment.

4.2.2.16 Compression test: The mechanical strength test was conducted with a vernier caliper and each data was collected for three times. Compressive strength was measured in non-confined mode, using universal testing machine (Model Instron 5943) equipped with 1 kN load cell and stainless-steel compression plates.

4.2.2.17 Isothermal Titration Calorimetry (ITC): The ITC experiments were performed on a Malvern MicroCal PEAQ-ITC microcalorimeter having 20 (19+1) injection cycle method capacity, the sample volume of 280 μL with a sample cell size of 200 μL and injection syringe volume of 40 μL for each set of experiments.

4.2.2.18 3D X-ray tomography: Aerogels were imaged using X-ray microtomography (Xradia 510 Versa X-ray Microscope, Zeiss X-ray Microscopy, Pleasanton, CA, USA) to study its morphology, porosity and pore-size distribution. Specimens were loaded onto the sample holder, kept in between the X-ray source and the detector assembly. Detector assembly consisted of a scintillator, 20X optics and a CCD camera. X-ray source was ramped up to 60 kV and 5 W. The tomographic image acquisitions were completed by acquiring 3201 projections over 360° of rotation with a pixel size of 0.80 microns for a sample size of 0.8 x 0.8 x 0.8 mm³. Each projection was recorded with 5 seconds of exposure time. In addition, projections without the samples in the beam (reference images) were also collected and averaged. The filtered back-projection algorithm was used for the reconstruction of the projections to generate two-dimensional (2D) virtual cross-sections of the specimens. Image de-noising, filtration, segmentation and further processing were performed using GeoDict software package (GeoDict® 2018, Math2Market GmbH, Germany). 2D images were trimmed down to a sub-volume (100 x 100 x 100 voxels with 0.80 cubic micron per voxel), filtered to remove noise and segmented after OTSU threshold selection based on local minima from the grayscale histogram. Resultant 3D reconstructed model was used to estimate the pore characteristics such as porosity, pore-size distribution, etc. using PoroDict® software package (GeoDict® 2018, Math2Market GmbH, Germany), where radius pore is determined by fitting spheres into the pore volume.

4.2.2.19 IPcomp-6 digestion process and ¹H NMR analysis: ~30 mg of NH₂-MOP@MOA composite material was digested in ~1 mL of 1 mol/L NaOH solution over ~6 hours. Then, 2.0 mL of DI water was added to the mixture and the overall solution was then sonicated properly for a certain time. Thereafter, the solution was left standing for one day with aqueous Al(OH)₃ precipitating. Further, the

ppt of $\text{Al}(\text{OH})_3$ was removed by a membrane filtration (0.2 μm pores) to give a clear solution containing the corresponding organic ligands of metal-organic gel (BTC^{3-}) and metal-organic polyhedron (ATA^{2-}). Now, in order to remove the solvent molecules, the mixture was subjected to undergo dynamic vacuum at 60 °C overnight. Thus, resultant residual solid was ground in a mortar pestle to give fine powder, which was further put under dynamic vacuum at 80 °C for 10 hours. After that the powder was dispersed in 1.2 mL of D_2O and followed by the addition of few drops of 40 wt% NaOD, which result a clear solution. This clear solution was than analyzed for ^1H NMR.

4.2.3 Detailed procedures for synthetic preparation

4.2.3.1 Synthesis of Metal-Organic Aerogel (MOA) and Xerogel: The Al-MOG was synthesized with slight modification based on the report from Cheng-Yong Su et al.^[38] In a simple reaction setup, 105 mg of the organic ligand (trimesic acid [H_3BTC]) and 281.4 mg of $\text{Al}(\text{NO}_3)_3 \cdot 9\text{H}_2\text{O}$ metal salt were each dissolved in DMF (~7.5 mL), followed by rapid mixing of the solution with the addition of triethylamine. Thereafter, the resulting transparent solution was transferred in a closed container and allowed to stand in oven at 110 °C for ~10 h, when the gelation was occurred. The gelation process was further aged for next 36 h. After cooling to room temperature, the wet-gel was subjected to wash followed by solvent exchanged with EtOH. Now, to obtain the aerogel compound from the wet-gel, a typical supercritical CO_2 activation process was performed using a TOUSIMIS Samdri instrument. (See section 4.2.3.4 for details) Moreover, to obtain the xerogel, thus, prepared wet-gel was further dried in an oven after spreading it on a petri dish leading to formation of the shrunk xerogel. Finally, the resulting material was dried under vacuum for overnight to obtain the product.

4.2.3.2 Synthesis of NH_2 -MOP: The NH_2 -MOP was synthesized with slight modification based on the report from Zhao et al.^[39] 2-aminoterephthalic acid (50 mg) and Zirconocene dichloride (150 mg) were dissolved in N, N-dimethylacetamide (DMA, 10 mL) with a trace amount of water (40 drops) and kept it at room temperature and left undisturbed state for 72 hours. The yellow cubic block crystals were collected by filtration and dried under vacuum.

4.2.3.3 Synthesis of BDC-MOP: The BDC-MOP was synthesized with slight modification based on the report from Hong et al.^[54] Terephthalic acid (48 mg) and Zirconocene dichloride (150 mg) were dissolved in N, N-dimethylacetamide (DMA, 10 mL) with a trace amount of water (40 drops) and kept it at 65 °C and left undisturbed state for 24 hours. The white cubic block crystals were collected by filtration and dried under vacuum.

4.2.3.4. Synthesis of NH_2 -MOP@MOA (IPcomp-6): The hybrid materials were synthesized by ‘bottle-around-ship’ encapsulation strategy in a two steps procedure. In the first step, the wet-gel form

of the composite was synthesized. At first, a certain number of NH₂-MOPs was dissolved in an aqueous DMF solution (few drops of H₂O in DMF). In another mixture 35 mg of H₃BTC and 95.6 mg of Al(NO₃)₂·9H₂O were individually dissolved in DMF solution. After that, all these solutions were mixed well together in a closed container, followed by addition of triethylamine which was then placed in an oven for gelation at 110 °C for ~10-12 h. After, ~12 hours the wet-gel was formed. This wet-gel was further aged for 36 h at 80 °C to get the final product. Primarily, the high luminescent nature of the compound indicated encapsulation of the NH₂-MOP inside the mesoporous cavities of the MOG(Al) (Appendix 4.1). Now, in order to get the aerogel (MOA) form of the hybrid composite materials, in the second step, thus-prepared hybrid wet-gel compound was subjected to through solvent exchange with ethanol before being carefully transferred into a plastic cell, which was then placed to the supercritical CO₂ activation instrument (TOUSIMIS Samdri). After that, a typical supercritical drying process was performed by cooling to 0 °C to 5 °C and filling the instrument chamber with liquid CO₂, followed by purge, soaked in liquid CO₂. The purge and soaking cycle (each ~20 min) were repeated for 6 times. Then the temperature of the system was raised to 35-40 °C for next ~2 h. After transforming the system to the supercritical temperature and pressure, it was allowed to slowly bleed overnight. At last, the auto venting of the SC-CO₂ equipment result the light weight aerogel monolith, which was used for further characterization and application. It should be pointed out that the proper number of purge-soaking cycles is essential for the final structure and robustness of the aerogel monoliths. Subsequently the xerogel form of the composite (NH₂-MOP@MOG) was synthesized via direct drying of the wet-gel hybrid compound at room temperature followed by in an oven at 80 °C.

In addition to this, different batches of the hybrid composite materials were synthesized by varying the amount of the NH₂-MOPs (5 mg, 25 mg, 45 mg, 50 mg, 60 mg, 75 mg, 80 mg, 100 mg, and 120 mg) and keeping the fixed amount of the precursors of the MOG. Now, for the primary screening test, we performed the As(V) oxoanion capture studies with all of these hybrid materials. However, the composite material fabricated with 45 mg of NH₂-MOP, demonstrated the most efficient capture performance (Appendix 4.28 and Appendix Table 4.7). Therefore, in this work, we chose 45 mg NH₂-MOP@MOA composite material (termed as IPcomp-6) for further study.

4.2.3.5 Synthesis of BDC-MOP@MOA: Another hybrid composite material BDC-MOP@MOA was synthesized by taking the BDC-MOP (BDC: terephthalic acid) as guest material, following the similar protocol, described in the above paragraph.

4.2.4 Oxoanions capture study

4.2.4.1 General consideration: The aqueous solution of different oxoanions was prepared by dissolving a certain amount of sodium or potassium salts of different oxoanions into deionized water

and the different concentrations were obtained by diluting the stock solution with the proper amount of distilled water unless otherwise indicated. The pH values of the solutions were adjusted by HNO₃ or NaOH aqueous solution. The concentrations of oxoanions during all the experiments were detected by ICP-AES and ICP-MS (for ultra-low concentrations) analysis. All the adsorption experiments were performed at ambient conditions. All the data has been collected three times through ICP analysis to plot the final adsorption results.

4.2.4.2 Adsorption kinetics studies: The standard procedure that we adopted for the adsorption kinetics experiments was as follows. The capture study of various oxoanions (HAsO₄²⁻, SeO₄²⁻, ReO₄⁻, CrO₄²⁻, MnO₄⁻) was performed in 15 mL glass vial equipped with magnetic stir bars with a constant stirring rate of 350 r.p.m. Firstly; 5 mg of material was taken in 5 mL of 50 ppm stock solution of different oxoanions, individually. After continuous stirring for different time at room temperature the solution was collected by a syringe with having 0.22 μm nylon membrane filter. The concentration of this filtrate was measured through ICP-AES (for HAsO₄²⁻, SeO₄²⁻, ReO₄⁻) and UV-vis spectroscopy (for CrO₄²⁻, MnO₄⁻) and the kinetic adsorption study were measured at different time intervals. From the time-dependent study, we calculated the removal % and decreasing concentration of the respective oxoanions with time using the following equations:

$D_t = (C_o - C_t) * 100 / C_o = (A_o - A_t) * 100 / A_o$, Where, D_t = oxoanions removal efficiency (%), C_o = initial concentration, A_o = initial absorbance, C_t = final concentration, A_t = final absorbance at specific time.

4.2.4.3 As(V) adsorption isotherm experiment: 5 mg of material was immersed in 10 mL aqueous solution of arsenate having different concentrations. After ~10 hours the filtrate was collected through syringe filter (0.22 μm) and measured the concentration through ICP-AES and further fitted with following equations,

Langmuir model, $Q_e = Q_m \cdot C_e / (K_d + C_e)$; Where, C_e (ppm) and Q_e (mg.g⁻¹) are the As(V) concentration at equilibrium and amount of HAsO₄²⁻ adsorbed at equilibrium respectively. Q_m (mg.g⁻¹) is the maximum amount of As(V) per mass of adsorbent to form a complete monolayer. K_d (mg.L⁻¹) is a constant to the affinity of the binding sites.

Freundlich model, $Q_e = K_f \cdot C_e^{1/n}$; Where, K_f and $1/n$ are the Freundlich model constant, indicating capacity and intensity of adsorption respectively.

4.2.4.4 Pseudo-second-order model: The pseudo-second-order equation can be expressed as follows:

$t/q_t = 1/K_2 q_e^2 + t/q_e$ Where, q_t and q_e represent the adsorbed amount (mg.g⁻¹) at time and at equilibrium t (min), respectively, k_2 represent the Pseudo-second-order rate constant of adsorption (g.mg⁻¹.min⁻¹).

The experimental data was fitted using Pseudo-second-order kinetic model.

4.2.4.5 Distribution coefficient (K_d) value calculation: The distribution coefficient (K_d) value as used for the determination of the affinity and selectivity of sorbents for oxoanions, is given by the equation:

$$K_d = [V\{(C_o - C_e)/C_e\}]/m;$$

Where, V is the volume of the testing solution (mL), m is the amount of solid adsorbent (g), C_o is the initial concentration of As(V), and C_e is the equilibrium concentration of As(V).

4.2.4.6 Oxoanions capture capacity: The amount of oxoanions adsorbed per gram of material was determined by exposing 5 mg of material to 10 mL of ~500/1000 ppm concentrated solution of respective oxoanions salts for ~12 hours under stirring conditions at room temperature. After 24 hours, the composite material was filtered off and the filtrate was characterized through ICP-AES/UV-vis by diluting the solution. The adsorption capacity per gm was calculated using following equation:

$$Q_t = (C_o - C_t) * V / m;$$

Where, Q_t , C_o , C_t , V and m are the capacity of adsorbent, initial concentration of the oxoanions solution, final concentration of oxoanions at a specific time, volumes of the solution and mass of the material used for the adsorption study respectively.

4.2.4.7 Oxoanions capture study in presence of other competing ions: For testing the influence of competing ions, large excess (~100-fold) of competing salts such as, NaCl, NaBr, NaNO₃, NaClO₄, Na₂SO₄ were added to the different aforementioned oxoanions aqueous solution and carried out the capture studies by following the aforementioned method. The capture studies were monitored through ICP-AES (for HAsO₄²⁻, SeO₄²⁻, ReO₄⁻,) and UV-vis spectroscopy (for CrO₄²⁻, MnO₄⁻).

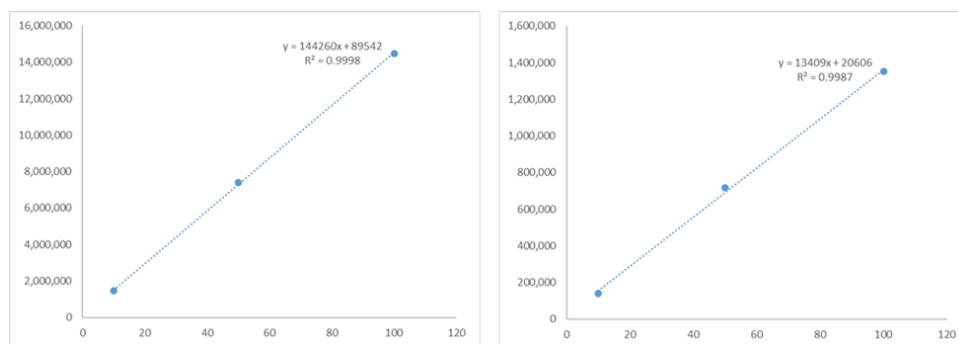
4.2.4.8 pH-dependent As(V) extraction study: The effect of pH on As(V) removal performance was recorded in a wide range of pH and compared with the data at pH-7 to check the relative performance. The variation of pH values was realized by the addition of either acid (HCl) or base (NaOH). We adopted the similar adsorption experiment for this study.

4.2.4.9 Trace amount capture study: Trace amount (1 ppm) of As(V) capture study was performed following the similar kinetic adsorption experiment described above. The kinetic adsorption study was measured at different particular time interval, taking ~1000 ppb stock solution of As(V) in water. The ICP-MS experiments were carried out for analyse the removal efficiency of the materials.

4.2.4.10 Recyclability test: The first cycle of As(V) uptake in the recyclable experiment was performed according to the aforementioned adsorption protocol. After the first run of adsorption, the As(V) containing material was regenerated by treatment with a saturated Na₂SO₄ aqueous solution. The resulting solid was dried and washed three times with pure deionized water. After being finally dried under vacuum, the resultant material was used for the next cycle adsorption experiments.

4.2.4.11 Dynamic column exchange-based flow-through As(V) capture study: To check the continuous As(V) oxoanion removal efficiency by the hybrid aerogel material (IPcomp-6), a column exchange-based flow-through experiment was conducted by packing the hybrid aerogel inside a column as bed for oxoanion capture. After that, to mimic the simulated industrial waste water system different volume of stock ~19.8 ppm of As(V) aqueous solution along with ~100-fold excess concentration of other interfering anions (such as NO_3^- , Cl^- , Br^- , ClO_4^- , SO_4^{2-}) were mixed. Thereafter, this mixture was passed through the column bed with a flow rate of 0.5 mL/min, which was controlled by a water-flow-regulator, and the drops per minute was recorded with the help of a stopwatch. A bed-volume of ~4.2 mL of column eluted solution was collected in a different respective container. The concentration of As(V) in these solutions were then analyzed through ICP-MS analysis. The recyclability test of the column exchanged-based As(V) capture study was performed by washing the column with pure water, followed by saturated Na_2SO_4 solution after each cycle. The filtrate of each cycle was collected at the bottom of the column (Appendix 4.39). Before and after capture studies, the concentration of As(V) solutions were analyzed through ICP-MS analysis. We have also performed the IPcomp-6 embedded column-exchange based As(V) capture experiment with the natural groundwater samples having initial concentration of ~56 ppb for sample-1 and ~43 ppb for sample-2. This samples were run through the column as received from their location of availability, without any further modification.

4.2.4.12 ICP Calibration: The calibration curve was recorded before each ICP measurement using various standard samples prepared by dilution of respective oxoanion salts aqueous solution of a known concentration with 2% w/w HNO_3 . The following calibration curves indicated the regression line with high correlation coefficient ($R^2 = 0.999$, $R^2 = 0.998$). Most of the ICP data were conducted triplicate. Whereas, few critical ICP data (such as kinetics of oxoanions capture, capacities of oxoanions removal) has been collected and verified from three different instruments.



Scheme 4.2 Regression line from the ICP measurement indicated calibration for oxoanion measurement.

4.2.5 Theoretical calculation and simulation studies

Determination of electrostatic-potential surface (ESP), binding sites and binding energy of interactions:

The molecular-level interactions between the amino functionalized cationic MOP and oxoanion, HAsO_4^{2-} were simulated using Discovery Studio 2017 (Accelrys). The DFT simulation was performed at fine quality calculation level. At first, using DMOL3 and B3LYP hybrid function the single unit of the MOP was fully geometry relaxed by keeping the Multiplicity factor to Auto mode, double numeric plus polarizing (DNP+) basis set with water as solvent. Using simulated annealing technique structural simulation on the geometry relaxed MOP structure was realized to find a feasible interaction site of the HAsO_4^{2-} within the relaxed MOP unit. The electrostatic potential (ESP) on the van der Waals (VDW) surfaces (isodensity = 0.001 a.u.) of MOP unit was derived from ground-state electron density of the system.

The Static binding energies (ΔE) at 0 K in vacuum were calculated using the following expression

$$\Delta E = E(\text{MOP} + \text{Anion}) - E(\text{MOP}^+) - E_{\text{Anion}}$$

Where, E_x refers, respectively, to the total energies of the MOP + Anion complex, the charged MOP+ alone, and the anion molecule respectively.

4.3 Results and Discussion

The choice of cage-topology-based framework materials as host matrix is suitable for encapsulating guest molecules by “bottle-around-ship” strategy to fabricate excellent composite materials, as the probability of leaching of guest become reduced due to the benefit of larger cavity size than lower pore window.^[46] Keeping this in mind, in this work, in-situ realization of an ionic host-guest hybrid composite materials has been constructed with a hydrolytically stable hierarchical porous metal (Al) organic gel having two distinct mesoporous cages with size 2.5 nm and 2.9 nm in its MTN topology (MTN = zeolite socony mobilthirtynine)^[47] as host matrix along with a stable cationic nanosized (~2 nm) Zr(IV)-based polyhedra as guest molecules (Appendix 4.2 and 4.3).^[39]

The amino-functionalized cationic MOP ($\{[\text{Cp}_3\text{Zr}_3\text{O}(\text{OH})_3]_4(\text{NH}_2\text{-BDC})_6\} \cdot \text{Cl}_4$) and Al-metal organic xerogel (MOG) and further, metal-organic aerogel (MOA) was synthesized and characterized by previously reported method (Appendix 4.4 and 4.5).^[39,47] While, single step “bottle-around-ship” encapsulating strategy has been adopted to fabricated the composite material. Briefly, individual mixture of aqueous N,N'-dimethylformamide (DMF) solution of MOPs and DMF solution of mixture of metal $[\text{Al}(\text{NO}_3)_3 \cdot 9\text{H}_2\text{O}]$ and bridging ligand (1,3,5-trimisisic acid) were mixed together to get a homogeneous solution. Then, the complete mixture was heated at an optimized temperature to afford

the hybrid composite gel-type luminescent material (Figure 4.1). Thereafter, the composite material was carefully dried under supercritical CO₂ drying procedure to fabricate nanotrap-MOP embedded cationic hybrid composite aerogel material (NH₂-MOP@MOA) (IPcomp-6) (Figure 4.1, see experimental section for detail synthetic procedure). It should be pointed out that the direct air or hot drying of the composite, yielded xerogel-type material (NH₂-MOP@MOG) due to mass losses of the pore-entrapped solvents molecules. Thus, synthesized cationic composite materials has been characterized by following physical and spectroscopic techniques. Powder X-ray diffraction (PXRD) analysis of IPcomp-6 indicated well resolved diffraction peaks that precisely match with the simulated patterns of the reported Al-MIL-100, MOF (Appendix 4.6).^[47] However, the PXRD patterns of both wet gel and xerogel composite exhibited broad peaks, which further indicated relative lower crystalline nature than aerogel composite (IPcomp-6). The Fourier transform infrared spectroscopy (FT-IR) spectra of IPcomp-6 established both the formation of host aerogel (MOA) matrix (characteristic peaks at ~1072 cm⁻¹, ~1525 cm⁻¹ and ~950 cm⁻¹, corresponding to -C=O, Al-O and bridging μ -OH group bond frequencies, respectively)^[47] and the presence of guest amino-functionalized Zr(IV)-MOP (characteristic peaks at ~1380 cm⁻¹, ~3515 cm⁻¹, ~3390 cm⁻¹, corresponding to Zr-O, symmetric and asymmetric stretching frequencies of -NH₂ group, respectively)^[48, 49] in the composite material (Appendix 4.7). After that, to check the existence as well as leaching test of guest (cationic MOP) from IPcomp-6, nuclear magnetic resonance (NMR), high resolution mass spectrometry (HRMS) and inductively coupled plasma (ICP) experiments have been performed. Initially, HRMS, ¹H NMR spectra and ICP data of without washing as-synthesized composite materials indicated existence of MOP molecules, which can be explained by the easy release of MOP molecules present on the surface of the composite (Appendix 4.8).^[48] After through washing with aqueous methanolic solution, the HRMS and ¹H NMR spectra along with ICP data of IPcomp-6 treated supernatant exhibited no presence of MOPs, which ruled out the existence of excess MOPs on the surface of IPcomp-6 along with no liberation of MOPs from the cage-based cavity of the host-MOA (Appendix 4.9). Moreover, the relevant peaks of corresponding organic linkers of both MOA and MOP in ¹H NMR spectra along with the presence of Zr-metal in the ICP data of digested sample of IPcomp-6 support the presence of trapped cationic MOPs inside the porous MOA matrix (Appendix 4.10). These results validated the advantage of “bottle-around-ship” strategy to successfully encapsulate nanosized MOP inside the relatively larger cavity with smaller window size of the host-Al-MOA matrix, along with no leaching of guest molecules (Figure 4.1).

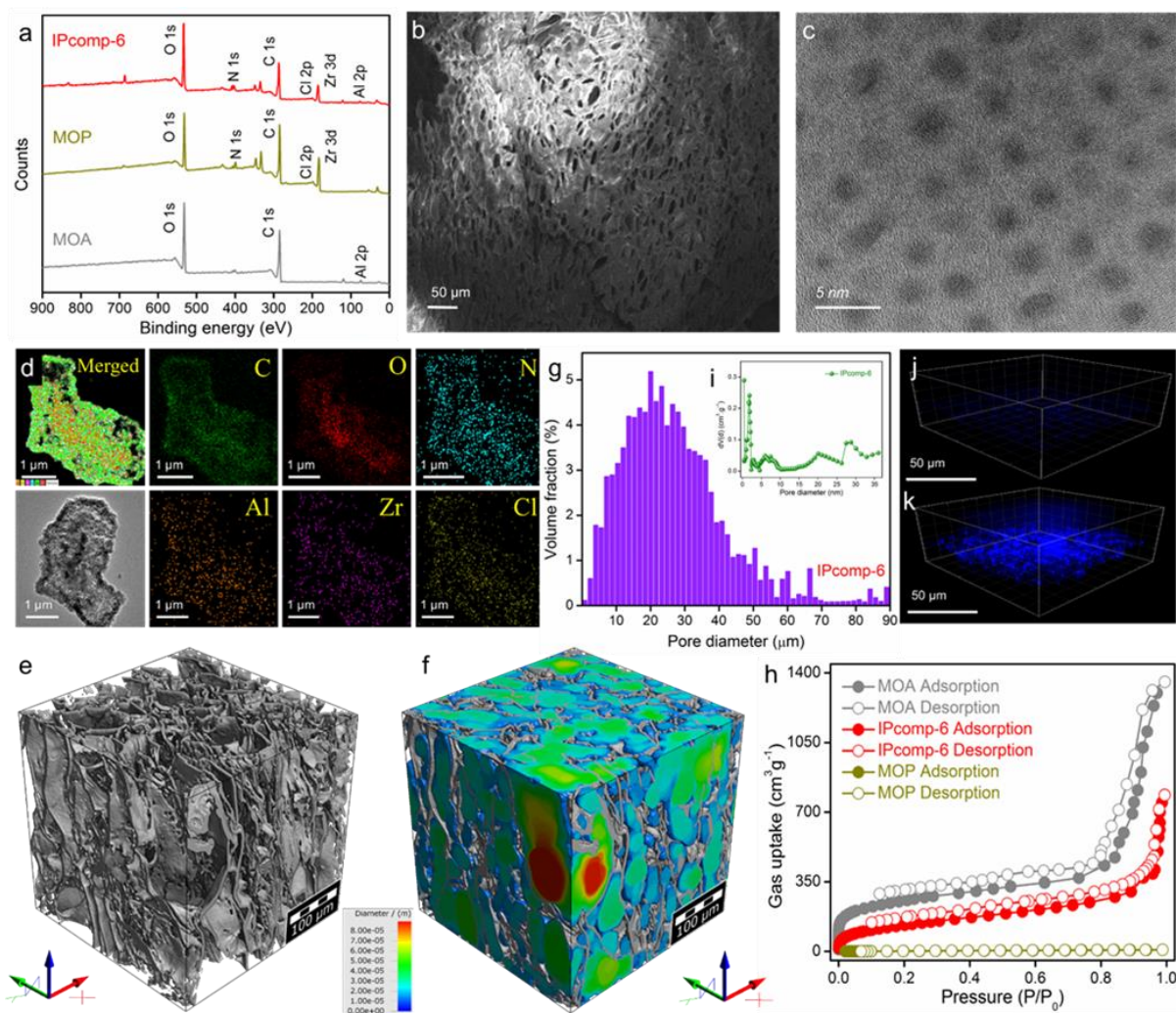


Figure 4.2 (a) XPS survey spectra of IPcomp-6 along with pristine MOP and MOA. (b) FESEM image of IPcomp-6. (c) HR-TEM image of the composite material. (d) STEM image with High-angle annular dark-field TEM (HAADF-TEM) elemental mapping of IPcomp-6. (e) Segmented 3D volume-rendered X-ray tomographic image of IPcomp-6. (f) Visualization of micron pore-size distribution with color-scale CT image. (g) Micron size pore distribution histogram. (h) Low temperature N_2 gas sorption measurement. (i) Pore size distribution from N_2 gas sorption data of IPcomp-6. (j, k) Confocal fluorescence microscopic images of MOA and hybrid aerogel materials, respectively.

Compared with pristine MOA, the X-ray photoelectron spectroscopy (XPS) survey spectra of IPcomp-6 exhibited peaks corresponding to elements Zr and N along with Al, C and O indicated successful grafting of MOPs in the porous MOA matrix (Figure 4.2a). Moreover, compared with MOA, the characteristic peaks for Al at binding energy ~ 75.5 eV was observed to be shifted towards relatively higher binding energy with peak broadening in case of IPcomp-6, which suggest significant interaction

between the host matrix and guest-MOP molecules (Appendix 4.11). The thermogravimetric analysis (TGA) of IPcomp-6 showed properties of both MOP and MOA, and disclosed the improved thermal behaviour of MOP in the composite (Appendix 4.12). Thereafter, the surface morphology of IPcomp-6 has been characterized by field emission scanning electron microscopy (FESEM) and transmission electron microscopy (TEM). Compared with cubic microcrystalline MOPs and sponge-like MOA, the morphology of the IPcomp-6 was found wormhole-like with disordered arrangement of interconnected large void spaces, suggesting the highly porous nature of the hybrid aerogel materials (Figure 4.2b and Appendix 4.13). The SEM images of IPcomp-6 exhibited the existence of macropores (~ 1 to ~ 50 μm) throughout the aerogel composite. Moreover, the high-magnification SEM images of MOP embedded hybrid aerogel revealed nanoparticles cross-linked with interparticle voids of the composite materials (Appendix 4.13). TEM images showed the interconnected agglomerated particles in the hybrid aerogel material with large void spaces (Appendix 4.14). Further, the high-resolution TEM (HR-TEM) images demonstrated the entity of nanosized MOPs throughout the host-matrix with an average diameter of ~ 2.1 nm (Figure 4.2c and Appendix 4.15). The appearance of few non-identical sizes of MOPs in the aerogel matrix might be attributed to the minimal aggregation of several MOPs throughout the hierarchical pores of host gel matrix.^[40] Apart from this, a close inspection in the energy-dispersive X-ray (EDX) data from both SEM and TEM, exposed the elements Zr/Cl ratio ~ 3.0 (accord with the crystallographic information of the Zr(IV)-MOP) in IPcomp-6, validated the stable existence of cationic MOPs in the hybrid aerogel (Appendix Tables 4.1-4.6). In addition, High-angle annular dark-field (HAADF) TEM elemental mapping exhibited the expected homogeneous distribution of all relevant elements throughout the composite (Figure 4.2d). Similar result was observed from SEM elemental mapping data (Appendix 4.16-4.18). Furthermore, in order to explore the hierarchical porous nature of the hybrid nanocomposite, microscale X-ray computed tomography (CT) experiment has been performed. From the 2D cross-sectional CT images, it was found that the heterogeneous distribution of large micrometer range pores (~ 1 to ~ 50 μm) within the aerogel-composite material (Appendix 4.19). Further, for better understanding, segmented 3D models of IPcomp-6 were obtained via reconstruction of the 2D images stacking. The volume-rendered 3D CT images of IPcomp-6 exhibited disorder packing of interconnected macropores throughout its volume (Figure 4.2e, 4.2f and Appendix 4.20). Along with this, the large pore size distribution (average pore size of 20 microns) with void space $\sim 89.2 \pm 2$ % within the total volume of IPcomp-6 was clearly realized by the respective color code in the 3D CT images (Figure 4.2f and Appendix 4.21). Moreover, the pore-size distribution of IPcomp-6 was calculated, which demonstrated large volume fraction in the micron size range (~ 1 to ~ 50 μm with maximum at 20 μm) (Figure 4.2g). These results clearly indicated the 3D morphological features with existence of extrinsic macroporous throughout the nanocomposite.

Low temperature N₂ gas adsorption measurement has been performed in order to evaluate the micro and meso porosity of the nanocomposite along with the pristine materials. The sorption data of IPcomp-6 at 77K exhibited a steep uptake of N₂ gas at low pressure along with high gas adsorption at ~1 bar pressure, indicated the presence of both microporous and mesoporous characteristic, respectively (Figure 4.2h).^[38] Whereas, the pristine aerogel material showed similar sorption profile with relative higher N₂ uptake, especially in high relative pressure (mesoporous region) (Figure 4.2h). Compared with pristine aerogel, the reduction in the porosity of IPcomp-6 is majorly attributed to the occupation of nonporous guest-MOP molecules in the mesopores of the host. Further, the pore size distribution of IPcomp-6 was calculated by non-local density functional theory (NLDFT) and Barrett-Joyner-Halenda (BJH) model, which indicated the presence of micropores (<2 nm) and meso/macropores (>2 nm to 150 nm), within the hybrid composite, respectively (Figure 4.2i and Appendix 4.22). Again, the decrease in the pore sizes with compared to pristine material, demonstrated encapsulation of guest-MOP molecules in the gel matrix (Appendix 4.23). In aggregate, the afore-discussed X-ray tomographic analysis together with N₂ gas adsorption measurement revealed that IPcomp-6 possess hierarchical porosity with macropores (~20 μm), mesopores (>2 nm) and micropores (<2 nm).

Furthermore, the successful loading of amino-functionalized cationic MOPs in the hybrid material was characterized by optical properties of IPcomp-6. The UV-vis diffuse reflectance spectroscopy (DRS) spectra of IPcomp-6 exhibited characteristic adsorption bands for both MOA and MOP (Appendix 4.24). Similar observation was found in case of solid-state photoluminescence spectra of the composite with a significant blue-shift in the characteristics peak, which is due to the confinement of nanosized discrete MOP molecules inside the gel-matrix. (Appendix 4.25). In addition, with compared to the non-emissive pristine MOA, the confocal fluorescent microscopic imaging displayed highly-emissive nature of IPcomp-6, which might be due to the effective grafting of emissive MOP molecules into the host (Figure 4.2j and 4.2k). Along with this, the confocal 3D images also indicated the presence of plenty of extrinsic large open pores (μm-sized macropores), distributed throughout the scattered inter-connected nanoparticles morphology of the hybrid aerogel material (Appendix 4.26). Apart from this, the IPcomp-6 demonstrated promises mechanical stability as shown in appendix 4.27.

Now, an optimized reaction condition exhibited that the loading capacity of the guest-MOP molecules in the composite aerogel using 45 mg of MOPs showed maximum capture efficiencies towards arsenate in water (Appendix 4.28 and Appendix Table 4.7). We hypothesized that utilization of a greater number of MOPs causes unavoidable aggregation through interconnected mesoporous network of the host matrix, which causes deduction in the porosity as well as making unavailability of the active sites of the overall nanocomposite. Which result, further diminished in the segregation efficiencies.

4.4 Capture Study

Owing to the creation of unique multifunctional properties, such as hierarchical (micro to macro) porosity, cationic nature with free exchangeable Cl^- ions, pendant amine functional groups, Zr(IV) SBU and stable 3D micro-structure of hybrid aerogel, the sequestration capability of IPcomp-6 towards removal of various metalloid and metal-based toxic oxoanions [i.e.; HAsO_4^{2-} , SeO_4^{2-} , CrO_4^{2-} , MnO_4^- and ReO_4^- (later two are consider as surrogate oxoanion for radioactive TcO_4^-)] was investigated. A typical adsorption capture experiment (see experimental section for details) was performed in water to detoxify the aforementioned oxoanions contaminated water samples by the hybrid nano-adsorbent. Inductively coupled plasma atomic emission spectroscopy/mass spectrometry (ICP-AES/MS) analysis and UV-vis spectroscopy techniques were employed for monitoring the decrease in the concentration of As(V), Se(VI), Re(VII) and Cr(VI), Mn(VII), respectively. Initially, the removal kinetic study was performed using high concentration (~50 ppm) of all oxoanions, individually in water. The ICP-AES analysis exhibited rapid entrapment of As(V), Se(VI) and Re(VII) by IPcomp-6 with respect of contact time (Appendix 4.29). Similarly, the UV-vis spectra indicated fastest diminishing of Cr(VI) and Mn(VII) concentration in water (Appendix 4.30 and 4.31). This result also demonstrated the rapid removal kinetics (up to ~98% within 5 min) of all oxoanions from water by IPcomp-6 (Appendix 4.32 and 4.33). The sorption kinetic rates towards oxoanions were found to follow pseudo-second-order model, with high correlation coefficient and rate constant values, further indicated ultrafast capture efficiencies (Appendix 4.34). Hereafter, considering the “real-world” application, such as detoxification of industrial wastewater or groundwater, an ideal adsorbent should selectively eliminate targeted pollutants in presence of large excess of other interfering pollutants in water. In general, oxoanions contaminated industrial wastewater contains various anions, such as NO_3^- , Cl^- , Br^- , ClO_4^- , SO_4^{2-} , etc. in high excess amount, which seriously affects the overall sorption performance of the adsorbent.^[50] Therefore, keeping this in mind, along with to explore the selectivity of the hybrid nano-adsorbent, the capture experiments of oxoanions were performed in presence of ~100-fold excess interfering coexisting anions. From the ICP-AES and UV-vis data, it was found that the scaffold, IPcomp-6 rapidly eliminated all the oxoanions, individually, from the contaminated water samples in presence of ~100-fold excess competitive anions (Figure 4.3a-4.3e). Almost >80% removal efficiencies of all oxoanions within 1 min and further complete removal within 5 min were achieved, which validated the negligible impact of other coexisting anions on the fastest sequestration ability of the hybrid aerogel material (Figure 4.3a-4.3f). That being said, among all the selected oxoanions, arsenic is considered as one of the most problematic groundwater pollutants, due to its pernicious consequences on human health as well as upon entire ecosystem, commonly exist in the natural drinking water.

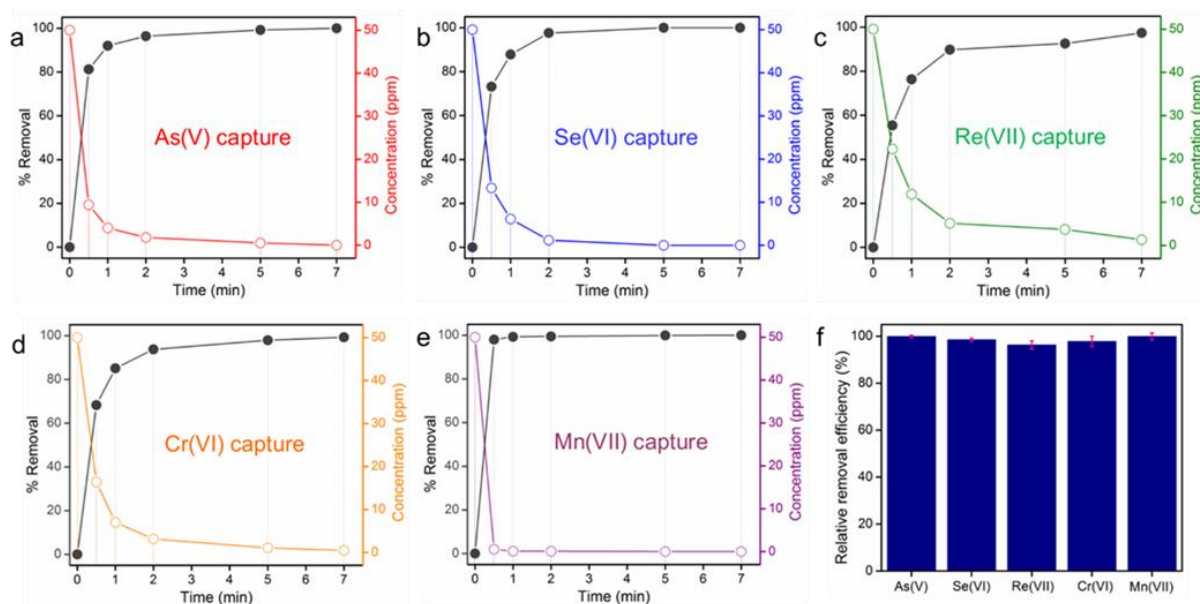


Figure 4.3 Oxoanions removal studies: % removal with respect to contact time profiles of high concentration (~50 ppm) of respective oxoanions in presence of ~100-fold excess of other non-metal-based anions (a) HAsO_4^{2-} , (b) SeO_4^{2-} , (c) ReO_4^- , (d) CrO_4^{2-} , (e) MnO_4^- , (f) Overall different oxoanions removal efficiencies of IPcomp-6.

Therefore, in this report, the further capture studies by IPcomp-6 have been performed using HAsO_4^{2-} , as a model oxoanion in water. In order to elucidate the advancement of the hybrid composite material (IPcomp-6) towards efficient capture performance, a comparison study of As(V) removal kinetic experiment by nanocomposite was performed along with the host-pristine metal-organic aerogel (MOA) and guest-MOP molecules. Compared with both MOP and MOA, the IPcomp-6 demonstrated high removal rate (~93% removal within 1 min) with exceptional selectivity for As(V) in water (Figure 4.4a). In line, pristine MOP and MOA exhibited significantly lower capture efficiencies, ~28% and ~16% within 1 min, respectively. This result explored the advanced role of hybrid composite over individual materials towards decontamination application. Thereafter, the adsorption of As(V) by IPcomp-6 was found to follow the Langmuir isotherm model (Figure 4.4b and Appendix 4.35). The exchange capacity of arsenic (As) was calculated as 157 mg per gram of adsorbent. Moreover, the hybrid aerogel material showed efficient As(V) segregation performance in a wide pH range (Appendix 4.36). In addition, IPcomp-6 exhibited excellent recyclability towards removal of As(V), as it retained its removal efficiency up to ~84% even after five cycles (Figure 4.4c). Such ultrafast capture efficiencies along with unparalleled selectivity towards a group of metalloids and metal-based oxoanions in water, positioned IPcomp-6 as a potential adsorbent in comparison to other existing materials (Appendix Tables 4.11-4.14).

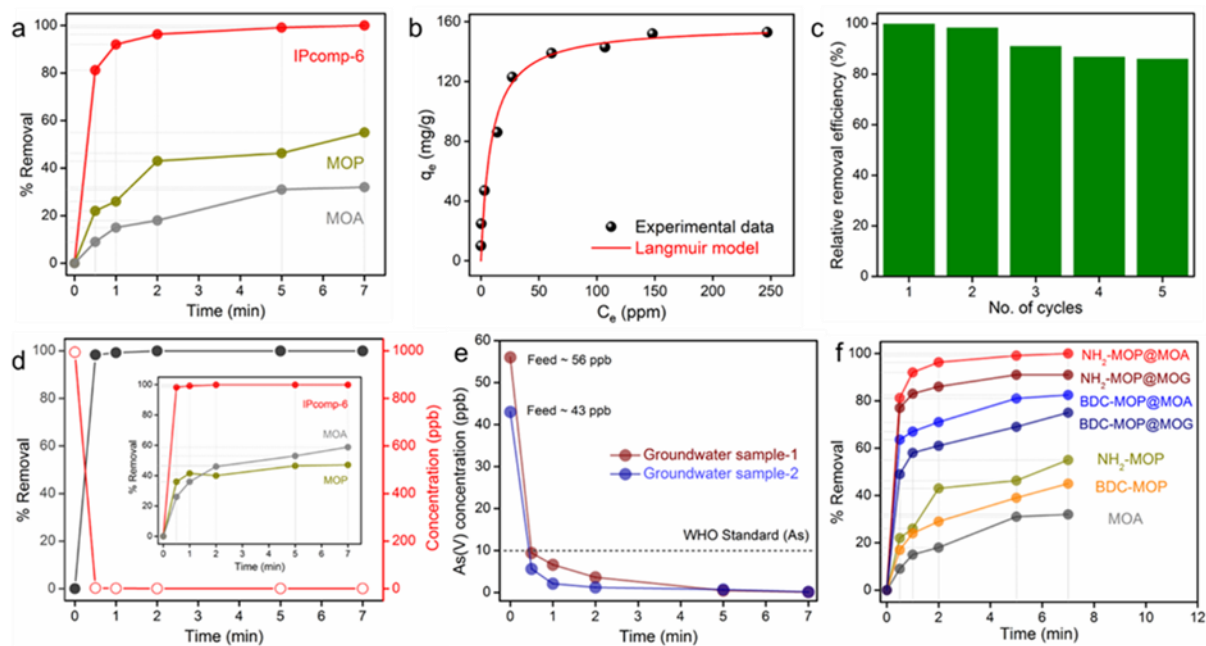


Figure 4.4 (a) Comparison of As(V) capture kinetics between IPcomp-6 and pristine MOP and MOA. (b) Adsorption isotherms of IPcomp-6 towards HAsO_4^{2-} uptake. (c) As(V) recyclable study of IPcomp-6. (d) Sorption kinetics study of low concentration (~ 1 ppm) of HAsO_4^{2-} by IPcomp-6 (inset: comparison of ~ 1 ppm As(V) removal studies between hybrid material and pristine compounds). (e) Arsenic removal study on natural ground water sample. (f) Comparison of As(V) capture studies between various composites and their respective pristine materials.

It is worthy to note, in literature, most of the reported oxoanions removal studies have been performed using high concentration samples only, and focused mostly on the removal kinetics along with exchange capacity (Appendix Tables 4.11-4.14). But scanty attention has been devoted to the selective and rapid extraction of oxoanions from very low concentration in presence of large excess concentration of other interfering anions, which is immensely important for real-time water-treatment application.^[51] Motivated by the excellent capture efficiencies of IPcomp-6 at high concentration, further, we sought to investigate the removal performance of the cationic nanotrap composite towards a very low concentration (~ 1 ppm) oxoanions contaminated water samples in presence of ~ 100 -fold other competitive nonmetal-based anions. In order to check the efficiency of the hybrid material to satisfy the current EPA standards for metal-based oxoanions in drinking water, a ~ 1000 ppb aqueous solution of HAsO_4^{2-} oxoanion was selected for capture and the lowering in the concentration was monitored through ICP-MS analysis. Within 1 min, the concentration of As(V) in the sample was found to be decreased to much below the permitted level in drinking water, set by WHO (Figure 4.4d). In

comparison, the pristine MOP and MOA compounds showed relatively less selective capture efficiencies towards As(V) even in low concentration (Inset: Figure 4.4d). Inspired from this, we performed the real, naturally polluted water treatment by IPcomp-6, taking arsenic-contaminated groundwater samples, collected from two well-known arsenic contamination affected areas (viz. Sample-1; Englishbazar, As, 43 ppb; and Sample-2; Kaliachalk block-I, As, 56 ppb from Malda, West Bengal, India).^[52,53] Notably, the hybrid aerogel demonstrated rapid elimination of As(V) from the drinking water samples to much below the EPA permitted level (10 ppb) (Figure 4.4e). These results promoted IPcomp-6 as a potential scavenger for the successful detoxification of hazardous oxoanions contaminated synthetic industrial water samples as well as natural drinking water samples.

Hereafter, to reveal the role of multifunctionalities of IPcomp-6 towards efficient oxoanion sorption performance, a comparative control study on As(V) capture has been performed using xerogel analogue (NH₂-MOP@MOG) of hybrid composite material (IPcomp-6) and non-amino functionalized MOP-based^[54] hybrid aerogel (BDC-MOP@MOA) and xerogel (BDC-MOP@MOG). The removal percentage of As(V) anions with contact time indicated that IPcomp-6 demonstrated highest removal efficiency, in comparison with other hybrid materials (Figure 4.4f). The overall removal efficiency order was found as, IPcomp-6 (NH₂-MOP@MOA) > NH₂-MOP@MOG > BDC-MOP@MOA > BDC-MOP@MOG (Figure 4.4f). In comparison to IPcomp-6, the relatively less sorption efficiency of BDC-MOP@MOA can be ascribed to the absence of amino functionality, which is potential for toxic oxoanion capture.^[43] On the other hand, the deduction in the removal efficiencies of xerogel-analogue composites might be attributed to the inexistence of macropores throughout its matrix, which are commonly present in the hybrid aerogels, that triggered the fast large mass diffusion of analytes.^[38, 55, 56] This result indicated the key role of both large hierarchical (nm to μm) porosity along with free amino functionality of IPcomp-6 over other hybrid cationic materials for excellent oxoanion sequestration capability in water. Again, the potential advantage of host-guest-based hybrid composite materials, constructed through “bottle-around-ship” encapsulation strategy was demonstrated by a comparison capture study over the composite material, prepared by physical mixing of MOPs and MOA or with post MOP loaded MOA composite material (Appendix 4.37). Taking advantage of the ultrafast capture efficiency of IPcomp-6 by its functionalized hierarchical porosity, we are encouraged to further performed the flow-through adsorption experiment by the nano-adsorbent packed column, towards arsenate with simulated-industrial and natural drinking water sample (Figure 4.5a, Appendix 4.39, appendix section 4.6.4).

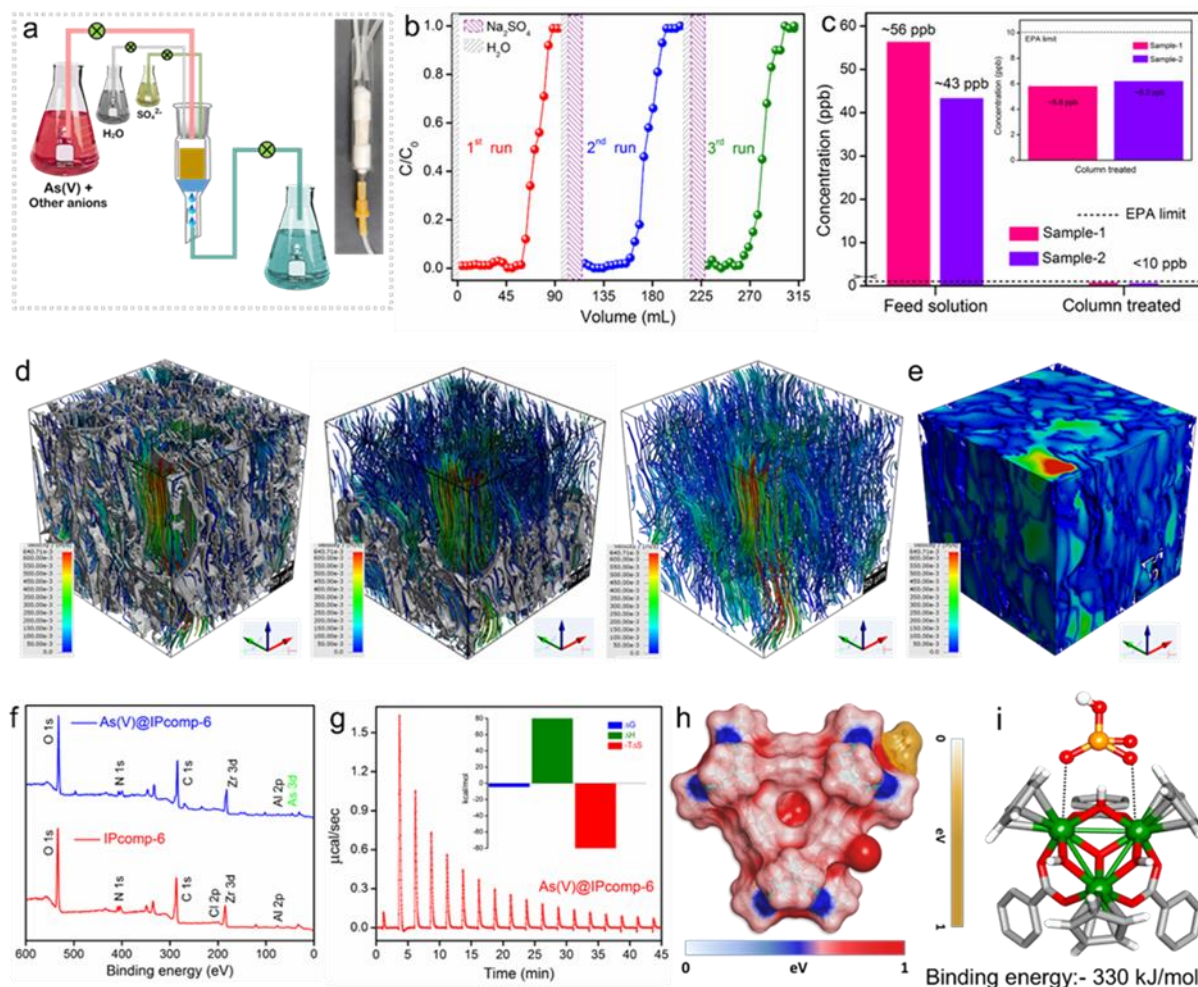


Figure 4.5 (a) Schematic diagram of dynamic column-exchange-based As(V) adsorption experiment. (b) Result of dynamic sorption-based recyclable As(V) capture. (c) Concentration decreases of As(V) in natural drinking water samples by column sorption experiment. (d, e) 3D Visualization of average flow-velocity inside the large pores of hybrid aerogel material with respective color-code. (f) XPS survey spectra of pristine and As(V) treated IPcomp-6. (g) ITC thermogram and thermodynamic parameter (inset) for injections of HAsO_4^{2-} titrated against IPcomp-6. (h, i) Energy optimized structure of interaction between HAsO_4^{2-} and Zr-SBU of the MOP shows the possible binding sites and the respective zoom view of the interaction sites.

For this typical experiment, ~ 19.8 ppm As(V) stock solution along with other interfering anions was passed through the hybrid aerogel fitted column with flow rate of 0.5 mL/min, and the concentration of the column eluted solution was measured by ICP-MS. Interestingly, almost 99% removal efficiency of As(V) was observed passing ~ 58.8 mL of arsenate solution (Figure 4.5b). Moreover, the regeneration ability of the column was investigated using saturated Na_2SO_4 solution that demonstrated significant

removal efficiency (~94.8%) in all the three cycles (Figure 4.5b). Further, the column successfully reduced the level of arsenate to far below the WHO set limit (10 ppb), when treated with toxic natural drinking water sample (Figure 4.5c). From the viewpoint of practical application, this result indicated the remarkable segregation efficiency of IPcomp-6 packed column towards As(V) in both environmental and industrial contaminated water. Such excellent selective separation capability of IPcomp-6 is believed to result from the cooperative effect of large macropores along with high surface area, presence of Zr-SBU, free -NH₂ group and exchangeable Cl⁻ ions of the overall nanocomposite.

Thereafter, following experiments and characterizations were carried out to support this probable mechanism. At first, to explore the role of interconnected large voids (macropores) of the hybrid aerogel towards efficient capture, the in-silico mass transport simulation was performed in the real 3D porous structure of hybrid aerogel, for an evidence-based prediction of dynamic events taken place during the water purification process (appendix section 4.6.4). Numerical simulator computes digital flow experiments in all three directions viz. X, Y and Z axis, using appropriate solver at 250 °C, 20 Pa pressure-drop, etc, and the outcome visualizes the average flow velocity profiles. Results of the numerical simulation process predicts the feasible average flow profiles through the inter-connected pore-structure of hybrid aerogel (Figure 4.5d, Appendix 4.40). The result indicated the average flow velocity in the X, Y and Z-directions are 1.42, 2.59 and 7.78 x 10⁻² m.s⁻¹, respectively. Such high mass-flow range in the hybrid aerogel exhibited the interconnected hierarchical pores, which significantly helps for the efficient sorption performance (Figure 4.5e). Thereafter, we further gain insight to the adsorption mechanism both by experimental and theoretical understanding. The retained structural integrity of the composite material was found from the identical PXRD analysis after the capture study (Appendix 4.41). In literature, Zr(IV)-SBU and amino functional groups are well explored for their selective oxoanions binding ability.^[43, 57, 58] Therefore, the cationic guest (NH₂-MOPs) in the composite material plays the key role for the selective oxoanion capture owing to its multifunctional properties. However, the pristine MOP molecules undergo unavoidable random self-aggregation,^[31] which make the functional groups inaccessible to interact with the oxoanions, subsequently, reduced the capture efficiency. Nevertheless, in case of hybrid composite, most of the nanosized MOPs are encapsulated separately in the mesoporous cavities of the host MOA matrix, which restricts the aggregation process and consequently exposed all the functional moieties towards efficient capture. Furthermore, detail XPS analysis, isothermal titration calorimetry (ITC) measurement, FT-IR and EDX-mapping (see appendix section 4.6.5) established the oxoanion sorption mechanism of IPcomp-6 by multiple functionalities, such as, oxoanions exchange with free Cl⁻ ions,^[44, 59] strong H-bonding between HAsO₄²⁻ and free -NH₂ group of MOP, and especially, optimum interaction with Zr-SBU (Figure 4.5f, 4.5g and Appendix 4.42-4.49).^[43, 58] Moreover such strong interaction between the oxoanions and MOPs of the composite was further validated by theoretical calculation using Density Functional Theory (DFT) simulation

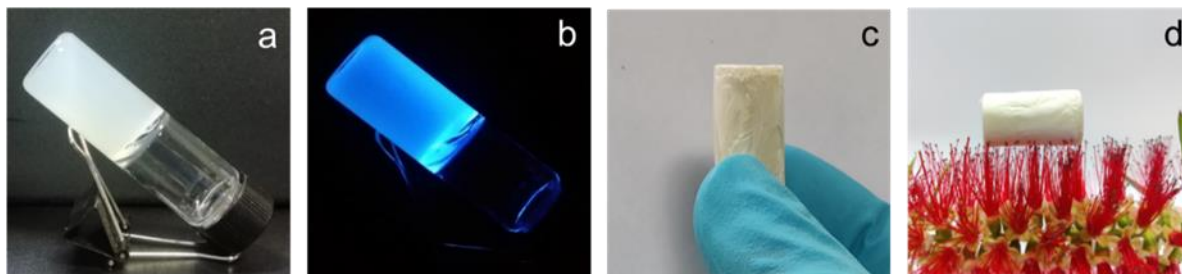
study, which support the experimental values (see appendix section 4.6.6) (Figure 4.5h, 4.5i and Appendix 4.50-4.53). The calculations showed that Zr(IV)-SBU of the MOPs selectively interacts with HAsO_4^{2-} at a binding energy -330 kJ/mol and other binding through a hydroxy group (OH^-) mediated interaction way. Additional interactions with relatively lower binding energies are presented in the supporting information file.

4.5 Conclusion

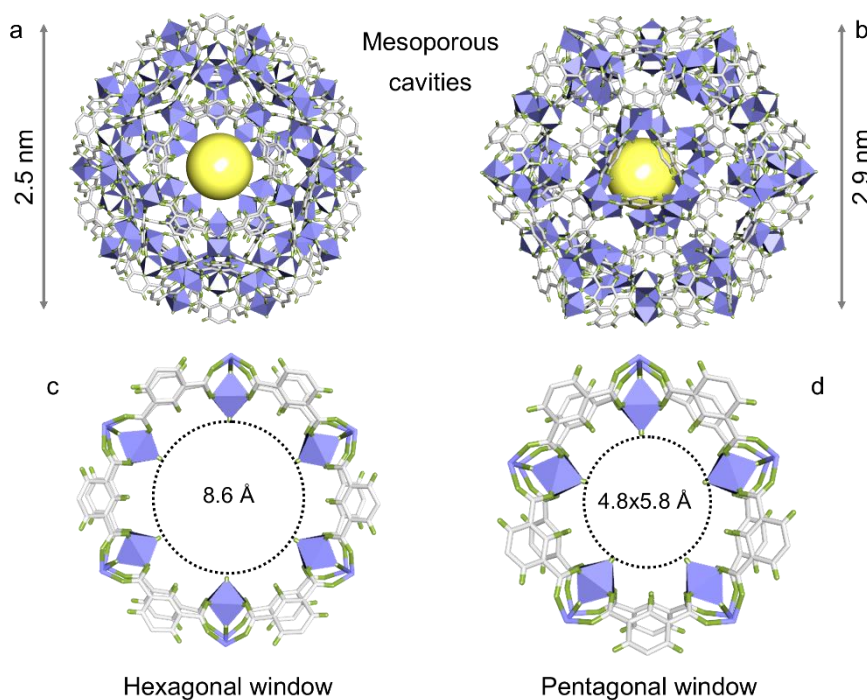
In conclusion, a successful demonstration of excellent chemical segregation performance towards a group of metal-based oxoanions has been conducted by synthesizing a unique efficient anion exchangeable hybrid composite material by encapsulating nanosized cationic MOPs in a hierarchical porous MOA matrix, utilizing “bottle-around-ship” strategy. The systematic structural and optical characterizations have been performed to elucidate the detailed insight of the hybrid aerogel material. The inter-connected large hierarchical porous composite matrix along with deliberately embedded Zr-SBU and free amino group-based discrete cationic nanotrap (MOP) exhibited a rapid and very selective, excellent sorption ability towards various oxoanions in water. Notably, the hybrid aerogel demonstrated a remarkable uptake performance especially towards HAsO_4^{2-} both in batch as well as dynamic column sorption method for simulated industrial waste water and natural ground water samples. An optimizing development of the hybrid material explored the multifunctional role towards fast, selective and recyclable adsorption capability, which render the material as a potential adsorbent for continuous wastewater treatment application. We believe that the present finding i.e.; efficient chemical separation with the hybrid aerogel material can pave the way to the development of a variety of promising materials for efficient water remediation application.

4.6 Appendix Section

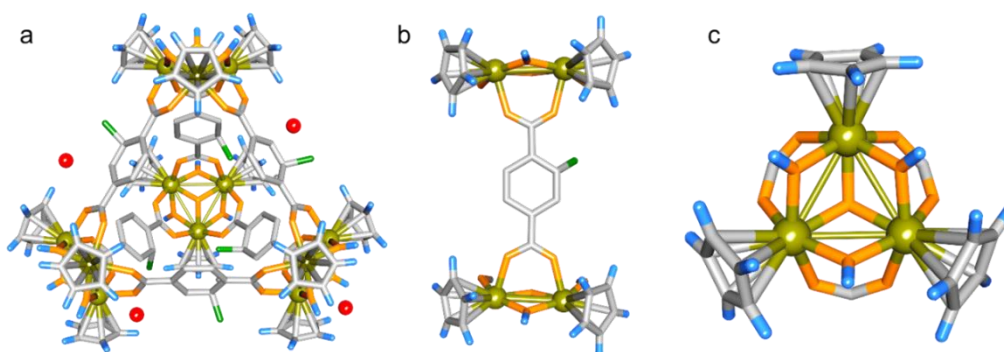
Appendix Section-4.6.1: Structural characterization of materials



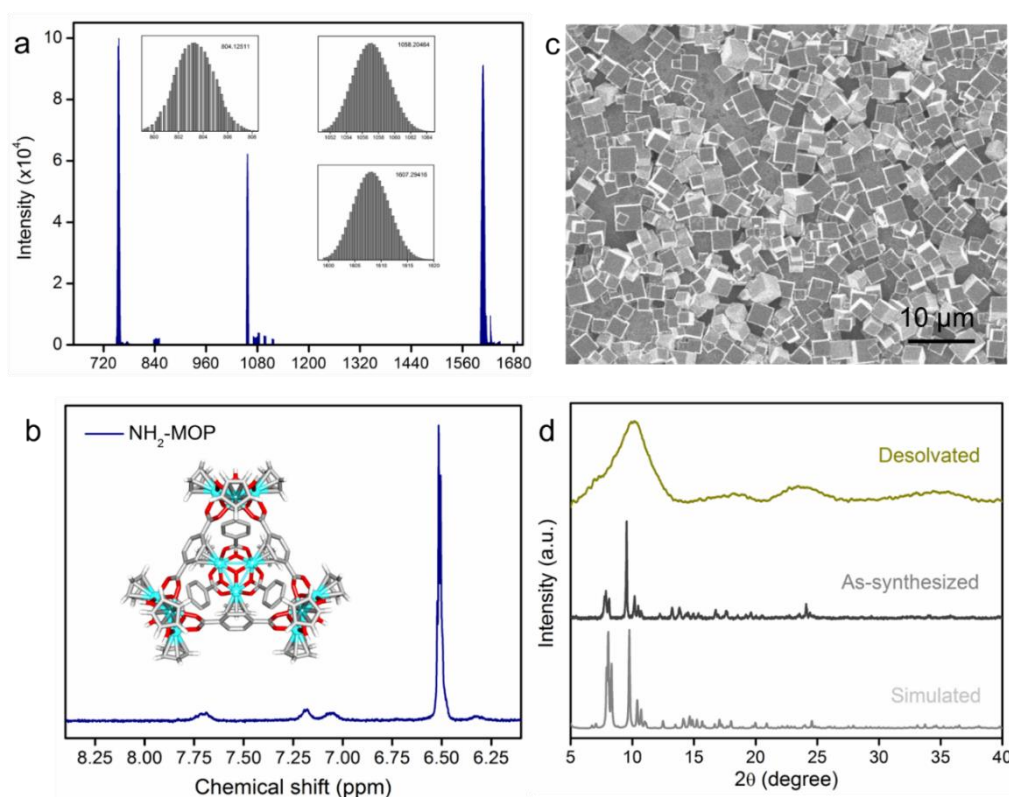
Appendix 4.1: Digital images of hybrid composite material. (a) The as-synthesized wet-gel of IPcomp-6. (b) Luminescent nature of the hybrid composite material. (c) Hybrid aerogel material (IPcomp-6). (d) Light weight nature of the hybrid aerogel material.



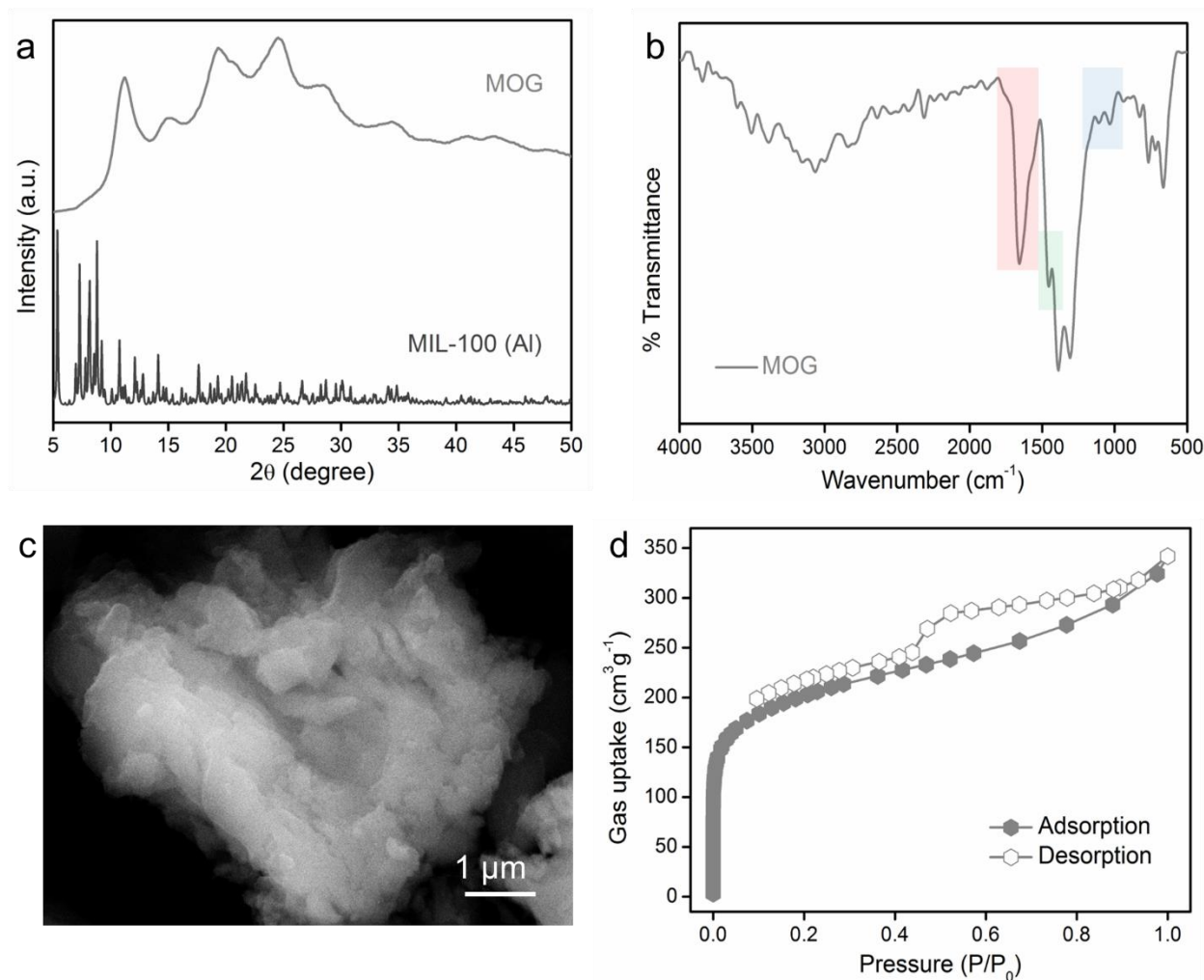
Appendix 4.2: Structural features of the metal-organic gel, MOG(Al): (a, b) Two different types of mesoporous cages exist in the framework structure of the MOG. (c, d) Hexagonal and pentagonal windows of the mesoporous cavities of the MOG.



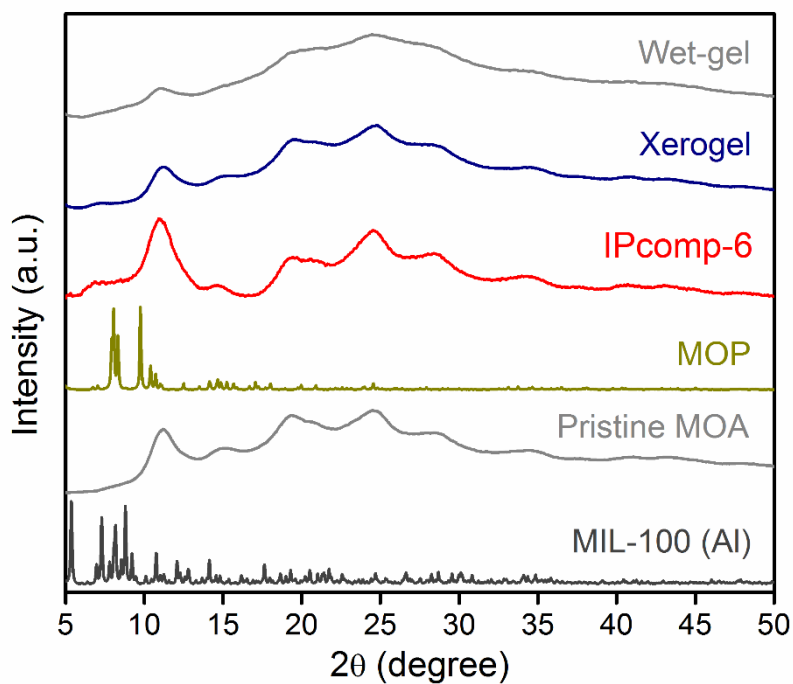
Appendix 4.3: Structural features of the (a) Zr(IV)-based amino functionalized metal-organic polyhedra (MOPs). (b) Organic linker, (c) Zr(IV)-based secondary building unit (SBU) of the MOP.



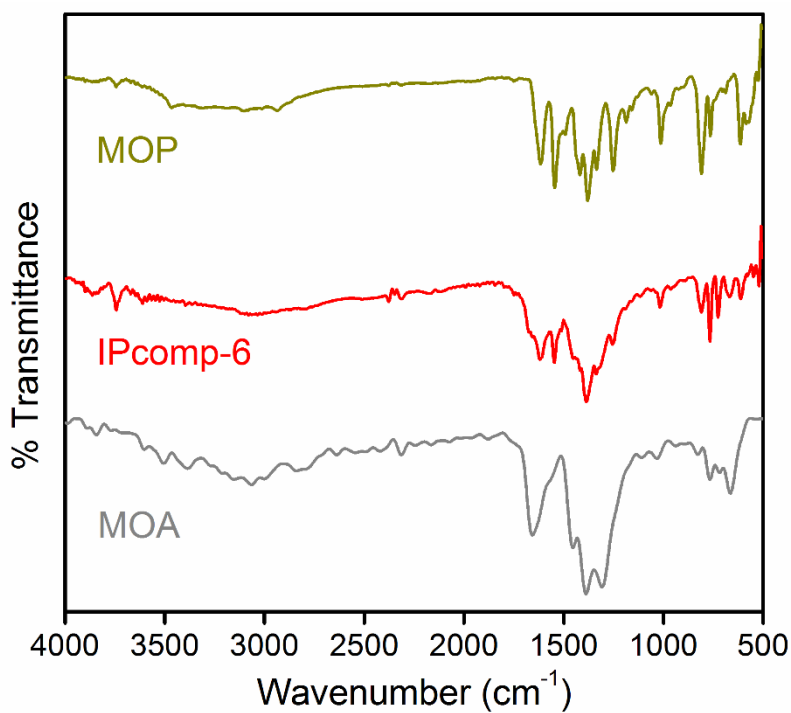
Appendix 4.4: Structural characterization of the metal-organic polyhedra (MOPs): (a) ESI-TOF-MS analysis of as-synthesized NH₂-MOP, indicated the formation of the MOPs. (b) ¹H NMR spectra of the NH₂-MOPs in MeOD and D₂O. (c) FESEM image of the MOPs, indicated highly cubic microcrystalline morphology. (d) PXRD analysis of the NH₂-MOP indicated formation of bulk phase purity of the MOP in as-synthesized phase, also the PXRD data of the desolvated phase showed the weak crystalline nature of the MOPs, which is cause of self-aggregation upon desolvation.



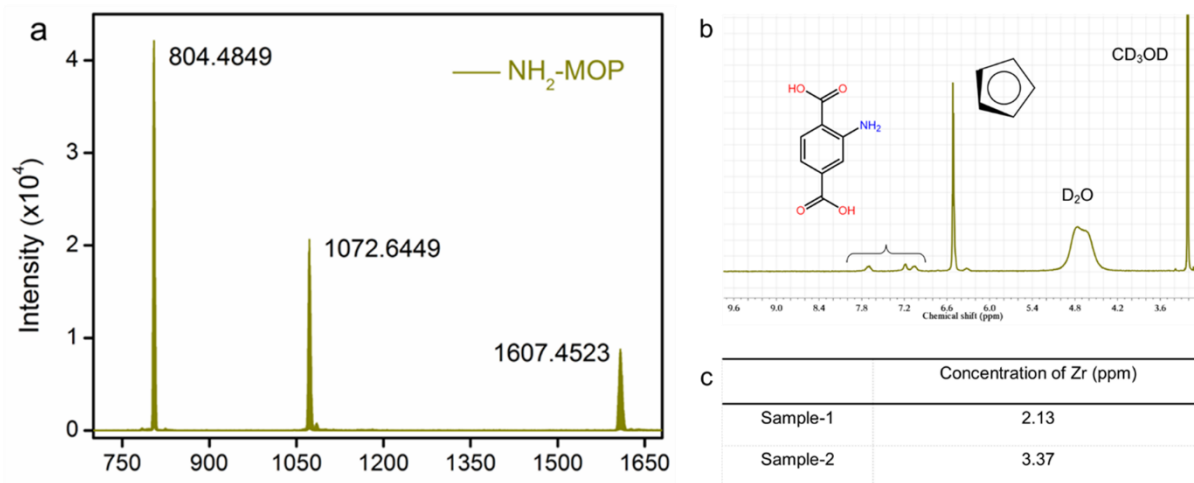
Appendix 4.5: Structural characterization of the metal-organic gel: (a) PXRD pattern of simulated MIL-100(Al) MOF and as-synthesized MOG. (b) FT-IR spectra of the MOG show the characteristic peaks corresponding to relevant frequencies [(C=C), (C=O), (Al-O)]. (c) FESEM image of the pristine MOA. (d) Nitrogen gas adsorption-desorption measurement at 77K of the MOG, suggested the existence of hierarchical (meso and micro) porosity. (MOG = metal-organic xerogel, MOA = metal-organic aerogel).



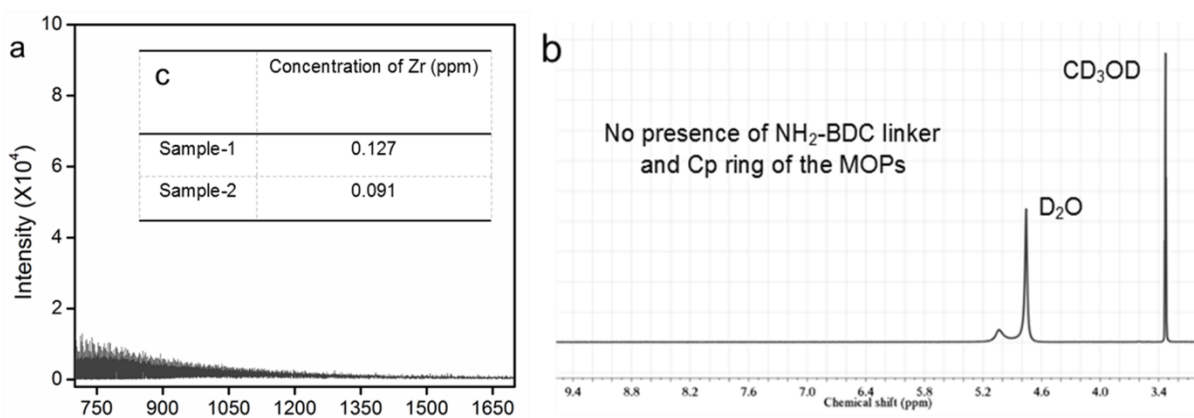
Appendix 4.6: PXRD pattern of IPcomp-6, along with simulated MIL-100(Al) MOF, as-synthesized MOA, MOP, hybrid xerogel and hybrid wet-gel material.



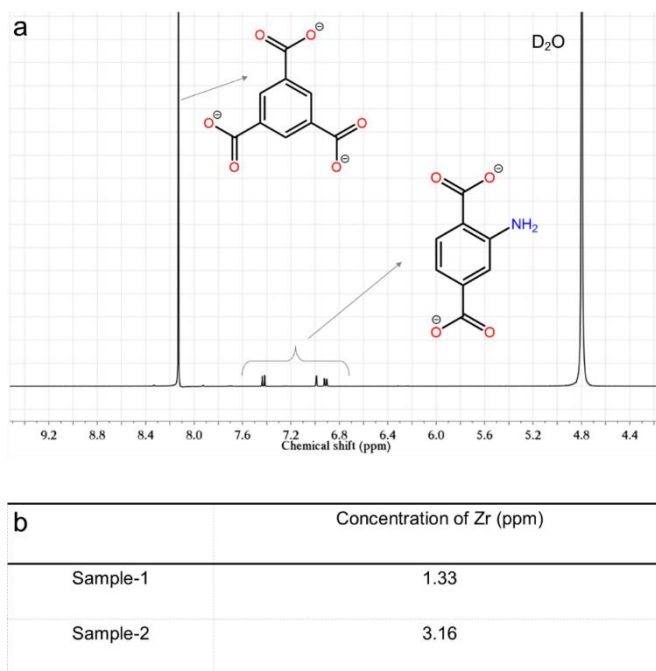
Appendix 4.7: FT-IR spectra of IPcomp-6, along with pristine MOA and MOP.



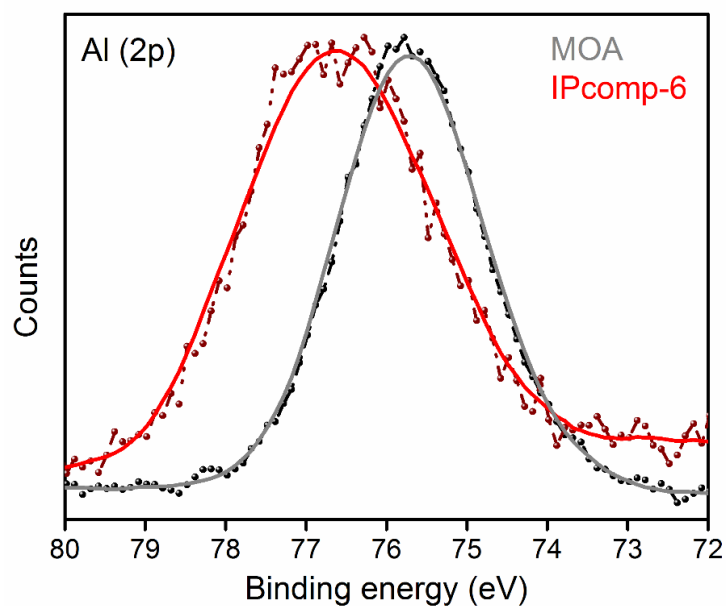
Appendix 4.8: Characterizations of the MOPs before washing the hybrid material: (a) HRMS spectra of MOPs, (b) ^1H NMR spectra of MOPs in MeOD, D_2O mixture, (c) ICP analysis of Zr(IV) metal in the supernatant of hybrid material exposed to aqueous methanolic solution.



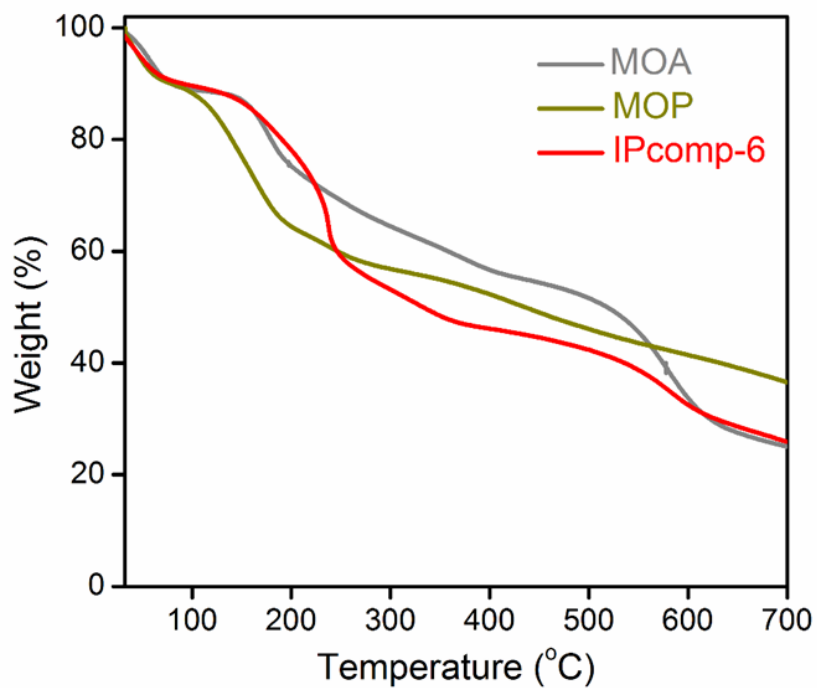
Appendix 4.9: Characterizations of the MOPs after washing the hybrid material: (a) HRMS spectra of MOPs, (b) ^1H NMR spectra of MOPs, (c) ICP analysis of Zr(IV) metal in the supernatant of hybrid material exposed to aqueous methanolic solution. These results suggested that no existence of MOPs on the surface of the MOA as well as no leaching of MOPs from the mesoporous cages of the MOA matrix could be detected by both mass-spectroscopy and ^1H NMR.



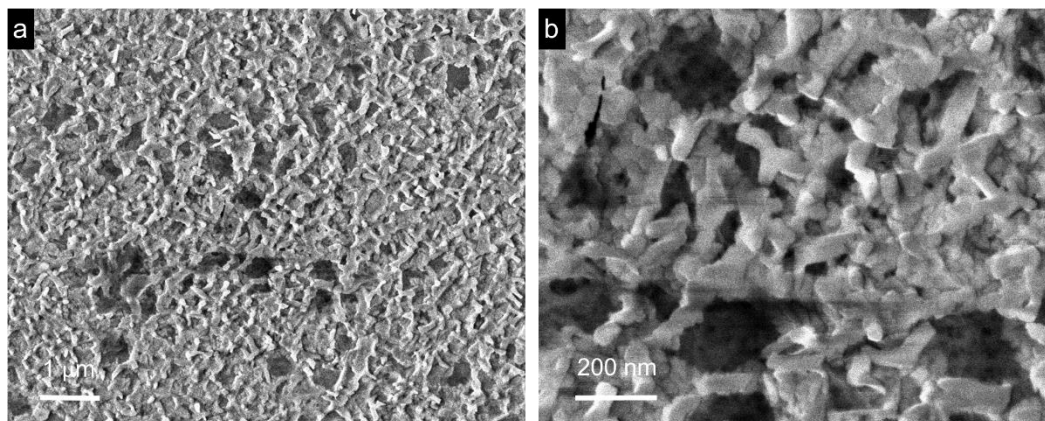
Appendix 4.10: Characterizations of the digested sample of the composite: (a) ^1H NMR spectra of the respective organic linkers of MOA and MOPs, in NaOD/D₂O solvent. (b) ICP analysis of Zr(IV) metal in the supernatant of the digested hybrid material.



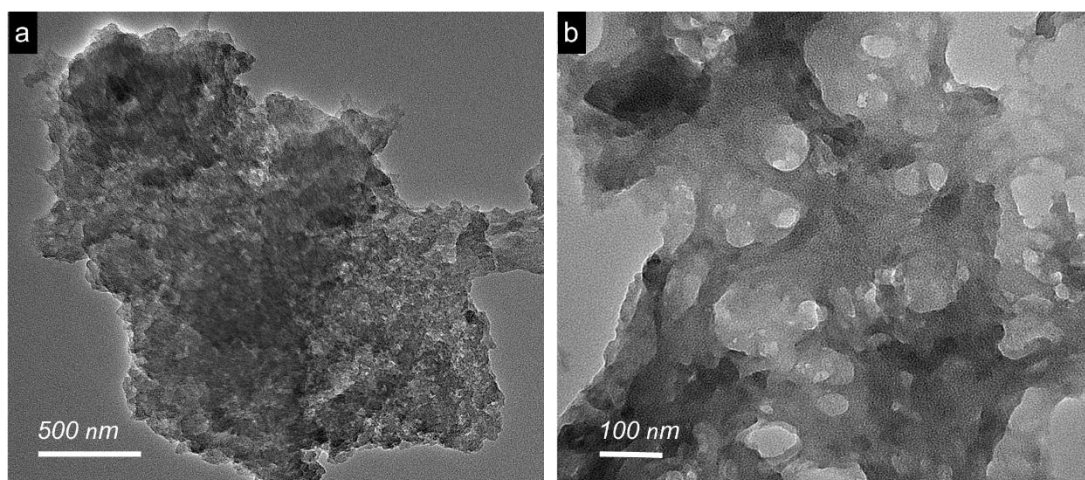
Appendix 4.11: XPS spectra of Al 2p of pristine MOA and IPcomp-6.



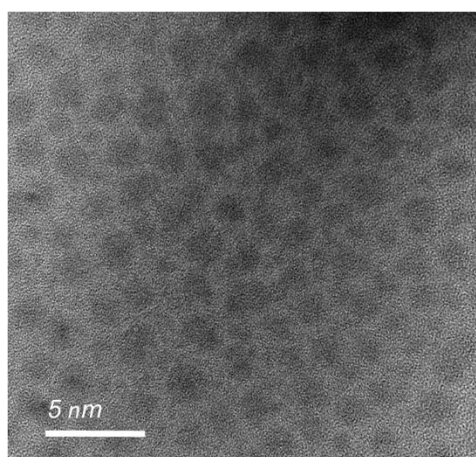
Appendix 4.12: TGA profile of IPcomp-6 along with pristine MOP and MOA.



Appendix 4.13: SEM analyses of the hybrid aerogel (IPcomp-6) showing interconnected nanoparticles of the gel materials, (a) 1 μm , (b) 200 nm. (The numerical values represent the scale bars of the images).

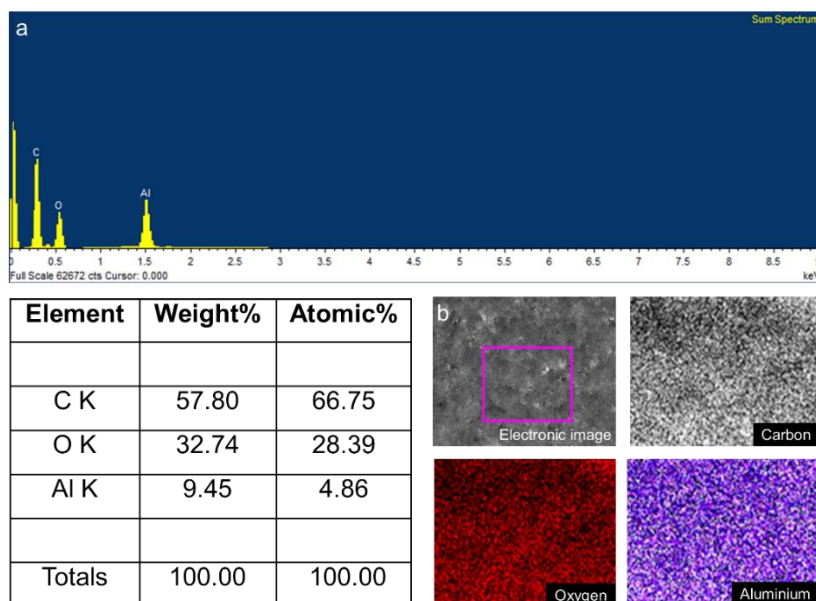


Appendix 4.14: TEM analyses of the hybrid aerogel (IPcomp-6) confirm the existence of interconnected nanoparticles of the gel matrix. (a) 500 nm, (b) 100 nm. (The numerical values represent the scale bars of the images).



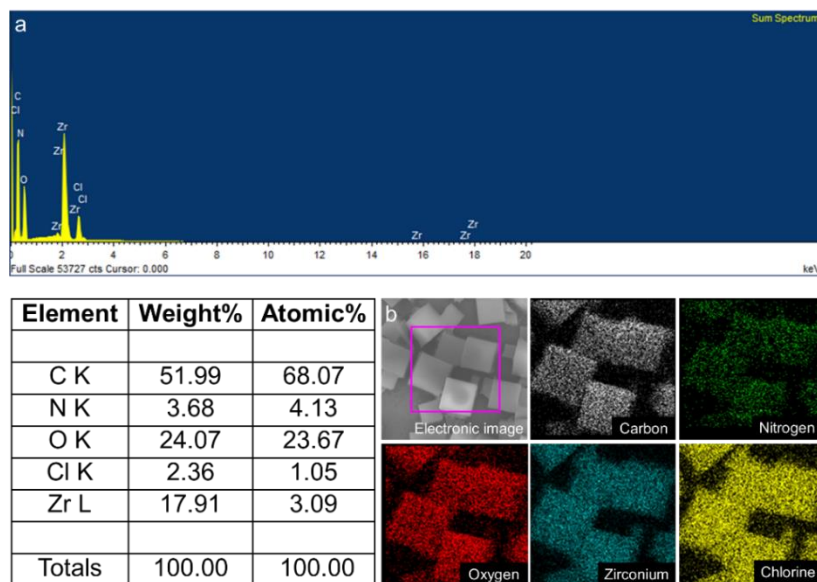
Appendix 4.15: HRTEM analyses of the hybrid aerogel (IPcomp-6) confirm the presence of dispersed nanoparticles of MOPs into the MOA matrix.

Appendix Table 4.1: EDX elemental analyses from FESEM experiment of pristine gel compound showing presence of C, O and Al elements (a).



Appendix 4.16: SEM elemental mapping analyses of pristine gel compound (b).

Appendix Table 4.2: EDX elemental analyses from FESEM experiment of NH₂-MOP molecules showing presence of C, N, O, Cl and Zr elements (a).



Appendix 4.17: SEM elemental mapping analyses of NH₂-MOP molecules (b).

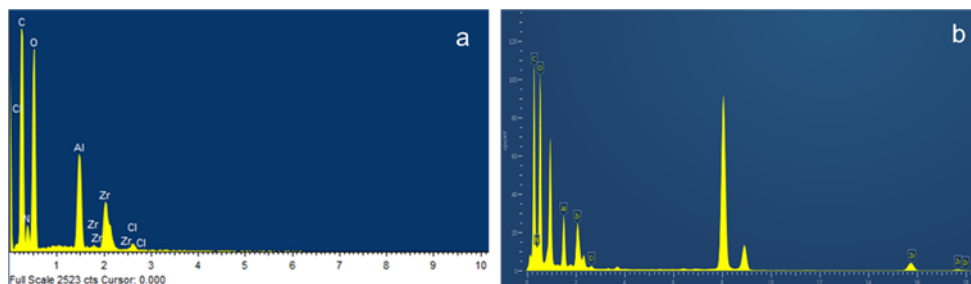
Appendix Table 4.3: EDX elemental analyses from FESEM experiment of hybrid composite, constructed with ~5 mg of MOPs showing presence of C, N, O, Al, Cl and Zr elements.

Element	Weight%	Atomic%
C K	47.87	49.27
N K	9.47	8.29
O K	24.08	28.75
Al K	14.08	12.27
Cl K	0.59	0.34
Zr L	3.91	1.08
Totals	100.00	100.00

Appendix Table 4.4: EDX elemental analyses from FESEM experiment of hybrid composite, constructed with ~25 mg of MOPs showing presence of C, N, O, Al, Cl and Zr elements.

Element	Weight%	Atomic%
C K	44.59	53.98
N K	11.13	9.52
O K	23.77	21.65
Al K	14.18	12.35
Cl K	0.97	0.61
Zr L	5.36	1.89
Totals	100.00	100.00

Appendix Table 4.5: EDX elemental analyses from (a) FESEM and (b) TEM experiment of IPcomp-6, constructed with ~45 mg of MOPs showing presence of C, N, O, Al, Cl and Zr elements.

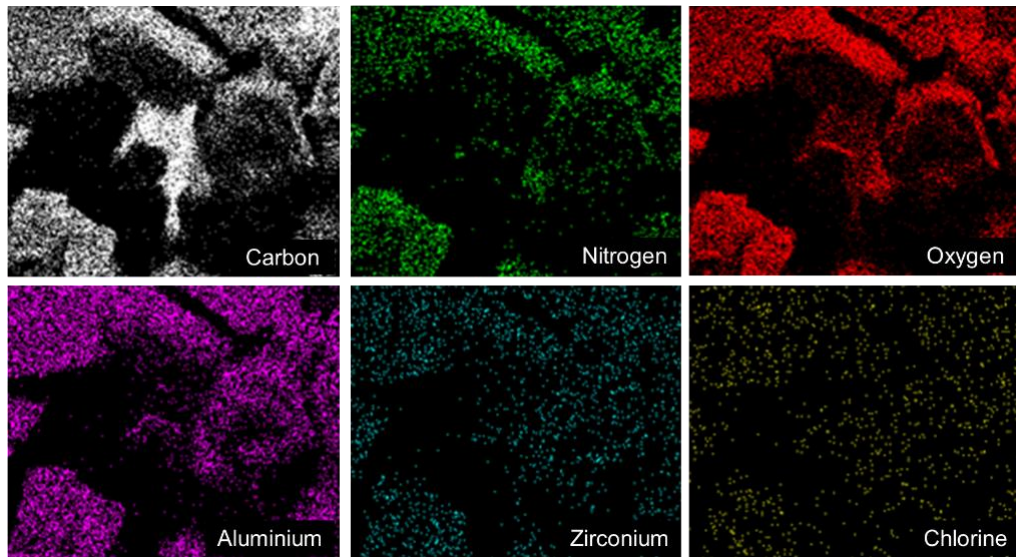


Element	Weight%	Atomic%
C K	40.63	46.22
N K	9.27	10.15
O K	22.59	26.75
Al K	18.37	13.42
Cl K	1.01	0.85
Zr L	8.13	2.61
Totals	100.00	100.00

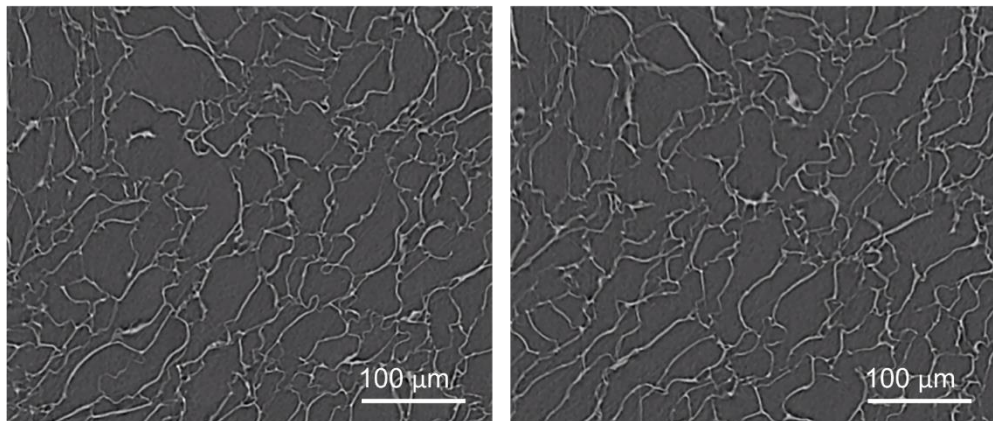
Element	Weight%	Atomic%
C	55.4	62.79
N	6.56	4.67
O	25.19	24.55
Al	9.8	7.36
Cl	0.69	0.15
Zr	2.36	0.48
Totals	100.00	100.00

Appendix Table 4.6: EDX elemental analyses from FESEM experiment of hybrid composite, constructed with ~80 mg of MOPs showing presence of C, N, O, Al, Cl and Zr elements.

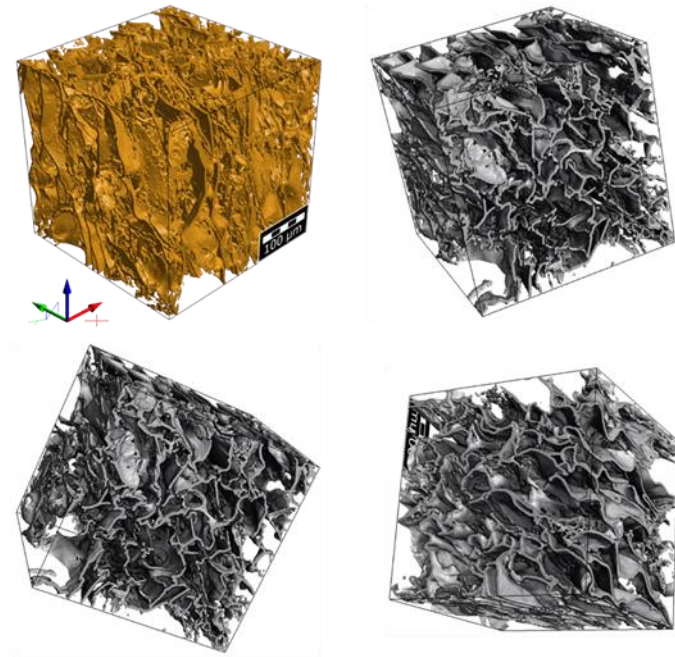
Element	Weight%	Atomic%
C K	36.71	44.9
N K	8.83	9.74
O K	19.36	28.19
Al K	17.91	12.24
Cl K	2.48	1.19
Zr L	14.71	3.74
Totals	100.00	100.00



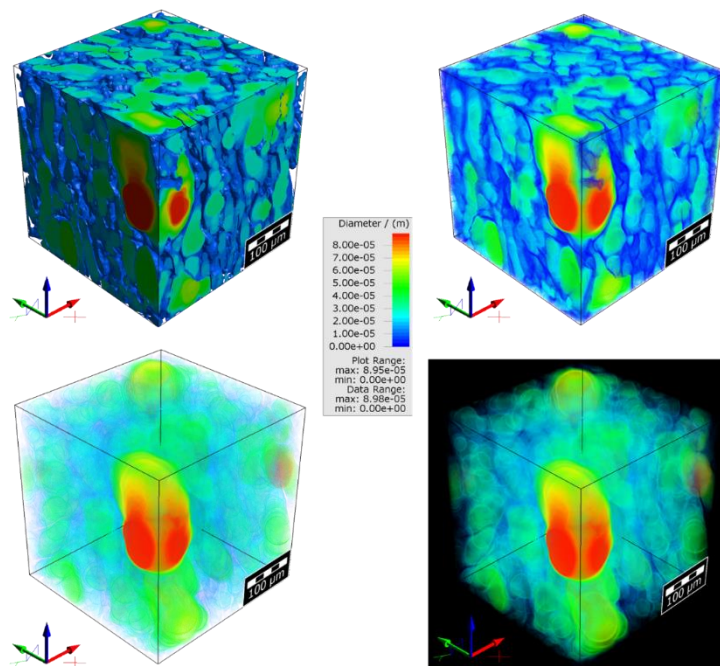
Appendix 4.18: SEM elemental mapping of IPcomp-6 composite material indicated homogeneous distribution of all relevant elements.



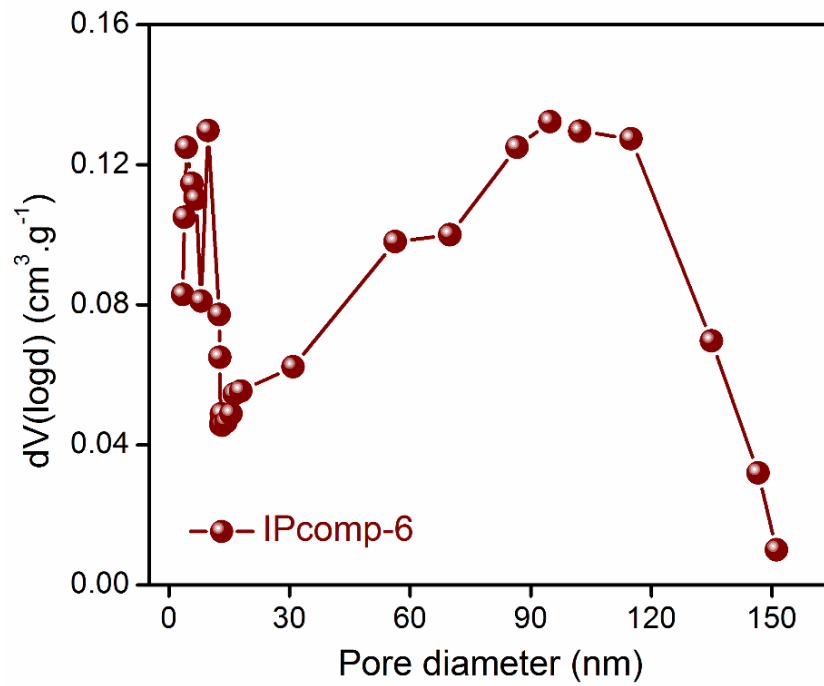
Appendix 4.19: Two-dimensional cross-sectional tomography images of IPcomp-6 showing the large macropores distributed throughout the matrix.



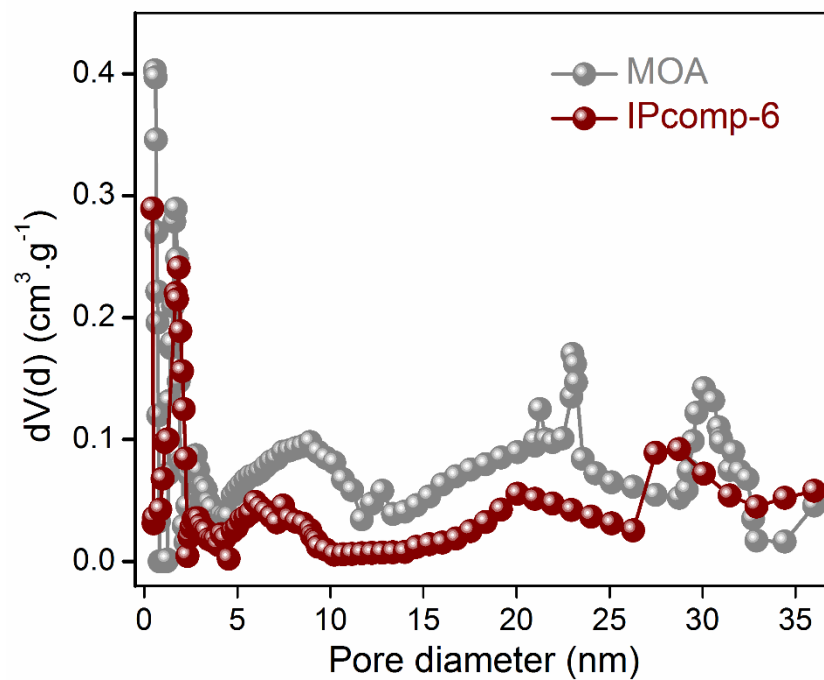
Appendix 4.20: Computed X-ray tomographic 3D image of IPcomp-6 showing the large macropores distributed throughout the matrix.



Appendix 4.21: Visualization of color-coded pore size distribution from tomography images of IPcomp-6 showing the large macropores distributed throughout the matrix.

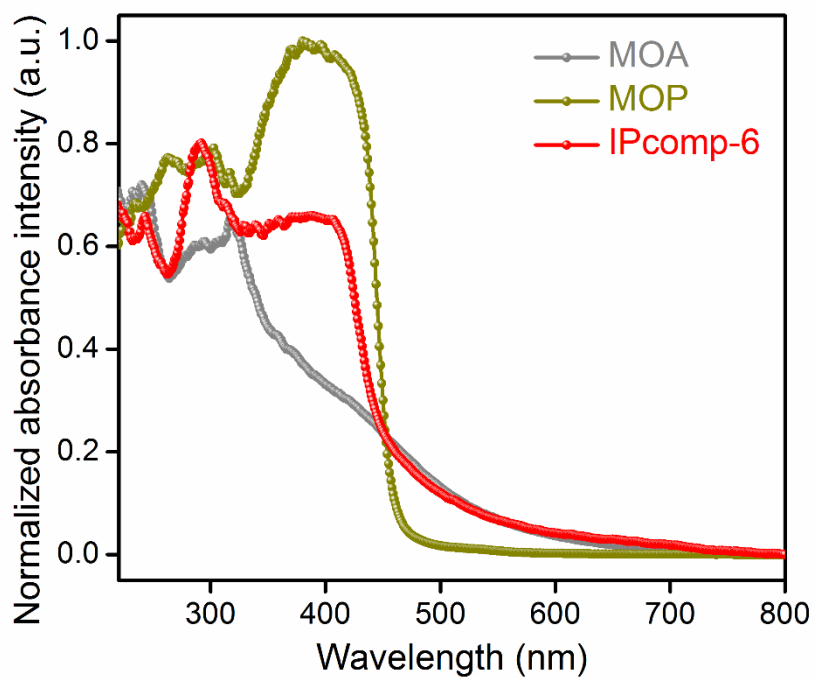


Appendix 4.22: Pore size distributions of IPcomp-6 calculated in Barrett-Joyner-Halenda (BJH) method.

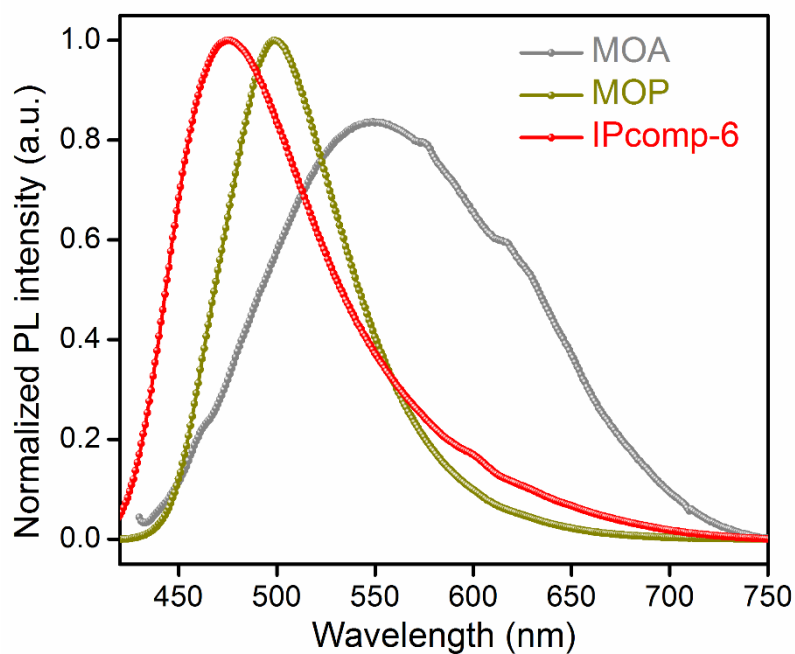


Appendix 4.23: Pore size distributions of IPcomp-6 and pristine MOA based on 77K N₂ sorption data.

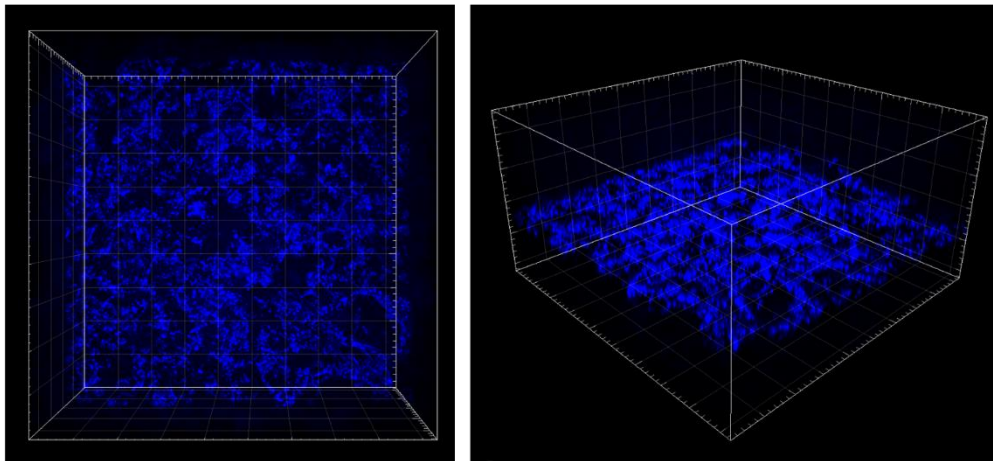
Appendix Section-4.6.2: Optical characterization and mechanical strength



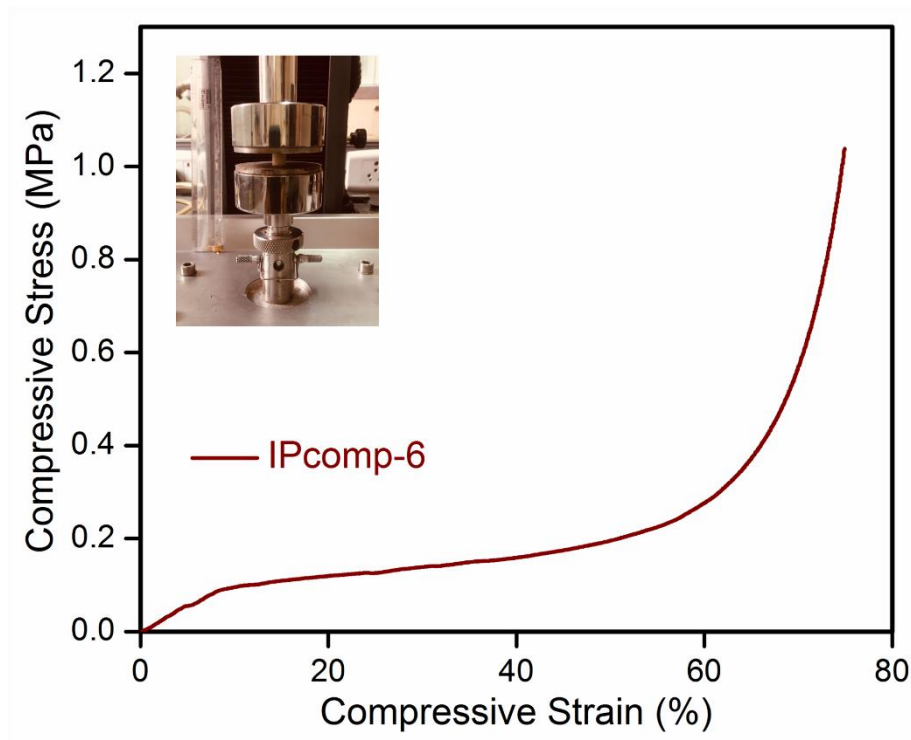
Appendix 4.24: Solid-state UV-vis spectra of IPcomp-6, along with pristine MOP and MOA.



Appendix 4.25: Solid-state photoluminescence spectra of IPcomp-6, along with pristine MOP and MOA.

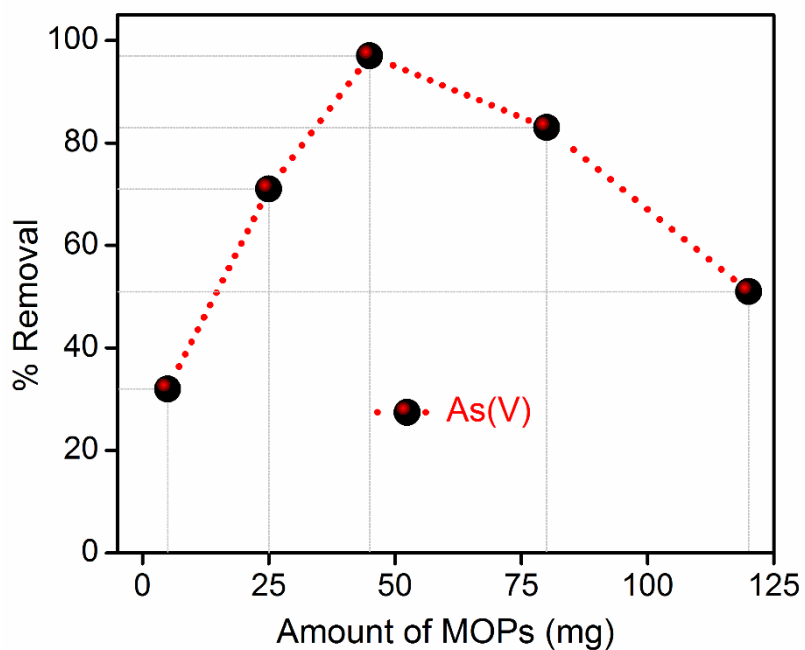


Appendix 4.26: Confocal 3D fluorescence images of IPcomp-6 showing existence of large pores throughout the hybrid matrix.



Appendix 4.27: Compressive stress-strain curves of the hybrid aerogel show promising mechanical stability. The hybrid aerogel shows compressive stress as 1039 ± 39 KPa and strain as $75 \pm 4\%$.

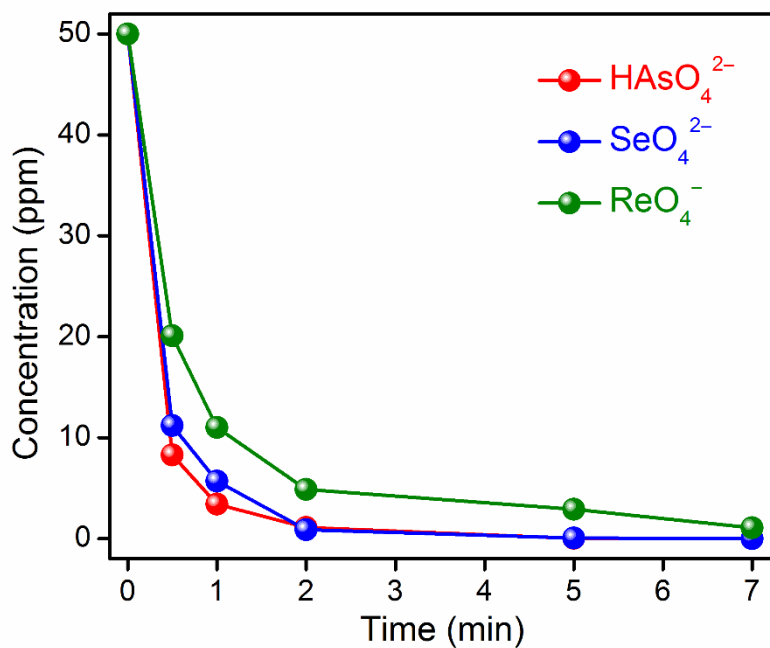
Appendix Section-4.6.3: Capture studies



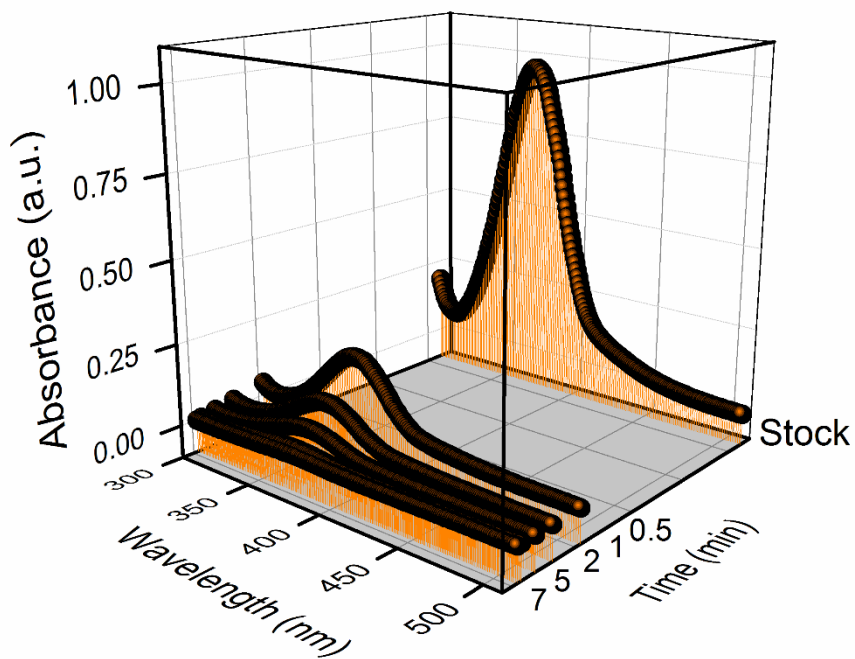
Appendix 4.28: An optimization study of As(V) capture, using different amounts of guest-MOP molecules in the hybrid materials exhibiting, hybrid material constructed by ~45 mg MOPs showed highest removal efficiency. [Condition: initial As(V) concentration = ~50 ppm, adsorbent amount = 5 mg, contact time = 5 min]

Appendix Table 4.7: Sorption kinetics data for As(V) uptake by different amount of MOPs containing hybrid composite materials.

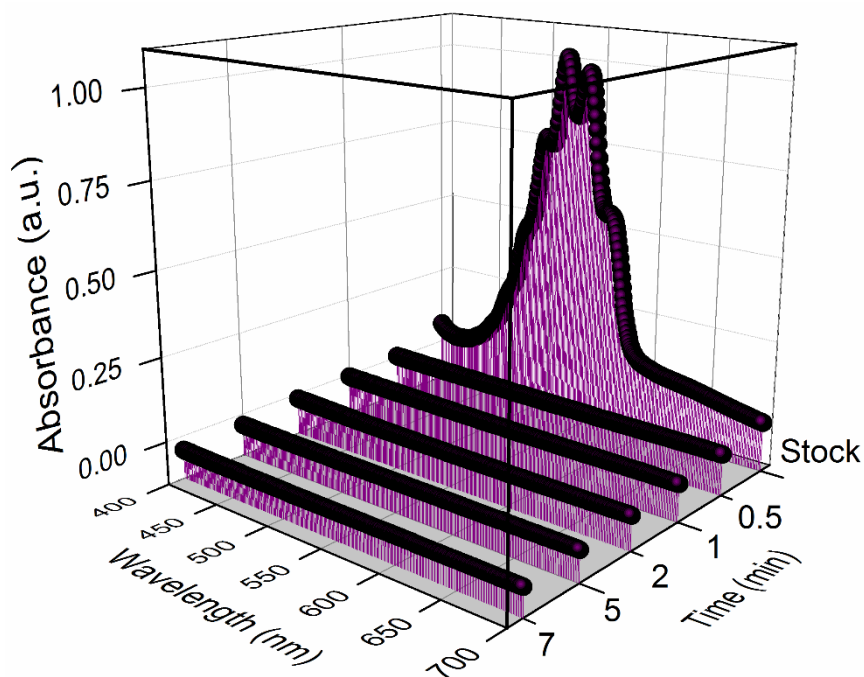
MOPs	Time (min)	C_o (ppm)	C_f (ppm)	% Removal
5 mg	5 min	43.6	29.29	32.8
25 mg	5 min	43.6	12.64	71
45 mg	5 min	43.6	0.78	98.2
80 mg	5 min	43.6	7.36	83.1
120 mg	5 min	43.6	20.92	52



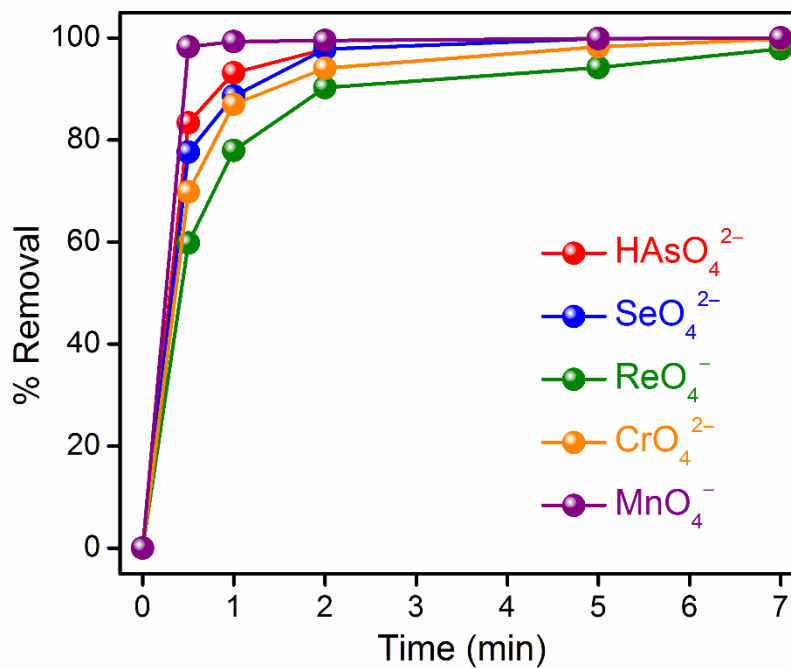
Appendix 4.29: ICP analyses of decrease in the concentration of As(V), Se(VI) and Re(VII) by IPcomp-6.



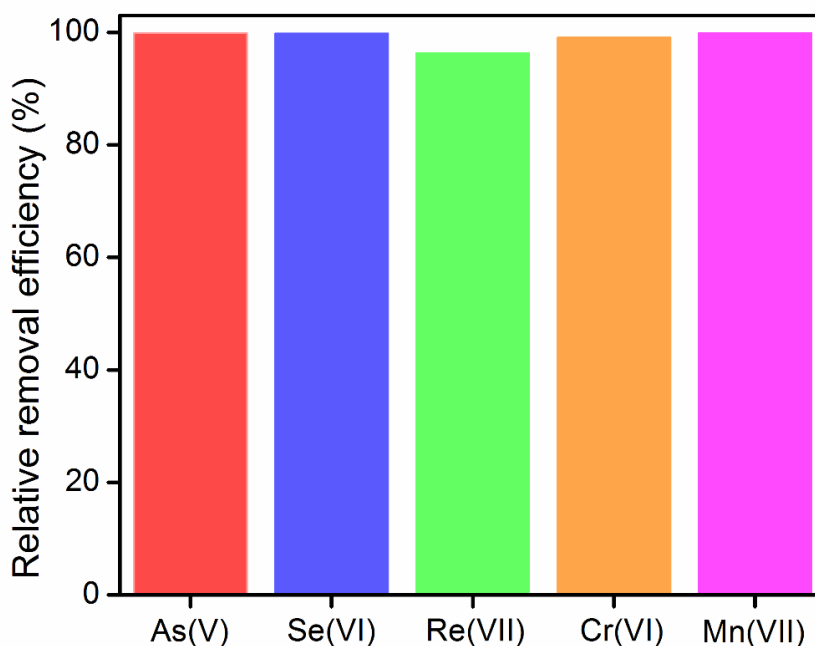
Appendix 4.30: UV-vis spectra of Cr(VI) solution showing rapid dismissing by the treatment of IPcomp-6.



Appendix 4.31: UV-vis spectra of Mn(VII) solution showing rapid disappearing by the treatment of IPcomp-6.



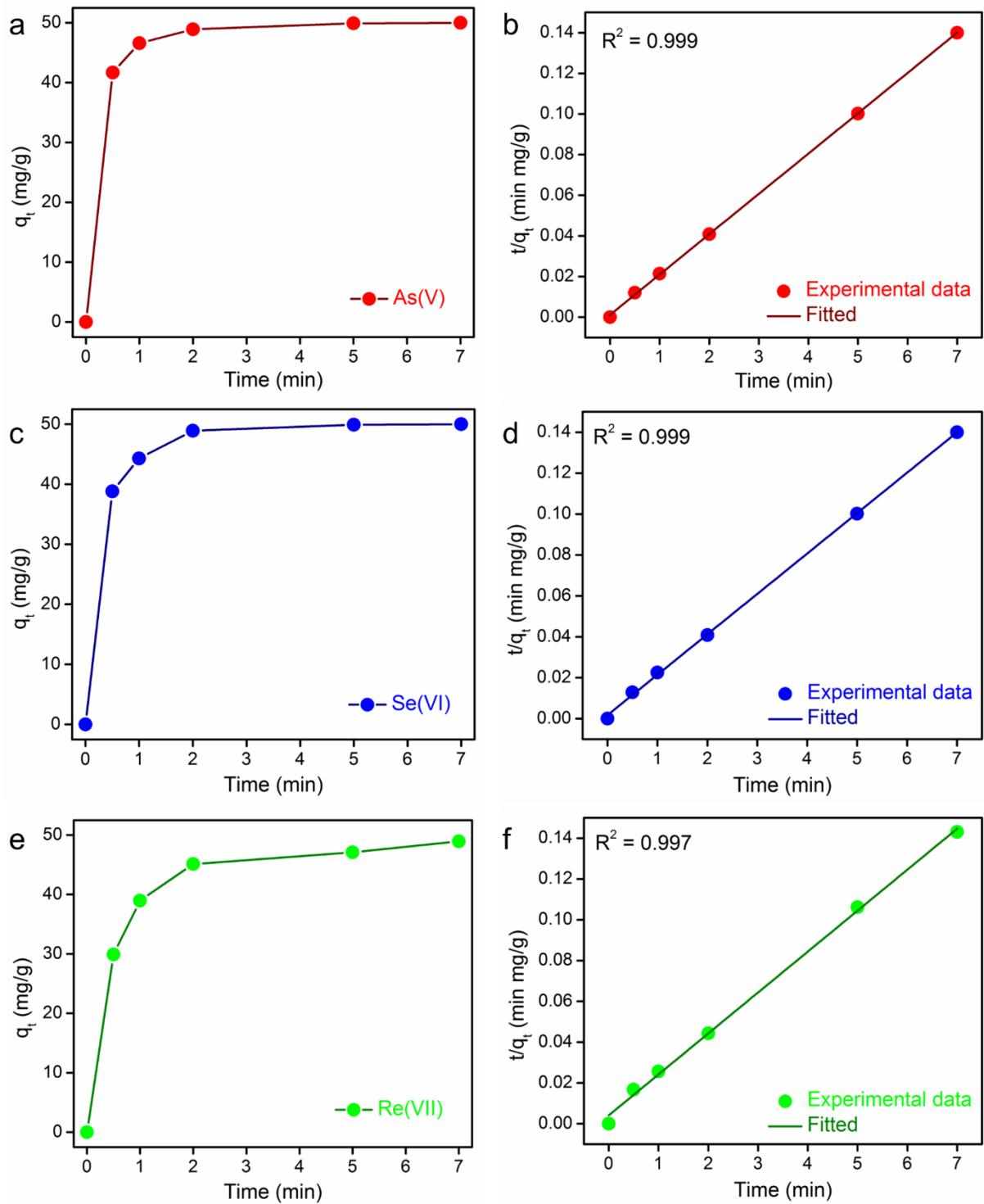
Appendix 4.32: Removal % with contact time: As(V), Se(VI), Re(VII), Cr(VI) and Mn(VII) oxoanions removal profile by IPcomp-6.



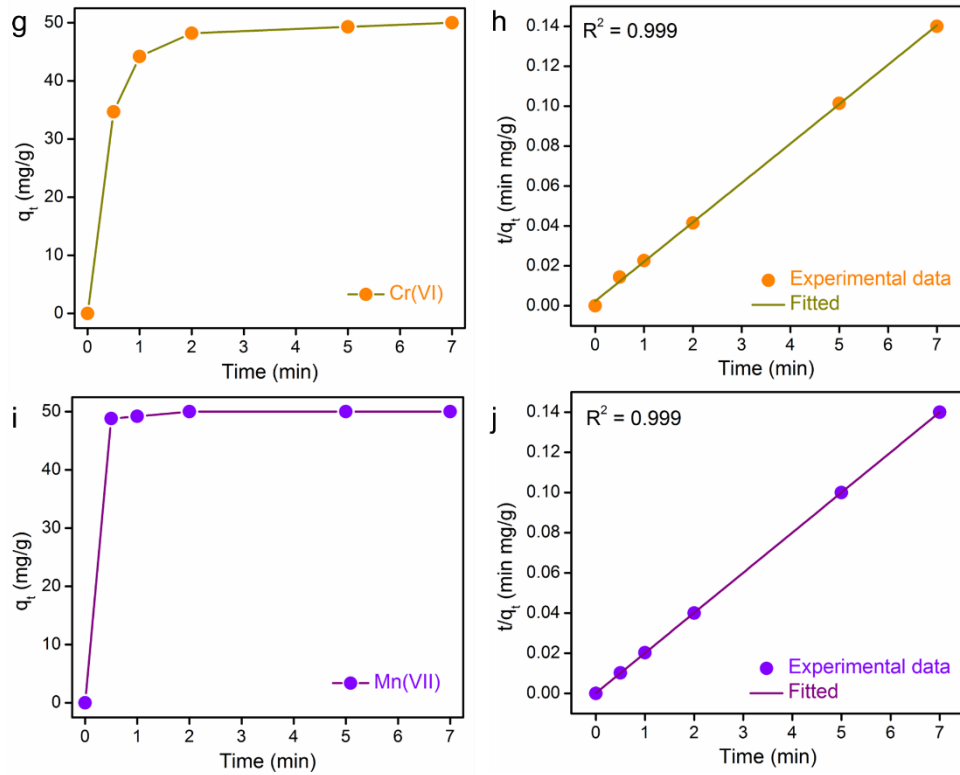
Appendix 4.33: Relative % removal efficiencies for different oxoanions by IPcomp-6, within contact time of 5 min.

Appendix Table 4.8: Sorption kinetics data from ICP measurement for uptake of As(V) by IPcomp-6.

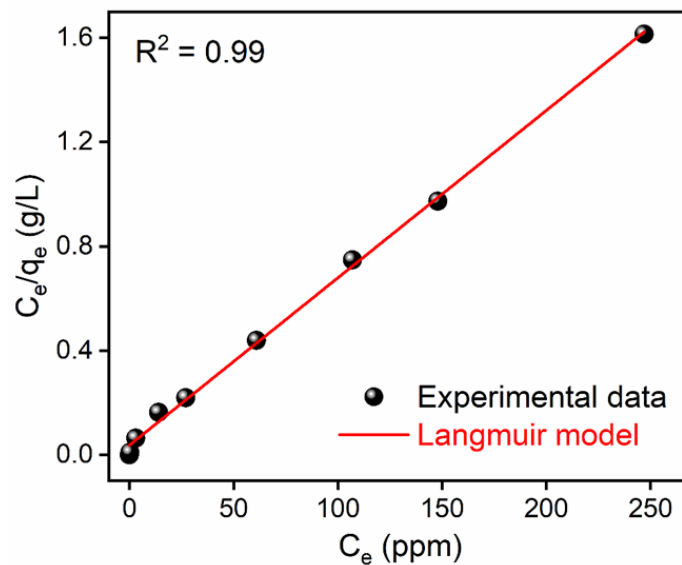
C_o (ppm)	Time (t) (min)	C_f (ppm)	% Removal	K_d (mL/g)	q_t (mg/g)
50.6	0	50.6	0	0	0
	0.5	9.41	81.42	4.37×10^3	41.19
	1	3.98	92.13	1.17×10^4	46.62
	2	1.79	96.46	2.72×10^4	48.81
	5	0.06	99.86	8.42×10^5	50.54
	7	N.D.	>99.99	5.06×10^6	50.60



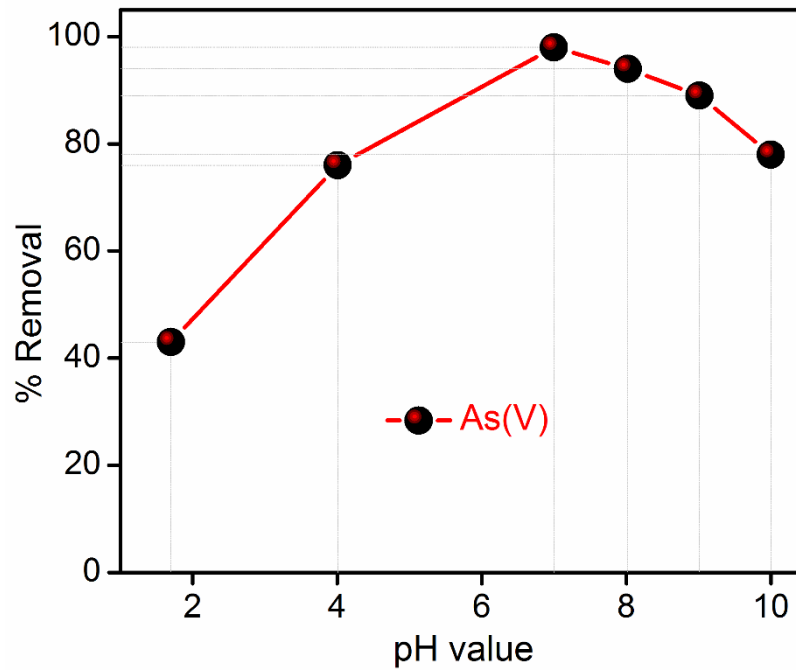
Appendix 4.34a: Sorption capacity with time and Pseudo-second-order model fitting for different oxoanions: (a, b) As(V), (c, d) Se(VI), (e, f) Re(VII).



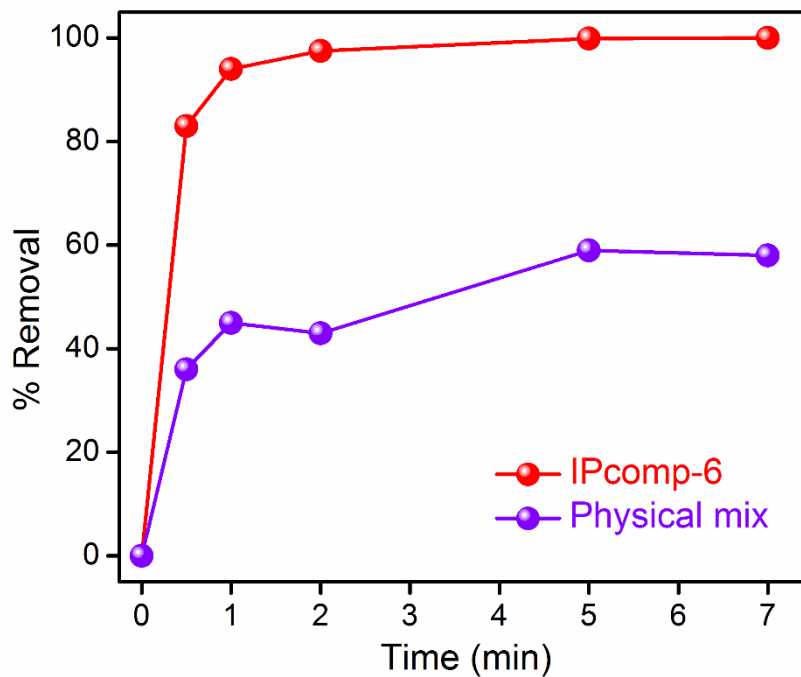
Appendix 4.34b: Sorption capacity with time and Pseudo-second-order model fitting for different oxoanions: (g, h) Cr(VI) and (i, j) Mn(VII).



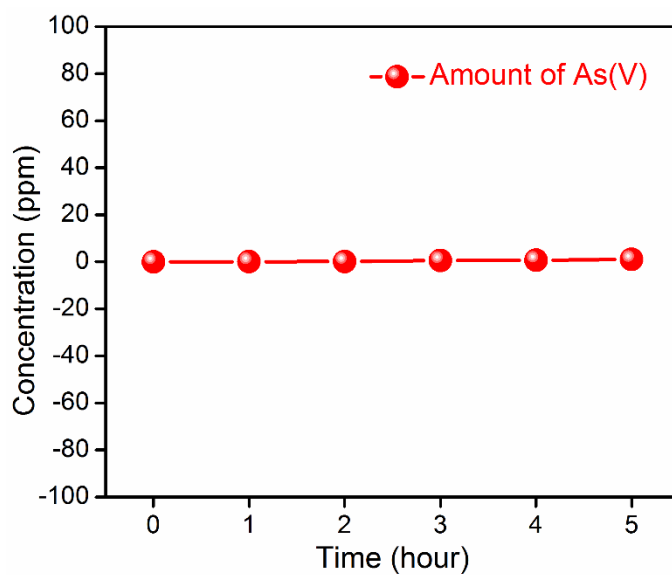
Appendix 4.35: Concentration dependent adsorption profiles of IPcomp-6 towards As(V) with corresponding Langmuir linear fitting model.



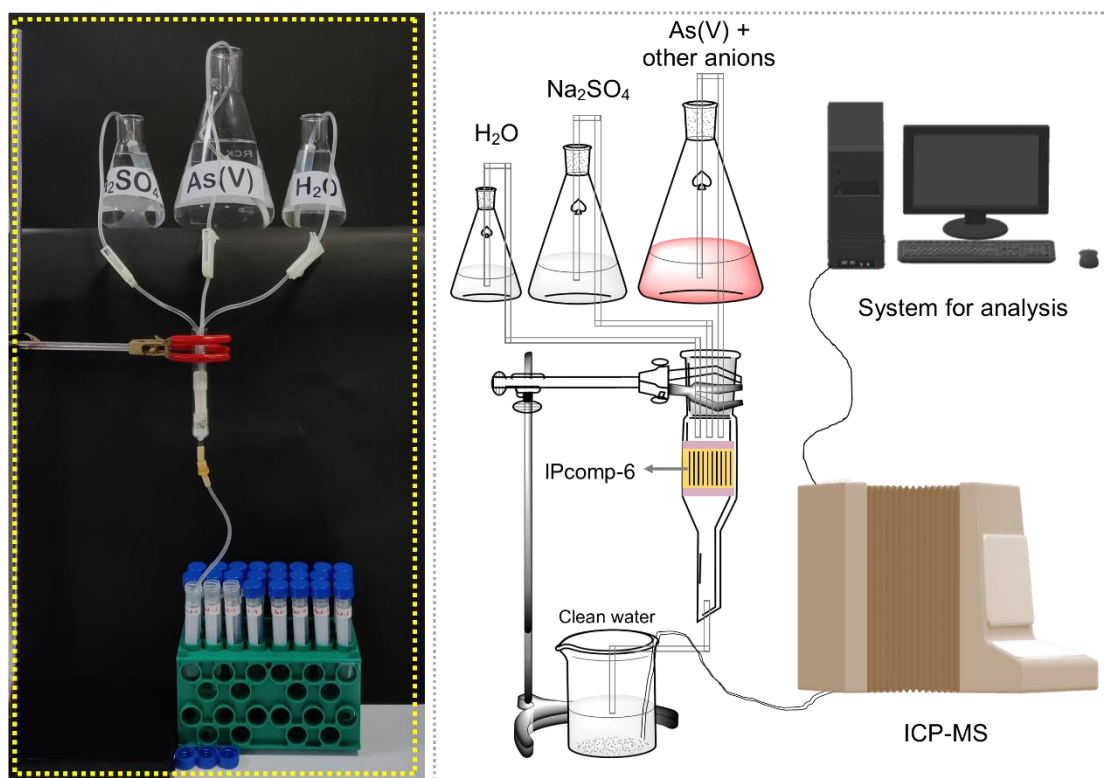
Appendix 4.36: pH dependent As(V) capture study by IPcomp-6.



Appendix 4.37: Removal % of As(V) with time, comparison study of IPcomp-6 and physical mixing of MOP and MOA.



Appendix 4.38: Leaching test of oxoanion: As(V) from IPcomp-6. (No significant leaching of As(V) from the hybrid aerogel materials indicated strong binding affinity).

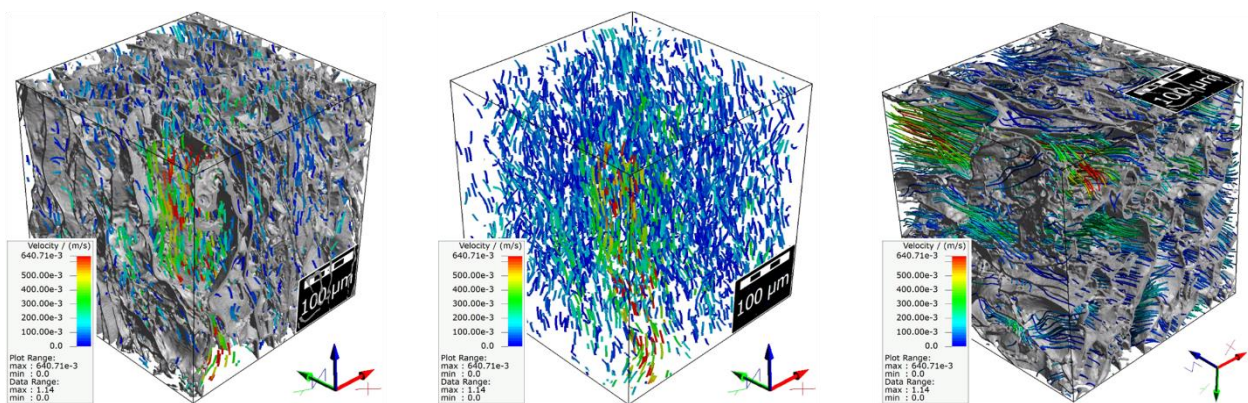


Appendix 4.39: Digital image and schematic diagram of experimental set-up of dynamic column-exchange based As(V)-oxoanion sorption experiment.

Appendix Section-4.6.4: Numerical simulation studies

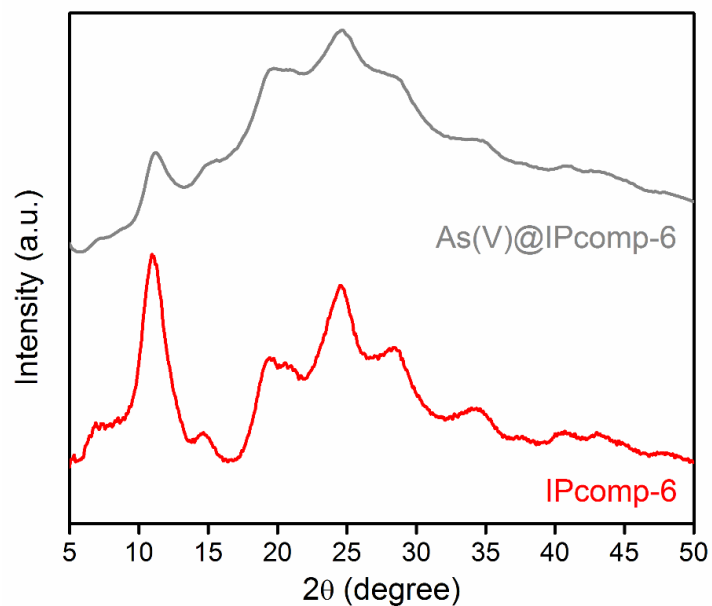
Simulation studies: Numerical simulation of mass transport properties in the hybrid aerogels were performed on their real 3D reconstructed model, using *FlowDict*[®] software package (*GeoDict*[®] 2018, Math2Market GmbH, Germany). Explicit jump solver is employed which follows Stokes equation, and are ideal for application in flows when the flow velocity dependence is linear. Flow of water at 25 °C is simulated with a pressure drop of 20 Pa, from all three directions (X, Y and Z axis) of the real 3D structure. Iterations in the range of 250 to 450 were undertaken with maximum error bound less than 0.8 %. Average flow velocity fields are calculated by explicit jump solver in the three directions by setting up the virtual pressure drop and selecting the computation directions or boundary conditions.

Considering the dynamic events taken place during the filtration process, these velocity profiles also predict the possible flow direction of As(V) stock solution through the stacked layers of the hybrid aerogel, in ZY plane. Such events involving the transport of aqueous arsenate solution, typically results in overall wetting of the hybrid aerogel walls with the solute. The process ultimately facilitates the deposition or adsorption of solute across all the interconnected pores of the hybrid aerogel. Therefore, these velocity profiles itself may be considered as an effective evidence for the higher saturation of pore channels in aerogels with As(V) solution.

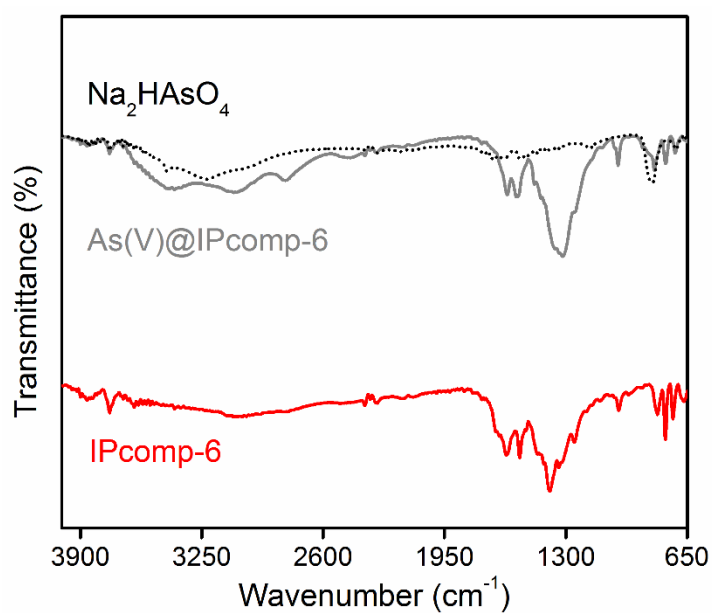


Appendix 4.40: Flow velocity measurement: The flow velocity simulation study has been performed for IPcomp-6. The average flow velocity has been calculated from the numerical simulation study.

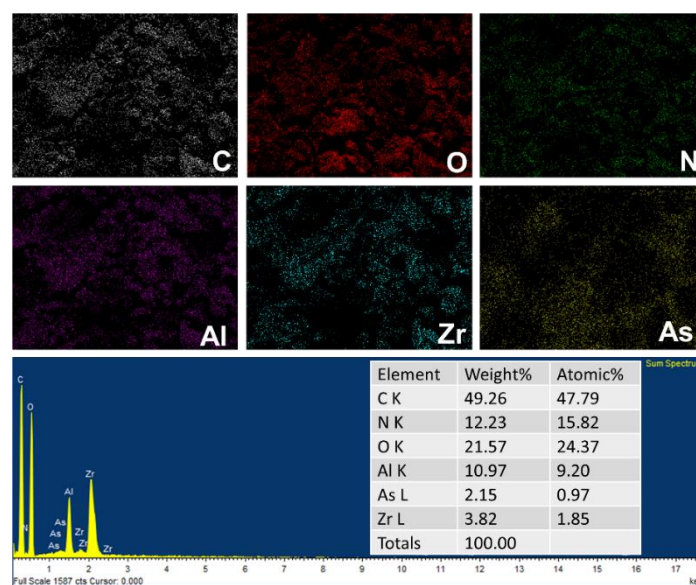
Appendix Section-4.6.5a: Post capture characterizations



Appendix 4.41: PXRD analysis of IPcomp-6, before and after As(V) capture study.



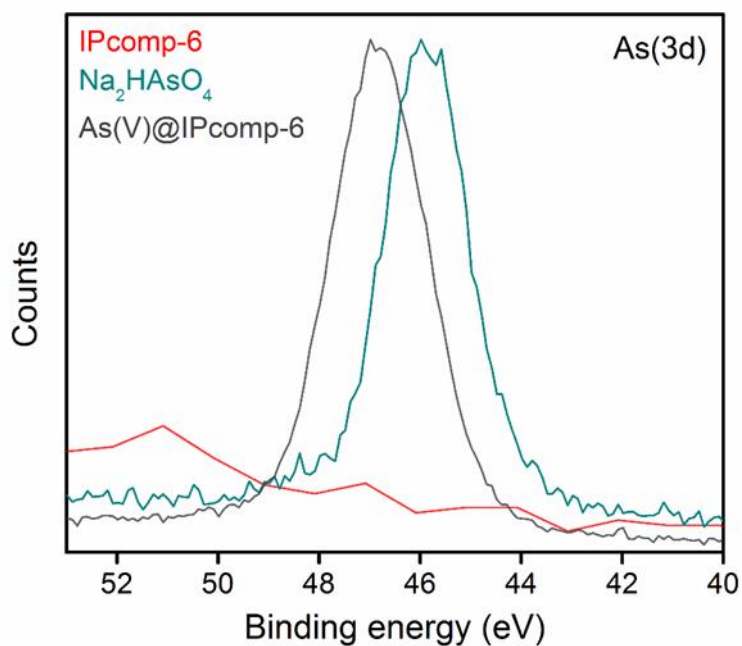
Appendix 4.42: FT-IR analysis of IPcomp-6 and before and after As(V) capture study. The intense peak at 841 cm⁻¹ is assigned to the stretching vibration of As–O, indicating the successful adsorption of As(V) species onto IPcomp-6.



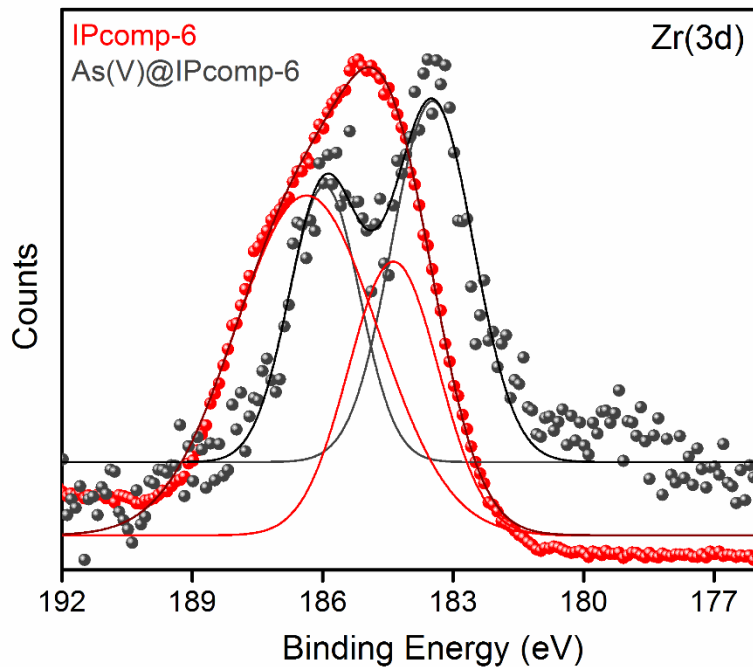
Appendix 4.43: SEM EDX and elemental mapping analysis of IPcomp-6 after exposed to As(V) aqueous solution. The corresponding EDX surface scan and elemental mapping data showing the homogeneous distribution of all relevant elements, especially arsenic in the surface of the As(V) treated compound.

Appendix Section-4.6.5b: X-ray Photoelectron Spectroscopy (XPS) studies

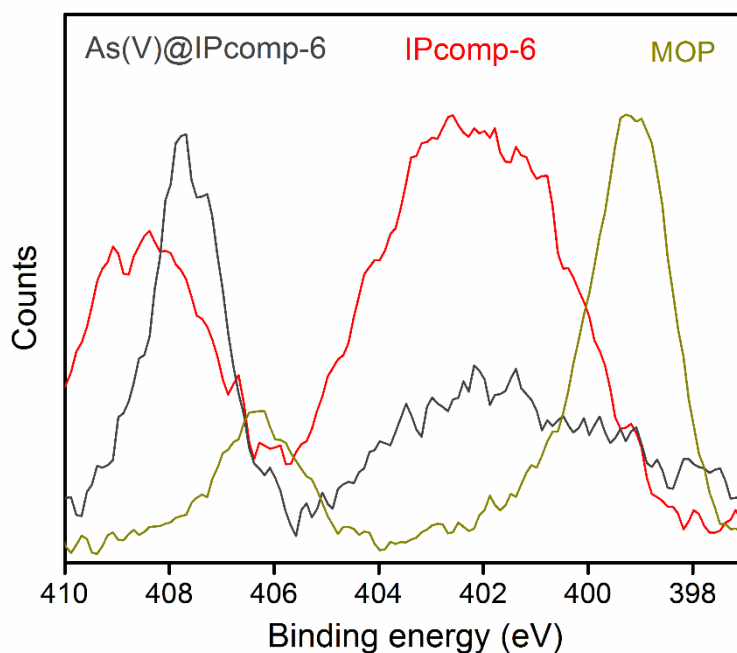
The X-ray photoelectron spectroscopy (XPS) was conducted in order to investigate the surface composition as well as to elucidate the interactions of As(V) with the hybrid composite materials along with all the relevant pristine materials. The XPS survey spectra in the main text (Figure 4.5f) of the IPcomp-6 before and after exposure to 50 ppm stock arsenate aqueous solution indicated the presence of all the relevant elements (Al, Zr, O, N, C, Cl for IPcomp-6 and Al, Zr, O, N, C, As for As(V) treated compound confirms the successful sorption of As(V) by hybrid material. Whereas, the high resolution As 3d XPS spectrum of the As(V)@IPcomp-6 along with Na₂HAsO₄ and pristine IPcomp-6, indicate that the characteristics peaks for As 3d in the XPS spectra of As(V)@IPcomp-6, shifted to higher binding energy (~0.8 eV) with compare to As 3d core peak of Na₂HAsO₄, which support the strong interaction between As(V) and the composite material (Appendix 4.44).^[58] Apart from this, with compare to the pristine IPcomp-6, the characteristics peaks for Zr 3d in the XPS spectra of the As(V) treated IPcomp-6 was found to be shifted to lower binding energy (~0.3 eV), which is attributed to the direct interaction between As(V) and the Zr SBU of the cationic MOP molecules in the composite (Appendix 4.45).^[60, 61] Similarly, the binding energy of the nitrogen (N) 1s orbital of the amino functionalized MOP molecules was observed to be fine altered with compared to the pristine IPcomp-6 and As(V) treated hybrid compound, which indicated the hydrogen bonding interaction between the guest-MOP molecules and host-MOG matrix as well as between As(V) and IPcomp-6 (Appendix 4.46).



Appendix 4.44: As 3d XPS spectra of the source of As(V)-sodium arsenate metal salt (Na₂HAsO₄) and the hybrid materials (IPcomp-6) before and after exposure to 50 ppm of stock As(V) solution.



Appendix 4.45: Zr 3d XPS spectra of the hybrid materials (IPcomp-6) before and after exposure to 50 ppm of stock As(V) solution.

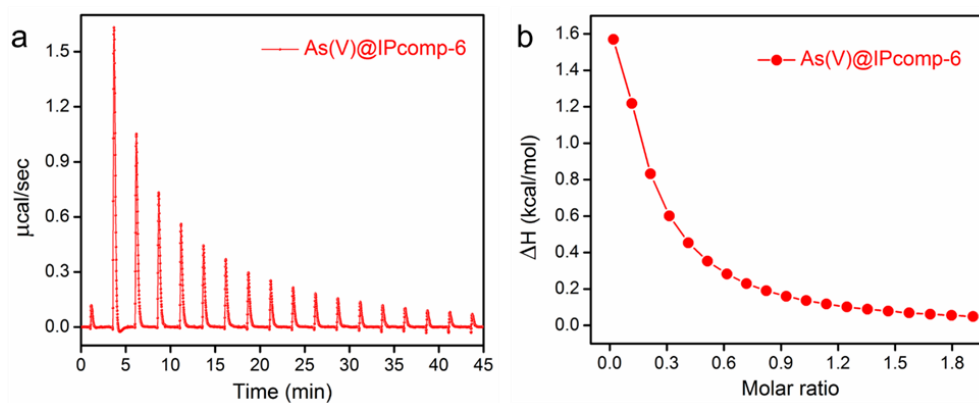


Appendix 4.46: N 1s XPS spectra of the pristine MOPs and hybrid materials (IPcomp-6) before and after exposure to 50 ppm of stock As(V) solution.

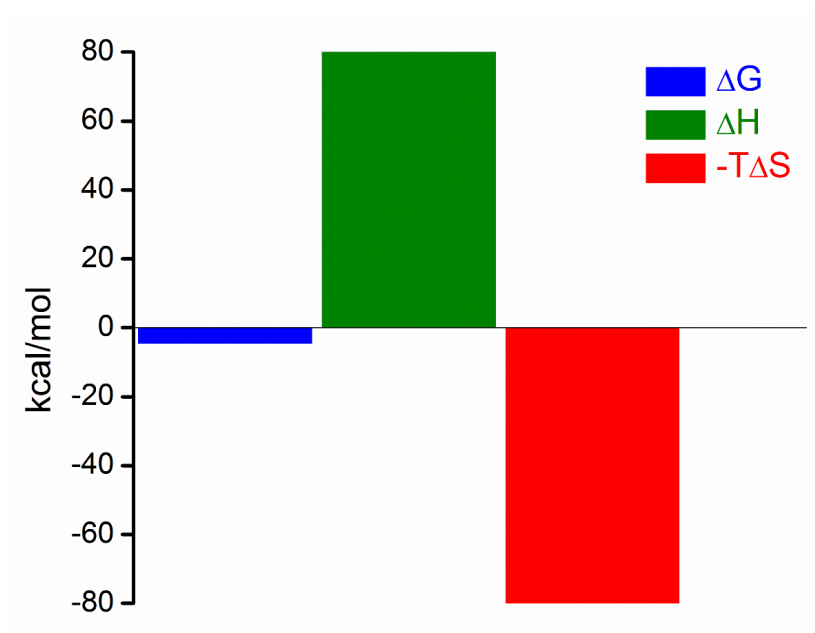
Appendix Section-4.6.5c: Isothermal titration calorimetry (ITC) studies

Further, beyond the XPS and other experimental investigations, we have also performed isothermal titration calorimetry (ITC) for the thermodynamic validation of such favourable interactions between targeted oxoanion (HAsO_4^{2-}) and hybrid aerogel material in aqueous medium.^[62] ITC experiment quantitatively provides the change in enthalpy, entropy and Gibbs free energy associated with the adsorption followed by the ion-exchange process between adsorbent and adsorbate.^[63] In this typical experiment, first, the reference cell was filled with deionized water, and a homogeneous aqueous suspension of 1 mmol adsorbate (IPcomp-6) (which was grounded into fine powder) was poured into the sample cell and the 10 mmol concentration of adsorbent (As(V)) aqueous solution was placed into the syringe, while the complete mixture was stirring at 750 rpm. In aqueous medium at pH 7, the arsenate [As(V)] oxoanion exists as the HAsO_4^{2-} anions.^[45] Therefore, in this study, we recorded the thermograms for hydrogen arsenate adsorption in the composite. The first injection of each titration was fixed at 0.4 μL . The analyte concentration was determined by ICP-MS. At least two titrations for each analyte-compound pair were collected. Data analysis was performed in y. MicroCal PEAQ-ITC analysis software. The heats of injection for blank titrations (analyte [As(V)] into blank) were subtracted from the heats of injection into compound suspensions. The recorded thermogram (Figure 4.5g), (Appendix 4.49) demonstrated a high association constant with the endothermic binding event along with the following thermodynamic parameters (Appendix Table 4.9 and Appendix 4.50). This

result indicated the adsorption of HAsO_4^{2-} by IPcomp-6 was thermodynamically favourable as the Gibbs free energy of the process was found to be negative with positive association constant (K_a) and positive entropy.^[64] Thus, these ITC data clearly indicated the similarities between the thermodynamic parameters and the bulk-scale experimental data of strong interactions of HAsO_4^{2-} with IPcomp-6 in water.



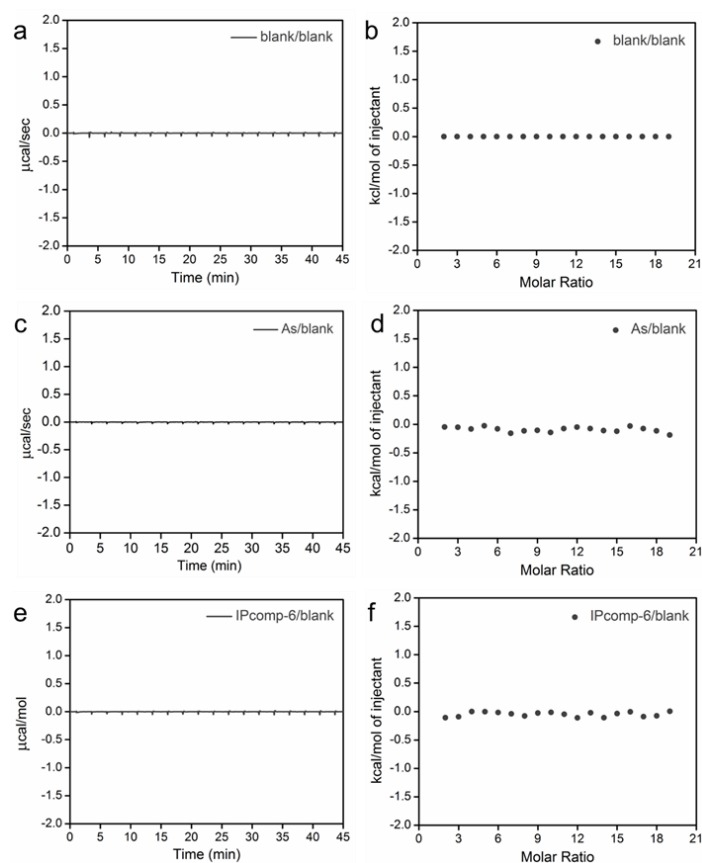
Appendix 4.47: (a) ITC thermograms and (b) integrated heat plots simultaneously for injections of HAsO_4^{2-} titrated against IPcomp-6.



Appendix 4.48: Thermodynamic parameters for interacting analytes HAsO_4^{2-} indicating changes in Gibbs free energy, enthalpy, entropy for the interactions with IPcomp-6.

Appendix Table 4.9: The concentration and thermodynamic parameters derived from ITC experiment for injections of HAsO_4^{2-} titrated against IPcomp-6.

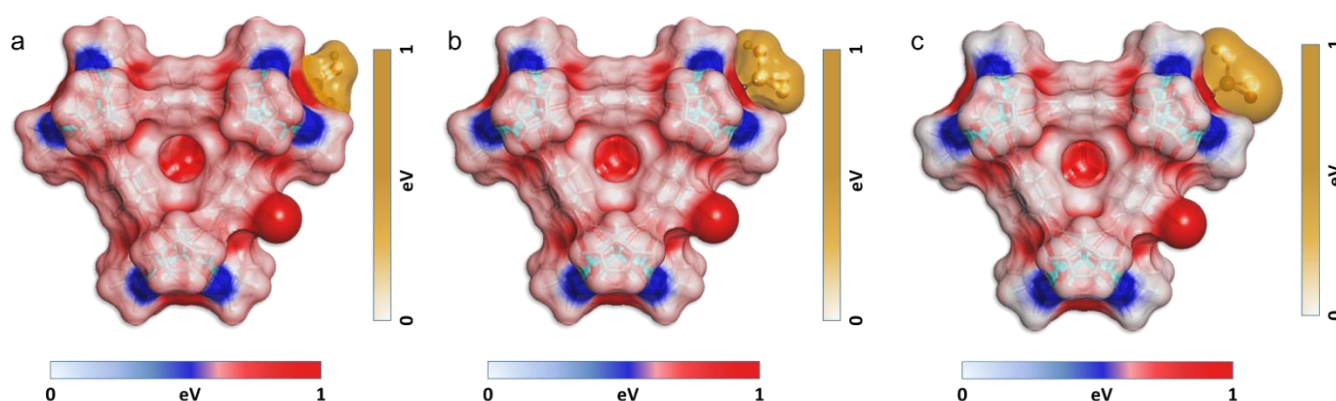
Ion	HAsO_4^{2-}
Temperature (oC)	25.1
Bin	Binding
[Syr] (M)	10.0e-03
[Cell] (M)	1.00e-03
Model	One Set of Sites
N (sites)	$8.5e-3 \pm 4.9e-2$
KD (M)	$406e-6 \pm 61.9e-6$
ΔH (kcal/mol)	80.0 ± 461
ΔG (kcal/mol)	-4.63
$-\text{T}\Delta\text{S}$ (kcal/mol)	-84.6



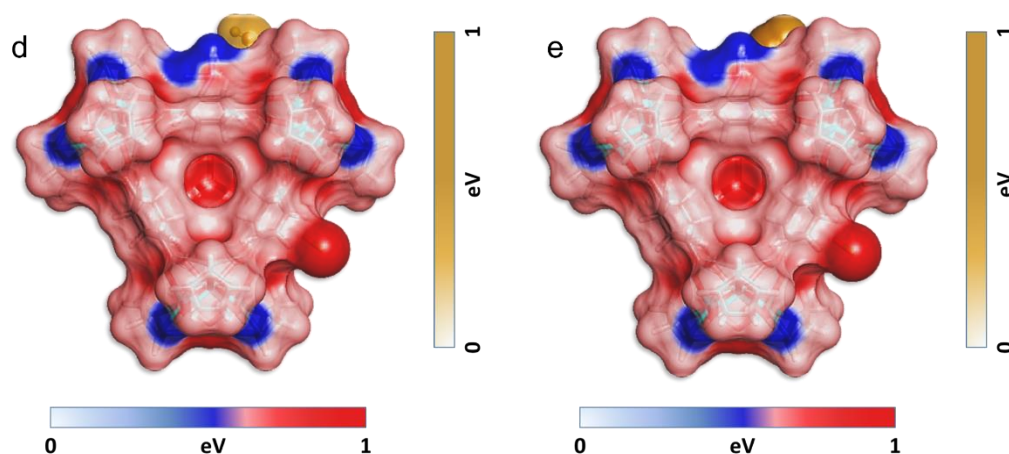
Appendix 4.49: ITC thermograms and integrated heat plots for injections for (a) & (b) Blank titrated against blank (syringe, cell, pH=7). (c) & (d) Aqueous HAsO_4^{2-} (10 mM, syringe loaded, pH 7) titrated against blank (cell loaded, pH 7) and (e) & (f) Blank (syringe loaded, pH 7) is titrated against suspension of IPcomp-6 (1 mM, cell loaded, pH 7).

Appendix Section-4.6.6: DFT simulation studies

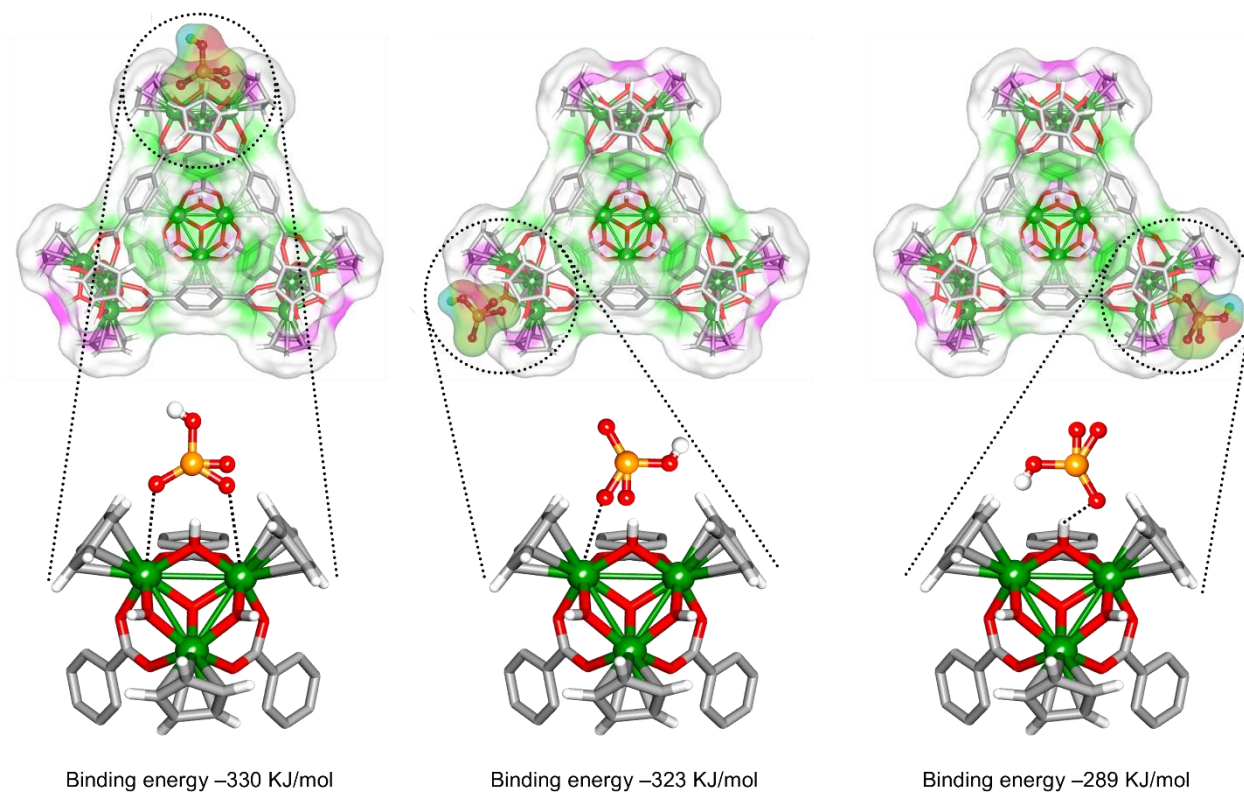
IPcomp-6 exhibited highly efficient selective removal of different oxoanions, such as HAsO_4^{2-} , SeO_4^{2-} , ReO_4^- , CrO_4^{2-} and MnO_4^- from the contaminated water system. The multifunctional nature of the hybrid aerogel material is caused for such good capture efficiencies. Among them, the hierarchical (micro-macro) porous structure of the composite material helps for fast mass diffusion of oxoanions (HAsO_4^{2-}) through its large open pores towards the main active sites (guest- amino functionalized Zr(IV)-SBU-based cationic MOPs) of the hybrid aerogel. Thereafter, the oxoanion HAsO_4^{2-} interact with the Zr-SBU and the free $-\text{NH}_2$ group of the cationic MOP, followed by exchange with Cl^- ions. Such interactions are majorly attributed to the dispersive interactions or supramolecular interactions, dipole interactions of the HAsO_4^{2-} with the functional groups of MOP molecules of the composite material. To validate this, we have calculated the respective binding energies of HAsO_4^{2-} with the MOP molecules of the hybrid compound. The molecular-level interactions between the amino functionalized cationic MOP and oxoanion, HAsO_4^{2-} were simulated using Discovery Studio 2017 (Accelrys). The DFT simulation was performed at fine quality calculation level. At first, using DMOL3 and B3LYP hybrid function the single unit of the MOP was fully geometry relaxed by keeping the Multiplicity factor to Auto mode, double numeric plus polarizing (DNP+) basis set with water as solvent. Using simulated annealing technique structural simulation on the geometry relaxed MOP structure was realized to find a feasible interaction site of the HAsO_4^{2-} within the relaxed MOP unit. The electrostatic potential (ESP) on the van der Waals (VDW) surfaces (isodensity = 0.001 a.u.) of MOP unit was derived from ground state electron density of the system. The DFT calculation reveals that the HAsO_4^{2-} interact with Zr-SBU and free amine ($-\text{NH}_2$) groups of the MOP with following major possible binding sites, with binding energies of 330, 323, 289, 256, 242 kJ/mol (Appendix 4.50-4.53).



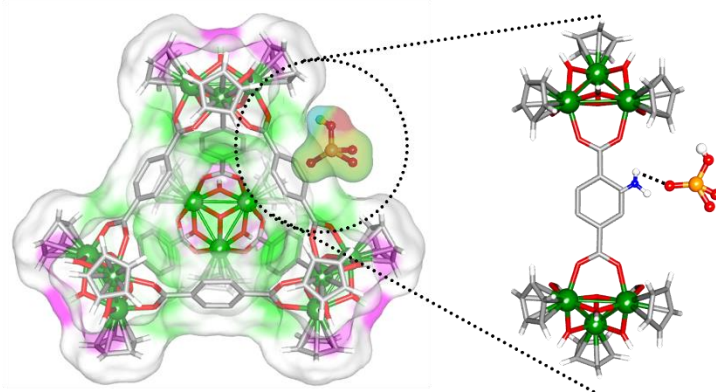
Appendix 4.50: Electrostatic Potential (ESP) diagram of different interaction between Zr-SBU of MOP in the hybrid composite and oxoanions viz. HAsO_4^{2-} , (a) Binding energy: -330 kJ/mol, (b) -323 kJ/mol and (c) -289 kJ/mol.



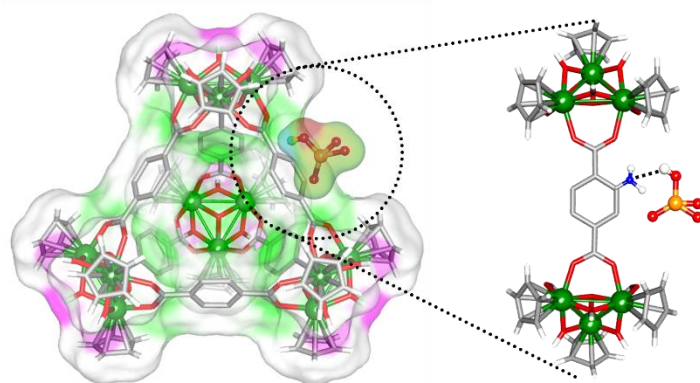
Appendix 4.51: Electrostatic Potential (ESP) diagram of different interaction between -NH_2 group of MOPs in the hybrid composite and oxoanions viz. HAsO_4^{2-} , (d) Binding energy: -256 kJ/mol , and (e) -242 kJ/mol .



Appendix 4.52: DFT optimized structures with corresponding binding energies showing hydrogen bonding interactions between Zr-SBU of the MOP of IPcomp-6 with oxoanions viz. HAsO_4^{2-} .



Binding energy -256 KJ/mol



Binding energy -242 KJ/mol

Appendix 4.53: DFT optimized structures with corresponding binding energies showing hydrogen bonding interactions between the $-\text{NH}_2$ group of MOPs of IPcomp-6 with oxoanions viz. HAsO_4^{2-} .

Appendix Section-4.6.7: Comparison tables

Appendix Table 4.11: Comparison of this work with other related investigations of As(V) capture by various adsorbents. (N.D.: Not Done).

Compound name	Contact time for removal	In presence of other ions/Selectivity	Capture capacity	Reference
IPcomp-6	~ 5 min	Cl ⁻ , Br ⁻ , SO ₄ ²⁻ , NO ₃ ⁻ , ClO ₄ ⁻	157 mg/g	This work
IPcomp-3(200)	< 2 min	Cl ⁻ , Br ⁻ , SO ₄ ²⁻ , NO ₃ ⁻ , ClO ₄ ⁻	N.D	<i>ACS Cent. Sci.</i> 2020 , 6, 1534-1541
Fe-BTC	10 min	N.D.	57.705 mg/g	<i>J. Phys. Chem. C</i> 2012 , 116, 8601-8607.
NH ₂ -MIL-88(Fe)	60 min	Various cations and anions	125 mg/g	<i>J. Mater. Chem. A</i> 2017 , 5, 23794-23804.
Fe ₃ O ₄ @UiO-66	100 min	N.D.	73.2 mg/g	<i>Microporous and Mesoporous Mater.</i> 2018 , 276, 68-75.
Zn-MOF-74	150 min	Cl ⁻ , NO ₃ ⁻ , PO ₄ ³⁻	325 mg/g	<i>Journal of Solid-State Chemistry.</i> 2019 , 269, 264-270.
AUBM-1	3 h	CO ₃ ²⁻ , NO ₃ ⁻	103.1 mg/g	<i>Dalton Trans.</i> 2018 , 47, 799-806.
MOF-808	4 h	N.D.	24.83 mg/g	<i>Materials Letters.</i> 2015 , 160, 412-414.
ZIF-8	7 h	Cl ⁻ , F ⁻ , NO ₃ ⁻ , SO ₄ ²⁻ , PO ₄ ³⁻	76.5 mg/g	<i>J. Phys. Chem. C.</i> 2014 , 118, 27382-27387.
MIL-53(Al)	11 h	Cl ⁻ , F ⁻ , NO ₃ ⁻ , SO ₄ ²⁻ , PO ₄ ³⁻	106.5 mg/g	<i>Water Sci. Technol.</i> 2014 , 70, 1391-139.
UiO-66	24 h	Cl ⁻ , NO ₃ ⁻ , CO ₃ ²⁻ , SO ₄ ²⁻	303.4 mg/g at pH=2	<i>Sci Rep.</i> 2015 , 5, 16613.
Fe ₃ O ₄ @MIL101(Cr)	24 h	Ca ²⁺ , Mg ²⁺ , PO ₄ ³⁻	12.29 mg/g	<i>Eur. J. Inorg. Chem.</i> 2016 , 4395-4401.
UiO-66-(SH) ₂	24 h	N.D.	40 mg/g	<i>Chem. Sci.</i> 2016 , 7, 6492-6498.
Fe-Mn chitosan beads	36 h	SO ₄ ²⁻ , HCO ₃ ⁻ , SiO ₄ ²⁻ , HPO ₄ ²⁻ , Ca ²⁺ , Mg ²⁺	39.1 mg/g	<i>Bioresource Technology.</i> 2015 , 193, 243-249.
iMOF-1C	72 h	Cl ⁻ , NO ₃ ⁻ , CO ₃ ²⁻ , SO ₄ ²⁻ , HCO ₃ ⁻	84 mg/g	<i>Angew. Chem. Int. Ed.</i> 2020 , 59, 7788-7792.
iMOF-3C	5 min	Cl ⁻ , NO ₃ ⁻ , CO ₃ ²⁻ , SO ₄ ²⁻ , HCO ₃ ⁻	75.5 mg/g	<i>J. Mater. Chem. A.</i> 2021 , 9, 6499-6507.

Appendix Table 4.12: Comparison of this work with other related investigations of Se(VI) capture by various adsorbents. (N.D.: Not Done).

Compound name	Contact time for removal	In presence of other ions/Selectivity	Capture capacity	Reference
IPcomp-6	~ 5 min	Cl ⁻ , Br ⁻ , SO ₄ ²⁻ , NO ₃ ⁻ , ClO ₄ ⁻	109 mg/g	This work
NU-1000	<1 min	N.D.	85 mg/g	<i>J. Am. Chem. Soc.</i> 2015 , <i>137</i> , 7488-7494.
IPcomp-3(200)	<2 min	Cl ⁻ , Br ⁻ , SO ₄ ²⁻ , NO ₃ ⁻ , ClO ₄ ⁻	N.D.	<i>ACS Cent. Sci.</i> 2020 , <i>6</i> , 1534-1541.
MOF-808	5 min	N.D.	118 mg/g	<i>CrystEngComm.</i> 2018 , <i>20</i> , 6140-6145.
MgAl-MoS ₄ -LDH	30 min	N.D.	85 mg/g	<i>J. Am. Chem. Soc.</i> 2017 , <i>139</i> , 12745-12757.
Mg-Al LDH	-	-	120 mg/g at pH=7	<i>J. Mater. Chem. A</i> 2014 , <i>2</i> , 15995-16007.
UiO-66	-	-	-	<i>Environ. Sci.: Nano.</i> 2018 , <i>5</i> , 1441-1453.
UiO-66-NH ₂	-	-	-	
Y ₂ (OH) ₅ Cl	12 h	NO ₃ ⁻ , SO ₄ ²⁻ , CO ₃ ²⁻ , HPO ₄ ²⁻	124 mg/g	<i>Environ. Sci. Technol.</i> 2017 , <i>51</i> , 8606-8615.
MgFeAl LDH	120 min	N.D.	N.D.	<i>RSC Adv.</i> 2014 , <i>4</i> , 61817-61822.
UiO-66-HCl	10 h	N.D.	N.D.	<i>Chem. Eng. J.</i> 2017 , <i>330</i> , 1012-1021.
Iron oxide impregnated CNTs	4 h	N.D.	N.D.	<i>J. Bioinorg. Chem. Appl.</i> 2017 , 4323619.
Al ₂ O ₃ /Chitosan	1440 min	N.D.	N.D.	<i>Water Research.</i> 2014 , <i>50</i> , 373-381.
Polyamine-type Ion Exchange Resin	180 min	SO ₄ ²⁻ and Cl ⁻	243 mg/g	<i>Separation Science and Technology.</i> 2014 , <i>42</i> , 3155-3167.
Cu ⁺ @diamino-functionalized MCM-41	600 min	SO ₄ ²⁻ , Cl ⁻ , NO ₃ ⁻	83 mg/g	<i>Bull. Chem. Soc. Jpn.</i> 2003 , <i>76</i> , 2225-2232.
iMOF-1C	72 h	Cl ⁻ , NO ₃ ⁻ , CO ₃ ²⁻ , SO ₄ ²⁻ , HCO ₃ ⁻	100 mg/g	<i>Angew. Chem. Int. Ed.</i> 2020 , <i>59</i> , 7788-7792.
iMOF-3C	5 min	Cl ⁻ , NO ₃ ⁻ , CO ₃ ²⁻ , SO ₄ ²⁻ , HCO ₃ ⁻	73 mg/g	<i>J. Mater. Chem. A.</i> 2021 , <i>9</i> , 6499-6507.

Appendix Table 4.13: Comparison of this work with other related investigations of Re(VII) capture by various adsorbents. (N.D.: Not Done).

Compound name	Contact time for removal	In presence of other ions/Selectivity	Capture capacity	Reference
IPcomp-6	~ 5 min	Cl ⁻ , Br ⁻ , SO ₄ ²⁻ , NO ₃ ⁻ , ClO ₄ ⁻	529 mg/g	This work
SCU-COF-1	1 min	CO ₃ ²⁻ , SO ₄ ²⁻ , PO ₄ ³⁻ , NO ₃ ⁻	702.4 mg/g	<i>Chem. Sci.</i> 2019 , <i>10</i> , 4293-4305.
IPcomp-3(200)	< 2 min	Cl ⁻ , Br ⁻ , SO ₄ ²⁻ , NO ₃ ⁻ , ClO ₄ ⁻	600.1 mg/g	<i>ACS Cent. Sci.</i> 2020 , <i>6</i> , 1534-1541.
α-MOC-1 and α-MOC-2	10 min	Cl ⁻ , NO ₃ ⁻ , Br ⁻ , SO ₄ ²⁻ , CO ₃ ²⁻	350 mg/g 583.9 mg/g	<i>ACS Appl. Nano Mater.</i> 2019 , <i>2</i> , 5824-5832.
SCU-100 (ReO ₄ ⁻ /TcO ₄ ⁻)	30 min (TcO ₄ ⁻)	CO ₃ ²⁻ , NO ₃ ⁻ , SO ₄ ²⁻ , PO ₄ ³⁻	541 mg/g (ReO ₄ ⁻)	<i>Environ. Sci. Technol.</i> 2017 , <i>51</i> , 3471-3479.
SCU-101 (ReO ₄ ⁻ /TcO ₄ ⁻)	10 min (TcO ₄ ⁻)	CO ₃ ²⁻ , NO ₃ ⁻ , SO ₄ ²⁻ , PO ₄ ³⁻	217 mg/g (ReO ₄ ⁻)	<i>J. Am. Chem. Soc.</i> 2017 , <i>139</i> , 14873-14876.
SLUG-21	60 min	N.D.	602 mg/g	<i>J. Am. Chem. Soc.</i> 2010 , <i>132</i> , 7202-7209.
Compound-1	60 min	Cl ⁻ , NO ₃ ⁻ , Br ⁻ , SO ₄ ²⁻	517 mg/g	<i>Chem. Sci.</i> 2018 , <i>9</i> , 7874-7881.
PAF-1-F	24 h	SO ₄ ²⁻ , PO ₄ ³⁻	420 mg/g	<i>Chem. Eur. J.</i> 2016 , <i>22</i> , 17581-17584.
iPOP-3	25 min	SO ₄ ²⁻ , Cl ⁻ , Br ⁻ , NO ₃ ⁻	515.5 mg/g	<i>Chem. Eur. J.</i> 2021 , <i>27</i> , 13442-13449.
iPOP-4	30 min	SO ₄ ²⁻ , Cl ⁻ , Br ⁻ , NO ₃ ⁻	350.3 mg/g	<i>Chem. Eur. J.</i> 2021 , <i>27</i> , 13442-13449.
TbDa-COF	2 min	Cl ⁻ , NO ₃ ⁻ , CO ₃ ²⁻ , SO ₄ ²⁻ , PO ₄ ³⁻	952 mg/g	<i>Chem.</i> 2020 , <i>6</i> , 2796-2809.
bis-PC ₂ (Cl)@MIL-101	30 sec	N.D.	362 mg/g	<i>ACS Cent. Sci.</i> 2020 , <i>6</i> , 12, 2354-2361.
SCU-CPN-1	30 sec	NO ₃ ⁻ , SO ₄ ²⁻	876 mg/g	<i>Nat. Comm.</i> 2018 , <i>9</i> , 3007.
CPN-tpm	20 min	NO ₃ ⁻ , SO ₄ ²⁻ , AsO ₄ ³⁻	1133 mg/g	<i>Small.</i> 2021 , <i>17</i> , 2007994.
SCU-CPN-4	1 min	NO ₃ ⁻ , SO ₄ ²⁻	437 mg/g	<i>ACS Cent. Sci.</i> 2021 , <i>7</i> , 1441-1450.

Appendix Table 4.14: Comparison of this work with other related investigations of Cr(VI) capture by various adsorbents. (N.D.: Not Done).

Compound name	Contact time for removal	In presence of other ions/Selectivity	Capture capacity	Reference
IPcomp-6	~ 5 min	Cl ⁻ , Br ⁻ , SO ₄ ²⁻ , NO ₃ ⁻ , ClO ₄ ⁻	243 mg/g	This work
MOR-2	1 min	Cl ⁻ , NO ₃ ⁻ , HCO ₃ ⁻	194 mg/g	<i>J. Mater. Chem. A</i> 2017 , 5, 14707-14719.
IPcomp-3(200)	< 2 min	Cl ⁻ , Br ⁻ , SO ₄ ²⁻ , NO ₃ ⁻ , ClO ₄ ⁻	274.4 mg/g	<i>ACS Cent. Sci.</i> 2020 , 6, 1534-1541.
POP-Ims (Cr ₂ O ₇ ²⁻)	5 min	Cl ⁻ , NO ₃ ⁻ , SO ₄ ²⁻	171.99 mg/g	<i>ACS Appl. Mater. Interfaces</i> 2016 , 8, 18904-18911.
Zn-Co-SLUG-35	4 h	NO ₃ ⁻ , SO ₄ ²⁻	68.5 mg/g	<i>Chem. Mater.</i> 2013 , 25, 647-652.
IMIP-Br(Cr ₂ O ₇ ²⁻)	30 min	NO ₃ ⁻ , SO ₄ ²⁻ , Cl ⁻ , BF ₄ ⁻	318 mg/g	<i>J. Mater. Chem. A</i> 2016 , 4, 12554-12560.
Compound-1	30 min	Cl ⁻ , NO ₃ ⁻ , Br ⁻ , SO ₄ ²⁻	133 mg/g	<i>Chem. Sci.</i> 2018 , 9, 7874-7881.
FIR-53 and FIR-54	4 h	Cl ⁻ , Br ⁻ , NO ₃ ⁻ , CO ₃ ²⁻ , ClO ₄ ⁻ , SO ₄ ²⁻	74.2 mg/g 103 mg/g	<i>Chem. Mater.</i> 2015 , 27, 205-210.
1-ClO ₄	8 h	Halide anions	62.88 mg/g	<i>Chem. Commun.</i> 2012 , 48, 8231-8233.
ZJU-101	10 min	Cl ⁻ , F ⁻ , I ⁻ , Br ⁻ , NO ₃ ⁻ , SO ₄ ²⁻	245 mg/g	<i>Chem. Commun.</i> , 2015 , 51, 14732-14734.
aMOC-1 and aMOC-2	6 min	Cl ⁻ , Br ⁻ , NO ₃ ⁻ , SO ₄ ²⁻ , CO ₃ ²⁻	157.4 mg/g 242.0 mg/g	<i>ACS Appl. Nano Mater.</i> 2019 , 2, 5824-5832.
1-SO ₄ (Cr ₂ O ₇ ²⁻)	24 h	CF ₃ SO ₃ ⁻ , BF ₄ ⁻ , NO ₃ ⁻ , ClO ₄ ⁻	166 mg/g	<i>Angew. Chem. Int. Ed.</i> 2016 , 55, 7811-7815.
TJU-1	24 h	Cl ⁻ , HCO ₃ ⁻ , NO ₃ ⁻ , SO ₄ ²⁻	279 mg/g	<i>Chem. Commun.</i> 2017 , 53, 7064-7067.
ABT.2ClO ₄ (Cr ₂ O ₇ ²⁻)	48 h	CF ₃ SO ₃ ⁻ , BF ₄ ⁻ , NO ₃ ⁻	0.73 mol/mol	<i>Angew. Chem. Int. Ed.</i> 2013 , 52, 13769-13773.
iPOP-3	60 min	SO ₄ ²⁻ , Br ⁻ , Cl ⁻ , NO ₃ ⁻	170 mg/g	<i>Chem. Eur. J.</i> 2021 , 27, 13442-13449.
iPOP-4	30 min	SO ₄ ²⁻ , Br ⁻ , Cl ⁻ , NO ₃ ⁻	141 mg/g	<i>Chem. Eur. J.</i> 2021 , 27, 13442-13449.

4.7 Reference

- [1] World Economic Forum, Global Risks 2015, 10th Edition (World Economic Forum, Geneva, Switzerland, **2015**).
- [2] M. C. M. V. Loosdrecht, D. Brdjanovic, *Science* **2014**, *344*, 6191.
- [3] Grant, S. B. et. al. *Science* **2012**, *337*, 681 – 685.
- [4] R. P. Schwarzenbach, B. I. Escher, K. Fenner, T. B. Hofstetter, C. A. Johnson, U. V. Gunten, B. Wehrli, *Science* **2006**, *313*, 1072 –1077.
- [5] L. N. Pincus, H. E. Rudel, P. V. Petrovic, S. Gupta, P. Westerhoff, C. L. Muhich, J. B. Zimmerman, *Environ. Sci. Technol.* **2020**, *54* (16), 9769 – 9790.
- [6] S. Rojas, P. Horcajada, *Chem. Rev.* **2020**, *120*, 8378 – 8415.
- [7] A. K. Mohammed, D. Shetty, *Environ. Sci. Water Res. Technol.*, **2021**, *7*, 1895 –1927.
- [8] M. A. Shannon, P. W. Bohn, M. Elimelech, J. G. Georgiadis, B. J. Marinas, A. M. Mayes, *Nature* **2008**, *452*, 301 – 310.
- [9] J. R. Werber, C. O. Osuji, M. Elimelech, *Nat. Rev. Chem.* **2016**, *2*, 16018.
- [10] Y. Zhang, J. R. Vallin, J. K. Sahoo, F. Gao, B. W. Boudouris, M. J. Webber, W. A. Phillip, *ACS Cent. Sci.* **2018**, *4*, 1697 – 1707.
- [11] A. A. Uliana, N. T. Bui, J. Kamcev, M. K. Taylor, J. J. Urban, J. R. Long, *Science* **2021**, *372*, 296 – 299.
- [12] J. Li, X. Wang, G. Zhao, C. Chen, Z. Chai, A. Alsaedi, T. Hayat, X. Wang, *Chem. Soc. Rev.* **2018**, *47*, 2322 – 2356.
- [13] P. Kumar, A. Pournara, K. -H. Kim, V. Bansal, S. Rapti, M. J. Manos, *Prog. Mater. Sci.* **2017**, *86*, 25 – 74.
- [14] X. Liu, H. Pang, X. Liu, Q. Li, N. Zhang, L. Mao, M. Qiu, B. Hu, H. Yang, X. Wang, *The Innovation.* **2021**, *2*, 100076.
- [15] J. Li, B. Li, N. Shen, L. Chen, Q. Guo, L. Chen, L. He, X. Dai, Z. Chai, S. Wang, *ACS Cent. Sci.* **2021**, *7*, 8, 1441–1450.
- [16] S. Rapti, D. Sarma, S. A. Diamantis, E. Skliri, G. S. Armatas, A. C. Tsipis, Y. S. Hassan, M. Alkordi, C. D. Malliakas, M. G. Kanatzidis, T. Lazarides, J. C. Plakatouras, M. J. Manos, *J. Mater. Chem. A* **2017**, *5*, 14707–14719.

- [17] B. Moulton, M. J. Zaworotko, *Chem. Rev.* **2001**, *101*, 1629–1658.
- [18] G. Cai, P. Yan, L. Zhang, H. C. Zhou, H. L. Jiang, *Chem. Rev.* **2021**, *121*, 20. 12278 – 12326.
- [19] M. J. Kalmutzki, C. S. Diercks, O. M. Yaghi, *Adv. Mater.* **2018**, *30*, 1704304.
- [20] C. R. Kim, T. Uemura, S. Kitagawa, *Chem. Soc. Rev.* **2016**, *45*, 3828 – 3845.
- [21] G. Distefano, H. Suzuki, M. Tsujimoto, S. Isoda, S. Bracco, A. Comotti, P. Sozzani, T. Uemura, S. Kitagawa, *Nat. Chem.* **2013**, *5*, 335 – 341.
- [22] M. Muschi, C. Serre, *Coord. Chem. Rev.* **2019**, *387*, 262 – 272.
- [23] Z. Chen, X. Li, C. Yang, K. Cheng, T. Tan, Y. Lv, Y. Liu, *Adv. Sci.* **2021**, *8*, 2101883.
- [24] T. Kitao, Y. Zhnag, S. Kitagawa, B. Wang, T. Uemura, *Chem. Soc. Rev.* **2017**, *46*, 3108 – 3133.
- [25] N. Ahmad, A. H. Chughtai, H. A. Younus, F. Verpoort, *Coord. Chem. Rev.* **2014**, *280*, 1 – 27.
- [26] E. J. Gosselin, C. A. Rowland, E. D. Bloch, *Chem. Rev.* **2020**, *120*, 16, 8987 – 9014.
- [27] F. J. Rizzuto, L. K. S. Krbek, J. R. Nitschke, *Nat. Rev. Chem.* **2019**, *3*, 204 – 222.
- [28] H. S. Lee, S. Jee, R. Kim, H. -T. Bui, B. Kim, J. -K. Kim, K. S. Park, W. Choi, W. Kim, K. M. Choi, *Energy Environ. Sci.* **2020**, *13*, 519 – 526.
- [29] W. -H. Xing, H. -Y. Li, X. -Y. Dong, S. -Q. Zang, *J. Mater. Chem. A* **2018**, *6*, 7724 – 7730.
- [30] J. Liu, W. Duan, J. Song, X. Guo, Z. Wang, X. Shi, J. Liang, J. Wang, P. Cheng, Y. Chen, et al. *J. Am. Chem. Soc.* **2019**, *141*, 12064 – 12070.
- [31] S. Mollick, S. Fajal, S. Mukherjee, S. K. Ghosh, *Chem. – Asian J.* **2019**, *14*, 3096 – 3108.
- [32] X. Qiu, W. Zhong, C. Bai, Y. Li, *J. Am. Chem. Soc.* **2016**, *138*, 1138 – 1141.
- [33] Y. -H. Kang, X. D. Liu, N. Yan, Y. Jiang, X. -Q. Liu, L. -B. Sun, J. -R. Li, *J. Am. Chem. Soc.* **2016**, *138*, 6099 – 6102.
- [34] S. Mollick, S. Fajal, S. Saurabh, D. Mahato, S. K. Ghosh, *ACS Cent. Sci.* **2020**, *6*, 1534 – 1541.
- [35] K. Sumida, K. Liang, J. Reboul, I. A. Ibarra, S. Furukawa, P. Falcaro, *Chem. Mater.* **2017**, *29*, 2626 – 2645.
- [36] B. M. Connolly, D. G. Madden, A. E. H. Wheatley, D. Fairenjimenez, *J. Am. Chem. Soc.* **2020**, *142*, 8541 – 8549.
- [37] J. Hou, A. F. Sapnik, T. D. Bennett, *Chem. Sci.* **2020**, *11*, 310 – 323.

- [38] L. Li, S. Xiang, S. Cao, J. Zhang, G. Ouyang, L. Chen, C. -Y. Su, *Nature Comm.* **2013**, *4*, 1774.
- [39] G. Liu, Y. D. Yuan, J. Wang, Y. Cheng, S. B. Peh, Y. Wang, Y. Qian, J. Dong, D. Yuan, D. Zhao, *J. Am. Chem. Soc.* **2018**, *140*, 6231 – 6234.
- [40] S. Mollick, T. N. Mandal, A. Jana, S. Fajal, S. K. Ghosh, *Chem. Sci.* **2019**, *10*, 10524 – 10530.
- [41] J. Liang, V. Gvilava, C. Jansen, S. Ozturk, A. Spieß, J. Lin, S. Xing, Y. Sun, H. Wang, C. Janiak, *Angew. Chem. Int. Ed.* **2021**, *60*, 15365 – 15370.
- [42] A. J. Howarth, M. J. Katz, T. C. Wang, A. E. Platero-Prats, K. W. Chapman, J. T. Hupp, O. K. Farha, *J. Am. Chem. Soc.* **2015**, *137*, 7488 – 7494.
- [43] R. Lv, J. Wang, Y. Zhang, H. Li, L. Yang, S. Liao, W. Gu, X. Liu, *J. Mater. Chem. A* **2016**, *4*, 15494 – 15500.
- [44] Q. Sun, B. Aguila, Y. Song, S. Ma, *Acc. Chem. Res.* **2020**, *53*, 812 – 821.
- [45] D. Mohan, C. U. J. Pittman, *Hazard. Mater.* **2007**, *142* (1), 1 – 53.
- [46] S. Mollick, T. N. Mandal, A. Jana, S. Fajal, A. V. Desai, S. K. Ghosh, *ACS Appl. Nano Mater.* **2019**, *2*, 1333 – 1340.
- [47] K. Jayaramulu, F. Geyer, M. Petr, R. Zboril, D. Vollmer, R. A. Fischer, *Adv. Mater.* **2017**, *29*, 1605307.
- [48] D. Nam, J. Huh, J. Lee, J. H. Kwak, H. Y. Jeong, K. Choi, W. Choe, *Chem. Sci.* **2017**, *8*, 7765 – 7771.
- [49] M. Kandiah, S. Usseglio, S. Svelle, U. Olsbye, K. P. Lillerud, M. Tilset, *J. Mater. Chem.* **2010**, *20*, 9848 – 9851.
- [50] S. R. J. Oliver, *Chem. Soc. Rev.* **2009**, *38*, 1868-1881.
- [51] M. Ateia, D. E. Helbling, W. R. Dichtel, *ACS Materials Lett.* **2020**, *2*, 1532-1544.
- [52] B. Purkait, A. Mukhaerjee, *Front. Earth Sci. China* **2008**, *2*(3), 292–301.
- [53] S. K. Acharyya, P. Chakraborty, S. Lahiri, B. C. Raymahashay, S. Guha, A. Bhowmik, *Nature* **1999**, *401*, 545.
- [54] G. Liu, Z. Ju, D. Yuan, M. Hong, *Inorg. Chem.* **2013**, *52*, 13815 – 13817.
- [55] S. Karak, K. Dey, A. Torris, A. Halder, S. Bera, F. Kanheerampockil, R. Banerjee, *J. Am. Chem. Soc.* **2019**, *141*, 7572 – 7581.

- [56] W. Xia, X. Zhang, L. Xu, Y. Wang, J. Lin, R. Zou, *RSC Adv.* **2013**, *3*, 11007 – 11013.
- [57] R. J. Drout, K. Otake, A. J. Howarth, T. Islamoglu, L. Zhu, C. Xiao, S. Wang, O. K. Farha, *Chem. Mater.* **2018**, *30*, 1277–1284.
- [58] C. O. Audu, H. G. T. Nguyen, C. -Y. Chang, M. J. Katz, L. Mao, O. K. Farha, S. T. Nguyen, *Chem. Sci.* **2016**, *7*, 6492–6498.
- [59] G. Zhang, K. Tan, S. Xian, K. Xing, H. Sun, G. Hall, L. Li, J. Li, *Inorg. Chem.* **2021**, *60*, 11730-11738.
- [60] S. M. Prabhu, S. Kancharla, C. M. Park, K. Sasaki, *CrystEngComm.* **2019**, *21*, 2320-2332.
- [61] N. Mahanta, J. P. Chen, *J. Mater. Chem. A.* **2013**, *1*, 8636-8644.
- [62] R. J. Drout, S. Kato, H. Chen, F. A. Son, K. Otake, T. Islamoglu, R. Q. Snurr, O. K. Farha, *J. Am. Chem. Soc.* **2020**, *142*, 12357-12366.
- [63] E. Freire, O. L. Mayorga, M. Straume, *Anal. Chem.* **1990**, *62* (18), 950-959.
- [64] R. J. Drout, M. A. Gaidimas, O. K. Farha, *ACS Appl. Mater. Interfaces.* **2021**, *13*, 51886-51893.

Chapter 5

Nano-snare Implanted Ultralight Crystalline Hybrid Composite Material for Multiple Cooperative Interactions Mediated Efficient Sequestration of Radioiodine

5.1 Introduction

The limitations associated with the spent nuclear fuel reprocessing and improper disposal of radionuclides wastes have thwarted the further sustainable development of nuclear energy.^[1-5] In nuclear plant, during reprocessing and in subsequent steps of spent nuclear fuel by dissolving in hot nitric acid solution, various highly toxic radionuclides are generated.^[6, 7] Among them, volatile radioactive iodine isotopes (e.g., ¹²⁹I and ¹³¹I) has attracted significant attention to the environment and safety point of view, owing to its hazardous impact with radiological (longest half-life $t_{1/2} = 1.6 \times 10^7$ years), chemical (high-mobility) and biological (rapid bioaccumulation) toxicity.^[8-10] Moreover, water discharged from nuclear reactor chiller plants contain a significant amount of radioactive iodine, directly contaminating substantial watery environments.^[11-14] Therefore, considering both the importance of sustainable future development of nuclear energy and water purification along with the practical relevance for essential medical uses, efficient and selective sequestration of radioactive iodine both from vapor and aqueous phase counts as a priority research topic.^[15-17]

To address this cardinal issue, recently, utilizing rational synthetic strategies, pioneering endeavours have been devoted to develop various excellent porous materials for the exceptional enrichment of iodine from contaminated samples.^[17-31] Nevertheless, most of the studies are still limited to exploration of fast kinetics, high capacity, capture at high temperature and improved selectivity, which has actuated researchers to develop novel materials for the efficient capture of iodine. Not but what, few of these performance criterion were full-filled by individual adsorbents, due to the scarcity of systematic synthetic strategies, development of a single material that enable highly selective entrapment of iodine with fast kinetics, high capacity, large retention efficiency, recyclability and capture in different relevant temperatures from both air and water medium is remain an unexplored territory.

To accomplish this, it is important to gain insights into the underlying chemistry of the active interaction sites. This can be revamped by taking into account the specific interactions between iodine and the sorbent material at molecular level. With this aim, designing an effective adsorbent for high performance iodine capture, we reconsidered the previous studies and investigated their insight mechanism towards efficient iodine uptake. The high adsorption capacity of iodine is predominantly governed by the textural features (such as surface area, pore size and pore volume) of the porous sorbents.^[26-28] Moreover, the strong interactions between the electron-deficient iodine molecules with the optimistic dense binding sites of electronically rich low-density porous materials are favourable for high iodine uptake, owing to the formation of suitable charge-transfer complex.^[23-29] On the other hand, several individual or collective effect of multiple functionalities, such as induction of pi-electron rich conjugated frameworks,^[28] presence of heterocyclic moieties,^[29] incorporation of specific heteroatoms,^[32] have shown clear benefits towards improved I₂ capture efficiency. Among the

heterocyclic sites, various N-doped structural moieties, including imine, triazine, pyridine, amine, etc. have been infused inside aromatic networks to expedite a large iodine enrichment.^[26, 29] In addition, integration of cationic functionality bearing free anions inside the adsorbent can trigger the I₂ vapor adsorption competence by generating strong electrostatic interactions with in-situ formed polyiodide species.^[5, 25, 26] These framework integrated counter anions facilitate energetically favourable interactions with iodine in vapor phase.^[5] Also, these exchangeable free anions aid in the trapping of I₃⁻ anions in aqueous phase.^[12] Other studies demonstrated that in comparison to its powder counterparts, the strategic fabrication of crystalline aerogels enable greatly enhanced I₂ capture with rapid kinetics.^[33, 34] Furthermore, studies suggest that materials featuring Zr-secondary building units (SBU) with hydroxyl groups exhibit selective strong interactions with iodine than that of other interference e.g., NO₂, a major off-gas species.^[19]

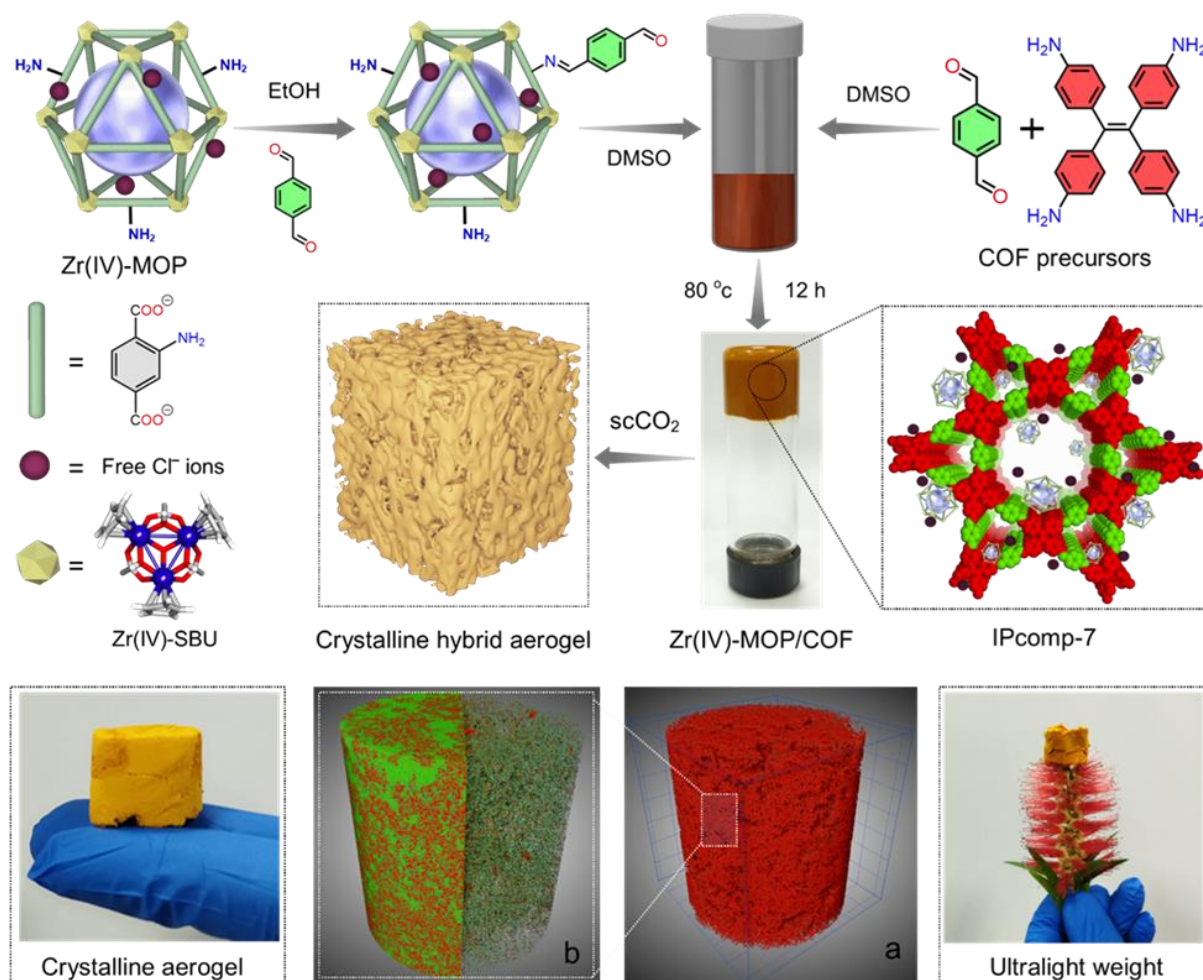


Figure 5.1: Schematic representation of fabrication of NH₂-Zr(IV)-MOP embedded COF hybrid aerogel (IPcomp-7). IPcomp-7 aerogel is crystalline and light weight in nature. The schematic illustration of the MOP exhibiting Zr(IV)-SBU, free Cl⁻ ions and 2-aminoterephthalate ligand. (a, b) 3D

X-ray tomographic images of the hybrid aerogel showing presence of hierarchical macropores throughout the structure.

Integrating all these features in a single material to develop an excellent I_2/I_3^- adsorbent is challenging, and remains largely unexplored due to shortfall of systematic synthetic preparation. In this regard, development of advanced hybrid composite porous materials can be beneficial in order to achieve upgraded performance toward target specific applications. Through carefully orchestrated molecular engineering, several innovative porous materials have recently been acknowledged as viable platforms for numerous activities due to their predesigned adjustable reticular structure.^[35, 36] That being said, efficacious performance with collective excellence of different functional materials can be achieved through the fabrication of composite materials.^[37, 38] Towards this aim, in case of host-guest hybrid material-based ideal adsorbents, the guest should be evenly dispersed throughout the host matrix and adorned with chelating groups that can strongly interact with the host surface. In this sense, metal-organic polyhedra (MOP) and covalent organic framework (COF), could be the perfect choice for guest and host matrix, respectively. MOPs and COFs are two well-known crystalline porous solid materials, constructed from coordination assembly of metal ions/cluster with organic ligands and covalent threading of pure organic molecules, respectively.^[39-42] The unique solution processable nature of MOPs and high chemical stability with long-range order of COFs promote them as promising compatible materials towards fabrication of composites. Nevertheless, unfortunately, MOPs fall short of their conceivable potential pertaining to their inevitable aggregation-induced blocking of the active sites in solid-state after the removal of guest.^[43] With this interest, only a few efforts have been performed to alleviate these key issues by encapsulating MOPs into various porous matrix including MOFs and silica or connecting with other polymer membranes.^[44-46] However, development of hybrid composite porous material by covalently strapping of MOPs with COFs, utilizing unique hybridization strategy and further construction of crystalline hybrid aerogel is still an unfinished challenge.

Taking all these factors into consideration, herein, we designed and fabricated a crystalline hybrid ionic aerogel material (IPcomp-7, where “IP” stands for IISER Pune, and “comp” stands for composite) by covalent grafting of amino functionalized Zr(IV)-MOP with COF, which exhibited highly efficient sequestration efficacy towards I_2 and I_3^- from both vapor and aqueous medium (Figure 5.1). The strategic embedding of free amine groups pendent cationic discrete chemically stable MOP with a imine functionalized non-interpenetrated 2D COF with 1D open channelled dual-pores, showcased unique structural features with multifunctional properties including, high crystallinity with large surface area, presence of heteroatoms, highly dense N-containing moieties, e.g., imine, amine groups, cationic nature with free Cl^- ions, $Cp_3Zr_3O(OH)_3$ SBU, and low density ultralight aerogel scaffold (Figure 5.1). Owing to these multifunctional characteristics, IPcomp-7 displayed unprecedented sequestration efficiency in terms of high adsorption capacity, fast kinetics, superior selectivity, retention, recovery and

recyclability towards I₂ and polyiodides under static and dynamic conditions at different temperatures in both vapor and aqueous medium. Moreover, the hybrid composite exhibited rapid and highly selective enrichment of both molecular iodine and polyiodine anions in the presence of large excess of other interference from different challenging water systems. Consequently, in order to demonstrate the practical utility, as a proof-of-concept device, IPcomp-7 embedded column breakthrough test manifested cyclic efficient capture and recovery of iodine/polyiodides.

5.2 Experimental

5.2.1 Materials: All the reagents, starting materials and solvents were commercially purchased from Sigma-Aldrich, TCI Chemicals, Alfa aesar depending on their availability and used without further purification.

5.2.2 Safety Note: Iodine vapor is toxic in nature and proper protective gear (masks, gloves) is always to be used. The iodine capture protocol described in this article, that uses acid (in dynamic sorption) in a packed tube at high temperature must be carried out under strict safety precautions.

5.2.3 General Characterizations and Physical Measurements:

5.2.3.1 Powder X-ray diffraction (PXRD): Powder X-ray diffraction (PXRD) experiments were performed on a Bruker D8 Advanced X-ray diffractometer at room temperature using Cu K α radiation ($\lambda = 1.5406 \text{ \AA}$) at a scan speed of $0.5^\circ \text{ min}^{-1}$ and a step size of 0.01° in 2θ .

5.2.3.2 Fourier transform infrared spectroscopy (FT-IR): The FT-IR spectra were acquired by using NICOLET 6700 FT-IR spectrophotometer using KBr pellet in $500\text{-}4000 \text{ cm}^{-1}$ range. The AIR Spectra were acquired by using a Bruker Optics ALPHA-E spectrometer with a universal Zn-Se ATR (attenuated total reflection) accessory. FT-IR/ATR data are reported with a wave number (cm^{-1}) scale in $500\text{-}4000 \text{ cm}^{-1}$ range.

5.2.3.3 Thermogravimetric analysis (TGA): Thermogravimetric analyses were recorded on Perkin-Elmer STA 6000 TGA analyzer by heating the samples from 40 to 800°C under N₂ atmosphere with a heating rate of $10^\circ\text{C min}^{-1}$.

5.2.3.4 Field emission scanning electron microscopy (FESEM): The morphology of the materials was recorded with a Zeiss Ultra Plus field-emission scanning electron microscope.

5.2.3.5 Transmission electron microscopy (TEM): TEM, High-resolution TEM imaging and STEM-EDS were performed on the HRTEM (JEM-2200FS, JEOL) operating at acceleration voltage of 200 kV . For TEM analysis, all the samples were dispersed in isopropanol (0.5 mg/mL) and sonicated for 15

min. Then, the samples were left for 2 min, and the upper part of the solution was taken for preparing TEM samples on a lacey carbon-coated copper grid (Electron Microscopy Science, 200 mesh).

5.2.3.6 Solid-state nuclear magnetic resonance (NMR) spectroscopy: Solid-state ^{13}C cross-polarization-magic angle spinning (CP-MAS) spectra were conducted on a Bruker 500 MHz NMR spectrometer with a CP-MAS probe. Carbon chemical shifts are expressed in parts per million (δ scale).

5.2.3.7 Nuclear magnetic resonance (NMR): ^1H NMR spectra were recorded on Bruker 400 MHz NMR spectrometer. The chemical shifts are expressed in parts per million (δ scale).

5.2.3.8 High-resolution mass spectroscopy (HRMS): The mass analysis of the MOPs were carried out using high-resolution mass spectrometry (HRMS-ESI-Q-TOF LC-MS) and Applied Bio system 4800 PLUS matrix-assisted laser desorption/ionization (MALDI) TOF/TOF analyzer.

5.2.3.9 Nitrogen adsorption-desorption isotherm measurements: N_2 gas adsorption-desorption measurements were performed using BelSorp-Max instrument (Bel Japan). Prior to adsorption measurements, the activated samples were heated at $120\text{ }^\circ\text{C}$ under vacuum for 12 hours using BelPrepvacII.

5.2.3.10 UV-visible absorption spectra: UV-vis absorption studies were performed on a Shimadzu UV 3600 UV /vis /NIR spectrophotometer in an optical quartz cuvette (10 mm path length) over the entire range of 200-800 nm.

5.2.3.11 Steady state photoluminescence spectra: The steady-state photoluminescence studies were recorded on a Fluorolog-3 spectrofluorometer (HORIBA Scientific).

5.2.3.12 Fluorescence measurements: All fluorescence measurements were done on Jobin Yvon Fluoromax-4 spectrofluorometer.

5.2.3.13 X-ray photoelectron spectroscopy (XPS): As-obtained powder samples was stuck to conductive paste and then measured by X-ray photoelectron spectroscopy using K-Alpha+model (Thermo Fischer Scientific, UK) with $\text{Al K}\alpha$ source.

5.2.3.14 Zeta potential: Zeta potential measurements were performed on Anton Paar Litesizer 500 series instrument. Measurement cell: Omega cuvette Mat. No. 155765, Target temperature $25.0\text{ }^\circ\text{C}$, Equilibration time – (Series parameter), Henry factor 1.1 (Other), Adjusted voltage (Automatic Mode), Number of runs 20, Solvent – water.

5.2.3.15 Raman measurements: Raman spectra were acquired with an Xplora PLUS Raman microscope (Horiba Company) (785 nm laser and a 1200 lines/mm grating).

5.2.3.16 Raman mapping analysis: Raman mapping images were acquired with a Renishaw, UK model-Invia Reflex make Raman microscope. Spectrograph equipped with a research-grade microscope capable of producing Raman (wavenumber transfer 50 to 4000 cm^{-1}) and PL (330 nm to 1.6 microns). Spectral Range of spectrometer: 200 nm – 1600 nm.

5.2.3.17 Supercritical CO₂ activation: Supercritical CO₂ activation process was performed using a TOUSIMIS Samdri instrument. A freshly filled liquid CO₂ cylinder was used for the experiment.

5.2.3.18 Compression test: The mechanical strength test was conducted with a vernier caliper and each data was collected for three times. Compressive strength was measured in non-confined mode, using universal testing machine (Model Instron 5943) equipped with 1 kN load cell and stainless-steel compression plates. The mechanical compression data was collected at room temperature.

5.2.3.19 Electron paramagnetic resonance (EPR) spectroscopy: EPR spectroscopy was carried out on a Bruker EMX plus spectrometer.

5.2.3.20 Conductivity measurement: Four probe DC conductivity measurements were done on pressed pellets of compounds in Keithley 6221 source meter instrument.

5.2.3.21 Fluorescence microscopy imaging: Fluorescence microscopy imaging (Leica Microscopes Model D3) was used to achieve background free high-resolution images of all the compounds. Hamamatsu orca flash4 camera with 20x objective (HC PI APO 20x/0.80) was used for capturing the digital images of the compound.

5.2.4 Detailed procedures for synthetic preparation

5.2.4.1 Synthesis of TPE-NO₂ (tetrakis(4-nitrophenyl)ethylene): TPE-NO₂ was synthesized by following a previously reported procedure.^[21] In an ice bath, 40 mL of acetic acid and 40 mL of fuming nitric acid were added to a 250 mL round bottom flask. Then 5 gm of TPE (15 mmol) was added in small portions over a 20 min period before the reaction was warmed to room temperature with stirring for 3h. After that the reaction mixture was poured into 300 mL ice water, which yielded yellow precipitation. This precipitate was collected by filtration, washed with an excess of water, and air dried, affording a light yellow powder with high yield (Scheme 5.1).

5.2.4.2 Synthesis of TPE-NH₂ (tetrakis(4-aminophenyl)ethylene): TPE-NH₂ was synthesized by following a previously reported procedure.^[21] 2.50 gm of tetrakis(4-nitrophenyl)ethylene (4.34 mmol) was dissolved in 25 mL of anhydrous THF in a 250 mL round bottom flask under nitrogen atmosphere. After that 500 mg of palladium on carbon (wt 10 % Pd) and 25 mL of NH₂NH₂·H₂O (516 mmol) were added to the solution slowly before the reaction mixture was refluxed for 48 hours. Then the reaction

temperature in undisturbed state for 72 hours. The yellow cubic block crystals were collected by filtration and dried under vacuum.

5.2.4.5 General Synthesis of NH₂-Zr(IV)-MOP/COF hybrid composites aerogel (IPcomp-7): In a typical synthesis procedure, at first, certain amount of -NH₂ functionalized Zr(IV)-MOP was reacted with TPD in ethanolic solution with catalytic amount of 3M acetic acid for 12 hours at 65 °C under mild-stirring condition. Upon completion of the reaction, the yellow coloured precipitate was collected by centrifugation at 7500 rpm for 5 min and dried under vacuum. This product was termed as TPD@NH₂-Zr(IV)-MOPs.

The hybrid materials were synthesized by systematic hybridization synthetic strategy via two steps procedure. In the first step, the hybrid wet-gel form of the composite was synthesized. At first, a certain amount of TPD@NH₂-Zr(IV)-MOPs were dissolved in an aqueous dimethyl sulfoxide (DMSO) solution (few drops of H₂O in DMSO). In another vial, precursor of COF, i.e., 23.5 mg (0.06 mmol) of 4, 4', 4'', 4'''-(ethene-1, 1, 2, 2-tetrayl)tetraaniline [ETTA] and 16.1 mg (0.12 mmol) terephthalaldehyde [TPD] were each dissolved completely in 0.45 mL dimethyl sulfoxide (DMSO). Thereafter, both of these two solution were mixed with each other in a 4 mL reaction glass vial. In this solution, 0.1 mL 6M acetic acid aqueous solution was introduced, upon which the mixture became cloudy immediately and underwent a gelation process within a few minutes. Thereafter, the resulting cloudy solution was sealed using Teflon tape to prevent the solvent leakage and further transferred in a closed container and allowed to stand in oven at 80 °C for ~12 h. In this time period the gelation was occurred. After, ~12 hours the hybrid wet-gel was formed (Appendix 5.1), which was further aged for another ~12 h at room temperature.

Now, in order to get the hybrid aerogel (IPcomp-7), in the second step, thus-prepared hybrid wet-gel compound was subjected to through solvent exchange with tetrahydrofuran, acetone and ethanol (each exchange for three times) before being carefully transferred into a plastic cell, which was then placed to the supercritical CO₂ (ScCO₂) activation chamber of the automated critical point dryer instrument (TOUSIMIS Samdri). After that, a typical supercritical drying process was performed by addition of ~20 mL of pure ethanol, cooling to 0 to 5 °C and filling the instrument chamber with liquid CO₂, followed by purge, soaked in liquid CO₂. The purge and soaking cycle (each ~10 min) were repeated for 8 times. Then the temperature of the system was raised to 35-40 °C for next ~2 h. After transforming the system to the supercritical temperature and pressure, it was allowed to slowly bleed overnight. At last, the auto venting of the ScCO₂ equipment result the light weight aerogel monolith of the hybrid composite (Appendix 5.1), which was used for further characterization and application. It should be pointed out that the proper number of purge-soaking cycles is essential for the final structure and robustness of the hybrid aerogel monoliths. Thereafter, these hybrid aerogels were further reactivated in dioxane (~2 mL) solvent with catalytic amount of 6M acetic acid (0.1 mL) at 80 °C for another one

day. After 24 hours, again, these reactivated aerogels were subjected to solvent exchange and drying under supercritical CO₂ condition with the similar protocol mentioned above. Finally, the resulting material was dried under vacuum for overnight to obtain the hybrid aerogel. In addition to this, different batches of the hybrid composite materials were synthesized by varying the amount of the TPD@NH₂-Zr(IV)-MOPs (1 mg, 5 mg, 15 mg, 25 mg, 35 mg, 45 mg, 50 mg, 100 mg) and keeping the fixed amount of the precursors of the COF. Now, for the primary screening test, we performed the vapor phase static iodine capture studies with all of these hybrid materials. As a result, the composite material fabricated with ~15 mg of TPD@NH₂-Zr(IV)-MOPs, demonstrated the most efficient capture performance (Appendix 5.34). Therefore, in this work, we chose ~15 mg NH₂-Zr(IV)-MOP@COF hybrid aerogel material (termed as IPcomp-7) for further study.

5.2.4.6 Digestion process and ¹H NMR analysis of IPcomp-7: Almost, 30 mg of NH₂-Zr(IV)-MOP/COF composite aerogel material (IPcomp-7) was digested in ~2 mL of 1 mol/L NaOH solution over ~6 hours. Then, 2 mL of DI water was added to the mixture and the overall solution was then sonicated properly for a certain time. Thereafter, the solution was left standing for one day for precipitating. Further, the precipitate was removed by a membrane filtration (0.2 μm pores) to give a clear solution containing the corresponding organic ligands of metal-organic polyhedron, 2-aminoterephthalate (2ATA²⁻). Now, in order to remove the solvent molecules, the mixture was subjected to undergo dynamic vacuum at 80 °C overnight to obtain the solid powder with very low yield. After that the powder was dispersed in 1.2 mL of D₂O and followed by the addition of few drops of 40 wt% NaOD, which result a clear solution. This clear solution was than analysed for ¹H NMR.

5.2.5 Iodine Sequestration studies

5.2.5.1 General Consideration: The aqueous or organic solution of iodine (I₂) or triiodide (I₃⁻) were prepared by dissolving a certain amount of solid iodine or iodine-potassium iodide (I₂/KI) into deionized water or n-hexane solution and the different concentrations were obtained by diluting the stock solution with the proper amount of distilled water/n-hexane unless otherwise indicated. The concentrations of I₂/I₃⁻ during all the experiments were detected by UV-vis spectroscopic analysis. All the adsorption experiments were performed at ambient conditions. All the data has been collected three times through UV-vis analysis to plot the final adsorption results.

5.2.5.2 Vapor phase static iodine uptake studies: IPcomp-7 (10 mg) was weighted in a small glass vial, and this vial was exposed to molecular iodine for 24 h at 75 °C in a closed system. After the corresponding adsorption time, the glass vial was taken out, cooled to room temperature, and weighed. Iodine uptake capacity of the compound was calculated by the weight difference of glass vials before and after adsorption, using the formula:

$$W = ((m_2 - m_1)) / m_1 \times 100\% \quad \dots\dots\dots(1)$$

Where, w ($\text{g}\cdot\text{g}^{-1}$) is the adsorption capacity of iodine uptake, m_1 (g) and m_2 (g) are the mass of compounds with the glass vial before and after being exposed to iodine vapor. The values of uptake capacity are the average values of at least three experiments.

5.2.5.3 Recyclability test in static condition: To study the recyclability for iodine-loaded material in static system we followed a reported protocol with slight modification.^[34] We first investigated the desorption efficiency. A certain amount of iodine-loaded compound (I_2 @IPcomp-7) with maximum adsorption capacity was taken in an open glass vial and heated at ~ 150 °C for a certain period of time. The iodine desorption efficiency was calculated by weight difference: Desorption efficiency = $(w_3 - w_2) / w_1 \times 100\%$, where w_1 (g) is the weight of iodine in I_2 @IPcomp-7 before desorption. w_2 (g) is the weight of I_2 @IPcomp-7 after desorption, and w_3 (g) is the weight of I_2 @IPcomp-7 before desorption. For the recyclability test, the I_2 @IPcomp-7 powder was heated at ~ 150 °C for ~ 16 h to achieve the complete desorption and used for the next cycle of iodine adsorption.

5.2.5.4 Retention ability test: To study the adsorption stability for iodine-loaded material in static system, a certain amount of iodine-loaded material (I_2 @IPcomp-7) was taken in an open glass vial, and the vial was placed in an empty large bottle, which was placed at room temperature and ambient pressure. After one day, the weight of the vial containing iodine-adsorbed material was recorded and the vial was placed back into the empty large bottle. The large bottle was opened to further continue the experiment for next 7 days.

5.2.5.5 Iodine (I_2) release studies in hexane: Time-dependent UV-Vis measurements were carried out in n-hexane to record the I_2 releasing efficiency from the I_2 @IPcomp-7. In a typical experiment, 2 mg of I_2 @IPcomp-7 was immersed in ~ 4 mL of n-hexane in a reaction vial with mild shaking. The UV-Vis adsorptions were recorded by periodically removing a 2 mL of n-hexane solution from the mother solution and then transferred back.

5.2.5.6 Vapor phase dynamic iodine uptake studies: The gaseous iodine adsorption in dynamic system was performed in a home-built setup. 20 mg IPcomp-7 was packed into a glass tube with glass wool filling the void space of both ends, which served as the adsorption cell. The temperature control system was set to 75 °C, and valve 1 and valve 2 were opened and valve 3 was closed. A nitrogen flow ($10 \text{ cm}^3/\text{min}$) passed through the iodine vapor generator to blow the iodine vapor into the hybrid composite material in the adsorption cell. The flow rate of I_2 gas was about $\sim 41 \pm 2$ mg/h, determined through trial and error. The effluent from the adsorption cell was treated with 0.1 M NaOH solution in outlet. The adsorption capacity for iodine was calculated from the weight difference of compound containing glass tubes before and after adsorption.

5.2.5.7 Recyclability test in dynamic condition: To study the recyclability for iodine-loaded compound in dynamic system, valve 1 and valve 2 were closed and valve 3 was opened. The iodine-loaded compound with maximum adsorption capacity in the adsorption cell was heated at ~150 °C for 16 h with a nitrogen flow (10 cm³/min) to achieve the complete desorption, Then, valve 1 and valve 2 were opened and valve 3 was closed, and the temperature control system was set to 75 °C for the next cycle of iodine adsorption.

5.2.5.8 Aqueous phase static molecular iodine (I₂) capture studies: To study the iodine adsorption performance in aqueous solution system, we first prepared the molecular iodine (I₂) solutions in water. To prepare the saturated iodine aqueous solution, an excess of iodine was added into 1 L deionized water, and after stirred for ~6 h the mixture was filtered to remove the undissolved iodine. The iodine concentration in the saturated iodine aqueous solution is about 300 ppm.

5.2.5.9 Aqueous phase static triiodide (I₃⁻) capture studies: The I₃⁻ solutions were freshly prepared before experiments by mixing 300 mg I₂ and 600 mg KI in 20 mL deionized water sonication. The iodine concentration in this I₂/KI aqueous solution is 15000 ppm.

5.2.5.10 Static iodine (I₂) capture studies in hexane: 3000 mg of iodine was dissolved in 1 L n-hexane to prepare the n-hexane solution of iodine (3000 ppm).

5.2.5.11 Solution phase adsorption kinetic studies: For the time-dependent study for I₃⁻ removal, we took 3 mL of 100 ppm stock aqueous I₃⁻ solution in a cuvette. We recorded the initial absorbance value with the help of UV-visible (UV-vis) spectroscopy. Then, 3 mg of IPcomp-7 was added to the cuvette. After treating the compound, we recorded the absorbance spectra of the supernatant solution at regular time intervals. We calculated the % removal data of I₃⁻, decrease in the concentration of the I₃⁻ vs time, and uptake of I₃⁻ from this study using the following equations:

$$D_t = ((C_0 - C_t))/C_0 \times 100\% = ((A_0 - A_t))/A_0 \times 100\% \quad \dots\dots(2)$$

$$(C_0 - C_t)/C_0 = (A_0 - A_t)/A_0 \quad \dots\dots\dots(3)$$

$$C_t = C_0 \times [1 - (A_0 - A_t)/A_0] \quad \dots\dots\dots(4)$$

$$Q_t = (C_t - C_0) \times v/m \quad \dots\dots\dots(5)$$

D_t is the exchange capacity, C₀ and A₀ are the initial concentration and absorbance of the I₃⁻ solution, respectively, and C_t and A_t are the concentration and absorbance of the I₃⁻ solution at specific times, respectively. Q_t is the uptake amount in time t in mg g⁻¹, V is the volume of the solution in mL, and m is the mass of the compound in gm. The kinetics data were fitted to a pseudo-second-order kinetic model using the following equation.

5.2.5.12 Pseudo-second-order model fitting: To investigate the kinetic adsorption behaviour towards iodine, pseudo-second-order kinetic model was used to evaluate the adsorption data, and its linear form can be expressed as follow:

$$t/Q_t = 1/(k_2 Q_e^2) + t/Q_e \quad \dots\dots\dots(6)$$

Where, Q_t and Q_e represent the adsorbed amount (mg.g^{-1}) at time and at equilibrium t (min), respectively, k_2 represent the Pseudo-second-order rate constant of adsorption ($\text{g mg}^{-1} \text{min}^{-1}$). The experimental data was fitted using Pseudo-second-order kinetic model, and R_2 is the correlation coefficient of the fitting curve.

5.2.5.13 Iodine uptake capacity studies: 5 mg of IPcomp-7 were kept in contact with 5 mL of I_3^- solutions bearing different concentrations (15000 to 50 ppm solution) for 24 h under stirring conditions. After 24 h, compounds were filtered out, and the filtrate was analysed by UV-vis studies. The absorbance was recorded by diluting the solution, and the uptake amount was calculated from the initial and final absorbance value of the filtrate using equations (2–5).

Langmuir model, $Q_e = Q_m \cdot C_e / (K_d + C_e)$; Where, C_e (ppm) and Q_e (mg.g^{-1}) are the I_3^- concentration at equilibrium and amount of I_3^- adsorbed at equilibrium respectively. Q_m (mg.g^{-1}) is the maximum amount of I_3^- per mass of adsorbent to form a complete monolayer. K_d (mg L^{-1}) is a constant to the affinity of the binding sites.

Freundlich model, $Q_e = K_f \cdot C_e^{1/n}$; Where, K_f and $1/n$ are the Freundlich model constant, indicating capacity and intensity of adsorption respectively.

5.2.5.14 Distribution coefficient (K_d) value calculation: The distribution coefficient (K_d) value as used for the determination of the affinity and selectivity of sorbents for triiodide (I_3^-), is given by the equation:

$$K_d = ((C_0 - C_e) / C_e) \times v / m \quad \dots\dots\dots(7)$$

Where, v is the volume of the testing solution (mL), m is the amount of solid adsorbent (g), C_0 is the initial concentration of I_3^- , and C_e is the equilibrium concentration of I_3^- .

5.2.5.15 Selectivity test in presence of other competing ions: For testing the influence of competing ions, in this study, 2 mg each of IPcomp-7 was kept in contact separately with a binary solution containing 1 mL of I_3^- solution and 1 mL each of various competing anions solution (NO_3^- , Cl^- , Br^- , ClO_4^- , SO_4^{2-}) with equal concentration as well as ~100-fold excess for 24 h under stirring conditions. Then, after 24 h, the compounds were filtered, and the filtrate was analysed by UV-vis studies using the protocol discussed above. The efficiency of the capture process in the presence of competing anions was measured with respect to a blank where 1 mL of water is used instead of the competing anion

solution. The absorbance was recorded by diluting the solution, and the uptake amount was calculated from the initial and final absorbance value of the filtrate using equations 2–5. The iodine uptake in the presence of a mixture of competing ions was also carried using the same protocol.

5.2.5.16 I_3^- capture study in different water systems: A stock solution of 100 ppm I_3^- was prepared using different water matrix, such as seawater, river water, lake water, etc. Then, 5 mg of IPcomp-7 was kept in contact with 5 mL of I_3^- ion those water stock solution for 12 h under stirring conditions. After 12 h, compounds were filtered out, and the filtrate was analysed by UV–vis studies. The absorbance was recorded by diluting the solution, and the uptake amount was calculated from the initial and final absorbance value of the filtrate using equations 2–5.

5.2.5.17 Dynamic column-based flow-through I_2 capture study in water: We conducted a dynamic column-based flow-through I_2 capture experiment with the flow of saturated iodine aqueous solution. IPcomp-7 was packed into a glass column with addition of cotton, and the saturated iodine aqueous solution was passed through the cell with a flow rate of $0.75 \text{ mL}\cdot\text{min}^{-1}$. The colour of IPcomp-7 material gradually became darker when iodine was adsorbed. The filtrate was clear, and the iodine concentrations of filtrate and the original solution were detected by UV-Vis spectrophotometer (Appendix 5.68).

5.2.5.18 Dynamic column-based flow-through I_3^- capture study in water: To check the continuous I_3^- capture efficiency by the hybrid aerogel material (IPcomp-7), a column exchange-based flow-through experiment was conducted by packing the hybrid aerogel inside a column as bed. After that, to mimic the ground water system different volume of stock ~ 100 ppm of I_3^- aqueous solution along with ~ 100 -fold excess concentration of other interfering anions (such as NO_3^- , Cl^- , Br^- , ClO_4^- , SO_4^{2-}) were mixed. Thereafter, this mixture was passed through the column bed with a flow rate of $0.5 \text{ mL}/\text{min}$, which was controlled by a water-flow-regulator, and the drops per minute was recorded with the help of a stopwatch. A bed-volume of ~ 4.2 – ~ 4.5 mL of column eluted solution was collected in a different respective container. The concentration of I_3^- in these solutions were then analysed through UV-vis analysis. The recyclability test of the column exchanged-based I_3^- capture study was performed by washing the column with pure water, followed by excess n-hexane and saturated NaCl solution after each cycle. The filtrate of each cycle was collected at the bottom of the column (Appendix 5.70). Before and after capture studies, the concentration of I_3^- solutions were analysed through UV-vis analysis.

5.2.5.19 Recovery of solid iodine by heating: The recovery of solid iodine was performed in a home-built setup as shown in appendix 5.72. A certain amount of iodine loaded (captured through vapor phase) compound (I_2 @IPcomp-7) was heated in a closed chamber at ~ 150 °C under the flow of nitrogen. The iodine vapor generated from the compound upon heating was further subjected to condense in a separate glass flask, which was dipped in an ice-cool bath for a period of time. After that the glass flask

was removed from the system. It was found that solid crystals of iodine was condensed on the surface of the glass flask. These solid iodine crystals were then measured and recovered in a separate storage vial.

5.2.5.20 Recovery of solid iodine by treating in pentane: A certain amount of iodine loaded (captured through vapor phase) compound ($I_2@IPcomp-7$) was treated with excess amount of pentane. Upon this treatment the colour of pentane solution was become dark violet colour, which indicated liberation of large amount of iodine from $I_2@IPcomp-7$. Thereafter, this iodine containing pentane was transferred into a glass petri dish, which was further kept at room temperature for evaporation for few minutes. After complete evaporation of pentane a large amount of solid iodine was found to crystalize on the top of the glass dish. This recovered iodine crystals were then stored in a separate glass vial (Appendix 5.73).

5.2.6 Determination of electrostatic surface potential (ESP), binding sites and binding energy of different interactions:

The molecular-level interactions between the amino functionalized cationic Zr(IV)-MOP and repeating unit of COF along with iodine/polyiodide species were simulated using Discovery Studio 2017 (Accelrys). The DFT simulation was performed at fine quality calculation level. At first, using DMOL3 and B3LYP hybrid function the single unit of the MOP and repeating unit of the COF was fully geometry relaxed by keeping the Multiplicity factor to Auto mode, double numeric plus polarizing (DNP+) basis set with water as solvent. Using simulated annealing technique structural simulation on the geometry relaxed MOP and COF structure was realized to find a feasible interaction site of the I_2/I_3^- within the relaxed MOP and COF unit. The electrostatic potential (ESP) on the van der Waals (VDW) surfaces (isodensity = 0.001 a.u.) of MOP and COF unit was derived from ground-state electron density of the system.

The Static binding energies (ΔE) at 0 K in vacuum were calculated using the following expression

$$\Delta E = E(\text{MOP} + I_2/I_3^-) - E(\text{MOP}^+) - E(I_2/I_3^-)$$

$$\Delta E = E(\text{COF} + I_2/I_3^-) - E(\text{COF}^+) - E(I_2/I_3^-)$$

Where E_x refers, respectively, to the total energies of the $\text{MOP} + I_2/I_3^-$ or $\text{COF} + I_2/I_3^-$ complex, the charged MOP^+ and COF^+ alone, and the I_2/I_3^- molecule/anions respectively.

5.3 Results and Discussion

To construct the host-guest-based unique hybrid composite ionic aerogel material, a cationic MOP and a 2D imine COF was selected as suitable guest and host materials, respectively. At first, the individual components, i.e., the nanosized Zr(IV)-based chemically stable amino-functionalized MOP ($\{[\text{Cp}_3\text{Zr}_3\text{O}(\text{OH})_3]_4(\text{NH}_2\text{-BDC})_6\}\cdot\text{Cl}_4\}$)^[47] (Figure 5.1 and Appendix 5.2) and the tetradentate core based 1D channel-type dual-pore containing hierarchical porous COF^[48, 49] aerogel^[33] (Figure 5.1 and Appendix 5.3) were synthesized and thoroughly characterized (Appendix 5.4-5.13). The hybrid material (IPcomp-7) was synthesized via stepwise systematic covalent hybridization synthetic strategy. Initially, the amino-group pendent MOP was functionalized with terephthaldehyde and further reacted with the precursors of the COF, tetraamino-tetraphenylethylene along with excess terephthaldehyde to construct the hybrid wet-gel material (Figure 5.1). In the subsequent step, after the reactivation and solvent-exchange process this hybrid wet-gel was subjected to conversion into aerogel by applying supercritical CO₂ drying procedure to fabricate a covalently threaded nano-snare(Zr(IV)-MOP) decorated cationic crystalline ultralight hybrid composite aerogel material (Zr(IV)-MOP/COF) (IPcomp-7) (Figure 5.1, see the experimental section for the detailed synthetic procedure).^[33] The following physical and spectroscopic techniques were employed to characterize the structural and morphological features of the synthesized composite material. Powder X-ray diffraction (PXRD) analysis of IPcomp-7 indicated well-resolved strong diffraction peaks that precisely match with the simulated patterns of the reported COF system, suggesting the highly crystalline nature along with dual-pore structure of the composite (Figure 5.2a).^[48, 49] The Fourier transform infrared spectroscopy (FT-IR) spectra of IPcomp-7 verified both the formation of the imine COF-based aerogel host-matrix (characteristic peaks at ~1622 and ~1691 cm⁻¹, corresponding to the appearance of C=N stretching vibration band, and the attenuation of aldehyde frequencies, respectively)^[47-49] and the presence of guest amino-functionalized Zr(IV)-MOP (characteristic peaks at ~1380, ~3515, ~3390 cm⁻¹, corresponding to metal-carboxylate (Zr-O) bonds, symmetric and asymmetric stretching frequencies of free -NH₂ group, respectively)^[50] in the hybrid composite material (Appendix 5.14). This data evidenced the grafting of NH₂-MOP into the COF aerogel matrix along with exposed Zr(IV)-SBU and excessive free amino functional groups. Furthermore, as compared to pristine COF aerogel, the X-ray photoelectron spectroscopy (XPS) survey spectra of IPcomp-7 showed peaks related to elements Zr and Cl along with C, N and O, indicating successful implantation of cationic MOPs into the COF aerogel matrix (Figure 5.2b). Also, the Zr 3d XPS spectra of the pristine MOP was found to shift notably after binding with COF-aerogel, indicating significant interaction between host and guest (Figure 5.2c). The elevated thermal behaviour of the MOPs in the composite was observed by the thermogravimetric analysis (TGA) of IPcomp-7, which also displayed features of both MOPs and COF aerogel (Appendix 5.15).

In addition to this, ^{13}C solid-state nuclear magnetic resonance (NMR) analysis was performed in order to structurally characterize the types of molecular level interactions that occur between the host-COF matrix and guest-MOP molecules in IPcomp-7.

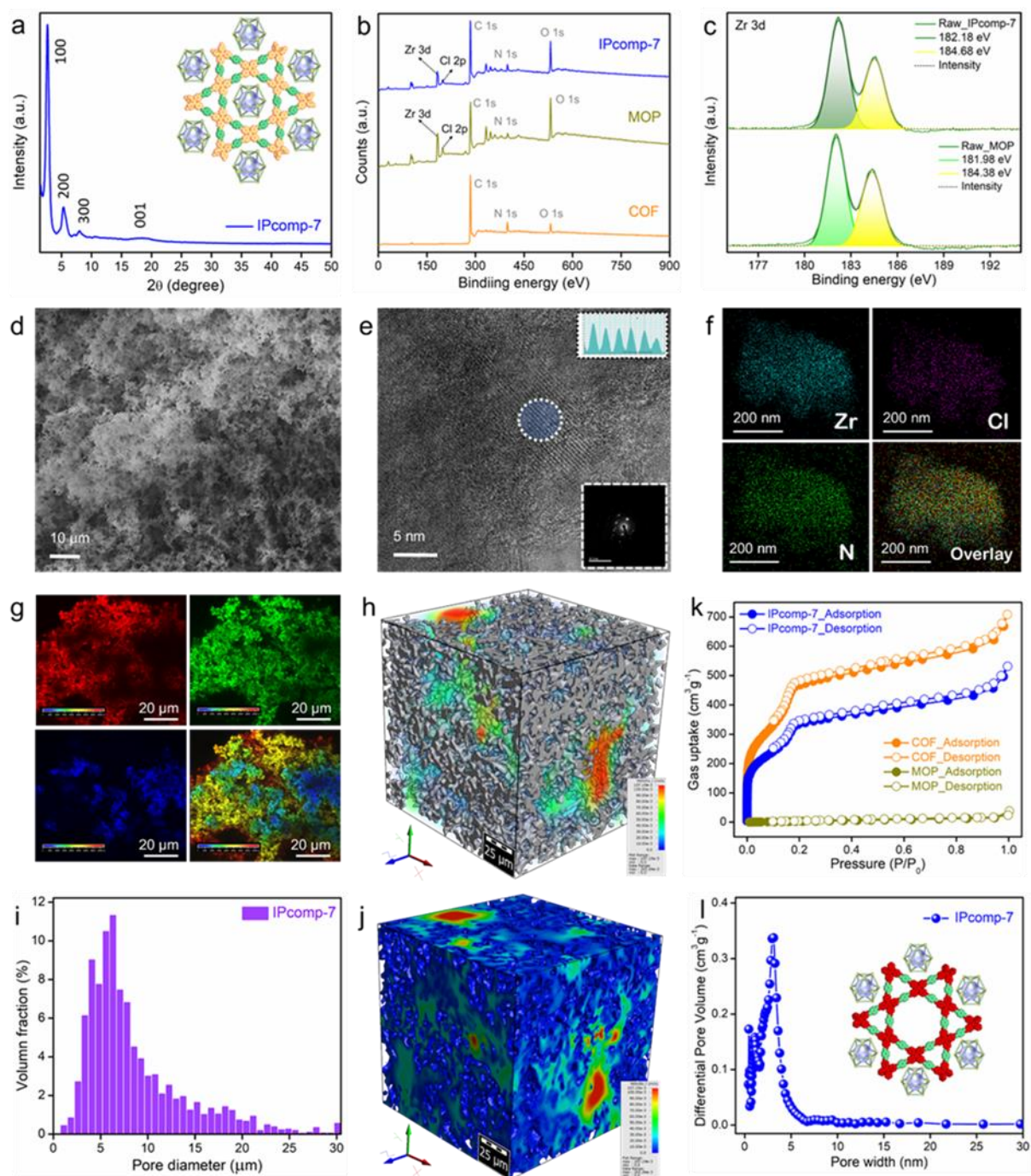


Figure 5.2: (a) PXRD pattern of IPcomp-7. (b) XPS survey spectra of IPcomp-7 with MOP and COF. (c) Zr 3d XPS spectra for MOP and IP-comp-7. (d) FESEM image, (e) HRTEM with d-spacing and FFT image, (f) HAADF-TEM elemental mapping of the composite. (g) Color-coded 3D confocal microscopic image of IPcomp-7. (h) Colour-scale visualization of 3D X-ray tomographic image with

pore-size distribution of IPcomp-7 (grey colour represents solid volume). (j) Void volume of IPcomp-7 with colour-scale (blue to red colour represents void volume). (k) N₂ gas sorption data. (i, l) Micron size and NLDFT pore distribution histogram of IPcomp-7, respectively.

The presence of distinct peaks in the spectra of IPcomp-7 demonstrates that the hybrid composite contained both MOP and COF functionalities (Appendix 5.16). Additionally, the appearance of new characteristic signal at ~171 ppm in the spectra of IPcomp-7 indicated formation of novel imine bond between the amine group of MOP and aldehyde moiety of COF.^[51, 52] Following this, NMR, high-resolution mass spectrometry (HRMS), and inductively coupled plasma (ICP) experiments have been carried out to verify the presence, as well as leaching test of guest MOP molecules from IPcomp-7.^[47, 50]

The analysis of the aqueous supernatant collected from the unwashed pristine composite using ¹H NMR, HRMS, and ICP data revealed the presence of MOP molecules (Appendix 5.17). This finding can be attributed to the simple liberation of non-covalently bonded MOP molecules from the surface of IPcomp-7. However, the analysis of IPcomp-7 treated supernatant, showed no presence of MOPs after through washing with aqueous methanolic solution, arguing out the occurrence of excess MOPs on the surface of the composite and the absence of MOP liberation from the COF aerogel matrix (Appendix 5.18). Additionally, the appearance of Zr metal in the ICP data of digested sample of IPcomp-7 and the relevant peaks of the corresponding organic linkers of MOP in the ¹H NMR spectra confirmed the existence of covalently connected amino-Zr(IV)-MOPs in the hierarchical porous COF aerogel matrix (Appendix 5.19).

Afterwards, the surface morphological investigation of IPcomp-7 was performed by field emission scanning electron microscopy (FESEM), transmission electron microscopy (TEM) and confocal laser microscopy. It was discovered from the FESEM images of IPcomp-7, the morphology resembled sponge-like architecture, in which COF nanolayers were assembled into fiber-like microstructure (Figure 5.2d and Appendix 5.20).^[33] Moreover, the high-magnification FESEM images of MOP-embedded hybrid COF aerogel revealed a disordered pattern of interconnecting fibers with meso-macro hierarchical large void spaces (~5-50 μm), which suggested the 3D hybrid aerogel was highly porous in nature (Appendix 5.20). Analysis of TEM images revealed the interconnected agglomerated particles with irregular large voids caused by the random stacking of the fiber-like nanolayers (Appendix 5.21). Further, to gain insight into the nanostructure of the hybrid aerogel we closely analysed the high-resolution transmission electron microscopy (HRTEM) images of IPcomp-7. The HRTEM images displayed a characteristic interplanar spacing of 0.23 nm, which is in good agreement with the d-spacing of the COF structure (Figure 5.2e).^[48, 49] This observation established the highly ordered/crystalline nature of the MOP loaded hybrid COF aerogel system (fast Fourier transformation, (FFT) data, inset of figure 5.2e).^[29, 53] A detailed examination of the FESEM and TEM energy-dispersive X-ray (EDX) data

of IPcomp-7 revealed the element Zr/Cl ratio ~ 3.0 , which is in agreement with the crystallographic composition of the Zr(IV)-MOP,^[47] supported the stable existence of the cationic MOPs in the hybrid COF aerogel (Appendix Table 5.1-5.6). Moreover, high-angle annular dark-field (HAADF) TEM and FESEM elemental mapping demonstrated the consistent homogenous distribution of all pertinent elements of the cationic MOPs throughout the structure of the composite (Figure 5.2f and Appendix 5.22-5.25). Furthermore, the confocal fluorescent microscopic 3D imaging of IPcomp-7 indicated plenty of extrinsic micron sized pores (macropores) with weakly interconnected nanoparticles surface morphology (Figure 5.2g and Appendix 5.26).

Additionally, microscale X-ray computed tomography (CT) experiments were carried out to investigate the 3D macroscopic hierarchical porous structure of the hybrid nanocomposite. The 2D cross-sectional CT images of the hybrid aerogel material was discovered to include a heterogeneous distribution of large micron-sized pores ($\sim 1\text{-}20\ \mu\text{m}$) throughout the structure (Appendix 5.27). The segmented 3D models of IPcomp-7 were created using reconstruction of 2D CT images for improved comprehension. A disordered pattern of interconnecting macropores was visible across the volume of IPcomp-7 in the segmented 3D CT image (Figure 5.2h and Appendix 5.28). Also, the corresponding color-coded 3D CT images made it easy to recognize the large pore size distribution (PSD) (high volume fraction within $\sim 1\text{-}20\ \mu\text{m}$ with maximum size of $5\text{-}7\ \mu\text{m}$) and $80.2\pm 2\%$ void space inside the entire volume of IPcomp-7 (Figure 5.2i, 5.2j and Appendix 5.29). These findings demonstrated the presence of extrinsic macropores throughout the nanocomposite together with 3D morphological characteristics, all of which are advantageous for rapid mass transfer within porous materials along with easy and complete accessibility of functional sites, and shortened diffusion paths, beneficial towards effective iodine adsorption.^[54]

Furthermore, the micro- and mesoporosity of IPcomp-7 was examined using low-temperature (77K) N_2 gas sorption studies. A sharp uptake at low pressure (below $P/P_0 = 0.01$) (type I) with a step at $P/P_0 = 0.15\text{-}0.20$ bar pressure (type IV) were identified from the sorption data of IPcomp-7, demonstrating the presence of both microporous and mesoporous features, respectively (Figure 5.2k).^[38, 55, 56] Similar observation was noted in the case of pristine COF-aerogel (Figure 5.2k). However, it was found that compared to the bare COF-aerogel, IPcomp-7 exhibited significant lower gas uptake or less porosity. This phenomenon can be explained due to the accommodation of nonporous guest-MOP molecules into the hierarchical porous COF-aerogel matrix. The Brunauer–Emmett–Teller (BET) surface area of IPcomp-7 was calculated to be $1463\ \text{m}^2\text{g}^{-1}$. The pore size distribution was calculated using nonlocal density functional theory (NLDFT) methods revealed the presence of micropores ($< 2\ \text{nm}$) and mesopores ($> 2\ \text{nm}$) within the hybrid material (Figure 5.2l). All these experiments collectively confirmed that IPcomp-7 exhibited hierarchical porosity with micropores ($< 2\ \text{nm}$), mesopores ($> 2\ \text{nm}$) and macropores ($\sim 5\ \mu\text{m}$). In addition, optical characterizations also indicated successful formation of

the MOP/COF hybrid composite.^[51, 55] The optical characteristics of IPcomp-7 were further utilized to demonstrate the successful grafting of amino-functionalized cationic MOPs in the structure of the COF aerogel. The UV-vis diffuse reflectance spectroscopy (DRS) spectra exhibited typical adsorption bands for MOP and COF-aerogel, demonstrating the presence of both constituents in the hybrid nanocomposite (Appendix 5.30). The solid-state photoluminescence spectra of IPcomp-7 yielded identical observation with a noticeable blue shift in the characteristic peak due to the entrapment of discrete MOP molecules inside the COF aerogel matrix (Appendix 5.31). In addition, once the amino group containing MOP molecules were successfully grafted, the weakly emissive COF aerogel was transformed into a highly emissive material, which is further emphasized by fluorescence microscopic imaging (Appendix 5.32). To our delight, in spite of their low density and high porosity, IPcomp-7 demonstrated excellent mechanical flexibility, making them sturdy enough to be used in sequestration applications (Appendix 5.33).^[33]

5.4 Iodine Sequestration Study

Initially, we examined the optimal amount MOPs utilized in the hybrid composite synthesis that enabled the highest efficacy toward iodine vapor capture under optimized conditions. It was found that the composite synthesized by taking ~15 mg of MOP molecules gave the best result (Appendix 5.34). We postulated that using excess MOPs lead to the inevitable aggregation through the host matrix's interconnected hierarchical framework, which reduces porosity and renders a large number of active sites of the over-all nanocomposite inaccessible. This ultimately resulted in lowering of the I₂ sequestration efficiencies. The static iodine capture performance of the nano-adsorbent (IPcomp-7) along with the pristine materials was investigated following a typical procedure (see Supporting Information for details). Interestingly, the colour of the samples became dark-black upon exposure of iodine indicating excess occlusion of iodine into the porous structure of the hybrid composite (Appendix 5.35). From the kinetics experiment, it was found the maximum or equilibrium adsorption capacity of IPcomp-7 was 9.98 g.g⁻¹ within 24h of operation, with a sequestrate step of 7.87 and 9.18 g.g⁻¹ in 6 and 12h, respectively (Figure 5.3a). The maximum capacity of IPcomp-7 was found to be much higher than the pristine MOP (2.31 g.g⁻¹) and COF-aerogel (6.11 g.g⁻¹) materials, which clearly indicated the advanced role of the multi-functional optimum hybrid composite over individual materials towards efficient sequestration of gaseous iodine (Figure 5.3a). The iodine adsorption kinetic of IPcomp-7 was found to follow pseudo-second-order model, which explored the kinetic rate constant as high as 0.0707 g.g⁻¹h⁻¹ (Appendix 5.36). This value suggested the rapid iodine sequestration rate of IPcomp-7, owing to its macro-micro hierarchical interconnected low-density 3D porous structure. Furthermore, considering the industrially relevant conditions, the iodine capture experiment has been performed at different

temperatures, such as 25 and 150 °C in both dry and humid condition. The result indicated 4.27 and 2.89 g.g⁻¹ iodine capture capacities at 25 and 150 °C temperature, respectively, at dry condition (Figure 5.3b). In addition, under humid condition, only a small reduction in the adsorption capacities of IPcomp-7 were recorded (Figure 5.3b). These results demonstrates that humidity had a negligible impact on the ability to efficiently extract iodine from vapor by IPcomp-7. That being said, reusability is an important parameter for an ideal adsorbent towards effective iodine sequestration.

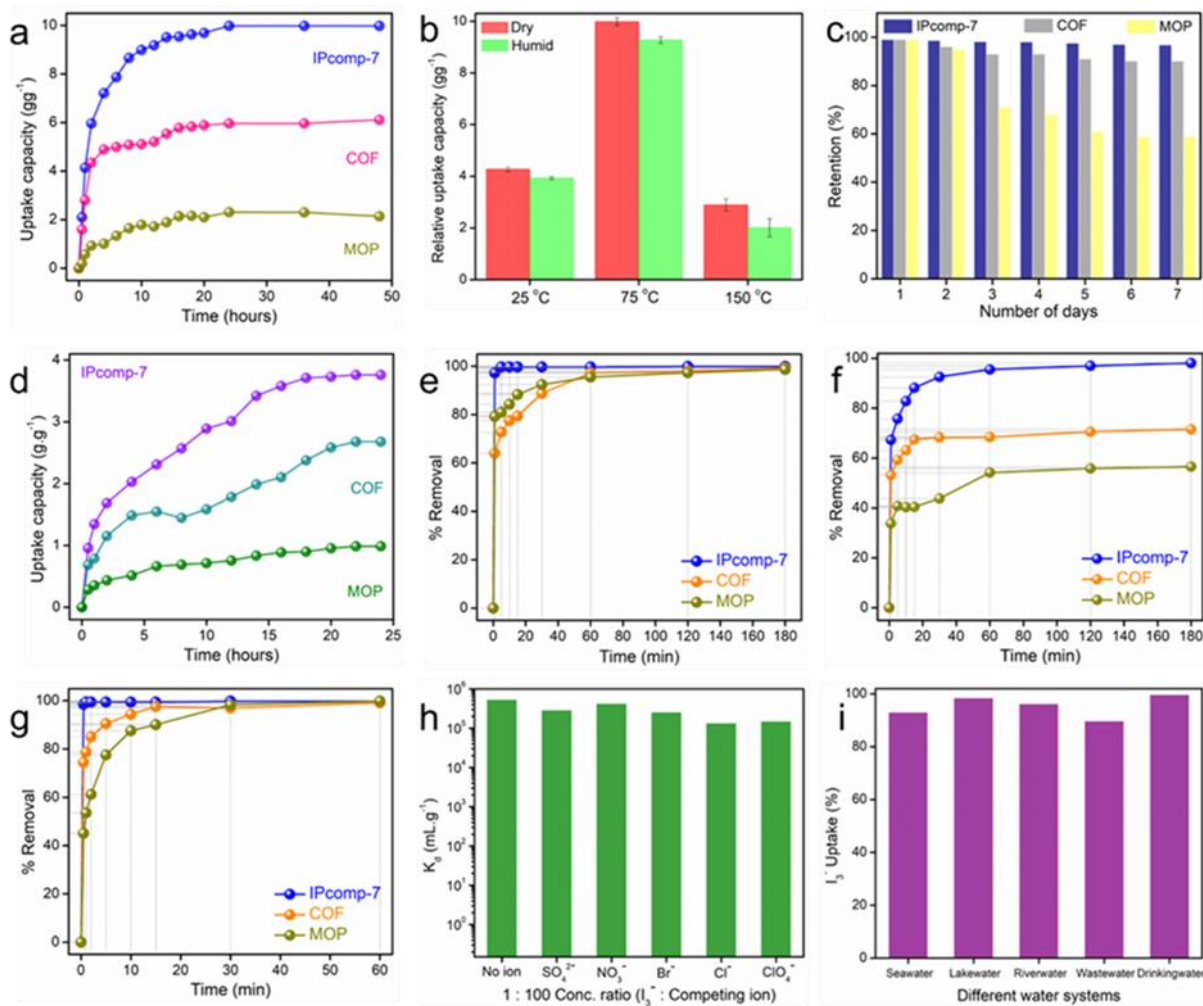


Figure 5.3: (a) Gaseous iodine uptake capacities of IPcomp-7, COF and MOP in static system at 75 °C. (b) Relative static iodine uptake capacities of IPcomp-7 at different temperatures. (c) Iodine retention efficiency of IPcomp-7, COF and MOP. (d) Iodine uptake capacities of IPcomp-7, COF and MOP in dynamic condition at 75 °C. Iodine removal efficiency of IPcomp-7, COF and MOP in (e) water as I₂, (f) n-hexane, (g) water as I₂/KI. (h) Distribution coefficient (K_d) profile of IPcomp-7 for I₃⁻ uptake. (i) Relative I₃⁻ uptake efficiency by IPcomp-7 in different water systems.

Therefore, recyclability of IPcomp-7 was evaluated by performing the desorption test of iodine laden composite. The desorption test resulted ~97% iodine release efficiency in the first cycle. IPcomp-7

demonstrated high sorption capacity ($>7.61 \text{ g.g}^{-1}$) even after five consecutive capture-release cycles indicating superior reusability of the material (Appendix 5.37). The release of captured iodine was also performed by treating the $\text{I}_2@\text{IPcomp-7}$ with hexane solution. Based on the UV-vis data, the concentration of iodine in n-hexane increased as the treatment progressed, which resulted $>96\%$ release of iodine within 2 h of contact time (Appendix 5.38 and 5.39). In this way, IPcomp-7 can be reused for iodine vapor capture, which demonstrated improved recyclability up to five cycles maintaining high efficiency and capacity. Apart from recyclability, another important parameter for an ideal iodine sorbent is retention efficiency. IPcomp-7 exhibited very high adsorption stability ($>94\%$ up to 7 days) with minimal liberation of iodine, indicating strong binding affinity of iodine with the nano-adsorbent (Figure 5.3c). However, in comparison to IPcomp-7, the retention efficiency of the pristine COF-aerogel and MOP was found to be significantly lower.

Pertaining to the practical implementation of the material towards efficient iodine adsorption application, dynamic vapor phase iodine sorption experiments were carried out following the standard procedure as described in the supporting information file (Appendix 5.40 and 5.41). The dynamic iodine adsorption test at $75 \text{ }^\circ\text{C}$ of IPcomp-7 resulted 3.76 g.g^{-1} capture capacity (Figure 5.3d). Also, the kinetic constant of IPcomp-7 for dynamic iodine capture was calculated to be high $0.0837 \text{ g.g}^{-1}\text{h}^{-1}$ indicating fast diffusion of iodine within hierarchical pores of hybrid aerogel (Appendix 5.42). However, when compared to IPcomp-7, the pristine COF-aerogel and MOP exhibited significantly lower dynamic iodine adsorption capacity. Moreover, the recyclability test of IPcomp-7 under dynamic condition was elucidated. As was observed, after five capture and release cycles, the iodine capacity of IPcomp-7 was found to be more than 2.48 g.g^{-1} (Appendix 5.43).

Notably, the majority of the described iodine uptake experiments only demonstrated vapor-phase iodine extraction, and primarily examined the exchange capacity. Yet, despite being crucial for real-time water treatment applications, selective and speedy extraction of iodine from aqueous-phase extremely low concentrations in the presence of a significant excess of other interfering anions has received scant attention. Therefore, the ability of iodine uptake from its aqueous solution was evaluated with IPcomp-7 along with the pristine MOP and COF-aerogel materials. The UV-vis studies indicated the almost instantaneous diminishing of iodine concentration from the saturated aqueous solution upon treating with IPcomp-7 (Appendix 5.44). However, the decrement in the intensity/concentration of iodine by MOP and COF-aerogel was relatively less compared to IPcomp-7 (Appendix 5.45-5.48). This result demonstrated the rapid uptake kinetics ($\sim 99.3\%$ removal within 1 min) of molecular iodine from water by IPcomp-7 (Figure 5.3e). Conversely, the iodine uptake efficiency of pristine MOP and COF-aerogel was found to be inferior to that of IPcomp-7 (Figure 5.3e). The aqueous phase iodine removal kinetics of IPcomp-7 was found to follow pseudo-second-order kinetics model (Appendix 5.49 and 5.50). Moreover, the iodine uptake capacity of IPcomp-7 from water was calculated to be 4.74 g.g^{-1} . In

addition, IPcomp-7 was further applied for sequester iodine from n-hexane medium, which demonstrated highly efficient capture as ~97.9% removal of iodine was observed from the stock solution within 60 min of contact time (Figure 5.3f and Appendix 5.51). Whereas, relatively lower efficiency in iodine uptake was found in case of pristine MOP and COF-aerogel (Figure 5.3f and Appendix 5.52-5.55). The rate constant and Langmuir model-based maximum iodine uptake capacity of IPcomp-7 in n-hexane was $0.00311 \text{ g.mg}^{-1}.\text{min}^{-1}$ and 5.89 g.g^{-1} , respectively (Appendix 5.56-5.57). Furthermore, considering the cationic nature of IPcomp-7 with free exchangeable chloride anions, sequestration of iodine in the form of polyiodide species (such as I_3^-) from water was performed by treating IPcomp-7 with concentrated aqueous solution of KI and I_2 . From the time-dependent UV-vis studies, it was found that IPcomp-7 exhibited ultrafast iodide (I_3^-) removal kinetics (>99% removal within 1 min) from KI/ I_2 solution, whereas, pristine materials showed relatively sluggish uptake rate (Figure 3g and Appendix 5.58-5.62). The I_3^- uptake process by IPcomp-7 found to follow pseudo-second-order kinetics model with rate constant $0.5148 \text{ g.mg}^{-1}.\text{min}^{-1}$, which suggested the ultrafast capture efficiency (Appendix 5.63). Moreover, the concentration-dependent equilibrium uptake capacities of KI/ I_2 were fitted well with the Langmuir isotherm model, which determined the maximum iodine sorption capacity of IPcomp-7, was 5.16 g.g^{-1} (Appendix 5.64). Furthermore, the distribution coefficient (K_d) value is an important parameter, which suggests the affinity of a sorbent material toward the sorbate, and $K_d > 10^3 \text{ mL.g}^{-1}$ is considered as exceptional.^[12] Hence, the K_d value for I_3^- capture by IPcomp-7 was also investigated and calculated to be in the range of $\sim 10^6 \text{ mL.g}^{-1}$, indicating a significant affinity for I_3^- in water (Figure 5.3h).

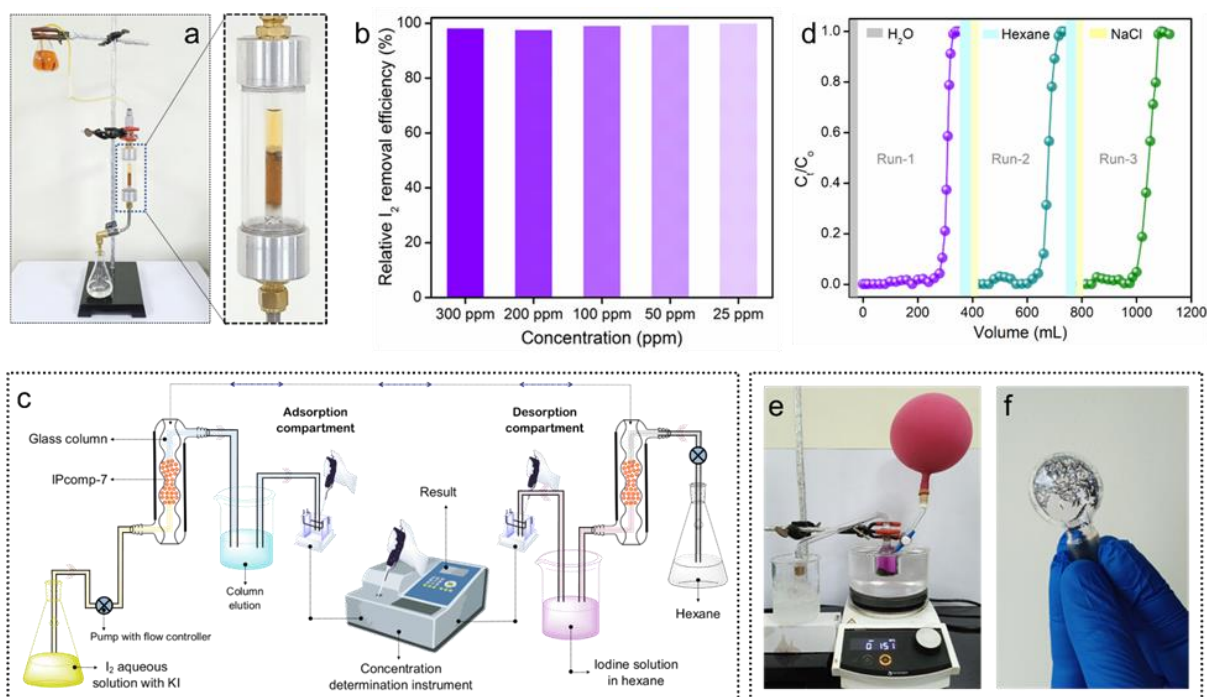


Figure 5.4: (a) Digital image of dynamic column-based aqueous phase molecular iodine capture test. (b) Result of dynamic column-based I_2 capture experiment. (c) Schematic diagram of IPcomp-7 embedded column-based flow-through I_2/KI capture study. (d) Break-through profile of column-based I_2/KI capture test. (e, f) Images of solid iodine recovery test set-up and recovered iodine crystals.

Henceforth, considering the real-world applications, such as detoxification of groundwater, an ideal adsorbent should selectively remove targeted contaminants in the presence of a large excess of other interferences in water. Typically, anions like NO_3^- , Cl^- , SO_4^{2-} , Br^- etc. are present in significant excess amounts with I_3^- contaminated water, which negatively impacts the adsorbent's overall sorption effectiveness.^[56] Therefore, to test the binary and mixture selectivity, I_3^- capture study has been performed in the presence of equimolar as well as ~100-fold excess other competing anions. IPcomp-7 demonstrated highly efficient extraction of I_3^- with removal efficiency of >97.9% in case of both equimolar and ~100-fold excess anions (Appendix 5.65, 5.66). Moreover, the corresponding K_d values for all the binary/mix-competing mixture were evaluated and were found in the order of $\sim 10^5/10^6$ mL.g⁻¹, advocating exceptional binding affinity of IPcomp-7 towards I_3^- (Figure 5.3h). Motivated by such highly efficient and selective entrapment of I_3^- anions by IPcomp-7 in water, further sequestration of I_3^- from different complex water matrixes, including seawater, lake-water, river-water, etc. have been performed. Interestingly, in all the water systems, the hybrid composite exhibited almost >85% removal efficiency of I_3^- anions within 1 min (Figure 5.3i). Additionally, the maximum capture capacity and K_d value of IPcomp-7 for I_3^- in seawater was calculated as 5.09 g.g⁻¹ and $\sim 10^5$ mL.g⁻¹, respectively. Given the seawater contain large excess of competing ions and fouling agents, these values are extraordinarily high.

Inspired by the ultrafast and efficient sequestration of molecular iodine and triiodides from water, we sought to explore further the potential of the hybrid composite toward dynamic column-based aqueous phase iodine capture experiments. Initially, to test the flow-through-based iodine capture from water, a column was packed with IPcomp-7 and aqueous iodine solution having range of different concentration was passed through it (Appendix section for details) (Figure 5.4a and Appendix 5.68). The initial dark/light-yellow iodine solution eventually turned colourless after passing through the column. Additionally, the UV-vis analyses indicated that IPcomp-7 was able to capture more than ~96% of iodine from water across all the concentrations (Figure 5.4b and Appendix 5.69). Furthermore, we were encouraged to perform the aqueous phase I_3^- breakthrough adsorption experiment with IPcomp-7 embedded column as schematically represented in figure 5.4c and Appendix 5.70 (Appendix section for details). In this typical experiment, the column was charged with aqueous solution of I_2+KI along with other competing anions with a flow-rate of 0.5 mL.min⁻¹, and the concentration of the column-eluted solution was determined by UV-vis analyses. Noteworthy, almost >99% elimination efficiency of triiodide was observed passing >200 mL of solution in the first cycle of the breakthrough test (Figure

5.4d). Additionally, the column's capability toward regeneration was examined using aqueous NaCl and hexane solution, which revealed notable removal efficiency with admirable uptake capacity over the course of three cycles (Figure 5.4d and Appendix 5.71). In view of practical implication, these results demonstrated impressive segregation effectiveness of IPcomp-7 packed column towards iodine in both environmental and industrially contaminated water. Such selective, regenerable and large iodine uptake capacities of the overall nano-composite is believed to an outcome of the cooperative effect of Zr(IV)-SBU, free -NH₂ groups, cationic nature with exchangeable Cl⁻ ions of the guest-MOP molecules combined with heteroatom functionality, hierarchical macro-micro porosity with large surface area of low density COF-aerogel matrix.

Moving ahead, we performed the recovery test of solid iodine both from vapor and organic solvent medium as described in the appendix section. In a typical experimental setup, vapor-phase iodine loaded compound was heated at a specific temperature to produce substantial amounts of solid molecular iodine (Figure 5.4e, 5.4f and Appendix 5.72). Moreover, the compound embedded iodine was also recovered by treating the I₂@IPcomp-7 with pentane solvent (Appendix 5.73). The rapid evaporation of pentane at room temperature afforded large quantity of iodine crystals (Appendix 5.74). These experiments demonstrated the facile and potential recovery of iodine form vapor phase by IPcomp-7.

Investigation of the Iodine Adsorption Mechanism:

We were inspired to investigate the adsorption mechanism of IPcomp-7 because of its exceptional iodine capture performance. To understand the iodine sorption mechanism, a series of experiments were implemented on I₂@IPcomp-7. FESEM images of IPcomp-7 taken before and after I₂ absorption show nearly unaltered morphologies, demonstrating high stability of the material (Appendix 5.75). The homogenous iodine distribution over IPcomp-7 was revealed by FESEM-EDX data and elemental mapping images, which implies that excessive I₂ was absorbed by the hybrid composite (Appendix 5.76, 5.77). The X-ray 3D CT images of I₂@IPcomp-7 indicated the retention of micron-sized macroscopic hierarchical porous structure (Appendix 5.78). Moreover, the pore size distribution with high volume percentage within ~1 to ~20 μm of IPcomp-7 after the iodine adsorption were clearly visible on the accompanying color-coded 3D CT images (Figure 5.5a and Appendix 5.79). The fluorescence microscopic imaging of I₂@IPcomp-7 displayed significant quenching of intensity after the iodine adsorption (Appendix 5.80).

Next, the time-resolved FT-IR spectra of iodine treated compound indicated obvious shift or reduced intensities of C=N bond stretching vibration from ~1622 cm⁻¹ for IPcomp-7 to ~1631 cm⁻¹ for I₂@IPcomp-7 (Figure 5.5b).^[24] Similar diminished intensities in the vibration bands of C=C, C-H and C-N bonds of phenyl rings at ~1556, ~1410 and ~1196 cm⁻¹ were observed. In addition, the bands

associated with the Zr-metal-carboxylate (Zr-O) bonds at $\sim 1380\text{ cm}^{-1}$ of the MOP underwent a gradual shift after adsorbing iodine. All these spectral changes suggested the occurrence of strong charge-transfer induced interaction between the adsorbed iodine molecules and the multiple functionalities, including imine, amine, phenyl and other heteroatoms of the composite.^[25, 29] Thereafter, XPS was employed to investigate in detail the existing state of trapped iodine as well as the binding nature of iodine/polyiodide anions with the hybrid composite. As compared to IPcomp-7, the XPS survey spectra of I_2 @IPcomp-7 clearly indicated the appearance of characteristic peaks for iodine (Appendix 5.81). The I 3d XPS spectra of I_2 @IPcomp-7 displayed two noticeable peaks located at 618.9 and 630.3 eV associated to I $3d_{5/2}$ and I $3d_{3/2}$ orbitals of iodine molecules respectively, which further indicated that the adsorbed iodine partially exists as molecule (Figure 5.5c).^[25, 57] There were also two additional peaks, with energies of 620.6 and 631.9 eV, which are ascribed to the generation of polyiodide anions like I_3^- and I_5^- .^[14, 57, 58] Also, after iodine adsorption, the N 1s spectra of IPcomp-7 was found to shift from 400.1 eV to 400.2 eV, respectively, indicated interaction of iodine with heteroatom-N (from imine and amine moieties) of the composite (Appendix 5.82). In addition, the emergence of a new peak fraction at 401.3 eV related to the N-I bond revealed the formation of charge-transfer complexes between I_2 and N-center of IPcomp-7.^[26, 29] Importantly, the Zr 3d XPS peaks of I_2 @IPcomp-7 was observed to shift towards relatively higher binding energy, suggesting potential interaction of iodine with Zr-SBU of the MOP of hybrid composite (Figure 5.5d).^[19] Moreover, after I_2 adsorption on IPcomp-7, the peak of the Cl 2p core energy level shifted from 197.5 and 198.9 eV to 198.8 and 200.2 eV, respectively, suggesting that Cl^- was also engaged in the I_2 uptake (Figure 5.5e).^[5, 9] All these results demonstrated that along with the COF matrix, the amino functionalized cationic Zr(IV)-MOP (as nano-snare) actively participate in the iodine sorption process. Further, the Raman spectra of I_2 @IPcomp-7 showed distinct bands at ~ 106.1 , ~ 141.2 and $\sim 168.7\text{ cm}^{-1}$ following iodine adsorption, indicating strong charge-transfer inter-action of iodine with IPcomp-7 and generation of multitude of anionic polynuclear iodide species (Figure 5.5g and Appendix 5.83).^[14] Among them band at ~ 106.1 and $\sim 141.2\text{ cm}^{-1}$ can be assigned to the symmetric and asymmetric stretching vibration of I_3^- , respectively, whereas, band at 168.7 cm^{-1} is attributed to the stretching vibration of I_5^- polyiodide species.^[14, 25, 26, 29, 57, 58] In addition to this, peaks associated with symmetric and asymmetric stretching vibration bands of $[\text{I}_2\text{Cl}]^-$ at 112.8 and 145.9 cm^{-1} , respectively, and stretching vibration bands of $[\text{2I}_2\text{Cl}]^-$ at 171.2 cm^{-1} were observed, which indicated potential interaction of iodine with free Cl^- anions of the composite.^[5, 25] Moreover, the spatial distribution of iodine species throughout the structure of IPcomp-7 was investigated by Raman spectroscopy mapping analysis. The color-coded Raman mapping of I_2 @IPcomp-7 exhibited distribution of adsorbed iodine species with significant intensities of respective bands (Figure 5.5f and Appendix 5.84). The solid-state UV-vis spectra of I_2 @IPcomp-7 displayed characteristic broad absorption peak, which indicated formation of charge-transfer complexes between polyiodide anions and IPcomp-7 (Appendix 5.85).^[14] Further, to confirm the existence of such charge transfer interactions,

electron paramagnetic resonance (EPR) studies was conducted. The iodine loaded compo-site revealed sharp EPR signals, however, almost no paramagnetic signals were observed in case of pristine IP-comp-7 (Figure 5.5h). Importantly, the EPR signal was noticeably less after desorption of iodine from IPcomp-7. These findings compel us to hypothesize that $I_2@IPcomp-7$ contains radicals, which most likely originate from an electron transfer between the electron-rich moieties of IPcomp-7 and entrapped iodine species.^[14] Also, notably following the capture of I_2 , the signal in the solid-state ^{13}C NMR spectra of $I_2@IPcomp-7$ clearly broadens (Appendix 5.86).

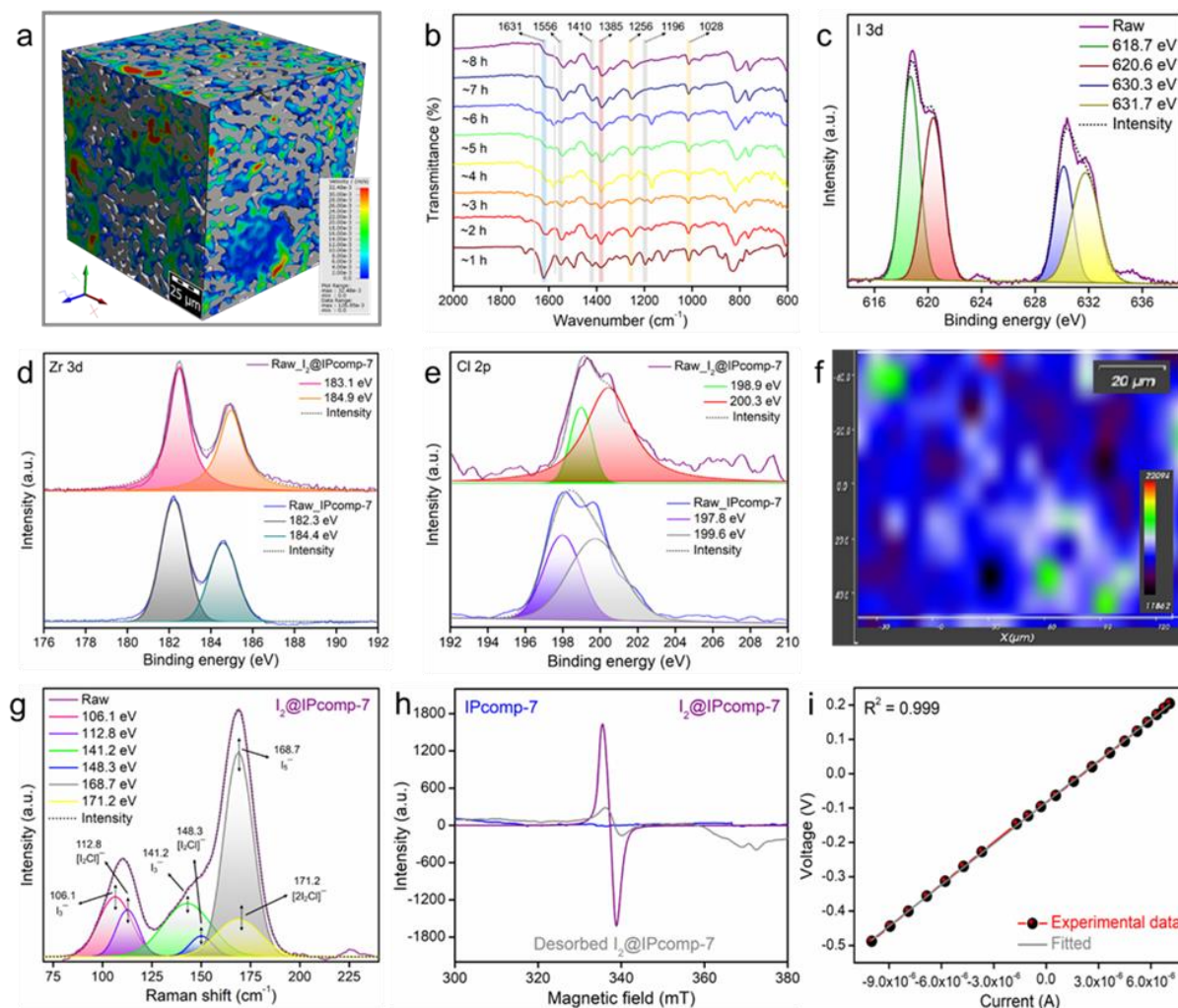


Figure 5.5: (a) Colour-scale 3D CT image of $I_2@IPcomp-7$. (b) Time-dependent FT-IR spectra of $I_2@IPcomp-7$. (c) I 3d, (d) Zr 3d, (e) Cl 2p XPS spectra of IPcomp-7 before and after iodine adsorption. (f) Raman mapping, (g) Raman spectra of $I_2@IPcomp-7$. (h) EPR spectra of IPcomp-7, $I_2@IPcomp-7$ and desorbed $I_2@IPcomp-7$. (i) Current-voltage (I-V) plots of $I_2@IPcomp-7$.

This may result from a strong affinity between the π -electron rich moieties of IPcomp-7 and the electron-deficient iodine molecules.^[26, 29] The PXRD patterns of $I_2@IPcomp-7$ exhibited no diffraction

peaks, indicated loading of amorphous iodine in the pores of the composite as well as eliminating the possibility of deposition or recrystallization of I_2 on the surface of IPcomp-7 (Appendix 5.87).^[26, 29] The TGA profile of I_2 @IPcomp-7 indicated high weight loss, demonstrating large quantity of iodine occupied into the pores of IPcomp-7 (Appendix 5.88). Furthermore, the electrical conductivity (σ) of the iodine loaded composite was measured, which yielded bulk σ value of $\sim 7.83 \times 10^{-5} \text{ S.cm}^{-1}$ (Figure 5.5i). This value suggested the successful occupation of excess iodine or polyiodide anions into the pores of IPcomp-7.^[12, 20] Moreover, in order to investigate the role of NH_2 -MOP towards iodine adsorption, 1H NMR time-dependent titration experiments of I_2 @ NH_2 -MOP were performed, which disclosed the significant degree of shift in the signals for the protons of the respective moieties (Appendix 5.89). This shift in the signals demonstrated that these moieties had a preferential location for interacting with iodine species. All of these findings demonstrated that contribution of both physisorption and chemisorption were at play in tandem to selectively adsorb the iodine species by the different multiple functionalities, including heteroatomic sites, amine, imine, phenyl moieties, Zr(IV)-SBU, free Cl^- counter-anions, etc. of IPcomp-7.

We were also encouraged to disseminate the advancement of low-density hybrid aerogel with hierarchical micron sized interconnected macropores towards the ultrafast iodine capture kinetics of IPcomp-7 in both vapor and aqueous phase. For this, confocal microscopic experiment and flow velocity analysis of iodine contaminated vapor and water was estimated by numerical simulations studies. The 3D confocal images of IPcomp-7 showed existence of large number of open voids (macropores) throughout the surface (Appendix 5.90). These large open pores enable easy encapsulation of iodine molecules or polyiodide anions through the inter-connected pore channels, which allow continuous rapid mass flow. The 2.5D confocal images shown were acquired from several layers of the composite. The modified 2.5D images of different layers (5th, 25th, 45th, and 65th) displayed dispersive adsorption of analyte within the different 2D layers of the whole matrix of IPcomp-7, as opposed to only surface of the composite. This support the easy and fast penetration of water or vapor through the open pores of IPcomp-7 further promotes the excessive adsorption of iodine and polyiodide anions (Figure 5.6a(I-IV) and Appendix 5.91). Moreover, in order to make an evidence-based forecast of the rapid and dynamic events occurring throughout the porous structure towards I_2/I_3^- entrapment process in vapor and water, an in-silico mass transport simulation was carried out in the segmented 3D tomographic model of IPcomp-7. Using an appropriate numerical solver at 25 °C, 20 Pa pressure-drop, etc., a simulation study was performed to visualize flow in the vertical axis (Y axis), and the outcome visualizes the average flow velocity profiles. The findings of the numerical simulation method forecast the practicable average flow profiles through the inter-connected void-space of IPcomp-7 (Figure 5.6b). The simulation results indicated entrapment of vapor through the porous structure of the hybrid aerogel. The average flow velocity in Y-direction was calculated as $\sim 4.2 \times 10^{-3}$

ms^{-1} , with flow resistivity of $3.4 \times 10^7 \text{ kg}/(\text{m}^3\text{s})$ and permeability of $5.3 \times 10^{-13} \text{ m}^2$, respectively (Figure 5.6c and Appendix 5.92-5.93). The result of water flow-velocity range in the hybrid aerogel demonstrated interconnected hierarchical pores of IPcomp-7 greatly aids in the massive mass-transport for rapid and high iodine uptake efficiency. This study further suggests the significance of low-density aerogel materials for effective iodine sequestration.

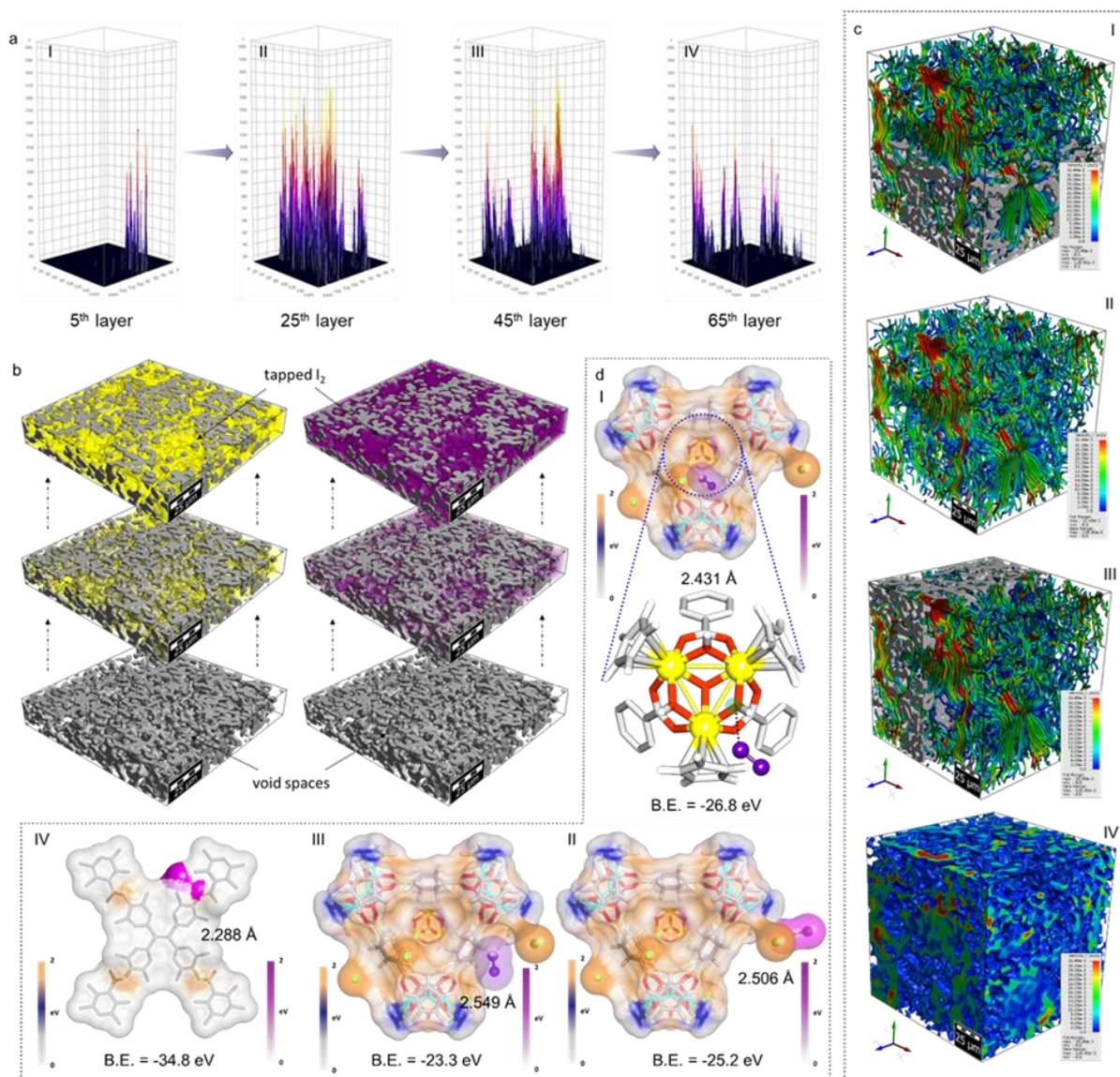


Figure 5.6: (a) The 2.5D confocal fluorescence microscopic images of IPcomp-7 with different 2D layers. (b) 3D images of IPcomp-7, generated by the numerical solver, depicting the entrapment process of iodine vapor, at three different stages, in the voids of the hybrid aerogel. (c) The water flow-velocity profile inside IPcomp-7, estimated by the numerical solver, visualizing the flow paths. (d) Energy-optimized structure of various interaction between iodine molecule and (I) Zr-SBU, (II) Cl^- ions, (III)

free -NH_2 group of the MOP, and (IV) imine functional group of the COF shows the possible binding sites.

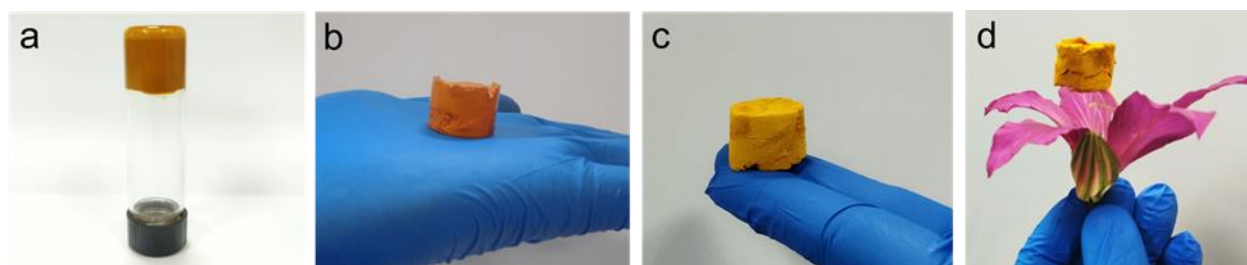
The potential of Zr(IV)-SBU and amino functional groups to selectively interact with iodine/polyiodides is well established in the literature.^[11, 19] Therefore, the cationic nano-snare (NH_2 -Zr(IV)-MOPs) in the hybrid composite effectively contributes towards the selective iodine capture owing to its multifunctional properties. However, the functional groups of the pristine MOPs become inaccessible to interact with I_2/I_3^- as a result of inevitable random self-aggregation, which significantly lowers the capture efficiency. However, in regard to the hybrid composite, the host COF-matrix wired up the MOPs separately, keeping the majority of the active sites well exposed, facilitating the diffusion of I_2/I_3^- species toward the active nano-snare through the macroscopic hierarchical porosity. All these discussions established the iodine or polyiodide uptake mechanism of IPcomp-7 by the cooperative interactions of multiple functionalities, such as strong interaction between heteroatom containing electron rich moieties of the composite with iodine, H-bonding with free -NH_2 group of MOP, energetically favourable binding as well as exchange with free Cl^- ions in vapor and aqueous phase, respectively, and the selective preferential affinity towards I_2 with deliberately grafted unique Zr(IV)-SBU of the MOP.

Additionally, the theoretical calculation utilizing the density functional theory (DFT) simulation study was conducted, which corroborated with the experimental findings, further verifying the strong interaction between iodine/polyiodide anions and host-guest of the hybrid composite. We used TPE backbone of the COF and crystal structure of the NH_2 -MOP as model molecules for calculating the binding energies with I_2/I_3^- species. The calculations showed that along with others the imine functionality of COF, binding with hydroxy group (-OH) of Zr(IV)-SBU, free -NH_2 group and Cl^- ions of the MOPs selectively interacts with iodine with binding energies of -34.8 , -26.8 , -23.3 and -25.2 eV, respectively (Figure 5.6d(I-IV) and Appendix 5.94-5.100). Particularly, the optimized geometries disclosed the selective strong interaction between the terminal -OH group of Zr-cluster and iodine/polyiodide anions, which further donates the maximum negative charges to the adsorbed iodine, indicating the maximum charge separation between the iodine atoms (Figure 5.6d and Appendix 5.94-5.95).^[19] Moreover, the DFT calculation displayed that the adsorption configuration of the I_2 molecule interacting directly with Cl^- was found energetically favourable (Figure 5.6dII).^[5] According to these studies, installation of ionic functionality with free Cl^- ions, Zr-metal cluster, amino and other electron-rich moieties by covalent grafting of the cationic MOP into the imine-COF-aerogel matrix increases the number and strength of selective binding sites for I_2/I_3^- adsorption by virtue of Coulomb interactions to generate thermodynamically more stable complexes.^[26]

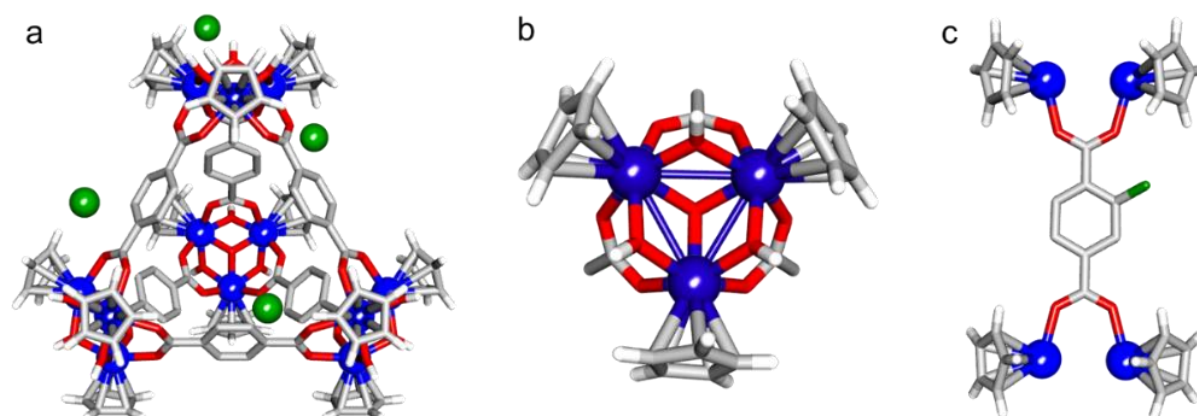
5.5 Conclusion

In summary, remarkable sequestration efficacy towards iodine have been demonstrated by successfully synthesizing a unique crystalline hybrid aerogel material by covalent-linking of nanosized cationic MOPs with a hierarchical porous COF-aerogel matrix, utilizing systematic hybridization synthetic strategy. We intensively investigated the structural, morphological and optical properties of such novel hybrid aerogel to elucidate detailed insights of the multifunctional composite material. Effective entrapment of iodine being the key targeted criterion, the combined interconnected hierarchical macro-microporosity, low-density ultralight weight, high mechanical stiffness along with deliberately grafted Zr(IV)-SBU and free amino group-based discrete cationic nano-snare (MOP) into a imine-COF aerogel matrix exhibited ultrafast, selective and high enrichment towards iodine uptake. Importantly, the hybrid aerogel illustrated a striking performance towards rapid and selective uptake with outstanding capacities of iodine or polyiodides in both static and dynamic vapor phase as well as aqueous phase condition, which underscore its full potential for large-scale real-time applications. The results revealed that the newly developed hybrid composite is of great scientific significance as a potential adsorbent for effective radioiodine sequestration owing to its rapid uptake kinetics, high sorption capacity, exceptional selectivity, superior retention, recovery and satisfying recyclability. We expect that the insight gained in this research are of fundamental importance to understand the rational design and development of novel innovative hybrid composite materials for efficient sequestration and other applications demanding for porous and macroscopic scaffolds.

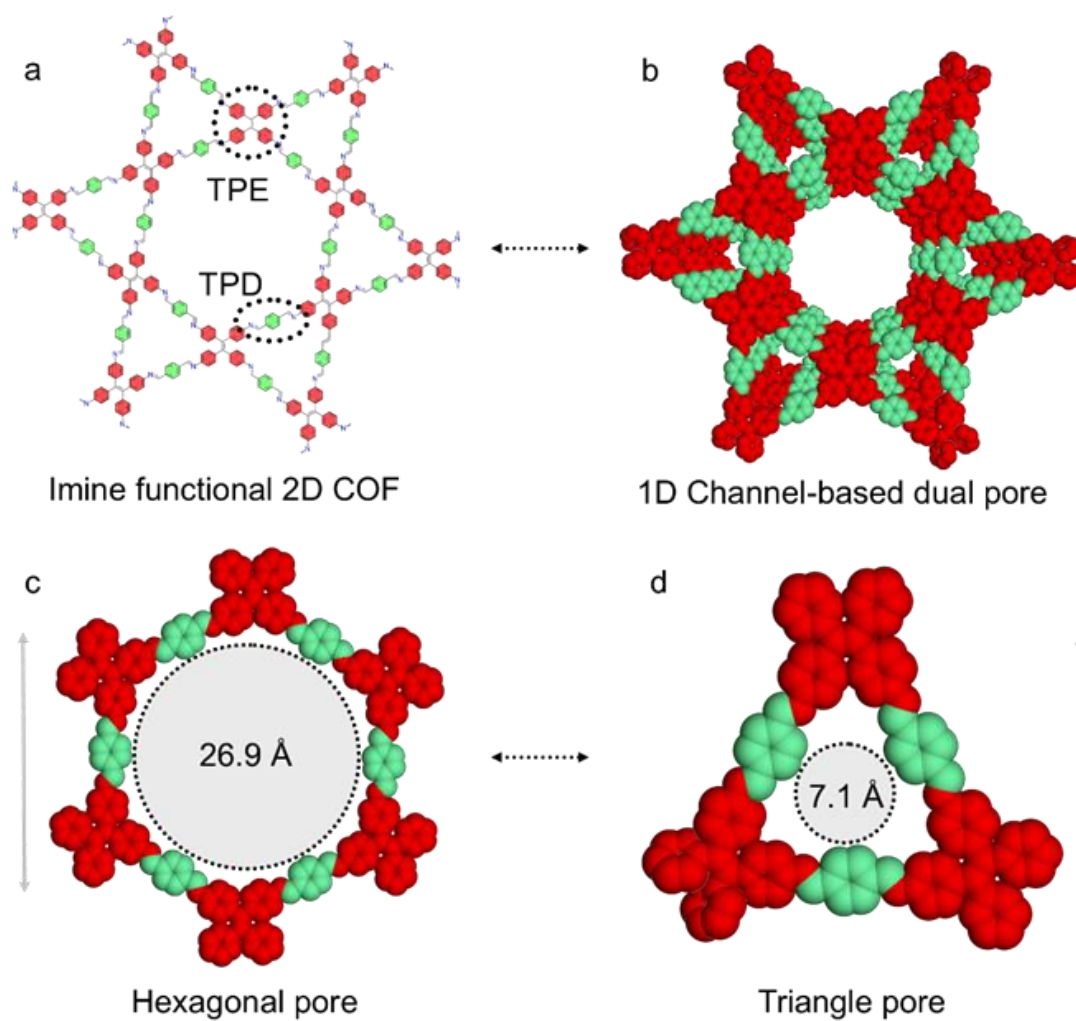
5.6 Appendix Section



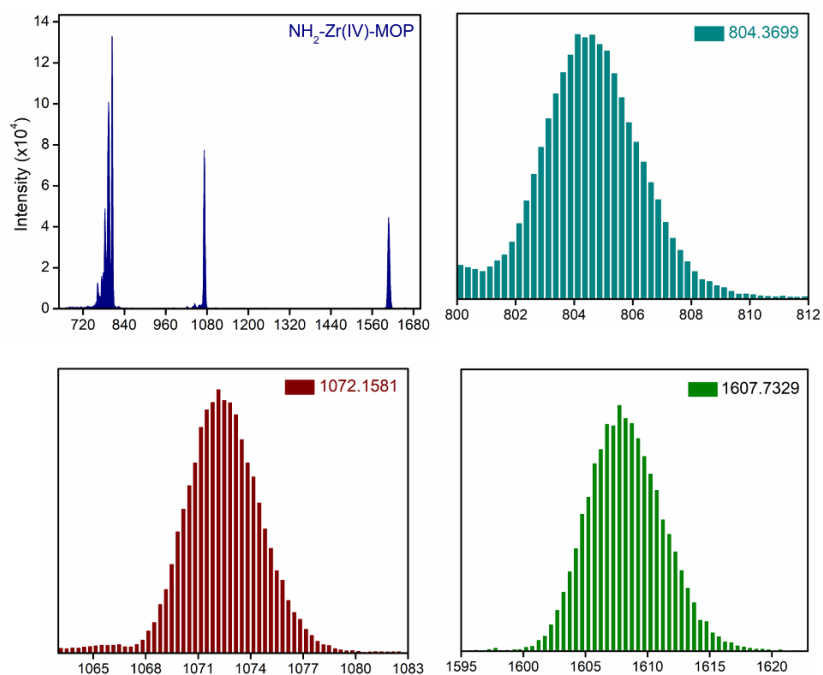
Appendix 5.1: Digital images of the hybrid composite material (IPcomp-7). (a, b) The as-synthesized wet-gel form of IPcomp-7. (b) Ultra-light weight nature of the crystalline hybrid aerogel.



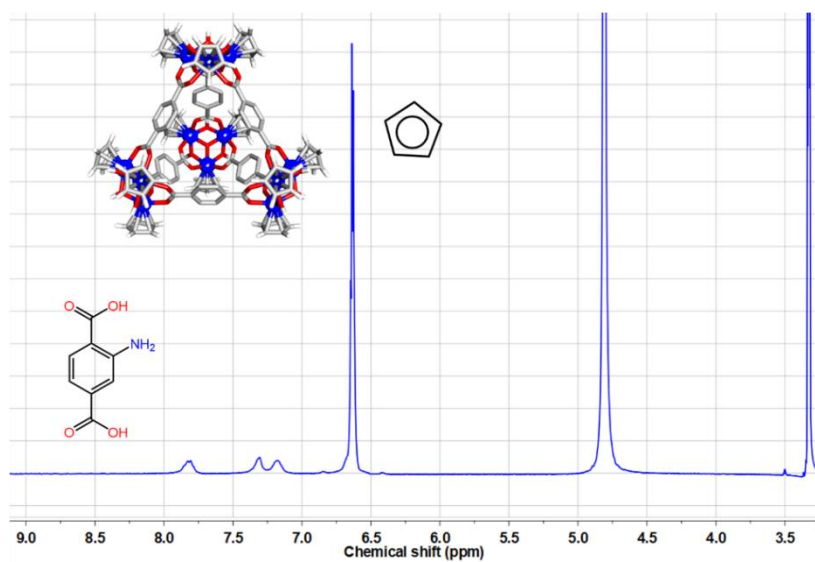
Appendix 5.2: Structural features of the (a) $\text{NH}_2\text{-Zr(IV)}$ -based cationic metal-organic polyhedra (MOPs), (b) Zr(IV) -based secondary building unit (SBU), (c) Organic linker (2-aminoterephthalate) of the MOP.



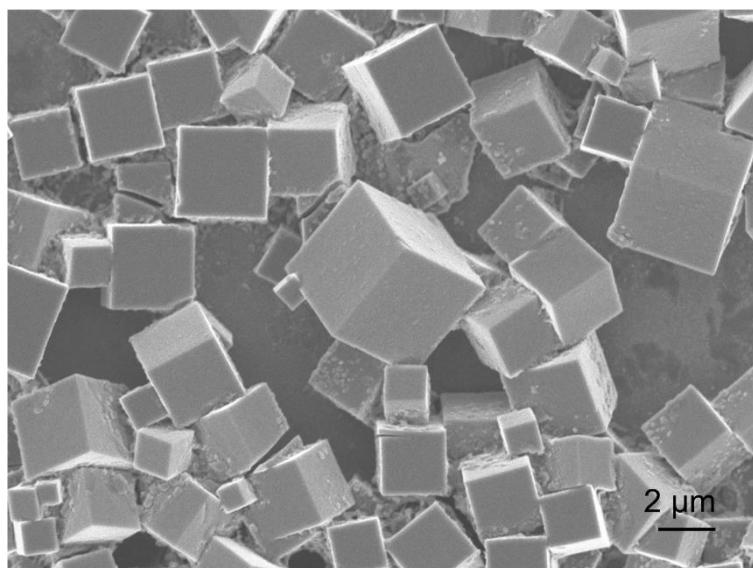
Appendix 5.3: Structural features of the covalent-organic framework (COF): (a) Chemical structure of the TPE core-based imine functional 2D COF. (b) Packing structure of 1D channel-based dual pore TPE-COF. (c, d) Hexagonal and triangle pores of the COF, respectively.



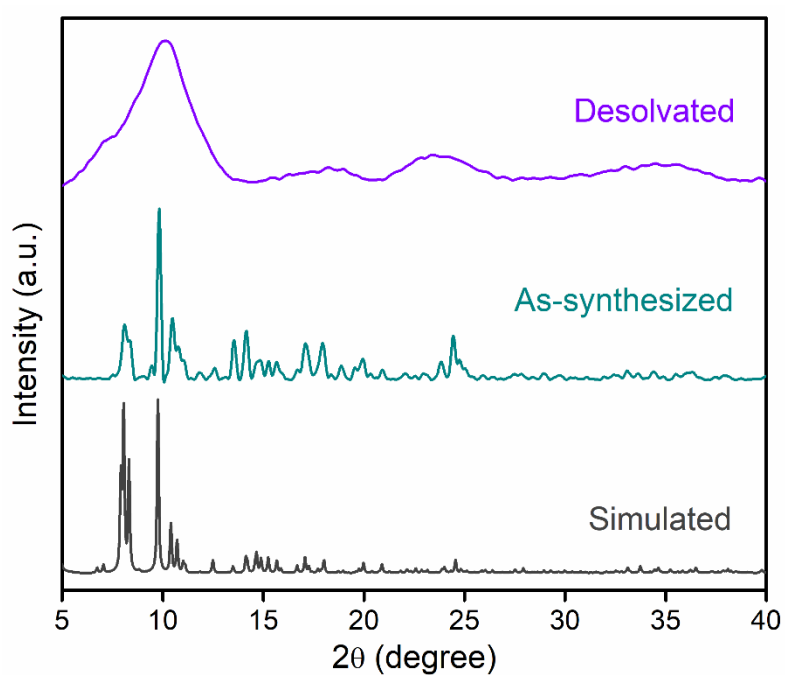
Appendix 5.4: Structural characterization of the metal-organic polyhedra (MOPs): ESI-TOF-MS analysis of as-synthesized Zr(IV)-MOP, indicated the formation of the MOPs.



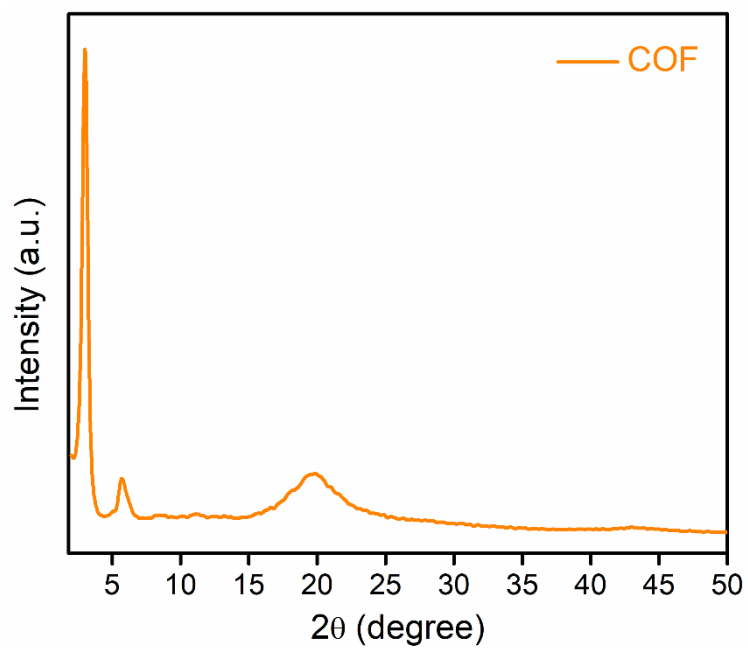
Appendix 5.5: ^1H NMR spectra of the Zr(IV)-MOPs in MeOD and D_2O .



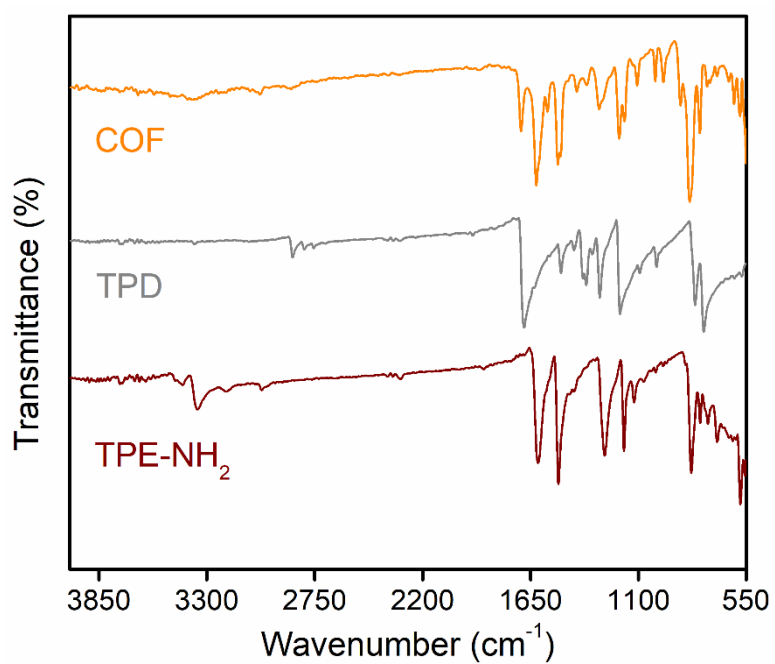
Appendix 5.6: FESEM image of the Zr(IV)-MOPs, indicated highly cubic micro-crystalline morphology.



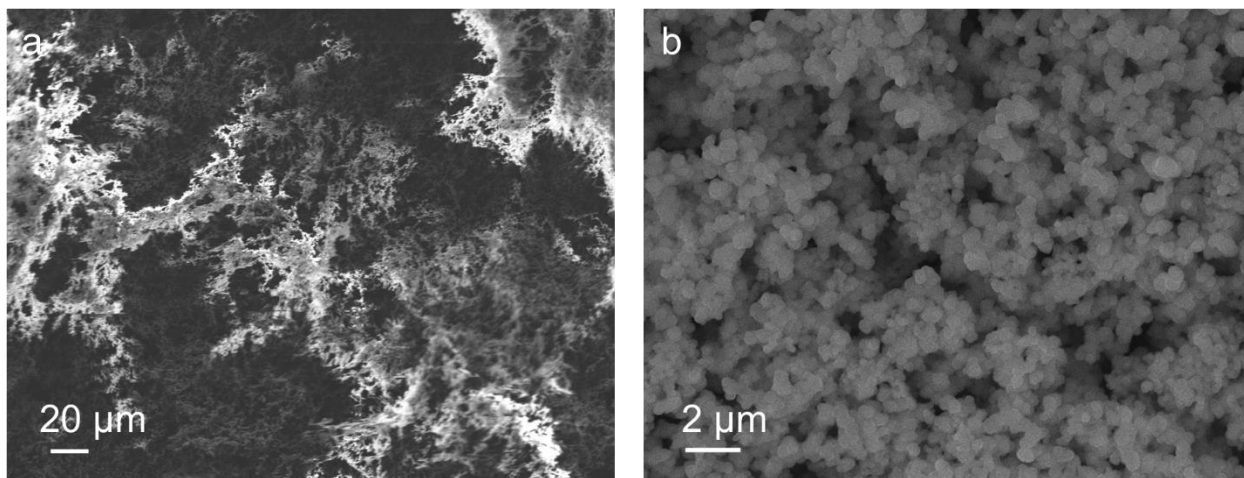
Appendix 5.7: PXRD analysis of the Zr(IV)-MOP indicated formation of bulk phase purity of the MOP in as-synthesized phase, also the PXRD data of the desolvated phase showed the weak crystalline nature of the MOPs, which is cause of self-aggregation upon desolvation.



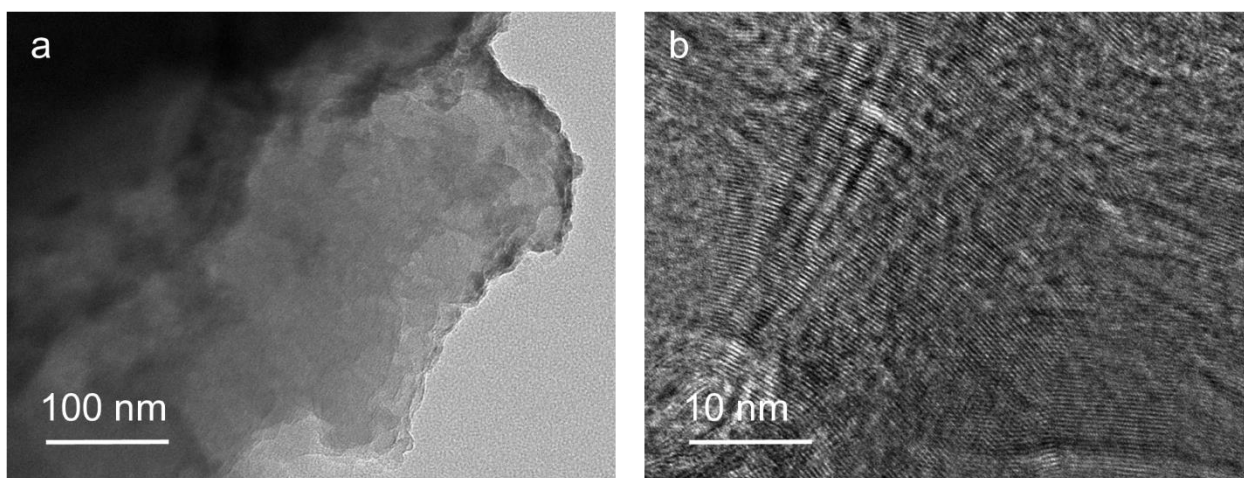
Appendix 5.8: PXRD profile of the COF aerogel.



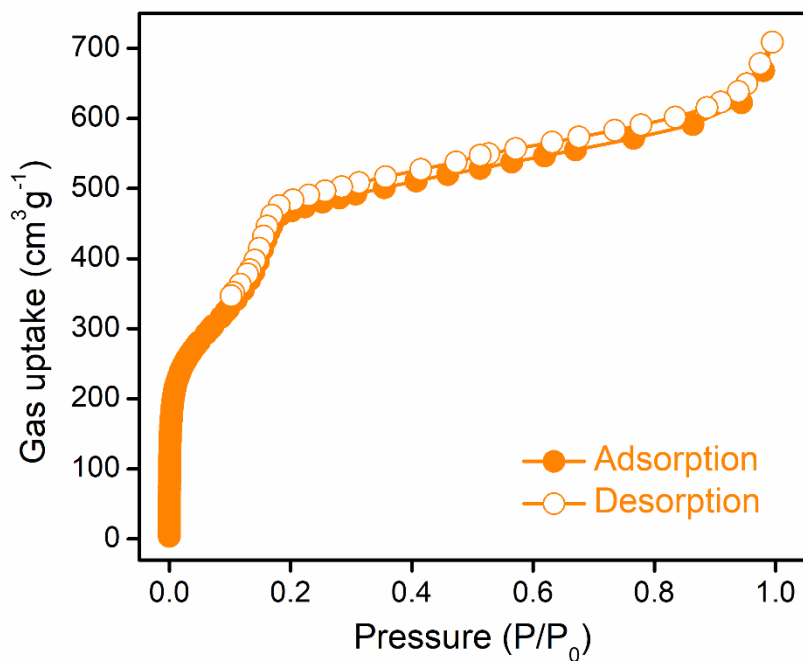
Appendix 5.9: FT-IR spectra of the COF aerogel along with its precursors.



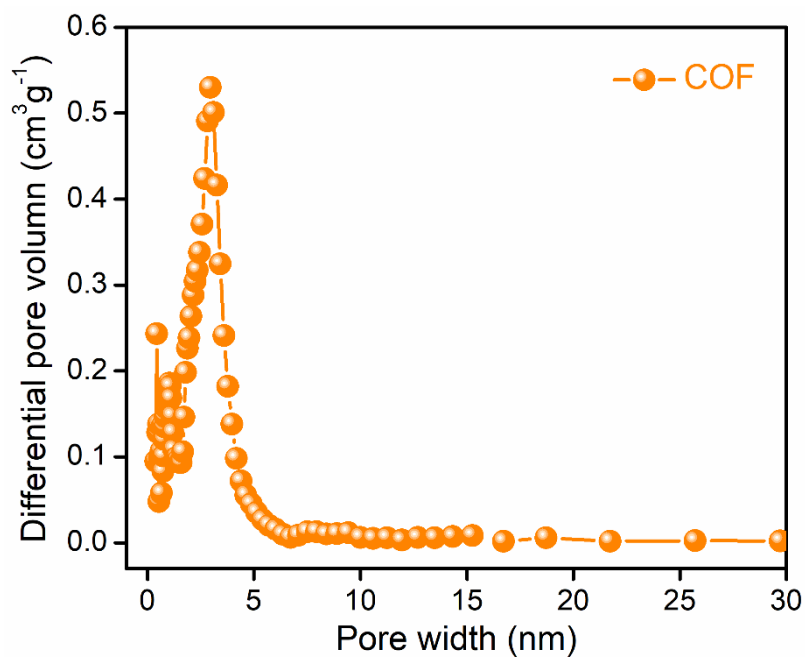
Appendix 5.10: (a) SEM and (b) FESEM images of the pristine COF aerogel.



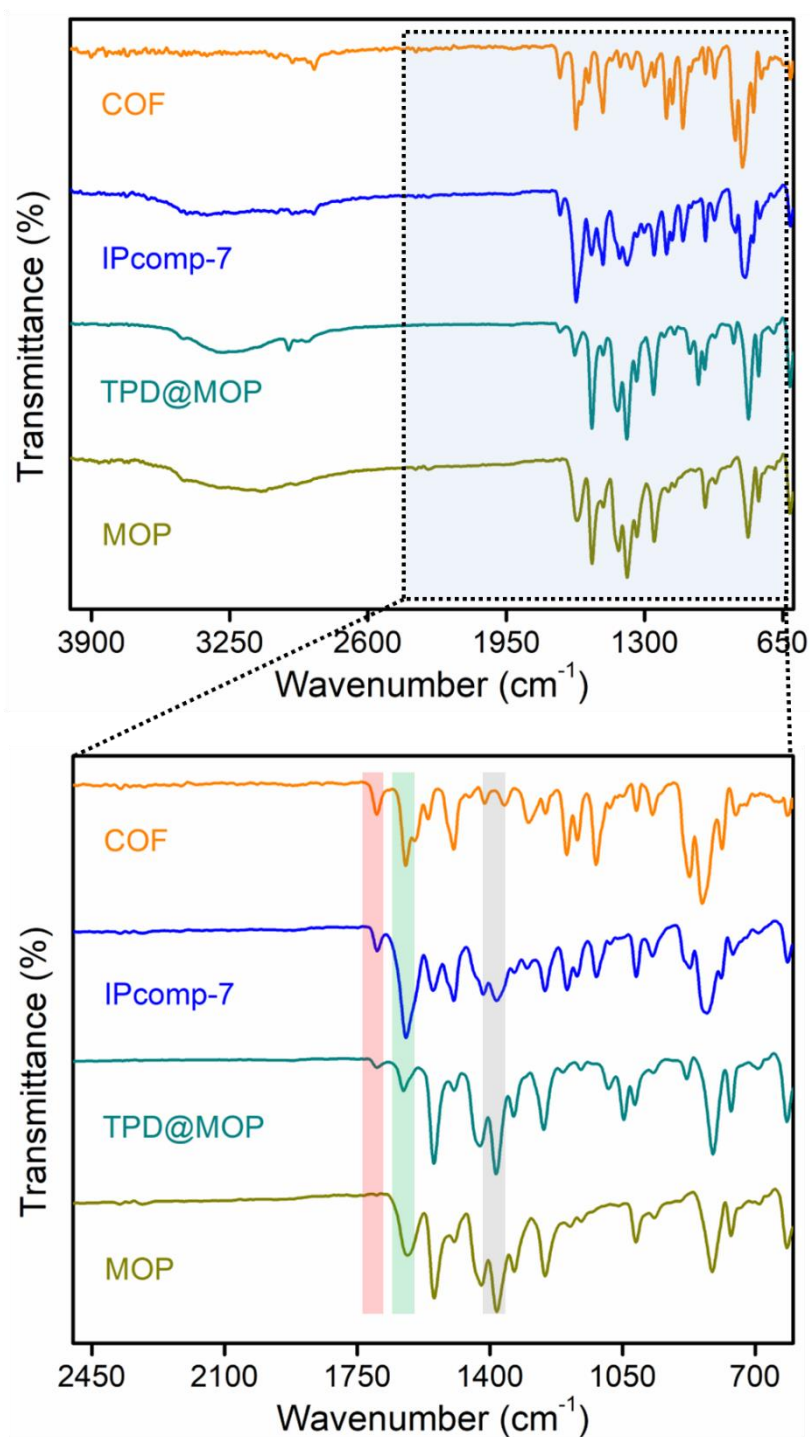
Appendix 5.11: (a) TEM and (b) HRTEM images of the pristine COF aerogel.



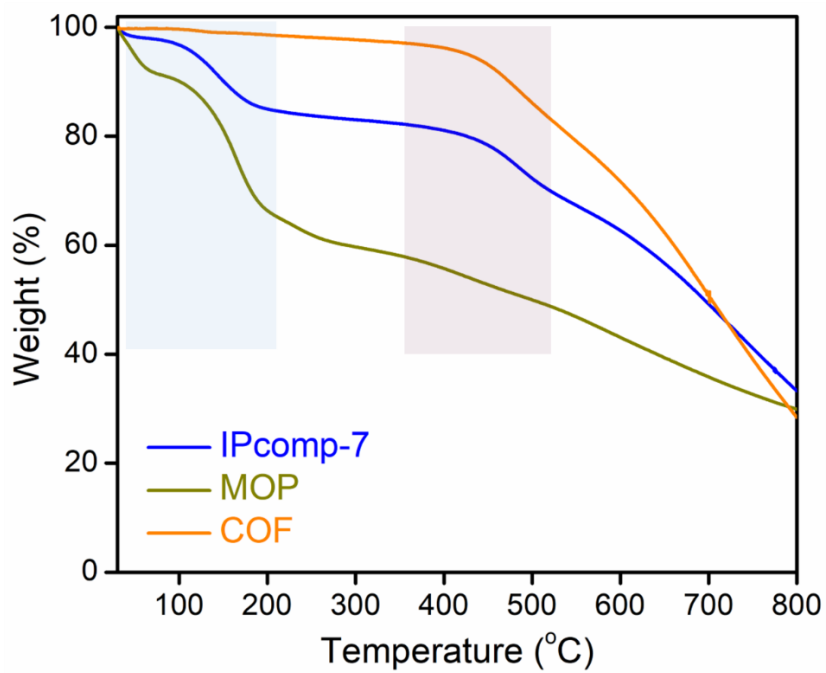
Appendix 5.12: Nitrogen gas adsorption-desorption measurement of the COF aerogel at 77K, indicating the existence of hierarchical (micro and meso) porosity.



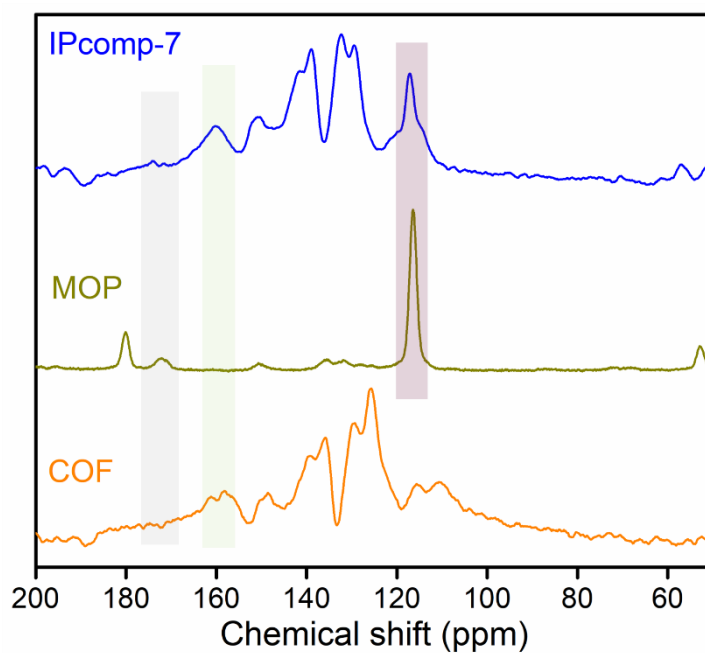
Appendix 5.13: NLDTF pore size distribution profile of the dual-pore COF aerogel.



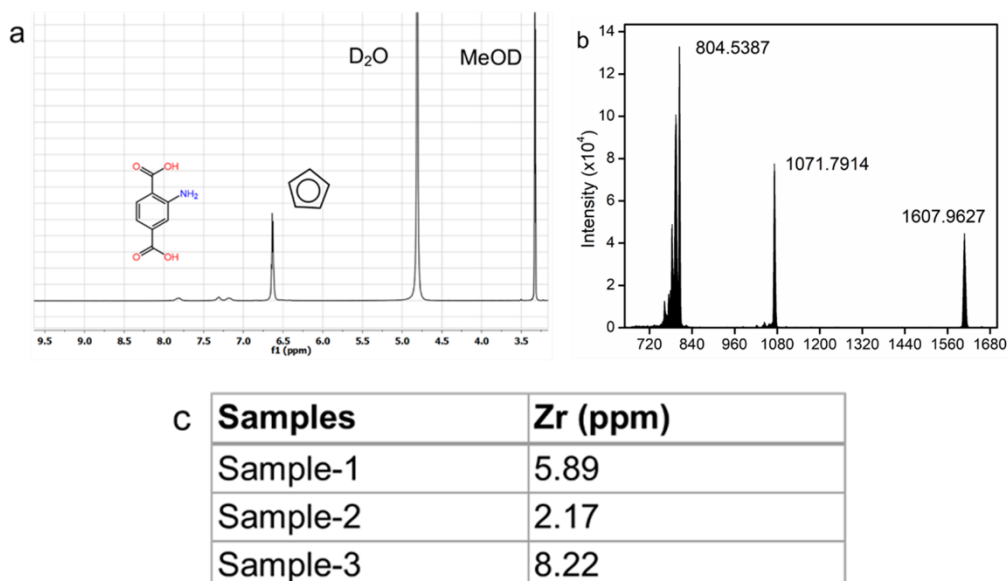
Appendix 5.14: FT-IR spectra of IPcomp-7, along with the pristine MOP, TPD@MOP, COF-aerogel.



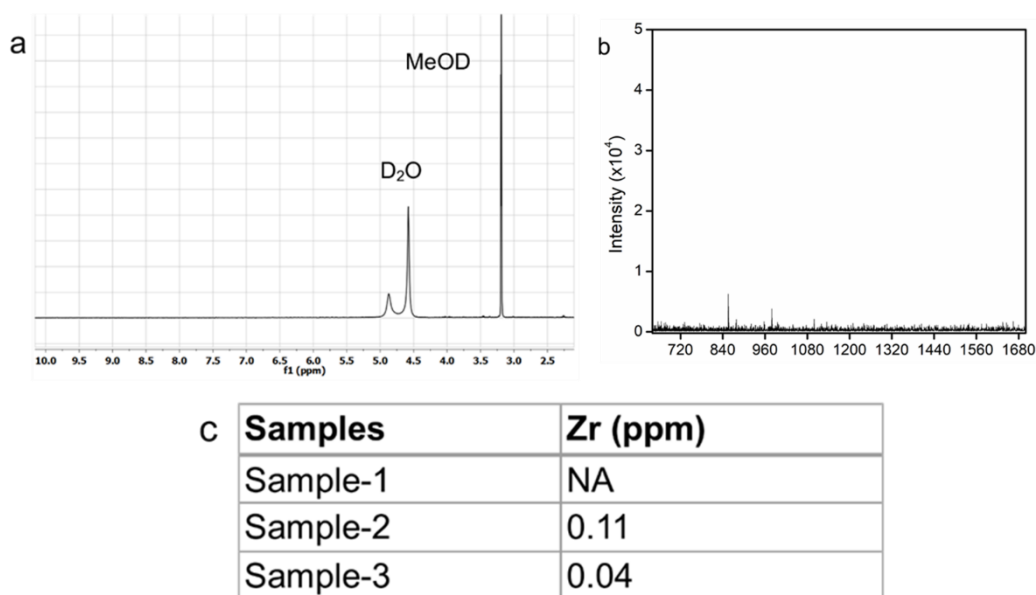
Appendix 5.15: TGA profile of IPcomp-7, along with pristine COF-aerogel and MOP.



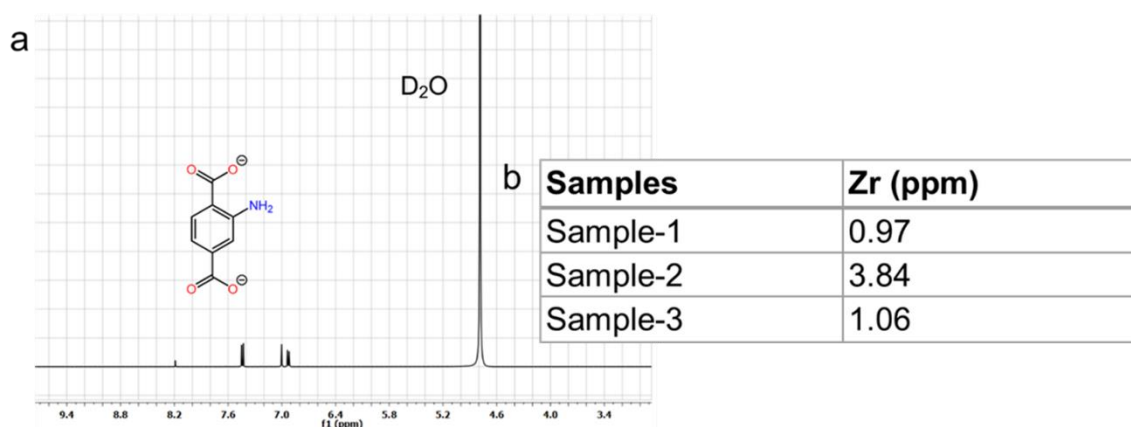
Appendix 5.16: ^{13}C CP-MAS NMR spectra of IPcomp-7, along with pristine COF-aerogel and MOP.



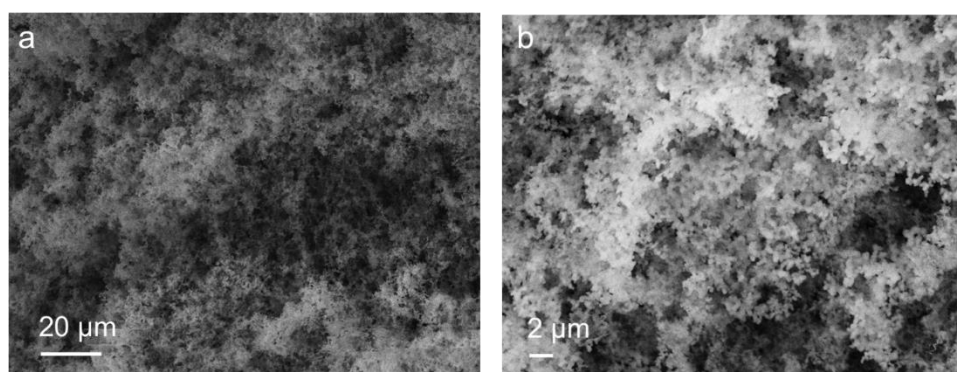
Appendix 5.17: Characterizations data of IPcomp-7 treated supernatant, indicating the presence of guest-MOP molecules before washing IPcomp-7 with aqueous methanolic solution: (a) ^1H NMR spectra of the MOP in MeOD, D_2O mixture, (b) HRMS spectra of the MOP, (c) ICP analysis of Zr(IV) metal in the supernatant of hybrid material exposed to aqueous methanolic solution.



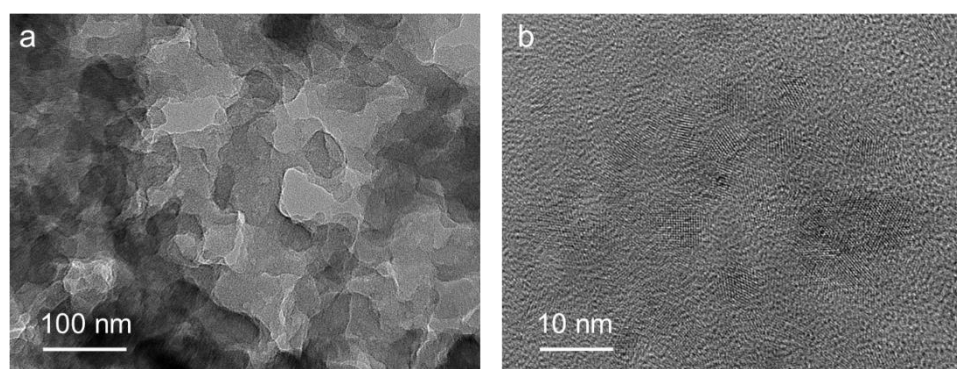
Appendix 5.18: Characterizations data of IPcomp-7 treated supernatant, indicating no presence of guest-MOP molecules after washing IPcomp-7 with aqueous methanolic solution: (a) ^1H NMR spectra, (b) HRMS spectra, (c) ICP analysis of Zr(IV) metal in the supernatant of hybrid material exposed to aqueous methanolic solution.



Appendix 5.19: Characterizations of the digested sample of IPcomp-7: (a) ^1H NMR spectra of the organic linker of MOP in NaOD/D₂O solvent. (b) ICP analysis of Zr(IV) metal in the supernatant of the digested hybrid material.

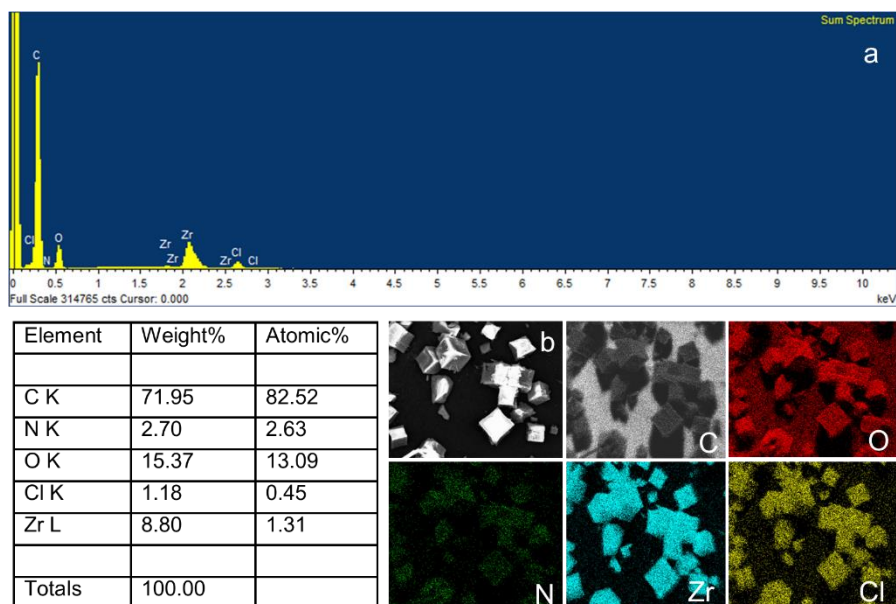


Appendix 5.20: FESEM images of the hybrid aerogel (IPcomp-7) (a) 20 μm , (b) 2 μm . (The numerical values represent the scale bars of the images).



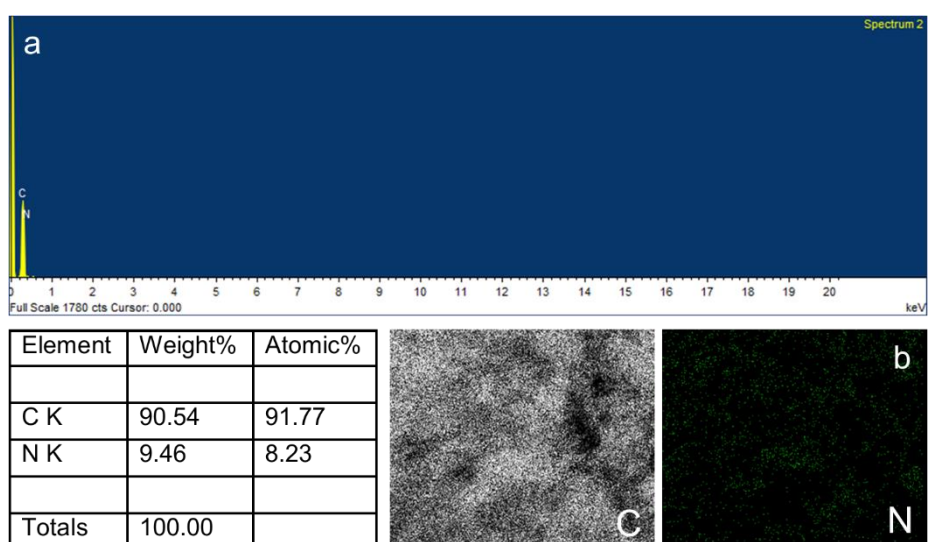
Appendix 5.21: TEM/HRTEM images of the hybrid composite (IPcomp-7) (a) 100 nm, (b) 10 nm. (The numerical values represent the scale bars of the images).

Appendix Table 5.1: EDX elemental analyses from FESEM experiment of $\text{NH}_2\text{-Zr(IV)-MOP}$ molecules showing presence of C, N, O, Cl and Zr elements (a).



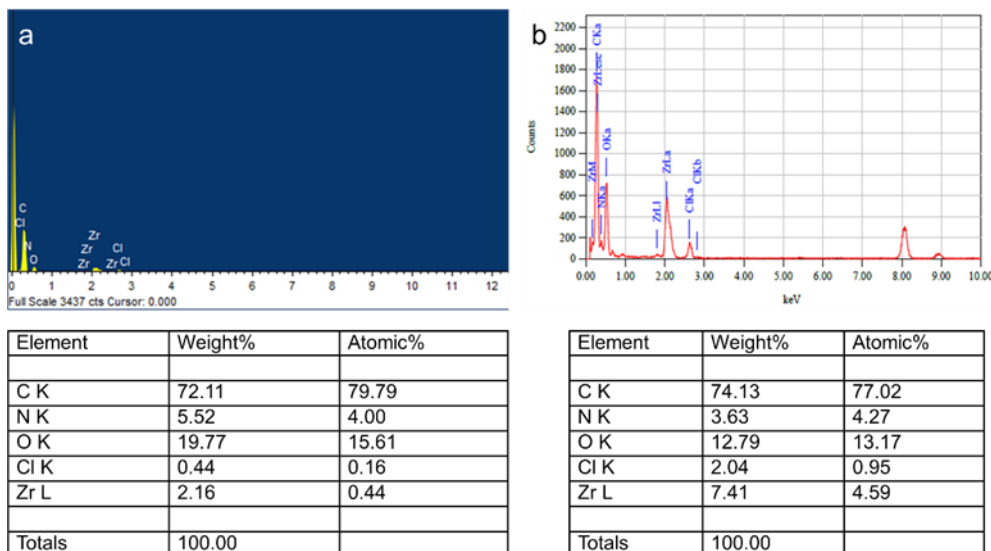
Appendix 5.22: (b) SEM elemental mapping images of the $\text{NH}_2\text{-Zr(IV)-MOP}$ molecules.

Appendix Table 5.2: EDX elemental analyses from FESEM experiment of the COF-aerogel showing presence of C and N elements (a).



Appendix 5.23: (b) SEM elemental mapping images of the COF-aerogel.

Appendix Table 5.3: EDX elemental analyses from (a) FESEM and (b) TEM experiment of IPcomp-7, constructed with ~15 mg of MOPs showing the presence of C, N, O, Al, Cl and Zr elements.



Appendix Table 5.4: EDX elemental analyses from FESEM experiment of the hybrid composite, constructed with ~35 mg of MOPs showing presence of C, N, O, Al, Cl and Zr elements.

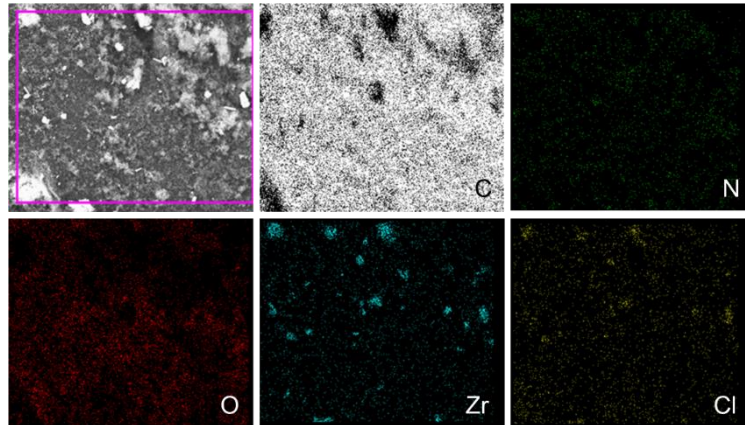
Element	Weight%	Atomic%
C K	75.62	81.99
N K	6.29	5.66
O K	13.87	11.22
Cl K	0.74	0.27
Zr L	3.48	0.86
Totals	100.00	

Appendix Table 5.5: EDX elemental analyses from FESEM experiment of the hybrid composite, constructed with ~50 mg of MOPs showing presence of C, N, O, Al, Cl and Zr elements.

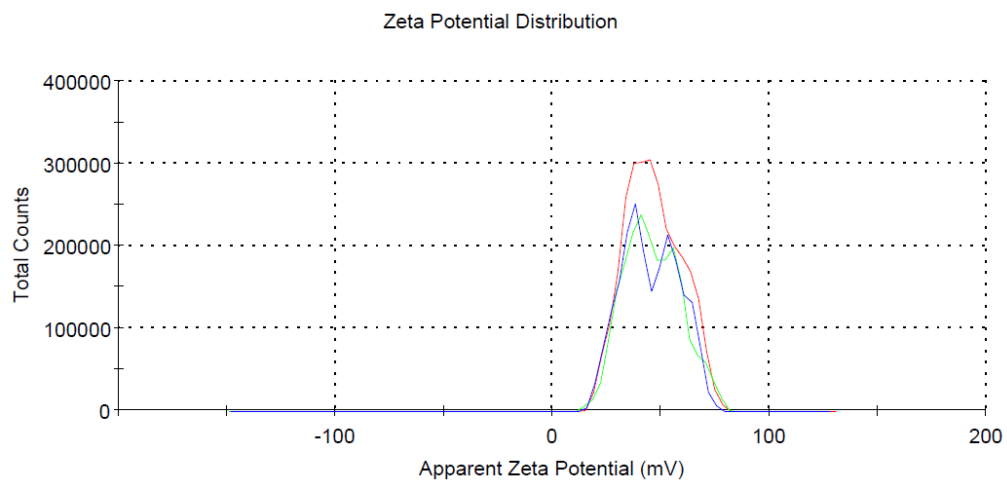
Element	Weight%	Atomic%
C K	76.92	85.84
N K	-0.77	-0.74
O K	15.42	12.98
Cl K	1.13	0.43
Zr L	7.30	1.49
Totals	100.00	

Appendix Table 5.6: EDX elemental analyses from FESEM experiment of the hybrid composite, constructed with ~100 mg of MOPs showing presence of C, N, O, Al, Cl and Zr elements.

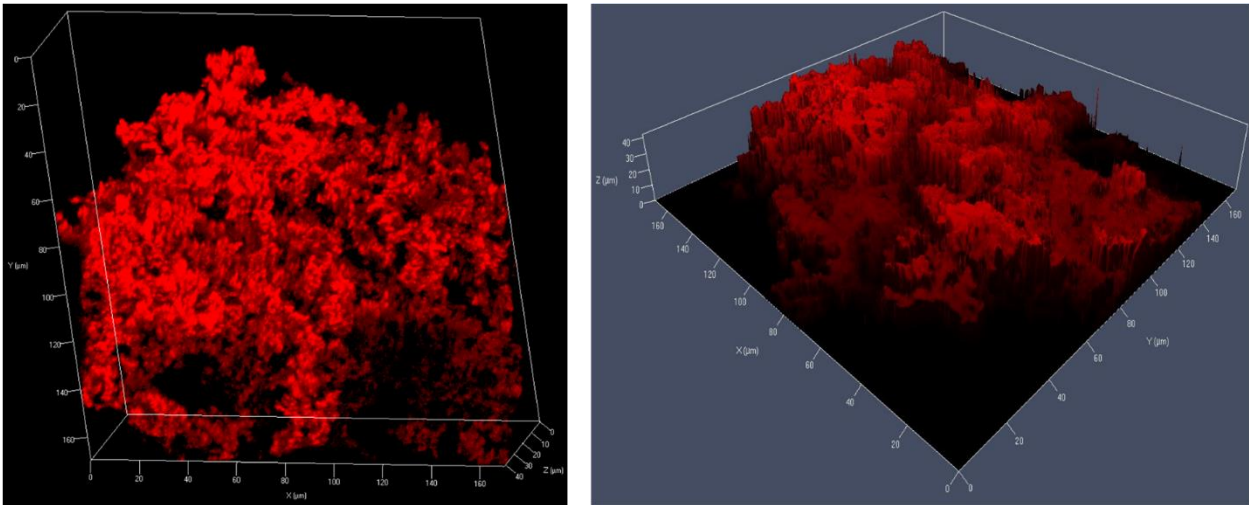
Element	Weight%	Atomic%
C K	74.77	79.33
N K	7.58	5.31
O K	11.66	10.56
Cl K	1.08	1.16
Zr L	4.91	3.64
Totals	100.00	



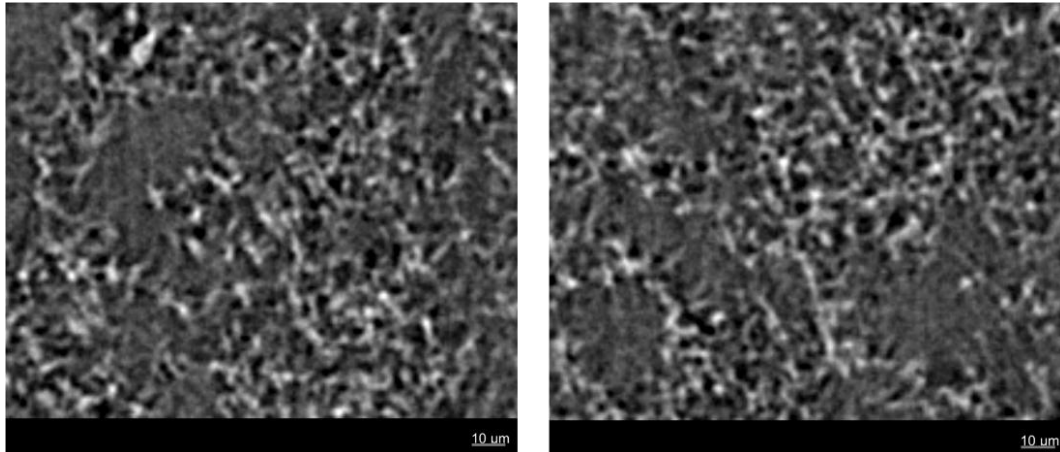
Appendix 5.24: SEM elemental mapping images of IPcomp-7 indicated homogeneous distribution of all relevant elements (Carbon (C), Nitrogen (N), Oxygen (O), Zirconium (Zr) and Chlorine (Cl)).



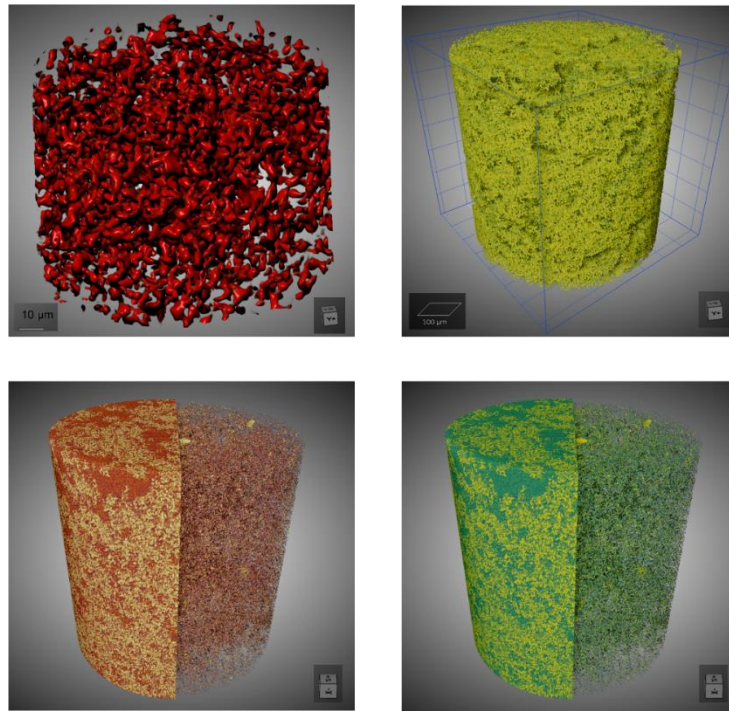
Appendix 5.25: Zeta potential measurement of IPcomp-7 indicated cationic nature of the composite with potential value of +46.3 mV.



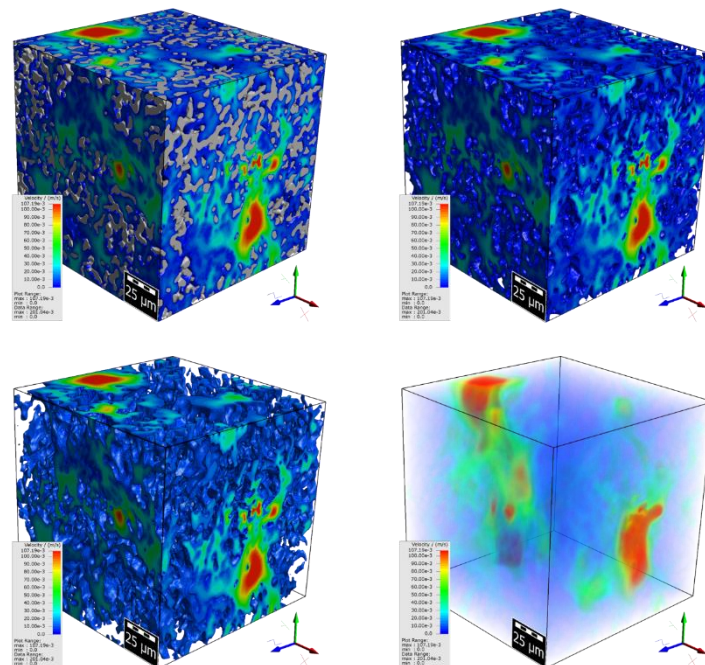
Appendix 5.26: Confocal fluorescence 3D images of IPcomp-7 indicated the distribution of extrinsic macropores throughout the surface of the composite.



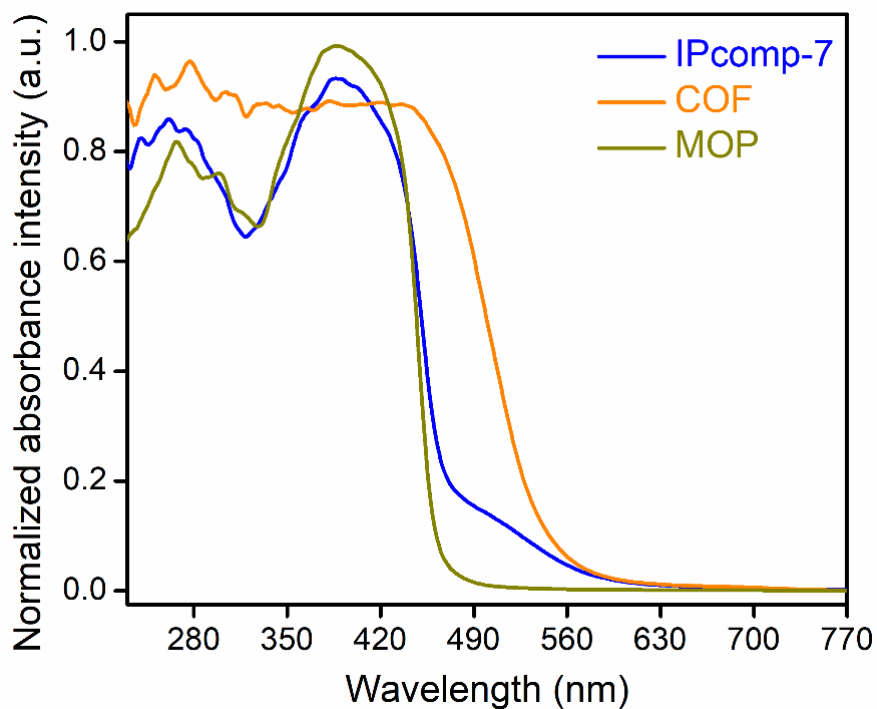
Appendix 5.27: Two-dimensional cross-sectional tomography images of IPcomp-7 indicated distribution of large macropores throughout the composite matrix.



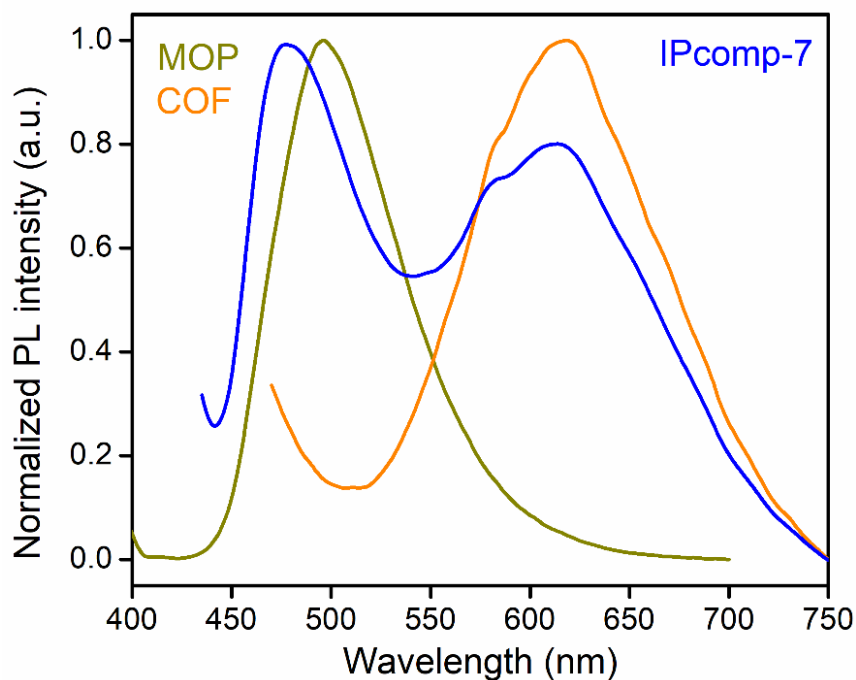
Appendix 5.28: Computed X-ray tomographic segmented 3D models of IPcomp-7 showing the distribution of large open voids (macropores) throughout the structure of the composite.



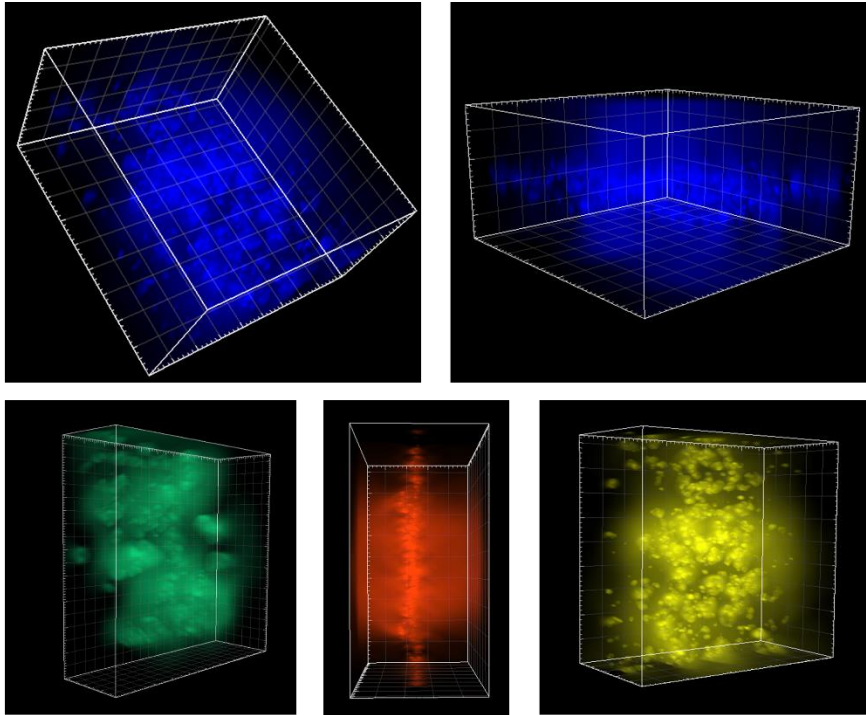
Appendix 5.29: Color-coded 3D CT images of IPcomp-7 demonstrating the visualization of pore size distribution of the large macropores throughout the structure.



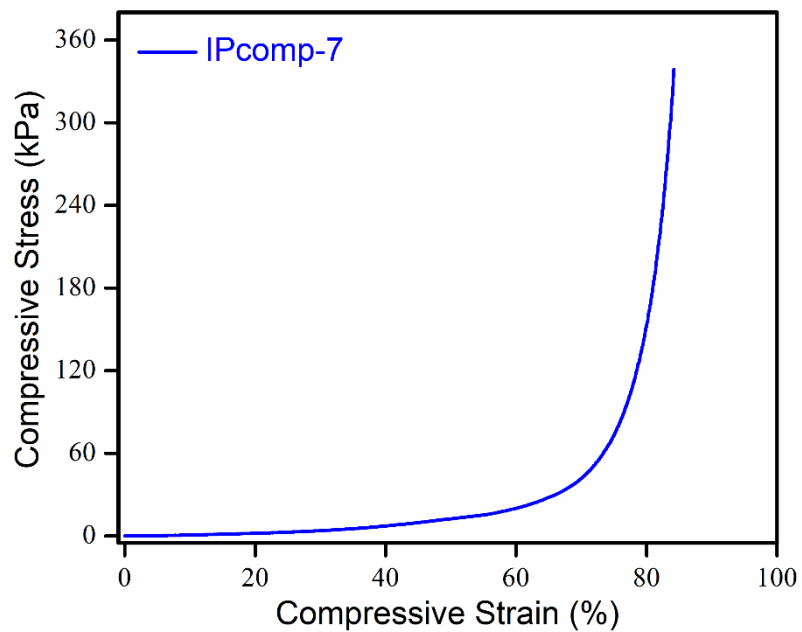
Appendix 5.30: Solid-state UV-vis spectra of IPcomp-7, along with pristine MOP and COF-aerogel.



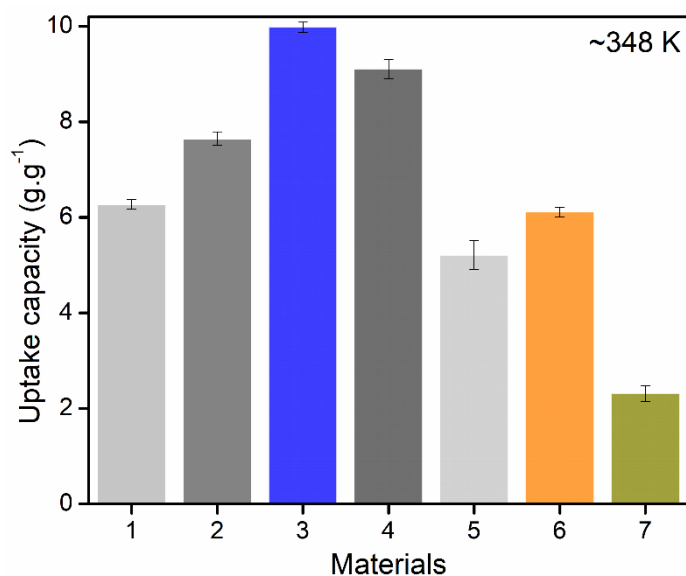
Appendix 5.31: Solid-state PL spectra of IPcomp-7, along with pristine MOP and COF-aerogel.



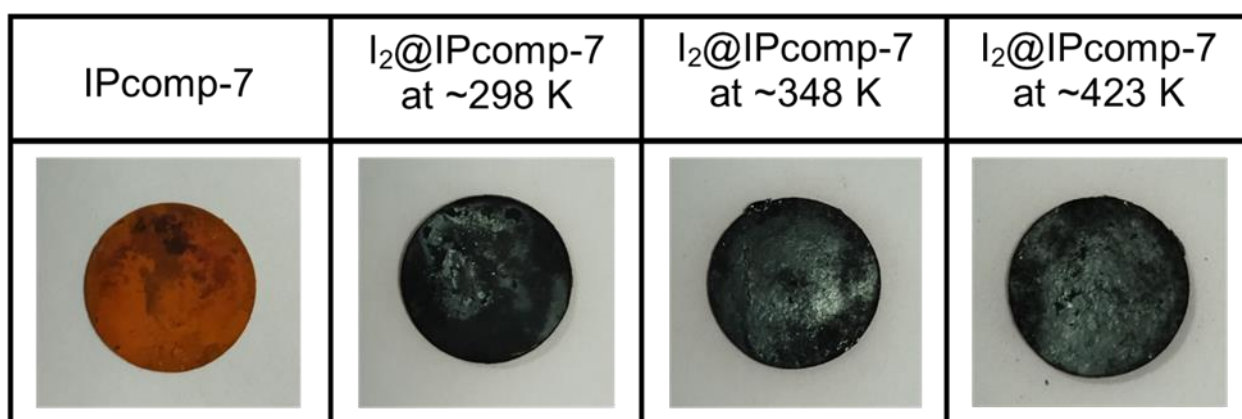
Appendix 5.32: 3D fluorescence images of IPcomp-7 showing the highly emissive nature of the composite.



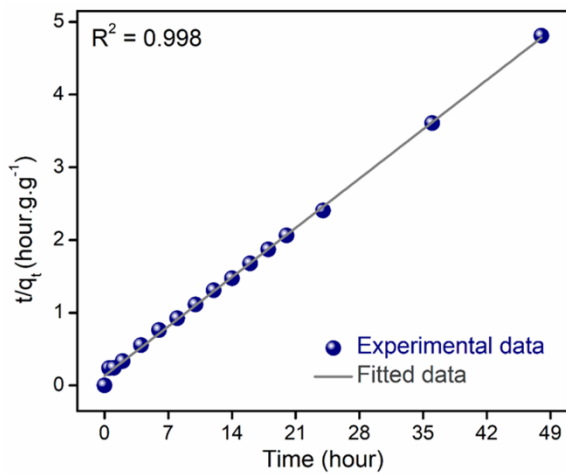
Appendix 5.33: Compressive stress-strain curves of the hybrid aerogel show promising mechanical stability.



Appendix 5.34: An optimization study of iodine capture, using different amounts of guest-MOP molecules in the hybrid composite exhibiting, IPcomp-7 constructed by ~15 mg MOPs showed highest sequestration capacity. (1 = 1 mg, 2 = 5 mg, 3 = 15 mg (IPcomp-7), 4 = 25 mg, 5 = 50 mg MOPs used in the synthesis of the composite, 6 = COF, and 7 = MOP) [Condition: adsorbent amount = 10 mg, contact time = 24 hours].



Appendix 5.35: Digital images of IPcomp-7 before and after exposing to iodine at different temperatures for 24 hours.



Kinetic parameters for the vapor phase static iodine adsorption by IPcomp-7

$$q_e (\text{exp}) = 9.98 \text{ g g}^{-1}$$

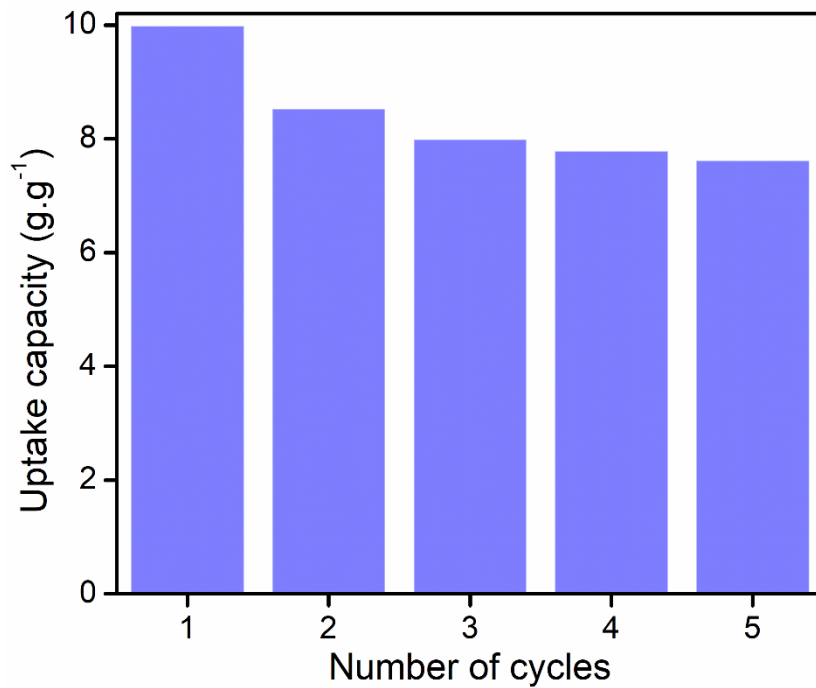
Pseudo-second-order

$$t/q_t = t/q_e + 1/k_2(q_e)^2$$

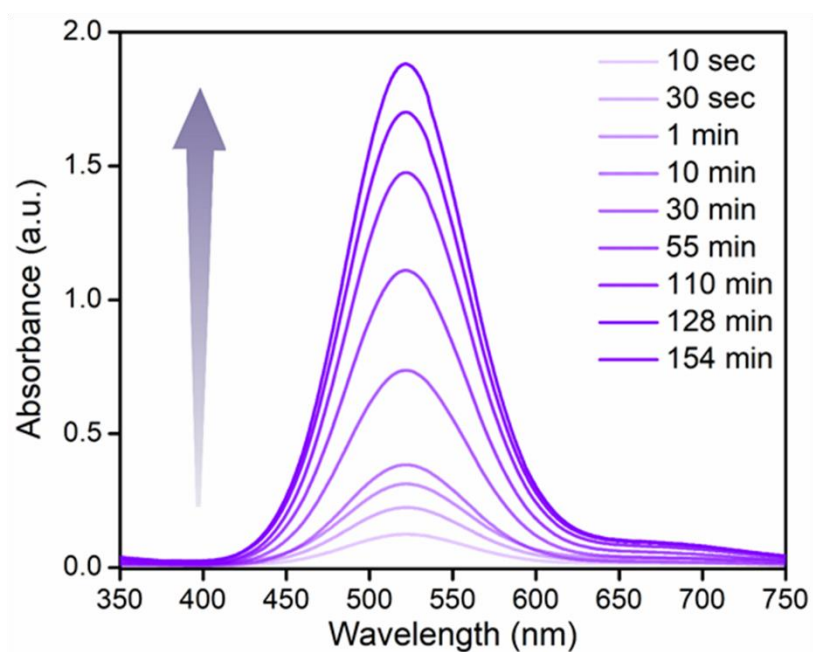
$$y = mx + c \quad y = 0.0968x + 0.1325$$

$q_e (\text{g g}^{-1})$	$k_2 (\text{g g}^{-1} \text{hour}^{-1})$	R^2
10.3305	0.0707	0.998

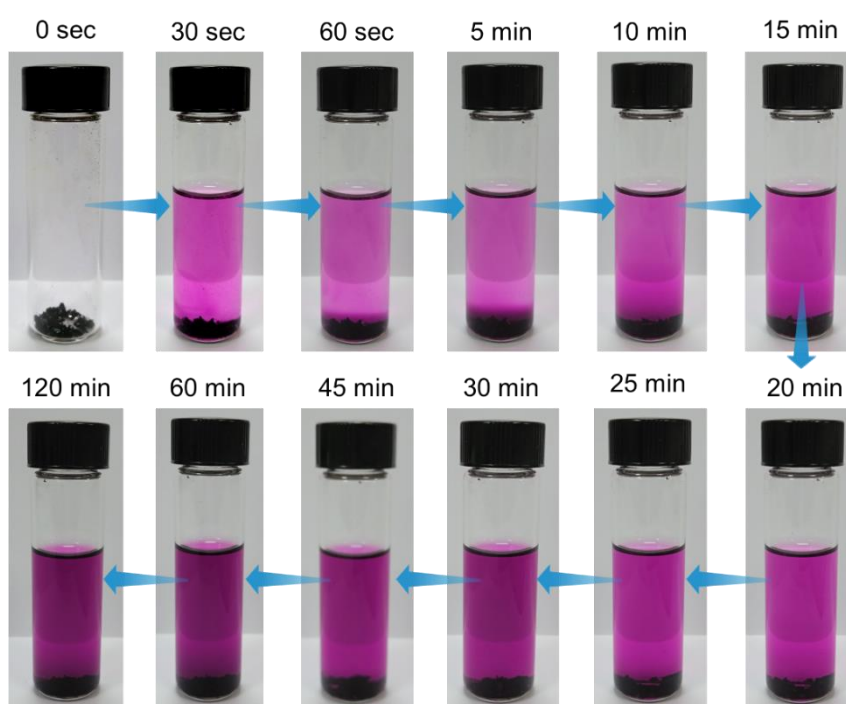
Appendix 5.36: Pseudo-second-order model fitting for vapor phase static iodine capture study by IPcomp-7 at 75 °C.



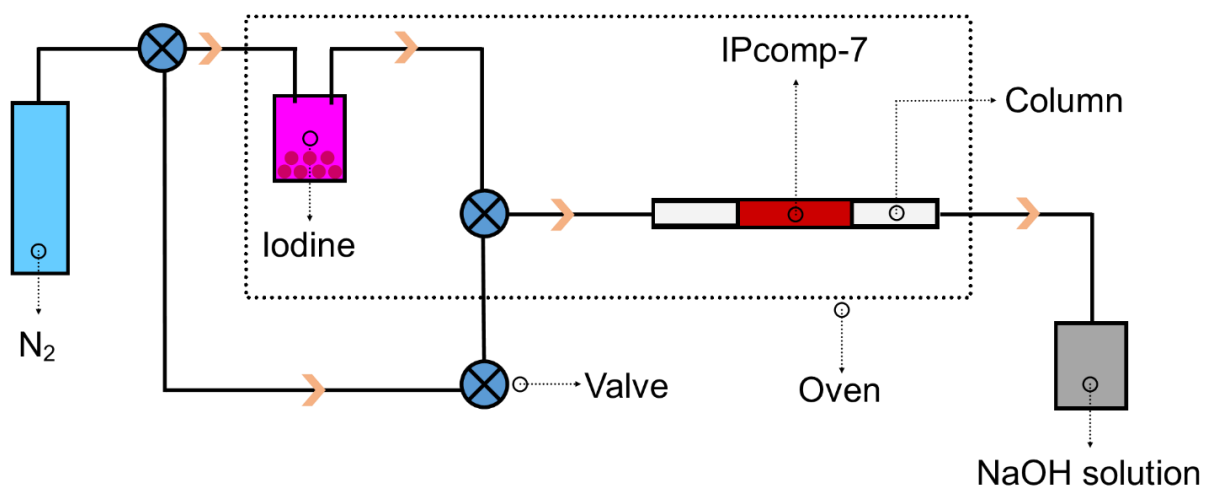
Appendix 5.37: The recyclability result of IPcomp-7 towards vapor phase iodine capture in static system.



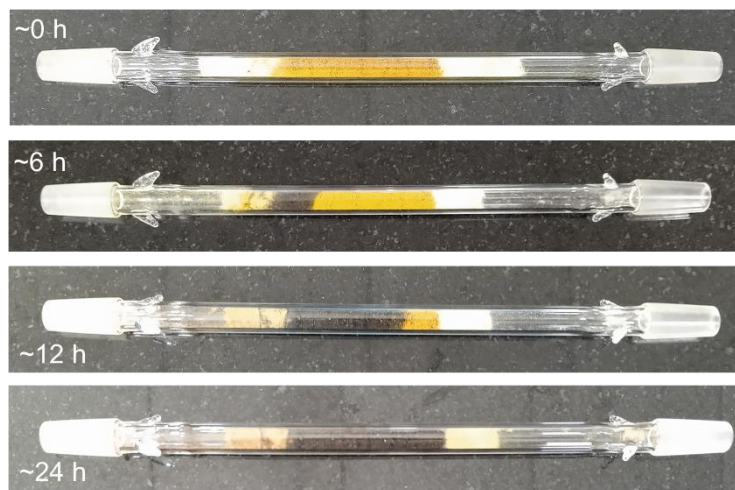
Appendix 5.38: Time-dependent UV-vis spectra of iodine released from I₂@IPcomp-7 in n-hexane solution.



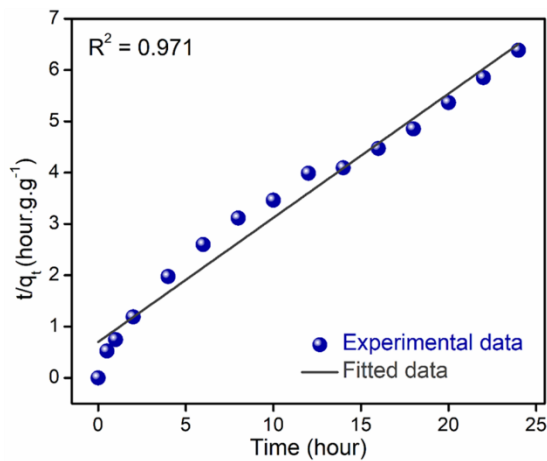
Appendix 5.39: Time-dependent images of the iodine released process from I₂@IPcomp-7 in n-hexane solution as the treatment progressed.



Appendix 5.40: Schematic representation of the instrument setup for dynamic gaseous iodine adsorption experiment at high temperature.



Appendix 5.41: Digital images of IPcomp-7 packed glass columns before and after dynamic gaseous iodine adsorption experiment at 348 K.



Kinetic parameters for the vapor phase dynamic iodine adsorption by IPcomp-7

$$q_e (\text{exp}) = 3.76 \text{ g g}^{-1}$$

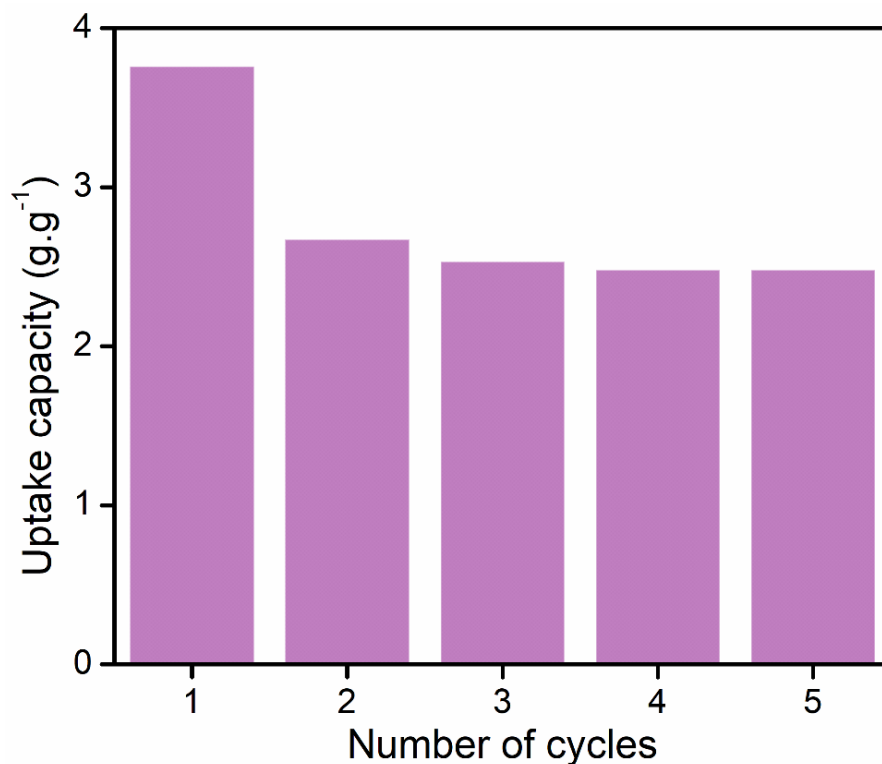
Pseudo-second-order

$$t/q_t = t/q_e + 1/k_2(q_e)^2$$

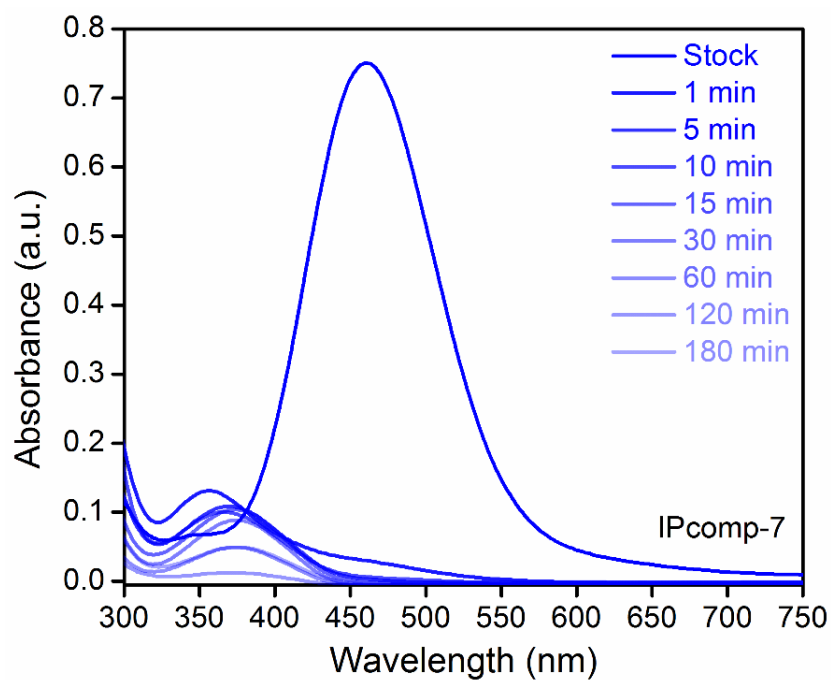
$$y = mx + c \quad y = 0.2419x + 0.6988$$

q_e (g g ⁻¹)	k_2 (g g ⁻¹ hour ⁻¹)	R^2
4.1339	0.0837	0.971

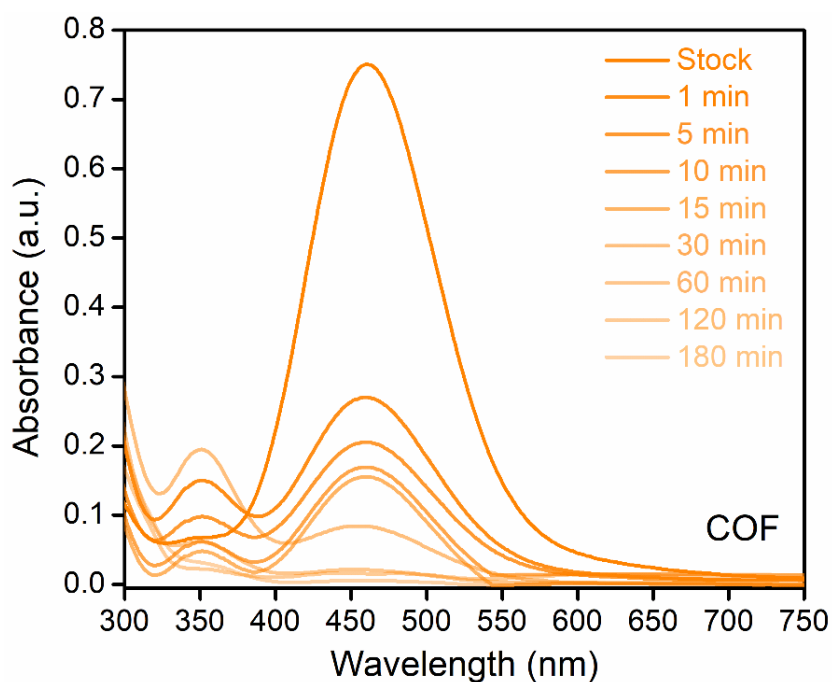
Appendix 5.42: Pseudo-second-order model fitting for vapor phase dynamic iodine capture study by IPcomp-7 at 75 °C.



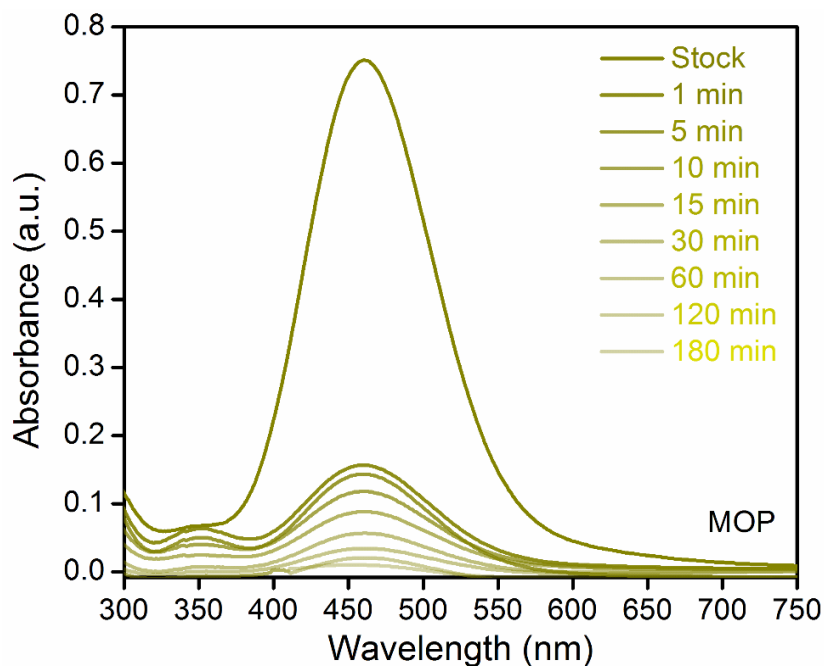
Appendix 5.43: The recyclability result of IPcomp-7 towards vapor phase dynamic iodine capture.



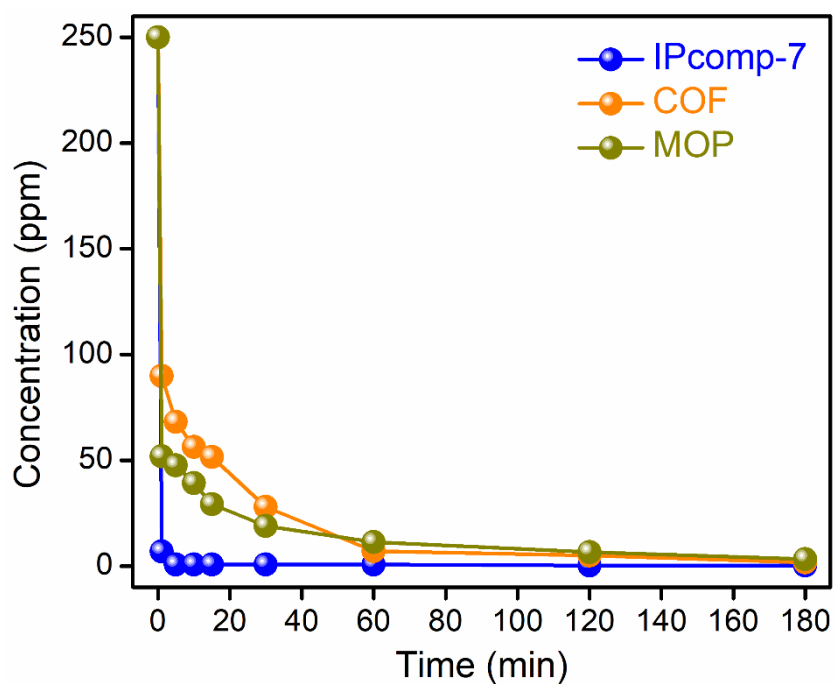
Appendix 5.44: Time-dependent UV-vis spectra of molecular iodine (I_2) in water showing rapid dismissing by the treatment of IPcomp-7.



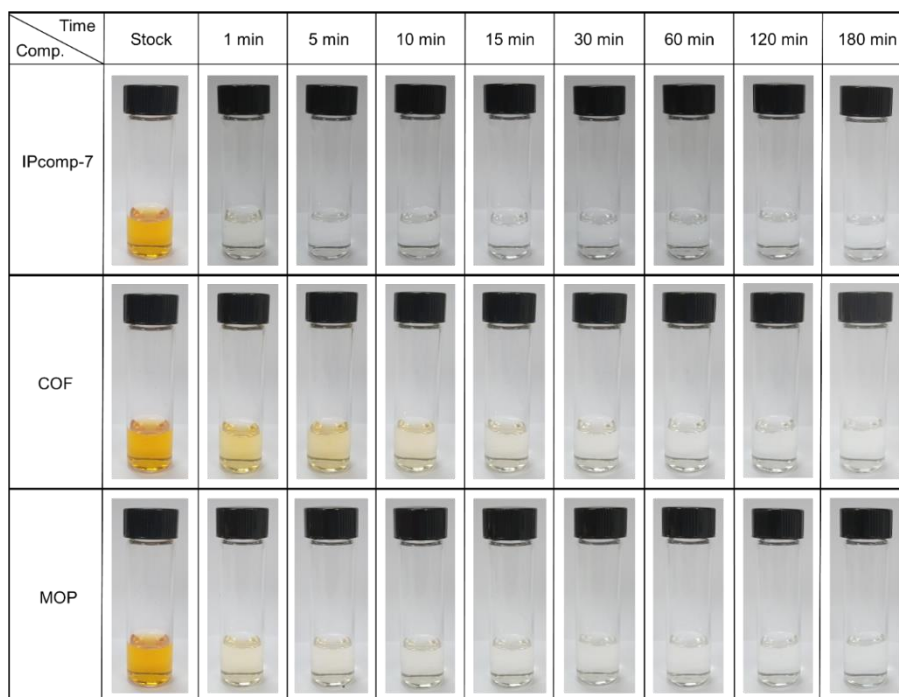
Appendix 5.45: Time-dependent UV-vis spectra of molecular iodine (I_2) in water showing rapid dismissing by the treatment of COF-aerogel.



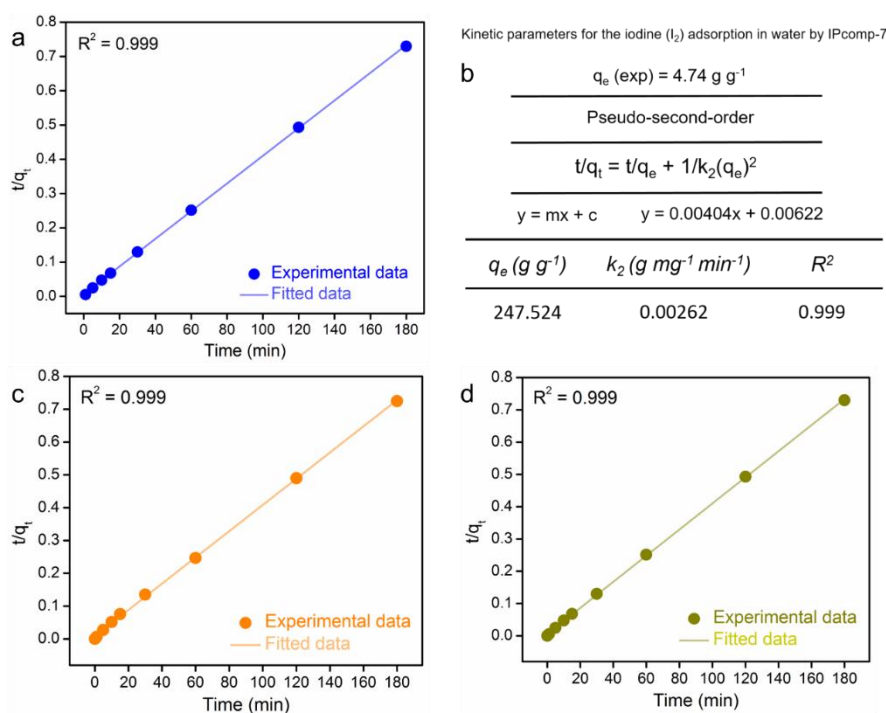
Appendix 5.46: Time-dependent UV-vis spectra of molecular iodine (I_2) in water showing rapid dismissing by the treatment of MOP.



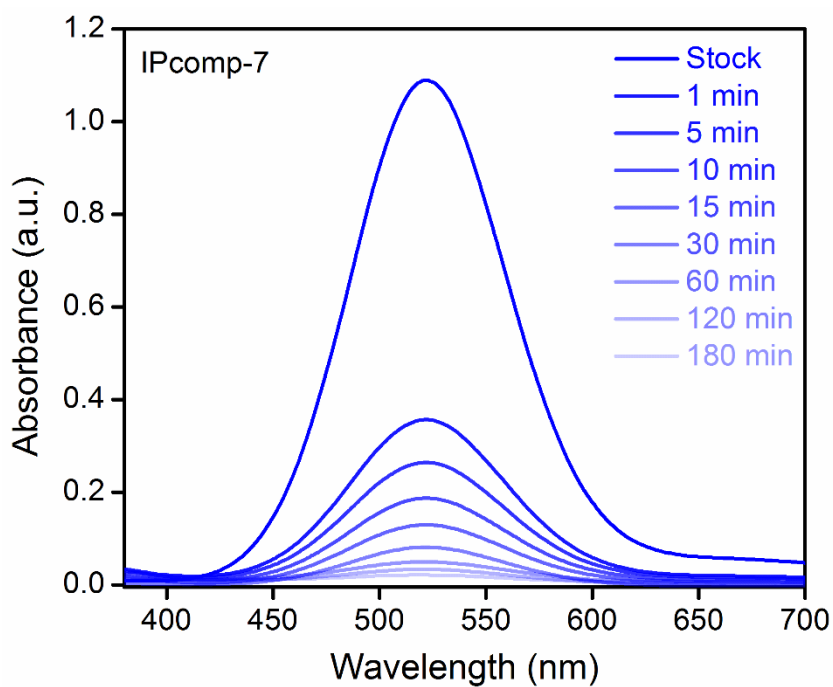
Appendix 5.47: Profile of decrease in the concentration of iodine in water with time by the treatment of IPcomp-7, COF-aerogel and MOP.



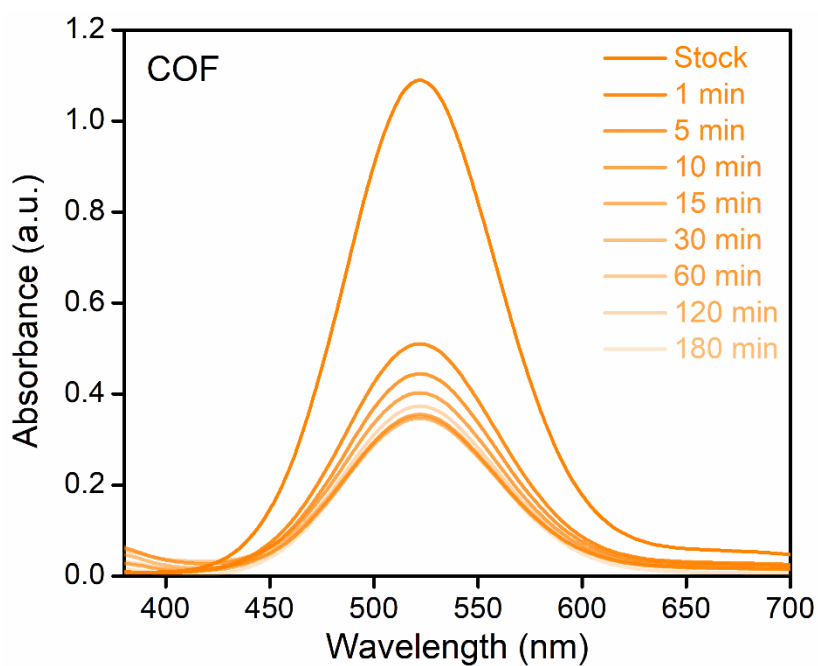
Appendix 5.48: Digital images of color changes of the saturated iodine aqueous solutions with time upon treatment of IPcomp-7, COF-aerogel and MOP.



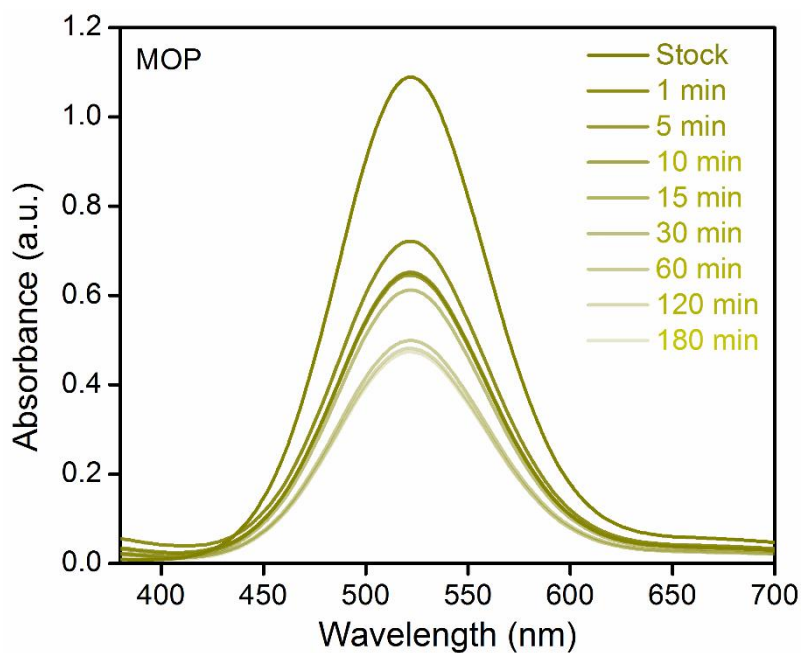
Appendix 5.49, 5.50: Pseudo-second-order kinetic model fitting plots and parameters for capture of a saturated iodine aqueous solution by (a, b) IPcomp-7, (c) COF-aerogel and (d) MOP.



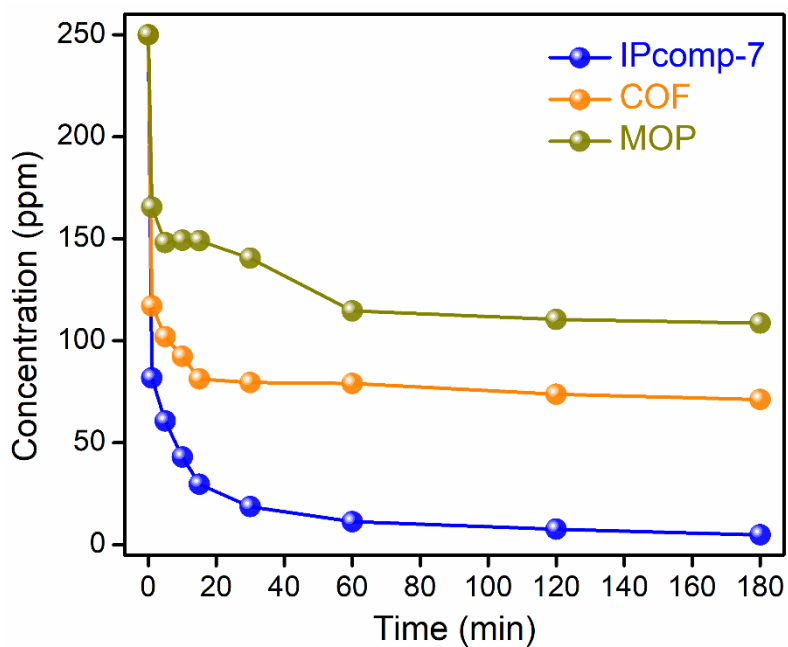
Appendix 5.51: Time-dependent UV-vis spectra of molecular iodine (I_2) in n-hexane showing rapid dismissing by the treatment of IPcomp-7.



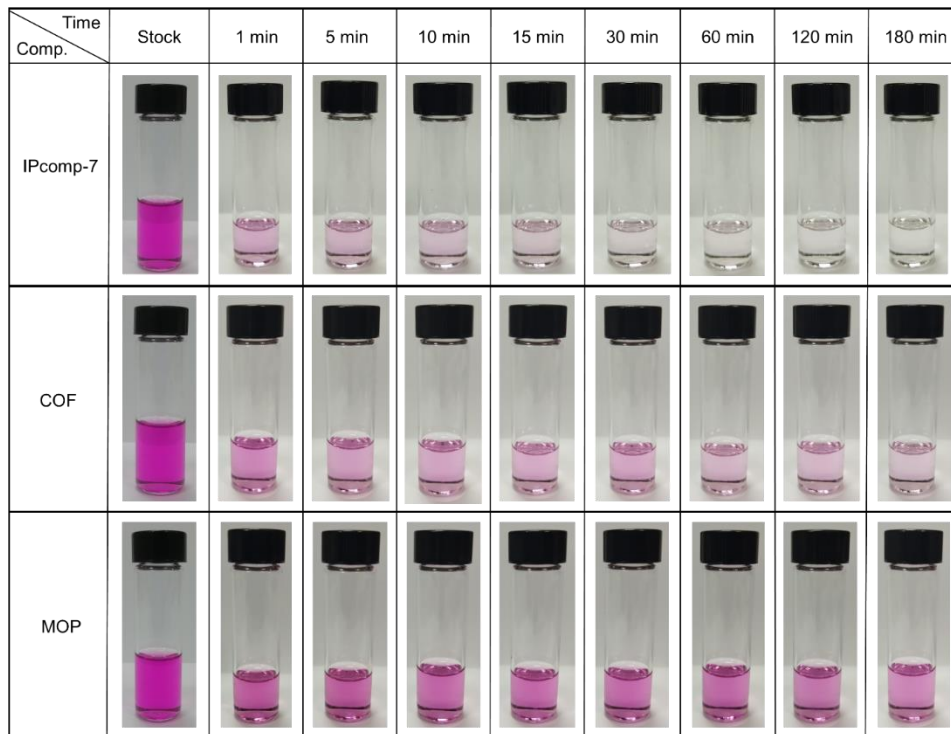
Appendix 5.52: Time-dependent UV-vis spectra of molecular iodine (I_2) in n-hexane showing rapid dismissing by the treatment of COF-aerogel.



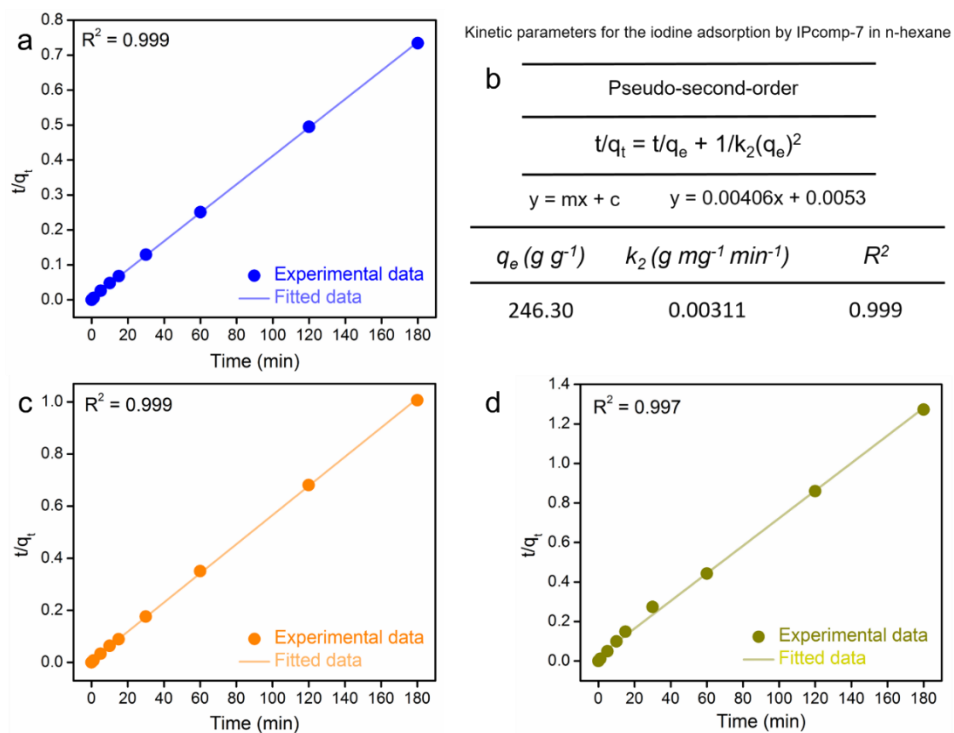
Appendix 5.53: Time-dependent UV-vis spectra of molecular iodine (I_2) in n-hexane showing rapid dismissing by the treatment of MOP.



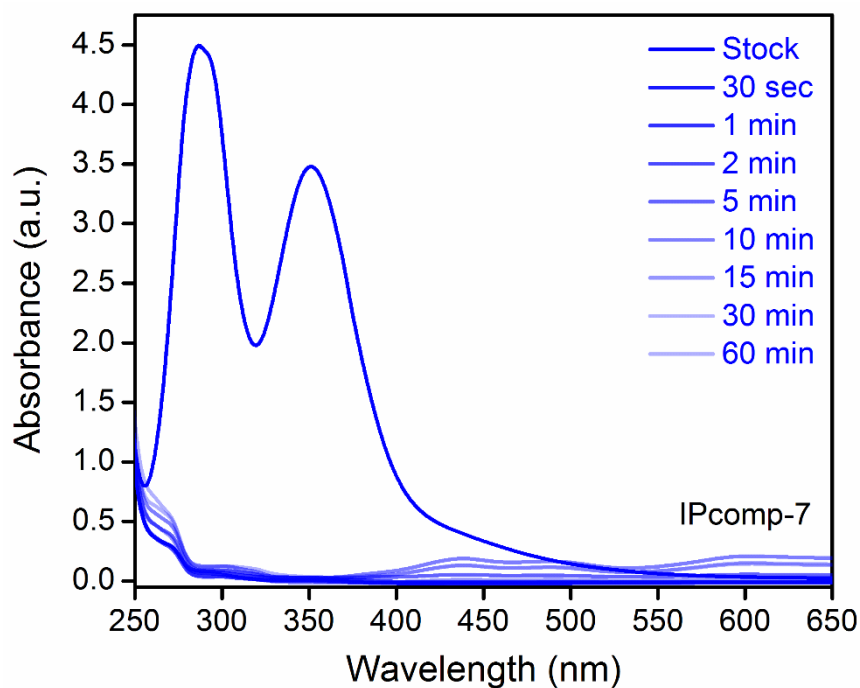
Appendix 5.54: Profile of decrease in the concentration of iodine in n-hexane with time by the treatment of IPcomp-7, COF-aerogel and MOP.



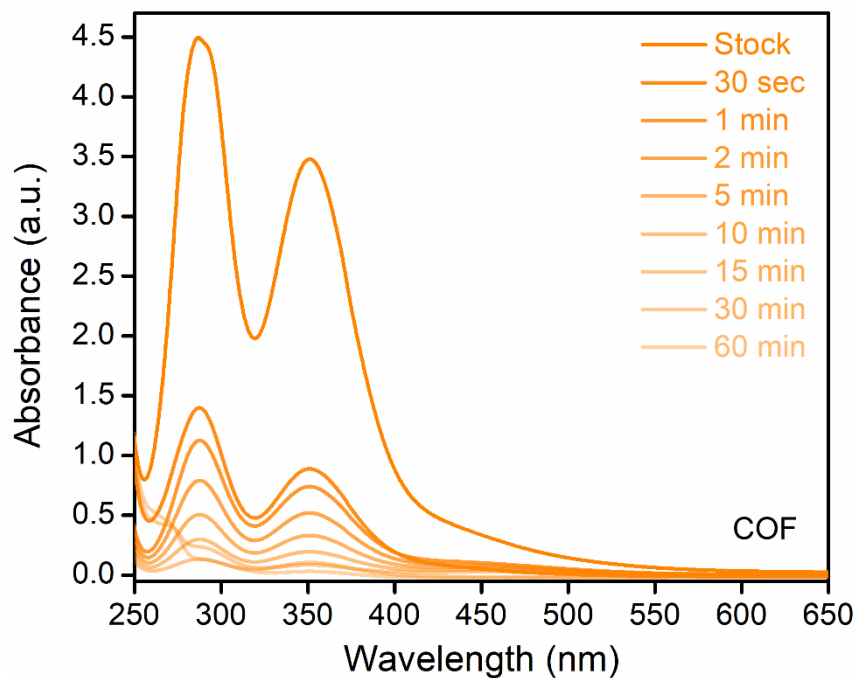
Appendix 5.55: Digital images of color changes of the iodine solutions in n-hexane with time upon treatment of IPcomp-7, COF-aerogel and MOP.



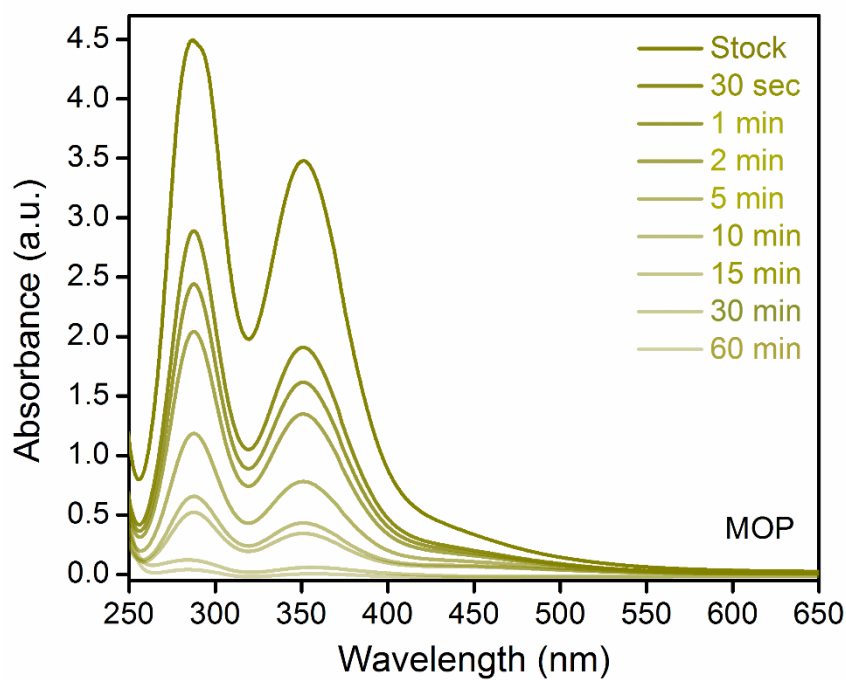
Appendix 5.56, 5.57: Pseudo-second-order kinetic model fitting plots and parameters for capture of iodine solution in n-hexane by (a, b) IPcomp-7, (c) COF-aerogel and (d) MOP.



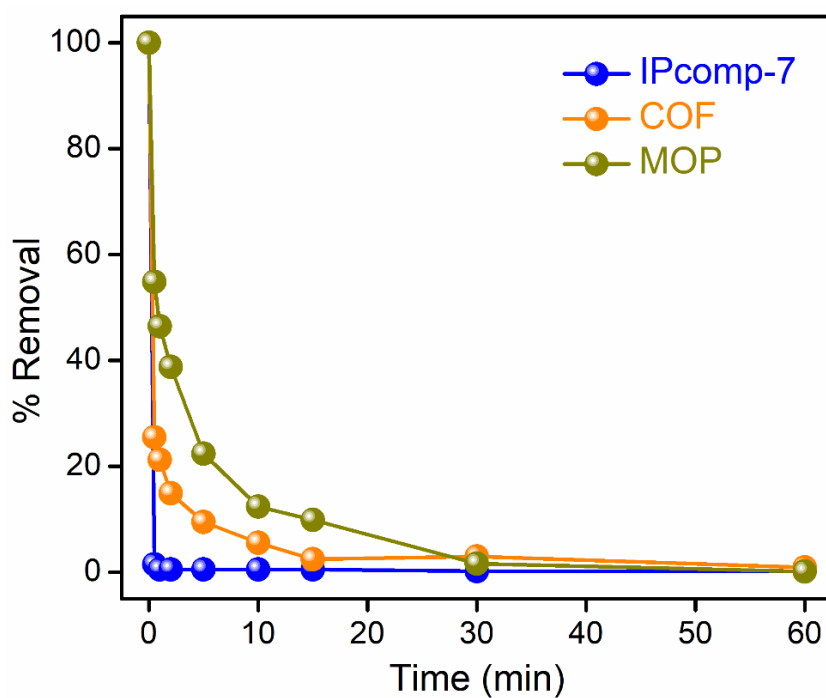
Appendix 5.58: Time-dependent UV-vis spectra of triiodides (I_3^-) (KI/I_2) in water showing rapid dismissing by the treatment of IPcomp-7.



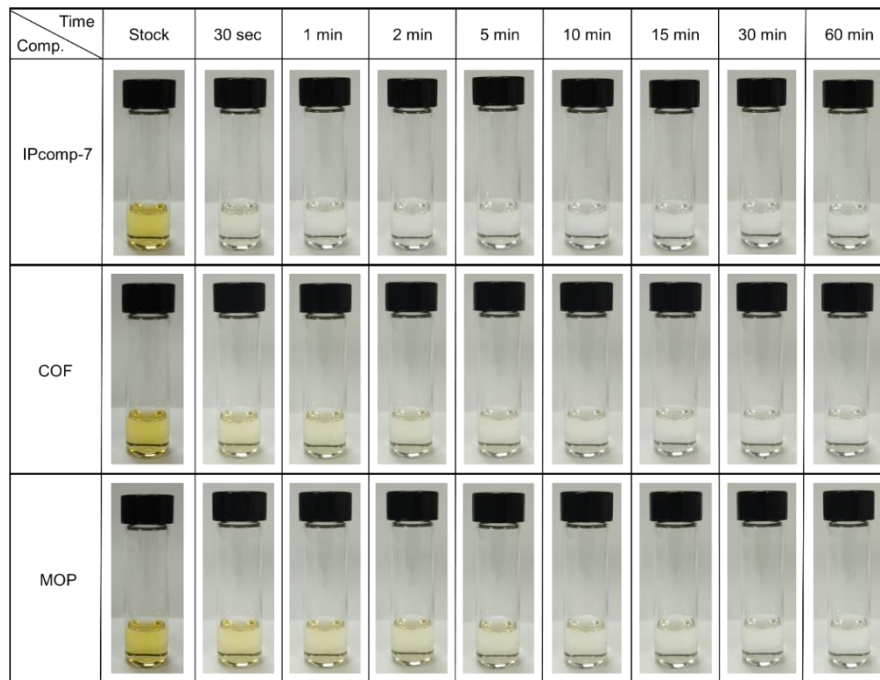
Appendix 5.59: Time-dependent UV-vis spectra of triiodides (I_3^-) (KI/I_2) in water showing rapid dismissing by the treatment of COF-aerogel.



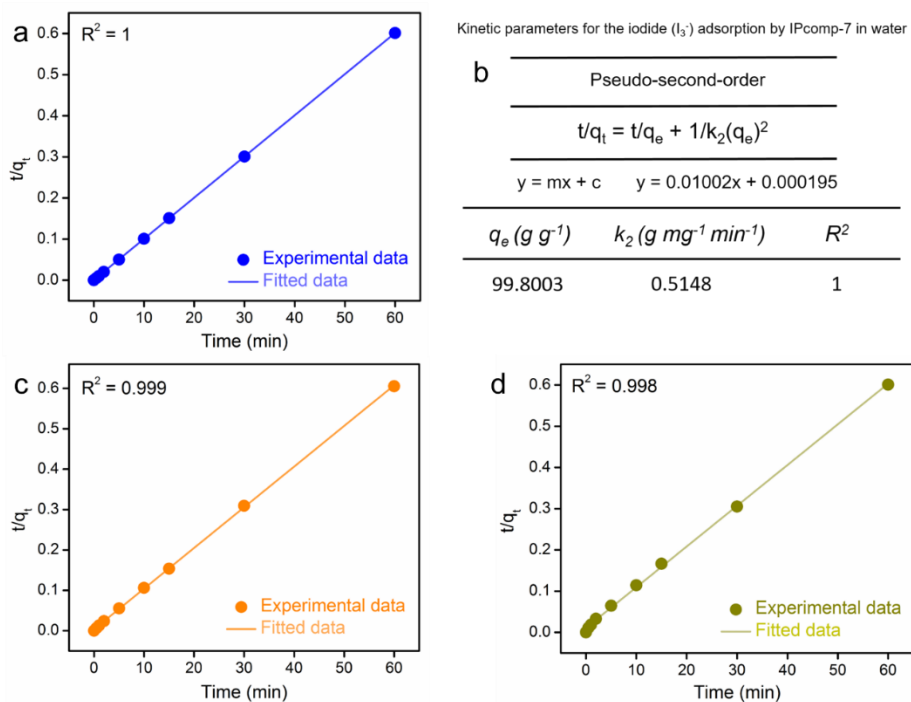
Appendix 5.60: Time-dependent UV-vis spectra of triiodides (I_3^-) (KI/ I_2) in water showing rapid dismissing by the treatment of MOP.



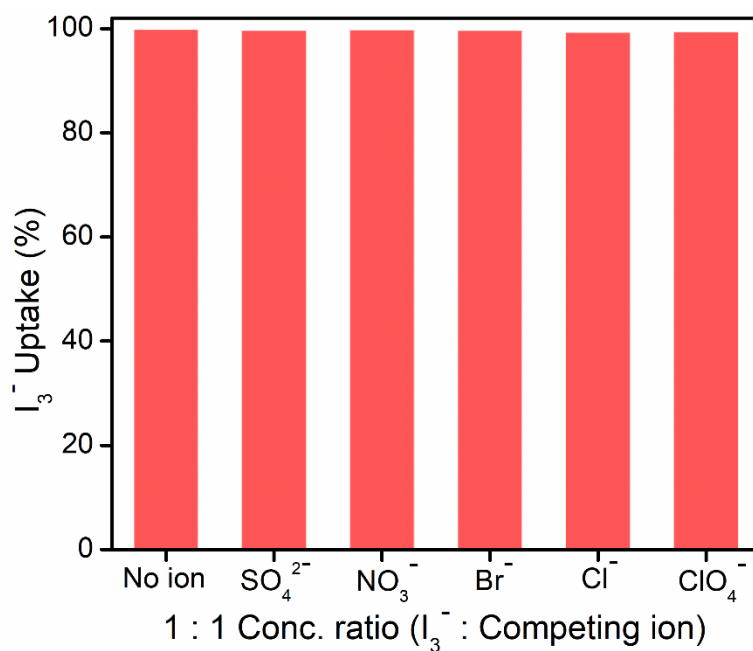
Appendix 5.61: Profile of decrease in the concentration of triiodides (I_3^-) (KI/ I_2) in water with time by the treatment of IPcomp-7, COF-aerogel and MOP.



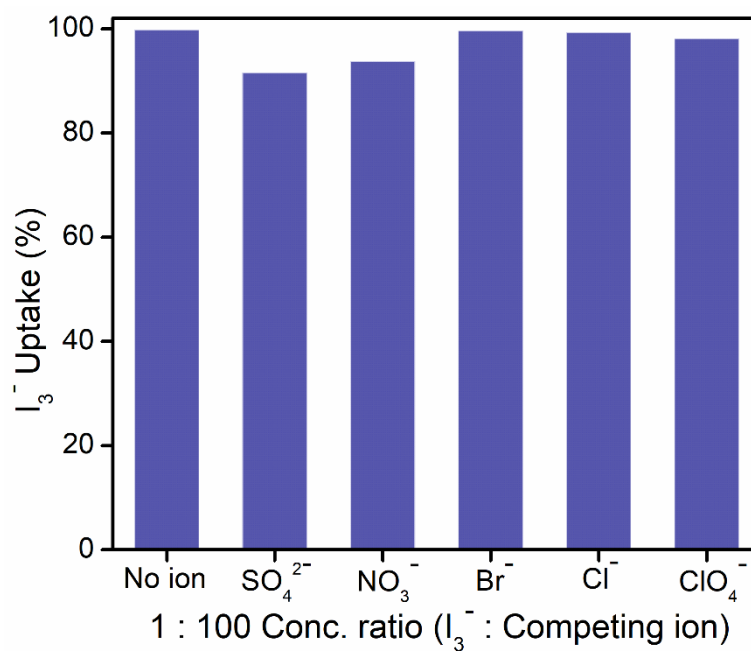
Appendix 5.62: Digital images of color changes of the triiodides (I_3^-) (KI/I_2) solution in water with time upon treatment of IPcomp-7, COF-aerogel and MOP.





















Appendix 5.63, 5.64: Pseudo-second-order kinetic model fitting plots and parameters for capture of triiodides (I_3^-) (KI/I_2) solution in water by (a, b) IPcomp-7, (c) COF-aerogel and (d) MOP.



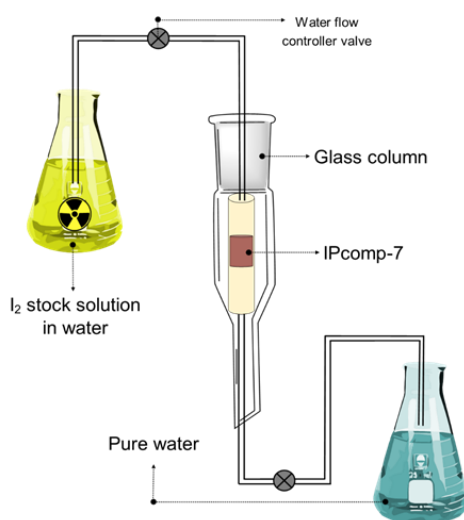
Appendix 5.65: Selectivity test: relative uptake for I_3^- anions in equimolar binary mixture of competing anions.



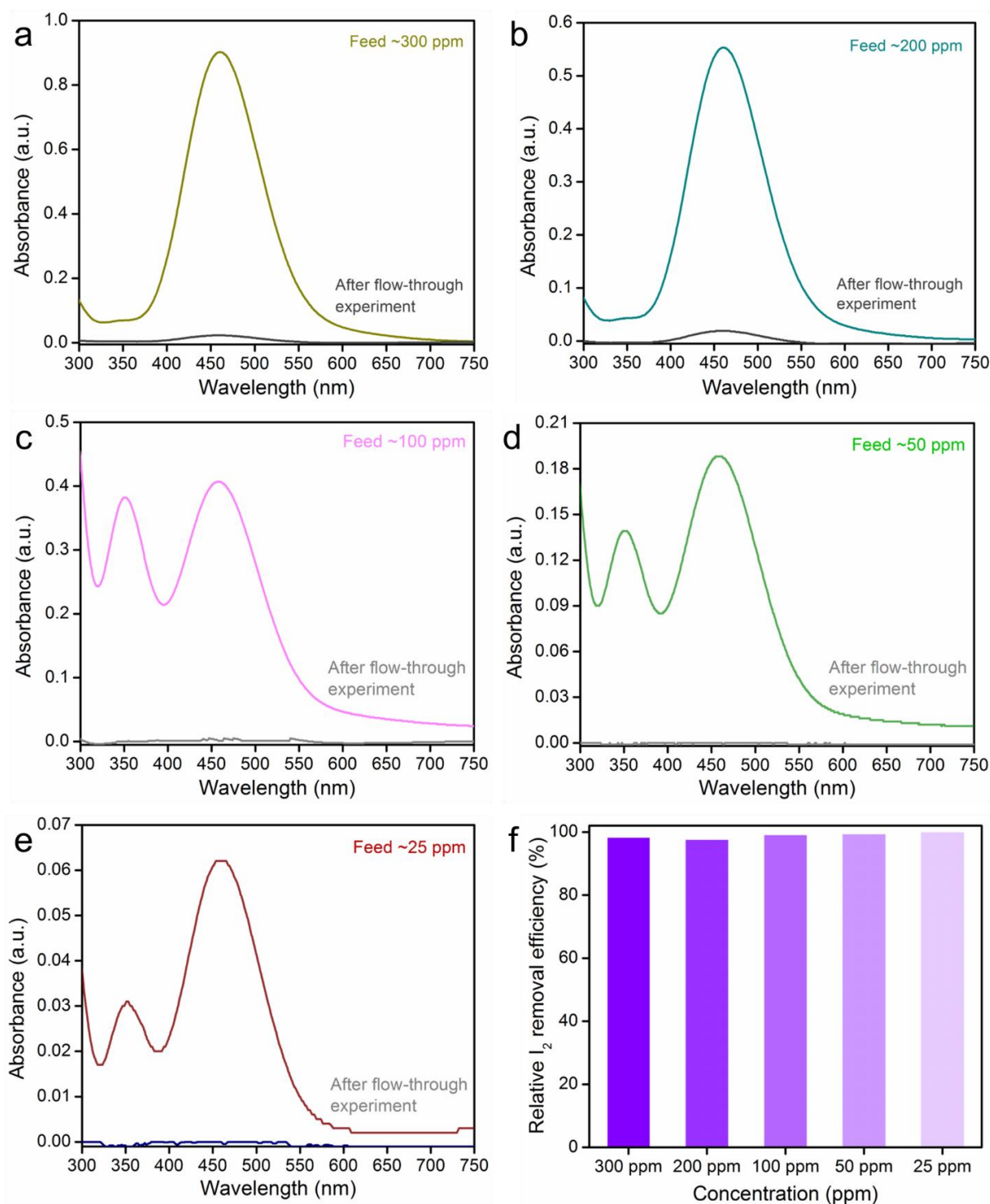
Appendix 5.66: Selectivity test: relative uptake for I_3^- anions in ~100-fold excess binary mixture of competing anions.

Time Solvent	IPcomp-7 weight	Feed	0 hour	1 hour	6 hours	12 hours	24 hours	48 hours	Total weight
I ₃ ⁻ solution in water	15.35 mg	15000 ppm							91.48 mg
I ₂ solution in cyclohexane	15.30 mg	6500 ppm							78.56 mg
I ₂ solution in n-hexane	15.26 mg	6500 ppm							83.47 mg

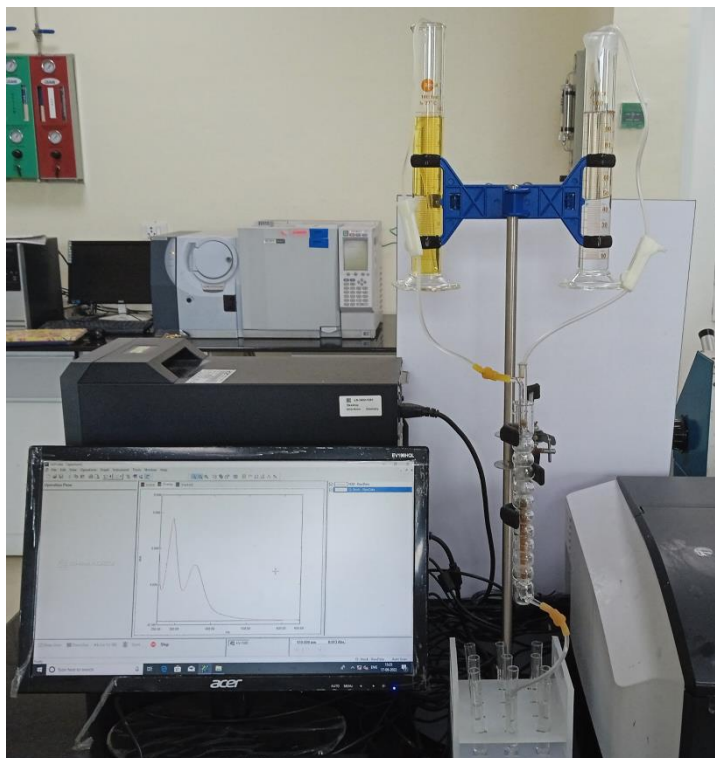
Appendix 5.67: Digital images of I₂ or I₃⁻ uptake study by IPcomp-7 in different solvents, 15000 ppm I₂/KI in water, 6500 ppm I₂ in cyclohexane, and 6500 ppm I₂ in n-hexane. [Condition: slution 2 mL, time 48 hours].



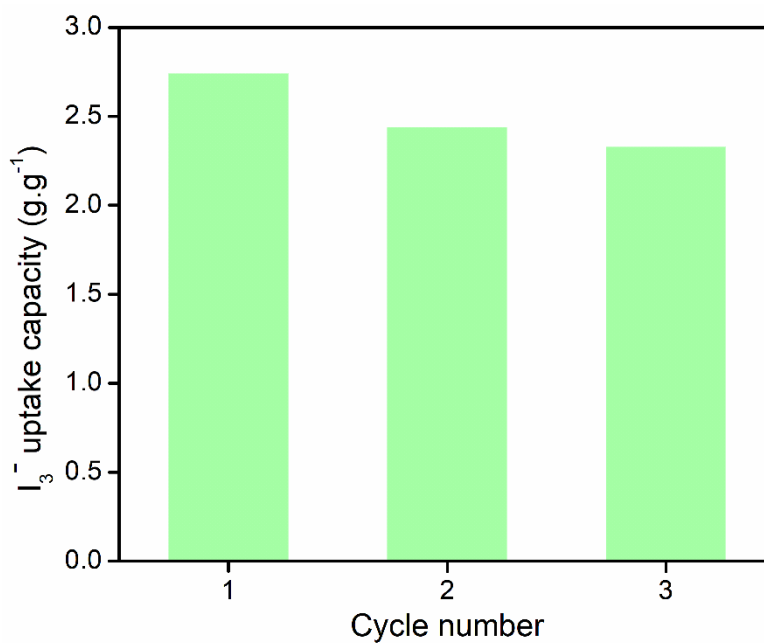
Appendix 5.68: Schematic representation of column-based aqueous phase iodine capture experiments.



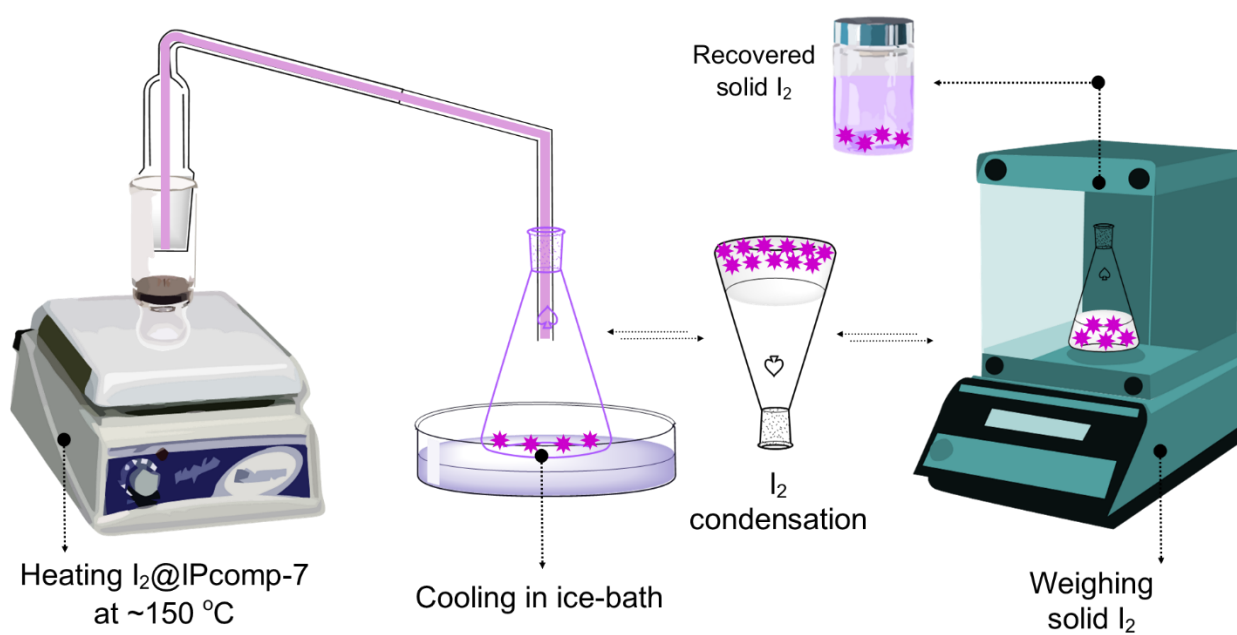
Appendix 5.69: (a-e) UV-vis spectra of aqueous solutions of iodine at different concentrations, before and after column-based capture experiments. (f) Relative I_2 uptake efficiency of IPcomp-7 embedded column at different concentrations.



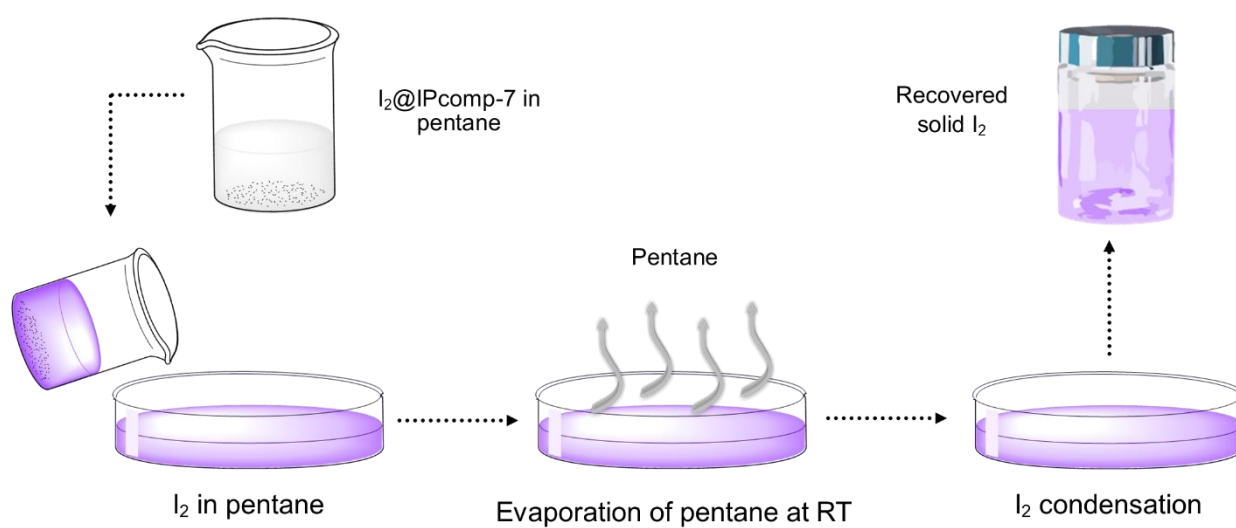
Appendix 5.70: Digital image of IPcomp-7 embedded column-based flow-through I_2/KI capture experiment.



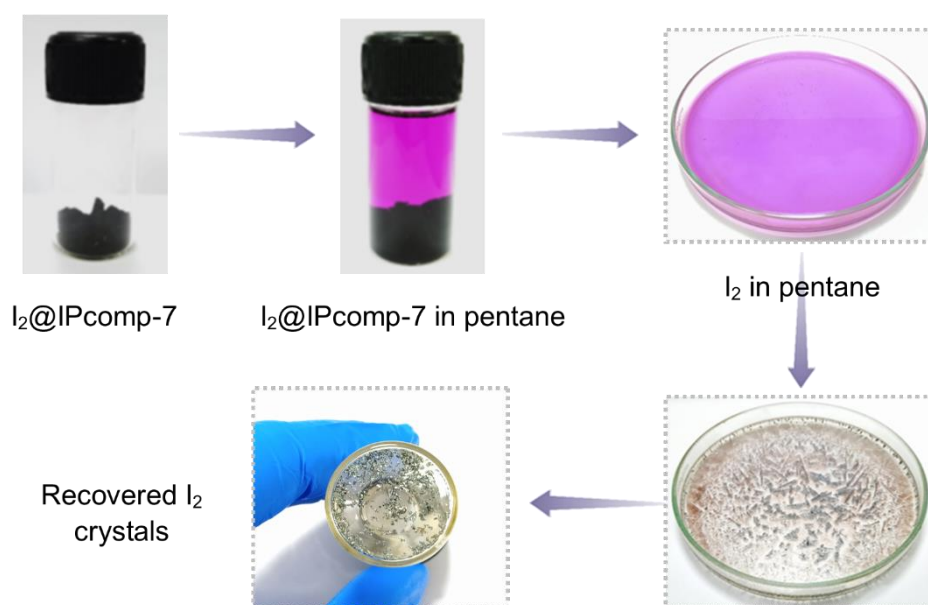
Appendix 5.71: Iodide uptake capacities in different cycles in case of column-based flow-through I_2/KI capture experiment.



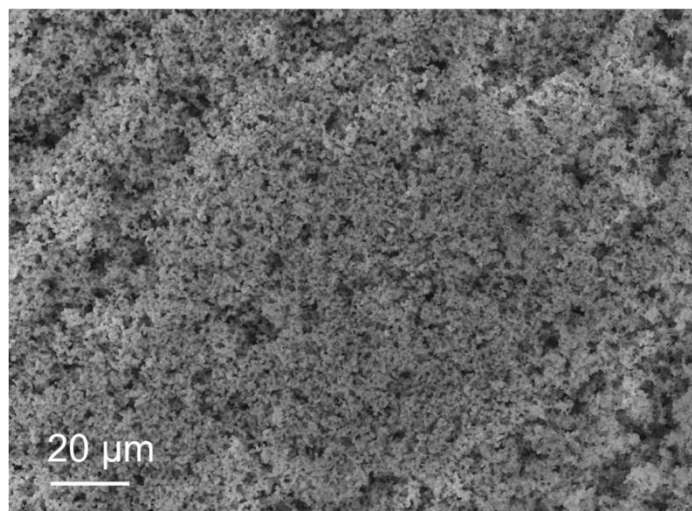
Appendix 5.72: Schematic representation and digital image of recovery of solid iodine setup by heating of I_2 @IPcomp-7 at $150^\circ C$.



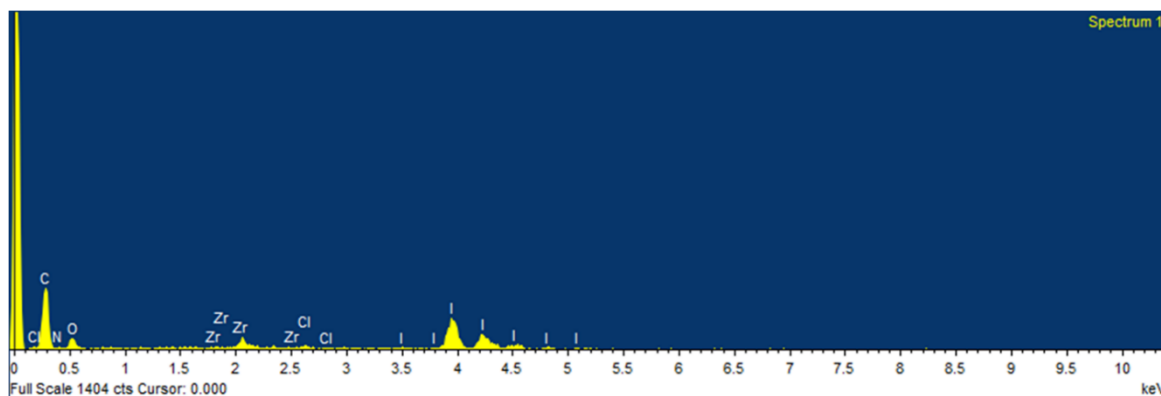
Appendix 5.73: Schematic representation of recovery of solid iodine crystals by treating of I₂@IPcomp-7 in pentane solvent.



Appendix 5.74: Digital images of recovery of solid iodine crystals by treating of I₂@IPcomp-7 in pentane solvent.

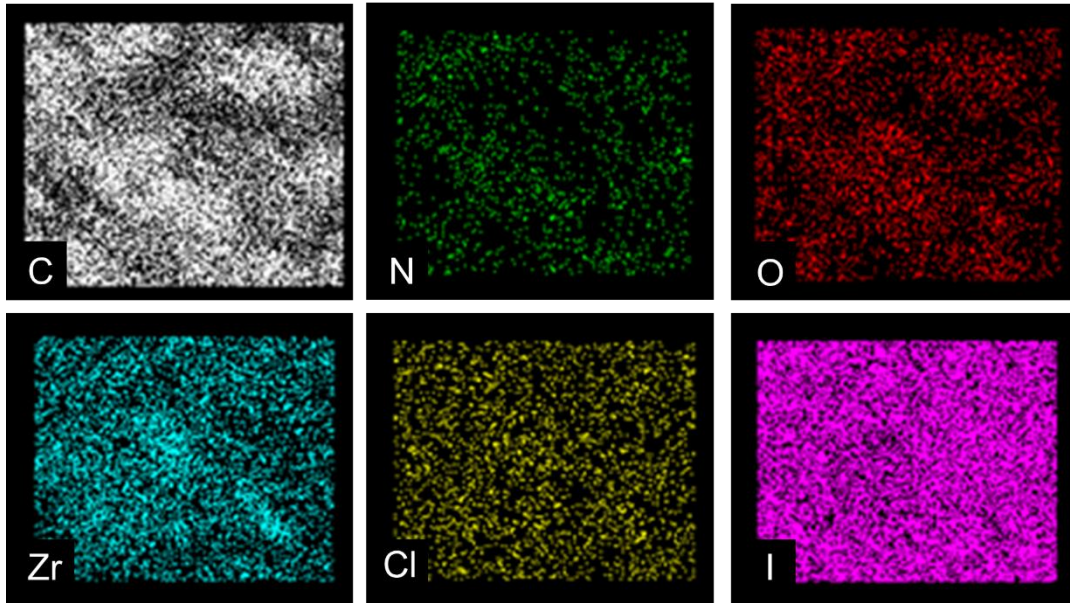


Appendix 5.75: FESEM image of IPcomp-7 after I₂ absorption test.

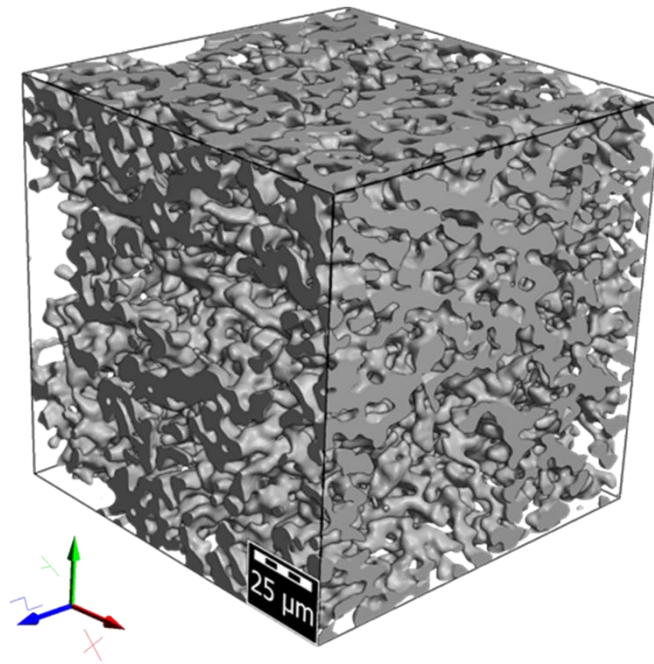


Element	Weight%	Atomic%
C K	40.55	79.50
N K	0.05	0.08
O K	6.67	9.82
Cl K	0.85	0.57
Zr L	5.50	1.42
I L	46.37	8.61
Totals	100.00	

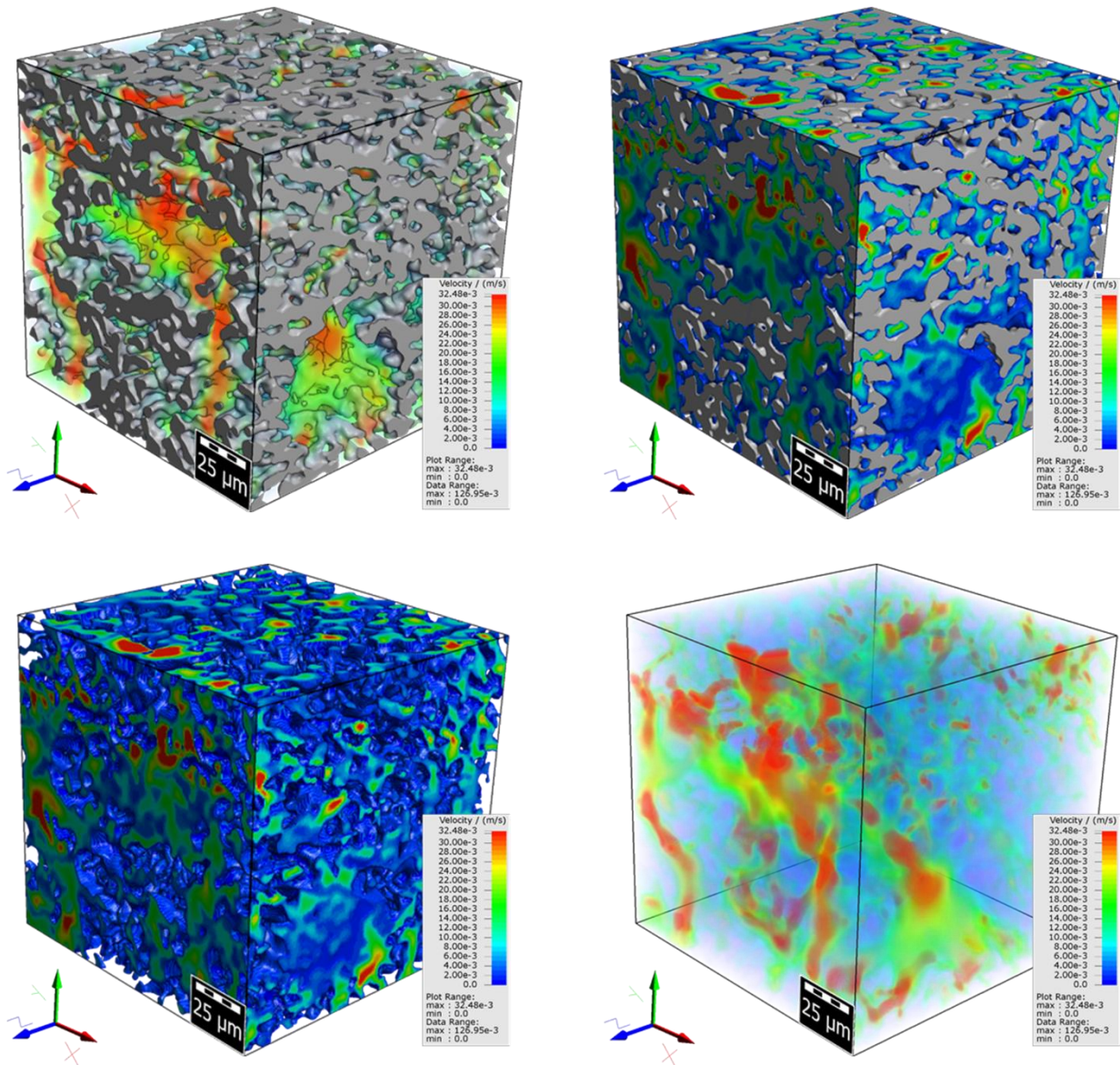
Appendix 5.76: FESEM-EDX data of IPcomp-7 after I₂ absorption test.



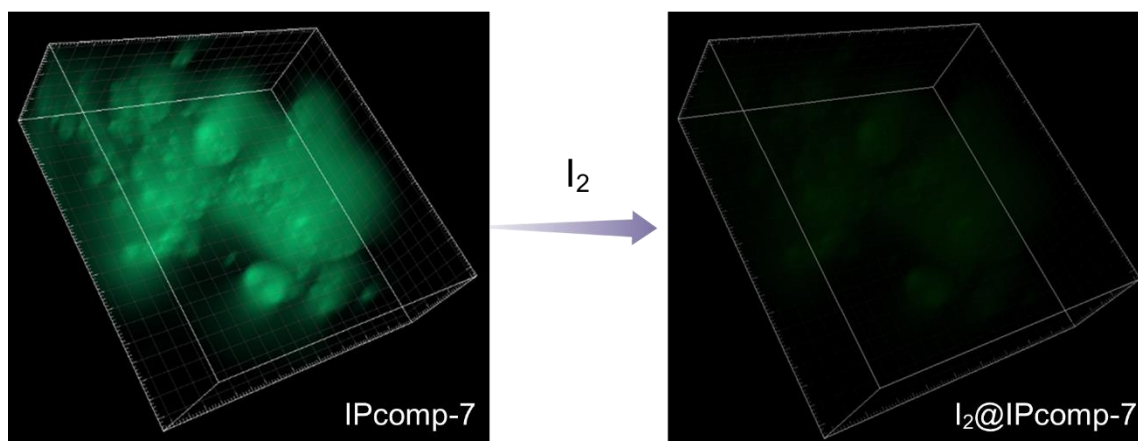
Appendix 5.77: Elemental mapping images from FESEM experiment of IPcomp-7 after I₂ absorption test.



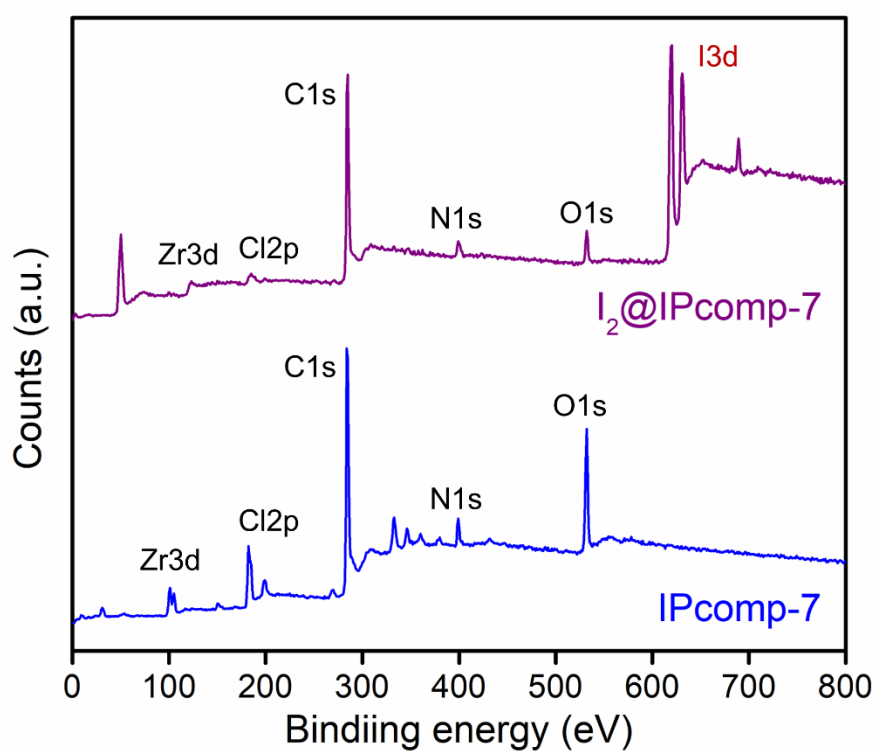
Appendix 5.78: X-ray 3D tomographic image of IPcomp-7 after I₂ absorption test.



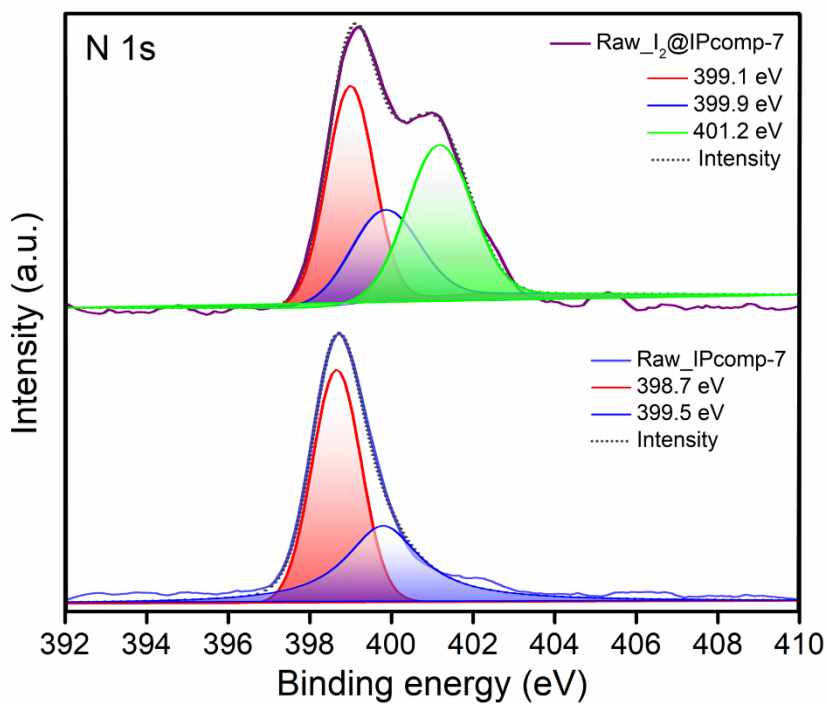
Appendix 5.79: Color-coded X-ray 3D tomographic image of $I_2@IPcomp-7$ showing the retention of micron size pores even after the iodine adsorption.



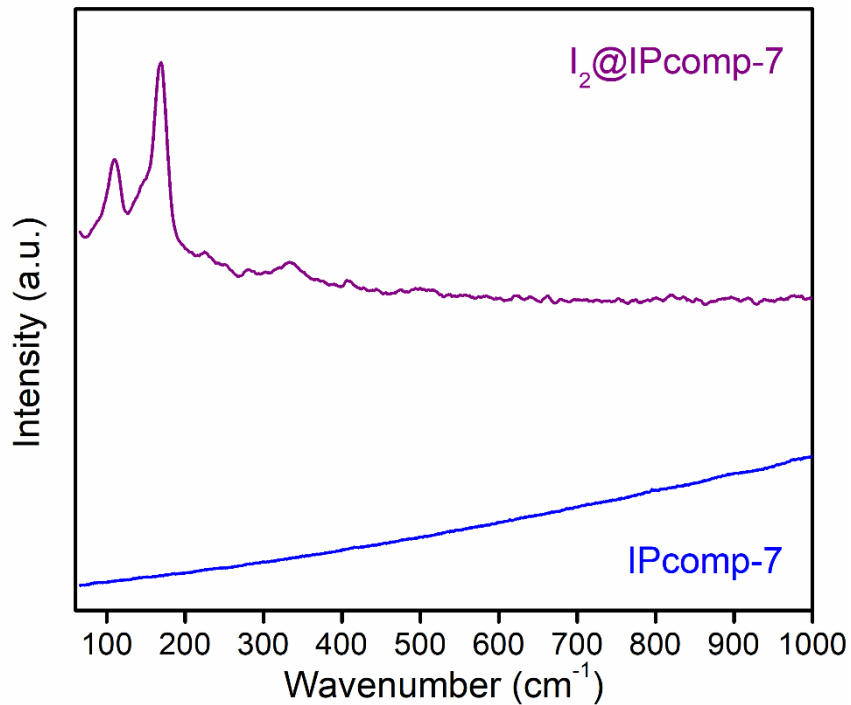
Appendix 5.80: Fluorescence microscopic images of IPcomp-7 before and after I₂ absorption test.



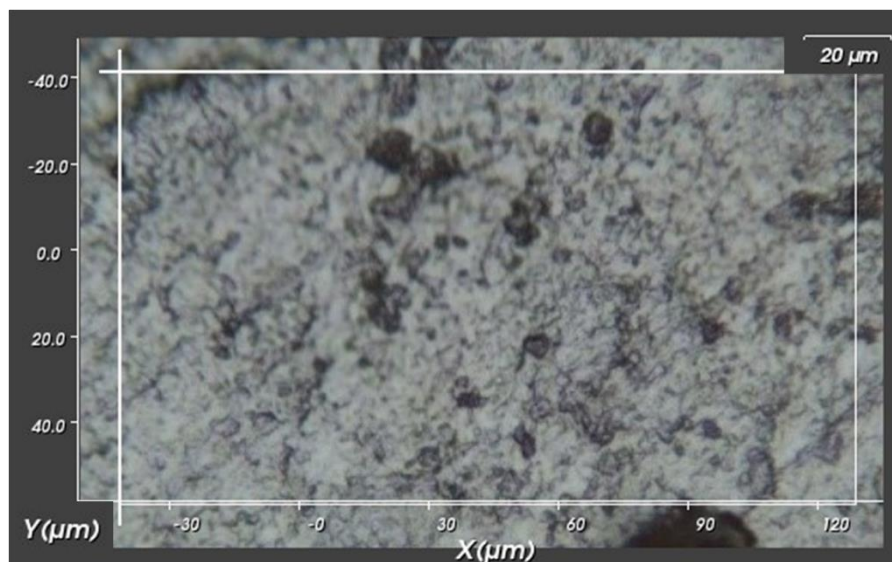
Appendix 5.81: XPS survey spectra of IPcomp-7 before and after I₂ absorption test.



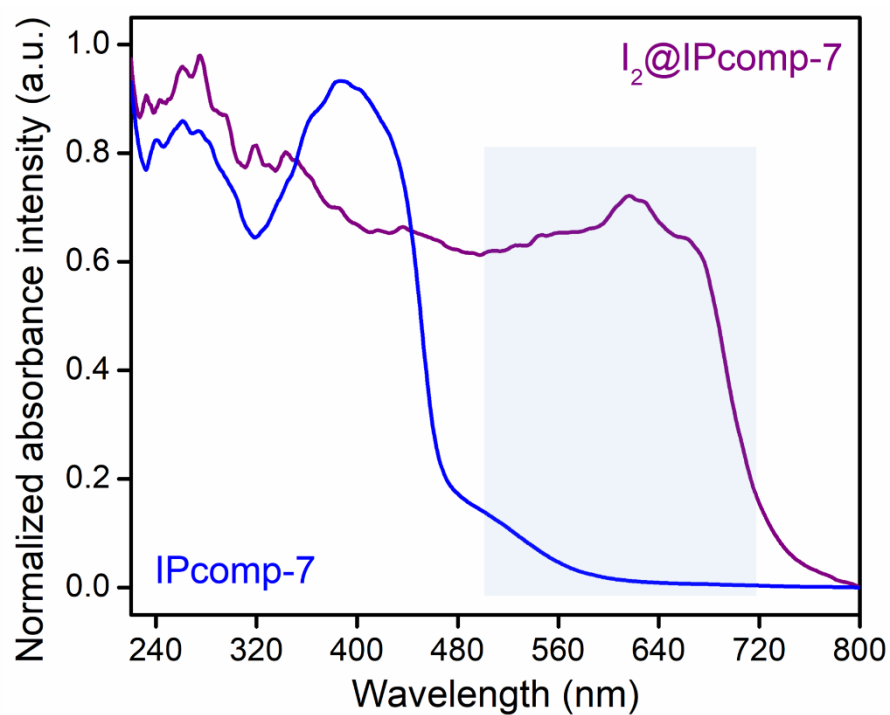
Appendix 5.82: N 1s XPS spectra of IPcomp-7 before and after I₂ absorption test.



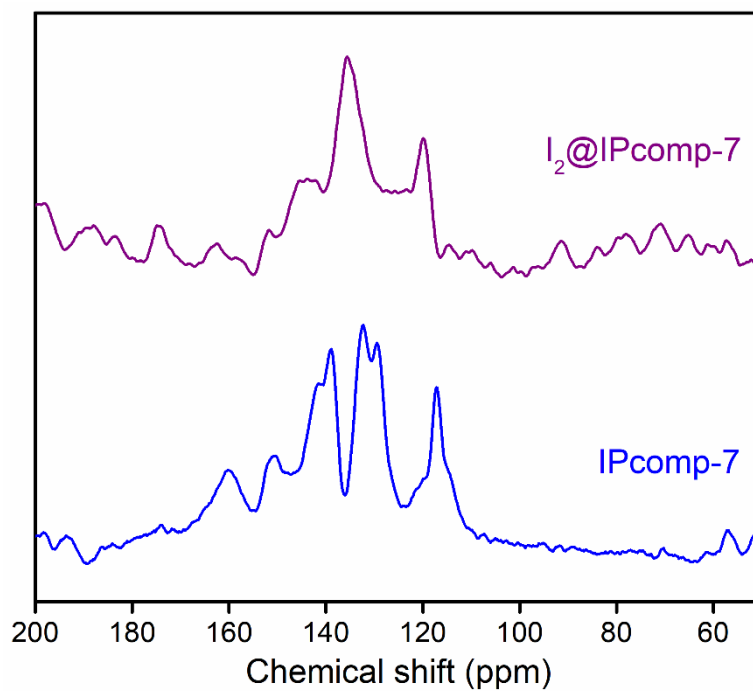
Appendix 5.83: Raman spectra of IPcomp-7 before and after I₂ absorption test.



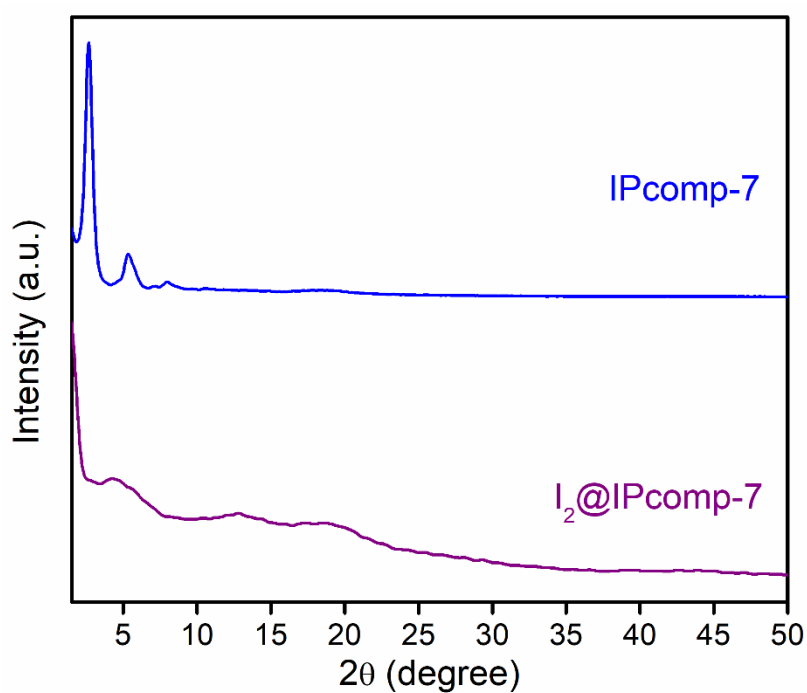
Appendix 5.84: Corresponding Raman spectroscopy image for mapping of IPcomp-7 after I_2 absorption test.



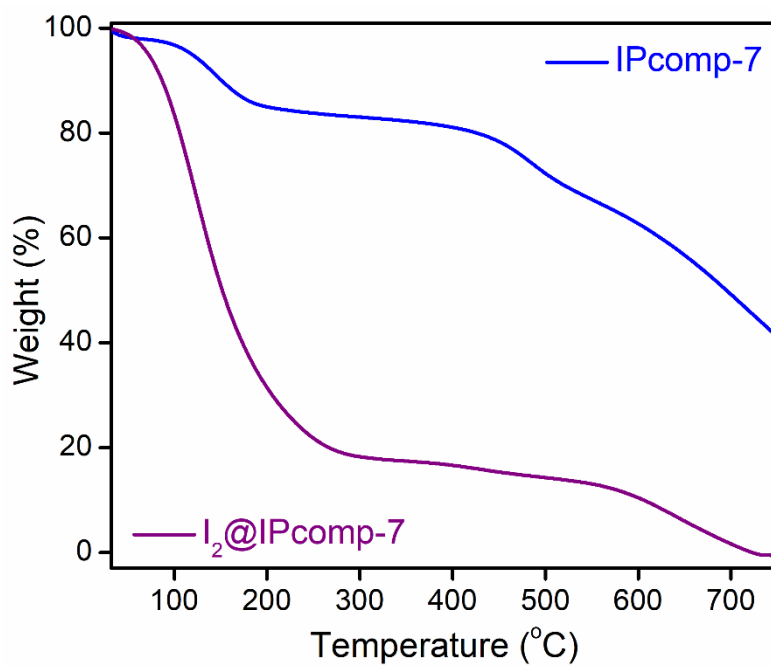
Appendix 5.85: Solid-state UV-vis spectra of IPcomp-7 before and after I_2 absorption test.



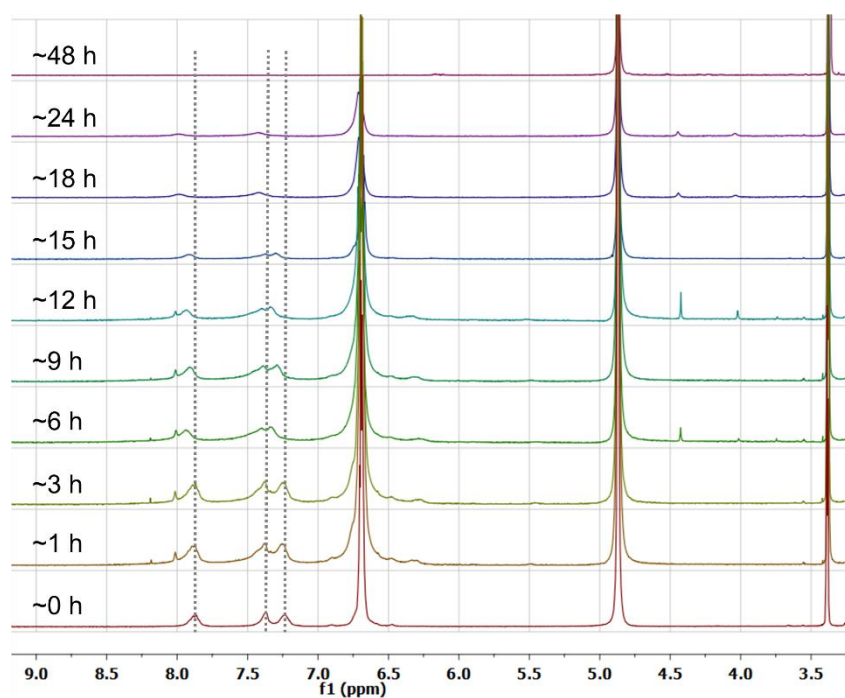
Appendix 5.86: Solid-state ^{13}C NMR spectra of IPcomp-7 before and after I_2 absorption test.



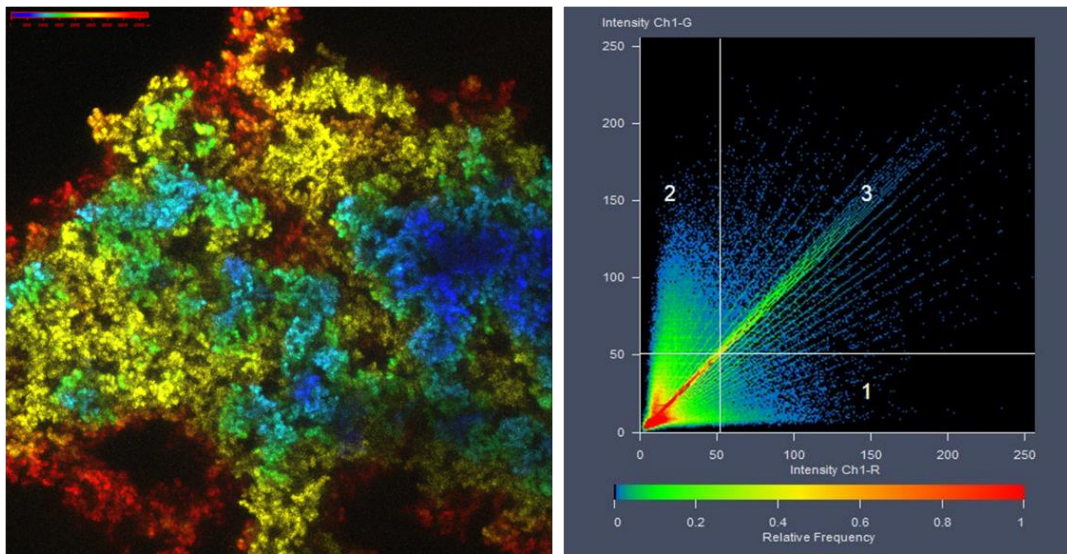
Appendix 5.87: PXRD profile of IPcomp-7 before and after I_2 absorption test.



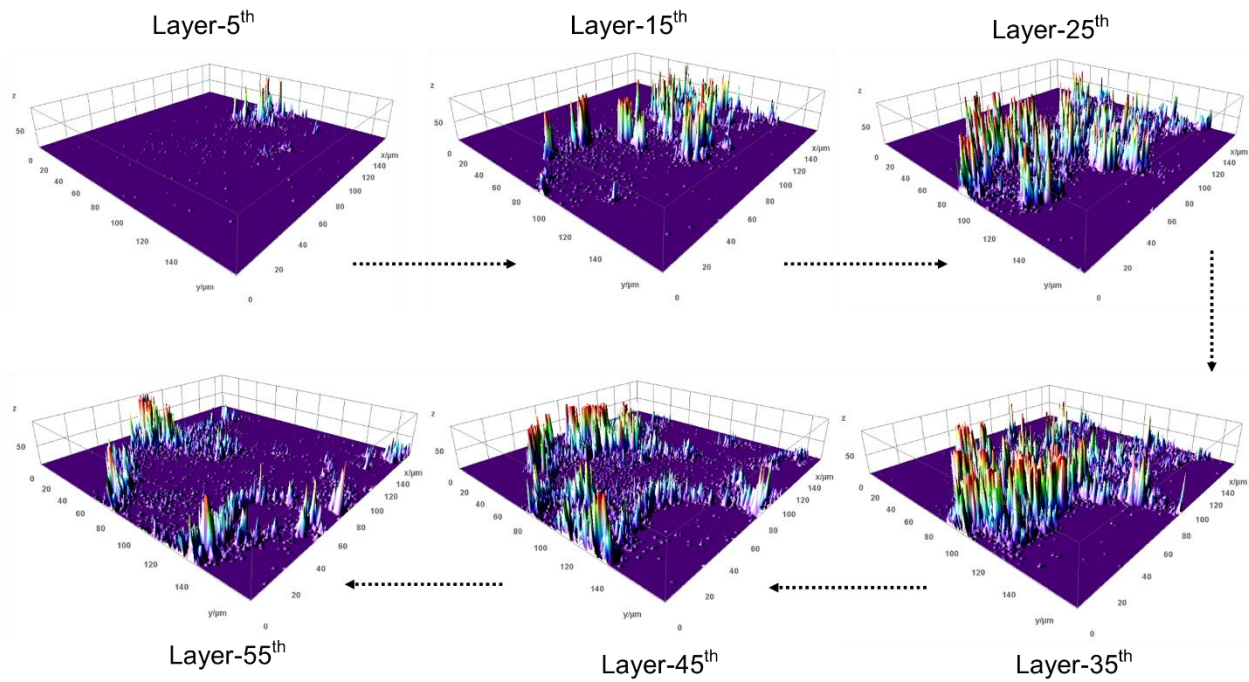
Appendix 5.88: TGA profile of IPcomp-7 before and after I₂ absorption test.



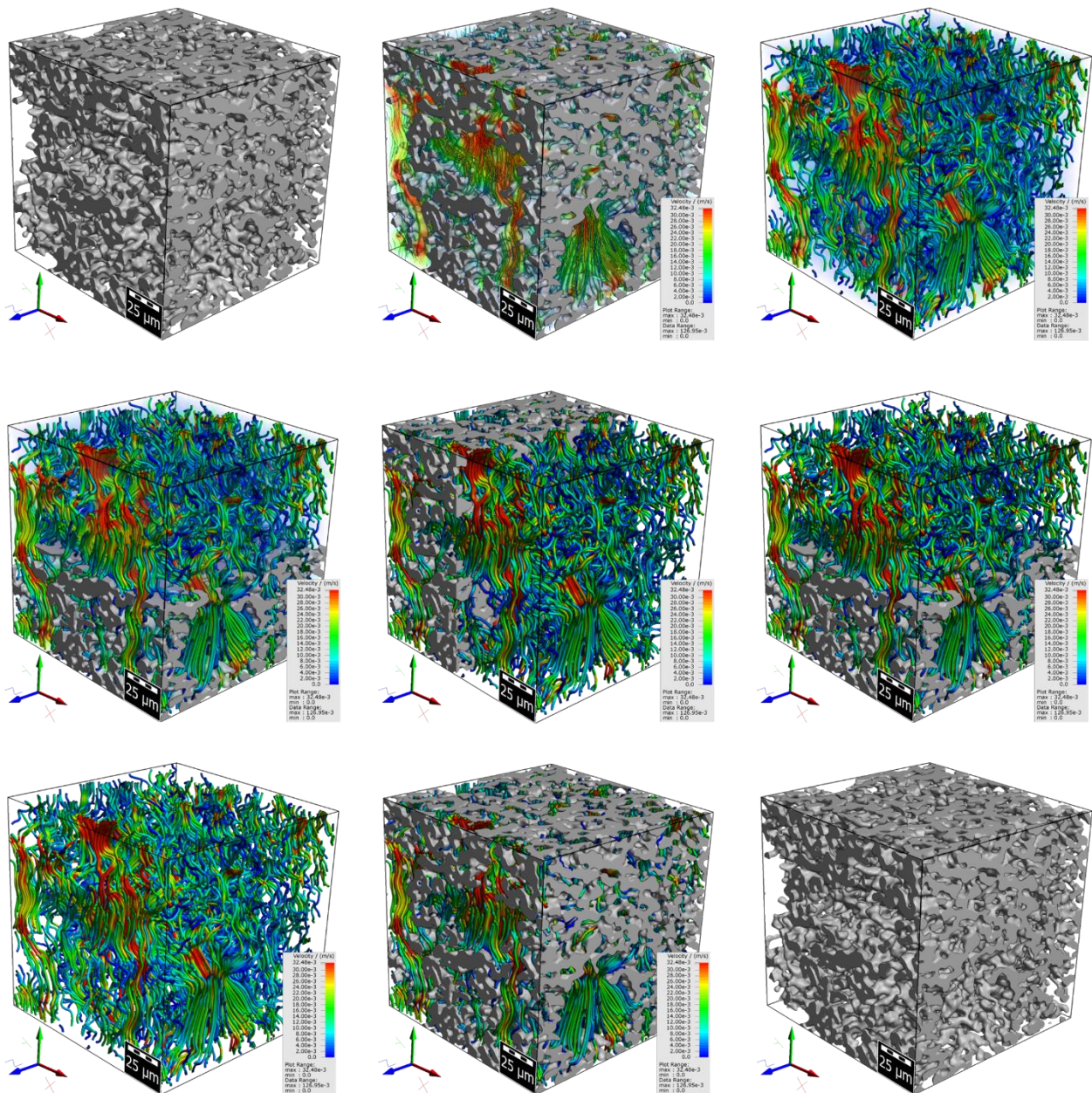
Appendix 5.89: Time-dependent ¹H NMR spectra of the stepwise treatment of I₂ to NH₂-Zr(IV)-MOP.



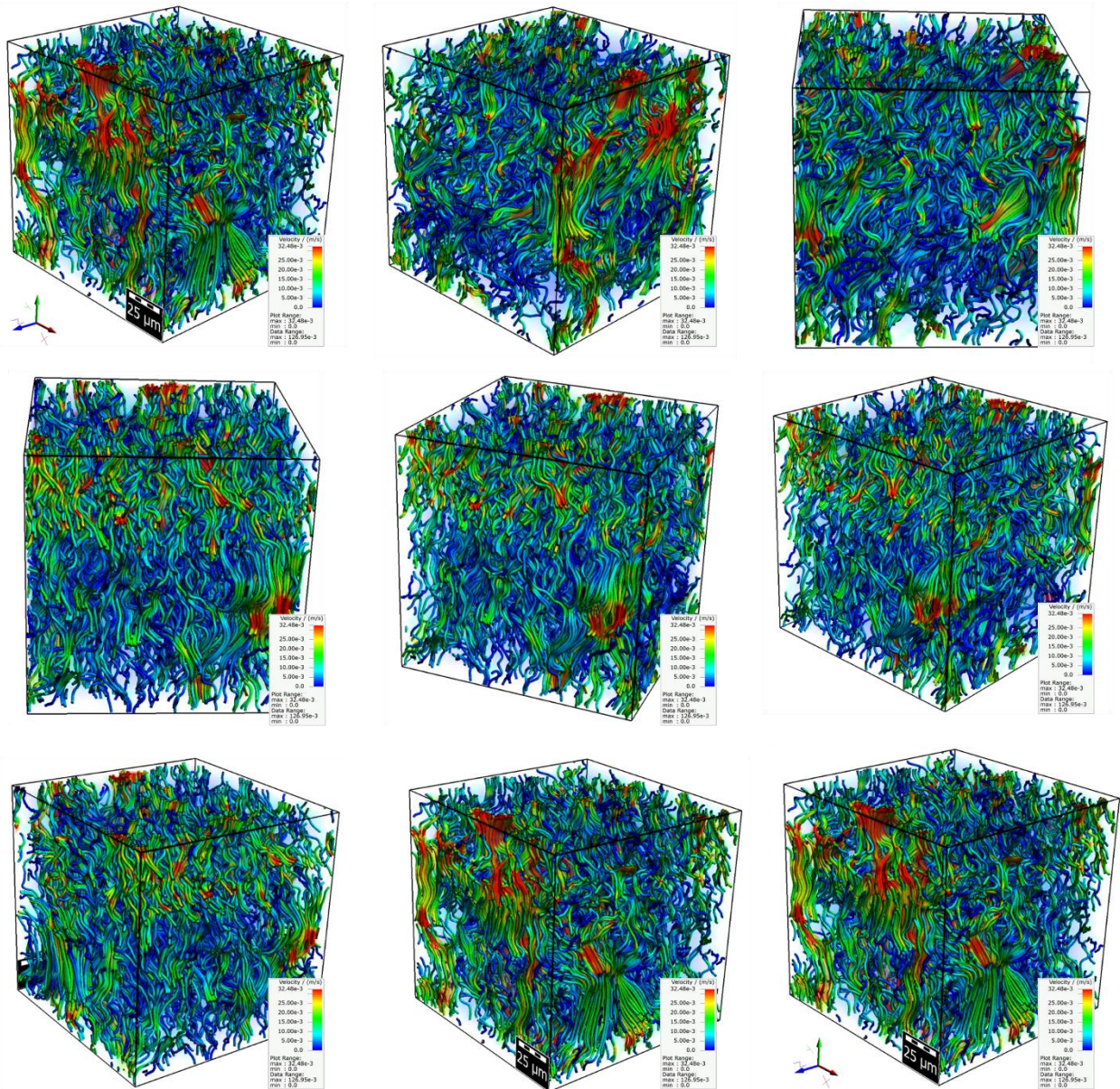
Appendix 5.90: Color-coded 3D confocal laser scanning microscopic images of IPcomp-7.



Appendix 5.91: 2.5 D confocal laser scanning microscopic processed images of different 2D layers of IPcomp-7 after treatment of dye.



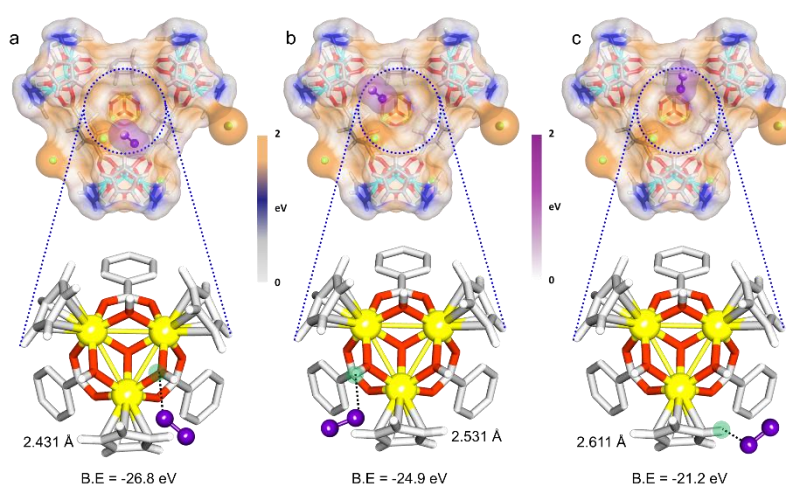
Appendix 5.92: The water flow velocity simulation analysis for IPcomp-7 by X-ray tomography. The average flow velocity has been calculated from the numerical simulation study.



Appendix 5.93: The average water flow velocity simulation analysis in all three x, y, z direction for IPcomp-7 by X-ray tomography. The average flow velocity has been calculated from the numerical simulation study.

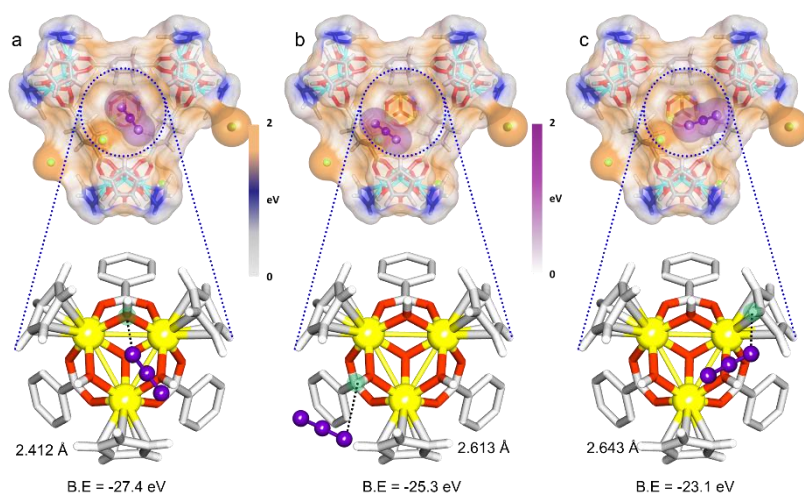
DFT simulation studies

IPcomp-7 exhibited highly efficient selective uptake of iodine or triiodide anion from both vapor and aqueous phase. The multifunctional nature of the hybrid aerogel material is caused for such potent capture efficiencies. Among them, the hierarchical (micro-macro) porous structure of the composite material helps for fast mass diffusion of iodine/iodides through its large open pores towards the main active sites (guest-amino functionalized Zr(IV)-SBU-based cationic MOPs) of the hybrid composite. Thereafter, the iodine/iodides species interact with the Zr-SBU, free -NH_2 group and with the free chlorine anions of the cationic MOP. Such interactions are majorly attributed to the dispersive interactions or supramolecular interactions, dipole interactions of the iodine/iodides species (I_2/I_3^-) with the functional groups of MOP molecules of the composite material. To validate this, we have calculated the respective binding energies of I_2/I_3^- with the MOP molecules and unit of COF structure of the hybrid compound. The molecular-level interactions between the amino functionalized cationic MOP, imine functionalized 2D COF and iodine/iodides species were simulated using Discovery Studio 2017 (Accelrys). The DFT simulation was performed at fine quality calculation level. At first, using DMOL3 and B3LYP hybrid function the single unit of the MOP and COF was fully geometry relaxed by keeping the Multiplicity factor to Auto mode, double numeric plus polarizing (DNP+) basis set. Using simulated annealing technique structural simulation on the geometry relaxed MOP/COF (unit) structure was realized to find a feasible interaction site of the I_2/I_3^- within the relaxed MOP/COF unit. The electrostatic potential (ESP) on the van der Waals (VDW) surfaces (isodensity = 0.001 a.u.) of MOP/COF unit was derived from ground state electron density of the system. The DFT calculation reveals that I_2/I_3^- interact with Zr-SBU, free amine (-NH_2) groups, free Cl^- ions of the MOP and imine or other functional groups of COF unit with following major possible binding sites, (Supplementary Figure-94-100). Furthermore, we also optimized the Zr-SBU of the MOP interacting with H_2O and NO_2 molecules.

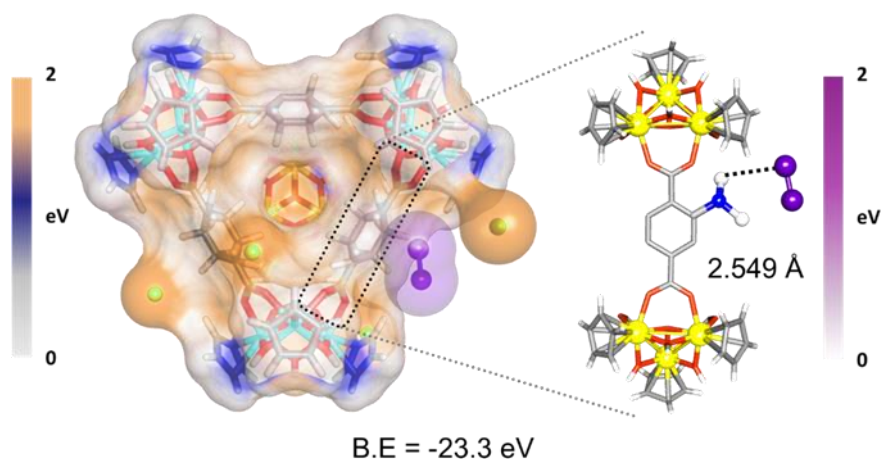


Appendix 5.94: Electrostatic Potential (ESP) diagram and corresponding DFT optimized structures with respective binding energies of different interaction between Zr-SBU of MOP in the hybrid composite with iodine molecule. (a) Interaction between iodine and oxygen of hydroxyl group of the Zr-SBU, (b)

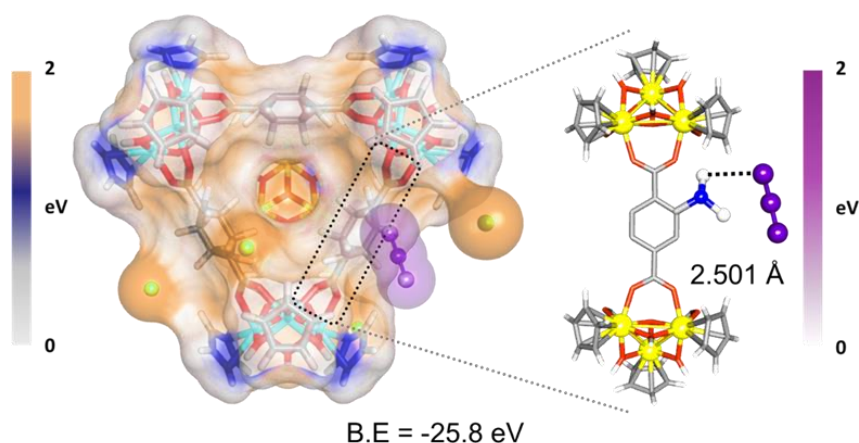
Interaction between iodine and hydrogen of hydroxyl group of the Zr-SBU, (c) Interaction between iodine and hydrogen of Cp-ring of the Zr-SBU, respectively.



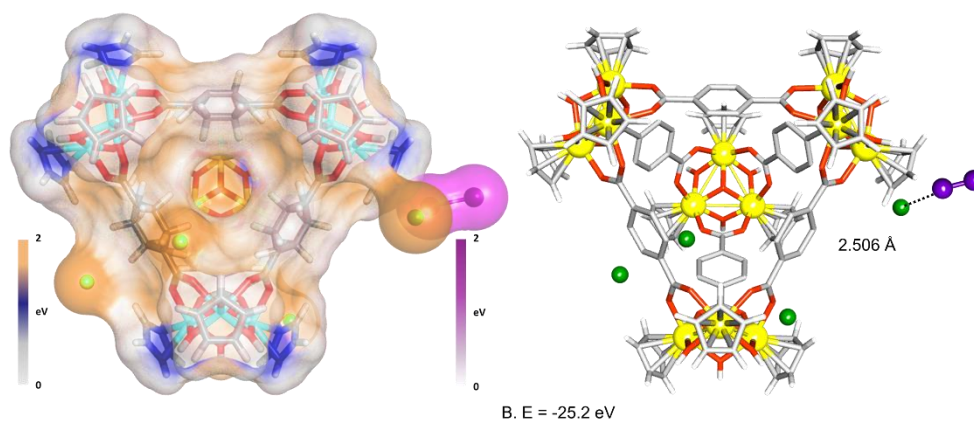
Appendix 5.95: Electrostatic Potential (ESP) diagram and corresponding DFT optimized structures with respective binding energies of different interaction between Zr-SBU of MOP in the hybrid composite with triiodide anions. (a) Interaction between triiodide and oxygen of hydroxyl group of the Zr-SBU, (b) Interaction between triiodide and hydrogen of hydroxyl group of the Zr-SBU, (c) Interaction between triiodide and hydrogen of Cp-ring of the Zr-SBU, respectively.



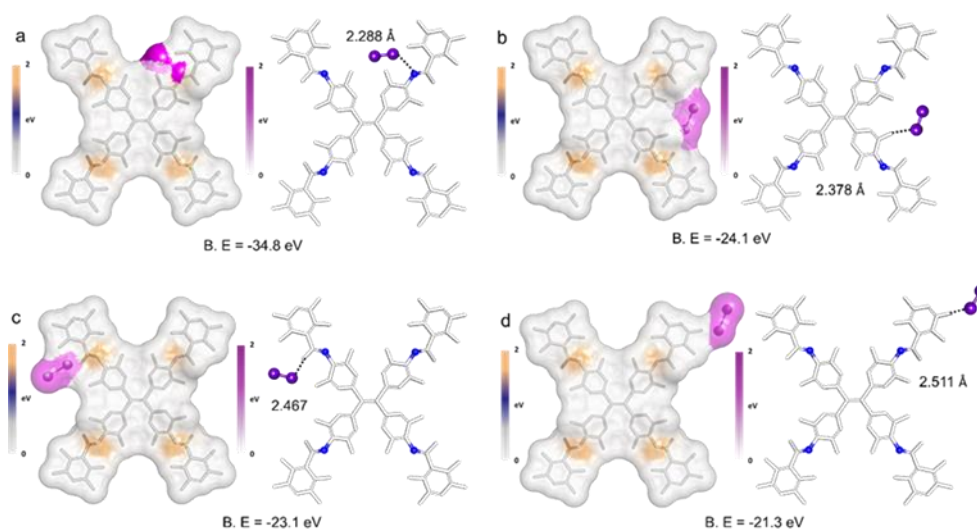
Appendix 5.96: Electrostatic Potential (ESP) diagram and corresponding DFT optimized structures with respective binding energies of interaction between -NH_2 groups of MOP in the hybrid composite with iodine molecule.



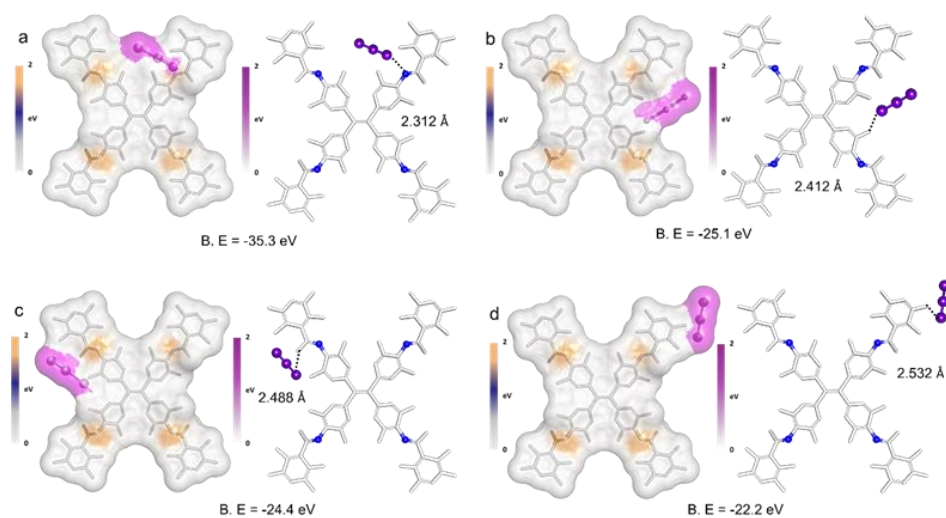
Appendix 5.97: Electrostatic Potential (ESP) diagram and corresponding DFT optimized structures with respective binding energies of interaction between $-\text{NH}_2$ groups of MOP in the hybrid composite with triiodide anions.



Appendix 5.98: Electrostatic Potential (ESP) diagram and corresponding DFT optimized structures with respective binding energies of interaction between free chlorine (Cl^-) anions of MOP in the hybrid composite with iodine molecule.



Appendix 5.99: Electrostatic Potential (ESP) diagram and corresponding DFT optimized structures with respective binding energies of different interaction between the TPE-core based COF units of the hybrid composite with iodine molecule. (a) Interaction between iodine and imine-N site of the COF, (b) Interaction between iodine and hydrogen of TPE-core of the COF, (c, d) Interaction between iodine and hydrogen of TPD-core of the COF, respectively.



Appendix 5.100: Electrostatic Potential (ESP) diagram and corresponding DFT optimized structures with respective binding energies of different interaction between the TPE-core based COF units of the hybrid composite with triiodide anions. (a) Interaction between triiodide and imine-N site of the COF, (b) Interaction between triiodide and hydrogen of TPE-core of the COF, (c, d) Interaction between triiodide and hydrogen of TPD-core of the COF, respectively.

5.7 References

- [1] J. D. Vienna, *Int. J. Appl. Glass Sci.* **2010**, *1*, 309–321.
- [2] R. C. Ewing, F. N. V. Hippel, *Science*, **2009**, *325*, 151–152.
- [3] A. Macfarlane, R. Ewing, *Science*, **2017**, *356*, 1313.
- [4] T. C. T. Pham, S. Docao, I. C. Hwang, M. K. Song, D. Y. Choi, D. Moon, P. Oleynikov, K. B. Yoon, *Energy Environ. Sci.* **2016**, *9*, 1050–1062.
- [5] Z. Zhang, X. Dong, J. Yin, Z.-G. Li, X. Li, D. Zhang, T. Pan, Q. Lei, X. Liu, Y. Xie, F. Shui, J. Li, M. Yi, J. Yuan, Z. You, L. Zhang, J. Chang, H. Zhang, W. Li, Q. Fang, B. Li, X.-H. Bu, Y. Han, *J. Am. Chem. Soc.* **2022**, *144*, 6821–6829.
- [6] D. R. Haefner, T. J. Tranter, Methods of gas phase capture of iodine from fuel reprocessing off-gas: a literature survey, INL/EXT-07-12299, Idaho National Laboratory, Idaho Falls, ID, **2007**.
- [7] Treatment, conditioning and disposal of iodine-129, Technical Reports Series No. 276, IAEA, Vienna, **1987**.
- [8] J. Wang, Z. Li, Y. Wang, C. Wei, K. Ai, L. Lu, *Mater. Horiz.* **2019**, *6*, 1517–1525.
- [9] P. H. Svensson, L. Kloo, *Chem. Rev.* **2003**, *103*, 1649 – 1684.
- [10] B. Li, X. Dong, H. Wang, D. Ma, K. Tan, S. Jensen, B. J. Deibert, J. Butler, J. Cure, Z. Shi, T. Thonhauser, Y. J. Chabal, Y. Han, J. Li, *Nat. Commun.* **2017**, *8*, 485.
- [11] W. Xie, D. Cui, S.-R. Zhang, Y.-H. Xu, D.-L. Jiang, *Mater. Horiz.* **2019**, *6*, 1571–1595.
- [12] A. Sen, S. Sharma, S. Dutta, M. M. Shirolkar, G. K. Dam, S. Let, S. K. Ghosh, *ACS Appl. Mater. Interfaces*, **2021**, *13*, 34188–34196.
- [13] M. P. little, R. Wakeford, A. Bouville, S. L. Simson, *Proc. Natl. Acad. Sci.* **2016**, *113*, 3720–3721.
- [14] L. Xie, Z. Zheng, Q. Lin, H. Zhou, X. Ji, J. L. Sessler, H. Wang, *Angew. Chem. Int. Ed.* **2022**, *61*, e202113724.
- [15] J. C. Sisson, J. Freitas, L. R. McDougall, L. T. Daur, J. R. Hurley, J. D. Brierley, C. H. Edinboro, D. Rosenthal, M. J. Thomas, J. A. Wexler, E. Asamoah, A. M. Avram, M. Milas, C. Greenlee, *Thyroid* **2011**, *21*, 335 – 346.
- [16] W. Wei, Z. T. Rosenkrans, J. Liu, G. Huang, Q.-Y. Luo, W. Cai, *Chem. Rev.* **2020**, *120*, 3787–3851.
- [17] X. Guo, Y. Li, M. Zhang, K. Cao, Y. tian, Y. Qi, S. Li, K. Li, X. Yu, L. Ma, *Angew. Chem. Int. Ed.* **2020**, *59*, 2 – 11.
- [18] X. Zhang, J. Maddock, T. M. Nenoff, M. A. Denecke, S. Yang, M. Schroder, *Chem. Soc. Rev.* **2022**, *51*, 3243–3262.

- [19] P. Chen, X. he, M. Pang, X. Dong, S. Zhao, W. Zhang, *ACS Appl. Mater. Interfaces*, **2020**, *12*, 20429–20439.
- [20] Z. Yin, Q.-X. Wang, M.-H. Zeng, *J. Am. Chem. Soc.* **2012**, *134*, 4857–4863.
- [21] Y. Lin, X. Jiang, S. T. Kim, S. B. Alahakoon, X. Hou, Z. Zhang, C. M. Thompson, R. A. Smaldone, C. Ke, *J. Am. Chem. Soc.* **2017**, *139*, 7172–7175.
- [22] X. jiang, X. Cui, A. J. E. Duncan, L. Li, R. P. Hughes, R. J. Staples, E. V. Alexandrov, D. M. Proserpio, Y. Wu, C. Ke, *J. Am. Chem. Soc.* **2019**, *141*, 10915–10923.
- [23] C. liu, Y. Jin, Z. Yu, L. Gong, H. Wang, B. Yu, W. Zhang, J. Jiang, *J. Am. Chem. Soc.* **2022**, *144*, 27, 12390–12399.
- [24] D. Luo, Y. He, J. Tian, J. L. Sessler, X. Chi, *J. Am. Chem. Soc.* **2022**, *144*, 1, 113–117.
- [25] Z. Yan, Y. Yuan, Y. Tian, D. Zhang, G. Zhu, *Angew. Chem. Int. Ed.* **2015**, *54*, 12733–12737.
- [26] Y. Xie, T. Pan, Q. Lei, C. Chen, X. Dong, Y. Yuan, J. Shen, Y. Cai, C. Zhou, I. Pinnau, Y. Han, *Angew. Chem. Int. Ed.* **2021**, *60*, 22432–22440.
- [27] Y. Xie, T. Pan, Q. Lei, C. Chen, X. Dong, Y. Yuan, W. A. Maksoud, L. Zhao, L. Cavallo, I. Pinnau, Y. Han, *Nat. Comm.* **2022**, *13*, 2878.
- [28] P. Wang, Q. Xu, Z. Li, W. Jiang, Q. Jiang, D. Jiang, *Adv. Mater.* **2018**, *30*, 1801991.
- [29] L. He, L. Chen, X. Dong, S. Zhang, M. Zhang, X. Dai, X. Liu, P. Lin, K. Li, C. Chen, T. Pan, F. Ma, J. Chen, M. Yuan, Y. Zhang, L. Chen, R. Zhou, Y. Han, Z. Chai, S. Wang, *Chem* **2021**, *7*, 699–714.
- [30] B. Valizadeh, T. N. Nguyen, B. Smit, K. C. Stylianou, *Adv. Funct. Mater.* **2018**, *28*, 1801596.
- [31] X.-H. Xu, Y.-X. Li, L. Zhou, N. Liu, Z.-Q. Wu, *Chem. Sci*, **2022**, *13*, 1111–1118.
- [32] X. Guo, Y. Li, M. Zhang, K. Cao, Y. Tian, Y. Qi, S. Li, K. Li, X. Yu, L. Ma, *Angew. Chem. Int. Ed.* **2020**, *59*, 22697–22705.
- [33] D. Zhu, Y. Zhu, Q. Yan, M. Barnes, F. Liu, P. Yu, C.-P. Tseng, N. Tjahjono, P.-C. Huang, M. M. Rahman, E. Egap, P. M. Ajayan, R. Verduzco, *Chem. Mater.* **2021**, *33*, 4216–4224.
- [34] X. Li, Z. Jia, J. Zhang, Y. Zou, B. Jiang, Y. Zhang, K. Shu, N. Liu, Y. Li, L. Ma, *Chem. Mater.* **2022**, *34*, 24, 11062–11071.
- [35] B. Moulton, M. J. Zawortko, *Chem. Rev.* **2001**, *101*, 1629–1658.
- [36] G. cai, P. Yan, L. Zhang, H.-C. Zhou, H.-L. Jiang, *Chem. Rev.* **2021**, *121*, 12278–12326.
- [37] G. Distefano, H. Suzuki, M. Tsujimoto, S. Isoda, S. Bracco, A. Comotti, P. Sozzani, T. Uemura, S. Kitagawa, *Nat. Chem.* **2013**, *5*, 335–341.
- [38] T. Kitao, Y. Zhang, S. Kitagawa, B. Wang, T. Uemura, *Chem. Soc. Rev.* **2017**, *46*, 3108–3133.
- [39] A. J. Gosselin, C. A. Rowland, E. D. Bloch, *Chem. Rev.* **2020**, *120*, 8987–9014.

- [40] F. Rizzuto, L. S. Krbeek, J. Nitschke, *Nat. Rev. Chem.* **2019**, *3*, 204–222.
- [41] C. S. Diercks, O. M. Yaghi, *Science* **2017**, *355*, eaal1585.
- [42] M. S. Lohse, T. Bein, *Adv. Funct. Mater.* **2018**, *28*, 1705553.
- [43] S. Mollick, S. Fajal, S. Mukherjee, S. K. Ghosh, *Chem. Asian J.* **2019**, *14*, 3096–3108.
- [44] X. Qiu, W. Zhong, C. Bai, Y. Li, *J. Am. Chem. Soc.* **2016**, *138*, 4, 1138–1141.
- [45] Y.-H. kang, X.-D. Liu, N. Yan, Y. Jiang, X.-Q. Liu, L.-B. Sun, J.-R. Li, *J. Am. Chem. Soc.* **2016**, *138*, 19, 6099–6102.
- [46] J. Liu, W. Duan, J. Song, X. Guo, Z. Wang, X. Shi, J. Liang, J. Wang, P. Cheng, Y. Chen, M. J. Zaworotko, Z. Zhang, *J. Am. Chem. Soc.* **2019**, *141*, 30, 12064–12070.
- [47] G. Liu, Y. D. Yuan, J. Wang, Y. Cheng, S. B. Peh, Y. Wang, Y. Qian, J. Dong, D. Yuan, D. Zhao, *J. Am. Chem. Soc.* **2018**, *140*, 6231–6234.
- [48] L. Chen, K. Furukawa, J. Gao, A. Nagai, T. Nakamura, Y. Dong, D. Jiang, *J. Am. Chem. Soc.* **2014**, *136*, 28, 9806–9809.
- [49] N. Huang, L. Zhai, D. E. Coupry, M. A. Addicoat, K. Okushita, K. Nishimura, T. Heine, D. Jiang, *Nat. Chem.*, **2016**, *8*, 310–316.
- [50] D. Nam, J. Huh, J. Lee, J. H. Kwak, H. Y. Jeong, K. Choi, W. Choe, *Chem. Sci.* **2017**, *8*, 7765–7771.
- [51] S. Mollick, S. Fajal, S. Saurabh, D. Mahato, S. K. Ghosh, *ACS Cent. Sci.* **2020**, *6*, 9, 1534–1541.
- [52] Y. Peng, M. Zhao, B. Chen, Z. Zhang, Y. Huang, F. Dai, Z. Lai, X. Cui, C. Tan, H. Zhang, *Adv. Mater.* **2018**, *30*, 1705454.
- [53] R.-R. Liang, S.-Y. Jiang, R.-H. A, X. Zhao, *Chem. Soc. Rev.* **2020**, *49*, 3920–3951.
- [54] S. Fajal, A. Hassan, W. Mandal, M. M. Shirolkar, S. Let, N. Das, S. K. Ghosh, *Angew. Chem. Int. Ed.* **2023**, *62*, e202214095.
- [55] S. Fajal, W. Mandal, S. Mollick, Y. D. More, A. Torris, S. Saurabh, M. M. Shirolkar, S. K. Ghosh, *Angew. Chem. Int. Ed.* **2022**, *61*, e202203385.
- [56] M. Zhang, J. Samanta, B. A. Atterberry, R. Staples, A. J. Rossini, C. Ke, *Angew. Chem. Int. Ed.* **2022**, *61*, e202214189.
- [57] J. Chang, H. Li, J. Zhao, X. Guan, C. Li, G. Yu, V. Valtchev, Y. Yan, S. Qiu, Q. Fang, *Chem. Sci.* **2021**, *12*, 8452–8457.
- [58] S. L. Hsu, A. J. Signorelli, G. P. Pez, R. H. Baughman, *Chem. Phys.* **1978**, *69*, 106.

Chapter 6

Summary, Critical Comments and Perspectives

6.1 Summary, Critical Comments and Perspectives

Advanced functional porous materials (AFPMs) and their hybrid composites have earned great deal of research attention in the recent past owing to their potential applicability in wide range of applications. The studies documented in the current thesis work include in-depth research into rational design and development of various advanced functional porous organic materials and their composites with inorganic-organic hybrid materials for energy efficient chemical separation application, particularly those fostering environmental sustainability. In the first section of the thesis, strategic synthesis of task-specific porous organic materials (POMs) have been done in order to demonstrate efficient sequestration of radioactive waste species such as organic iodides as well as inorganic/organic persistent pollutants from contaminated water. Briefly, the role of framework integrated functionalities along with textural properties of POMs towards toxic gas (i.e. methyl iodide) capture has been investigated by rationally fabricating a series of covalent organic frameworks (COFs). Moreover, the role of higher order porosity such as inducing ordered interconnected macroporosity into charged organic framework material towards enhanced pollutants separation performance has been studied. Conversely, recently, hybrid composite porous materials catches topical research interest over individual porous materials due to their ingenious characteristics, collective benefits and effective performance. Motivated by this, in the second section of the thesis work focuses on the fabrication of porous hybrid composite materials based adsorbents to sequester hazardous water contaminants and toxic gaseous iodine or polyiodide species. A MOPs embedded MOG-based hybrid nanocomposite has been developed to act as active nanotrap towards a class of heavy metal-based toxic oxoanionic chemicals in wastewater. Following this, another ultralight aerogel based multifunctional hybrid composite has been constructed by unique covalent hybridization strategy between an amino functional MOP with a 2D imine COF. Thus developed hybrid was utilized in efficient sequestration of molecular iodine as well as polyiodide species from gaseous phase and aqueous medium with large sorption capacity, high retention efficiency, superior selectivity and recyclability. All the works are highlighted in their potency toward practical implementation in terms of efficiency, scope, processability as well as ‘proof of concept’ based real-time applicability towards chemical separation application.

Despite the exceptional accomplishments that have been made in this thesis works in the field of AFPMs and their hybrid composites development for potential utility in energy efficient chemical separation application, there are still many challenges that need to be addressed. These critical comments associated with each of these works are described below. (I) In case of COFs based organic iodide capture work, although, along with the exploration of insightful molecular level adsorption chemistry, the adsorbents demonstrated high sorption capacity towards methyl iodide in both static and dynamic condition, the chemical, thermal and radiation stability of the COFs under extreme practical radioactive conditions is a challenge that remains to be clarified. The stability or retention of framework

configuration in high radiation and strong acidic environment (actual radioactive waste condition) is a serious matter of concern for practical implementation. Also, due to the robust adsorption mechanism of CH_3I with COFs, the higher order recyclability of these adsorbents is difficult. (II) In case of hierarchically porous cationic viologen organic network based chemical separation work, the homogeneous distribution of interconnected ordered macropores along with active ionic sites throughout the complete area of the material is still a significant challenge. Apart from this, the scalability and the high chemical stability of the material towards large-scale practical chemical separation application is a major problem. In the investigation of multifunctional hybrid composites, a major challenge remains the distribution of active sites with acceptable porosity while maintaining numerous specific components. (III) Although, the hybrid composite synthesized with MOP and MOG exhibited efficient segregation of toxic metal oxoanions, their molecular level reproducible synthesis and fabrication into light weight aerogel is quite challenging. In this line, specific positioning of individual active nanotrap (MOPs) into the pores of MOG is not always 'easy to syntheses'. The use of super critical drying technique during synthesis of this material is not feasible in terms of operational cost, time and labour. Moreover, the chemical and thermal stability of this particular material is quite less with respect to the practical toxic chemicals segregation application. (IV) In the last work, where surrogate radioactive iodine species was sequestered by developing another MOP@COF hybrid aerogel material, the composite invariably experience compromised surface areas as a result of pore blockage due to the placement of MOPs inside the COF. Again, there are still unresolved issues regarding the material's chemical, thermal, and radiation stability in extremely realistic radioactive environments. The retention of similar efficiency, processability as well as stability in real-time application towards radioactive iodine waste sequestration is great challenge for this material. Aside from each of these particular problems, the enthalpy of adsorption—a crucial thermodynamic parameter that needs further study—is closely linked to other parameters associated with the adsorption of chemical species, including diffusion kinetics, sorption capacity, molecular sieving, etc. Above all, there is a need to relentlessly seek the industrial use of these high-performance materials that have been evaluated in laboratories in this thesis works. Moreover, comparatively expensive raw ingredients like as solvents, catalysts, and monomers, together with challenging reaction methods and processability of these works, obstruct large-scale manufacturing and efficient material processing for immediate industrial use.

The most significant learning from the present thesis work is the strategic design and synthesis of materials that combine the benefits of structural robustness, function-led design, and improved performance. Understanding the intricate roles played by the hierarchical porosities and molecular level functionalities of porous materials in separation is crucial for designing and developing new adsorbents that will be useful in various applications. It also provides guidance for adsorption mechanisms.

Additionally, composite preparation techniques, including shaping of AFPMs such as aerogels, solve a significant flaw in powder materials' processability. The significance of prudent structural alterations is further underscored by the creation of diverse porous organic materials that may be effectively utilized in different applications. Moreover, the advancement of developing hybrid composites out of the individual porous materials towards improved sorption performance has been demonstrated. The main goal of all the scientific research done for this thesis has been to create task-specific functionality for applications that are target-specific. Giving AFPMs iconicity and ordered macroporosity can be beneficial, but they are currently understudied and need further investigation. Much more in-depth understanding into the complex chemical structure of hybrid composites and their improved performance should be investigated in detail, which can be done by through characterizations and analysis of the materials. Long-term performance retention under operating conditions and cost-effective scaling are other critical issues that require a lot of focus. An abundance of expertise and information in this field is provided by the commercial successes of several well-known porous materials, such as polymeric separation membranes and ion exchange and adsorption resins. Therefore, there is a lot of potential for academics to expand on and help create task-specific AFPMs in the next years to address significant industrial and environmental challenges.



From the journal:
Journal of Materials Chemistry A

Unraveling mechanistic insights into covalent organic frameworks for highly efficient sequestration of organic iodides from simulated nuclear waste †



Sahel Fajal, ^a Dipanjan Majumder, ^a Writakshi Mandal, ^a Sumanta Let, ^a Gourab K. Dam, ^a Mandar M. Shirolkar ^{bc} and Sujit K. Ghosh ^{*ad}

Author affiliations

Abstract

Over the last few decades, given the impending global energy and environmental crises, paramount development in nuclear energy as an alternative high power density and low-carbon energy source has been widely observed. However, this development is hindered due to certain problems associated with nuclear reactors, including the emission of volatile radioactive substances, like organic iodides and iodine, which must be eliminated before

About

Cited by

Related

Unraveling mechanistic insights into covalent organic frameworks for highly efficient sequestration of organic iodides from simulated nuclear waste

S. Fajal, D. Majumder, W. Mandal, S. Let, G. K. Dam, M. M. Shirolkar and S. K. Ghosh, *J. Mater. Chem. A*, 2023, Advance Article, DOI: 10.1039/D3TA04995G

To request permission to reproduce material from this article, please go to the [Copyright Clearance Center request page](#).

If you are **an author contributing to an RSC publication, you do not need to request permission** provided correct acknowledgement is given.

If you are **the author of this article, you do not need to request permission to reproduce figures and diagrams** provided correct acknowledgement is given. If you want to reproduce the whole article in a third-party publication (excluding your thesis/dissertation for which permission is not required) please go to the [Copyright Clearance Center request page](#).

Read more about [how to correctly acknowledge RSC content](#).

JOHN WILEY AND SONS LICENSE TERMS AND CONDITIONS

Dec 04, 2023

This Agreement between IISER Pune -- SAHEL FAJAL ("You") and John Wiley and Sons ("John Wiley and Sons") consists of your license details and the terms and conditions provided by John Wiley and Sons and Copyright Clearance Center.

License Number 5681980436216

License date Dec 04, 2023

Licensed Content
Publisher John Wiley and Sons

Licensed Content
Publication Angewandte Chemie International Edition

Licensed Content Title Ordered Macro/Microporous Ionic Organic Framework for
Efficient Separation of Toxic Pollutants from Water

Licensed Content
Author Sahel Fajal, Atikur Hassan, Writakshi Mandal, et al

Licensed Content
Date Dec 7, 2022

Licensed Content
Volume 62

Licensed Content
Issue 1

Licensed Content
Pages 10

Type of use	Dissertation/Thesis
Requestor type	Author of this Wiley article
Format	Print and electronic
Portion	Full article
Will you be translating?	No
Title of new work	Advanced Functional Porous Materials and their Hybrid Composites for Energy-Efficient Chemical Separation Application
Institution name	IISER Pune
Expected presentation date	Jan 2025
	IISER Pune IISER Pune, Pashan
Requestor Location	Pune, Maharashtra 411008 India Attn: IISER Pune
Publisher Tax ID	EU826007151
Total	0.00 USD
Terms and Conditions	

TERMS AND CONDITIONS

This copyrighted material is owned by or exclusively licensed to John Wiley & Sons, Inc. or one of its group companies (each a "Wiley Company") or handled on behalf of a society with which a Wiley Company has exclusive publishing rights in relation to a particular work (collectively "WILEY"). By clicking "accept" in connection with completing this licensing transaction, you agree that the following terms and conditions apply to this transaction (along with the billing and payment terms and conditions established by the

JOHN WILEY AND SONS LICENSE TERMS AND CONDITIONS

Dec 04, 2023

This Agreement between IISER Pune -- SAHEL FAJAL ("You") and John Wiley and Sons ("John Wiley and Sons") consists of your license details and the terms and conditions provided by John Wiley and Sons and Copyright Clearance Center.

License Number 5681980269244

License date Dec 04, 2023

Licensed Content
Publisher John Wiley and Sons

Licensed Content
Publication Angewandte Chemie International Edition

Licensed Content Title Trap Inlaid Cationic Hybrid Composite Material for Efficient Segregation of Toxic Chemicals from Water

Licensed Content
Author Sujit K. Ghosh, Mandar M. Shirolkar, Satyam Saurabh, et al

Licensed Content Date May 19, 2022

Licensed Content
Volume 61

Licensed Content
Issue 32

Licensed Content
Pages 10

Type of use	Dissertation/Thesis
Requestor type	Author of this Wiley article
Format	Print and electronic
Portion	Full article
Will you be translating?	No
Title of new work	Advanced Functional Porous Materials and their Hybrid Composites for Energy-Efficient Chemical Separation Application
Institution name	IISER Pune
Expected presentation date	Jan 2025
	IISER Pune IISER Pune, Pashan
Requestor Location	Pune, Maharashtra 411008 India Attn: IISER Pune
Publisher Tax ID	EU826007151
Total	0.00 USD

Terms and Conditions

TERMS AND CONDITIONS

This copyrighted material is owned by or exclusively licensed to John Wiley & Sons, Inc. or one of its group companies (each a "Wiley Company") or handled on behalf of a society with which a Wiley Company has exclusive publishing rights in relation to a particular work (collectively "WILEY"). By clicking "accept" in connection with completing this licensing transaction, you agree that the following terms and conditions apply to this transaction (along with the billing and payment terms and conditions established by the



RightsLink

Ultralight crystalline hybrid composite material for highly efficient sequestration of radioiodine



Author: Sahel Fajal et al
Publication: Nature Communications
Publisher: Springer Nature
Date: Feb 10, 2024

Copyright © 2024, The Author(s)

Creative Commons

This is an open access article distributed under the terms of the [Creative Commons CC BY](#) license, which permits unrestricted use, distribution, and reproduction in any medium, provided the original work is properly cited.

You are not required to obtain permission to reuse this article.

To request permission for a type of use not listed, please contact [Springer Nature](#)

© 2024 Copyright - All Rights Reserved | [Copyright Clearance Center, Inc.](#) | [Privacy statement](#) | [Data Security and Privacy](#)
| [For California Residents](#) | [Terms and Conditions](#) Comments? We would like to hear from you. E-mail us at customercare@copyright.com



Cite this: DOI: 10.1039/d3ta04995g

Unraveling mechanistic insights into covalent organic frameworks for highly efficient sequestration of organic iodides from simulated nuclear waste†

Sahel Fajal, ^a Dipanjan Majumder, ^a Writakshi Mandal, ^a Sumanta Let, ^a Gourab K. Dam, ^a Mandar M. Shirolkar ^{bc} and Sujit K. Ghosh ^{*ad}

Over the last few decades, given the impending global energy and environmental crises, paramount development in nuclear energy as an alternative high power density and low-carbon energy source has been widely observed. However, this development is hindered due to certain problems associated with nuclear reactors, including the emission of volatile radioactive substances, like organic iodides and iodine, which must be eliminated before releasing the off-gas. These substances include methyl iodide (CH_3I), ethyl iodide ($\text{CH}_3\text{CH}_2\text{I}$), and iodine, which are exceedingly harmful to both the environment and human health. Although several porous solid adsorbents have been successfully employed to sequester organic iodides (generally CH_3I) from the vapor phase, the majority of the earlier investigations have largely focused on the saturation capacity and kinetic study of CH_3I capture. However, the importance of the porous adsorbents' strategic functions in the unique binding interaction with organic iodides has been grossly underappreciated and poorly understood. Also, certain crucial difficulties pertaining to the practical capturing of radioactive organic iodides from nuclear waste were thwarted in the endeavors to construct innovative adsorbents. Herein, we have demonstrated a systematic strategy-driven study to understand the roles of framework-integrated functionalities towards organic iodide sequestration by varying the number of N-heteroatomic sites in a series of chemically stable porous covalent organic frameworks (COFs). The CH_3I adsorption capacity was found to be positively correlated with the porosity or surface area as well as with the N-heteroatomic or heterocyclic functionalities, such as the imine, pyridine, and triazine sites of these COFs. Under both static and dynamic conditions, all the COFs exhibited high CH_3I sorption capacities through the N-methylation reaction mechanism. This work is of fundamental importance to understanding the CH_3I adsorption mechanisms and also offers direction for the design and development of novel adsorbents for relevant applications.

Received 20th August 2023
Accepted 16th October 2023

DOI: 10.1039/d3ta04995g

rsc.li/materials-a

1. Introduction

The usage of nuclear power for global energy systems has attracted significant interest and is predicted to increase in the near future due to the urgently growing needs for high-efficiency and economical, potential, and sustainable energy.^{1,2} In nuclear plants, during the generation of nuclear energy, the used nuclear fuel rods need to be reprocessed by dissolving in concentrated

hot nitric acid. In this dissolution protocol, apart from the molecular iodine, nitric acid vapor, NO_2 , and N_2O_5 , another highly radioactive dissolved off-gas (DOG) species, organic iodides, *e.g.*, methyl iodide (CH_3I) and ethyl iodide ($\text{CH}_3\text{CH}_2\text{I}$), are generated.^{3–5} Radioactive organic iodide (ROI) vapor is extremely harmful to living beings due to its substantially higher activity and has therefore attracted a significant amount of public attention, especially in the event of a nuclear disaster.^{5–7} Therefore, considering both the environmental as well as human health concerns along with future development and the safe generation of nuclear energy, efficient sequestration of these radioactive species from the air has attracted much research interest in recent years. However, it was found that trapping these ROI species is considerably difficult owing to their lower adsorption rate towards specific adsorbents (Ag@MOR)^{5–7} and poor retention efficiency. Past studies have established the use of solid sorbent-based fixed-bed technologies for radionuclide

^aDepartment of Chemistry, Indian Institute of Science Education and Research (IISER) Pune, Dr Homi Bhabha Road, Pashan, Pune 411 008, India

^bAdvanced Bio-Agro Tech Pvt. Ltd, Baner, Pune 411045, India

^cNorel Nutrient Bio-Agro Tech Pvt. Ltd, Baner, Pune 411045, India

^dCentre for Water Research (CWR), Indian Institute of Science Education and Research (IISER) Pune, Dr Homi Bhabha Road, Pashan, Pune 411 008, India.

E-mail: sghosh@iiserpune.ac.in

† Electronic supplementary information (ESI) available. See DOI: <https://doi.org/10.1039/d3ta04995g>


 Water Purification
How to cite: *Angew. Chem. Int. Ed.* **2023**, *62*, e202214095

International Edition: doi.org/10.1002/anie.202214095

German Edition: doi.org/10.1002/ange.202214095



Ordered Macro/Microporous Ionic Organic Framework for Efficient Separation of Toxic Pollutants from Water

Sahel Fajal, Atikur Hassan⁺, Writakshi Mandal⁺, Mandar M. Shirolkar, Sumanta Let, Neeladri Das, and Sujit K. Ghosh*

Dedicated to Professor Susumu Kitagawa on the occasion of 10th publication from our group in this journal.

Abstract: In case of pollutant segregation, fast mass diffusion is a fundamental criterion in order to achieve improved performance. The rapid mass transport through porous materials can be achieved by availing large open pores followed by easy and complete accessibility of functional sites. Inducing macroporosity into such materials could serve as ideal solution providing access to large macropores that offer unhindered transport of analyte and full exposure to interactive sites. Moreover, the challenge to configure the ionic-functionality with macroporosity could emerge as an unparalleled avenue toward pollutants separation. Herein, we strategized a synthetic protocol for construction of a positively charged hierarchically-porous ordered interconnected macro-structure of organic framework where the size and number of macropores can easily be tuned. The ordered macropores with strong electrostatic interaction synergistically exhibited ultra-fast removal efficiency towards various toxic pollutants.

toxic anions as a potential water pollutants.^[1] Organic species such as dyes and antibiotics are considered as potentially toxic even at very low concentration.^[2] Environmental self-purification process is unable to degrade these complicated, highly-toxic, water soluble organic pollutants which further causes diverse health issues to the living organism.^[3] In addition, inorganic pollutants such as metal-based oxoanions and iodine present in wastewater are generated owing to rapid industrial development. These are also being tagged as carcinogenic and radioactive pollutants posing threat to the entire ecosystem.^[4,5] Therefore, segregation of such hazardous water contaminants by innovative materials has received significant research attention in both scientific and industrial communities. Although, a variety of techniques have either been tested or are under consideration for water-purification, ion-exchange-based adsorption has been recently considered as favored choice, owing to its high efficiency, selectivity, low cost and simplicity.^[6]

The past few years has witnessed revolutionary development followed by ion-exchange-based separation by porous materials as potential alternatives to energy-intensive sequestration process.^[7,8] The removal mechanism in such materials are primarily governed by analyte diffusion followed by accessibility of the ion-exchangeable-sites within the pores.^[9,10] In this regard, ionic porous organic-frameworks, such as viologen-based frameworks have gained immense interest and are considered more expedient over neutral frameworks, owing to its fascinating intrinsically charged potential porous nature.^[11,12] Constructed from rigid covalent bonds, these are furnished with stronger electrostatic interactions that are suitable for host-guest recognition generated from the charged backbone of viologen-unit. Such ionic materials have shown promising application toward elimination of toxic anions from water.^[13-15] Although, until now, several synthetic strategies have reported been to construct ionic organic-network for specific sequestration of pollutants, these systematically developed strategies have been restricted to uniform pores.^[11,16] Therefore, the pollutant separation performance, especially in terms of removal kinetics has been typically limited to a great extent due to inadequate mass-transfer through the small pores and less accessibility of active sites on account of pore blocking by the presence of free exchangeable counter anions in the cationic porous skeleton.^[17] Consequently, ionic porous-organic-polymers have frequently demonstrated sluggish

Introduction

Since the incarnation of the industrial revolution together with agriculture, human activities have generated various

[*] S. Fajal, W. Mandal,⁺ S. Let, S. K. Ghosh
 Department of Chemistry,
 Indian Institute of Science Education and Research Pune
 Dr. Homi-Bhabha-Road, Pashan, Pune 411008 (India)
 E-mail: sghosh@iiserpune.ac.in
 Homepage: <https://skg-lab.acads.iiserpune.ac.in/home>

A. Hassan,⁺ N. Das
 Department of Chemistry,
 Indian Institute of Technology Patna
 Patna 801106, Bihar (India)

M. M. Shirolkar
 Symbiosis Center for Nanoscience and Nanotechnology (SCNN),
 Symbiosis International (Deemed University)
 Lavale, Pune 412115 (India)

S. K. Ghosh
 Centre for Water Research (CWR),
 Indian Institute of Science Education and Research Pune
 Dr. Homi-Bhabha-Road, Pashan, Pune 411008 (India)

[[†]] These authors contributed equally to this work.


Mesoporous Materials Hot Paper
How to cite: *Angew. Chem. Int. Ed.* **2022**, *61*, e202203385

International Edition: doi.org/10.1002/anie.202203385

German Edition: doi.org/10.1002/ange.202203385

Trap Inlaid Cationic Hybrid Composite Material for Efficient Segregation of Toxic Chemicals from Water

Sahel Fajal, Writakshi Mandal, Samraj Mollick, Yogeshwer D. More, Arun Torris, Satyam Saurabh, Mandar M. Shirolkar, and Sujit K. Ghosh*

Abstract: Metal-based oxoanions are potentially toxic pollutants that can cause serious water pollution. Therefore, the segregation of such species has recently received significant research attention. Even though several adsorbents have been employed for effective management of chemicals, their limited microporous nature along with non-monolithic applicability has thwarted their large-scale real-time application. Herein, we developed a unique anion exchangeable hybrid composite aerogel material (IPcomp-6), integrating a stable cationic metal–organic polyhedron with a hierarchically porous metal–organic gel. The composite scavenger demonstrated a highly selective and very fast segregation efficiency for various hazardous oxoanions such as, HAsO_4^{2-} , SeO_4^{2-} , ReO_4^- , CrO_4^{2-} , MnO_4^- , in water, in the presence of 100-fold excess of other coexisting anions. The material was able to selectively eliminate trace HAsO_4^{2-} even at low concentration to well below the As^{V} limit in drinking water defined by WHO.

mand for clean water, coupled with the potential influence of these hazardous oxoanions in contaminated water, environmental remediation has attracted intense attention for sustainable life and has become a topical research interest in recent years.^[6,7] Both environment and human health concerns are driving efforts to develop various efficient technologies to disinfect and de-contaminate wastewater.^[8,9] Among them, adsorption followed by ion-exchange-based purification techniques are emerging, and are considered as promising over other conventional methods.^[10,11] Although several adsorbents have been devoted to remove waste from wastewater, the poor selectivity towards isolating trace toxic ions, in the presence of a high concentration of coexisting salts and slow removal kinetics limits the overall efficiency of the materials.^[12,13] Therefore, to address these issues, tremendous development of effective regenerable materials with substantially improved segregation properties has received special attention. That being said, pioneering endeavors have been employed to identify efficient adsorbents for the removal of specific oxoanions from contaminated water.^[14–16] However, as a long-term battle, improvement in terms of high selectivity, fast kinetics and capacities towards a group of toxic oxoanions at trace concentration, from natural groundwater sources to point-of-use are still needed for practical application, which is unexplored due to the lack of rational synthetic strategies.

In this regard, by virtue of predesigned tunable reticular structure, advanced porous materials have been recognized as promising platforms for various leading applications.^[17–19] Recently, composite materials are emerging as advantageous over individual materials, owing to their collective benefits and effective performance.^[20,21] Based on this view, hybrid composite materials have commanded research interest in recent years because of their unique and ingenious properties towards task-specific applications.^[22–24] Now, for host–guest hybrid composite material-based ideal adsorbents, the guest should be homogeneously distributed throughout the host matrix and decorated with functional groups that can strongly interact with the host matrix. In this context, discrete metal–organic polyhedra (MOP), a zero-dimensional crystalline material, constructed from predesigned organic linkers with a metal cluster, could be an ideal solution as a guest material and therefore attract interest in various applications, such as separation, catalysis, gas storage, sensing, biology, etc.^[25,26] However, most of the MOPs are found to be less chemically stable which limits their practical utility in aqueous or chemical

Introduction

In terms of significant impact, the World Economic Forum documented water crisis as the largest worldwide risk.^[1] Due to accelerating urbanization along with rapid industrialization, an ever growing number of toxic contaminants are entering the fresh water supplies.^[2–4] In the priority list, the Environment Protection Agency (EPA) listed metal-based oxoanions as potential toxic inorganic pollutants in wastewater.^[5] In response, considering the escalating de-

[*] S. Fajal, W. Mandal, S. Mollick, Y. D. More, S. Saurabh, S. K. Ghosh
Department of Chemistry, and Centre for Water Research,
Indian Institute of Science Education and Research
Dr. Homi Bhabha Road, Pashan, Pune 411008 (India)
E-mail: sghosh@iiserpune.ac.in
Homepage: <http://skg-lab.acads.iiserpune.ac.in>

A. Torris
Polymer Science and Engineering Division,
CSIR-National Chemical Laboratory
Dr. Homi Bhabha Road, Pune 411008 (India)

M. M. Shirolkar
Symbiosis Center for Nanoscience and Nanotechnology (SCNN),
Symbiosis International (Deemed University) (SIU)
Lavale, Pune 412115 (India)

Ultralight crystalline hybrid composite material for highly efficient sequestration of radioiodine

Received: 1 August 2023

Accepted: 29 January 2024

Published online: 10 February 2024

Check for updates

Sahel Fajal¹, Writakshi Mandal¹, Arun Torris², Dipanjan Majumder¹, Sumanta Let¹, Arunabha Sen¹, Fayis Kanheerampockil², Mandar M. Shirolkar^{3,4} & Sujit K. Ghosh^{1,5}✉

Considering the importance of sustainable nuclear energy, effective management of radioactive nuclear waste, such as sequestration of radioiodine has inflicted a significant research attention in recent years. Despite the fact that materials have been reported for the adsorption of iodine, development of effective adsorbent with significantly improved segregation properties for widespread practical applications still remain exceedingly difficult due to lack of proper design strategies. Herein, utilizing unique hybridization synthetic strategy, a composite crystalline aerogel material has been fabricated by covalent stepping of an amino-functionalized stable cationic discrete metal-organic polyhedra with dual-pore containing imine-functionalized covalent organic framework. The ultralight hybrid composite exhibits large surface area with hierarchical macro-micro porosity and multi-functional binding sites, which collectively interact with iodine. The developed nano-adsorbent demonstrate ultrahigh vapor and aqueous-phase iodine adsorption capacities of 9.98 g.g⁻¹ and 4.74 g.g⁻¹, respectively, in static conditions with fast adsorption kinetics, high retention efficiency, reusability and recovery.

The limitations associated with the spent nuclear fuel reprocessing and improper disposal of radionuclides wastes have thwarted the further sustainable development of nuclear energy^{1–5}. In nuclear plant, during reprocessing and in subsequent steps of spent nuclear fuel by dissolving in hot nitric acid solution, various highly toxic radionuclides are generated^{6,7}. Among them, volatile radioactive iodine isotopes (e.g., ¹²⁹I and ¹³¹I) has attracted significant attention from the environment and safety point of view, owing to its hazardous impact with radiological (longest half-life $t_{1/2} = 1.6 \times 10^7$ years), chemical (high-mobility) and biological (rapid bio-accumulation) toxicity^{8–10}. Moreover, water discharged from nuclear reactor chiller plants contain a significant amount of radioactive iodine, directly contaminating substantial

watery environments^{11–14}. Therefore, considering both the importance of sustainable future development of nuclear energy and water purification along with the practical relevance for essential medical uses, efficient and selective sequestration of radioactive iodine both from vapor and aqueous phase counts as a priority research topic^{15–17}.

To address this cardinal issue, recently, utilizing rational synthetic strategies, pioneering endeavors have been devoted to develop various excellent porous materials for the exceptional enrichment of iodine from contaminated samples^{17–31}. Nevertheless, most of the studies are still limited to the exploration of fast kinetics, high capacity, capture at high temperature and improved selectivity, which has actuated researchers to develop novel materials for the efficient

¹Department of Chemistry, Indian Institute of Science Education and Research (IISER) Pune, Dr. Homi Bhabha Road, Pashan, 411008 Pune, India. ²Polymer Science and Engineering Division, CSIR-National Chemical Laboratory, Dr. Homi Bhabha Road, Pune 411008, India. ³Advanced Bio-Agro Tech Pvt. Ltd, Baner, Pune 411045, India. ⁴Norel Nutrient Bio-Agro Tech Pvt. Ltd, Baner, Pune 411045, India. ⁵Centre for Water Research (CWR), Indian Institute of Science Education and Research (IISER) Pune, Dr. Homi Bhabha Road, Pashan, Pune 411008, India. ✉e-mail: sghosh@iiserpune.ac.in